

POLISH SOCIETY OF THEORETICAL AND APPLIED MECHANICS

**JOURNAL OF THEORETICAL
AND APPLIED MECHANICS**

No. 2 • Vol. 56

Quarterly

WARSAW, APRIL 2018

JOURNAL OF THEORETICAL AND APPLIED MECHANICS

(until 1997 Mechanika Teoretyczna i Stosowana, ISSN 0079-3701)

Beginning with Vol. 45, No. 1, 2007, *Journal of Theoretical and Applied Mechanics* (JTAM) has been selected for coverage in Thomson Reuters products and custom information services. Now it is indexed and abstracted in the following:

- **Science Citation Index Expanded** (also known as SciSearch®)
- **Journal Citation Reports/Science Edition**

Advisory Board

MICHAŁ KLEIBER (Poland) – Chairman

- JORGE A.C. AMBROSIO (Portugal) ★ ANGEL BALTOV (Bulgaria) ★ ROMESH C. BATRA (USA)
★ ALAIN COMBESCURE (France) ★ JÜRI ENGELBRECHT (Estonia) ★ WITOLD GUTKOWSKI (Poland)
★ JÓZEF KUBIK (Poland) ★ ZENON MRÓZ (Poland) ★ RYSZARD PARKITNY (Poland)
★ EKKEHARD RAMM (Germany) ★ EUGENIUSZ ŚWITOŃSKI (Poland) ★ HISAAKI TOBUSHI (Japan)
★ ANDRZEJ TYLIKOWSKI (Poland) ★ DIETER WEICHERT (Germany) ★ JOSE E. WESFREID (France)
★ JÓZEF WOJNAROWSKI (Poland) ★ JOSEPH ZARKA (France)
★ VLADIMIR ZEMAN (Czech Republic)

Editorial Board

Editor-in-Chief – **WŁODZIMIERZ KURNIK**

Section Editors: IWONA ADAMIEC-WÓJCIK, PIOTR CUPIAŁ, KRZYSZTOF DEMS,
WITOLD ELSNER, ELŻBIETA JARZĘBOWSKA, OLEKSANDR JEWTUSZENKO,
PIOTR KOWALCZYK, ZBIGNIEW KOWALEWSKI, TOMASZ KRZYŻYŃSKI, STANISŁAW KUKLA,
TOMASZ ŁODYGOWSKI, EWA MAJCHRZAK, WIESŁAW NAGÓRKO, JANUSZ NARKIEWICZ,
PIOTR PRZYBYŁOWICZ, BŁAŻEJ SKOCZEŃ, ANDRZEJ STYCZEK,
JACEK SZUMBARSKI, UTZ VON WAGNER (Germany), JERZY WARMIŃSKI

Language Editor – PIOTR PRZYBYŁOWICZ

Technical Editor – EWA KOISAR

Secretary – ELŻBIETA WILANOWSKA



Articles in JTAM are published under Creative Commons Attribution – Non-commercial 3.0. Unported License <http://creativecommons.org/licenses/by-nc/3.0/legalcode>. By submitting an article for publication, the authors consent to the grant of the said license.



The journal content is indexed in Similarity Check, the Crossref initiative to prevent plagiarism.

* * * * *

Editorial Office

Al. Armii Ludowej 16, room 650

00-637 Warszawa, Poland

phone (+48 22) 825 7180, (+48) 664 099 345, e-mail: biuro@ptmts.org.pl

www.ptmts.org.pl/jtam.html

* * * * *



Publication supported by Ministry of Science and Higher Education of Poland

(Journal of Theoretical and Applied Mechanics: 1) digitalizacja publikacji i monografii naukowych w celu zapewnienia i utrzymania otwartego dostępu do nich przez sieć Internet, 2) stworzenie anglojęzycznych wersji wydawanych publikacji, 3) wdrożenie procedur zabezpieczających oryginalność publikacji naukowych oraz zastosowane techniki zabezpieczeń – są finansowane ze środków Ministra Nauki i Szkolnictwa Wyższego przeznaczonych na działalność upowszechniającą naukę)

FROM THE EDITORS

This special issue of *JTAM* (Vol. 56/2018, No. 2) is entirely devoted to the Polish Society of Theoretical and Applied Mechanics (PSTAM), the Publisher of *JTAM*, on the occasion of its 60th anniversary.

PSTAM was established in 1958 as an initiative of eminent Polish mechanics at that time – Witold Nowacki, Waclaw Olszak, Jerzy Mutermilch, Sylwester Kaliski, Witold Wierzbicki and many other scientists having outstanding achievements and international recognition. The initiators referred to a long tradition of Polish Mechanics going back to the time of Adam Adamandy Kochanski (1631-1700) and then intensively developed in the 19th and 20th centuries by world-known scientists like Jan Nepomucen Franke (1846-1918), Feliks Jasiński (1856-1899), Marian Smoluchowski (1872-1917) and Maksymilian Tytus Huber (1872-1950). PSTAM was a new scientific organization in Poland that entered into relation with the International Union of Theoretical and Applied Mechanics (IUTAM) formed in 1949. Today PSTAM incorporates more than 1000 members and considerably contributes to the development of Mechanics and international scientific collaboration.

Exceptionally, this special issue includes invited papers only. Our invitations went to the scientists whom we know for their excellent research, conference activities and top-level earlier publications. It is an international group of authors. Part of them are members of the Editorial Board of *JTAM* who usually do not publish in our Journal. We would like to emphasize that all the invited papers have been reviewed within the standard editorial procedure of *JTAM*.

This special issue contains 16 articles reflecting research activities of the invited authors and their research teams. The papers comprise the following thematic areas:

- Thermo-elastic phenomena in continua,
- Instability and bifurcations in machinery,
- Mechanical properties of materials and structures,
- Numerical methods in mechanics,
- Solid-fluid interactions,
- Dynamic contact problems,
- Modelling and simulation of structures.

The topics being presented indicate problems in Mechanics that attract attention of scientists and are important for technological innovations and their applications in modern industry.

We would like to thank all the authors of the articles in this issue for accepting our invitation and contributing to the publishing output of *JTAM*.

The Publisher is grateful to the Ministry of Science and Higher Education of Poland for financial support aiming at increase of the scientific quality, impact and international reputation of our Journal.

Włodzimierz Kurnik
Editor-in-Chief of *JTAM*

Zbigniew Kowalewski
Chairman of PSTAM

FRACTIONAL HEAT CONDUCTION IN A SPHERE UNDER MATHEMATICAL AND PHYSICAL ROBIN CONDITIONS

STANISŁAW KUKLA, URSZULA SIEDLECKA

Czestochowa University of Technology, Institute of Mathematics, Czestochowa, Poland

e-mail: stanislaw.kukla@im.pcz.pl; urszula.siedlecka@im.pcz.pl

In this paper, the effect of a fractional order of time-derivatives occurring in fractional heat conduction models on the temperature distribution in a composite sphere is investigated. The research concerns heat conduction in a sphere consisting of a solid sphere and a spherical layer which are in perfect thermal contact. The solution of the problem with a classical Robin boundary condition and continuity conditions at the interface in an analytical form has been derived. The fractional heat conduction is governed by the heat conduction equation with the Caputo time-derivative, a Robin boundary condition and a heat flux continuity condition with the Riemann-Liouville derivative. The solution of the problem of non-local heat conduction by using the Laplace transform technique has been determined, and the temperature distribution in the sphere by using a method of numerical inversion of the Laplace transforms has been obtained.

Keywords: heat conduction, fractional heat equation, Robin boundary condition

1. Introduction

The classical heat conduction model based on the Fourier law has a non-physical property that the heat propagates with an infinite speed (Özişik, 1993). This property is a consequence of the dependence between the heat flux vector and the temperature gradient which is established by the Fourier law. This disadvantage does not appear when the non-local time dependence between the flux vector and the temperature gradient is assumed (Povstenko, 2014; Sur and Kanoria, 2014). This assumption leads to a differential equation and/or boundary conditions with derivatives of a non-integer order. The properties of fractional derivatives and different analytical methods to solve fractional differential equations are presented in (Atanacković *et al.*, 2014; Klimek, 2009; Leszczyński, 2011; Magin, 2006; Mainardi, 2010; Povstenko, 2015). Approximate numerical methods were applied to solving fractional initial-boundary problems in numerous papers, for example in (Błaszczyk and Ciesielski, 2017; Ciesielski and Błaszczyk, 2013; Dimitrov, 2014).

The heat conduction modelled by using the fractional order derivative is the subject of many papers. A mathematical model of one-dimensional heat conduction in a slab was proposed in paper (Žecová and Terpák, 2015). The Grünwald-Letnikov derivative with respect to a time variable was used. A solution to the problem of fractional heat conduction in a two-layered slab with the Caputo time-derivative in the heat conduction equation was presented in (Kukla and Siedlecka, 2015). Heat transfer for non-contacting face seals described by the time-fractional heat conduction equation in the cylindrical coordinate system was considered in (Błasiak, 2016). The fractional model of thermal energy transport in rigid bodies was derived in (Raslan, 2016). The effect of the order of the Marchand-type derivative in the heat transfer equation on the temperature distribution in a rigid conductor was numerically investigated. An application of the fractional order theory to a problem of thermal stress distribution in a spherical shell was

studied in (Zingales, 2014). In the paper by Atangana and Bildik (2013), the time fractional calculus was employed in the mathematical model of groundwater flow. Applications of fractional order systems to an ultracapacitor and beam heating problems were presented in (Dzieliński *et al.*, 2010). An application of fractional calculus in continuum mechanics to a problem of linear elasticity under small deformation was shown in (Sumelka and Blaszczyk, 2014). Some applications of the fractional calculus were also discussed in the papers (Abbas, 2012; Dalir and Bashour, 2010; Rahimy, 2010).

Solutions to time-fractional heat conduction problems in a spherical coordinate system are presented in many papers. In the paper by Ning and Jiang (2011), for the problem of fractional heat conduction in a sphere, the method of the Laplace transform and the variable separation were used. An analytical solution to the problem of the time-fractional radial heat conduction in a multilayered sphere under the Robin boundary condition was presented by Kukla and Siedlecka (2017). Fundamental solutions to the Cauchy problem and to the source problem of the heat conduction fractional equation in a spherical coordinate system in an analytical form were derived by article Povstenko and Klekot (2017).

The fractional heat conduction equation is complemented by initial and boundary conditions. Mathematical and physical formulations of the initial and boundary conditions can be considered in fractional heat conduction models (Povstenko, 2013). The mathematical formulations of Dirichlet, Neumann and Robin boundary conditions are the same as these in the classical theory of heat conduction. Also, the physical Dirichlet condition has the same form as the classical boundary condition of the first kind, while the physical Neumann and the physical Robin boundary conditions contain the fractional time-derivative. If two solids are in perfect thermal contact, the physical formulation of the condition of heat flux equality through the contact surface also contain the fractional time-derivative (Povstenko, 2013).

The solution to the problem of linear fractional heat conduction in a sphere under mathematical boundary conditions can be determined in an analytical form. However, in solving such problems of heat conduction under physical Neumann or Robin boundary conditions, an approximate methods must be used. Application of the Laplace transform method to a linear problem allows one to obtain a solution in the Laplace domain. For the fractional heat conduction problems under physical Neumann or Robin boundary conditions and physical continuity conditions, the inverse Laplace transform in an analytical form can not be determined. The solution to the problem is obtained by applying numerical inversion of the Laplace transform. The methods for numerical inversion of the Laplace transform, which are used in the classical problems, can be also applied to the Laplace transform obtained in fractional analysis. A review of the methods to numerical inversion of the Laplace transform was presented by Kuhlman (2013). An application of selected methods to determine the inverse Laplace transform in fractional calculus were presented in (Brzeziński and Ostalczyk, 2016; Sheng *et al.*, 2011). Modification of the method introduced by Gaver (1966) was presented in (Abate and Valkó, 2004; Valkó and Abate, 2004).

In this paper, the fractional heat conduction problem in a solid sphere under the mathematical and physical boundary condition is studied. The considered sphere consists of an inner sphere and a spherical layer. We assume perfect thermal contact of the inner sphere and the spherical layer which is modeled by mathematical or physical conditions. The exact solution of the problem for the mathematical boundary condition and the solution in the Laplace domain for the physical formulation of boundary and continuity conditions are presented. The effect of the order of the Riemman-Liouville derivative in the Robin physical condition and in the contact condition at the interface on the temperature distribution in the sphere has been numerically investigated.

2. Formulation of the problem

We consider the problem of heat conduction in a sphere which consists of a solid sphere occupying the region $0 \leq r \leq r_1$ and a spherical layer defined by $r_1 \leq r \leq b$, in the spherical coordinates system. The time-fractional heat conduction in the inner sphere ($i = 1$) and in the spherical layer ($i = 2$) is governed by the following equation

$$\frac{1}{r^2} \frac{\partial}{\partial r} \left(r^2 \frac{\partial T_i}{\partial r} \right) = \frac{1}{a_i} \frac{\partial^{\alpha_i} T_i}{\partial t^{\alpha_i}} \quad i = 1, 2 \tag{2.1}$$

where a_i is the thermal diffusivity, λ_i is the thermal conductivity and α_i denotes the fractional order of the left Caputo derivative with respect to time t . The Caputo derivative is defined by (Podlubny, 1999)

$${}_a^C D_t^\alpha f(t) = \frac{d^\alpha f(t)}{dt^\alpha} = \frac{1}{\Gamma(m - \alpha)} \int_a^t (t - \tau)^{m - \alpha - 1} \frac{d^m f(\tau)}{d\tau^m} d\tau \quad m - 1 < \alpha < m \tag{2.2}$$

We consider the case of $a = 0$ and $\alpha \in (0, 1]$. Note, that the thermal diffusivity coefficient can be interpreted as a measure of the distance on which the thermal front propagates in a medium at the given time. The thermal conductivity is a measure of the ability of the medium to transfer heat.

The condition at the centre of the sphere, the continuity conditions at the interface, the Robin boundary condition on the outer surface and the initial condition are (Povstenko, 2013a,b)

$$|T(0, t)| < \infty \quad T_1(r_1, t) = T_2(r_1, t) \tag{2.3}$$

$$\lambda_1 D_{RL}^{1-\beta_1} \frac{\partial T_1}{\partial r}(r_1, t) = \lambda_2 D_{RL}^{1-\beta_2} \frac{\partial T_2}{\partial r}(r_1, t) \tag{2.4}$$

$$\lambda_2 D_{RL}^{1-\beta_2} \frac{\partial T_2}{\partial r}(b, t) = a_\infty (T_\infty(t) - T_2(b, t))$$

$$T(r, 0) = F_i(r) \tag{2.5}$$

where a_∞ is the outer heat transfer coefficient and T_∞ is the ambient temperature. The left Riemann-Liouville fractional derivative $D_{RL}^{1-\beta}$ which occurs in equations (2.4) is defined by (Die-thelm, 2010)

$$D_{RL}^\beta f(t) = \frac{d}{dt} \left(\frac{1}{\Gamma(1 - \beta)} \int_0^t \frac{f(\tau)}{(t - \tau)^\beta} d\tau \right) \quad 0 < \beta \leq 1 \tag{2.6}$$

Conditions (2.4) for $\beta_1 = \alpha_1$ and $\beta_2 = \alpha_2$ for $\alpha_1, \alpha_2 \in (0, 1)$ are called the physical conditions (Rahimt, 2010; Raslan, 2016). If $\beta_1 = \beta_2 = 1$, the conditions are called the mathematical conditions. In this case, the D_{RL}^0 means an identity operator and can be omitted in equations (2.4).

3. Solution to the problem

The fractional heat conduction problem defined by equations (2.1) and (2.3)-(2.5) can be transformed to a new problem for functions $U_i(r, t)$ by using the formula

$$U_i(r, t) = r (T_i(r, t) - T_\infty(t)) \quad i = 1, 2 \tag{3.1}$$

Taking into account relationship (3.1) in equation (2.1) and conditions (2.3)-(2.5), we obtain a formulation of the initial-boundary problem in the form

$$a_i \frac{\partial^2 U_i(r, t)}{\partial r^2} = \frac{\partial^{\alpha_i} U_i(r, t)}{\partial t^{\alpha_i}} + r \frac{d^{\alpha_i} T_\infty(t)}{dt^{\alpha_i}} \quad i = 1, 2 \tag{3.2}$$

$$U_1(0, t) = 0 \quad U_1(r_1, t) = U_2(r_1, t) \tag{3.3}$$

$$\lambda_1 D_{RL}^{1-\beta_1} \left(\frac{\partial U_1(r_1, t)}{\partial r} - \frac{1}{r_1} U_1(r_1, t) \right) = \lambda_2 D_{RL}^{1-\beta_2} \left(\frac{\partial U_2(r_1, t)}{\partial r} - \frac{1}{r_1} U_2(r_1, t) \right) \tag{3.4}$$

$$\lambda_2 D_{RL}^{1-\beta_2} \left(\frac{\partial U_2(b, t)}{\partial r} - \frac{1}{b} U_2(b, t) \right) = -a_\infty U_2(b, t)$$

$$U_i(r, 0) = r (F_i(r) - T_\infty(0)) \quad i = 1, 2 \tag{3.5}$$

The solution to initial-boundary problem (3.2)-(3.5) for $\beta_1 = \beta_2 = 1$ (mathematical formulation) and for $\beta_1 = \alpha_1, \beta_2 = \alpha_2$ (physical formulation) will be presented below.

3.1. Mathematical conditions

An analytical solution to time-fractional heat conduction problem (3.2)-(3.5) under mathematical conditions (3.4) for $\alpha_1 = \alpha_2 = \alpha$ will be determined by using the method of separation of variables. As a result, we find a solution to the problem in the form of a series

$$U_i(r, t) = \sum_{k=1}^{\infty} \Lambda_k(t) \Phi_{i,k}(r) \quad i = 1, 2 \tag{3.6}$$

The functions $\Phi_{1,k}(r)$ and $\Phi_{2,k}(r)$ for $k = 1, 2, \dots$ are obtained as a solution to the corresponding eigenvalue problem

$$\frac{d^2 \Phi_{i,k}(r)}{dr^2} + \frac{\gamma_k^2}{a_i} \Phi_{i,k}(r) = 0 \quad i = 1, 2 \tag{3.7}$$

$$\Phi_{1,k}(0) = 0 \quad \Phi_{1,k}(r_1) = \Phi_{2,k}(r_1) \tag{3.8}$$

$$\lambda_1 \frac{d\Phi_1(r_1)}{dr} + \frac{1}{r_1} (\lambda_2 - \lambda_1) \Phi_1(r_1) = \lambda_2 \frac{d\Phi_2(r_1)}{dr} \quad \frac{d\Phi_2(b)}{dr} = \left(\frac{1}{b} - \frac{a_\infty}{\lambda_2} \right) \Phi_2(b) \tag{3.9}$$

The eigenfunctions $\Phi_{i,k}(r)$ are given by

$$\Phi_{1,k}(r) = B_{1,k} \sin \mu_{1,k} r \quad \Phi_{2,k}(r) = A_{2,k} \cos \mu_{2,k} (r - r_1) + B_{2,k} \sin \mu_{2,k} (r - r_1) \tag{3.10}$$

where $\mu_{i,k} = \gamma_k / \sqrt{a_i}$ and γ_k are the roots of the eigenvalue equation

$$M_1 \lambda_2 \mu_1 \sin \mu_1 r_1 + M_2 M_3 = 0 \tag{3.11}$$

where

$$M_1 = \left(\frac{a_\infty}{\lambda_2} - \frac{1}{b} \right) \cos \mu_2 (b - r_1) - \mu_2 \sin \mu_2 (b - r_1)$$

$$M_2 = \left(\frac{a_\infty}{\lambda_2} - \frac{1}{b} \right) \sin \mu_2 (b - r_1) + \mu_2 \cos \mu_2 (b - r_1)$$

$$M_3 = \lambda_1 \mu_1 \cos \mu_1 r_1 + \frac{\lambda_2 - \lambda_1}{r_1} \sin \mu_1 r_1$$

The coefficients $B_{1,k}, A_{2,k}$ and $B_{2,k}$ are determined by using continuity and boundary conditions (3.8) and (3.9). Assuming $B_{1,k} = 1$, we obtain $A_{2,k} = \sin \mu_{1,k} r_1$ and $B_{2,k} = M_3 / \lambda_2 \mu_{2,k}$.

The function $\Lambda_k(t)$, occurring in equation (3.6), is a solution to the fractional initial problem which is obtained by using the orthogonality condition in the form

$$\frac{\lambda_1}{a_1} \int_0^{r_1} \Phi_{1,k}(r)\Phi_{1,k'}(r) dr + \frac{\lambda_2}{a_2} \int_{r_1}^b \Phi_{2,k}(r)\Phi_{2,k'}(r) dr = \begin{cases} 0 & \text{for } k' \neq k \\ N_k & \text{for } k' = k \end{cases} \tag{3.12}$$

Assuming $F_i(r) = T_{init} = \text{const}$ for $i = 1, 2$ and condition (3.12) in equation (3.2) and (3.5), the initial problem is obtained

$$\begin{aligned} \frac{d^\alpha \Lambda_k(t)}{dt^\alpha} + \gamma_k^2 \Lambda_k(t) &= 0 \\ \Lambda_k(0) &= \frac{T_{init} - T_\infty}{N_k^r} \left(\frac{\lambda_1}{a_1} \int_0^{r_1} r \Phi_{1,k}(r) dr + \frac{\lambda_2}{a_2} \int_{r_1}^b r \Phi_{2,k}(r) dr \right) \end{aligned} \tag{3.13}$$

A solution to problem (3.13) is given by (Diethelm, 2010)

$$\Lambda_k(t) = \frac{T_{init} - T_\infty}{N_k^r} E_\alpha(-\gamma_k^2 t^\alpha) \left(\frac{\lambda_1}{a_1} \int_0^{r_1} r \Phi_{1,k}(r) dr + \frac{\lambda_2}{a_2} \int_{r_1}^b r \Phi_{2,k}(r) dr \right) \tag{3.14}$$

where $E_\alpha(z)$ is the Mittag-Leffler function (Kilbas *et al.*, 2006)

$$E_\alpha(z) = \sum_{k=0}^{\infty} \frac{z^k}{\Gamma(\alpha k + 1)} \tag{3.15}$$

Finally, the functions $T_i(r, t)$ are given by equations (3.1), (3.6), (3.10) and (3.14). Assuming that the following conditions are fulfilled: $a_1 = a_2 = a$, $\lambda_1 = \lambda_2 = \lambda$, $\alpha_1 = \alpha_2 = \alpha$ and $\beta_1 = \beta_2 = 1$, we obtain the temperature $T(r, t)$ in the homogeneous sphere

$$T(r, t) = T_\infty + \frac{4(T_{init} - T_\infty)}{r} \sum_{k=1}^{\infty} \frac{b\mu_k \cos b\mu_k - \sin b\mu_k}{\mu_k(\sin 2b\mu_k - 2b\mu_k)} E_\alpha(-\gamma_k^2 t^\alpha) \sin \mu_k r \tag{3.16}$$

In this case, $\mu_k = \gamma_k/\sqrt{a}$ and γ_k are the roots of the equation

$$\left(1 - \frac{ba_\infty}{\lambda}\right) \sin b\mu - b\mu \cos b\mu = 0 \tag{3.17}$$

3.2. Physical conditions

We obtain a solution to problem (3.2)-(3.5) under physical boundary and continuity conditions ($\beta_1 = \alpha_1$, $\beta_2 = \alpha_2$ in equations (3.4) and (3.5)) by using the Laplace transform method. The Laplace transform $\bar{f}(s)$ of a function $f(t)$ is defined by

$$\bar{f}(s) = \int_0^{\infty} f(t)e^{-st} dt \tag{3.18}$$

where s is a complex parameter. Using the properties of the Laplace transform, equations (3.2)-(3.4) can be rewritten in the Laplace domain as

$$\frac{d^2 \bar{U}_i}{dr^2} - \frac{s^{\alpha_i}}{a_i} \bar{U}_i(r, s) = \frac{rs^{\alpha_i}}{a_i} \left(\bar{T}_\infty(s) - \frac{F_i(r)}{s} \right) \tag{3.19}$$

$$\bar{U}_1(0, s) = 0 \quad \bar{U}_1(r_1, s) = \bar{U}_2(r_1, s) \tag{3.20}$$

$$\begin{aligned} \lambda_1 s^{1-\alpha_1} \left(\frac{d\bar{U}_1(r_1, s)}{dr} - \frac{1}{r_1} \bar{U}_1(r_1, s) \right) &= \lambda_2 s^{1-\alpha_2} \left(\frac{d\bar{U}_2(r_1, s)}{dr} - \frac{1}{r_1} \bar{U}_2(r_1, s) \right) \\ \lambda_2 s^{1-\alpha_2} \left(\frac{d\bar{U}_2(b, s)}{dr} - \frac{1}{b} \bar{U}_2(b, s) \right) &= -a_\infty \bar{U}_2(b, s) \end{aligned} \quad (3.21)$$

The general solution to equation (3.19) for $i = 1, 2$ has the form

$$\begin{aligned} \bar{U}_1(r, s) &= B_1 \sinh S_1 r + \frac{1}{S_1} \int_0^r P_1(u) \sinh S_1(r-u) du \\ \bar{U}_2(r, s) &= A_2 \cosh S_2(r-r_1) + B_2 \sinh S_2(r-r_1) + \frac{1}{S_2} \int_{r_1}^r P_2(u) \sinh S_2(r-u) du \end{aligned} \quad (3.22)$$

where

$$S_i = \frac{s^{\alpha_i/2}}{\sqrt{a_i}} \quad P_i(r) = \frac{r s^{\alpha_i}}{a_i} \left(\bar{T}_\infty(s) - \frac{F_i(r)}{s} \right)$$

The constants B_1 , A_2 and B_2 are determined by using conditions (3.20)₂ and (3.21). After some transformations, the functions $\bar{U}_1(r, s)$ and $\bar{U}_2(r, s)$ can be written as

$$\bar{U}_1(r, s) = \tilde{B}_1 \sinh S_1 r \quad \bar{U}_2(r, s) = \tilde{A}_2 \cosh S_2(r-r_1) + \tilde{B}_2 \sinh S_2(r-r_1) \quad (3.23)$$

where

$$\begin{aligned} \tilde{B}_1 &= -s^{\alpha_1-2} \frac{a_\infty}{\lambda_1 d} S_2 b^2 & \tilde{A}_2 &= -s^{\alpha_1-2} \frac{a_\infty b}{\lambda_1 d} S_2 b \sinh S_1 r_1 \\ \tilde{B}_2 &= s^{\alpha_2-2} \frac{b}{r_1} \frac{a_\infty b}{\lambda_2 d} \left[\left(1 - s^{\alpha_1-\alpha_2} \frac{\lambda_2}{\lambda_1} \right) \sinh S_1 r_1 - S_1 r_1 \cosh S_1 r_1 \right] \\ d &= s^{\alpha_1-\alpha_2} \frac{\lambda_2}{\lambda_1} S_2 r_1 \sinh S_1 r_1 [w \cosh S_2(b-r_1) + S_2 b \sinh S_2(b-r_1)] \\ &\quad + \left[S_1 r_1 \cosh S_1 r_1 - \left(1 - s^{\alpha_1-\alpha_2} \frac{\lambda_2}{\lambda_1} \right) \sinh S_1 r_1 \right] [S_2 b \cosh S_2(b-r_1) + w \sinh S_2(b-r_1)] \\ w &= \frac{a_\infty b}{\lambda_2 s^{1-\alpha_2}} - 1 \end{aligned}$$

Assuming $F_i(r) = T_{init} = \text{const}$ for $i = 1, 2$, the temperature distribution in the sphere is given by

$$T_i(r, t) = T_\infty + (T_{init} - T_\infty) \frac{r_1}{r} L^{-1}[\bar{U}_i(r, s)] \quad (3.24)$$

For the homogeneous sphere, the following conditions are fulfilled $a_1 = a_2 = a$, $\lambda_1 = \lambda_2 = \lambda$, $\alpha_1 = \alpha_2 = \alpha$, $\beta_1 = \beta_2 = \beta$ and $S_1 = S_2 = S$. In this case, the function $T_i(r, t) = T(r, t)$ has the form

$$T(r, t) = T_\infty + (T_{init} - T_\infty) \frac{b}{r} L^{-1}[\bar{U}(r, s)] \quad (3.25)$$

where

$$\bar{U}(r, s) = -\frac{1+w}{s(Sb \cosh Sb + w \sinh Sb)} \sinh Sr$$

The inverse of the Laplace transform of the functions $\bar{U}_1(r, s)$ and $\bar{U}_2(r, s)$ are numerically determined. The calculation has been performed by the Gaver method using the sequence of

functionals presented in Gaver (1966) and Valkó and Abate (2004). Applying this method, the approximate values of the original function $U_i(r, t) = L^{-1}[\bar{U}_i(r, s)]$ are determined using the formula

$$U_i(r, t) \simeq n\tau \binom{2n}{n} \sum_{i=0}^n (-1)^i \binom{n}{i} \bar{U}_i(r, (n+i)\tau) \tag{3.26}$$

where $\tau = (\ln 2)/t$ and n is a fixed positive integer number.

The functions $T_i(r, t)$ and $T(r, t)$ obtained for the mathematical and physical conditions will serve for investigation of the influence of the orders of the Caputo and Riemann-Liouville derivatives occurring in the heat conduction models on the temperature distribution in the sphere.

4. Results of numerical calculations

The effect of the order of the fractional derivative in the heat conduction equation on the temperature distribution in the sphere has been numerically investigated. The results for the mathematical boundary condition obtained by using numerical inversion of the Laplace transforms has been compared with the exact solution. The computations were performed for the homogeneous sphere (Sphere A) and for the sphere consisting of a solid sphere and a spherical layer (Sphere B). The radius of both Spheres was $b = 1.0$ m and the interface in Sphere B was at $\hat{r}_1 = r_1/b = 0.9$. The thermal diffusivity $a = 3.352 \cdot 10^{-6} \text{ m}^2/\text{s}^\alpha$ and the thermal conductivity $\lambda = 16 \text{ W}/(\text{m}\cdot\text{K})$ were assumed for Sphere A. The thermal diffusivities $a_1 = 2.3 \cdot 10^{-5} \text{ m}^2/\text{s}^\alpha$, $a_2 = 3.352 \cdot 10^{-6} \text{ m}^2/\text{s}^\alpha$ and the thermal conductivities $\lambda_1 = 80 \text{ W}/(\text{m}\cdot\text{K})$, $\lambda_2 = 16 \text{ W}/(\text{m}\cdot\text{K})$ were assumed for Sphere B. Subscript 1 was used for the inner sphere and subscript 2 – for the spherical layer of Sphere B. For both Spheres, the outer heat transfer coefficient was $a_\infty = 200 \text{ W}/(\text{m}^2\cdot\text{K})$, the ambient temperature was $T_\infty = 100^\circ\text{C}$ and the initial temperature was assumed as $T_{init} = 25^\circ\text{C}$.

In Table 1, the non-dimensional temperature $\hat{T} = T/T_{init}$ in Sphere A for different orders of the Caputo derivative α at the reference time $\hat{t} = tb^2/a = 1.0$ is presented. The calculation has been performed for the mathematical Robin boundary condition, i.e. for $\beta = 1.0$. The results were obtained by using the exact solution, Eq. (3.16), and by the Gaver method of numerical inversion of the Laplace transforms, Eq. (3.26), and using relationship (3.1). A similar comparison of numerically obtained non-dimensional temperatures have been performed for Sphere B. The results are presented in Table 2. The relative error evaluated on the basis of the results given in Tables 1 and 2 fulfils the condition: $|Exact - NILT|/Exact < 3.6 \cdot 10^{-5}$. The good accordance of the results obtained for mathematical formulation of the boundary and continuity condition allows one to use the NILT method to the heat conduction problem under physical formulation of the boundary and continuity condition.

Table 1. Non-dimensional temperature $\hat{T}(\hat{r}, \hat{t})$ for $\hat{t} = 1.0$, computed by using the exact solution and by using numerical inversion of the Laplace transform (NILT) for Sphere A

\hat{r}	$\alpha = 0.8$		$\alpha = 0.9$		$\alpha = 1.0$	
	Exact	NILT	Exact	NILT	Exact	NILT
0	1.12416	1.12412	2.41882	2.41882	3.91149	3.91145
0.25	1.19635	1.19634	2.52818	2.52818	3.91902	3.91900
0.50	1.49058	1.49058	2.84104	2.84103	3.93932	3.93932
0.75	2.21186	2.21186	3.30678	3.30678	3.96637	3.96629
1.00	3.50777	3.50776	3.83398	3.83398	3.99254	3.99251

Table 2. Non-dimensional temperature $\widehat{T}(\widehat{r}, \widehat{t})$ for $\widehat{t} = 1.0$, computed by using the exact solution and by using numerical inversion of the Laplace transform (NILT) for Sphere B

\widehat{r}	$\alpha = 0.8$		$\alpha = 0.9$		$\alpha = 1.0$	
	Exact	NILT	Exact	NILT	Exact	NILT
0	2.35412	2.35407	3.66988	3.66988	3.99982	3.99969
0.25	2.39527	2.39526	3.67879	3.67880	3.99983	3.99969
0.50	2.51791	2.51791	3.70498	3.70498	3.99984	3.99971
0.75	2.71870	2.71870	3.74679	3.74679	3.99987	3.99974
1.00	3.48174	3.48172	3.89885	3.89885	3.99995	3.99988

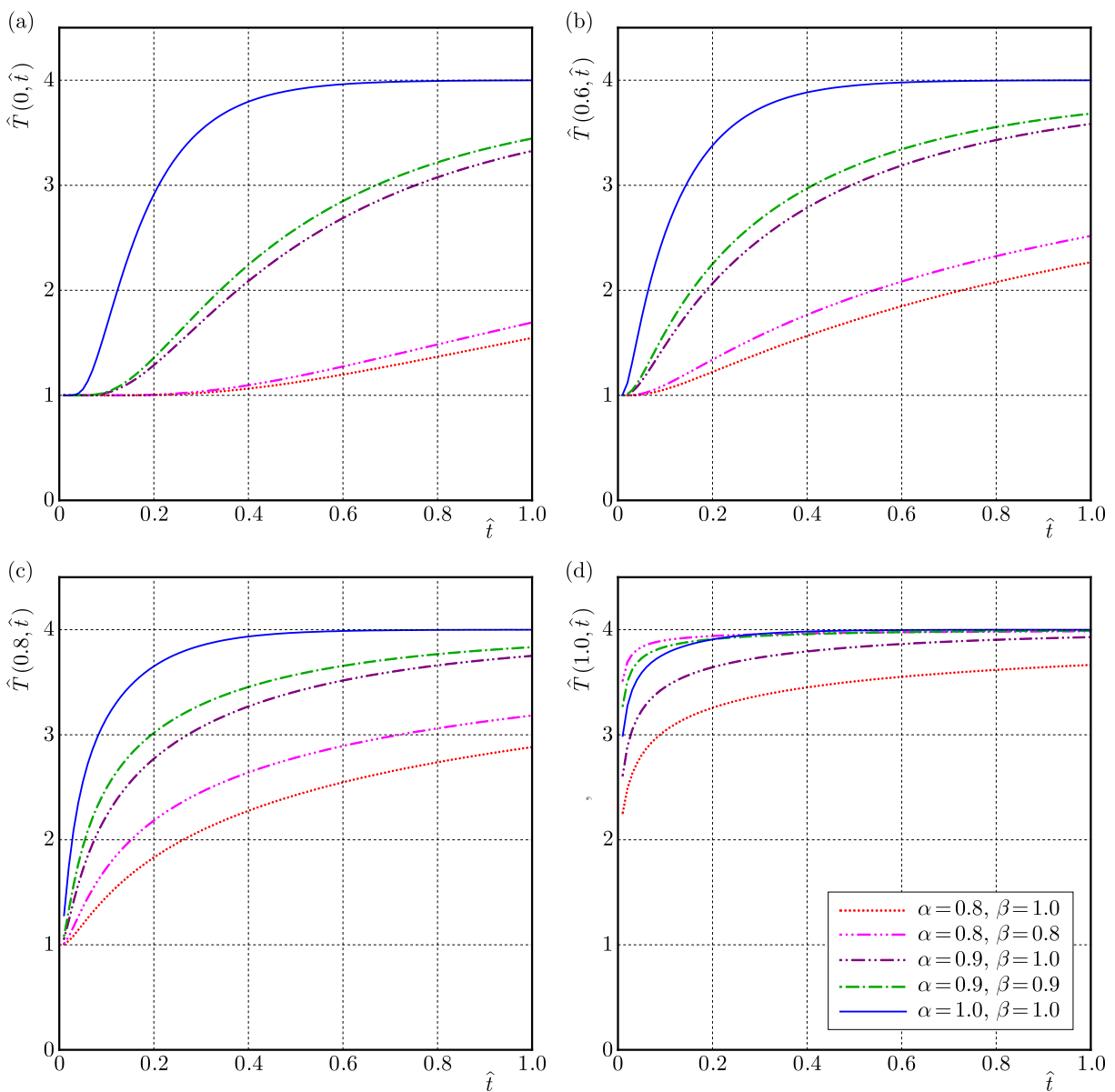


Fig. 1. Non-dimensional temperature $\widehat{T}(\widehat{r}, \widehat{t})$ as a function of time \widehat{t} in Sphere A for various values of fractional derivatives α and β : (a) $\widehat{r} = 0$, (b) $\widehat{r} = 0.6$, (c) $\widehat{r} = 0.8$, (d) $\widehat{r} = 1.0$

The non-dimensional temperatures \hat{T} as functions of the time \hat{t} for various radial coordinates are presented in Fig. 1. The pairs of curves obtained for mathematical and physical formulations of the Robin condition show the effect of the order of the Riemann-Liouville derivative occurring in the physical boundary condition on the temperature in the sphere. Significant differences can be observed in the temperatures obtained for the classical heat conduction model ($\alpha = \beta = 1$) and fractional models ($\alpha = 0.8$ and $\alpha = 0.9$), particularly in the inner points of the sphere.

The curves presented in Fig. 2 represent the non-dimensional temperatures \hat{T} as functions of the reference time \hat{t} for Sphere B. In numerical calculations with the mathematical conditions (MC) the following values have been assumed $\alpha_1 = \alpha_2 = \alpha = 0.8, 0.9, 1.0$ and $\beta_1 = \beta_2 = 1.0$. The numerical calculations to the problem with the physical conditions (PC) have been carried out for: $\alpha_1 = \beta_1 = 0.9, \alpha_2 = \alpha = 0.8, 0.9, 1.0$ and $\beta_2 = \beta = \alpha_2$. A higher temperature is observed for the heat conduction with the physical boundary and continuity conditions than in the model with the mathematical formulation of these conditions. A significant effect on the temperature distribution in the sphere has the order of the Caputo derivative in the heat conduction model.

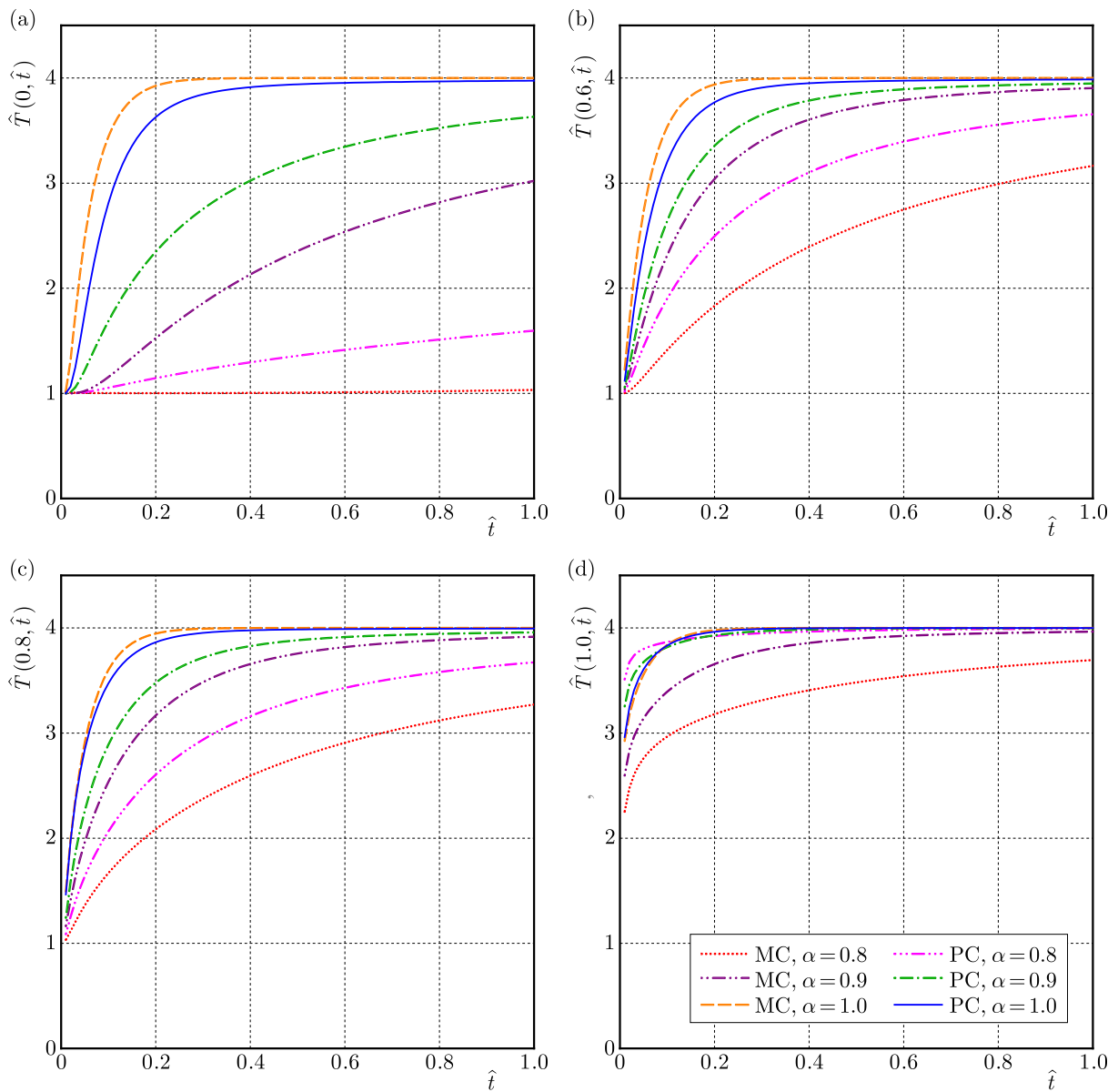


Fig. 2. Non-dimensional temperature $\hat{T}(\hat{r}, \hat{t})$ as a function of the time \hat{t} in Sphere B for various values of fractional derivatives α and β : (a) $\hat{r} = 0$, (b) $\hat{r} = 0.6$, (c) $\hat{r} = 0.8$, (d) $\hat{r} = 1.0$

5. Conclusions

A solution to the problem of fractional heat conduction in a homogeneous sphere and a composite sphere consisting with a solid sphere and a spherical layer has been presented. The mathematical and physical formulations of the Robin boundary condition and the continuity conditions at the interface have been considered. The temperature distribution in the sphere, under the physical boundary and continuity conditions, has been obtained by using the Laplace transform technique. Numerical results show a significant effect of the order of the Caputo derivative occurring in the heat conduction equation on the time-history of temperature in the sphere. The order of the Riemann-Liouville derivative occurring in the boundary and continuity conditions of the fractional model of heat conduction has a smaller effect on the time-history of temperature in the sphere than the order of the fractional Caputo derivative in the heat conduction equation.

References

1. ABATE J., VALKÓ P.P., 2004, Multi-precision Laplace transform inversion, *International Journal for Numerical Methods in Engineering*, **60**, 979-993
2. ABBAS I.A., 2012, On a thermoelastic fractional order model, *Journal of Physics*, **1**, 2, 24-30
3. ATANACKOVIĆ T.M., PILIPOVIĆ S., STANKOVIĆ B., ZORICA D., 2014, *Fractional Calculus with Applications in Mechanics*, John Wiley & Sons, New York
4. ATANGANA A., BILDIK N., 2013, The use of fractional order derivative to predict the groundwater flow, *Mathematical Problems in Engineering*, Article ID 543026
5. BLASIAK S., 2016, Time-fractional heat transfer equations in modeling of the non-contacting face seals, *International Journal of Heat and Mass Transfer*, **100**, 79-88
6. BŁASZCZYK T., CIESIELSKI M., 2017, Numerical solution of Euler-Lagrange equation with Caputo derivatives, *Advances in Applied Mathematics and Mechanics*, **9**, 173-185
7. BRZEZIŃSKI D.W., OSTALCZYK P., 2016, Numerical calculations accuracy comparison of the inverse Laplace transform algorithms for solution of fractional order differential equations, *Nonlinear Dynamics*, **84**, 1, 65-77
8. CIESIELSKI M., BŁASZCZYK T., 2013, An approximation of the analytical solution of the fractional Euler-Lagrange equation, *Journal of Applied Mathematics and Computational Mechanics*, **12**, 4, 23-30
9. DALIR M., BASHOUR M., 2010, Applications of fractional calculus, *Applied Mathematical Sciences*, **4**, 21, 1021-1032
10. DIETHELM K., 2010, *The Analysis of Fractional Differential Equations*, Springer-Verlag Berlin Heidelberg
11. DIMITROV Y., 2014, Numerical approximations for fractional differential equations, *Journal of Fractional Calculus and Applications*, **5**, 38, 1-45
12. DZIELIŃSKI A., SIEROCIUK D., SARWAS G., 2010, Some applications of fractional order calculus, *Bulletin of the Polish Academy of Sciences – Technical Sciences*, **58**, 4, 583-592
13. GAVER D.P. JR., 1966, Observing stochastic processes and approximate transform inversion, *Operational Research*, **14**, 444-459
14. KILBAS A., SRIVASTAVA H., TRUJILLO J., 2006, *Theory and Applications of Fractional Differential Equations*, Elsevier, Amsterdam
15. KLIMEK M., 2009, *On Solutions of Linear Fractional Differential Equations of a Variational Type*, The Publishing Office of Czestochowa University of Technology, Czestochowa

16. KUHLMAN K.L., 2013, Review of inverse Laplace transform algorithms for Laplace-space numerical approaches, *Numerical Algorithms*, **63**, 2, 339-355
17. KUKLA S., SIEDLECKA U., 2015, Laplace transform solution of the problem of time-fractional heat conduction in a two-layered slab, *Journal of Applied Mathematics and Computational Mechanics*, **14**, 4, 105-113
18. KUKLA S., SIEDLECKA U., 2017, An analytical solution to the problem of time-fractional heat conduction in a composite sphere, *Bulletin of the Polish Academy of Sciences – Technical Sciences*, **65**, 2, 179-186
19. LESZCZYŃSKI J.S., 2011, *An Introduction to Fractional Mechanics*, The Publishing Office of Czestochowa University of Technology, Czestochowa
20. MAGIN R.L., 2006, *Fractional Calculus in Bioengineering*, Begell House Publishers, Connecticut
21. MAINARDI F., 2010, *Fractional Calculus and Waves in Linear Viscoelasticity: an Introduction to Mathematical Models*, Imperial College Press, London
22. NING T. H., JIANG X. Y., 2011, Analytical solution for the time-fractional heat conduction equation in spherical coordinate system by the method of variable separation, *Acta Mechanica Sinica*, **27**, 6, 994-1000
23. ÖZİŞİK M.N., 1993, *Heat Conduction*, Wiley, New York
24. PODLUBNY I., 1999, *Fractional Differential Equations*, Academic Press, San Diego
25. POVSTENKO Y., 2013a, Fractional heat conduction in an infinite medium with a spherical inclusion, *Entropy*, **15**, 4122-4133
26. POVSTENKO Y., 2013b, Time-fractional heat conduction in an infinite medium with a spherical hole under Robin boundary condition, *Fractional Calculus and Applied Analysis*, **16**, 2, 354-369
27. POVSTENKO Y., 2014, Fractional heat conduction in a semi-infinite composite body, *Communications in Applied and Industrial Mathematics*, **6**, 1, e-482
28. POVSTENKO Y., 2015, *Linear Fractional Diffusion-Wave Equation for Scientists and Engineers*, Birkhäuser, New York
29. POVSTENKO Y., KLEKOT J., 2017, The fundamental solutions to the central symmetric time-fractional heat conduction equation with heat absorption, *Journal of Applied Mathematics and Computational Mechanics*, **16**, 2, 101-112
30. RAHIMY M., 2010, Applications of fractional differential equations, *Applied Mathematical Sciences*, **4**, 50, 2453-2461
31. RASLAN W.E., 2016, Application of fractional order theory of thermoelasticity to a 1D problem for a spherical shell, *Journal of Theoretical and Applied Mechanics*, **54**, 1, 295-304
32. SHENG H., LI Y., CHEN Y., 2011, Application of numerical inverse Laplace transform algorithms in fractional calculus, *Journal of the Franklin Institute*, **384**, 315-330
33. SUMELKA W., BLASZCZYK T., 2014, Fractional continua for linear elasticity, *Archives of Mechanics*, **66**, 3, 147-172
34. SUR A., KANORIA M., 2014, Fractional heat conduction with finite wave speed in a thermo-viscoelastic spherical shell, *Latin American Journal of Solids and Structures*, **11**, 1132-1162
35. VALKÓ P.P., ABATE J., 2004, Comparison of sequence accelerators for the Gaver method of numerical Laplace transform inversion, *Computers and Mathematics with Applications*, **48**, 629-636
36. ŽECOVÁ M., TERPÁK J., 2015, Heat conduction modeling by using fractional-order derivatives, *Applied Mathematics and Computation*, **257**, 365-373
37. ZINGALES M., 2014, Fractional-order theory of heat transport in rigid bodies, *Communications in Nonlinear Science and Numerical Simulation*, **19**, 3938-3953

THEORETICAL AND EXPERIMENTAL INVESTIGATIONS OF THE BIFURCATION BEHAVIOR OF CREEP GROAN OF AUTOMOTIVE DISK BRAKES

XINGWEI ZHAO, NILS GRÄBNER, UTZ VON WAGNER

Technische Universität Berlin, Chair of Mechatronics and Machine Dynamics (MMD), Berlin, Germany

e-mail: utz.vonwagner@tu-berlin.de

There are several low frequency vibration phenomena which can be observed in automotive disk brakes. Creep groan is one of them provoking noise and structural vibrations of the car. In contrast to other vibration phenomena like brake squeal, creep groan is caused by the stick-slip-effect. A fundamental investigation of creep groan is proposed in this paper theoretically and experimentally with respect to parameter regions of the occurrence. Creep groan limit cycles are observed while performing experiments in a test rig with an idealized brake. A nonlinear model using the bristle friction law is set up in order to simulate the limit cycle of creep groan. As a result, the system shows three regions of qualitatively different behavior depending on the brake pressure and driving speed, i.e. a region with a stable equilibrium solution and a stable limit cycle, a region with only a stable equilibrium solution, and a region with only a stable limit cycle. The limit cycle can be interpreted as creep groan while the equilibrium solution is the desired vibration-free case. These three regions and the bifurcation behavior are demonstrated by the corresponding map. The experimental results are analyzed and compared with the simulation results showing good agreement. The bifurcation behavior and the corresponding map with three different regions are also confirmed by the experimental results. At the end, a similar map with the three regions is also measured at a test rig with a complete real brake.

Keywords: creep groan, stick-slip limit cycle, equilibrium solution, bifurcation

1. Introduction

Creep groan is a low frequency vibration phenomenon in automotive disk brakes occurring in particular, when the brake is slowly released while the car starts moving (Abdelhamid, 1995; Abdelhamid and Bray, 2009; Zhao *et al.*, 2016, 2017; Brecht *et al.*, 1997; Brecht, 2000; Crowther and Singh, 2007, 2008). The frequency range is up to 500 Hz and it is caused by the stick-slip-effect. Like other brake noise problems, such as brake squeal (Cantoni *et al.*, 2009; von Wagner *et al.*, 2007), creep groan is mainly a comfort problem resulting in possible warranty claims and additional costs for the manufacturer.

The simplest usual way to describe the stick-slip-effect is to use Coulomb's friction law. A general study on friction induced vibrations has been performed by Ibrahim giving also an overview about contact mechanics and friction forces (Ibrahim, 1994a,b). With respect to creep groan, Brecht *et al.* (1997) and Brecht (2000) measured its vibration characteristics and studied the corresponding stick-slip limit cycle. Crowther and Singh (2007, 2008) modeled the creep groan phenomenon in terms of two dynamic sub-systems coupled with Coulomb's friction law. Vadari and Jackson (1999) considered the relationship of creep groan to vehicle dynamics by looking at the suspension response. A more complex nonlinear model with 7 degree-of-freedom (DOF) with Coulomb's friction law was utilized for studying the mechanism of creep groan by Wu and Jin (2014).

However, the models using Coulomb's friction law cannot explain all effects occurring during creep groan. In order to overcome this deficiency, Hetzler *et al.* (2007) presented an analytical investigation on stability and bifurcation behavior of stick-slip motions, where a friction coefficient depended on the relative velocity between the two contact partners.

Since friction induced vibrations are naturally highly related to the frictional contact, some works are concentrating on studying the characteristics of the involved pad materials. A study performed by Jang *et al.* (2001) on the creep groan propensity of different friction materials resulted in the conclusion that creep groan can be reduced when the friction material contains a small difference between the static and dynamic friction coefficients. Similar results can be obtained when considering elementary friction oscillators. Fuadi *et al.* (2009, 2010) studied creep groan by considering a caliper-slider experimental model, and derived a map showing necessary conditions for avoiding creep groan. Results of creep groan vehicle tests were shown by Neis *et al.* (2016) and their relation with stick-slip in laboratory tests was investigated. However, most of those works were experimental investigations, and a model showing high agreement with experimental results is still to be developed.

The present paper extends the prior work of the same authors (Zhao *et al.*, 2016, 2017) performing the fundamental work with minimal models for creep groan using the bristle friction law. Creep groan is first measured in a test rig with an idealized brake, which is in most parts similar to a real brake system but with less hard-to-model components. After that, creep groan is studied fundamentally through (compared to Zhao *et al.*, 2016, 2017) an extended minimal model using also the bristle friction law. The bristle friction law proposed by De Wit *et al.* (1995) and Johanaström and De Wit (2008) includes the Stribeck effect, hysteresis and spring-like characteristics for stick. By analyzing the bifurcation behavior of the resulting nonlinear model, three regions of qualitatively different behavior depending on the parameters can be identified. The main focus of this paper is to describe the detailed bifurcation behavior and the corresponding map with three different regions according to the occurrence and absence of creep groan, while experiments testified the existence of them in the test rig with the idealized brake. Furthermore, a similar map is also measured from the test rig with a real brake.

2. Test rig with an idealized brake

For the experimental investigation of creep groan, a test rig with an idealized brake has been designed and assembled at MMD TU Berlin. This set-up (Fig. 1) imitates the brake system of an automotive vehicle. The intention of the design was to concentrate on the pad-disk friction contact and to avoid other hard-to-model parts. In the real brake, there are additional hard-to-model parts, such as complicated structure of the carrier and its coupling with the caliper via bushings. These parts may also have an influence on the creep groan behavior but are considered to have minor influence compared to the frictional contact between the pad and the disk. Therefore, a carrier consisting of two L-shaped steel plates with high stiffness in the in-plane direction (but comparable order of stiffness similar to the real brake carrier) and low stiffness in the out-of-plane direction replaces the real brake carrier. The pads (from a serial brake) are fixed on the long legs of the carrier while its short legs are fixed to the base plate. A caliper from the same serial brake is attached to the long legs of the carrier providing the pressure force. The disk is driven by an AC motor coupled with a reduction gearbox, which can provide a low revolution speed (starting from 0.1 rad/s i.e. approximately 0.12 km/h) with a high torque. A drive shaft connects the gear box and the brake disk. This set-up is almost similar with a real brake system, since the pads, the disk, the drive shaft and the caliper of the test rig are taken from a real vehicle. Moreover, the set-up has advantages for the experimental investigation of creep groan, such as: 1. The set-up has a simple structure of the components and, therefore, its

parameters are easy to identify; 2. The set-up is easy to assemble with different types of sensors since the disk is directly driven by the shaft. In contrast to this, in industrial dynos, the disk is usually driven via wheel bolts, which complicates accessibility to the brake for measurements.

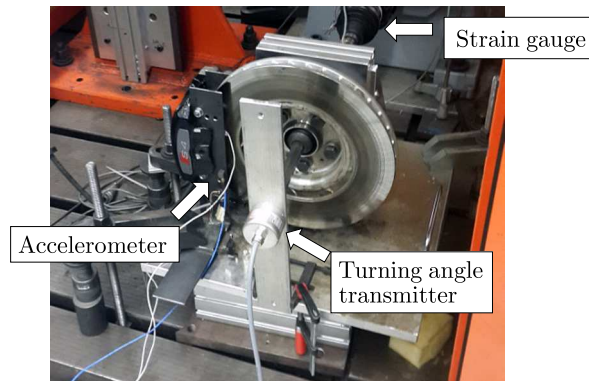


Fig. 1. Test rig with an idealized brake at MMD TU Berlin

The following sensors have been assembled to the set-up. A strain sensor is placed on the drive shaft measuring its torsional angle. It is calibrated through a static measurement (Muschalle, 2015). A turning angle transmitter (power supply 5 V DC, maximum sample rate 40 kHz, resolution 14 bit) is connected to the disk which allows for the measurement of the absolute angle and angular velocity of the disk. The pressure of the brake can be read from a pressure meter. An accelerometer (PCB 4507 ICP accelerometers, frequency range 0.3 Hz-6 kHz, sensitivity 101.2 mV/g) is attached to the long leg of the carrier, which measures the acceleration of the pad in the vertical direction. The measured signals are conditioned and subsequently driven into a data acquisition module (featuring eight 24-bit simultaneously sampled A/D channels, maximum sample rate 80 kHz, and analogue anti-aliasing filter).

The measured torsional angle $\Delta\theta$ of the shaft describing the difference between the rotation angle of the drive and the rotation angle of the disk (defined in Section 3), and the pad acceleration \ddot{x} are displayed in Fig. 2 without creep groan and Fig. 3 in the case of creep groan. One can differ the creep groan case from the non-creep groan case, where $\Delta\theta$ has large vibrations and impulses can be found in the acceleration signal \ddot{x} during creep groan. The kurtosis value, which is based on a scaled version of the fourth moment of the signal, can be used to detect creep groan from the non-creep groan case. A higher kurtosis is the result of extreme deviations, which is characteristic for non-stationary signals (Antoni, 2006; Antoni and Randall, 2006). For the non-creep groan case, the kurtosis value of the pad acceleration signal is shown in Fig. 2b is 2.85, while this kurtosis value increases to 7.06 when creep groan occurs as shown in Fig. 3b.

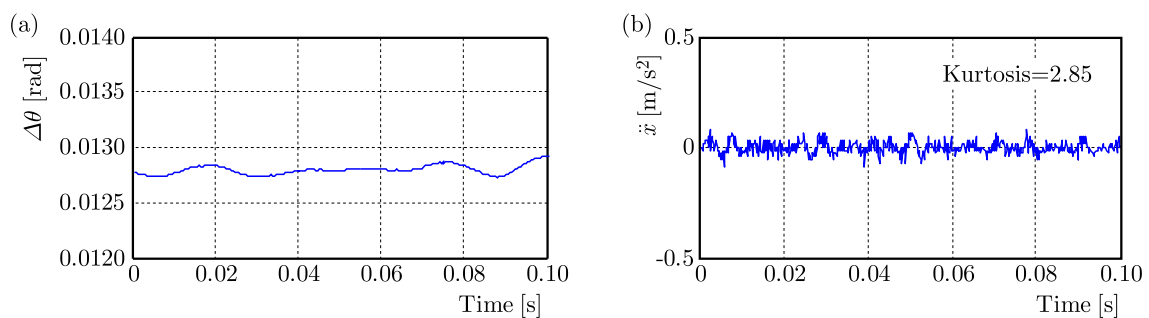


Fig. 2. Torsional angle of the shaft $\Delta\theta$ (a) and acceleration of the pad \ddot{x} (b) without creep groan

The frequency spectra of the signals during creep groan are exhibited in Fig. 3c,d by pursued Discrete Fourier transformations. The set-up consists of non-rotating parts in terms of the brake

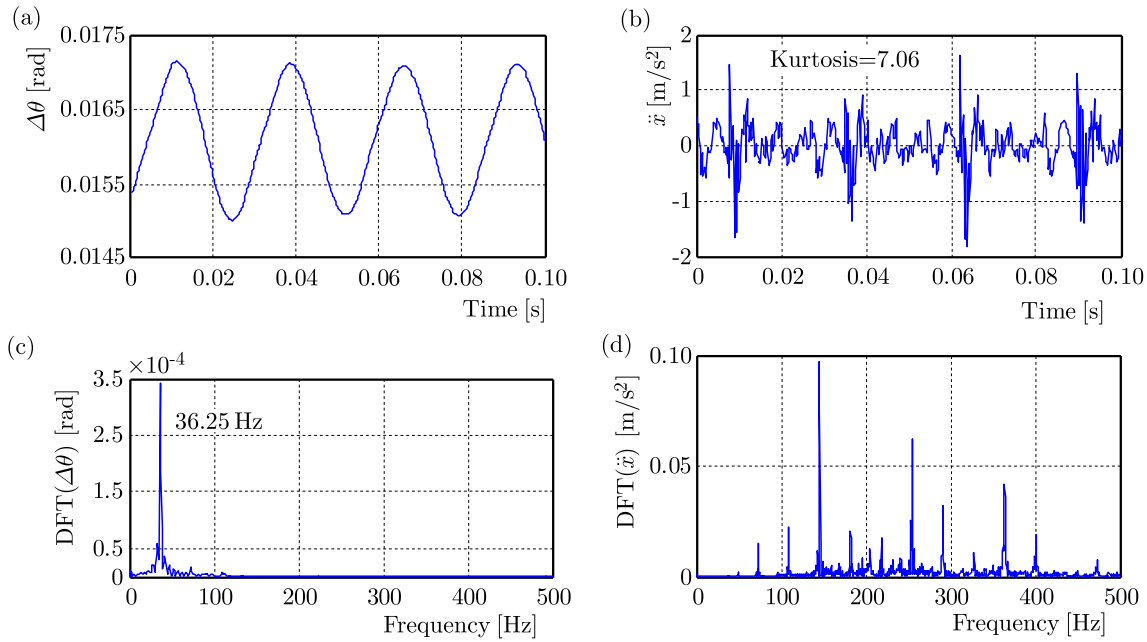


Fig. 3. Torsional angle of the shaft $\Delta\theta$ (a) and acceleration of the pads \ddot{x} (b), and their frequency spectra (c), (d) during creep groan

pads, the caliper, and the carrier, as well as rotating parts in terms of the disk, the drive shaft and the motor. In the rotating parts, the spectrum of $\Delta\theta$ shows a single peak at 36.25 Hz, which is the frequency related to the period of the stick-slip motion. In the non-rotating parts, the spectrum of \ddot{x} shows a lot of frequency peaks, also at much higher frequencies than the frequency of the stick-slip motion, and this vibration is what the human hear/feel during creep groan. According to the measured signals from both parts, it is clear that stick-slip happens during creep groan, and the creep groan is the resulted vibration of the brake system.

3. Fundamental theoretical investigations of creep groan

The chosen minimal model for the investigation of creep groan is shown in Fig. 4. It is considered as a two DOF system. Minimal models for creep groan with comparable low number of degrees of freedom are, as already mentioned in the introduction, discussed by Brecht (2000) with three degrees of freedom, in (von Wagner *et al.*, 2007) and (Ibrahim, 1994a) by Crowther and Singh (2007, 2009) with four degrees of freedom or by Fuadi *et al.* (2010) with two degrees of freedom. With our model, we focus on the stability and bifurcation analysis of the nonlinear model in comparison with our experimental results.

As we are in the low frequency range, the disk is considered as a rigid body which is connected to the motor by the drive shaft. During creep groan, the pads and the caliper move synchronously. Thus, the brake pads together with the caliper are considered as a rigid body and are connected to the base frame through the carrier. As the disk can only perform rotation but no wobbling motion, the number of pads can be reduced from two to one without any influence on the qualitative behavior of the model. The drive shaft is modeled as a rotational spring with stiffness k_θ and damping d_θ . With θ being the disk rotation angle and $\Omega_0 t$ the rotation angle of the drive with constant Ω_0 , the equation of motion of the disk is given by

$$I\ddot{\theta} + d_\theta(\dot{\theta} - \Omega_0) + k_\theta(\theta - \Omega_0 t) = -F_R r \quad (3.1)$$

where r is the radius of the point the pads act on the disk, I is the moment of inertia of the disk and F_R is the friction force in the contact between the disk and pads. Introducing $\Delta\theta$ as

the difference between the rotation angle of the drive $\Omega_0 t$ and the disk rotation angle θ , with $\Delta\theta = \Omega_0 t - \theta$, this equation of motion of the disk reads

$$I\Delta\ddot{\theta} + d_\theta\Delta\dot{\theta} + k_\theta\Delta\theta = F_R r \quad (3.2)$$

The carrier is considered as a spring with stiffness k_x and damping d_x , m is the mass of the pads with the caliper, and x is the displacement of the pads. The equations of motion of the system can then be described by

$$\begin{aligned} \mathbf{M}\ddot{\mathbf{Y}} + \mathbf{C}\dot{\mathbf{Y}} + \mathbf{K}\mathbf{Y} &= \mathbf{F} \\ \mathbf{Y} &= \begin{bmatrix} \Delta\theta \\ x \end{bmatrix} & \mathbf{M} &= \begin{bmatrix} I & 0 \\ 0 & m \end{bmatrix} & \mathbf{C} &= \begin{bmatrix} d_\theta & 0 \\ 0 & d_x \end{bmatrix} \\ \mathbf{K} &= \begin{bmatrix} k_\theta & 0 \\ 0 & k_x \end{bmatrix} & \mathbf{F} &= \begin{bmatrix} F_R r \\ F_R \end{bmatrix} \end{aligned} \quad (3.3)$$

Due to its definition, $\Delta\theta$ has in general due to the influence of the friction force a positive nonzero mean value.

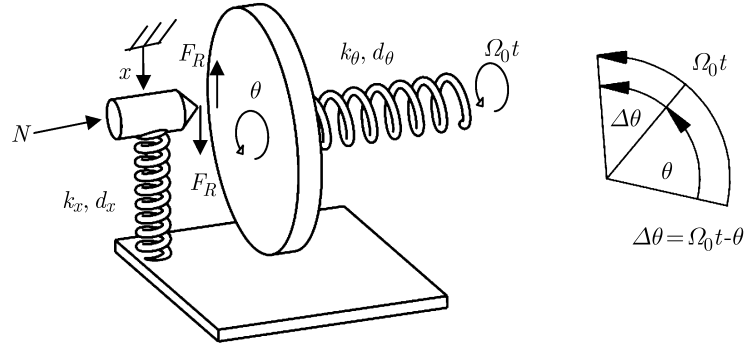


Fig. 4. Model of the test rig with an idealized brake

For the determination of F_R , the bristle friction law is used in the following. By imagining that two rigid bodies are in contact through elastic bristle surfaces (De Wit *et al.*, 1995; Johanaström and De Wit, 2008), the friction force F_R is generated by deformation of the bristle. The dynamic friction force F_R can in general be expressed as

$$F_R = \sigma_0 z + \sigma_1 \dot{z} \quad (3.4)$$

where σ_0 is the contact stiffness coefficient, σ_1 is the contact damping coefficient. z is the average deflection of the bristles described by

$$\dot{z} = \phi(\Delta\dot{\theta}, \dot{x}, z) = \Omega_0 r - \Delta\dot{\theta} r - \dot{x} - \frac{z}{g_0} |\Omega_0 r - \Delta\dot{\theta} r - \dot{x}| \quad (3.5)$$

Herein, g_0 is a scaling factor which includes the Stribeck effect. g_0 is given as

$$g_0 = \frac{1}{\sigma_0} \left(N\mu_d + N(\mu_s - \mu_d) \exp\left(-\left|\frac{(\Omega_0 - \Delta\dot{\theta})r - \dot{x}}{v_s}\right|^\alpha\right) \right) \quad (3.6)$$

where v_s is Stribeck velocity, N is the brake normal force, μ_s and μ_d are the static and dynamic friction coefficients, α is an empirical parameter which can be measured in experiments. In our test rig, the value $\alpha = 1$ is chosen as the more reasonable approach (Johanaström and De Wit, 2008; Tustin, 1947), since $\alpha = 1$ leads to better agreement between experimental and simulation

results. The bristle friction law can be described in such a way that the bristles will deflect like springs at a tangential force, which gives rise to the friction force. If the force is so large that some of the bristles deflect, slip occurs. This bristle friction law includes the Stribeck effect, hysteresis, pre-sliding characteristics of friction. The complete dynamic equations of the entire model can be, therefore, written as a set of first order ordinary differential equations

$$\begin{aligned} \dot{\mathbf{Y}} &= \begin{bmatrix} \Delta\dot{\theta} \\ \dot{x} \\ -\frac{d_\theta}{I}\Delta\dot{\theta} - \frac{k_\theta}{I}\Delta\theta + \frac{r}{I}\sigma_0 z + \frac{r}{I}\sigma_1\phi(\Delta\dot{\theta}, \dot{y}, z) \\ -\frac{d_x}{m}\dot{x} - \frac{k_x}{m}x + \frac{1}{m}\sigma_0 z + \frac{1}{m}\sigma_1\phi(\Delta\dot{\theta}, \dot{y}, z) \\ \phi(\Delta\dot{\theta}, \dot{y}, z) \end{bmatrix} \\ \mathbf{Y} &= [\Delta\theta \quad x \quad \Delta\dot{\theta} \quad \dot{x} \quad z]^T \\ \phi(\Delta\dot{\theta}, \dot{y}, z) &= \Omega_0 r - \Delta\dot{\theta} r - \dot{x} - \frac{z}{g_0} |\Omega_0 r - \Delta\dot{\theta} r - \dot{x}| \\ g_0 &= \frac{1}{\sigma_0} \left(N\mu_d + N(\mu_s - \mu_d) \exp\left(-\left|\frac{(\Omega_0 - \Delta\dot{\theta})r - \dot{x}}{v_s}\right|^\alpha\right) \right) \end{aligned} \tag{3.7}$$

where \mathbf{Y} is the vector of state variables of the system.

The equilibrium solution of equations (3.7), which is the equilibrium position of the system, is expressed as

$$\begin{aligned} \dot{\mathbf{Y}}_{eq} &= \mathbf{0} \\ \mathbf{Y}_{eq} &= \left[\frac{r\mathcal{A}}{k_\theta} \quad 0 \quad \frac{\mathcal{A}}{k_x} \quad 0 \quad \frac{\mathcal{A}}{\sigma_0} \right]^T \end{aligned} \tag{3.8}$$

where $\mathcal{A} = N\mu_d + N(\mu_s - \mu_d)e^{-\Omega_0 r/v_s}$.

Linearizing equation (3.7)₁ under its equilibrium position, we get

$$\dot{\mathbf{Y}} = \mathbf{A}\mathbf{Y} \tag{3.9}$$

$$\mathbf{A} = \begin{bmatrix} 0 & 1 & 0 & 0 & 0 \\ -\frac{k_\theta}{I} & -\frac{d_\theta}{I} + \frac{r\sigma_1}{I} \frac{\partial \tilde{\phi}}{\partial \Delta\dot{\theta}} & 0 & \frac{r\sigma_1}{I} \frac{\partial \tilde{\phi}}{\partial \dot{x}} & \frac{r\sigma_0}{I} + \frac{r\sigma_1}{I} \frac{\partial \tilde{\phi}}{\partial z} \\ 0 & 0 & 0 & 1 & 0 \\ 0 & \frac{\sigma_1}{m} \frac{\partial \tilde{\phi}}{\partial \Delta\dot{\theta}} & -\frac{k_x}{m} & -\frac{d_x}{m} + \frac{\sigma_1}{m} \frac{\partial \tilde{\phi}}{\partial \dot{x}} & \frac{\sigma_0}{m} + \frac{\sigma_1}{m} \frac{\partial \tilde{\phi}}{\partial z} \\ 0 & \frac{\partial \tilde{\phi}}{\partial \Delta\dot{\theta}} & 0 & \frac{\partial \tilde{\phi}}{\partial \dot{x}} & \frac{\partial \tilde{\phi}}{\partial z} \end{bmatrix}$$

where

$$\begin{aligned} \frac{\partial \tilde{\phi}}{\partial \Delta\dot{\theta}} &= \frac{\partial \phi(\Delta\dot{\theta}, \dot{x}, z)}{\partial \Delta\dot{\theta}} = \frac{(\mu_s - \mu_d)r^2\Omega_0}{v_s(\mu_s - \mu_d + \mu_d e^{\Omega_0 r/v_s})} \\ \frac{\partial \tilde{\phi}}{\partial \dot{x}} &= \frac{\partial \phi(\Delta\dot{\theta}, \dot{x}, z)}{\partial \dot{x}} = \frac{(\mu_s - \mu_d)r\Omega_0}{v_s(\mu_s - \mu_d + \mu_d e^{\Omega_0 r/v_s})} \\ \frac{\partial \tilde{\phi}}{\partial \Delta z} &= \frac{\partial \phi(\Delta\dot{\theta}, \dot{x}, z)}{\partial \Delta z} = \frac{-r\sigma_0\Omega_0}{N\mu_d + N(\mu_s - \mu_d)e^{-\Omega_0 r/v_s}} \end{aligned}$$

and \mathbf{A} is the corresponding system matrix. The eigenvalue of the matrix can be calculated as

$$\lambda = \text{eig}(\mathbf{A}) \quad (3.10)$$

The Lyapunov stability of the equilibrium solution can be analyzed by eigenvalues λ . The equilibrium solution is asymptotically stable, when the real parts of all the eigenvalues are negative. In contrast, the equilibrium solution is unstable when any of the real parts of eigenvalues is positive. With respect to the nonlinear behavior, we call an isolated periodic solution in a self-excited system a limit cycle (Hagedorn, 1978). The limit cycle of Eq. (3.7) is calculated in a transient analysis by using numerical integration.

According to the conditions for the existence of the stick-slip limit cycle and the stability of the equilibrium solution, the system has three different regions with different types of solutions. Corresponding results are shown exemplarily in Fig. 5 if both the speed Ω_0 and brake pressure p are varied. Detailed comparison with the experimental results is performed in Section 4. When the system has a stable equilibrium solution but no a stick-slip limit cycle, creep groan cannot occur in this parameter region, and this region is labeled as region I (white region in Fig. 5). When a stable stick-slip limit cycle and a stable equilibrium solution exist simultaneously, occurrence or absence of creep groan depends on its initial condition. We labeled this region as region II (green region in Fig. 5). When the system has a stable stick-slip limit cycle and an unstable equilibrium solution, creep groan will always occur, and this region is labeled as region III (yellow region in Fig. 5). Figure 5 exhibits also, for a constant Ω_0 with varying p and for a constant p with varying Ω_0 , respectively, the largest real part of the eigenvalues $\text{Re}(\lambda)$ of the system matrix \mathbf{A} (red line), and the torsional angle limit cycle amplitude A_{LC} (blue line). The boundary between regions II and III is defined as a curve, where the largest real part of the eigenvalues $\text{Re}(\lambda)$ of the system matrix is equal to 0. The way to determine the boundary between regions I and II is given as follows: for varying brake pressure and speed, the solution of the nonlinear system can be calculated by a numerical time integration of Eq. (3.7) with initial conditions in the stick region. If the solution is still the stick-slip limit cycle after a while, the stick-slip limit cycle is considered to exist and be asymptotically stable. In addition, due to the system with the negative real parts of the eigenvalues, its equilibrium solution is asymptotically stable and we have coexistence of the stable equilibrium solution and the limit cycle, i.e. we are in region II. If the solution diverges from the limit cycle and converges to the equilibrium solution, a stable stick-slip limit cycle is considered not to exist, i.e. we are in region I. By varying the brake pressure and driving speed, regions I and II as well as the boundary between them can be determined.

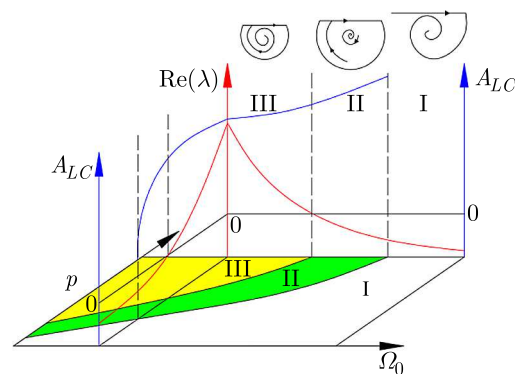


Fig. 5. Map of solution regions depending on the parameters Ω_0 and p : I only stable equilibrium solution, II coexistence of the stable equilibrium solution and the limit cycle solution, III only stable limit cycle solution. The largest real part of the eigenvalues $\text{Re}(\lambda)$ of the system matrix \mathbf{A} (red line) and the limit cycle amplitude A_{LC} (blue line) for a constant Ω_0 with varying p and for a constant p with varying Ω_0 , respectively

4. Comparison between experimental and simulation results

Experimental and theoretical results will be compared in this Section. Due to the simple structure of the idealized brake in the test rig, its physical parameters can comparably easy be identified by experiments. The stiffness and damping of the drive shaft and the carrier are determined by modal analyses. The mass of the disk and the caliper with the pads can be measured by a weighting device. The friction coefficients are estimated from comparison of the experimental and simulation limit cycle results. The chosen parameters are given in Table 1.

Table 1. Parameters of the system

Parameters	Values
I	0.2025 kgm^2
k_θ	$1.036 \cdot 10^4 \text{ Nm}$
d_θ	2 Nms
k_x	$9.87 \cdot 10^6 \text{ N/m}$
d_x	$1.5 \cdot 10^3 \text{ Ns/m}$
r	0.15 m
μ_d	0.325
$\mu_s - \mu_d$	0.009
σ_0	$3.97 \cdot 10^8 \text{ N/m}$
σ_1	$3.84 \cdot 10^5 \text{ Ns/m}$
v_s	0.025 m/s

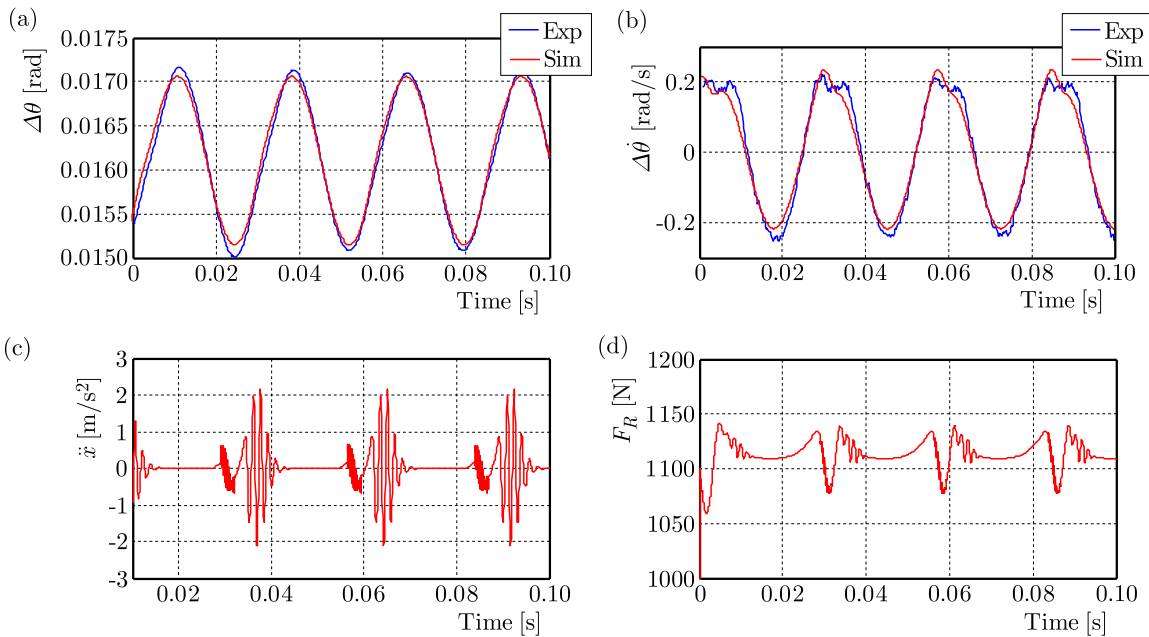


Fig. 6. Simulated and measured torsional angle and torsional velocity of the shaft (a), (b), simulated acceleration of the pad (c) and a simulated friction force (d) with a brake pressure 9 bar and speed 0.2 rad/s

Figures 6a and 6b show the measured and simulated torsional angle and torsional velocity of the drive shaft, with brake pressure 9 bar and driving speed 0.2 rad/s. The red line denotes the simulation results and the blue line presents the experimental results, where both of them show good agreement. The simulated acceleration of the brake pads and the corresponding friction force are proposed in Figs. 6c and 6d. When the system converts from the stick region to the

slip region, the friction force changes suddenly and a large impulse appears in the acceleration signal. The same effect can also be observed in the measured acceleration on the carrier shown in Fig. 2b. Figure 7 exhibits the simulated and measured stick-slip limit cycles in the phase plot with $\Delta\dot{\theta}$ as a function of $\Delta\theta$. At a constant driving speed, the amplitude of the limit cycle increases with an increase in the brake pressure. The measured and simulated stick-slip limit cycles at 5, 7, and 9 bar are plotted in Fig. 7.

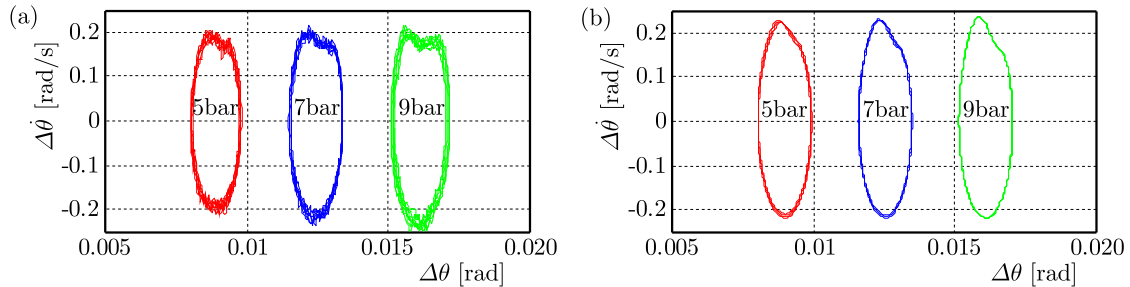


Fig. 7. Limit cycle of experimental results (a) and simulation results (b)

The map of the parameter regions is drawn in Fig. 8 with the identified parameters. Its horizontal axis is the speed of the motor and the vertical axis is the brake pressure, which is proportional to the normal brake force. This map shows different critical conditions of creep groan during accelerating and decelerating of a vehicle. If the operation starts with parameters in region III, creep groan must occur, as the equilibrium solution is unstable. Creep groan will proceed also in region II if we move slowly within this parameter map until the system enters in parameter region I, since the limit cycle does not exist in region I. Following the dotted line in Fig. 8, this is usually the case when the vehicle is accelerated. If the vehicle is decelerated, different things will happen, as shown in Fig. 8 with the solid line. In region I, the silent solution without creep groan is the only stable solution. The system will stay in the attractor of the silent solution even though it enters region II, and no creep groan is occurring. Creep groan will then occur once region III is entered, as the limit cycle is the only stable solution. This can explain that creep groan is more serious in the accelerating process than in the decelerating process, which agrees with the driving experience.

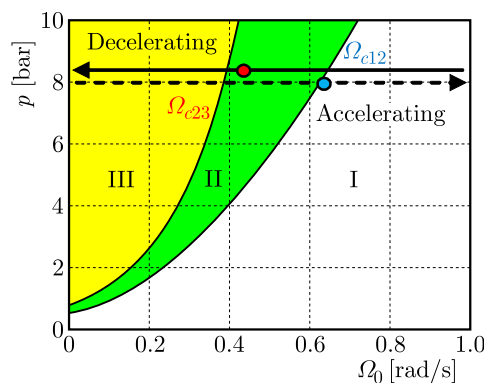


Fig. 8. Map of creep groan, the red point represents the measured boundary between regions II (green) and III (yellow), while the blue point represents the measured boundary between regions I (white) and II (green)

The determination of the critical velocities Ω_{c12} and Ω_{c23} is described in the following. The brake pressure is constant (8 bar) and the speed of the motor is varied. The corresponding experimental results are shown in Fig. 9. The red line describes the driving speed, while the blue line represents the torsional vibrations $\Delta\tilde{\theta}$, where $\Delta\tilde{\theta} = \Delta\theta - \Delta\theta_{eq}$. The torsional vibration

of the drive shaft becomes large when creep groan appears. In the accelerating process, the speed is slowly increased from 0.1 rad/s to 0.8 rad/s, creep groan occurs at a low speed but disappears when the speed is higher than the critical speed Ω_{c12} (0.62 rad/s with 8 bar), which is the boundary point between regions I and II. In the decelerating process, the speed is slowly decreased from 0.8 rad/s to 0.1 rad/s. Creep groan does not occur at a high speed but appears when the speed is lower than the other critical speed Ω_{c23} (0.42 rad/s with 8 bar), which is the boundary point between regions II and III. It should be noted here that similar boundary points can also be measured by varied pressure with a constant speed (Zhao *et al.*, 2017). For a constant speed with the increasing pressure, the onset of creep groan will occur at a higher brake pressure than the stopping of creep groan will happen when decreasing the brake pressure. This case is considered in Section 5 for the complete real brake.

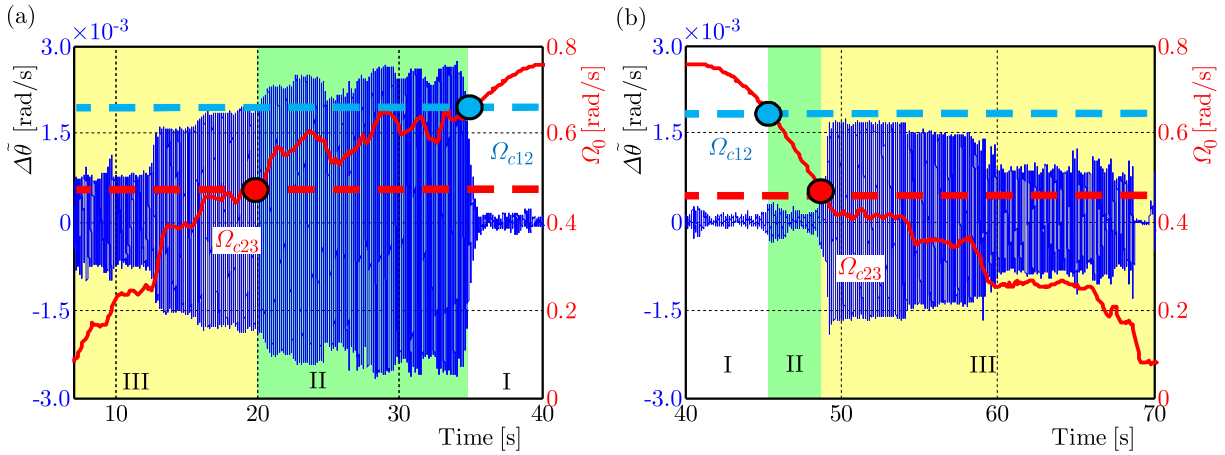


Fig. 9. Experiment: occurrence of creep groan with variation in the speed. Creep groan is always present in region III (yellow) and does not occur in region I (white), while creep groan occurs in region II (green) in the accelerating process (a) but not in the decelerating process (b) cf. Fig. 8

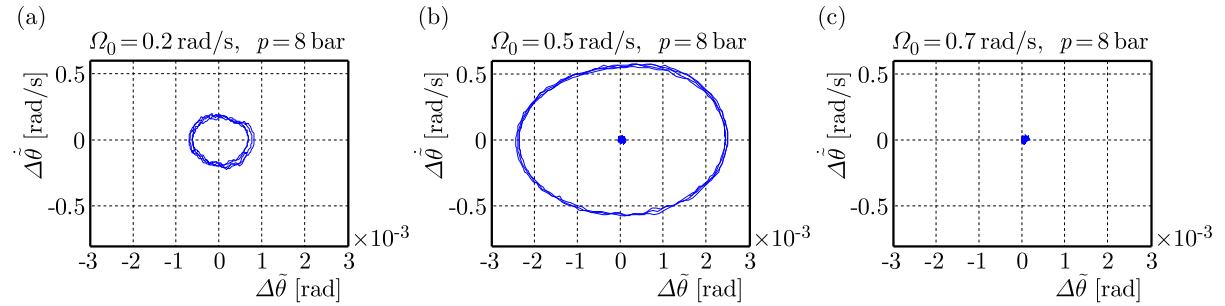


Fig. 10. The equilibrium solution and the stick-slip limit cycle with different driving speeds, (a) in region III with the stick-slip limit cycle, (b) in region II with coexistence of two stable solutions, (c) in region I with just an equilibrium solution

Figure 10 shows the limit cycles and the equilibrium solutions of the system with different speeds in the phase plot. When the speed is higher than Ω_{c12} (Fig. 10c), only the equilibrium solution can be measured in both accelerating and decelerating processes. The system under current conditions stays in region I and creep groan cannot occur. When the speed is lower than Ω_{c23} (Fig. 10a), only the stick-slip limit cycle can be measured in both processes, meaning that the system is in region III and creep groan always occurs. When the speed is higher than Ω_{c23} but lower than Ω_{c12} (Fig. 10b), creep groan can be measured in the accelerating process but not in the decelerating process, meaning that the system is in region II with both the stable equilibrium solution and the stable limit cycle, and the occurrence and absence of creep groan depends on its

initial conditions. The difference between these two limit speed values (Ω_{c12} and Ω_{c23}) actually proves the existence of region II with the coexistence of two stable solutions.

The main result therefore is that a linear stability analysis is not sufficient for the determination of the boundary of creep groan as thereby one can only calculate Ω_{c23} . E.g., in the acceleration case, which is in fact compared to the deceleration case, the one being more suspicious for creep groan, the boundary Ω_{c12} for that undesired vibration phenomenon can only be determined by performing a nonlinear analysis. The same holds in the case of brake pressure variation.

5. Creep groan bifurcation experimental behavior of a complete real brake

In this Section, some results on the test rig with a complete real brake will be expressed and compared to the results of the idealized brake. The set-up consists of a real brake system, a suspension system, as well as the same drive system as before, shown in Fig. 11. The similar

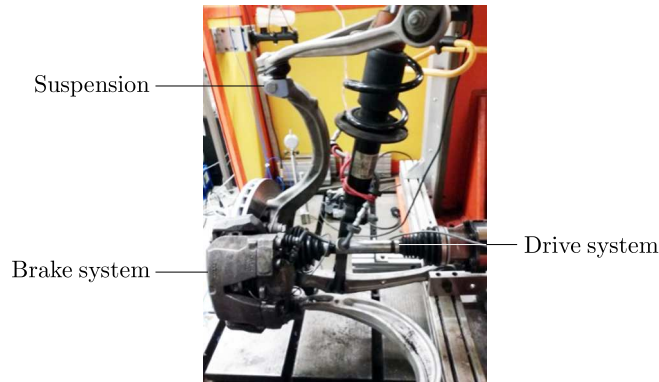


Fig. 11. Test rig with a complete real brake including the suspension

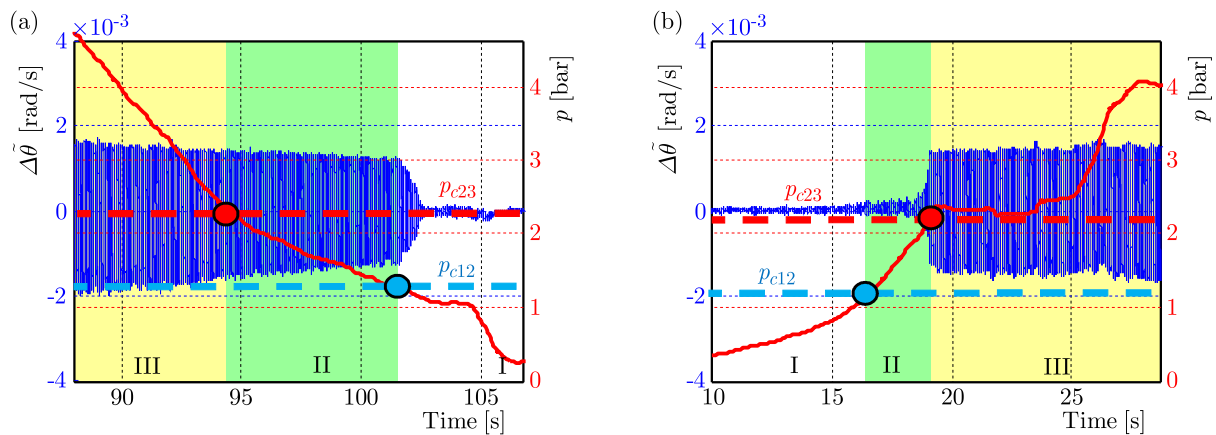


Fig. 12. Occurrence of creep groan with variation of the brake pressure during the pressure decreasing process (a) and pressure increasing process (b). Limits for the stopping and the onset of creep groan (p_{c12} and p_{c23} , respectively) are different proving the existence of region II with two stable solutions, while region III (yellow) and region I (white) contain only one stable solution

experimental method has been used to identify the bifurcation behavior and the corresponding map of creep groan of the complete real brake. According to the above analysis, the boundary between regions I and II is critical for stopping of creep groan in the acceleration process, which is the more suspicious case for creep groan. The boundary between regions II and III is critical

for the occurrence of creep groan starting from the equilibrium position which is the case while decelerating. We can choose the speed of motor and vary the brake pressure arbitrarily in the test rig and, therefore, the boundaries could be determined. The result for a single test run with decreasing and respectively increasing brake pressure is shown in Fig. 12. Again the boundaries for the stopping and the onset of creep groan are not the same, which proves the existence of region II with the coexistence of a stable limit cycle and a stable equilibrium solution. The measured boundary points as well as the polynomial regression boundary curves are exhibited in Fig. 13.

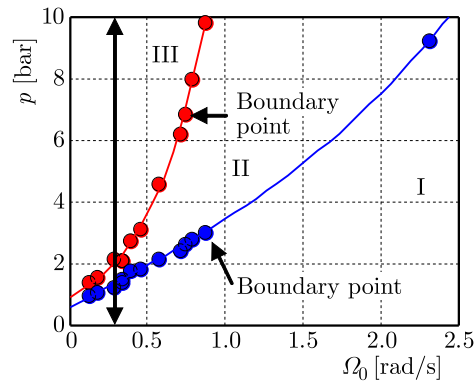


Fig. 13. Map of creep groan identified by experiments, the red points represent the measured boundary points between regions II and III while the blue points represent the measured boundary points between regions I and II, the red line and the blue line are polynomial regression curves of the measured boundary points

Compared to the map measured from the idealized brake, both maps show the same three regions I, II and III, and the boundaries among regions have the same qualitative behavior. It is, therefore, confirmed that the bifurcation behavior observed for the simplified brake can be conveyed in the complete real brake system.

6. Conclusions

In this paper, fundamentals of creep groan have been studied theoretically and experimentally. In order to concentrate on the friction contact between the disk and pads, a test rig with an idealized brake has been designed and assembled. Creep groan is measured for this set-up and for the test rig with a complete real brake including suspension.

A nonlinear model with the bristle friction law is proposed to explain the experimental results. Based on the model, creep groan is simulated through a minimal model. Furthermore, the bifurcation behavior and the corresponding map of creep groan are studied. Three parameter regions of the solutions exist in this map at varied brake pressure and driving speed. The parameter regions are denoted as follows: region I with no stick-slip limit cycle but a stable equilibrium solution, region II with both the stable stick-slip limit cycle and the equilibrium solution, and region III with a stable stick-slip limit cycle and an unstable equilibrium solution. The limit cycle can be interpreted as creep groan while the equilibrium solution is the desired vibration free case. In region I, no creep groan can occur, while in region III creep groan is always present. In region II, the occurrence or absence of creep groan depends on the initial conditions. From that, it can be concluded that a linear stability analysis is not sufficient for the determination of the boundary of creep groan. E.g., in the acceleration case, which is in fact compared to the deceleration case, the one being more suspicious for creep groan, the boundary for that undesired vibration phenomenon can only be determined by performing a nonlinear analysis.

Experimental results confirm the existence of the map with three regions, and the boundaries of the regions can be identified theoretically and experimentally. The simulation results show good agreement with the experimental results. At the end, a similar map is measured in the test rig with a complete real brake, which confirmed that the bifurcation behavior observed for the simplified brake can be conveyed to the complete real brake system.

Acknowledgements

The first author acknowledges the support by the China Scholarship Council (CSC). The authors thank Dr. Torsten Treyde, ZF TRW, for fruitful discussions and his helpful comments.

References

1. ABDELHAMID M.K., 1995, Creep groan of disc brakes, *SAE Technical Paper*, **951282**, 02-24
2. ABDELHAMID M.K., BRAY W., 2009, Braking systems creep groan noise: detection and evaluation, *SAE Technical Paper*, 10-11
3. ANTONI J., 2006, The spectral kurtosis: a useful tool for characterising non-stationary signals, *Mechanical Systems and Signal Processing*, **20**, 2, 282-307
4. ANTONI J., RANDALL R., 2006, The spectral kurtosis: application to the vibratory surveillance and diagnostics of rotating machines, *Mechanical Systems and Signal Processing*, **20**, 2, 308-331
5. BRECHT J., 2000, Untersuchungen zum Bremsenknarzen-ein Beitrag zur Beschreibung von Schwingungen in Bremssystemen, Shaker, Ph.D. Thesis University Siegen
6. BRECHT J., HOFFRICHTER W., DOHLE A., 1997, Mechanisms of brake creep groan, *SAE Technical Paper*, **106**, 2, 3405-3411, DOI: 10.4271/973026
7. CANTONI C., CESARINI R., MASTINU G., ROCCA G., SICIGLIANO R., 2009, Brake comfort – a review, *Vehicle System Dynamics*, **47**, 8, 901-947
8. CROWTHER A.R., SINGH R., 2007, Analytical investigation of stick-slip motions in coupled brake-driveline systems, *Nonlinear Dynamics*, **50**, 3, 463-481
9. CROWTHER A.R., SINGH R., 2008, Identification and quantification of stick-slip induced brake groan events using experimental and analytical investigations, *Noise Control Engineering Journal*, **56**, 4, 235-255
10. DE WIT C.C., OLSSON H., ASTROM K.J., LISCHINSKY P., 1995, A new model for control of systems with friction, *IEEE Transactions on Automatic Control*, **40**, 3, 419-425
11. FUADI Z., ADACHI K., IKEDA H., NAITO H., KATO K., 2009, Effect of contact stiffness on creep-groan occurrence on a simple caliper-slider experimental model, *Tribology Letters*, **33**, 3, 169-178
12. FUADI Z., MAEGAWA S., NAKANO K., ADACHI K., 2010, Map of low-frequency stick-slip of a creep groan, *Proceedings of the Institution of Mechanical Engineers. Part J: Journal of Engineering Tribology*, **224**, 12, 1235-1246
13. HAGEDORN P., 1978, *Nichtlineare Schwingungen*, Akad. Verlag Ges.
14. HETZLER H., SEEMANN W., SCHWARZER D., 2007, Steady-state stability and bifurcations of friction oscillators due to velocity dependent friction characteristics, *Proceedings of the Institution of Mechanical Engineers. Part K: Journal of Multi-body Dynamics*, **221**, 3, 401-412
15. IBRAHIM R., 1994a, Friction-induced vibration, chatter, squeal, and chaos. Part I: Mechanics of contact and friction, *Applied Mechanics Reviews*, **47**, 209-226
16. IBRAHIM R., 1994b, Friction-induced vibration, chatter, squeal, and chaos. Part II: Dynamics and modeling, *Applied Mechanics Reviews*, **47**, 227-253
17. JANG H., LEE J.S., FASH J.W., 2001, Compositional effects of the brake friction material on creep groan phenomena, *Wear*, **251**, 1, 1477-1483

18. JOHANASTROM K., DE WIT C.C., 2008, Revisiting the LuGre friction model, *IEEE Control Systems*, **28**, 6, 101-114
19. MUSCHALLE C., 2015, Experimentelle Modalanalyse an einem Versuchsaufbau zur Untersuchung an Kfz-Bremsen, Bachelor thesis, TU Berlin,
20. NEIS P.D., FERREIRA N.F., POLETTO J.C., MATOZO L.T., MASOTTI D., 2016, Quantification of brake creep groan in vehicle tests and its relation with stick-slip obtained in laboratory tests, *Journal of Sound and Vibration*, **369**, 63-76
21. TUSTIN A., 1947, Effects of backlash and of speed-dependent friction on the stability of closed-cycle control systems, *Electrical Engineers – Part IIA: Automatic Regulators and Servo Mechanisms*, **94**, 1, 143-151
22. VADARI V., JACKSON M., 1999, An experimental investigation of disk brake creep-groan in vehicles and brake dynamometer correlation, *SAE Technical Paper*, **1999-01-3408**
23. VON WAGNER U., HOCHLENERT D., HAGEDORN P., 2007, Minimal models for disk brake squeal, *Journal of Sound and Vibration*, **302**, 3, 527-539
24. WU G., JIN S., 2014, Combination of test with simulation analysis of brake groan phenomenon, *SAE International Journal of Passenger Cars-Mechanical Systems*, **7**, 1119-1127
25. ZHAO X., GRÄBNER N., VON WAGNER U., 2016, Experimental and theoretical investigation of creep groan of brakes through minimal models, *PAMM*, **16**, 1, 295-296
26. ZHAO X., GRÄBNER N., VON WAGNER U., 2017, Creep groan: fundamental experimental and theoretical investigations, *Eurobrake*, EB2017-FBR-002, Dresden

Manuscript received October 26, 2017; accepted for print November 8, 2017

SKIN FRICTION ESTIMATION IN A STRONG DECELERATING FLOW

ARTUR DRÓZDŹ, WITOLD ELSNER, DAWID SIKORSKI

Czestochowa University of Technology, Czestochowa, Poland

e-mail: welsner@imc.pcz.czyst.pl

The paper presents the analysis of the turbulent boundary layer developed on a flat plate subjected to an Adverse Pressure Gradient (APG) and approaching separation. The aim of the study is to examine the effects of pressure gradient on a non-equilibrium boundary layer while indicating local areas of the equilibrium flow. The emphasis is on the analysis of mean flow velocity and the estimation of skin friction. It is known that accurate measurements of skin friction were considered as a difficult and demanding task despite of various measuring techniques available. A great challenge is especially the measurement of a strong decelerated turbulent boundary layer because of low shear stress and possible large measuring errors. To date, the oil film or oil drop interferometry technique, because of its high accuracy, has become a basis of turbulent-boundary-layer research. In our research, this technique has been used as a reference method for comparing with the traditional Clauser chart method, which generally is considered as not suitably for non-canonical flows. In the paper, however, a correction of the method is proposed, which allows one to increase its range of applicability. This corrected Clauser chart method (CCCM) involves only one iteration while other proposed in the literature methods employ a twofold iterative procedure. The comparison of the methods for the non-canonical turbulent boundary layer, i.e. adverse pressure gradient with a strong flow history effect has been presented. It has been shown that CCCM can be successfully used for small and medium pressure gradients, where the Clauser-Rotta pressure gradient parameter β does not exceed level close to 11.

Keywords: turbulent boundary layer, separation, oil-film interferometry, Clauser chart

1. Introduction

The measurement of skin friction is presently recognized as a critical element of aerodynamic testing. It gives rise to crucially important flow phenomena such as viscous drag on air and ground vehicles, on wind turbine blades, and losses in internal flows. It provides critical information necessary for computational simulations and serves as a sensitive quantity for use in flow-control applications.

Until now, accurate measurements of skin friction were considered as a difficult and demanding task as it requires precise measurements of mean velocity in the viscous sublayer, where the determination of the velocity gradient is necessary (Hutchins and Choi, 2002). Most commonly used for this purpose is a measuring method relying on hot-wire technique. Despite theoretical basis, the accuracy of this method is strongly dependent on resolution and quality of measurements very close to the wall (Dixit and Ranesh, 2009). According to Castillo and Johansson (2002), this method works satisfactorily only for low Reynolds number flows. Concerning adverse pressure gradient (APG) flows, where the low velocity close the wall occurs, the results from hot-wire measurement are biased by heat transfer to the wall (Ikeya *et al.*, 2017). An indirect method based on the measurement of velocity profile, the so called Clauser plot or Clauser chart method (Clauser, 1956) (herein CCM), do not require precise measurements in the viscous sublayer as it is based on the logarithmic overlapping layer universality assumption. In its original form it

is however, restricted only to canonical flows. There are some modifications of the method for equilibrium or near-equilibrium pressure gradient flows, which are based on the non-universal or pressure-gradient-dependent log law in the inner scaling (Dixit and Ranesh, 2009), however their applications are limited as they provide different parameters in to the log-law function for pressure gradient changes without analyzing flow history effects (Bobke *et al.*, 2017; Drózdź and Elsner, 2017).

On the other hand, the method considered to be the most accurate is the oil film or oil drop interferometry technique which is based on the work of Tanner and Blows (1976). This technique uses the dependency between the thinning of an oil film deposited on the surface exposed to the flow and the local shear stress. According to (Segalini *et al.*, 2015), if carefully implemented, this method yields the true time averaged skin friction within the $\pm 1\%$ of measurement accuracy.

The paper presents results of skin friction measurements using the two above methods applied for a strong decelerated turbulent boundary layer developed on the flat plate being at the verge of separation.

The goal of the study is to verify applicability of this method for a very demanding case, where a low shear stress is present and where its estimation may be associated with large measuring errors. In the paper, the comparison of the measurements accuracy with the proposed correction to the Clauser chart method for a strong pressure gradient flow with the flow history effect, is presented.

2. Methodology and instrumentation

An open-circuit wind tunnel located at Czestochowa University of Technology has been used for this experiment. The facility consists of a blower, settling chamber, and a long rectangular channel with length of 5.035 m located upstream the test section. As a result, the turbulent boundary layer develops on a long plate what allows it to reach boundary layer thickness up to 90 mm at the inlet to the test section. The inlet rectangular channel has two pairs of suction gaps aimed, at maintaining overpressure, to control the two-dimensionality of the flow by minimizing the boundary layers on the side walls. Triangular corner inserts are used in the whole inlet channel to reduce the effect of secondary vortices developing along the rectangular channel. A slight inclination of the upper wall helps maintaining zero pressure gradient ($dP_\infty/dx \approx 0$, where P_∞ is external static pressure and x is the streamwise direction) conditions at the inlet.

The specially design diffuser shape test section with length of 1.835 m (see Fig. 1) is equipped with a perforated movable upper wall. Wall perforation of 10.1% is adopted, characterized by 0.5 mm circular holes. Modification of the shape and position of the upper wall and the suction flux enables generation of a wide range of pressure gradient conditions, while the zero pressure gradient conditions are maintained at the inlet channel. With specific pressure conditions, it is possible to obtain, on the bottom wall, a turbulent boundary layer which is at the verge of separation. Full separation on the lower flat plate does not occur even for the suction case. After that point, due to the cessation of suction, the flow returns to the attached state.

The velocity measurements have been performed with a single hot-wire anemometry probe of diameter $d = 3 \mu\text{m}$ and length $l = 0.4 \text{ mm}$ (modified Dantec Dynamics 55P31). The probe was a combined with hot-wire anemometry CCC developed by the Polish Academy of Science in Krakow.

The hot-wire bridge was connected to a 16 bit A/D converter. The acquisition was maintained at the frequency of 25 kHz, with minimum 30 s sampling records. The ambient conditions were carefully controlled during the measurements. During single profile measurements, the scatter of ambient temperature did not exceed $\pm 0.2^\circ$. If the measured temperature was different from

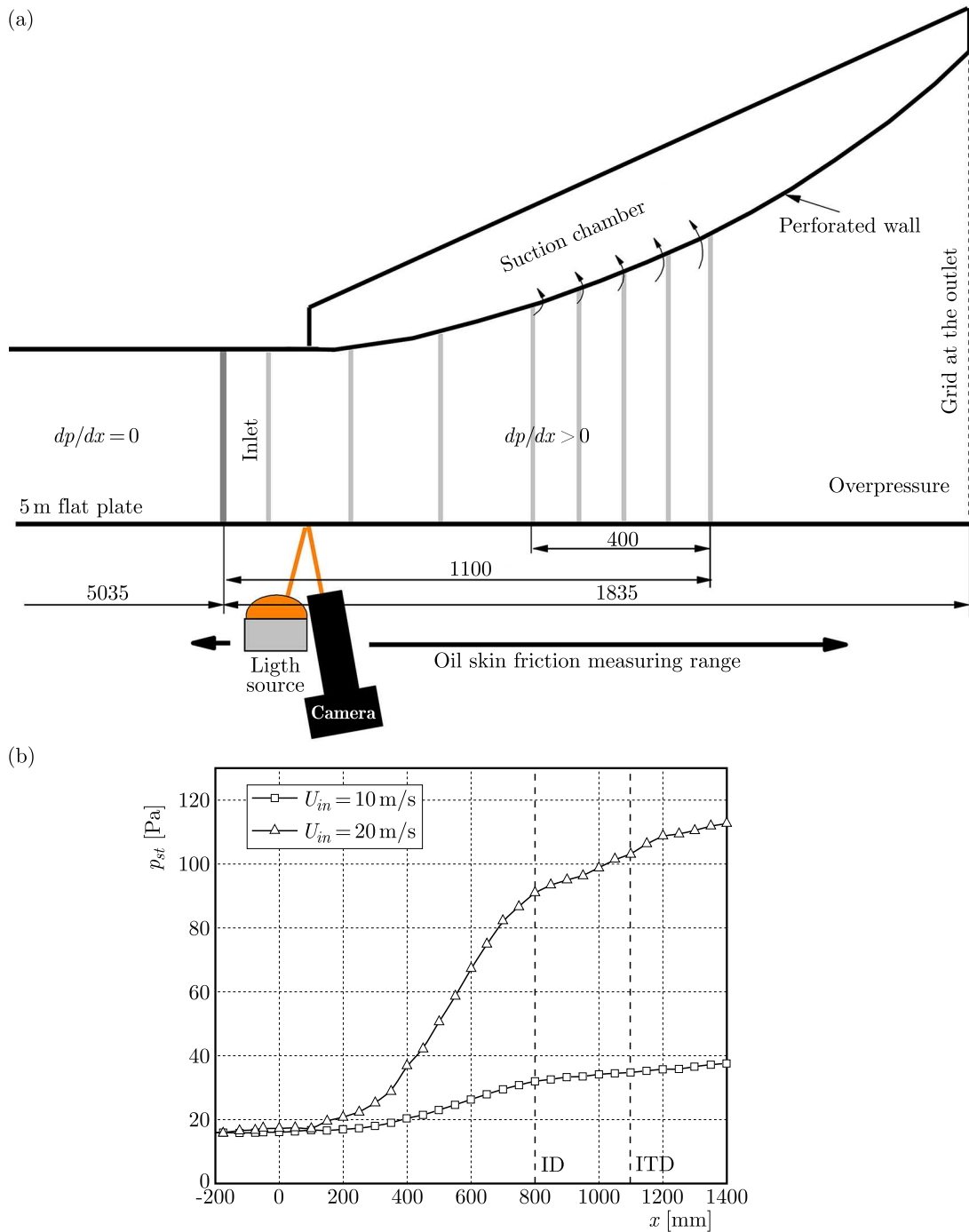


Fig. 1. Test section geometry (a) and pressure distribution (b)

the calibration temperature, the temperature correction of CTA voltage was used by Jorgensen (2002). Free-stream velocity was simultaneously monitored by means of the Prandtl tube.

The velocity measurements were performed for two inlet velocities $U_{in} = 10$ and 20 m/s, which corresponded to the Reynolds number based on momentum loss thickness 6300 and 10150. Basic inlet parameters are summarized in Table 1, where Tu is turbulence intensity, U_{in} mean velocity outside the turbulent boundary layer, u_τ friction velocity ($u_\tau = \sqrt{\tau_w/\rho}$), θ momentum loss thickness and $Re_\theta = U_{in}\theta/\nu$ is the Reynolds number, where ν is the kinematic viscosity. The pressure distribution imposed by the upper wall and the active suction is presented in Fig. 1b. Further details of the experiment can be found in (Drózdź and Elsner, 2017).

Table 1. Inlet conditions of ZPG turbulent boundary layer

	Tu [%]	U_{in} [m/s]	u_τ [m/s]	θ [mm]	Re_θ [-]
1	0.7%	10	0.37	8.26	6300
2	0.7%	20	0.72	10.3	10150

3. Methodology of direct skin friction estimation

The direct method of skin friction estimation is based on the fringe skin friction (FSF) technique introduced by Tanner and Blows (1976), who relate the evolution of oil droplet thickness to the skin friction τ_w . The method is based on the assumption of constant shear stress for a given measuring point already used in experimental investigations (Drózdź *et al.*, 2008; Pailhas *et al.*, 2009). Under the action of the flow shearing force the oil film is getting thinner leading, under lighting of the monochromatic lamp, to a series of interferometric fringes. These fringes are produced as a result of interference of the light reflected from the surface and from the air-oil interface. Distance between consecutive fringes is strictly related to the oil layer thickness and consequently to skin friction.

For the purpose of skin friction measurement, the optical equipment has been installed in the wind tunnel under the plate (see Fig. 1a). It consisted of commercial camera equipped with Macro lens and SOX Whitecroft Lighting sodium lamp emitting the monochromatic light of wavelength $\lambda = 0.5893 \mu\text{m}$ used to illuminate the oil droplet. For the measurements, the OM50 silicone oil with viscosity of about 0.048 Pas was used. The accuracy of wall shear data was in the range of 1%, which corresponded to 0.5% accuracy in friction velocity for the inlet u_τ . The oil viscosity is the most important parameter that has to be precisely controlled that is why temperature of the flow, which is also the temperature of the flat plate, was carefully measured using a temperature sensor. In the course of a single profile measurement the scatter of ambient temperature at the end of the test section did not exceed $\pm 0.2^\circ$ and the temperature difference between the flowing air and the wall was also below 0.1°C .

In the central part of the flat plate, an optical glass delivered by Schott Company has been mounted. This glass, used for radiological shields due to high lead contents, is characterized by a very smooth surface, which is necessary to get smallest distortion of the fringe pattern. The camera has been controlled by a computer program, which triggered the shutter from every 10 s up to 30 s depending on the flow speed. Pictures have been recorded as monochromatic and processing of the images obtained from experiments has been performed in Matlab Image Processing Toolbox. Quality of images has been improved by image contrast adjustment and histogram equalization procedures, which have been adopted from Matlab library (Drózdź *et al.*, 2008).

The direct estimation of skin friction has been obtained from a series of pictures (minimum 25) of fringe patterns forming on the oil droplet thinning under the influence of the flow shear force. An exemplary image of the thinning droplet is presented in Fig. 2. Extracted pixels of varying brightness from the single line from oil symmetry plane are used in order to estimate the fringe spacing. Having the estimated fringe spacing from all taken pictures, the distribution of the period versus time is obtained (Fig. 3). The approximation of the distribution with least squares algorithm allows one to determine the slope of the curve a .

The shear stresses τ_w [Pa] is calculated from the following equation

$$\tau_w = \frac{2n_o\mu_o a}{c\lambda} \cos \theta_o \quad (3.1)$$

where $n_o = 1.4$ is the index of refraction for the oil, μ_o – dynamic viscosity of the oil, c – calibration coefficient [pixels/mm], a – slope of the fringe spacing versus time [pixels/s]



Fig. 2. Oil droplet with the interferometry pattern

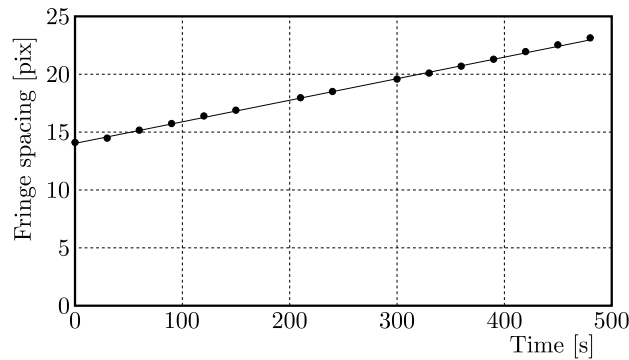


Fig. 3. Fringe spacing versus time

and θ_o is the angle between the incident light and the direction normal to the plate in the oil environment. In comparison with Pailhas *et al.* (2009), the present shear stresses formula (3.1) includes the influence of the view angle in the oil environment θ_o . It is important to know that the viewing angle can lead to overestimation of the skin friction error equal to 0.7% for the angle $\theta = 10^\circ$ in the air environment.

4. Methodology of corrected Clauser chart method (CCCM)

The indirect estimation of skin friction can be realized using the Clauser plot method (Clauser, 1956). It is based on the assumption of universality of the logarithmic overlap region for zero pressure gradient flows defined as

$$U^+ = \frac{1}{\kappa} \ln(y^+) + B \quad (4.1)$$

where the von Karman constant κ and constant B are independent of the Reynolds number. It is common knowledge that this method is considered not very accurate because, among others, there is no value of constant κ that would be widely accepted (Zanoun *et al.*, 2003). As often reported in the literature, e.g. (Kendall and Koochesfahani, 2007) the Clauser plot method produces artificially high friction velocities, especially at the low range of Reynolds numbers. For example, for Reynolds numbers in the range of $Re_\theta = 1000-10\,000$ (Blackwelder and Haritonidis, 1983), the friction velocity was reported to have an error varying between 8% and 20% while at

very high Reynolds numbers, the larger extent of a log-linear region improved the accuracy of the Clauser method provided that the value of κ was correctly adopted. According to Nagib *et al.* (2004) for a zero pressure gradient turbulent boundary layer the most of the data are very well represented using the log-law with $\kappa = 0.38$, $B = 4.1$, and the same constants are adopted in the current investigations.

Originally, Clauser chart method involved fitting of the velocity profile with log-line in the overlap layer by changing the value of friction velocity u_τ . In practice, there is also a need to select beginning and end of the region where the logarithmic velocity profile occurs. It introduces user subjectivity, which can result in substantial errors, especially for low Reynolds numbers and for TBL with a strong adverse pressure gradient, where the log region in the overlap layer is hardly observed. For the APG flow the region occupied by the log-law is progressively reduced and the mean velocity profiles will deviate from the logarithmic line resulting in a change of κ and B constants. In the absence of direct measurements of the shear stress, the attempt to preserve constants valid for the ZPG flow, the logarithmic region shifts the profile to the wall. This causes underestimation of shear stress values as shown at Fig. 4.

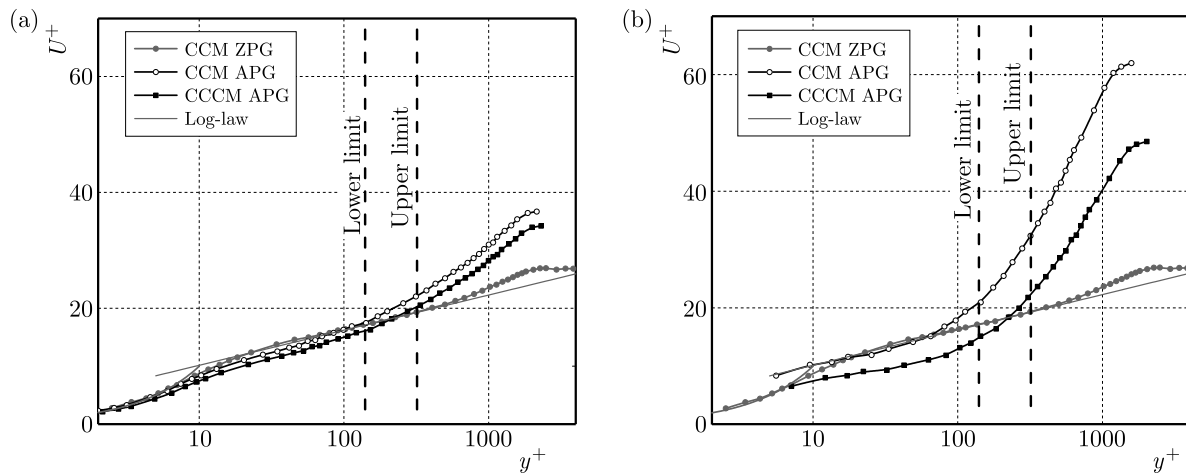


Fig. 4. Comparison of inner scaled mean velocity profiles for $U_{in} = 10$ m/s estimated by the original and corrected Clauser plot method for $x = 700$ mm and $x = 900$ mm

The aim of this study is to propose a very simple extension of the conventional Clauser chart method based on the assumption that the preceding ZPG turbulent boundary layers are correctly defined in viscous units and so that the lower and upper limits of the overlapping logarithmic layer for the analysed Reynolds number are known. It is generally accepted that the near-wall flow is vulnerable to changes in the pressure gradient, preserving however memory of the upstream flow features. As it was mentioned above, the basic problem for this type of flow is the reduction of the logarithmic zone with an increase in β while for the boundary layer approaching separation the mean velocity profile does not even reveal a log region at all. Our concept stems from Mathis *et al.* (2009) observation that for ZPG TBL the centre of large scale structures coincides well with the geometrical centre of the logarithmic region. It could be assumed, therefore, that large scales have an important effect on the shear stress at the wall. However, for APG flow, the region occupied by large-scales is extended above the log region that is why the range of occurrence of the large scale motions, which is the same as the overlap log layer properly defined for ZPG (Drózdź and Elsner, 2017), should be used rather than the log region. As it is suggested in a number of papers e.g. (Vinuesa and Nagib, 2015), the lower boundary of overlapping log layer for ZPG TBL is invariant with the Reynolds number ($y^+ \approx 150$), while the upper boundary can be calculated at a value of $y^+ = 0.15\delta^+$ (as the inner range of the near wall region is $y/\delta = 0.15$) (Mathis *et al.*, 2009), where $\delta^+ = \delta u_\tau/\nu$

is the zero pressure gradient turbulent boundary layer thickness δ presented in viscous units. The above boundaries can be estimated in few iterations using the Clauser chart for the zero pressure gradient case and should be kept constant for the consecutive profiles in APG region, even if there is no logarithmic profile. For flows with $\delta^+ < 1000$, the log region does not exist because the upper and lower boundaries are equal. In this case, the boundaries may be modified slightly by ± 50 viscous units (to obtain range 100-200) to cover at least a few measuring points. Assuming the invariable location of the logarithmic profile in the overlap region, already defined for ZPG where the large scales centers reside, the location of the experimental APG profile is modified using the least-square method such that the R-squared value of the fit, with the logarithmic curve within the above defined overlap layer limits, reaches a maximum (keeping constants equal $\kappa = 0.38$ and $B = 4.1$).

The concept is presented for a lower Reynolds number case in Fig. 4, where two selected mean velocity profiles for two locations $x = 700$ mm (Fig. 4a) and $x = 900$ mm (Fig. 4b) are drawn in inner scaling. Each figure contains the mean ZPG profile (grey dots), the profile plotted according to the original Clauser method (open circles) and the profile plotted according to the corrected Clauser method (dots) as well as the log law line for ZPG flow. In the figures, the boundaries of the defined overlap region are drawn as vertical dashed lines. The first location corresponds to the pressure gradient parameter $\beta = 11$ while the other location corresponds to the incipient detachment (ID) point according to the definition of Simpson (1989), where the pressure gradient parameter β equals to 28.

In both cases, the mean velocity profile drawn according to the conventional Clauser chart method (CCM) is fitted to the log-law but in the region much closer to the wall. Such a fit of the mean profile causes undervaluation of friction velocity u_τ . The CCCM allows one to correct the friction velocity by about 6.7% (from 0.235 to 0.252) for $\beta = 11$, which is consistent with the results obtained by the oil-film interferometry method and by about 21.7% (from 0.13 to 0.166) for $\beta = 28$. There is of course a question about the range of applicability of this methodology and it will be presented in the next Section of the paper.

5. Flow conditions

The diverging measuring section enables generation of a predetermined adverse pressure gradient. The flow conditions in the section can be best described by the pressure coefficient

$$C_p = 1 - \left(\frac{U_\infty}{U_{\infty 0}} \right)^2 \quad (5.1)$$

Here U_∞ is the local and $U_{\infty 0}$ is the inlet freestream velocity determined for $x = 0$ mm. The distributions of C_p are presented in Fig. 5a while Fig. 5b presents the Clauser-Rotta pressure gradient parameter β . The rise of β to 90 for the streamwise distance $x = 1100$ mm generates conditions that increase the susceptibility of the boundary layer to detachment. It should be also noted that, irrespective of two different Reynolds numbers, both C_p and β distributions match well. This confirms that from the point of view of the pressure gradient it is possible to obtain similar external conditions.

Prior to flow analysis in the APG area, verification of the inlet conditions is necessary. The first travers i.e. for $x = 0$ mm is located at the region of zero pressure gradient, so it is easy to check the measured skin friction data against explicit relation of Coles-Fernholz $C_f = 2[(1/\kappa) \ln(\text{Re}_\theta) + B]^{-2}$, which was modified by Nagib *et al.* (2004) (modification of κ and B is valid for the zero pressure gradient boundary layer). The measured, using oil film interferometry, values of skin friction are used to calculate friction coefficients applying $C_f = 2\tau_w/(\rho U_\infty^2)$ formula. The data presented in Fig. 6 confirm the agreement of oil film interferometry readings with the theoretical line in function of the Reynolds number.

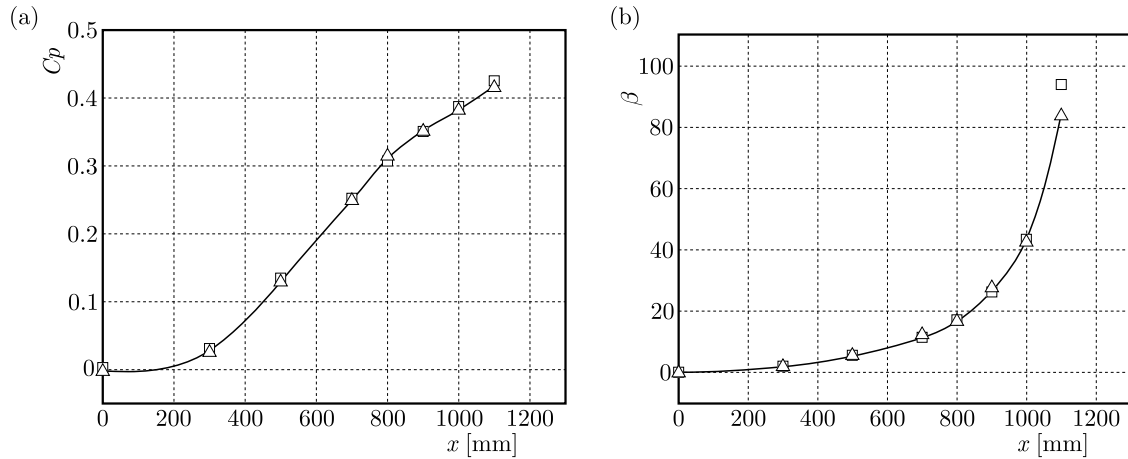


Fig. 5. Distributions of the flow parameters: pressure gradient parameter C_p (a) and Clauser-Rotta pressure gradient parameter β (b)

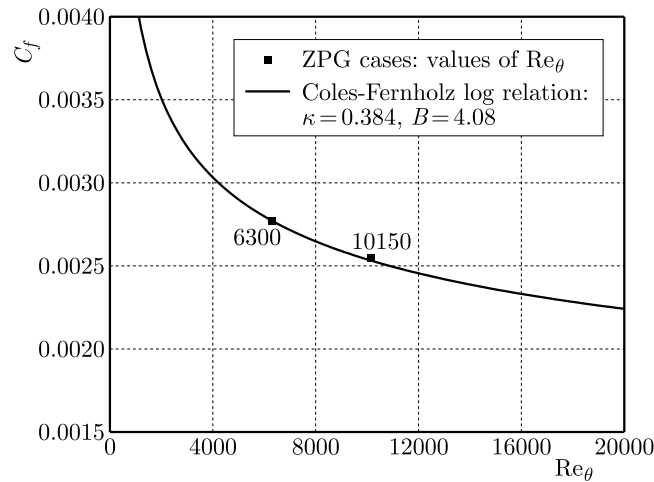


Fig. 6. Friction coefficient relation with the Reynolds number measured at the inlet plane

6. Discussion of the results

Having verified inlet conditions the indirect estimation of skin friction is performed using the Clauser chart method (Clauser, 1956) for consecutive APG traverses up to the incipient of separation. Figure 7 shows the distribution of skin friction along the plate using the CCM (squares) as well as CCCM (circles). Close to the separation, the values obtained by both methods are compared with the reference data obtained by oil-film interferometry (open triangles). For these latter data, the level of measurement uncertainty is shown. Since the measurement uncertainty in absolute terms is estimated to be at the level 0.006 Pa (which is 1% of the ZPG value), the relative value, shown by the uncertainty bars, is almost four times higher for 10 m/s (Fig. 7a) than for 20 m/s (Fig. 7b).

It is clear from Fig. 7a that for lower Reynolds numbers both indirect methods provide consistent results for the distance x up to 500 mm. However, further downstream, where the Clauser-Rotta pressure gradient parameter $\beta \gtrsim 5.0$, the consistency is lost. The first oil – fringe measurement was performed for the $x = 700$ mm and it was the same location where the difference between CCM and CCCM estimations did not agree. Results of the CCCM agree well with oil – fringe measurements and fall within the range of its measurement uncertainty. Further downstream for both Clauser based methods, a decrease of skin friction of about the same order

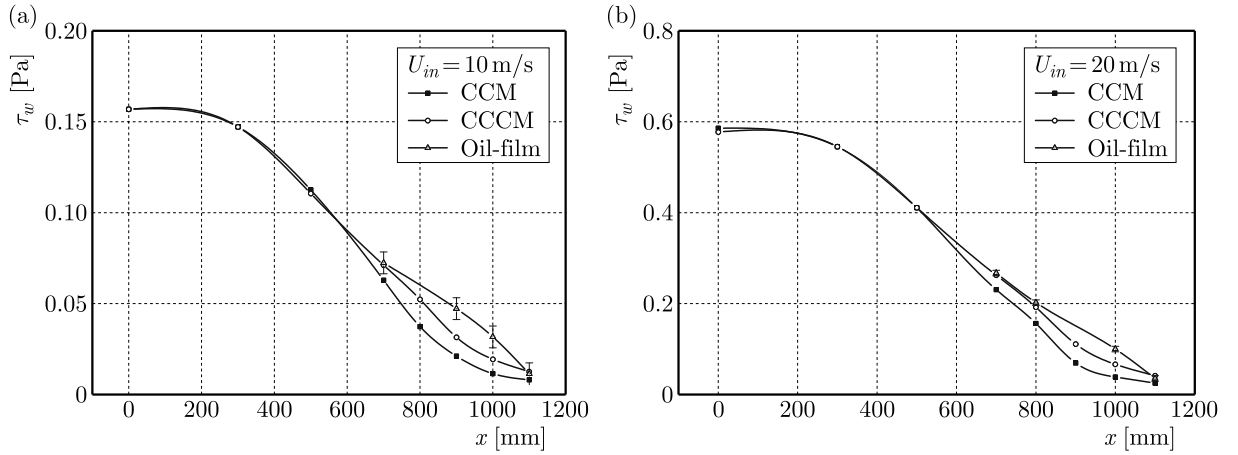


Fig. 7. Comparison of skin friction distributions of the Clauser chart and with the proposed correction verified with oil skin friction (a) 10 m/s and (b) 20 m/s

but with lower values for the original Clauser chart is observed. A slightly different in character is the trend measured for the reference technique. Surprisingly, at the ITD point ($x = 1100$) all three estimations are pretty much the same. For higher Reynolds numbers (Fig. 7b), the stress values are much higher, but the tendency in τ_w changes is maintained. In the latter case, attention shall be paid to the comparability of the CCCM estimation with oil measurements even for pressure parameter β close to 17 ($x = 800$ mm). All measurement data are collected in Table 2. The values which are comparable with OFI method are marked in bold.

Table 2. Comparison of skin friction values

x [mm]	β [-]	$U_{in} = 10$ m/s			$U_{in} = 20$ m/s		
		CCM [Pa]	CCCM [Pa]	OFI [Pa]	CCM [Pa]	CCCM [Pa]	OFI [Pa]
700	11	0.063	0.071	0.072	0.231	0.262	0.267
800	17	0.037	0.051	–	0.156	0.192	0.202
900	28	0.021	0.029	0.047	0.069	0.111	–
1000	43	0.011	0.019	0.032	0.039	0.066	0.100
1100	85	0.008	0.013	0.011	0.025	0.041	0.035

As can be seen at the beginning of detachment ($x = 800$ - 1000 mm), the Clauser chart method significantly lowers the skin friction. Lack of near wall flow similarity with canonical flow and a departure of the mean velocity profile from the log-line may be due to various reasons. According to Knopp *et al.* (2013), this could be attributed to a sudden change of the mean velocity in the streamwise direction. The explanation of this phenomenon can also be carried out based on the analysis of physics of the processes occurring near the wall of the considered flow as it was shown in (Drózdź and Elsner, 2017). It is known that the adverse pressure gradient enhances the large- and small-scale interaction which leads to the rise of small scale convection velocity near the wall. This mechanism is responsible for increasing the momentum near the wall, which leads to the rise of the wall skin friction. The Clauser plot method does not take account of this process because it is based on the assumption that the mean velocity is universal in the whole inner region including the log layer, which is not valid for APG. Since CCCM, to some extent, takes into account the influence of large scale motion that is why its estimations are closer to reality. Close to separation (ITD point), due to the drop of energy of the small scales (convection velocity is no longer efficient in increasing the momentum), this effect is weaker, which may be the reason for more consistent results obtained by all methods.

Available literature data (Madad *et al.*, 2010) suggest that the Clauser chart method is applicable only for zero and weak adverse pressure gradient flows. They showed that beyond $\beta = 2.0$ the difference in the reference to the oil interferometry method becomes significant (approximately 10% difference of C_f). However, the proposed modification extends the upper limit of usable range of the Clauser chart method from $\beta \approx 2.0$ (Monty *et al.*, 2011) up to $\beta \approx 11.0$. On the other hand, for low friction velocity and close to separation, the application of any method is problematical because of large uncertainty level.

It is well known that the impact of large-small scale interaction on the near wall region increases with the Reynolds number. As it was shown in (Drózdź and Elsner, 2017), the difference between velocity profiles for two considered Reynolds numbers was not significant even close the separation. However, the Reynolds stress profiles and spectral analysis shows the increase of small scale energy close the wall with the Reynolds number due to the process of modulation of near wall small scales by large scales from the outer zone. An increase of Reynolds stress indicates an increase of the strain rate (dU/dy) close the wall, therefore it can be expected that it will also be noticeable on skin friction. In order to show the effect of the Reynolds number on the turbulent boundary layer for the same distribution of C_p in this area the results from Fig. 7 (only CCCM and OFI) are reduced by the inlet zero pressure gradient (ZPG) friction velocity $u_{\tau ZPG}$ and are shown in Fig. 8. The oil fringe values are approximated by a linear function (dashed dot line for 10 m/s and dashed line for 20 m/s). The uncertainty levels are also provided in relevant scaling. The results demonstrate that for the same pressure conditions, although differing in the number of Re, the distributions of reduced friction velocity do not reveal influence (in the uncertainty range). The reason for the lack of the Reynolds number effect may be due to a low Reynolds number difference. Further research should be carried out for a wider range of Reynolds numbers to prove the effect.

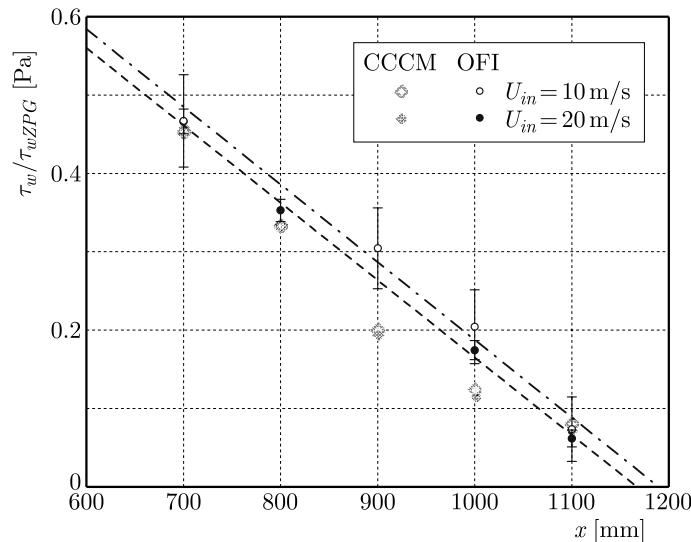


Fig. 8. Reduced skin friction distributions obtained with oil-film interferometry and CCCM. Reduced by its ZPG value

7. Summary and conclusions

The goal of the study is to verify applicability of the Clauser chart method and thin-oil film interferometry technique for a very demanding case. Difficulty of the analyzed problem does not rise only from a strong history effect of the flow, but also from a low shear stress, where their estimation may be associated with large measuring errors. The skin friction measurements in the turbulent boundary layer approaching separation are performed for two different Reynolds

numbers with the same distribution of the pressure coefficient C_P . The results are compared with the corrected Clauser chart method (CCCM) which is introduced in the paper. This corrected Clauser chart method involves only one iteration, while the other methods, as the modified Clauser chart method (MCCM), employ a twofold iterative procedure (one iteration on C_f and the other on pressure gradient coefficient). It is found that the skin friction distributions obtained by the CCCM method agree very well with the reference oil-film interferometry data (within the uncertainty range of oil-film interferometry) up to Incipient Detachment point. Further downstream, an underestimation of the CCCM in reference to the oil-film interferometry method is observed. An explanation of this effect is proposed, in which attention is paid to the importance of large-small scales interaction leading to deformation of the mean velocity profile near the wall which makes the Clauser plot method inapplicable for flows with strong pressure gradient. This effect is present up to Intermittent Transitory Detachment point, where due to increased fraction of reversed flow the drop of energy of the small scales is observed. Close to the separation ($\tau_w < 0.3$ m/s), applicability of any method is problematic because of large uncertainty of any applied techniques. The effect of the Reynolds number for the same pressure gradient conditions is not observable for the analysed Reynolds number range.

Acknowledgement

The investigation was supported by National Science Centre under Grant No. DEC-2012/07/B/ST8/03791.

References

1. BLACKWELDER R.F., HARITONIDIS J.H., 1983, Scaling of the bursting frequency in turbulent boundary layers, *Journal of Fluid Mechanics*, **132**, 1, 87
2. BOBKE A., VINUESA R., ÖRLÜ R., SCHLATTER P., 2017, History effects and near-equilibrium in adverse- pressure-gradient turbulent boundary layers adverse-pressure-gradient turbulent, *Journal of Fluid Mechanics*, **820** (April), 667-692
3. CASTILLO L., JOHANSSON T.G., 2002, The effects of the upstream conditions on a low Reynolds number turbulent boundary layer with zero pressure gradient, *Journal of Turbulence*, **3**, 31, 1-19
4. CLAUSER F.H., 1956, The turbulent boundary layer, *Advances in Applied Mechanics*, **4**, 1-51
5. DIXIT S.A., RAMESH O.N., 2009, Determination of skin friction in strong pressure-gradient equilibrium and near-equilibrium turbulent boundary layers, *Experiments in Fluids*, **47**, 6, 1045-1058
6. DRÓZDŹ A., ELSNER W., 2017, An experimental study of turbulent boundary layers approaching separation, *International Journal of Heat and Fluid Flow*, **68C** (April), 337-347
7. DRÓZDŹ A., ELSNER W., DROBNIAK S., 2008, Application of oil-fringe interferometry for measurements of wall shear stress, *Turbomachinery*, **133**, 103-110
8. HUTCHINS N., CHOI K.S., 2002, Accurate measurements of local skin friction coefficient using hot-wire anemometry, *Progress in Aerospace Sciences*, **38**, 4/5, 421-446
9. IKEYA Y., ÖRLÜ R., FUKAGATA K., ALFREDSSON P.H., 2017. Towards a theoretical model of heat transfer for hot-wire anemometry close to solid walls, *International Journal of Heat and Fluid Flow*, **68**, 248-256, DOI: 10.1016/j.ijheatfluidflow.2017.09.002
10. JORGENSEN F.E., 2002, *How to Measure Turbulence with Hot-Wire Anemometers – a Practical Guide*, Dantec Dynamics A/S, P.O. Box 121, Tonsbakken 16-18, DK-2740 Skovlunde, Denmark
11. KENDALL A., KOOCHEFAHANI M., 2007, A method for estimating wall friction in turbulent wall-bounded flows, *Experiments in Fluids*, **44**, 5, 773-780
12. KNOPP T., SCHANZ D., SCHRÖDER A., DUMITRA M., CIERPKA C., HAIN R., KÄHLER C.J., 2013, Experimental investigation of the log-law for an adverse pressure gradient turbulent boundary layer flow at $Re_\theta = 10000$, *Flow, Turbulence and Combustion*, **92**, 1/2, 451-471

13. MADAD R., HARUN Z., CHAUHAN K., MONTY J.P., MARUSIC I., 2010, Skin friction measurement in zero and adverse pressure gradient boundary layers using oil film interferometry, *17th Australasian Fluid Mechanics Conference 2010*
14. MATHIS R., HUTCHINS N., MARUSIC I., 2009, Large-scale amplitude modulation of the small-scale structures in turbulent boundary layers, *Journal of Fluid Mechanics*, **628** (2009), 311
15. MONTY J.P.P., HARUN Z., MARUSIC I., 2011, A parametric study of adverse pressure gradient turbulent boundary layers, *International Journal of Heat and Fluid Flow*, **32**, 3, 575-585
16. NAGIB H., CHRISTOPHOROU C., RÜEDI J.-D., MONKEWITZ P., OSTERLUND J., GRAVANTE S., CHAUHAN K., PELIVAN I., 2004, Can we ever rely on results from wall-bounded turbulent flows without direct measurements of wall shear stress?, *24th AIAA Aerodynamic Measurement Technology and Ground Testing Conference*
17. PAILHAS G., BARRICAU P., TOUVET Y., PERRET L., 2009, Friction measurement in zero and adverse pressure gradient boundary layer using oil droplet interferometric method, *Experiments in Fluids*, **47**, 2, 195-207
18. SEGALINI A., RÜEDI J.-D., MONKEWITZ P.A., 2015, Systematic errors of skin-friction measurements by oil-film interferometry, *Journal of Fluid Mechanics*, **773**, 298-326
19. SIMPSON R.L., 1989, Turbulent boundary-layer separation, *Annual Review of Fluid Mechanics*, **21**, 205-234
20. TANNER L.H., BLOWS L.G., 1976, A study of the motion of oil films on surfaces in air flow, with application to the measurement of skin friction, *Journal of Physics E*, **9**, 3, 194-202
21. VINUESA R., NAGIB H.M., 2015, Enhancing the accuracy of measurement techniques in high Reynolds number turbulent boundary layers for more representative comparison to their canonical representations, *European Journal of Mechanics – B/Fluids*, November
22. ZANOUN E.S., DURST F., NAGIB H., 2003, Evaluating the law of the wall in two-dimensional fully developed turbulent channel flows, *Physics of Fluids*, **15**, 10, 3079-3089

Manuscript received December 15, 2017; accepted for print December 21, 2017

A TWO-DIMENSIONAL FINITE ELEMENT MODEL OF THE GRAIN BOUNDARY BASED ON THERMO-MECHANICAL STRAIN GRADIENT PLASTICITY

YOUSEOB SONG, **GEORGE Z. VOYIADJIS**

*Louisiana State University, Department of Civil and Environmental Engineering, Baton Rouge, LA, USA
e-mail: voyiadjis@eng.lsu.edu*

In this work, a two-dimensional finite element model for the grain boundary flow rule is developed based on the thermo-mechanical gradient-enhanced plasticity theory. The proposed model is temperature-dependent. A special attention is given to physical and micromechanical nature of dislocation interactions in combination with thermal activation on stored and dissipated energy. Thermodynamic conjugate microforces are decomposed into energetic and dissipative components. Correspondingly, two different grain boundary material length scales are present in the proposed model. Finally, numerical examples are solved in order to explore characteristics of the proposed grain boundary flow rule.

Keywords: strain gradient plasticity, grain boundary, energetic, dissipative, 2D FEM

1. Introduction

It is well known that the free surface may act as a source of defect development and its propagation towards the grain inside, whereas the grain boundaries block this dislocation movement, consequently, give rise to the strain gradients to accommodate geometrically necessary dislocations (Hirth and Lothe, 1982). In addition, the grain boundaries can be a source of dislocations through transmission of plastic slip to the neighboring grains (Clark *et al.*, 1992). Besides these physical manifestations, from the mathematical viewpoint, nonstandard boundary conditions are necessary at the external boundary of a region for the well-posed governing equations in the implementation of higher order strain gradient plasticity models. Therefore, careful modeling of the grain boundary is important in the continued development of higher order strain gradient plasticity models.

The experimental observations on slip transmission motivate one to assume that the effect of surface/interfacial energy and the global nonlocal energy residual should be non-vanishing. Examples can be found from the in-situ TEM direct observations, see e.g., Lee *et al.* (1989), or using the geometrically necessary dislocation (GND) concept in the description of observations in bicrystallines, e.g., Sun *et al.* (2000) and nanoindentation tests close to the grain boundary, e.g., Soer *et al.* (2005). This results in a new type of the boundary condition, in the context of strain gradient plasticity incorporating the interfacial energy, accounting for the surface resistance to slip transfer due to grain boundary misalignment, see e.g., Aifantis and Willis (2005), Cermelli and Gurtin (2002), Fredriksson and Gudmundson (2007), Gudmundson (2004), Gurtin (2008).

Voyiadjis and co-workers (Voyiadjis *et al.*, 2014, 2017; Voyiadjis and Song, 2017) developed thermodynamically consistent and coupled thermo-mechanical strain gradient plasticity models incorporating the flow rules for both the grain interior and grain boundary to study characteristics of nano/micro-scale metallic materials. In those three works, the finite element analysis

was implemented via a one-dimensional model. As is well known, there is bound to be a fundamental difference between one-dimensional finite element implementation and two-dimensional one. For example, in the one-dimensional case, some special complications, e.g. the resonance between the physical scale and the mesh scale, cannot be considered during simulation. In terms of dimensional extension, there were simple modifications from one-dimensional finite element implementation for the strain gradient plasticity model to the two-dimensional one in Voyiadjis and Song (2017) and Song and Voyiadjis (2018). However, in Voyiadjis and Song (2017), the grain boundary modeling and the effects of temperature and its gradient were not considered, but just addressed the effect of the mechanical component of thermodynamic microforces in terms of the stress jump phenomenon. In addition, in Song and Voyiadjis (2018), only two null boundary conditions, i.e. microscopically free and hard boundary conditions, were considered at the grain boundary to describe the dislocation movement and the plastic flow at the grain boundary areas. In the current work, two-dimensional numerical simulation, in the context of the small deformation framework, is developed incorporating temperature and rate dependent flow rules for the grain interior and grain boundary. The proposed model is applied to the simple shear problem in order to examine the characteristics of the proposed model.

2. Thermodynamically consistent strain gradient plasticity model for grain interior

In this work, tensors are denoted by the subscripts i, j, k, l, m , and n . The superscripts e, p, int, ext, en, dis and etc. imply specific quantities such as elastic state, plastic state, internal, external, energetic, dissipative and etc., respectively. Also, the superimposed dot represents derivative with respect to time, and the indices after a comma represent partial derivatives.

2.1. Principle of virtual power (grain interior)

The internal power \mathcal{P}^{int} is presented with a combination of three energy contributions, i.e. the macro-, micro- and thermal-energy contributions, in an arbitrary region Ω_0 as follows

$$\mathcal{P}^{int} = \int_{\Omega_0} \left(\underbrace{\sigma_{ij} \dot{\epsilon}_{ij}^e}_{Macro} + \underbrace{x \dot{e}^p + Q_i \dot{e}_{,i}^p}_{Micro} + \underbrace{\mathcal{A} \dot{T} + \mathcal{B}_i \dot{T}_{,i}}_{Thermal} \right) dV \quad (2.1)$$

where ϵ_{ij}^e is the elastic part of the strain tensor, e^p is the accumulated plastic strain, x and Q_i are the thermodynamic microforces conjugate respectively to \dot{e}^p and $\dot{e}_{,i}^p$, \mathcal{A} and \mathcal{B}_i are the micromorphic scalar and vector generalized stresses conjugate to the temperature rate \dot{T} and the gradient of the temperature rate $\dot{T}_{,i}$ respectively, and σ_{ij} is the Cauchy stress tensor.

The internal power \mathcal{P}^{int} for Ω_0 is equated with the external power \mathcal{P}^{ext} expended by the macro and microtractions (t_i, m) on the external surface $\partial\Omega_0$ and the body forces acting within Ω_0 as follows

$$\mathcal{P}^{ext} = \int_{\Omega_0} \underbrace{b_i \dot{u}_i}_{Macro} dV + \int_{\partial\Omega_0} \left(\underbrace{t_i \dot{u}_i}_{Macro} + \underbrace{m \dot{e}^p}_{Micro} + \underbrace{a \dot{T}}_{Thermal} \right) dS \quad (2.2)$$

where b_i is the generalized external body force conjugate to the macroscopic velocity \dot{u}_i . Furthermore, it is assumed for the external power to have the term of a conjugate to \dot{T} for the thermal effect.

By using the equation, $\mathcal{P}^{int} = \mathcal{P}^{ext}$, in conjunction with the divergence theorem and factoring out the common terms, the balance equations for the macroscopic linear momentum, nonlocal

microforce and generalized stresses \mathcal{A} and \mathcal{B}_i for the volume Ω_0 can be obtained respectively as follows

$$\sigma_{ij,j} + b_i = 0 \quad \bar{\sigma}_{ij} = (x - Q_{k,k})N_{ij} \quad \mathcal{B}_{i,i} - \mathcal{A} = 0 \quad (2.3)$$

where $\bar{\sigma}_{ij}$ is the deviatoric part of σ_{ij} with the Kronecker delta δ_{ij} ($\bar{\sigma}_{ij} = \sigma_{ij} - \sigma_{kk}\delta_{ij}/3$).

On $\partial\Omega_0$, the balance equations for the local surface traction and the nonlocal microtraction are expressed with the outward unit normal vector to $\partial\Omega_0$, n_i , respectively, as

$$t_j = \sigma_{ij}n_i \quad m = Q_in_i \quad a = \mathcal{B}_in_i \quad (2.4)$$

2.2. Second law of thermodynamics (grain interior)

The second law of thermodynamics introduces a physical base to account for the GNDs distribution in the body. The following entropy production inequality can be obtained based on the basic statement of this law with the specific entropy s and the micromorphic approach by Forest (2009)

$$-\rho\dot{\mathcal{E}} + \rho s\dot{\mathcal{T}} + \sigma_{ij}\dot{\varepsilon}_{ij}^e + x\dot{e}^p + Q_i\dot{e}_{,i}^p + \mathcal{A}\dot{\mathcal{T}} + \mathcal{B}_i\dot{\mathcal{T}}_{,i} - q_i\frac{\dot{\mathcal{T}}_{,i}}{\mathcal{T}} \geq 0 \quad (2.5)$$

The entropy production vector is assumed in this work to be equal to the thermal flux vector divided by temperature, as given in Coleman and Noll (1963).

2.3. Energetic and dissipative thermodynamic microforces (grain interior)

The Helmholtz free energy Ψ (per unit volume) is obtained with the entropy s , internal energy \mathcal{E} and temperature \mathcal{T} describing the current state of the material as $\Psi = \mathcal{E} - \mathcal{T}s$. By using this equation along with Eq. (2.6), the Clausius-Duhem inequality is derived as follows

$$\sigma_{ij}\dot{\varepsilon}_{ij}^e + x\dot{e}^p + Q_i\dot{e}_{,i}^p + \mathcal{A}\dot{\mathcal{T}} + \mathcal{B}_i\dot{\mathcal{T}}_{,i} - \rho\dot{\Psi} - \rho s\dot{\mathcal{T}} - q_i\frac{\dot{\mathcal{T}}_{,i}}{\mathcal{T}} \geq 0 \quad (2.6)$$

For deriving the constitutive equations, the functional form of the Helmholtz free energy, $\Psi = \Psi(\varepsilon_{ij}^e, e^p, e_{,i}^p, \mathcal{T}, \mathcal{T}_{,i})$, is put forward in this work. By taking time derivative of the Helmholtz free energy, $\dot{\Psi}$ is expressed as follows

$$\dot{\Psi} = \frac{\partial\Psi}{\partial\varepsilon_{ij}^e}\dot{\varepsilon}_{ij}^e + \frac{\partial\Psi}{\partial e^p}\dot{e}^p + \frac{\partial\Psi}{\partial e_{,i}^p}\dot{e}_{,i}^p + \frac{\partial\Psi}{\partial\mathcal{T}}\dot{\mathcal{T}} + \frac{\partial\Psi}{\partial\mathcal{T}_{,i}}\dot{\mathcal{T}}_{,i} \quad (2.7)$$

Substituting Eq. (2.7) into Eq. (2.6) and factoring the common terms out gives

$$\begin{aligned} & \left(\sigma_{ij} - \rho\frac{\partial\Psi}{\partial\varepsilon_{ij}^e}\right)\dot{\varepsilon}_{ij}^e + \left(x - \rho\frac{\partial\Psi}{\partial e^p}\right)\dot{e}^p + \left(Q_i - \rho\frac{\partial\Psi}{\partial e_{,i}^p}\right)\dot{e}_{,i}^p \\ & + \left(\mathcal{A} - \rho s - \rho\frac{\partial\Psi}{\partial\mathcal{T}}\right)\dot{\mathcal{T}} + \left(\mathcal{B}_i - \rho\frac{\partial\Psi}{\partial\mathcal{T}_{,i}}\right)\dot{\mathcal{T}}_{,i} - \frac{q_i}{\mathcal{T}}\dot{\mathcal{T}}_{,i} \geq 0 \end{aligned} \quad (2.8)$$

Meanwhile, the thermodynamic conjugate microforces x , Q_i and \mathcal{A} are assumed to be decomposed into the energetic and the dissipative elements as follows

$$x = x^{en} + x^{dis} \quad Q_i = Q_i^{en} + Q_i^{dis} \quad \mathcal{A} = \mathcal{A}^{en} + \mathcal{A}^{dis} \quad (2.9)$$

Substituting Eq. (2.9) into Eq. (2.8) and rearranging them in accordance with the energetic and the dissipative parts results in the following expression

$$\begin{aligned} & \left(\sigma_{ij} - \rho\frac{\partial\Psi}{\partial\varepsilon_{ij}^e}\right)\dot{\varepsilon}_{ij}^e + \left(x^{en} - \rho\frac{\partial\Psi}{\partial e^p}\right)\dot{e}^p + \left(Q_i^{en} - \rho\frac{\partial\Psi}{\partial e_{,i}^p}\right)\dot{e}_{,i}^p + \left(\mathcal{A}^{en} - \rho s - \rho\frac{\partial\Psi}{\partial\mathcal{T}}\right)\dot{\mathcal{T}} \\ & + \left(\mathcal{B}_i - \rho\frac{\partial\Psi}{\partial\mathcal{T}_{,i}}\right)\dot{\mathcal{T}}_{,i} + x^{dis}\dot{e}^p + Q_i^{dis}\dot{e}_{,i}^p + \mathcal{A}^{dis}\dot{\mathcal{T}} - \frac{q_i}{\mathcal{T}}\dot{\mathcal{T}}_{,i} \geq 0 \end{aligned} \quad (2.10)$$

By assuming that the fifth term in Eq. (2.10) is strictly energetic, the energetic components of the thermodynamic microforces are defined as follows

$$\begin{aligned} \sigma_{ij} &= \rho \frac{\partial \Psi}{\partial \varepsilon_{ij}^e} & x^{en} &= \rho \frac{\partial \Psi}{\partial e^p} & Q_i^{en} &= \rho \frac{\partial \Psi}{\partial e_{,i}^p} \\ \mathcal{A}^{en} &= \rho \left(s + \frac{\partial \Psi}{\partial \mathcal{T}} \right) & \mathcal{B}_i &= \rho \frac{\partial \Psi}{\partial \mathcal{T}_{,i}} \end{aligned} \quad (2.11)$$

The dissipation density per unit time \mathcal{D} is then obtained as

$$\mathcal{D} = x^{dis} \dot{e}^p + Q_i^{dis} \dot{e}_{,i}^p + \mathcal{A}^{dis} \dot{\mathcal{T}} - \frac{q_i}{\mathcal{T}} \mathcal{T}_{,i} \geq 0 \quad (2.12)$$

The dissipative counterparts of the thermodynamic microforces are obtained from the dissipation potential $\mathcal{D}(\dot{e}^p, \dot{e}_{,i}^p, \dot{\mathcal{T}}, \mathcal{T}_{,i})$ as follows

$$x^{dis} = \frac{\partial \mathcal{D}}{\partial \dot{e}^p} \quad Q_i^{dis} = \frac{\partial \mathcal{D}}{\partial \dot{e}_{,i}^p} \quad \mathcal{A}^{dis} = \frac{\partial \mathcal{D}}{\partial \dot{\mathcal{T}}} \quad -\frac{q_i}{\mathcal{T}} = \frac{\partial \mathcal{D}}{\partial \mathcal{T}_{,i}} \quad (2.13)$$

2.4. Constitutive equations for the admissible potentials (grain interior)

2.4.1. Energetic constitutive relations

It is important to define the proper formulation of the Helmholtz free energy Ψ because it establishes the basis for the derivation of constitutive relations. In the current work, the Helmholtz free energy function is put forward as follows (Voyiadjis and Song, 2017; Voyiadjis *et al.*, 2017)

$$\begin{aligned} \Psi &= \frac{1}{2\rho} \varepsilon_{ij}^e E_{ijkl} \varepsilon_{kl}^e - \frac{\alpha^{th}}{\rho} (\mathcal{T} - \mathcal{T}_r) \varepsilon_{ij}^e \delta_{ij} + \frac{\mathcal{H}_0}{\rho(r+1)} \left[1 - \left(\frac{\mathcal{T}}{\mathcal{T}_y} \right)^n \right] (e^p)^{r+1} \\ &+ \frac{\sigma_0}{\rho(\vartheta+1)} [\ell_{en}^2 (e_{,i}^p e_{,i}^p)]^{\frac{\vartheta+1}{2}} - \frac{1}{2} \frac{c_\varepsilon}{\mathcal{T}_r} (\mathcal{T} - \mathcal{T}_r)^2 - \frac{1}{2\rho} a \mathcal{T}_{,i} \mathcal{T}_{,i} \end{aligned} \quad (2.14)$$

where α^{th} is the thermal expansion coefficient, E_{ijkl} is the elastic modulus tensor, \mathcal{H}_0 is the standard isotropic hardening parameter, r ($0 < r < 1$) is the isotropic hardening material parameter, \mathcal{T}_y and n are the thermal material parameters, $\sigma_0 > 0$ is the stress-dimensioned scaling parameter to explain the initial slip resistance, ℓ_{en} is the energetic material length scale describing the feature of short-range interaction of the GNDs, a is the material constant for the isotropic heat conduction, ϑ is the parameter of governing nonlinearity of the gradient dependent defect energy, $\mathcal{T}_r > 0$ is the reference temperature, and c_ε is the specific heat capacity at a constant stress.

One can now obtain the energetic thermodynamic forces by using Eqs. (2.11) and (2.14) as follows

$$\begin{aligned} \sigma_{ij} &= E_{ijkl} \varepsilon_{kl}^e - \alpha^{th} (\mathcal{T} - \mathcal{T}_r) \delta_{ij} & x^{en} &= \mathcal{H}_0 \left[1 - \left(\frac{\mathcal{T}}{\mathcal{T}_y} \right)^n \right] (e^p)^r \\ Q_i^{en} &= \sigma_0 \ell_{en}^2 [\ell_{en}^2 (e_{,k}^p e_{,k}^p)]^{\frac{\vartheta-1}{2}} e_{,i}^p \\ \mathcal{A}^{en} &= \rho s - \alpha^{th} (\mathcal{T} - \mathcal{T}_r) \varepsilon_{ij}^e \delta_{ij} - \frac{c_\varepsilon}{\mathcal{T}_r} (\mathcal{T} - \mathcal{T}_r) - \frac{\mathcal{H}_0 (e^p)^{r+1}}{r+1} \frac{\mathcal{T}}{\mathcal{T}_y} \left(\frac{\mathcal{T}}{\mathcal{T}_y} \right)^{n-1} \\ \mathcal{B}_i &= -a \mathcal{T}_{,i} \end{aligned} \quad (2.15)$$

2.4.2. Dissipative constitutive relations

In this work, the following functional form of the dissipation potential is put forward

$$\begin{aligned} \mathcal{D} = & \sigma_0 \sqrt{\mathcal{H}^2(e^p) + \ell_{N-G}\varepsilon^p} \left[1 - \left(\frac{\mathcal{T}}{\mathcal{T}_y} \right)^n \right] \left(\frac{\dot{e}^p}{\dot{p}_1} \right)^{m_1} \dot{e}^p \\ & + \sigma_0 \left[1 - \left(\frac{\mathcal{T}}{\mathcal{T}_y} \right)^n \right] \left(\frac{\dot{p}}{\dot{p}_2} \right)^{m_2} \dot{p} - \frac{\varsigma}{2} \dot{\mathcal{T}}^2 - \frac{1}{2} \frac{k(\mathcal{T})}{\mathcal{T}} \mathcal{T}_{,i} \mathcal{T}_{,i} \end{aligned} \quad (2.16)$$

where \dot{p}_1 and \dot{p}_2 are the non-negative reference rates, m_1 and m_2 are the non-negative rate sensitivity parameters, ς is the material constant characterizing the energy exchange between phonon and electron, and $k(\mathcal{T})$ is the thermal conductivity coefficient. The N-G material length scale ℓ_{N-G} was first introduced by Nix and Gao (1998). In the special case $\ell_{N-G} = 0$ and $\mathcal{H}(e^p) = 1$. The first term in RHS reduces to $\sigma_0 (1 - (\mathcal{T}/\mathcal{T}_y)^n) (\dot{e}^p/\dot{p}_1)^{m_1} \dot{e}^p$, a form used by Voyiadjis and Song (2017). ε^p is a scalar measure of an effective plastic strain gradient defined by $\varepsilon^p \stackrel{\text{def}}{=} \|\alpha_{ij}\| = b\rho_G$ with the magnitude of the Burgers vector b , Nye dislocation density tensor α_{ij} and the total GNDs density ρ_G .

The parameter \dot{p} is a scalar measuring the plastic strain rate gradient, which is defined by

$$\dot{p} \stackrel{\text{def}}{=} \ell_{dis} \|\dot{e}_{,i}^p\| = \ell_{dis} \sqrt{\dot{e}_{,i}^p \dot{e}_{,i}^p} \quad (2.17)$$

where ℓ_{dis} is the dissipative material length scale.

The dimensionless function $\mathcal{H}(e^p)$ is related to the strain hardening/softening behavior. In the current work, the following form of the mixed-hardening function is adopted (Voce, 1955)

$$\mathcal{H}(e^p) = 1 + (\chi - 1) [1 - \exp(-\omega e^p)] + \frac{\mathcal{H}_0}{\sigma_0} e^p \quad (2.18)$$

where χ and ω are the material parameters. The strain hardening, strain softening and strain hardening/softening can be modeled based on the particular choices for these parameters.

Using the dissipative potential given in Eq. (2.16) along with Eq. (2.13) and considering $k(\mathcal{T})/\mathcal{T} = k_0 = \text{const}$, the constitutive relations for the dissipative microforces are obtained as follows

$$\begin{aligned} x^{dis} &= \sigma_0 \sqrt{\mathcal{H}^2(e^p) + \ell_{N-G}\varepsilon^p} \left[1 - \left(\frac{\mathcal{T}}{\mathcal{T}_y} \right)^n \right] \left(\frac{\dot{e}^p}{\dot{p}_1} \right)^{m_1} \\ Q_i^{dis} &= \sigma_0 \ell_{dis}^2 (m_2 + 1) \left[1 - \left(\frac{\mathcal{T}}{\mathcal{T}_y} \right)^n \right] \left(\frac{\dot{p}}{\dot{p}_2} \right)^{m_2} \frac{\dot{e}_{,i}^p}{\dot{p}} \\ \mathcal{A}^{dis} &= -\varsigma \dot{\mathcal{T}} \quad \frac{q_i}{\mathcal{T}} = k_0 \mathcal{T}_{,i} \end{aligned} \quad (2.19)$$

2.5. Flow rule (grain interior)

The flow rule is established based on the nonlocal microforce balance, Eq. (2.3), and strengthened by thermodynamically consistent constitutive relations for energetic and dissipative microforces. By considering the backstress in the microforce equilibrium such as $\bar{\sigma}_{ij} - (-Q_{k,k}^{en}) N_{ij} = (x - Q_{k,k}^{dis}) N_{ij}$, one can obtain a second order partial differential flow rule as follows

$$\begin{aligned} \bar{\sigma}_{ij} - \left\{ -\sigma_0 \ell_{en}^2 [\ell_{en}^2 (e_{,i}^p e_{,i}^p)]^{\frac{q-1}{2}} e_{,kk}^p \right\} N_{ij} &= \left\{ \mathcal{H}_0 \left[1 - \left(\frac{\mathcal{T}}{\mathcal{T}_y} \right)^n \right] (e^p)^r \right. \\ &+ \sigma_0 \sqrt{\mathcal{H}^2(e^p) + \ell_{N-G}\varepsilon^p} \left[1 - \left(\frac{\mathcal{T}}{\mathcal{T}_y} \right)^n \right] \left(\frac{\dot{e}^p}{\dot{p}_1} \right)^{m_1} \\ &\left. - \sigma_0 \ell_{dis}^2 (m_2 + 1) \left[1 - \left(\frac{\mathcal{T}}{\mathcal{T}_y} \right)^n \right] \left(\frac{\dot{p}}{\dot{p}_2} \right)^{m_2} \frac{\dot{e}_{,kk}^p}{\dot{p}} \right\} N_{ij} \end{aligned} \quad (2.20)$$

where N_{ij} is the direction of plastic flow given by $N_{ij} = \dot{\varepsilon}_{ij}^p / \dot{e}^p$.

3. Thermodynamically consistent strain gradient plasticity model for the grain boundary

The main goal of this study is to develop a thermodynamically consistent gradient-enhanced plasticity model for the grain boundary, which should be also consistent with the one for the grain interior addressed in Section 2. Hereafter, the superscript GB and the expression GB will be used to denote specific variables at the grain boundary.

3.1. Principle of virtual power (grain boundary)

Two grains \mathcal{G}_1 and \mathcal{G}_2 separated by the grain boundary are taken into account in this work, and the displacement field is assumed to be continuous, i.e. $u_i^{\mathcal{G}_1} = u_i^{\mathcal{G}_2}$, across the grain boundary. The internal part of the principle of virtual power for the grain boundary is assumed to depend on the GB accumulated plastic strain rates $\dot{\epsilon}^{p^{GB\mathcal{G}_1}}$ at $S^{GB\mathcal{G}_1}$ and $\dot{\epsilon}^{p^{GB\mathcal{G}_2}}$ at $S^{GB\mathcal{G}_2}$ in the arbitrary surface S^{GB} of the grain boundary as follows

$$\mathcal{P}^{int^{GB}} = \int_{S^{GB}} (\mathbb{M}^{GB\mathcal{G}_1} \dot{\epsilon}^{p^{GB\mathcal{G}_1}} + \mathbb{M}^{GB\mathcal{G}_2} \dot{\epsilon}^{p^{GB\mathcal{G}_2}}) dS^{GB} \quad (3.1)$$

where the GB microscopic moment tractions $\mathbb{M}^{GB\mathcal{G}_1}$ and $\mathbb{M}^{GB\mathcal{G}_2}$ are assumed to expend the power over $\dot{\epsilon}^{p^{GB\mathcal{G}_1}}$ and $\dot{\epsilon}^{p^{GB\mathcal{G}_2}}$, respectively. In addition, the GB external power $\mathcal{P}^{ext^{GB}}$ is expended by the macrotractions $\sigma_{ij}^{\mathcal{G}_1}(-n_j^{GB})$ and $\sigma_{ij}^{\mathcal{G}_2}(n_j^{GB})$ conjugate to the macroscopic velocity \dot{u}_i , and the microtractions $\mathbb{Q}_k^{\mathcal{G}_1}(-n_k^{GB})$ and $\mathbb{Q}_k^{\mathcal{G}_2}(n_k^{GB})$ that are conjugate to $\dot{\epsilon}_{ij}^{p^{GB\mathcal{G}_1}}$ and $\dot{\epsilon}_{ij}^{p^{GB\mathcal{G}_2}}$, respectively, as follows

$$\mathcal{P}^{ext^{GB}} = \int_{S^{GB}} [(\sigma_{ij}^{\mathcal{G}_2} n_j^{GB} - \sigma_{ij}^{\mathcal{G}_1} n_j^{GB}) \dot{u}_i + \mathbb{Q}_k^{\mathcal{G}_2} n_k^{GB} \dot{\epsilon}^{p^{GB\mathcal{G}_2}} - \mathbb{Q}_k^{\mathcal{G}_1} n_k^{GB} \dot{\epsilon}^{p^{GB\mathcal{G}_1}}] dS^{GB} \quad (3.2)$$

where \mathbf{n}^{GB} is the unit outward normal vector of the grain boundary surface. From $\mathcal{P}^{int^{GB}} = \mathcal{P}^{ext^{GB}}$, the macro- and microforce balances for the grain boundary are obtained as follows

$$(\sigma_{ij}^{\mathcal{G}_1} - \sigma_{ij}^{\mathcal{G}_2}) n_j^{GB} \quad \mathbb{M}^{GB\mathcal{G}_1} + \mathbb{Q}_k^{\mathcal{G}_1} n_k^{GB} = 0 \quad \mathbb{M}^{GB\mathcal{G}_2} - \mathbb{Q}_k^{\mathcal{G}_2} n_k^{GB} = 0 \quad (3.3)$$

3.2. Laws of thermodynamics (grain boundary)

The first and second laws of thermodynamics are considered to construct the thermodynamically consistent gradient- and temperature-enhanced framework for the grain boundary as follows

$$\begin{aligned} \dot{\mathcal{E}}^{GB} &= \mathbb{M}^{GB} \dot{\epsilon}^{p^{GB}} + q_i^{GB} n_i^{GB} \\ \dot{s}^{GB} \mathcal{T}^{GB} - q_i^{GB} n_i^{GB} &\geq 0 \end{aligned} \quad (3.4)$$

where \mathcal{E}^{GB} is the GB surface energy density, q_i^{GB} is the GB heat flux vector and s^{GB} is the surface density of entropy of the grain boundary.

3.3. Energetic and dissipative thermodynamic microforces (grain boundary)

By using the time derivative of the equation, $\dot{\Psi}^{GB} = \dot{\mathcal{E}}^{GB} - \mathcal{T}^{GB} \dot{s}^{GB}$, and substituting it into Eqs. (3.4), the following Clausius-Duhem inequality for the grain boundary is obtained

$$\mathbb{M}^{GB} \dot{\epsilon}^{p^{GB}} - \dot{\Psi}^{GB} - s^{GB} \dot{\mathcal{T}}^{GB} \geq 0 \quad (3.5)$$

Suppose the isothermal condition for the grain boundary ($\dot{\mathcal{T}}^{GB} = 0$) and the Helmholtz free energy for the grain boundary is given by $\Psi^{GB} = \Psi^{GB}(e^{p^{GB}})$. Substituting the time derivative of Ψ^{GB} into Eq. (3.5) gives the following inequality

$$\mathbb{M}^{GB} \dot{e}^{p^{GB}} - \rho \frac{\partial \Psi^{GB}}{\partial e^{p^{GB}}} \dot{e}^{p^{GB}} \geq 0 \quad (3.6)$$

The GB thermodynamic microforce quantity \mathbb{M}^{GB} is further assumed to be decomposed into the energy and dissipative components such as $\mathbb{M}^{GB} = \mathbb{M}^{GB,en} + \mathbb{M}^{GB,dis}$. The components $\mathbb{M}^{GB,en}$ and $\mathbb{M}^{GB,dis}$ indicate the mechanisms for the pre- and post-slip transfer, and thus involve the plastic strain at the grain boundary prior to the slip transfer $e^{p^{GB(pre)}}$ and the one after the slip transfer $e^{p^{GB(post)}}$, respectively, ($e^{p^{GB}} = e^{p^{GB(pre)}} + e^{p^{GB(post)}}$). From Eq. (3.6)

$$\left(\mathbb{M}^{GB,en} - \rho \frac{\partial \Psi^{GB}}{\partial e^{p^{GB}}} \right) \dot{e}^{p^{GB}} + \mathbb{M}^{GB,dis} \dot{e}^{p^{GB}} \geq 0 \quad (3.7)$$

The GB energetic microforce can be obtained as

$$\mathbb{M}^{GB,en} = \rho \frac{\partial \Psi^{GB}}{\partial e^{p^{GB}}} \quad (3.8)$$

Hence the GB dissipative microforce can then be obtained as

$$\mathbb{M}^{GB,dis} = \frac{\partial \mathcal{D}^{GB}}{\partial \dot{e}^{p^{GB}}} \quad (3.9)$$

where \mathcal{D}^{GB} is the non-negative dissipation density per unit time for the grain boundary, given by $\mathcal{D}^{GB} = \mathbb{M}^{GB,dis} \dot{e}^{p^{GB}} \geq 0$. This non-negative plastic dissipation condition can be satisfied when the GB plastic dissipation potential is a convex function of the GB accumulated plastic strain rate.

3.4. Energetic and dissipative thermodynamic microforces (grain boundary)

In this work, it is assumed, following Fredriksson and Gudmundson (2007), that the GB Helmholtz free energy per unit surface has the form of a general power law as follows

$$\Psi^{GB}(e^{p^{GB}}) = \frac{1}{2} G \ell_{en}^{GB} (e^{p^{GB(pre)}})^2 \quad (3.10)$$

where G is the shear modulus in the case of isotropic linear elasticity, ℓ_{en}^{GB} is the GB energetic length scale. By substituting Eq. (3.10) into Eq. (3.8), the GB energetic microforce quantity can be obtained as follows

$$\mathbb{M}^{GB,en} = G \ell_{en}^{GB} e^{p^{GB(pre)}} \quad (3.11)$$

Note that $\mathbb{M}^{GB,en}$ is independent of the plastic strain rate and temperature since this variable comes from the recoverable stored energy.

Meanwhile, two major factors might be identified affecting energy dissipation when the dislocations move in the grain boundary area (Aifantis and Willis, 2005). When the dislocations encounter a grain boundary, they pile up there. Slip can transmit to the adjacent grain only when the stress field ahead of the pileup is high enough. Direct observation of the process using transmission electron microscopy (TEM) also shows that the main mechanisms for the aforementioned slip transmission are dislocation absorption and re-emission for low angle boundaries (Soer *et al.*, 2005) and the dislocation nucleation in the adjacent grain for high angle boundaries (Ohmura *et al.*, 2004), respectively. As soon as deformation initiates in the adjacent grain, the

grain boundary begins to deform and the plastic strain on the grain boundary increases. The energy associated with the deformation of the grain boundary in this case is taken to be mainly due to energy dissipation as the dislocations move in the grain boundary region. In addition, considering the resistance force to dislocation motion being temperature and rate dependent, this energy dissipation can be taken as a linear function of the GB plastic strain.

Moreover, a change in the grain boundary area can also affect the energy dissipation. The macroscopic accumulated plastic strain at the grain boundary, e^{pGB} , can be related to microscopic deformation of the grain boundary through the root-mean-square of the gradient of this deformation. In addition, the energy change after the grain boundary has yielded, i.e. the onset of slip transmission, can be approximated by a quadratic function of the aforementioned displacement gradient at microscale and hence the GB plastic strain at macroscale.

Combining both the aforementioned mechanisms, i.e. a change in the grain boundary area and deformation of the grain boundary due to the dislocation movement, involved in the energy dissipation due to plastic strain transfer across the grain boundary, one can postulate the following generalized expression for the GB dissipation potential

$$\mathcal{D}^{GB} = \frac{\ell_{dis}^{GB}}{m^{GB} + 1} (\sigma_0^{GB} + \mathcal{H}_0^{GB} e^{pGB(post)}) \left(1 - \frac{\mathcal{T}^{GB}}{\mathcal{T}_y^{GB}}\right)^{n^{GB}} \left(\frac{\dot{e}^{pGB(post)}}{\dot{p}^{GB}}\right)^{m^{GB}} \dot{e}^{pGB(post)} \geq 0 \quad (3.12)$$

where ℓ_{dis}^{GB} is the GB dissipative length scale, m^{GB} and \dot{p}^{GB} are the viscous related material parameters, σ_0^{GB} is a constant accounting for the GB yield stress, \mathcal{H}_0^{GB} is the GB hardening parameter, \mathcal{T}_y^{GB} is the scale-independent GB thermal parameter at the onset of yield, n^{GB} is the GB thermal parameter. The temperature- and rate-dependency of the GB energy are shown respectively in terms $(1 - \mathcal{T}^{GB}/\mathcal{T}_y^{GB})^{n^{GB}}$ and $(\dot{e}^{pGB(post)}/\dot{p}^{GB})^{m^{GB}}$.

By using Eqs. (3.9) and (3.12), the GB dissipative microforce $\mathbb{M}^{GB,dis}$ can be obtained as

$$\mathbb{M}^{GB,dis} = \ell_{dis}^{GB} (\sigma_0^{GB} + \mathcal{H}_0^{GB} e^{pGB(post)}) \left(1 - \frac{\mathcal{T}^{GB}}{\mathcal{T}_y^{GB}}\right)^{n^{GB}} \left(\frac{\dot{e}^{pGB(post)}}{\dot{p}^{GB}}\right)^{m^{GB}} \quad (3.13)$$

Therefore, the GB thermodynamic microforce \mathbb{M}^{GB} can be obtained as

$$\begin{aligned} \mathbb{M}^{GB} &= G \ell_{en}^{GB} e^{pGB(pre)} \\ &+ \ell_{dis}^{GB} (\sigma_0^{GB} + \mathcal{H}_0^{GB} e^{pGB(post)}) \left(1 - \frac{\mathcal{T}^{GB}}{\mathcal{T}_y^{GB}}\right)^{n^{GB}} \left(\frac{\dot{e}^{pGB(post)}}{\dot{p}^{GB}}\right)^{m^{GB}} \end{aligned} \quad (3.14)$$

It can be seen from Eq. (3.14) that the grain boundary may act like a free surface, i.e. microscopically free boundary condition, when $\ell_{en}^{GB} = \ell_{dis}^{GB} = 0$. On the other hand, the microscopically hard boundary condition can be compelled under the conditions $\ell_{en}^{GB} \rightarrow \infty$ and $\ell_{dis}^{GB} \rightarrow \infty$.

3.5. Flow rule (grain boundary)

The flow rule for the grain boundary can be derived by substituting Eq. (3.14) into the microforce balances for the grain boundary, Eq. (3.3), such as:

— for S^{GBG_1}

$$\begin{aligned} &\left\{ \sigma_0 \ell_{en}^2 [\ell_{dis}^2 (e_{,k}^p e_{,k}^p)]^{\frac{\vartheta-1}{2}} e_{,i}^p + \sigma_0 \ell_{dis}^2 (m_2 + 1) \left[1 - \left(\frac{\mathcal{T}}{\mathcal{T}_y}\right)^n\right] \left(\frac{\dot{p}}{\dot{p}_2}\right)^{m_2} \frac{\dot{e}_{,i}^p}{\dot{p}} \right\} n_k^{GB} + G \ell_{en}^{GB} e^{pGB(pre)} \\ &= -\ell_{dis}^{GB} (\sigma_0^{GB} + \mathcal{H}_0^{GB} e^{pGB(post)}) \left(1 - \frac{\mathcal{T}^{GB}}{\mathcal{T}_y^{GB}}\right)^{n^{GB}} \left(\frac{\dot{e}^{pGB(post)}}{\dot{p}^{GB}}\right)^{m^{GB}} \end{aligned} \quad (3.15)$$

— for $S^{GB\mathcal{G}_2}$

$$\left\{ \sigma_0 \ell_{en}^2 [\ell_{en}^2 (e_{,k}^p e_{,k}^p)]^{\frac{\nu-1}{2}} e_{,i}^p + \sigma_0 \ell_{dis}^2 (m_2 + 1) \left[1 - \left(\frac{\mathcal{T}}{\mathcal{T}_y} \right)^n \right] \left(\frac{\dot{p}}{\dot{p}_2} \right)^{m_2} \frac{\dot{e}_{,i}^p}{\dot{p}} \right\} n_k^{GB} - G \ell_{en}^{GB} e^{p^{GB(pre)}} \tag{3.16}$$

$$= \ell_{dis}^{GB} (\sigma_0^{GB} + \mathcal{H}_0^{GB} e^{p^{GB(post)}}) \left(1 - \frac{\mathcal{T}^{GB}}{\mathcal{T}_y^{GB}} \right)^{n^{GB}} \left(\frac{\dot{e}^{p^{GB(post)}}}{\dot{p}^{GB}} \right)^{m^{GB}}$$

where the second term in LHS of both equations represents the backstress. Note that, in a general case, the grain boundary model parameters are not identical on each side, however in this work, the same values are assumed to be considered for simplification.

Considering the GB flow rules as the boundary conditions of the grain interior flow rule, Eq. (2.20), results in a yield condition accounting for the temperature and rate dependent barrier effect of grain boundaries on the plastic slip and, consequently, the influence on the GNDs evolution in the grain interior.

4. Finite element implementation of the proposed SGP model

A two-dimensional finite element model for the derived grain interior/boundary flow rules is developed to account for the size dependent response for microscopic structures. In this finite element solution, the plastic strain field e^p as well as the displacement field u_i are discretized independently and both the fields are taken as fundamental unknown nodal degrees of freedom. The increments in the nodal displacement and plastic strains can be obtained by computing the system of linear equations shown in Eq. (4.1)

$$\underbrace{\begin{bmatrix} K_{u_i u_k}^{\Omega_{el}} & K_{u_i e^p}^{\Omega_{el}} \\ K_{e^p u_k}^{\Omega_{el}} & K_{e^p e^p}^{\Omega_{el}} \end{bmatrix}}_{\mathbf{K}^{\Omega_{el}}} \begin{Bmatrix} (\Delta \mathcal{U}_{u_k})_\eta \\ (\Delta \mathcal{E}_{e^p})_\eta \end{Bmatrix} = \begin{Bmatrix} (\mathbb{R}_{u_i})_\eta \\ (\mathbb{R}_{e^p})_\eta \end{Bmatrix} \tag{4.1}$$

where $\mathbf{K}^{\Omega_{el}}$ is the Jacobian (stiffness) matrix. The nodal displacement and the plastic strain in the iteration ζ at the node η are expressed as $(\mathcal{U}_{u_i}^\zeta)_\eta$ and $(\mathcal{E}_{e^p}^\zeta)_\eta$, respectively, and their increments are calculated by $(\Delta \mathcal{U}_{u_k})_\eta = (\mathcal{U}_{u_i}^{\zeta+1})_\eta - (\mathcal{U}_{u_i}^\zeta)_\eta$, $(\Delta \mathcal{E}_{e^p})_\eta = (\mathcal{E}_{e^p}^{\zeta+1})_\eta - (\mathcal{E}_{e^p}^\zeta)_\eta$. $(\mathbb{R}_{u_i})_\eta$ and $(\mathbb{R}_{e^p})_\eta$ are the nodal residuals for the displacement and plastic strain at the node η , respectively. The system of linear equations is solved via the user-defined element subroutine (UEL) in ABAQUS/standard using the Newton-Raphson iterative method.

Each component of the Jacobian matrix can be obtained respectively as follows

$$K_{u_i u_k}^{\Omega_{el}} = - \left. \frac{\partial \mathbb{R}_{u_i}}{\partial \mathcal{U}_{u_k}^\eta} \right|_{\mathcal{U}_{u_i}^\zeta} = \int_{\Omega_{el}} \left(E_{ijkl} \frac{\partial \mathbb{N}_u^\eta}{\partial x_j} \frac{\partial \mathbb{N}_u^\eta}{\partial x_l} \right) dV$$

$$K_{u_i e^p}^{\Omega_{el}} = - \left. \frac{\partial \mathbb{R}_{u_i}}{\partial \mathcal{E}_{e^p}^\eta} \right|_{\mathcal{E}_{e^p}^\zeta} = \int_{\Omega_{el}} \left(E_{ijkl} \frac{e^p}{\varepsilon_{kl}} \frac{\partial \mathbb{N}_u^\eta}{\partial x_j} \mathbb{N}_{e^p}^\eta \right) dV \tag{4.2}$$

$$K_{e^p u_k}^{\Omega_{el}} = - \left. \frac{\partial \mathbb{R}_{e^p}}{\partial \mathcal{U}_{u_k}^\eta} \right|_{\mathcal{U}_{u_i}^\zeta} = \int_{\Omega_{el}} \left(E_{ijkl} \frac{e^p}{\varepsilon_{ij}} \mathbb{N}_u^\eta \frac{\partial \mathbb{N}_{e^p}^\eta}{\partial x_l} \right) dV$$

and

$$\begin{aligned}
 K_{e^p e^p}^{\Omega_{el}} = & - \frac{\partial \mathbb{R}_{e^p}}{\partial \mathcal{E}_{e^p}^\eta} \Big|_{\mathcal{E}_{e^p}^\zeta} = \int_{\Omega_{el}} \left\{ \left(r \mathcal{H}_0(e^p)^r + \mathcal{H}_0 \left(\frac{\dot{e}^p}{\dot{p}_1} \right)^{m_1} \right. \right. \\
 & + \sigma_0 \sqrt{\mathcal{H}^2(e^p) + \ell_{N-G} \varepsilon^p} \frac{m_1 \dot{e}^{p^{m_1-1}}}{\dot{p}_1^{m_1} \Delta t} \left[1 - \left(\frac{\mathcal{T}}{\mathcal{T}_y} \right)^n \right] N_{e^p}^\eta N_{e^p}^\eta \\
 & + \sigma_0 \ell_{en}^2 [\ell_{en}^2 (e_{,k}^p e_{,k}^p)]^{\frac{\nu-1}{2}} \frac{\partial N_{e^p}^\eta}{\partial x_j} \frac{\partial N_{e^p}^\eta}{\partial x_j} \\
 & + \sigma_0 \ell_{dis}^4 (m_2^2 - 1) \left[1 - \left(\frac{\mathcal{T}}{\mathcal{T}_y} \right)^n \right] \frac{\dot{p}^{m_2-3}}{\dot{p}_2^{m_2} \Delta t} \left(\dot{e}_{,j}^p \frac{\partial N_{e^p}^\eta}{\partial x_j} \right) \left(\dot{e}_{,j}^p \frac{\partial N_{e^p}^\eta}{\partial x_j} \right) \\
 & + \sigma_0 \ell_{dis}^2 (m_2 + 1) \left[1 - \left(\frac{\mathcal{T}}{\mathcal{T}_y} \right)^n \right] \frac{\dot{p}^{m_2-1}}{\dot{p}_2^{m_2} \Delta t} \frac{\partial N_{e^p}^\eta}{\partial x_j} \frac{\partial N_{e^p}^\eta}{\partial x_j} \Big\} dV \\
 & - \left[G \ell_{en}^{GB} + \ell_{dis}^{GB} \frac{\sigma_0^{GB} + \mathcal{H}_0^{GB} e^{p^{GB(post)}}}{(\Delta t \dot{p}^{GB})^{m^{GB}}} \left(1 - \frac{\mathcal{T}^{GB}}{\mathcal{T}_y^{GB}} \right)^{n^{GB}} \dot{e}^{p^{GB(post) m^{GB} - 1}} \right] N_{e^p}^\eta N_{e^p}^\eta
 \end{aligned} \tag{4.3}$$

where Δt is the time step. The grain boundary terms in Eq. (4.3) are only applied for nodes on the grain boundary area.

5. Numerical examples

The assumption of the microscopically hard boundary condition is used in the authors’ previous work (Song and Voyiadjis, 2018). In this work, the governing differential equation is solved by imposing the proposed grain boundary flow rule to account for the deformable grain boundary. Furthermore, the characteristics of the proposed strain gradient plasticity theory incorporating the flow rules of both the grain interior and the grain boundary is addressed in this Section by solving the shear problem of a square plate with an edge of L . A schematic illustration of the problem, initial conditions and macroscopic and microscopic boundary conditions as well as the grain boundary area are shown in Fig. 1. The parameter $u^+(t)$ represents the prescribed displacement. The whole square is meshed using 1 600 (40×40) elements and split into 16 (4×4) grains by the grain boundary area, which is indicated by bold lines.

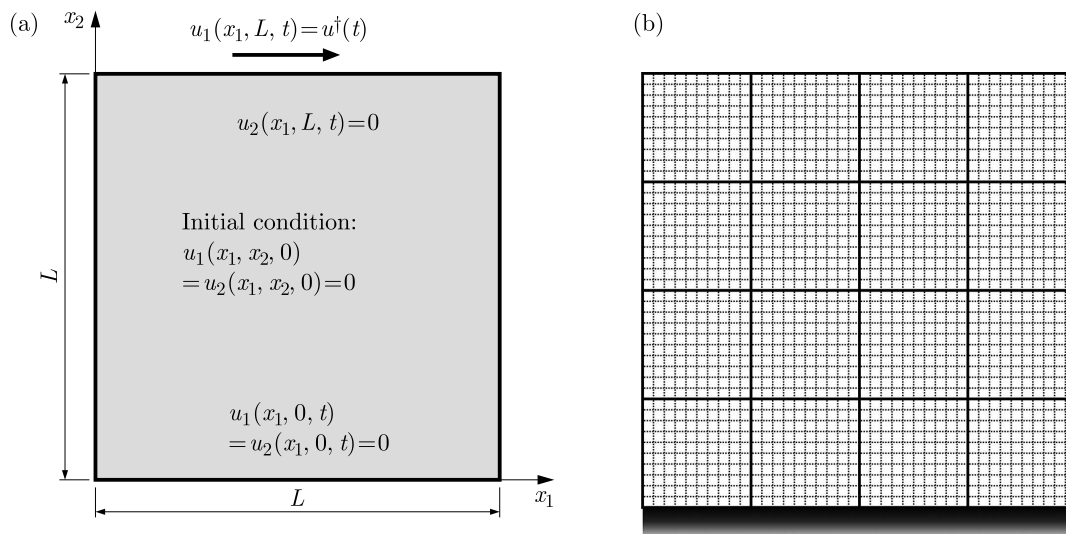


Fig. 1. The schematic illustration of the simple shear problem: (a) macroscopic, microscopic boundary conditions, and initial conditions, (b) 4×4 grains

The following material parameters are used in this Section unless stated otherwise: $E = 110$ GPa, $\nu = 0.343$, $\rho = 8.960$ g·cm⁻³, $c_\epsilon = 0.385$ J/(g·K), $\alpha^{th} = 16.0$ μ m/(m·K), $\dot{p}_1 = \dot{p}_2 = 0.04$ s⁻¹, $r = 0.6$, $m_1 = 0.05$, $m_2 = 0.2$, $\mathcal{T}_y = 1358$ K, $n = 0.3$, $\sigma_0 = 195$ MPa, $\mathcal{H}_0 = 0$ MPa, $\sigma_0^{GB} = 300$ MPa, $\mathcal{H}_0^{GB} = 300$ MPa, $\dot{p}^{GB} = 0.04$ s⁻¹, $m^{GB} = 1$, $\mathcal{T}_y^{GB} = 700$ K, $n^{GB} = 0.4$.

As mentioned in Section 3.4, the microscopically free and hard boundary conditions at the grain boundary can be introduced respectively by setting $\ell_{en}^{GB} = \ell_{dis}^{GB} = 0$ and $\ell_{en}^{GB} \rightarrow \infty$, $\ell_{dis}^{GB} \rightarrow \infty$. Firstly, the validity of these conditions is examined in this work. Next, a direct comparison between the classical plasticity theory ($\ell_{en}/L = \ell_{dis}/L = \ell_{N-G}/L = 0.0$) and the gradient-enhanced plasticity theory ($\ell_{en}/L = \ell_{dis}/L = \ell_{N-G}/L = 0.1$) is given in order to check the ability of the proposed flow rule on the size effect. The numerical results in terms of the accumulated plastic strain profile and the stress-strain curves are shown in Figs. 2 and 3. The

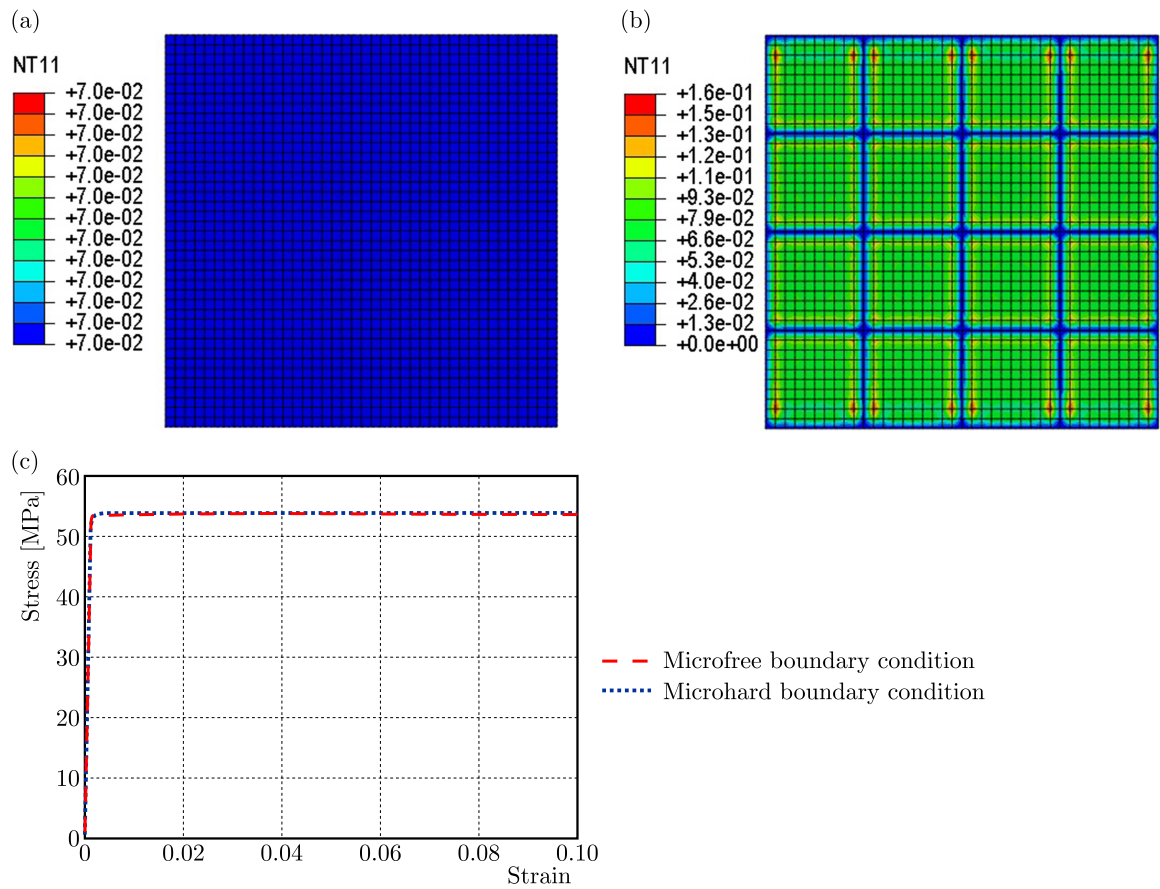


Fig. 2. Classical plasticity theory ($\ell_{en}/L = \ell_{dis}/L = \ell_{N-G}/L = 0$). Distributions of the accumulated plastic strain with: (a) microscopically free ($\ell_{en}^{GB} = \ell_{dis}^{GB} = 0$), and (b) microscopically hard boundary conditions ($\ell_{en}^{GB} \rightarrow \infty$, $\ell_{dis}^{GB} \rightarrow \infty$), and (c) stress-strain responses

terminology “NT11” in Figs. 2 and 3 indicates the accumulated plastic strain. As can be seen in these figures, the microscopically free and hard boundary conditions are well captured under the classical plasticity theory as well as the gradient-enhanced plasticity theory. In addition, in Fig. 2c, no size effect is observed in the classical plasticity theory with varying normalized material length scales as expected. In Fig. 3c, on the other hand, strain hardening and strengthening are more pronounced as the dimensions of the shear plate height are reduced ($\ell_{en}^{GB}/L \rightarrow \infty$, $\ell_{dis}^{GB}/L \rightarrow \infty$).

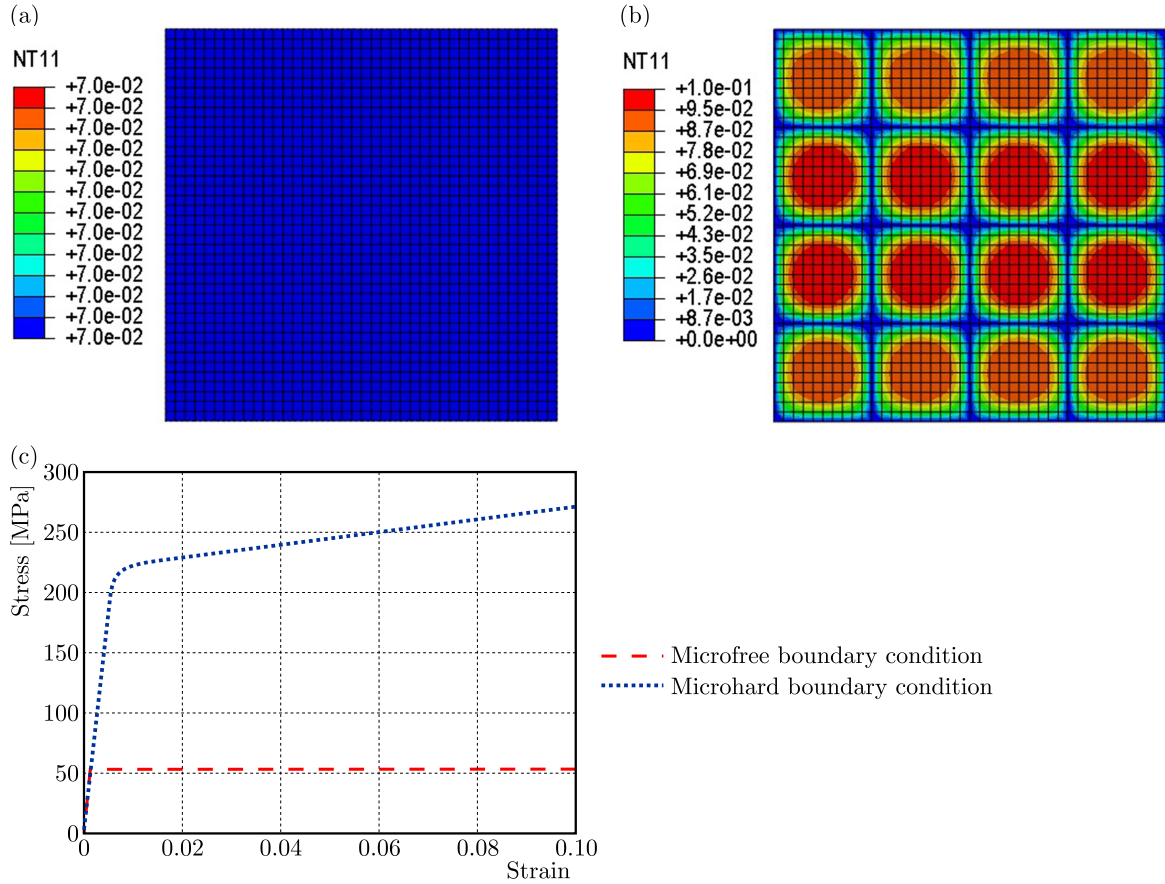


Fig. 3. Strain gradient plasticity theory ($\ell_{en}/L = \ell_{dis}/L = \ell_{N-G}/L = 0.1$). Distributions of the accumulated plastic strain with: (a) microscopically free ($\ell_{en}^{GB} = \ell_{dis}^{GB} = 0$), and (b) microscopically hard boundary conditions ($\ell_{en}^{GB} \rightarrow \infty, \ell_{dis}^{GB} \rightarrow \infty$), and (c) stress-strain responses

In Fig. 4, the effects of each material length scale parameter, i.e. ℓ_{en} , ℓ_{dis} and ℓ_{N-G} , along with the microscopically hard boundary condition are also examined through the profile of the accumulated plastic strain. In addition, the contributions of each length scale parameter on the stress-strain responses are shown in Fig. 4c.

Variations in the stress-strain responses and evolutions of the maximum temperature are investigated for various values of the normalized energetic and dissipative grain boundary material length scales as shown in Figs. 5 and 6. It is assumed by setting $\ell_{dis}^{GB}/\ell_{dis} = 0$ that all plastic work at the grain boundary is stored as surface energy which depends on the plastic strain state at the surface. In this case, ℓ_{en}^{GB}/ℓ_{en} reflects the grain boundary resistance to plastic deformation. Figures 5b and 6b show the size effects on the strain hardening and temperature evolution due to the grain boundary energetic length scale, and it is more pronounced in the more strongly constrained material, i.e. increasing ℓ_{en}^{GB}/ℓ_{en} . On the other hand, by setting $\ell_{en}^{GB}/\ell_{en} = 0$, it is assumed that the work performed at the grain boundary is dissipated in the absence of surface energy. In this case, $\ell_{dis}^{GB}/\ell_{dis}$ reflects the grain boundary resistance to slip transfer. As can be seen in Fig. 5c, the initial yield strength increases without strain hardening as $\ell_{dis}^{GB}/\ell_{dis}$ increases.

6. Conclusions

The two-dimensional finite element model for the thermodynamically consistent thermo-mechanical coupled gradient enhanced plasticity theory is proposed on the basis of the concept

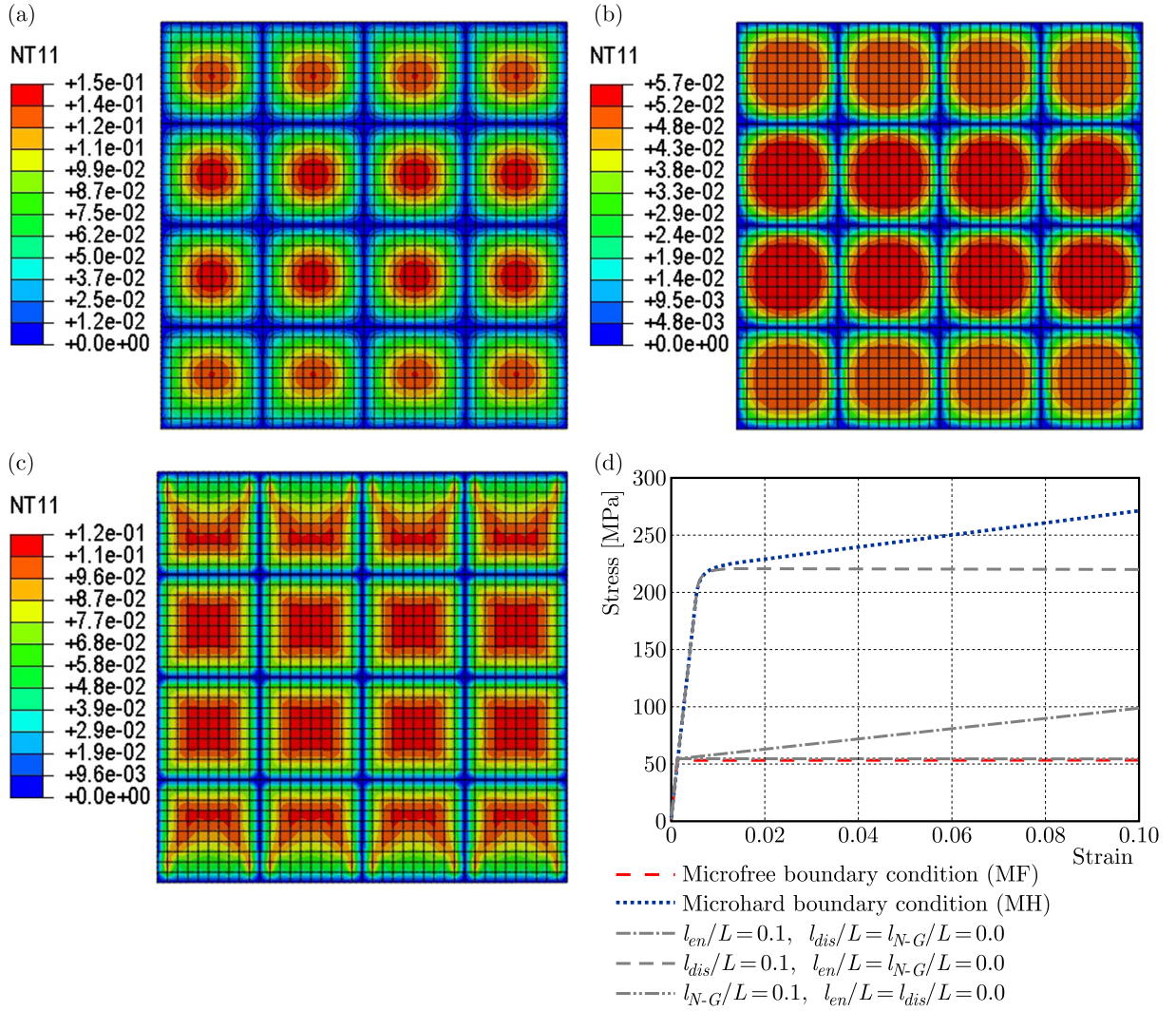


Fig. 4. Distributions of the accumulated plastic strain with the microscopically hard boundary condition ($\ell_{en}^{\text{GB}}/L \rightarrow \infty, \ell_{dis}^{\text{GB}}/L \rightarrow \infty$) under: (a) energetic length scale only ($\ell_{en}^{\text{GB}}/L = 0.1, \ell_{dis}^{\text{GB}}/L = \ell_{N-G}/L = 0$), (b) dissipative length scale only ($\ell_{dis}^{\text{GB}}/L = 0.1, \ell_{en}^{\text{GB}}/L = \ell_{N-G}/L = 0$), (c) N-G length scale only ($\ell_{N-G}/L = 0.1, \ell_{en}^{\text{GB}}/L = \ell_{dis}^{\text{GB}}/L = 0$), and (d) stress-strain responses

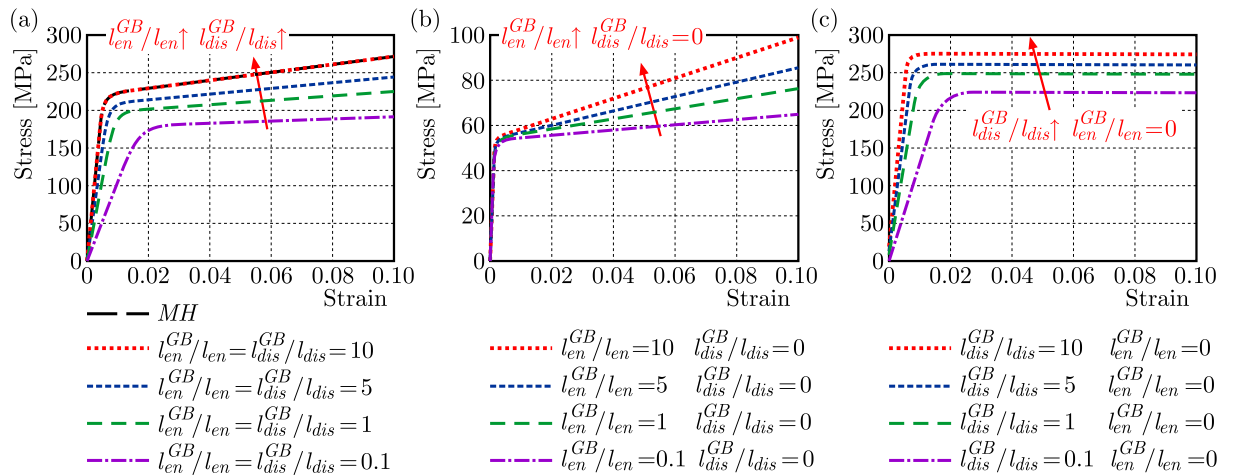


Fig. 5. Distributions of the accumulated plastic strain according to various values of $\ell_{en}^{\text{GB}}/\ell_{en}$ and $\ell_{dis}^{\text{GB}}/\ell_{dis}$: (a) combined $\ell_{en}^{\text{GB}}/\ell_{en}$ and $\ell_{dis}^{\text{GB}}/\ell_{dis}$, (b) $\ell_{en}^{\text{GB}}/\ell_{en}$ only, and (c) $\ell_{dis}^{\text{GB}}/\ell_{dis}$ only

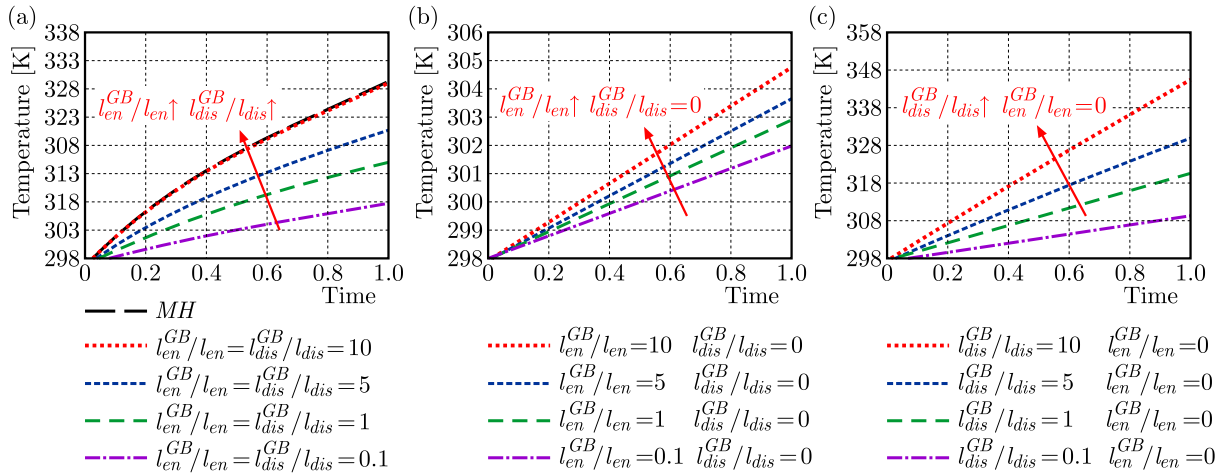


Fig. 6. Evolutions of the maximum temperature according to various values of ℓ_{en}^{GB}/ℓ_{en} and $\ell_{dis}^{GB}/\ell_{dis}$: (a) combined ℓ_{en}^{GB} and ℓ_{dis}^{GB} , (b) ℓ_{en}^{GB} only, and (c) ℓ_{dis}^{GB} only

of dislocation interaction mechanisms and thermal activation energy. The thermodynamic microstresses for the grain interior and grain boundary are respectively assumed to be divided into two components, i.e. energetic and dissipative components which, in turn, both energetic and dissipative material length scale parameters are incorporated in the governing constitutive equations and flow rules for both areas. These thermodynamic microstresses can be respectively obtained in a direct way from the Helmholtz free energy and the rate of dissipation potential by taking the maximum entropy production into account. In particular, the concept of GNDs density is additionally employed in the grain interior to interpret the microstructural strengthening mechanisms induced by the nonhomogeneous deformation. Correspondingly, the model in this work incorporates the terms related to GNDs-induced strengthening and the additional material length scale parameter.

In order to investigate the characteristics of the proposed strain gradient plasticity theory incorporating the flow rules for both the grain interior and grain boundary, the shear problem of a square plate is solved in this work. The microscopically free and hard boundary conditions are well captured under the classical plasticity theory as well as the gradient-enhanced plasticity theory by using the proposed grain boundary flow rule. In addition, the size effects on the stress-strain responses and the evolutions of the maximum temperature are well observed with the cases of (a) combined ℓ_{en}^{GB} and ℓ_{dis}^{GB} , (b) ℓ_{en}^{GB} only, and (c) ℓ_{dis}^{GB} only.

Acknowledgements

The financial support provided by a grant from the National Science Foundation EPSCoR CIMM (grant number #OIA-1541079) is gratefully acknowledged.

References

1. ABAQUS, 2012, User's Manual (Version 6.12). Dassault Systemes Simulia Corp., Providence, RI, USA
2. AIFANTIS K.E., WILLIS J.R., 2005, The role of interfaces in enhancing the yield strength of composites and polycrystals, *Journal of the Mechanics and Physics of Solids*, **53**, 5, 1047-1070
3. CERMELLI P., GURTIN M.E., 2002, Geometrically necessary dislocations in viscoplastic single crystals and bicrystals undergoing small deformations, *International Journal of Solids and Structures*, **39**, 26, 6281-6309

4. CLARK W.A.T., WAGONER R.H., SHEN Z.Y., LEE T.C., ROBERTSON I.M., BIRNBAUM H.K., 1992, On the criteria for slip transmission across interfaces in polycrystals, *Scripta Metallurgica et Materialia*, **26**, 2, 203-206
5. COLEMAN B.D., NOLL W., 1963, The thermodynamics of elastic materials with heat conduction and viscosity, *Archive for Rational Mechanics and Analysis*, **13**, 3, 167-178
6. FOREST S., 2009, Micromorphic approach for gradient elasticity, viscoplasticity, and damage, *Journal of Engineering Mechanics – ASCE*, **135**, 3, 117-131
7. FREDRIKSSON P., GUDMUNDSON P., 2007, Competition between interface and bulk dominated plastic deformation in strain gradient plasticity, *Modelling and Simulation in Materials Science and Engineering*, **15**, 1, S61-S69
8. GUDMUNDSON P., 2004, A unified treatment of strain gradient plasticity, *Journal of the Mechanics and Physics of Solids*, **52**, 6, 1379-1406
9. GURTIN M.E., 2008, A theory of grain boundaries that accounts automatically for grain misorientation and grain-boundary orientation, *Journal of the Mechanics and Physics of Solids*, **56**, 2, 640-662
10. HIRTH J.P., LOTHE J., 1982, *Theory of Dislocations*, Elsevier
11. LEE T.C., ROBERTSON I.M., BIRNBAUM H.K., 1989, Prediction of slip transfer mechanisms across grain-boundaries, *Scripta Metallurgica*, **23**, 5, 799-803
12. NIX W.D., GAO H.J., 1998, Indentation size effects in crystalline materials: A law for strain gradient plasticity, *Journal of the Mechanics and Physics of Solids*, **46**, 3, 411-425
13. OHMURA T., MINOR A.M., STACH E.A., MORRIS J.W., 2004, Dislocation-grain boundary interactions in martensitic steel observed through in situ nanoindentation in a transmission electron microscope, *Journal of Materials Research*, **19**, 12, 3626-3632
14. SOER W.A., AIFANTIS K.E., DE HOSSON J.T.M., 2005, Incipient plasticity during nanoindentation at grain boundaries in body-centered cubic metals, *Acta Materialia*, **53**, 17, 4665-4676
15. SONG Y., VOYIADJIS G.Z., 2018, Small scale volume formulation based on coupled thermo-mechanical gradient enhanced plasticity theory, *International Journal of Solids and Structures*, **134**, March 2018, 195-215
16. SUN S., ADAMS B.L., KING W.E., 2000, Observations of lattice curvature near the interface of a deformed aluminium bicrystal, *Philosophical Magazine a-Physics of Condensed Matter Structure Defects and Mechanical Properties*, **80**, 1, 9-25
17. VOCE E., 1955, A practical strain-hardening function, *Metallurgica*, 51219-51226
18. VOYIADJIS G.Z., FAGHIHI D., ZHANG Y.D., 2014, A theory for grain boundaries with strain-gradient plasticity, *International Journal of Solids and Structures*, **51**, 10, 1872-1889
19. VOYIADJIS G.Z., SONG Y., 2017, Effect of passivation on higher order gradient plasticity models for non-proportional loading: energetic and dissipative gradient components, *Philosophical Magazine*, **97**, 5, 318-345
20. VOYIADJIS G.Z., SONG Y., PARK T., 2017, Higher-order thermomechanical gradient plasticity model with energetic and dissipative components, *Journal of Engineering Materials and Technology – Transactions of the ASME*, **139**, 2

IMPLICIT SCHEME OF THE FINITE DIFFERENCE METHOD FOR THE SECOND-ORDER DUAL PHASE LAG EQUATION

EWA MAJCHRZAK

Silesian University of Technology, Gliwice, Poland

e-mail: ewa.majchrzak@polsl.pl

BOHDAN MOCHNACKI

University of Occupational Safety Management, Katowice, Poland

e-mail: bmochnacki@wszop.edu.pl

The second-order dual phase lag equation (DPLE) as a mathematical model of the microscale heat transfer is considered. It is known that the starting point determining the final form of this equation is the generalized Fourier law in which two positive constants (the relaxation and thermalization times) appear. Depending on the order of the generalized Fourier law expansion into the Taylor series, different forms of the DPLE can be obtained. As an example of the problem described by the second-order DPLE equation, thermal processes proceeding in the domain of a thin metal film subjected to a laser pulse are considered. The numerical algorithm is based on an implicit scheme of the finite difference method. At the stage of numerical modeling, the first, second and mixed order of the dual phase lag equation are considered. In the final part of the paper, examples of different solutions are presented and conclusions are formulated.

Keywords: microscale heat transfer, dual phase lag model, implicit scheme of finite difference method

1. Introduction

The Fourier heat conduction model is based on the assumption of instantaneous propagation of the thermal wave in the domain considered. Intuitively, this approach seems to be incorrect, but it has worked for solving a number of macroscopic heat conduction problems. However, it turned out that for certain non-typical materials with a complex internal structure, the Fourier model is insufficient (Roetzel *et al.*, 2003). Even more, deviations from the real course of the process can be seen in the case of microscale heat transfer.

It is obvious that accumulating enough energy to transfer to the nearest neighborhood would take time in the process of heat transfer (Zhang, 2007). So, the lag time of the heat flux in relation to the temperature gradient referred to as “a relaxation time” was introduced by Cattaneo (1948) and Vernotte (1958), and the appropriate energy equation (a hyperbolic PDE) became known as the Cattaneo-Vernotte equation. In the recent years, the heat conduction model in which two delay times appear has become more and more popular. This model is called the dual-phase lag one (Zhang, 2007; Tzou, 2015). The starting point for considerations is the generalized form of the Fourier law, e.g. (Faghri *et al.*, 2010; Smith and Norris, 2003). Depending on the number of terms in the Taylor series expansion of this law, different forms of the dual phase lag equation (DPLE) can be obtained (see Section 2). The lag times appearing in DPLE are called the relaxation time and the thermalization time. Some simple tasks described by this equation (supplemented by appropriate boundary and initial conditions) can be solved analytically, e.g. (Ciesielski, 2017a; Tang and Araki, 1999; Askarizadeh *et al.*, 2017; Mohammadi-

-Fakhar and Momeni-Masuleh, 2010). However, most of the practical problems have been solved using numerical methods. Examples of such solutions in the field of the microscale heat transfer may be the papers (Majchrzak and Mochnacki, 2014; Ciesielski, 2017b; Dai and Nassar, 2000; Mochnacki and Paruch, 2013; Chen and Beraun, 2001) concerning the first-order DPLE.

The similar problems have been considered for non-homogeneous (multilayered) domains. In this place, the papers (Majchrzak *et al.*, 2009; Qiu *et al.*, 1994; Al-Nimr *et al.*, 2004; Wang *et al.*, 2006, 2008) can be (as the examples) mentioned. The correct form of the boundary conditions between subdomains (here, the macroscopic boundary conditions are often used, which is a significant simplification) can be found in (Ho *et al.*, 2003) while the detailed mathematical considerations were shown in (Majchrzak and Kałuża, 2017). In turn, in the paper (Majchrzak and Mochnacki, 2016), the problem of stability condition (explicit scheme of the FDM) was analyzed.

The numerical solutions concerning the second-order DPLE (based on the finite difference method) are the subject of works prepared by Castro *et al.* (2016) and Deng *et al.* (2017). The similar problems are discussed in the paper presented, but the wider class of equations and the other numerical algorithm are taken into account.

The applications of DPLE in the scope of bioheat transfer will not be discussed here.

2. Dual-phase lag model

The following well known thermal diffusion equation is considered

$$c \frac{\partial T(X, t)}{\partial t} = -\nabla \cdot \mathbf{q}(X, t) + Q(X, t) \quad (2.1)$$

where c is a volumetric specific heat, \mathbf{q} is a heat flux vector, Q is a capacity of the internal volumetric heat source, X, t denote the geometrical co-ordinates and time.

The relationship between the heat flux \mathbf{q} and the temperature gradient ∇T is given in the form of the generalized Fourier law (Zhang, 2007; Smith and Norris, 2003), namely

$$\mathbf{q}(X, t + \tau_q) = -\lambda \nabla T(X, t + \tau_T) \quad (2.2)$$

where λ is thermal conductivity, τ_q and τ_T are the relaxation time and thermalization time, respectively. The relaxation time τ_q is the mean time for electrons to change their energy states, while the thermalization time τ_T is the mean time required for electrons and lattice to reach equilibrium.

Using the Taylor series expansions, the following second-order approximation of formula (2.2) can be taken into account

$$\mathbf{q}(X, t) + \tau_q \frac{\partial \mathbf{q}(X, t)}{\partial t} + \frac{\tau_q^2}{2} \frac{\partial^2 \mathbf{q}(X, t)}{\partial t^2} = -\lambda \left[\nabla T(X, t) + \tau_T \frac{\partial \nabla T(X, t)}{\partial t} + \frac{\tau_T^2}{2} \frac{\partial^2 \nabla T(X, t)}{\partial t^2} \right] \quad (2.3)$$

which means

$$-\mathbf{q}(X, t) = \tau_q \frac{\partial \mathbf{q}(X, t)}{\partial t} + \frac{\tau_q^2}{2} \frac{\partial^2 \mathbf{q}(X, t)}{\partial t^2} + \lambda \nabla T(X, t) + \lambda \tau_T \frac{\partial \nabla T(X, t)}{\partial t} + \lambda \frac{\tau_T^2}{2} \frac{\partial^2 \nabla T(X, t)}{\partial t^2} \quad (2.4)$$

From equation (2.4) it results that

$$\begin{aligned} -\nabla \cdot \mathbf{q}(X, t) &= \tau_q \frac{\partial [\nabla \cdot \mathbf{q}(X, t)]}{\partial t} + \frac{\tau_q^2}{2} \frac{\partial^2 [\nabla \cdot \mathbf{q}(X, t)]}{\partial t^2} + \nabla [\lambda \nabla T(X, t)] \\ &+ \tau_T \frac{\partial \{\nabla [\lambda \nabla T(X, t)]\}}{\partial t} + \frac{\tau_T^2}{2} \frac{\partial^2 \{\nabla [\lambda \nabla T(X, t)]\}}{\partial t^2} \end{aligned} \quad (2.5)$$

The last dependence is introduced in to equation (2.1), and then

$$c \frac{\partial T(X, t)}{\partial t} = \tau_q \frac{\partial [\nabla \cdot \mathbf{q}(X, t)]}{\partial t} + \frac{\tau_q^2}{2} \frac{\partial^2 [\nabla \cdot \mathbf{q}(X, t)]}{\partial t^2} + \nabla [\lambda \nabla T(X, t)] + \tau_T \frac{\partial \{\nabla [\lambda \nabla T(X, t)]\}}{\partial t} + \frac{\tau_T^2}{2} \frac{\partial^2 \{\nabla [\lambda \nabla T(X, t)]\}}{\partial t^2} + Q(X, t) \tag{2.6}$$

Equation (2.1) can also be written as

$$\nabla \cdot \mathbf{q}(X, t) = -c \frac{\partial T(X, t)}{\partial t} + Q(X, t) \tag{2.7}$$

Putting equation (2.7) into (2.6), one obtains

$$c \frac{\partial T(X, t)}{\partial t} = \tau_q \frac{\partial}{\partial t} \left[-c \frac{\partial T(X, t)}{\partial t} + Q(X, t) \right] + \frac{\tau_q^2}{2} \frac{\partial^2}{\partial t^2} \left[-c \frac{\partial T(X, t)}{\partial t} + Q(X, t) \right] + \nabla [\lambda \nabla T(X, t)] + \tau_T \frac{\partial \{\nabla [\lambda \nabla T(X, t)]\}}{\partial t} + \frac{\tau_T^2}{2} \frac{\partial^2 \{\nabla [\lambda \nabla T(X, t)]\}}{\partial t^2} + Q(X, t) \tag{2.8}$$

Assuming the constant value of the volumetric specific heat c , one has

$$c \left[\frac{\partial T(X, t)}{\partial t} + \tau_q \frac{\partial^2 T(X, t)}{\partial t^2} + \frac{\tau_q^2}{2} \frac{\partial^3 T(X, t)}{\partial t^3} \right] = \nabla [\lambda \nabla T(X, t)] + \tau_T \frac{\partial \{\nabla [\lambda \nabla T(X, t)]\}}{\partial t} + \frac{\tau_T^2}{2} \frac{\partial^2 \{\nabla [\lambda \nabla T(X, t)]\}}{\partial t^2} + Q(X, t) + \tau_q \frac{\partial Q(X, t)}{\partial t} + \frac{\tau_q^2}{2} \frac{\partial^2 Q(X, t)}{\partial t^2} \tag{2.9}$$

Additionally, for $\lambda = \text{const}$ the last equation takes form

$$c \left[\frac{\partial T(X, t)}{\partial t} + \tau_q \frac{\partial^2 T(X, t)}{\partial t^2} + \frac{\tau_q^2}{2} \frac{\partial^3 T(X, t)}{\partial t^3} \right] = \lambda \nabla^2 T(X, t) + \lambda \tau_T \frac{\partial [\nabla^2 T(X, t)]}{\partial t} + \lambda \frac{\tau_T^2}{2} \frac{\partial^2 [\nabla^2 T(X, t)]}{\partial t^2} + Q(X, t) + \tau_q \frac{\partial Q(X, t)}{\partial t} + \frac{\tau_q^2}{2} \frac{\partial^2 Q(X, t)}{\partial t^2} \tag{2.10}$$

As previously mentioned, dual phase lag equation (2.10) is often simplified by omitting appropriate components. For example, in several works (e.g. Tzou, 1995) the second order Taylor expression of heat flux and the first order Taylor expression of the temperature gradient are applied to take into account the phase lagging behavior. Ignoring the inner heat source (as in Tzou, 1995), the governing equation of temperature based on the DPL model is the following

$$c \left[\frac{\partial T(X, t)}{\partial t} + \tau_q \frac{\partial^2 T(X, t)}{\partial t^2} + \frac{\tau_q^2}{2} \frac{\partial^3 T(X, t)}{\partial t^3} \right] = \lambda \nabla^2 T(X, t) + \lambda \tau_T \frac{\partial [\nabla^2 T(X, t)]}{\partial t} \tag{2.11}$$

It is also possible to consider the energy equation in the form (assuming that $Q(X, t) = 0$)

$$c \left[\frac{\partial T(X, t)}{\partial t} + \tau_q \frac{\partial^2 T(X, t)}{\partial t^2} \right] = \lambda \nabla^2 T(X, t) + \lambda \tau_T \frac{\partial [\nabla^2 T(X, t)]}{\partial t} + \lambda \frac{\tau_T^2}{2} \frac{\partial^2 [\nabla^2 T(X, t)]}{\partial t^2} \tag{2.12}$$

The most popular DPLE results from the assumption that the first-order approximation of formula (2.2) is used, and then (e.g. Tang and Araki, 1999; Al-Nimr *et al.*, 2004; Majchrzak and Mochnacki, 2014)

$$c \left[\frac{\partial T(X, t)}{\partial t} + \tau_q \frac{\partial^2 T(X, t)}{\partial t^2} \right] = \lambda \nabla^2 T(X, t) + \lambda \tau_T \frac{\partial [\nabla^2 T(X, t)]}{\partial t} + Q(X, t) + \tau_q \frac{\partial Q(X, t)}{\partial t} \tag{2.13}$$

One can see that for $\tau_T = 0$, DPLE (2.13) takes form of the Cattaneo-Vernotte equation, while for $\tau_q = 0$ and $\tau_T = 0$ the well known macroscopic Fourier equation is obtained.

Taking into account the numerical examples presented in the final part of the paper, a modified form of the Neumann boundary condition must still be formulated, namely

$$\begin{aligned} q_b(X, t) + \tau_q \frac{\partial q_b(X, t)}{\partial t} + \frac{\tau_q^2}{2} \frac{\partial^2 q_b(X, t)}{\partial t^2} \\ = -\lambda \left[\mathbf{n} \cdot \nabla T(X, t) + \tau_T \frac{\partial [\mathbf{n} \cdot \nabla T(X, t)]}{\partial t} + \frac{\tau_T^2}{2} \frac{\partial^2 [\mathbf{n} \cdot \nabla T(X, t)]}{\partial t^2} \right] \end{aligned} \quad (2.14)$$

where $\mathbf{n} \cdot \nabla T(X, t)$ denotes normal derivative and $q_b(X, t)$ is the known boundary heat flux. In the case of simplified forms of the DPLE, the appropriate components in condition (2.14) should be neglected.

3. Formulation of the problem

Thermal processes proceeding in a thin metal film subjected to laser pulse are considered. A 1D problem is analyzed (heat transfer in the direction perpendicular to the layer is taken into account). The front surface $x = 0$ is irradiated by a laser pulse and according to (Tang and Araki, 1999; Kaba and Dai, 2005), the conduction heat transfer in the domain considered can be modeled using the DPLE in which the volumetric heat source $Q(x, t)$ is introduced. At the same time, for $x = 0$ and $x = L$, the non-flux conditions should be assumed. The laser irradiation is described by the following source term

$$Q(x, t) = \sqrt{\frac{\beta(1-R)}{\pi}} \frac{I_0}{t_p \delta} \exp\left[-\frac{x}{\delta} - \beta \frac{(t - 2t_p)^2}{t_p^2}\right] \quad (3.1)$$

where I_0 is the laser intensity, t_p is the characteristic time of the laser pulse, δ is the optical penetration depth, R is the reflectivity of the irradiated surface, and $\beta = 4 \ln 2$.

In the most general case, the following DPLE is considered:

— for $0 < x < L$

$$\begin{aligned} \frac{\partial T(x, t)}{\partial t} + \tau_q \frac{\partial^2 T(x, t)}{\partial t^2} + w_q \frac{\tau_q^2}{2} \frac{\partial^3 T(x, t)}{\partial t^3} = a \frac{\partial^2 T(x, t)}{\partial x^2} + a \tau_T \frac{\partial^3 T(x, t)}{\partial t \partial x^2} \\ + w_T a \frac{\tau_T^2}{2} \frac{\partial^4 T(x, t)}{\partial t^2 \partial x^2} + \frac{1}{c} Q(x, t) + \frac{\tau_q}{c} \frac{\partial Q(x, t)}{\partial t} + w_q \frac{\tau_q^2}{2c} \frac{\partial^2 Q(x, t)}{\partial t^2} \end{aligned} \quad (3.2)$$

where $a = \lambda/c$ is the diffusion coefficient, w_T and w_q are bivalent parameters. Here $w_T = 1$ and $w_q = 1$. For the “simplified” forms of DPLE, they are equal to (0, 1), (1, 0) and (0, 0).

As previously mentioned, $q_b(0, t) = q_b(L, t) = 0$ and the appropriate boundary conditions are of the form (Eq. (2.14)):

— for $x = 0$

$$\frac{\partial T(x, t)}{\partial x} + \tau_T \frac{\partial^2 T(x, t)}{\partial t \partial x} + w_T \frac{\tau_T^2}{2} \frac{\partial^3 T(x, t)}{\partial t^2 \partial x} = 0 \quad (3.3)$$

— for $x = L$

$$\frac{\partial T(x, t)}{\partial x} + \tau_T \frac{\partial^2 T(x, t)}{\partial t \partial x} + w_T \frac{\tau_T^2}{2} \frac{\partial^3 T(x, t)}{\partial t^2 \partial x} = 0 \quad (3.4)$$

The initial condition is also given for $t = 0$

$$T(x, 0) = T_p \quad \left. \frac{\partial T(x, t)}{\partial t} \right|_{t=0} = u(x) \quad \left. \frac{\partial^2 T(x, t)}{\partial t^2} \right|_{t=0} = v(x) \quad (3.5)$$

where T_p is the initial temperature, while $u(x)$ and $v(x)$ are known functions.

4. Numerical algorithm

The algorithm presented below is based on the implicit scheme of the finite difference method (FDM).

Let $T_i^f = T(x_i, f\Delta t)$, where Δt is the time step, $x_i = ih$ (h is the geometrical mesh step) and $f = 0, 1, \dots, F$. Taking into account initial conditions (3.5), on the assumption that $u(x) = v(x) = 0$, one has $T_i^0 = T_i^1 = T_i^2 = T_p$. For the transition $t^{f-1} \rightarrow t^f$ ($f \geq 3$), the approximate form of equation (3.2) resulting from the introduction of adequate differential quotients is as follows

$$\begin{aligned} & \frac{T_i^f - T_i^{f-1}}{\Delta t} + \tau_q \frac{T_i^f - 2T_i^{f-1} + T_i^{f-2}}{(\Delta t)^2} + w_q \frac{\tau_q^2 T_i^f - 3T_i^{f-1} + 3T_i^{f-2} - T_i^{f-3}}{(\Delta t)^3} \\ &= a \frac{T_{i-1}^f - 2T_i^f + T_{i+1}^f}{h^2} + \frac{a\tau_T}{\Delta t} \left(\frac{T_{i-1}^f - 2T_i^f + T_{i+1}^f}{h^2} - \frac{T_{i-1}^{f-1} - 2T_i^{f-1} + T_{i+1}^{f-1}}{h^2} \right) \\ &+ w_T \frac{a\tau_T^2}{2(\Delta t)^2} \left(\frac{T_{i-1}^f - 2T_i^f + T_{i+1}^f}{h^2} - 2 \frac{T_{i-1}^{f-1} - 2T_i^{f-1} + T_{i+1}^{f-1}}{h^2} + \frac{T_{i-1}^{f-2} - 2T_i^{f-2} + T_{i+1}^{f-2}}{h^2} \right) \\ &+ \frac{1}{c} Q_i^f + \frac{\tau_q}{c} \left(\frac{\partial Q}{\partial t} \right)_i^f + w_q \frac{\tau_q^2}{2c} \left(\frac{\partial^2 Q}{\partial t^2} \right)_i^f \end{aligned} \quad (4.1)$$

After mathematical transformations, one has

$$\begin{aligned} & - \frac{a[2(\Delta t)^2 + 2\tau_T \Delta t + w_T \tau_T^2]}{2h^2(\Delta t)^2} T_{i-1}^f + \left[\frac{2(\Delta t)^2 + 2\tau_q \Delta t + w_q \tau_q^2}{2(\Delta t)^3} \right. \\ & \left. + \frac{2a[2(\Delta t)^2 + 2\tau_T \Delta t + w_T \tau_T^2]}{2h^2(\Delta t)^2} \right] T_i^f - \frac{a[2(\Delta t)^2 + 2\tau_T \Delta t + w_T \tau_T^2]}{2h^2(\Delta t)^2} T_{i+1}^f \\ &= \frac{2(\Delta t)^2 + 4\tau_q \Delta t + 3w_q \tau_q^2}{2(\Delta t)^3} T_i^{f-1} - \frac{2\tau_q \Delta t + 3w_q \tau_q^2}{2(\Delta t)^3} T_i^{f-2} \\ &+ \frac{w_q \tau_q^2}{2(\Delta t)^3} T_i^{f-3} - \frac{a\tau_T(\Delta t + w_T \tau_T)}{h^2(\Delta t)^2} (T_{i-1}^{f-1} - 2T_i^{f-1} + T_{i+1}^{f-1}) \\ &+ \frac{aw_T \tau_T^2}{2h^2(\Delta t)^2} (T_{i-1}^{f-2} - 2T_i^{f-2} + T_{i+1}^{f-2}) + \frac{1}{c} Q_i^f + \frac{\tau_q}{c} \left(\frac{\partial Q}{\partial t} \right)_i^f + w_q \frac{\tau_q^2}{2c} \left(\frac{\partial^2 Q}{\partial t^2} \right)_i^f \end{aligned} \quad (4.2)$$

Denoting

$$\begin{aligned} A &= - \frac{a[2(\Delta t)^2 + 2\tau_T \Delta t + w_T \tau_T^2]}{2h^2(\Delta t)^2} & B &= \frac{2(\Delta t)^2 + 2\tau_q \Delta t + w_q \tau_q^2}{2(\Delta t)^3} - 2A \\ C_i^f &= \frac{2(\Delta t)^2 + 4\tau_q \Delta t + 3w_q \tau_q^2}{2(\Delta t)^3} T_i^{f-1} - \frac{2\tau_q \Delta t + 3w_q \tau_q^2}{2(\Delta t)^3} T_i^{f-2} + \frac{w_q \tau_q^2}{2(\Delta t)^3} T_i^{f-3} \\ & - \frac{a\tau_T(\Delta t + w_T \tau_T)}{h^2(\Delta t)^2} (T_{i-1}^{f-1} - 2T_i^{f-1} + T_{i+1}^{f-1}) + \frac{aw_T \tau_T^2}{2h^2(\Delta t)^2} (T_{i-1}^{f-2} - 2T_i^{f-2} + T_{i+1}^{f-2}) \\ & + \frac{1}{c} Q_i^f + \frac{\tau_q}{c} \left(\frac{\partial Q}{\partial t} \right)_i^f + w_q \frac{\tau_q^2}{2c} \left(\frac{\partial^2 Q}{\partial t^2} \right)_i^f \end{aligned} \quad (4.3)$$

one obtains

$$AT_{i-1}^f + BT_i^f + AT_{i+1}^f = C_i^f \quad (4.4)$$

The FDM equation resulting from the boundary condition for $x = 0$ is of the form

$$\begin{aligned} & \frac{T_1^f - T_0^f}{h} + \frac{\tau_T}{\Delta t} \left(\frac{T_1^f - T_0^f}{h} - \frac{T_1^{f-1} - T_0^{f-1}}{h} \right) \\ & + \frac{w_T \tau_T^2}{2(\Delta t)^2} \left(\frac{T_1^f - T_0^f}{h} - 2 \frac{T_1^{f-1} - T_0^{f-1}}{h} + \frac{T_1^{f-2} - T_0^{f-2}}{h} \right) = 0 \end{aligned} \quad (4.5)$$

or

$$\begin{aligned} & - [2(\Delta t)^2 + 2\tau_T \Delta t + w_T \tau_T^2] T_0^f + [2(\Delta t)^2 + 2\tau_T \Delta t + w_T \tau_T^2] T_1^f \\ & = (2\tau_T \Delta t + 2w_T \tau_T^2)(T_1^{f-1} - T_0^{f-1}) - w_T \tau_T^2 (T_1^{f-2} - T_0^{f-2}) \end{aligned} \quad (4.6)$$

Let us denote

$$D = 2(\Delta t)^2 + 2\tau_T \Delta t + w_T \tau_T^2 \quad E = 2\tau_T \Delta t + 2w_T \tau_T^2 \quad (4.7)$$

then

$$-DT_0^f + DT_1^f = E(T_1^{f-1} - T_0^{f-1}) - w_T \tau_T^2 (T_1^{f-2} - T_0^{f-2}) \quad (4.8)$$

In a similar way, for $x = L$, one has

$$-DT_{n-1}^f + DT_n^f = E(T_n^{f-1} - T_{n-1}^{f-1}) - w_T \tau_T^2 (T_n^{f-2} - T_{n-1}^{f-2}) \quad (4.9)$$

So, the final form of the system of equations corresponding to the transition $t^{f-1} \rightarrow t^f$ ($f \geq 3$) is the following

$$\begin{aligned} & -DT_0^f + DT_1^f = E(T_1^{f-1} - T_0^{f-1}) - w_T \tau_T^2 (T_1^{f-2} - T_0^{f-2}) \\ & AT_{i-1}^f + BT_i^f + AT_{i+1}^f = C_i^f \quad i = 1, 2, \dots, n-1 \\ & -DT_{n-1}^f + DT_n^f = E(T_n^{f-1} - T_{n-1}^{f-1}) - w_T \tau_T^2 (T_n^{f-2} - T_{n-1}^{f-2}) \end{aligned} \quad (4.10)$$

So, the transition from t^{f-1} to t^f ($f \geq 3$) requires solving of the system of equations with a three-band main matrix which is the fastest solved using the Thomas algorithm.

5. Examples of computations

Thin metal films ($L = 100$ nm) made of chromium, nickel and gold have been considered. The surface $x = 0$ of the domain is subjected to the laser pulse. The parameters determining the capacity of the internal heat source (Eq. (3.1)) are equal to $I_0 = 13.7$ J/m², $t_p = 0.1$ ps, $\delta = 15.3$ nm, $R = 0.93$. The initial temperature of the domain equals $T_p = 300$ K, while the initial values of functions are $u(x) = 0$, $v(x) = 0$. Differential mesh parameters are $n = 1000$, $\Delta t = 0.0001$ ps.

At the stage of numerical computations, constant values of thermophysical parameters have been assumed (mainly due to lack of other data in the literature) – see Table 1.

Table 1. Thermophysical parameters (Tzou, 2015)

	Chromium	Gold	Nickel
c [MJ/(m ³ K)]	3.21484	2.4897	4
λ [W/(mK)]	93	315	90.8
τ_q [ps]	0.136	8.5	0.82
τ_T [ps]	7.86	90	10

Computations have been performed in versions corresponding to $w_T = 0$, $w_q = 0$ (first-order DPLE), $w_T = 1$, $w_q = 1$ (second-order DPLE), $w_T = 0$, $w_q = 1$ and $w_T = 1$, $w_q = 0$ (mixed order DPLE). Additionally, for comparative purposes, numerical solutions of the classical Fourier problems have been also found. The results are presented in the form of heating/cooling curves at the irradiated surface. The set of solutions for the chromium layer is shown in Fig. 1. For the other materials (Figs. 2 and 3), the solutions corresponding to the Fourier model, $w_T = 0$, $w_q = 0$ and $w_T = 1$, $w_q = 1$ are distinguished. The discussion of the results obtained will be carried out in the next Section.

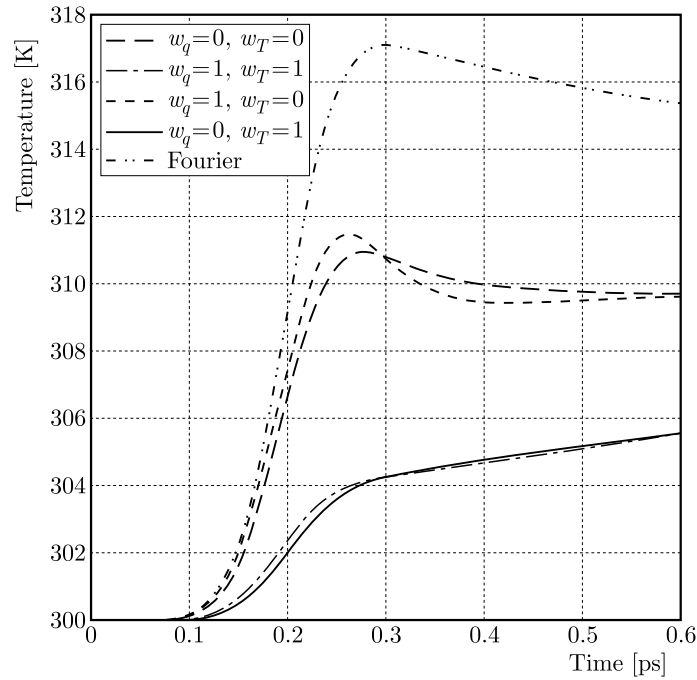


Fig. 1. Temperature history at the irradiated surface for different models (chromium)

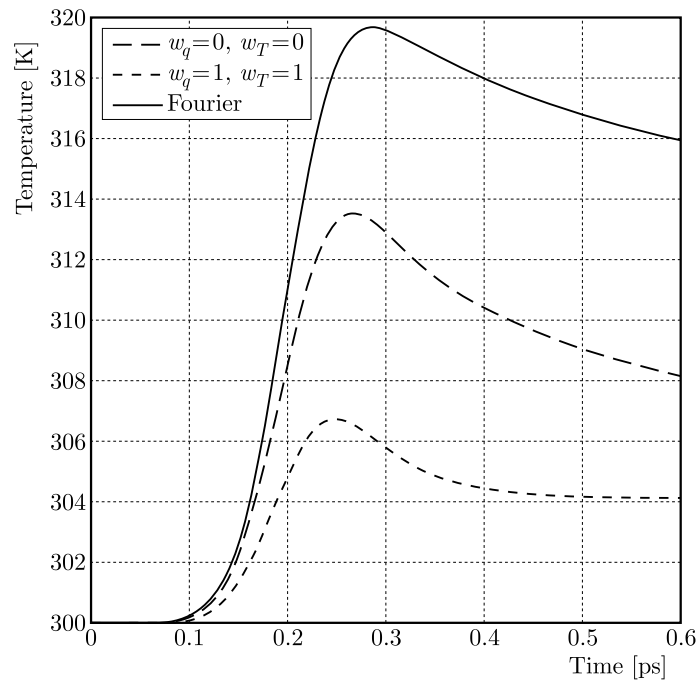


Fig. 2. Temperature history at the irradiated surface for different models (gold)

6. Conclusions

Different (in the sense of the order) models using the dual phase lag equation give different results. Here, one can see some regularities. In relation to the model based on the second-order DPLE, the solution resulting from the first-order equation is clearly overstated. This is the case for all the materials in question. The fact that the Fourier model gives a solution over DPLE has been repeatedly confirmed in numerous papers. This is a natural consequence of the delay

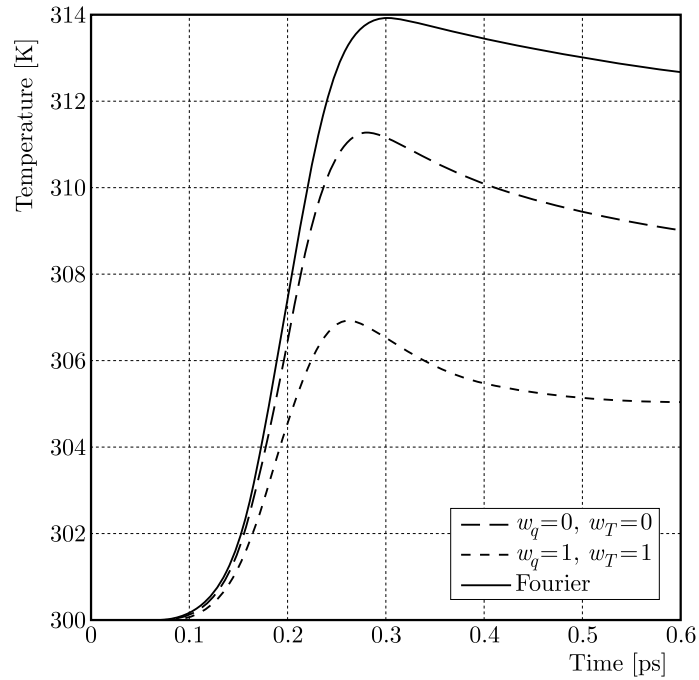


Fig. 3. Temperature history at the irradiated surface for different models (nickel)

times introduced. In the case of mixed models, the omission of the component containing τ_T^2 (Eq. (2.11)) leads to results close to the solution of the first-order DPLE – see Fig. 1. On the other hand, the omission of the component containing τ_q^2 (Eq. (2.12)) gives a solution similar to the solution of the second-order DPLE. The same trend is observed for the remaining materials. This results from the much larger (in the case of metals) value of the thermalization time versus the relaxation one. Therefore, more components of the Taylor series should be included on the right hand side of the generalized Fourier law. Summing up, the problems connected with the modeling of thermal processes in metal microdomains should be solved using the second-order dual phase lag equation. If the delay times vary less, then the solution based on the first-order model is sufficiently accurate.

Acknowledgement

The paper and research were financed within the project 2015/19/B/ST8/01101 sponsored by The National Science Centre (Poland).

References

1. AL-NIMR M.A., NAJI M., ABDALLAH R.I., 2004, Thermal behavior of a multi-layered thin slab carrying periodic signals under the effect of the dual-phase-lag heat conduction model, *International Journal of Thermophysics*, **25**, 3, 949-966
2. ASKARIZADEH H., BANIASADI E., AHMADIKIA H., 2017, Equilibrium and non-equilibrium thermodynamic analysis of high-order dual-phase lag heat conduction, *International Journal of Heat and Mass Transfer*, **104**, 301-309
3. CASTRO M.A., RODRIGUEZ F., CABRERA J., MARTIN, J.A., 2016, A compact difference scheme for numerical solution of second order dual-phase-lagging models of microscale heat transfer, *Journal of Computational and Applied Mathematics*, **201**, 432-440
4. CATTANEO M.C., 1948, Sulla conduzione de calor, *Atti de Seminario Matematico e Fisico Della Universita di Modena*, **3**, 3, 3-21

5. CHEN J. K., BERAUN J. E., 2001, Numerical study of ultrashort laser pulse interactions with metal films, *Numerical Heat Transfer A – Applications*, **40**, 1-20
6. CIESIELSKI M., 2017a, Analytical solution of the dual phase lag equation describing the laser heating of thin metal film, *Journal of Applied Mathematics and Computational Mechanics*, **16**, 1, 33-40
7. CIESIELSKI M., 2017b, Application of the alternating direction implicit method for numerical solution of the dual phase lag equation, *Journal of Theoretical and Applied Mechanics*, **55**, 3, 839-852
8. DAI W., NASSAR R., 2000, A compact finite difference scheme for solving a three-dimensional heat transport equation in a thin film, *Numerical Methods for Partial Differential Equations*, **16**, 441-458
9. DENG D., JIANG Y., LIANG D. L., 2017, High-order finite difference methods for a second-order dual-phase-lagging models of microscale heat transfer, *Applied Mathematics and Computation*, **309**, 31-48
10. FAGHRI A., ZHANG Y., HOWELL J., 2010, *Advanced Heat and Mass Transfer*, Global Digital Press
11. HO A.J.R., KUO CH.P., JIAUNG W.S., 2003, Study of heat transfer in multilayered structure within the framework of dual-phase-lag heat conduction model using lattice Boltzmann method, *International Journal of Heat and Mass Transfer*, **46**, 55-69
12. KABA I., DAI W., 2005, A stable three-level finite difference scheme for solving the parabolic two-step model in a 3D micro-sphere heated by ultrashort-pulsed lasers, *Journal of Computational and Applied Mathematics*, **181**, 125-147
13. MAJCHRZAK E., KAŁUŻA G., 2017, Analysis of thermal processes occurring in the heated multi-layered metal films using the dual-phase lag model, *Archives of Mechanics*, **69**, 4-5, 275-287
14. MAJCHRZAK E., MOCHNACKI B., 2014, Sensitivity analysis of transient temperature field in microdomains with respect to dual-phase-lag-model parameters, *International Journal for Multiscale Computational Engineering*, **12**, 1, 65-77
15. MAJCHRZAK E., MOCHNACKI B., 2016, Dual-phase lag equation. Stability conditions of a numerical algorithm based on the explicit scheme of the finite difference method, *Journal of Applied Mathematics and Computational Mechanics*, **15**, 3, 89-96
16. MAJCHRZAK E., MOCHNACKI B., SUCHY J.S., 2009, Numerical simulation of thermal processes proceeding in a multi-layered film subjected to ultrafast laser heating, *Journal of Theoretical and Applied Mechanics*, **47**, 2, 383-396
17. MOCHNACKI B., PARUCH M., 2013, Estimation of relaxation and thermalization times in micro-scale heat transfer model, *Journal of Theoretical and Applied Mechanics*, **51**, 4, 837-845
18. MOHAMMADI-FAKHAR V., MOMENI-MASULEH S. H., 2010, An approximate analytic solution of the heat conduction equation at nanoscale, *Physics Letters A*, **374**, 595-604
19. QIU T.Q., JUHASZ T., SUAREZ C., BRON N.E., TIEN C.L., 1994, Femtoscond laser heating of multi-layers metals. II Experiments, *International Journal of Heat and Mass Transfer*, **37**, 17, 2799-2808
20. SMITH A. N., NORRIS P. M., 2003, Microscale Heat Transfer, Chapter 18, [In:] *Heat Transfer Handbook*, John Willey & Sons
21. ROETZEL W., PUTRA N., DAS S.K., 2003, Experiment and analysis for non-Fourier conduction in materials with non-homogeneous inner structure, *International Journal of Thermal Sciences*, **42**, 541-552
22. TANG D.W., ARAKI N., 1999, Wavy, wavelike, diffusive thermal responses of finite rigid slabs to high-speed heating of laser-pulses, *International Journal of Heat and Mass Transfer*, **42**, 855-860
23. TZOU D.Y., 1995, A unified field approach for heat conduction from macro- to micro-scales, *Journal of Heat Transfer, ASME*, **117**, 1, 8-16

24. TZOU D.Y., 2015, *Macro to Microscale Heat Transfer: The Lagging Behavior*, John Wiley & Sons, Ltd.
25. VERNOTTE P., 1958, Les paradoxes de la theorie continue de l'equation de la chaleur, *Comptes Rendus de l'Academie des Sciences*, **246**, 3154-3155
26. WANG H., DAI W., MELNIK R., 2006, A finite difference method for studying thermal deformation in a double-layered thin film exposed to ultrashort pulsed lasers, *International Journal of Thermal Sciences*, **45**, 1179-1196
27. WANG H., DAI W., HEWAVITHARANA L.G., 2008, A finite difference method for studying thermal deformation in a double-layered thin film with imperfect interfacial contact exposed to ultrashort pulsed lasers, *International Journal of Thermal Sciences*, **47**, 7-24
28. ZHANG Z.M., 2007, *Nano/Microscale Heat Transfer*, McGraw-Hill

Manuscript received November 11, 2017; accepted for print January 9, 2018

THE USE OF VACUUM PACKED PARTICLES WITH ADAPTABLE PROPERTIES IN ACOUSTIC APPLICATIONS

ROBERT ZALEWSKI, MICHAŁ RUTKOWSKI

Warsaw University of Technology, Institute of Machine Design Fundamentals, Warsaw, Poland

e-mail: landranger@gmail.com; robertzalewski@wp.pl

The aim of this paper is to present possibilities of using a new type of granular media in acoustics as innovative sound absorbers. Most materials of this type have a porous or fibrous structure. It is constant, and once manufactured, does not easily change its configuration. The examined material – Vacuum Packed Particles (VPP) is of a changeable structure. It can be assumed that the acoustical absorption of such structures can be modified and partially adjusted by an external factor. First steps in an experimental approach have been made – the acquired results are optimistic. Additional tests are being planned to confirm the observed phenomenon and to apply VPP as novel materials in acoustics. Basing on the preliminary experimental tests, it can be concluded that the considered structures could become a significant part of a multilayered structure which would have controllable sound absorption properties.

Keywords: Vacuum Packed Particles, absorption coefficient, experiments, Voronina model

List of abbreviations

ABS	–	acrylonitrile butadiene styrene
MR	–	magnetorheological (fluid)
POL	–	poly(methyl methacrylate)
PP	–	polypropylene
PPt	–	polypropylene talc
PS	–	polystyrene
VPP	–	vacuum packed particles

1. Introduction

Nowadays, there is demand for more efficient sound absorbing materials. It is obvious that all classical materials (porous, fibrous) are tested, and their acoustic characteristics could be found in many scientific publications. Most of the above are artificial and expensive structures (Karliński *et al.*, 2014), and currently there is a general tendency to search for “green” and innovative solutions in the engineering. Many efforts have been made to increase the applicability of recyclable materials, production leftovers etc., as some recent publications demonstrate (Ersoy and Küçük, 2009; Hong *et al.*, 2007; Fatima and Mohanty, 2011). Most frequently, the investigated sound absorbing materials show good absorption/transmission loss properties and, since most of acoustic tests are comprehensive (considering e.g. various thicknesses, densities, particle size, etc.), it is quite easy to determine general application possibilities and limitations concerning the researched materials (Gawdzińska *et al.*, 2015, 2016).

The modeling of the behavior of various granular absorbing materials (mixes) in various states (compressed, loose) (Voronina and Horoshenkov, 2003; Swift *et al.*, 1999; Wilson, 1999)

has shown that although most of tested particles are made of widely known and well-tested materials, there are still possibilities of using them in a better and more effective way. Some general modifications to the porous materials structure are adding air gaps, combining few layers with different acoustic properties to create a novel sound absorber, adding an additional mass to the system or even active elements (Besset and Ichchou, 2011; Yamamoto *et al.*, 2009; Zieliński, 2011). Following this path, the next step is an active absorbing material which would be able to adjust accordingly to a control measure, its own structure to better suit the requirements.

The presented research does not concern “green” materials directly, but the investigated materials could be treated as a typical leftover from production processes or products of recycling. Granulates used in the experiment were made of 5 different plastics. Using them as the so-called Vacuum Packed Particles consists in packing them in a thin hermetic envelope in which a partial vacuum (the so called underpressure) is generated.

Vacuum Packed Particles (VPP), with some limitations, can be treated as a type of a smart structure. When subjected to a partial vacuum, the structure greatly increases its apparent viscosity to the point of becoming a viscoplastic solid. Importantly, the yield stress of the VPP when in its active (“on”) state can be controlled very accurately by varying the underpressure intensity (Bajkowski and Zalewski, 2014). The outcome of this is that the structure ability to transmit a force can be controlled with a vacuum pump, which increases the number of its possible control-based applications. Extensive discussions of the physics and applications of VPP fluids can be found in (Zalewski, 2013) or previous papers of the authors (Pyrz and Zalewski, 2010; Zalewski, 2010).

Controlling the vacuum range is controlling the structure properties, which is additionally a reversible process. As previously mentioned, VPP have some characteristics that are unique to smart materials. Moreover, their considerable advantage is the simplicity and a low price compared to other smart structures, e.g. MR fluids (Bajkowski *et al.*, 2012) or (Zalewski *et al.*, 2014), and common availability.

2. Experimental set-up

Acoustic properties have been tested according to an appropriate standard (ISO 10534-2) with the use of Brüel & Kjær equipment: the impedance tube (4206) with two microphones (2670), (3160-A-04/2) generator and the (2716C) amplifier. The experimental setup is depicted in Fig. 1. Additional equipment consisted of a PC with Pulse Lab Shop software and a vacuum pump with two gauges for pressure control. The proposed experimental stand enabled obtaining reliable results between 500 and 6400 Hz.



Fig. 1. The main part of the experimental setup

2.1. The range of experiments

Granular structures have been investigated to determine the influence of several factors on the sound absorption coefficient. The following factors are particularly worthy of being mentioned:

- the level of underpressure generated inside the sample (ten various underpressure levels ranging from 0 to 0.09 MPa with a step of 0.01 MPa were taken into consideration),
- length of a sample (two different cylindrical specimens, i.e. sample I and II, having 130 and 200 mm in length, respectively, diameter of the specimen was constant and equal $D = 29$ mm),
- the grains material (five various materials were considered: polypropylene (PP), polystyrene (PS), acrylonitrile butadiene styrene (ABS), poly(methyl methacrylate) (POL) and polypropylene talc (PPt)),
- the front surface of a specimen (three types of various thickness were tested: 0.05, 0.1 and, 0.2 mm for type 1, 2 and 3, respectively).

To minimize measurement errors, the tests were performed in three independent experimental series. It was assumed that the internal porosity of investigated granular samples was constant and equal $N = 0.28$. Dimensions of the considered barrel-roller shaped grains were 2-3 mm diameter and 4-5 mm length (Fig. 2). Densities of the tested materials are shown in Table 1 (values determined in separate laboratory tests).



Fig. 2. Particles used in the specimen construction

Table 1. Densities of tested materials

Grain material	Density [g/cm ³]
PP	0.92
PS	1.06
ABS	1.04
POL	1.18
PPt	1.21

2.2. Specimen construction

The necessity to generate a partial vacuum inside the investigated testing pieces forced the authors to design a special construction of the experimental sample. The grains were packed in a

thin plastic container as shown below in Fig. 3. The rear part of the sample was manufactured as a steel disc which acted as a “rigid” wall behind the test material. The sample previously mounted inside the impedance tube was in the next step connected to the vacuum pump. To verify such an approach to experimental research, a second type of specimen was designed, where the original parts of the mentioned impedance tube were used. Differences in the observed responses of the investigated materials were negligible.

Because the design of the test sample had to ensure tightness, its front was sealed by a thin plastic membrane (made of polypropylene, thicknesses 0.05-0.2 mm). To try and find out the impact of the material in front of the sample, three various thickness values were analyzed (Section 2.1).

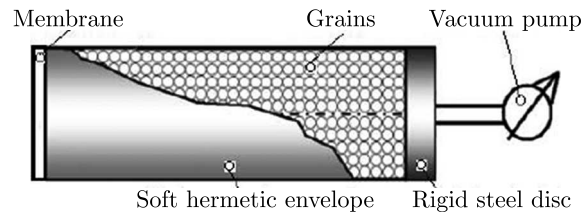


Fig. 3. Specimen construction details

3. Results and discussion

3.1. Influence of the underpressure

It can be observed in Figs. 4 and 5 (absorption coefficient of ABS and PP particles, respectively) that the underpressure generated inside the sample has a noticeable impact on acoustic properties of tested granular structures for the whole range of investigated frequencies. Moreover, the impact of a partial vacuum is nonlinear. The observed structural change, where the material is transforming from a semi-liquid to a semi-solid state (so called “jamming mechanism”), appears to be the strongest between the atmospheric pressure and 0.01 MPa underpressure. Additional experimental tests conducted on other granular materials revealed a similar phenomenon, where the full phase transition was observed near the 0.03 MPa underpressure limit. Beyond that threshold value, there is no evident difference in the recorded acoustic absorption variations. The changes in the granular structure are noticeable, since they affect every grain in the sample. Once submitted to underpressure, the grains are compacting. It results in a nonlinear increase in the number of contact points and simultaneously “intergranular” forces values (Pyrz and Zalewski, 2010). In this “jammed” state, the grains can no longer freely vibrate, also the air cavities surrounding them are greatly reduced or even eliminated (Brown *et al.*, 2010).

3.2. Influence of the front surface material

Figures 6 and 7, also Table 2 show the influence of the front membrane of investigated samples filled with ABS and POL grains respectively on their acoustic absorption coefficient measured in the atmospheric pressure. The analyzed thicknesses were ranging approximately from 0.2 mm (type 3) to 0.05 mm (type 1). It is clearly depicted that acoustic properties of the samples under test are very poor for type 3 membrane. For type 2 they are significantly better and membrane type 1 is evidently the best in the whole range of experimental frequencies.

The differences between type 1 and 3 material are several hundred percent. Another observation can be made that for frequencies below 2-2.5 kHz, an increase in the absorbing efficiency (with decreasing thickness of the membrane) is considerably slower than for higher frequencies. Also, the membrane thickness seems to have a lot more impact on the absorption above 2 kHz.

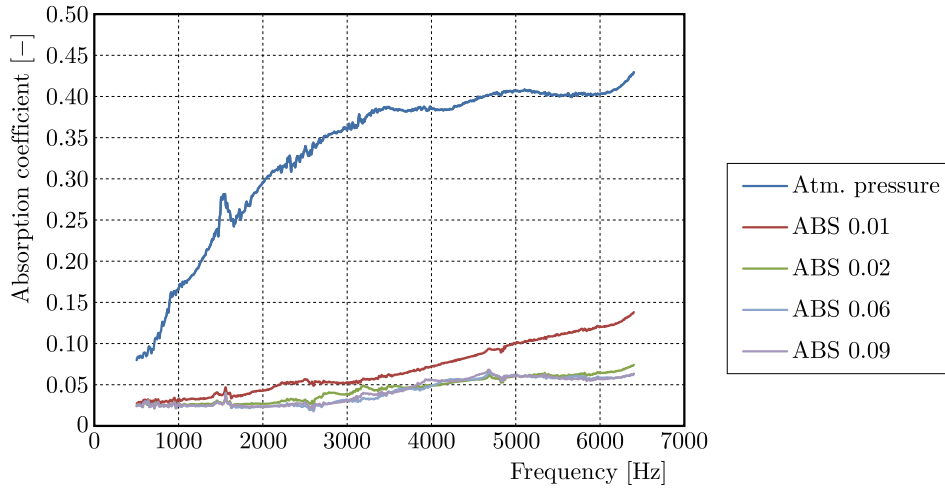


Fig. 4. Sound absorption coefficient for ABS grains and various underpressure values; sample II, front material type 2

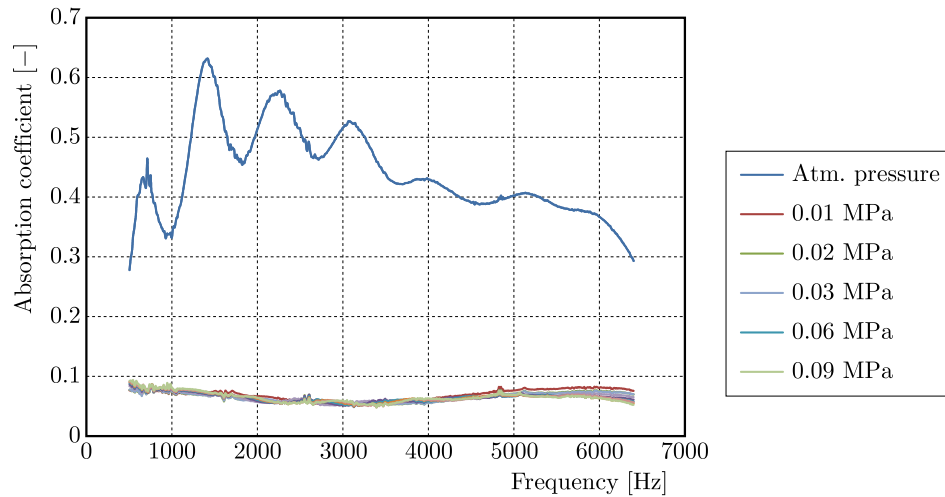


Fig. 5. Sound absorption coefficient for PP grains and various underpressure values; sample I, front material type 1

Table 2. Sound absorption coefficient of ABS and POL particles for various specimen front materials

Grain material	Sample front material type	Frequency [Hz]				
		500	1000	2000	4000	6400
ABS	3	0.057	0.052	0.058	0.059	0.088
	2	0.080	0.166	0.296	0.385	0.429
	1	0.267	0.448	0.429	0.547	0.464
POL	3	0.057	0.076	0.098	0.128	0.124
	2	0.126	0.239	0.390	0.482	0.407
	1	0.457	0.574	0.581	0.571	0.580

The cause for some differences mentioned above would probably be an increase of sound waves penetration with a reduction in the membrane thickness. It is obvious that using a supplementary material in front of the tested grains simply limits their dissipation capabilities but, nevertheless, it is the only way to use Vacuum Packed Particles as controllable sound absorbers.

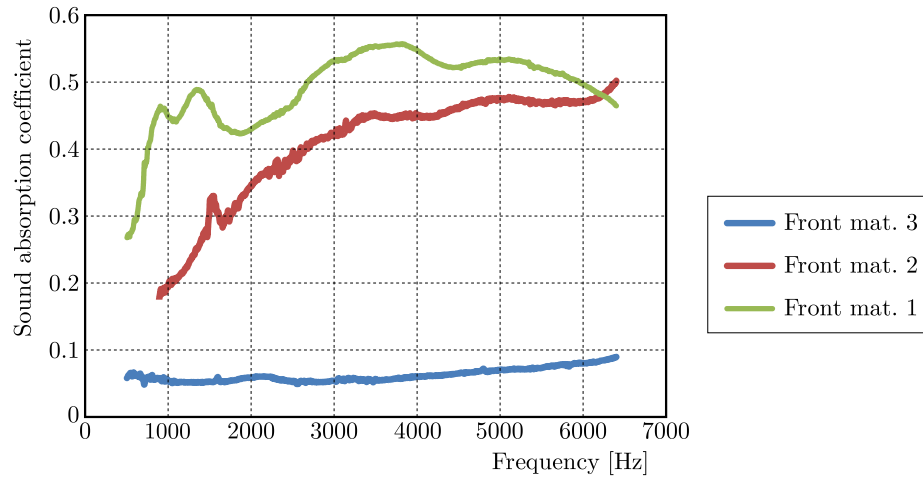


Fig. 6. Sound absorption coefficient for ABS grains subject to atmospheric pressure; sample I, various types of specimens front materials

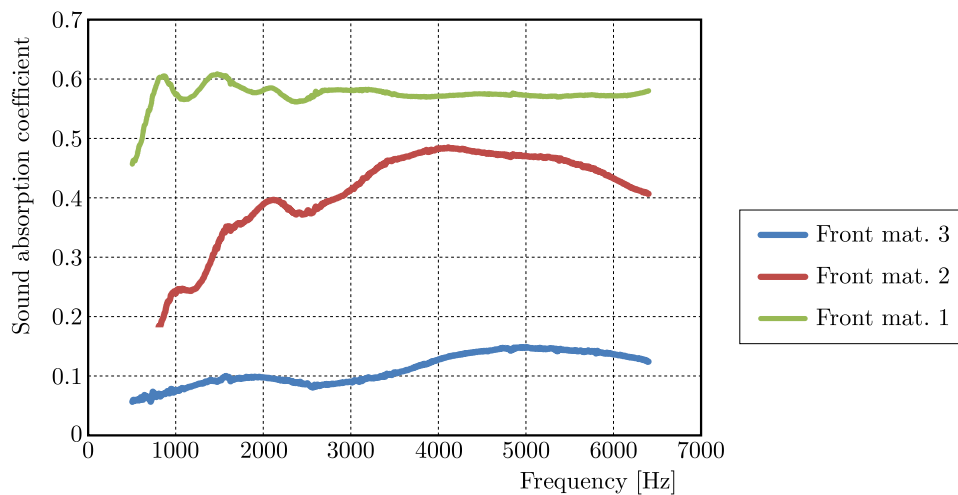


Fig. 7. Sound absorption coefficient for POL grains subject to atmospheric pressure; sample II, various types of specimens front materials

3.3. Influence of the grain material

In Fig. 8, various grains materials subjected to the atmospheric pressure are investigated and their sound absorption coefficient is depicted. It is additionally assumed that the front membrane is the same for all experiments analyzed in this Section (type 2). As for the shape of the curves, it can be stated that the characteristics of ABS and POL grains reveal many similarities, especially for the lower values of considered frequencies. Also in mid and high frequencies the value of coefficient seems to be close and stabilizing for both. The characteristics of PP and PS also seem to be close in shape with a clear highest value of the coefficient for both plastics. However, the highest value for both these materials is almost 1.5 kHz apart in frequency. The highest sound absorption properties have been obtained for PS structures, for frequencies below 2.5 kHz, other materials showed best performance between 3 and 5 kHz. Such characteristics probably result from slight size/shape variations in the grain mixes as well as the materials density scatter. A common feature for all 4 curves is a similar peak that can be found at about 1.5 kHz as well as the characteristic below the value of 1.5 kHz.

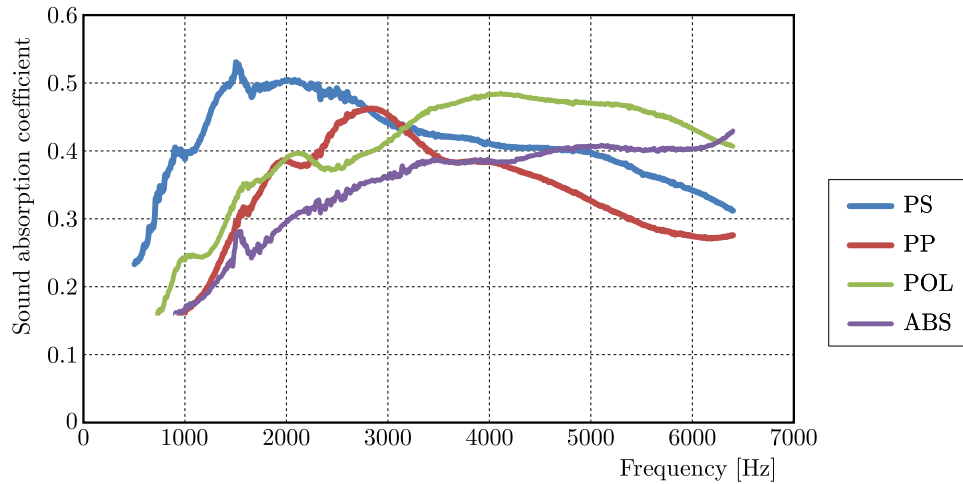


Fig. 8. Sound absorption coefficient for various granular materials subjected to the atmospheric pressure; sample II, front material type 2

3.4. Influence of the sample length

Figures 9-12 reveal the influence of length of the sample on the investigated acoustic properties. It is worth mentioning that many similarities between the compared characteristics can be encountered, e.g. the characteristic frequencies of resonance in the absorption coefficient spectra for corresponding specimens. The characteristics with front material type 1 (the thinnest) show more clearly that the shape of curves for sample I is similar for all materials which, thus, proves the impact of the sample front material is the least with type 1. With sample II, the results are also close for all grain types (there is a little variation with ABS).

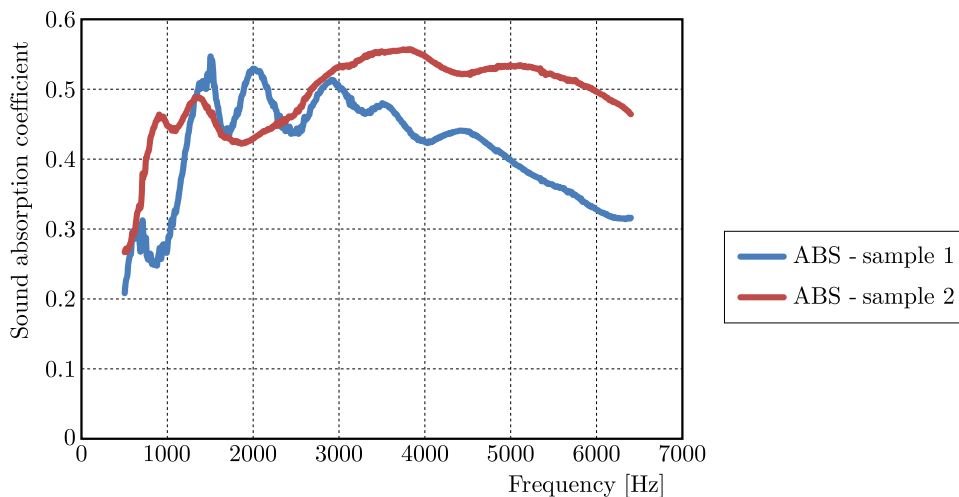


Fig. 9. Sound absorption coefficient for ABS grains; samples I and II, atmospheric pressure, front material type 1

The absorption coefficient is generally higher for sample II in comparison to sample I, which is particularly observable for frequencies above 3 kHz. Below that value, it depends on the sound frequency, since there are some regions with analogous properties for both specimens (500 Hz-2 kHz). It would mean that the sample length is not a decisive factor for this range of frequencies. On the other hand, sample II in most cases (besides ABS) provides a more steady constant performance throughout the whole tested range. The results for sample I show a peak of performance at about 1.5 kHz, then the absorption is decreasing, also the shape of curves is wavy (sinusoidal), which is interesting, as it is almost a negligible feature for sample II.

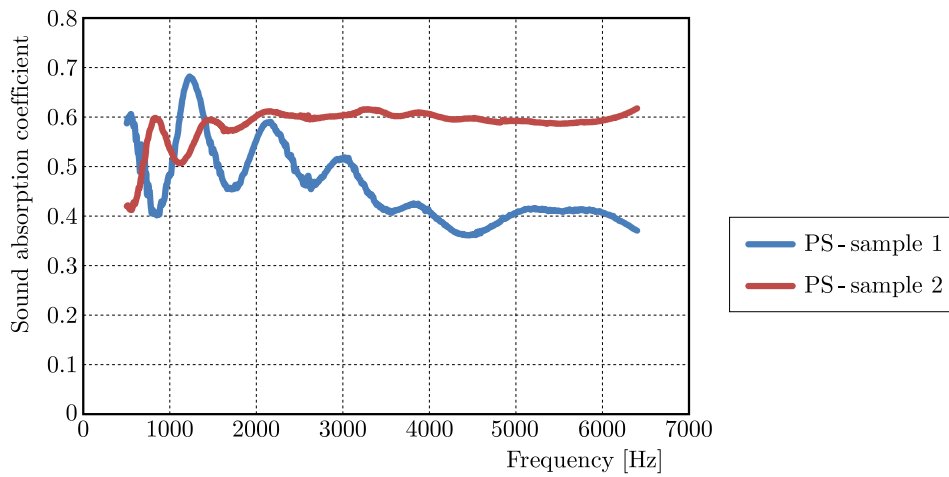


Fig. 10. Sound absorption coefficient for PS grains; samples I and II, atmospheric pressure, front material type 1

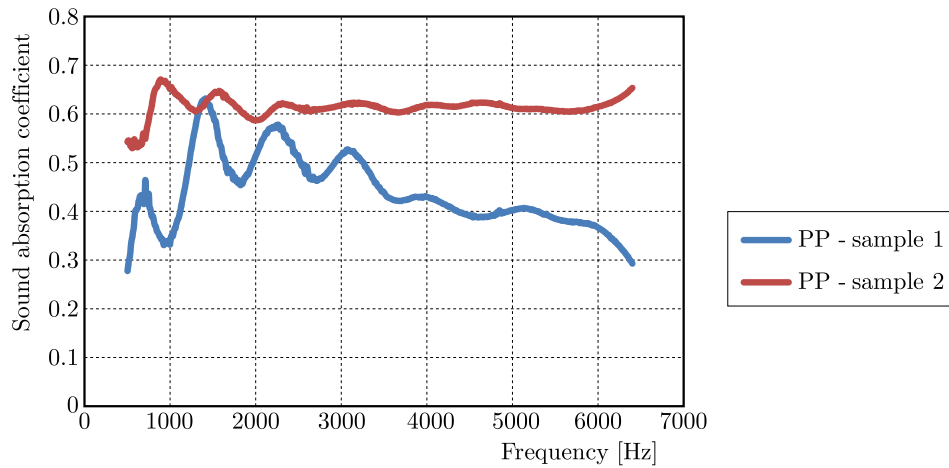


Fig. 11. Sound absorption coefficient for PP grains; samples I and II, atmospheric pressure, front material type 1

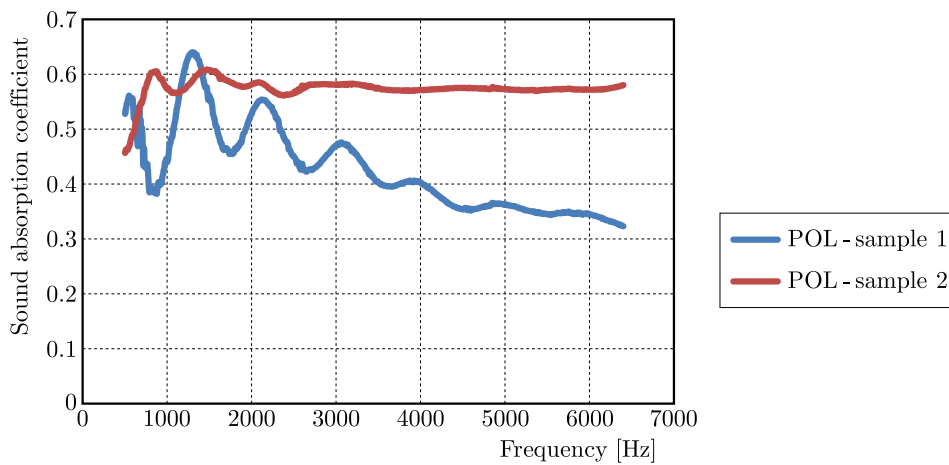


Fig. 12. Sound absorption coefficient for POL grains; samples I and II, atmospheric pressure, front material type 1

It should be pointed out that the recorded characteristics for ABS grains reveal a range between 1.1 and 3 kHz, where the absorption level of sample I is greater than for sample II. Another thing to emphasize is that all the tested materials are of the same kind (plastics). And although there are physical differences between them (slight size, shape, properties etc.), the overall test results remain, in some ways, similar.

4. Modeling

To model the acoustic behavior of VPP, several models have been considered. As it turned out, the best suited is the one being developed by Voronina, and finally presented e.g. in (Voronina and Horoshenkov, 2004). The model involves a number of material parameters such as the characteristic dimension of particles D , tortuosity q and porosity H (being a ratio of the void space volume to the whole volume of the material). The model equations are

$$\alpha_0 = 1 - \left| \frac{z_s - 1}{z_s + 1} \right|^2 \quad z_s = W \coth(\gamma l) \quad (4.1)$$

where α_0 is the absorption coefficient, $W = W_a + iW_i$ is the normalized surface impedance, $\gamma = \alpha + i\beta$ is the complex propagation constant, z_s is the normalized surface impedance and l is the thickness of the layer.

Also

$$\alpha = \frac{kQH}{1+A} \quad \beta = k[1 + QH(1+B)] \quad (4.2)$$

and

$$W_i = \frac{QH}{1+C} \quad W_a = \begin{cases} 1+Q & \text{for } f < f_{cr} \\ \frac{q}{H} & \text{for } f \geq f_{cr} \end{cases} \quad (4.3)$$

where k is the wavenumber in the air, Q is the structural characteristic (acoustic parameter), A , B and C are certain coefficients, and f_{cr} is the critical frequency.

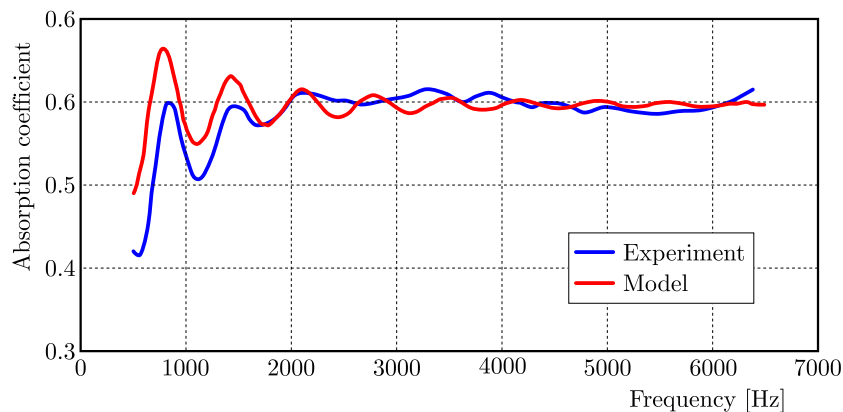


Fig. 13. Verification of experimental and numerical data for PS grains; sample II, atmospheric pressure, front material type 1

The first attempt of using the model for capturing the real acoustic behavior of VPP samples may be found in Fig. 13. It is clear that for normal conditions, the Voronina model works very well. The agreement between the model and experiment is satisfactory. Unlike other popular acoustic models (Biot, Allard, Delany-Bazley, etc.) proposed for various types of acoustic materials such as fibers or foams, the Voronina empirical formulation was developed especially for

granular media. Basing on the data depicted in Fig. 13, it can be noticed that the calculated values of the absorption coefficient are close to the direct experimental results recorded in laboratory tests. Moreover, the character of both numerical and experimental characteristics is similar. It is worth mentioning that the modeled and recorded frequencies of resonance (e.g. 0.8 kHz, 1,4 kHz) are coincident. Such observations confirm the correctness and reliability of the adopted Voronina model for capturing nonlinear acoustic properties of vacuum packed particles.

The Voronina model in presented form (4.1)-(4.3) does not include the underpressure parameter. To introduce nonlinear underpressure functions to the investigated model, additional laboratory tests have been carried out. The parameter of tortuosity was modified to compensate for the structural changes while introducing underpressure. It was observed that the mentioned changes did not include overall sample volume but, nevertheless, the grains were forced to closer contact and they could no longer freely vibrate, hence the tortuosity change. Two additional parameters α and β (both as a function of p) were introduced to the tortuosity equation

$$q = q_0 + \left(\frac{f}{\alpha}\right)^\beta \quad (4.4)$$

Two Figs. 14 and 15 show both parameters as a function of underpressure for two types of grains.

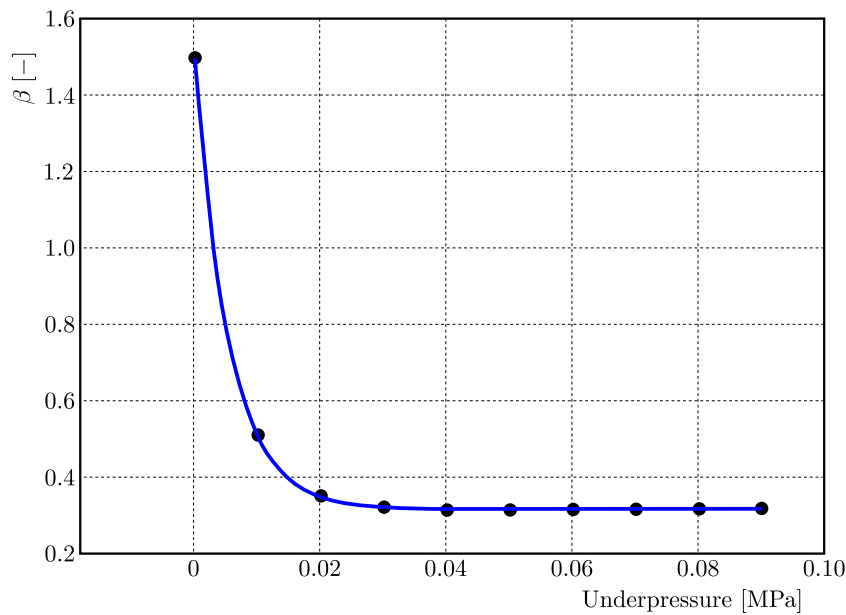


Fig. 14. Parameter β as a function of underpressure for ABS grains

Subsequent Figs. 16-18 show the modeling with the use of new expressions against the experimental results.

5. Conclusions and perspectives

The current work is a continuation of previous efforts aimed at commercialization of Vacuum Packed Particles. The former papers of the authors were mainly devoted to studies and modeling of mechanical properties of VPP. It was shown in (Zalewski and Szmids, 2014) that the Young modulus and proof stress (Szmids, Zalewski, 2014) of such structures are complex functions of underpressure. In (Zalewski, 2013) the authors revealed that the volume of the specimen had an impact on the physical properties of granular conglomerates. Extraordinary features of VPP

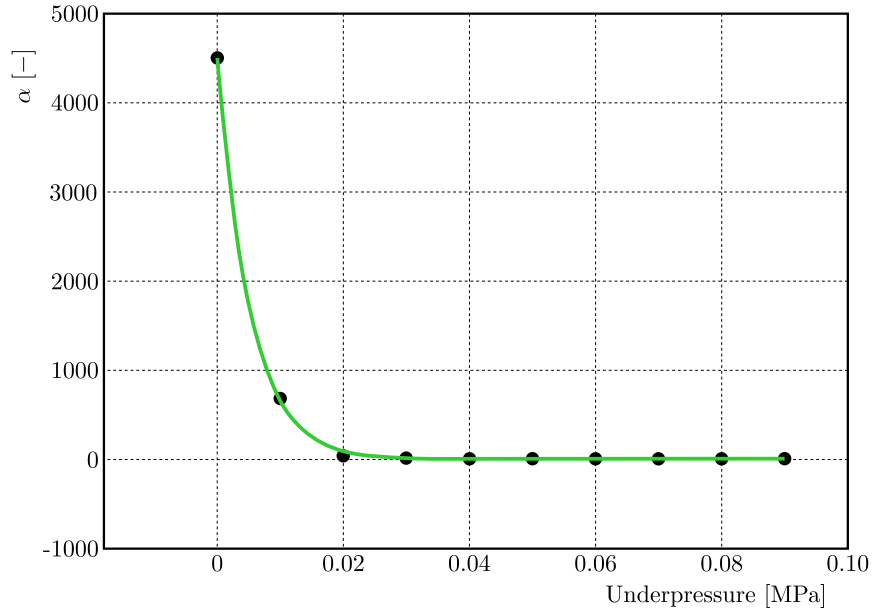


Fig. 15. Parameter α as a function of underpressure for PMMA grains

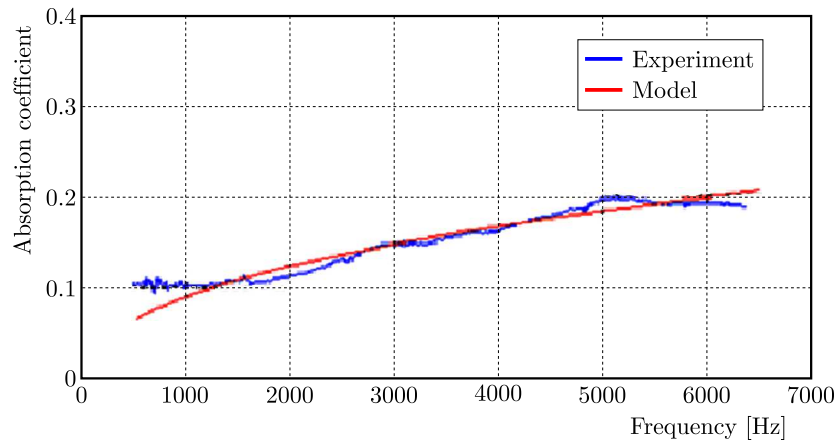


Fig. 16. Verification of experimental and numerical data for PMMA grains; sample I, underpressure 0.01 MPa, front material type 2

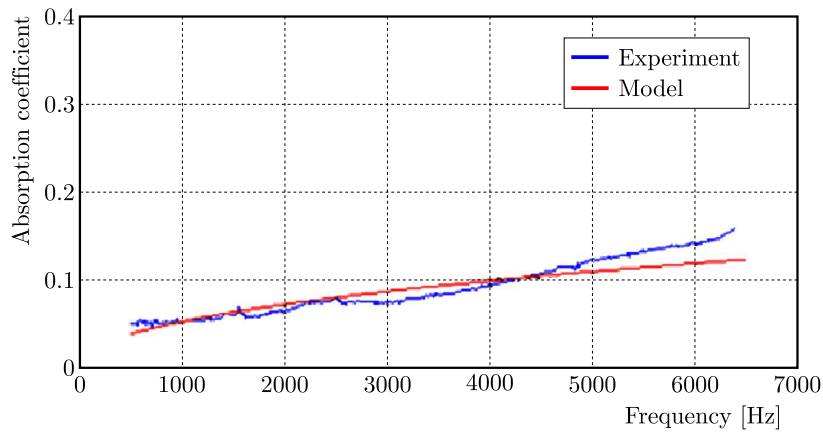


Fig. 17. Verification of experimental and numerical data for ABS grains; sample II, underpressure 0.01 MPa, front material type 2

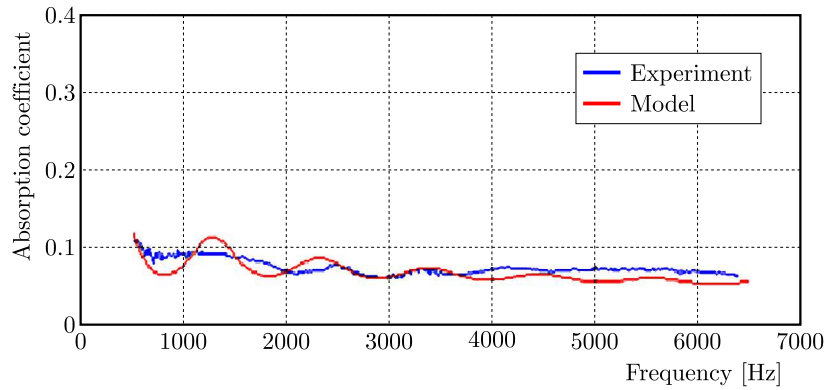


Fig. 18. Verification of experimental and numerical data for PMMA grains; sample I, underpressure 0.09 MPa, front material type 1

observed in the former experiments encouraged the authors to focus on the acoustic properties of VPP.

Studying sound absorbing characteristics of Vacuum Packed Particles has confirmed to be a very interesting and far-reaching task. It revealed that the simple mechanism of vacuum packing and changing the internal pressure can widely influence the acoustic characteristics of tested materials. Although there are some obvious limitations in practical engineering applications of VPP resulting from incomplete knowledge about their behavior, the control possibilities alone make the authors believe that the future work will help them to overcome issues that have been observed during the current research.

Moreover, using VPP as a part of an active sound absorber is possible but requires further work aiming at maximizing the sample absorption in a loose state of the granular mix while minimizing its thickness.

The presented results clearly depict that there is a simple way of influencing the structure and properties of VPP. Having performed several hundred measurements, the authors can clearly state that while materials selected for the test may seem similar in a physical way, the detailed comparison of complete results reveals many incoherences in their absorption characteristics (e.g. Figs. 8 or 9). It is clear that even small differences in the shape of the grains or in other micro-features will have a great impact on the macroscopic physical (acoustic) properties of VPP.

Nevertheless, there are still many aspects to be considered in further research. Open questions include among others the influence of the mentioned physical factors (dimension, shape) or the compression ratio of grains on the acoustic properties. These parameters seem to be particularly significant because they undoubtedly determine such parameters as porosity or tortuosity (Allard, 1993; Attenborough, 1983) of tested specimens.

Another interesting issue is the quantitative change of the absorption coefficient in the restricted range of internal underpressures from 0 to 0.01 MPa. In the perspective research, this range of partial vacuum will be closely examined to record and describe the nature of the mentioned changes. In further research, it will be also important to consider materials of different strength properties (Karliński *et al.*, 2016). Grains would probably demonstrate alternative behavior when made of rubber or another deformable elastic material.

References

1. ALLARD J.F., 1993, *Propagation of Sound in Porous Media. Modelling Sound Absorbing Materials*, Elsevier, Amsterdam

2. ATTENBOROUGH K., 1983, Acoustical characteristics of rigid fibrous absorbents and granular materials, *Journal of the Acoustical Society of America*, **73**, 785-799
3. BAJKOWSKI J., JASIŃSKI M., MAĆZAK J., RADKOWSKI S., ZALEWSKI R., 2012, The active magnetorheological support as an element of damping of vibrations transferred from the ground to large-scale structure supports, *Key Engineering Materials*, **518**, 350-357
4. BAJKOWSKI J.M., ZALEWSKI R., 2014, Transient response analysis of a steel beam with vacuum packed particles, *Mechanics Research Communications*, **60**, 1-6
5. BESSET S., ICHCHOU M.N., 2011, Acoustic absorption material optimisation in the mid-high frequency range, *Applied Acoustics*, **72**, 632-638
6. BROWN E., RODENBERG N., AMEND J., MOZEIKA A., STELTZ E., ZAKIN M.R., LIPSON H., JAEGER H.M., 2010, Universal robotic gripper based on the jamming of granular material, *Proceedings of the National Academy of Sciences of the United States of America*, **107**, 18809-18814
7. ERSOY S., KÜÇÜK H., 2009, Investigation of industrial tea-leaf-fibre waste material for its sound absorption properties, *Applied Acoustics*, **70**, 1, 215-220
8. FATIMA S., MOHANTY A.R., 2011, Acoustical and fire-retardant properties of jute composite materials, *Applied Acoustics*, **72**, 2/3, 108-114
9. GAWDZIŃSKA K., CHYBOWSKI L., BEJGER A., KRILE S., 2016, Determination of technological parameters of saturated composites based on SiC by means of a model liquid, *Metallurgija*, **55**, 4, 659-662
10. GAWDZIŃSKA K., CHYBOWSKI L., PRZETAKIEWICZ W., 2015, Proper matrix-reinforcement bonding in cast metal matrix composites as a factor of their good quality, *Archives of Civil and Mechanical Engineering*, **16**, 3, 553-563
11. HONG Z., BO L., GUANGSU H., JIA H., 2007, A novel composite sound absorber with recycled rubber particles, *Journal of Sound and Vibration*, **304**, 1/2, 400-406
12. ISO 10534-2, Acoustics – Determination of sound absorption coefficient and impedance in impedance tubes – Part 2: Transfer-function method
13. KARLIŃSKI J., PTAK M., DZIAŁAK P., RUSIŃSKI E., 2014, Strength analysis of bus superstructure according to Regulation No. 66 of UN/ECE, *Archives of Civil and Mechanical Engineering*, **14**, 342-353
14. KARLIŃSKI J., PTAK M., DZIAŁAK P., RUSIŃSKI E., 2016, The approach to mining safety improvement: accident analysis of an underground machine operator, *Archives of Civil and Mechanical Engineering*, **16**, 3, 503-512
15. PYRZ M., ZALEWSKI R., 2010, Modeling of granular media submitted to internal underpressure, *Mechanics Research Communications*, **37**, 2, 141-144
16. SZMIDT T., ZALEWSKI R., 2014, Inertially excited beam vibrations damped by Vacuum Packed Particles, *Smart Materials and Structures*, **23**, 2014, 105026 (9 pp)
17. SWIFT M.J., BRIŠ P., HOROSHENKOV K.V., 1999, Acoustic absorption in re-cycled rubber granulate, *Applied Acoustics*, **57**, 203-212
18. VORONINA N.N., HOROSHENKOV K.V., 2003, A new empirical model for the acoustic properties of loose granular media, *Applied Acoustics*, **64**, 415-432
19. VORONINA N.N., HOROSHENKOV K.V., 2004, Acoustic properties of unconsolidated granular mixes, *Applied Acoustics*, **64**, 673-691
20. WILSON D.K., 1997, Simple, relaxational models for the acoustical properties of porous media, *Applied Acoustics*, **50**, 3, 171-188
21. YAMAMOTO T., MARUYAMA S., NISHIWAKI S., YOSHIMURA M., 2009, Topology design of multi-material soundproof structures including poroelastic media to minimize sound pressure levels, *Computer Methods in Applied Mechanics and Engineering*, 1439-1455

22. ZALEWSKI R., 2010, Constitutive model for special granular structures, *International Journal of Non-Linear Mechanics*, **45**, 3, 279-285
23. ZALEWSKI R., 2013, *Modeling and Research of the Underpressure Influence on Mechanical Properties of Vacuum Packed Particles* (in Polish), WKŁ, Warsaw, ISBN 978-83-206-1851-8
24. ZALEWSKI R., NACHMAN J., SHILLOR M., BAJKOWSKI J., 2014, Dynamic model for a magneto-rheological damper, *Applied Mathematical Modelling*, **38**, 9/10, 2366-2376
25. ZALEWSKI R., SZMIDT T., 2014, Application of Special Granular Structures for semi-active damping of lateral beam vibrations, *Engineering Structures*, **65**, 13-20
26. ZIELIŃSKI T.G., 2011, Numerical investigation of active porous composites with enhanced acoustic absorption, *Journal of Sound and Vibration*, 5292-5308

Manuscript received December 11, 2017; accepted for print January 26, 2018

A NUMERICAL UPPER BOUND FORMULATION WITH SENSIBLY-ARRANGED VELOCITY DISCONTINUITIES AND ORTHOTROPIC MATERIAL STRENGTH BEHAVIOUR

MINGJING LI, JOSEF FÜSSL, MARKUS LUKACEVIC, JOSEF EBERHARDSTEINER

Vienna University of Technology, Vienna, Austria

e-mail: mingjing.li@tuwien.ac.at

CHRISTOPHER M. MARTIN

University of Oxford, Oxford, UK

Numerical limit analysis allows for fast estimates of the collapse load of structures exhibiting ideal plastic material behaviour. In numerical upper bound formulations, the description of the unknown velocity field can be extended by introducing velocity discontinuities between finite elements. Through these additional degrees of freedom, localised failure modes may be approximated more accurately and better upper bounds can be obtained. In the existing formulations, such discontinuities are typically introduced between all elements and the description is restricted to isotropic failure behaviour. In this work, a general 3D upper bound formulation is briefly proposed, allowing the consideration of both isotropic and orthotropic yield functions within finite elements as well as at velocity discontinuities. The concept of “projecting” a stress-based orthotropic yield function onto a certain discontinuity is presented, giving a traction-based yield function which allows for a consistent description of the material strength behaviour across the interface. The formulation is verified by means of two classical examples, the rigid strip footing and the block with asymmetric holes. Furthermore, based on the computation of potential orientations of plastic flow localisation, a simple concept for a sensible arrangement of velocity discontinuities is proposed. It is shown that this concept performs very well for isotropic as well as anisotropic material strength behaviour. A feature of the present work is that, velocity jumps are allowed only across the prescribed finite element interfaces determined from the sensible discontinuity arrangement. Good upper bounds similar to those in the existing works are obtained with far fewer degrees of freedom.

Keywords: numerical upper bound formulations, localised failure modes, traction-based yield function, sensible arrangement of velocity discontinuities, orthotropic material strength behaviour

1. Introduction

1.1. Numerical limit analysis

The main objective of limit analysis is the determination of load bearing capacities of structures exhibiting an elastoplastic material response. To achieve this, limit analysis concentrates on the critical energy dissipation rate at the time instant of structural failure, and the basic task can be expressed as follows: *Find the kinematically admissible velocity field which minimises energy dissipation over the set of all statically admissible stress fields which maximise the dissipated energy* (Ciria *et al.*, 2008). Statically admissible stress fields are required to be in equilibrium, fulfil the static boundary conditions and obey a plastic yield criterion at each point of the body. Kinematically admissible velocity fields are subject to compatibility, the kinematic

boundary conditions, and fulfil an associated plastic flow rule at each point of the body. Unfortunately, the so-defined saddle-point problem can be solved only for simple geometric and loading situations as well as for simple material behaviours. In more complex situations, the plastic flow compatibility in the so-called static principle or the static equilibrium in the so-called kinematic principle may be relaxed, providing lower and upper bounds on the exact load bearing capacity of a structure according to the bounding theorems by Drucker *et al.* (1951, 1952).

However, for complex problems, the application of these bounding theorems (in the context of limit analysis) in an analytical way is very limited and often not possible. Thus, finite-element-based formulations were first introduced in the 1970s (Belytschko and Hodge, 1970; Lysmer, 1970; Anderheggen and Knöpfel, 1972; Maier *et al.*, 1972), and gained popularity from then on. The computational efficiency and accuracy of such numerical formulations strongly depend on the mathematical programming method used to solve the underlying optimisation problems. At the early stage, the limit analysis theorems were formulated as linear optimisation problems, by linearising the applied plastic yield functions. At the turn of the millennium, Lyamin and Sloan (2002a,b) proposed more general lower and upper bound formulations allowing for nonlinear yield functions, which were solved using nonlinear programming concepts. However, local smoothing was required for yield functions with singularities, e.g. the Mohr-Coulomb yield function. Subsequently, during the past two decades, second-order cone programming (SOCP) has been proven to be an excellent alternative method by Makrodimopoulos and Martin (2006, 2007) and Ciria and Peraire (2004) for cohesive-frictional materials and Füssl *et al.* (2008) for composite materials, with sufficient robustness and efficiency to solve large-scale nonlinear optimisation problems of numerical limit analysis. Such implementations allow the applications of many different yield functions in their native form, since most of the commonly-used yield functions can be formulated as second-order cones. In this work, SOCP is employed to solve the nonlinear optimisation problems arising from the presented limit analysis formulations.

The efficiency and accuracy of such formulations is also strongly influenced by the chosen finite elements and related shape functions. In order to obtain rigorous upper bound solutions, for example, the associated plastic flow rule must be satisfied throughout the whole body. Basically, this can be achieved by using constant strain triangular elements, which are often combined with velocity discontinuities between element boundaries (Bottero *et al.*, 1980; Sloan and Kleeman, 1995; Lyamin and Sloan, 2002b). To improve the quality of upper bound solutions, the use of higher order interpolation functions is desired. Makrodimopoulos and Martin (2007) showed that the associated plastic flow rule could also be enforced throughout the whole body by using linear strain triangular elements, leading to a better performance than constant strain elements even without discontinuities. As a further development, the meshless method was implemented for numerical upper bound approaches in (Le *et al.*, 2010; Liu and Zhao, 2013; Yu *et al.*, 2016). However, in such implementations with high order shape functions, it is difficult to guarantee both compatibility and satisfaction of the associated plastic flow rule throughout each element.

Additionally or as an alternative to the use of high order elements, velocity discontinuities can be implemented in upper bound formulations to increase their effectiveness. In (Chen *et al.*, 2003; Milani and Lourenço, 2009), for example, rigid elements were used and plastic dissipation was only allowed between finite elements. Such approaches are highly dependent on the mesh and even adaptive mesh refinement cannot fully compensate for this issue. An approach without using classical finite elements is the so-called discontinuity layout optimisation (DLO), where velocity discontinuities are determined by using a truss layout optimisation algorithm based on a prescribed grid (Smith and Gilbert, 2007; Hawksbee *et al.*, 2013). This approach performs well for 2D problems, but the determination of complex failure mechanisms in 3D bodies requires a fine grid and large computational effort.

For this reason, in the authors' opinion, the most promising approach so far to obtain rigorous upper bound solutions still seems to be the use of solid finite elements with or without velocity

discontinuities. In Krabbenhøft *et al.* (2005) zero-thickness interface elements between constant strain elements are introduced, which perform well for a large number of applications. Another development can be found in Makrodimopoulos and Martin (2008), where velocity discontinuities are implemented between linear strain elements. In order to increase the efficiency of the upper bound formulations, adaptive mesh refinement was introduced by Ciria and Peraire (2004), Ciria *et al.* (2008) and Martin (2011). However, a targeted arrangement of discontinuities, as will be proposed in this work, has not been introduced until now.

1.2. Objective of the paper

In several previous works, e.g. in (Füssl *et al.*, 2017; Li *et al.*, 2018), anisotropic yield functions have been implemented in numerical upper bound formulations. To the authors' knowledge, the combination of anisotropic yield functions and velocity discontinuities has not previously been presented, although it could significantly improve the capability of upper bound approaches in handling localised plastic failure for anisotropic materials, like wood or fibre reinforced composites. In particular, it is beneficial if the alignment of discontinuities is tuned to the direction of localised plastic failure.

Thus, the main objectives of this work can be introduced as follows:

1. The formulation of 3D numerical upper bound approaches with anisotropic yield functions, quadratic shape functions for the velocity fields, and velocity discontinuities.
2. To allow for a consistent description of plastic failure also across velocity discontinuities, the derivation of a traction-based yield function which is in accordance with the stress-based yield function assigned to the solid finite elements/bulk material.
3. Implementation of an initial concept for a sensible introduction and arrangement of velocity discontinuities only in failure regions.

According to these objectives, the paper is structured as follows. A quite general numerical upper bound approach is briefly proposed in Section 2, able to consider plastic energy dissipation in both finite elements and discontinuities obeying an anisotropic failure criterion. Furthermore, the process for obtaining the required traction-based yield functions for the discontinuities is described. A verification of the implemented upper bound formulations by means of well-known examples can be found in Section 3, as well as a discussion about the performance of velocity discontinuities. Finally, a brief summary and concluding comments are given in Section 4.

2. Upper bound approaches

The upper bound theorem focuses exclusively on the kinematically admissible velocity fields $\dot{\mathbf{u}} = (\dot{u}_x, \dot{u}_y, \dot{u}_z)^T \in \mathfrak{R}^3$, and by minimising the internal plastic energy dissipation rate W_{int} , which has to be equal to the work rate of the external loads W_{ext} , the resulting failure state provides an upper bound for the exact collapse load. A kinematically admissible velocity field $\dot{\mathbf{u}}$ has to satisfy the compatibility, the associated plastic flow rule, and the kinematic boundary conditions at each point of the considered body. Additionally, a velocity-jump field $\Delta\dot{\mathbf{u}} = (\Delta\dot{u}_x, \Delta\dot{u}_y, \Delta\dot{u}_z)^T \in \mathfrak{R}^3$ is introduced, describing localised interface plastic failure across a prescribed interior surface.

The internal energy dissipation rate W_{int} is composed of a part referring to material failure in the continuum body Ω and a part related to the energy dissipation at interior surfaces Γ^{dis} , and reads

$$W_{int} = \int_{\Omega} d_p^{mat}(\dot{\boldsymbol{\varepsilon}}) dV + \int_{\Gamma^{dis}} d_p^{dis}(\Delta\dot{\mathbf{u}}) dA \quad (2.1)$$

with the plastic dissipation functions

$$\begin{aligned} d_p^{mat} &= \sup_{\boldsymbol{\sigma} \in \mathcal{F}} \boldsymbol{\sigma}^T \dot{\boldsymbol{\epsilon}} & \mathcal{F} &= \{\boldsymbol{\sigma} \mid f(\boldsymbol{\sigma}) \leq 0\} & \text{in } \Omega \\ d_p^{dis} &= \sup_{\mathbf{t} \in \mathcal{D}} \mathbf{t}^T \Delta \dot{\mathbf{u}} & \mathcal{D} &= \{\mathbf{t} \mid f(\mathbf{t}) \leq 0\} & \text{on } \Gamma^{dis} \end{aligned} \quad (2.2)$$

where $\dot{\boldsymbol{\epsilon}} = (\dot{\epsilon}_{xx}, \dot{\epsilon}_{yy}, \dot{\epsilon}_{zz}, \dot{\epsilon}_{xy}, \dot{\epsilon}_{yz}, \dot{\epsilon}_{xz})^T \in \mathfrak{R}^6$ represents the plastic strain-rate field, $\boldsymbol{\sigma} = (\sigma_{xx}, \sigma_{yy}, \sigma_{zz}, \tau_{xy}, \tau_{yz}, \tau_{xz})^T \in \mathfrak{R}^6$ the stress field and $\mathbf{t} = (t_x, t_y, t_z)^T \in \mathfrak{R}^3$ the surface traction field. $f(\boldsymbol{\sigma}) \leq 0$ and $f(\mathbf{t}) \leq 0$ denote the stress-based yield function for Ω and the traction-based yield function for Γ^{dis} , respectively.

The upper bound theorem can then be formulated as a nonlinear optimisation problem, reading

$$\begin{aligned} \min \quad & W_{int} \\ \text{s.t.} \quad & \dot{\boldsymbol{\epsilon}} = \text{div } \dot{\mathbf{u}} & \text{in } \Omega \\ & \dot{\mathbf{u}} = \dot{\mathbf{u}}_b & \text{on } \Gamma \\ & \dot{\boldsymbol{\epsilon}} = \dot{\lambda}_\sigma \partial f(\boldsymbol{\sigma}) / \partial \boldsymbol{\sigma} & \text{in } \Omega \\ & \Delta \dot{\mathbf{u}} = \dot{\lambda}_t \partial f(\mathbf{t}) / \partial \mathbf{t} & \text{on } \Gamma^{dis} \end{aligned} \quad (2.3)$$

in which the constraints enforce compatibility between the velocities and the plastic strain-rates, the kinematic boundary conditions, and the associated plastic flow rule both in the continuum Ω and at the interior surfaces Γ^{dis} . In the second constraint, $\dot{\mathbf{u}}_b$ refers to the prescribed velocity boundary conditions defined over the whole surface $\Gamma = \partial\Omega$ of the continuum body. In the last two constraints, $\dot{\lambda}_\sigma$ and $\dot{\lambda}_t$ are plastic multipliers, determining the magnitude of plastic flow within the continuum and at the discontinuities, respectively. Note that these two associated plastic flow constraints in Eq. (2.3) are valid only when the yield function is differentiable everywhere. If singular apex points exist, additional technology is required, and the use of SOCP in this work ensures that such points are handled naturally.

As shown in Makrodimopoulos and Martin (2007), using the duality of nonlinear programming, a mathematically equivalent optimisation problem to Eq. (2.3) can be formulated, reading

$$\begin{aligned} \max \quad & W_{ext} \\ \text{s.t.} \quad & \int_{\Omega} (\text{div } \dot{\mathbf{u}})^T \boldsymbol{\sigma} dV + \int_{\Gamma^{dis}} \Delta \dot{\mathbf{u}}^T \mathbf{t} dA = \int_{\Omega} \dot{\mathbf{u}}^T \beta \mathbf{g} dV + \int_{\Gamma} \dot{\mathbf{u}}^T \beta \mathbf{t} dA & \text{in } \Omega \\ & f(\boldsymbol{\sigma}) \leq 0 & \text{in } \Omega \\ & f(\mathbf{t}) \leq 0 & \text{on } \Gamma^{dis} \end{aligned} \quad (2.4)$$

in which the first constraint represents weak equilibrium of the dissipated energy, and the objective function is related to the external work rate given as

$$W_{ext} = \int_{\Omega} \dot{\mathbf{u}}^T \beta \mathbf{g} dV + \int_{\Gamma} \dot{\mathbf{u}}^T \beta \mathbf{t} dA \quad (2.5)$$

where β denotes a load multiplier applied to the surface traction field \mathbf{t} and the prescribed body force field $\mathbf{g} \in \mathfrak{R}^3$.

For the discretisation of the upper bound optimisation problem, tetrahedral linear-strain simplex elements are used, as introduced for the 2D upper bound problem under plane strain conditions in Makrodimopoulos and Martin (2007, 2008) and for the 3D upper bound problem in Martin and Makrodimopoulos (2008). Thus, the velocity field is approximated using quadratic interpolation functions and the plastic strain-rate field is described by linear shape functions. Worth mentioning is that each finite element has its own strain-rate evaluation nodes, which means that adjacent nodes from different elements share the same coordinates but can have different

strain-rate states. The exact representation of this approximation is given in Makrodimopoulos and Martin (2008). In this work, to assess the capability of the discontinuity arrangement, velocity jumps are allowed only across particular prescribed finite element interfaces determined by the arrangement, on which adjacent elements have their own velocity evaluation nodes.

Finally, as introduced in detail by the authors in Li *et al.* (2018), the discretised formulation of the dual upper bound optimisation problem, Eq. (2.4), can be written as

$$\begin{aligned}
& \max W_{ext} \\
& \text{s.t.} \quad \mathbf{A}_{UB}^{mat\text{T}} \hat{\mathbf{q}}_{\sigma} + \mathbf{A}_{UB}^{dis} \hat{\mathbf{q}}_t^{dis} = \beta \mathbf{A}_{UB}^{bc} \hat{\mathbf{q}}_t^{bc} \\
& \quad \hat{\mathbf{s}}_{\sigma}^{mat,i} = \hat{\mathbf{a}}_{\sigma}^{mat,i} + \mathbf{B}_{\sigma}^{mat} \mathbf{R}_{\dot{\epsilon}}^{mat} \hat{\mathbf{q}}_{\sigma}^{mat,i} \\
& \quad \hat{\mathbf{s}}_{\sigma}^{mat,i} \in \mathcal{C} \\
& \quad \hat{\mathbf{s}}_t^{dis,j} = \hat{\mathbf{a}}_t^{dis,j} + \mathbf{B}_t^{dis} \mathbf{R}_t^{dis} \hat{\mathbf{q}}_t^{dis,j} \\
& \quad \hat{\mathbf{s}}_t^{dis,j} \in \mathcal{C}
\end{aligned} \tag{2.6}$$

with the matrices \mathbf{A}_{UB} obtained by applying the linear compatibility operator to the related shape functions of the velocity (or the velocity jump), within the finite elements (*mat*), at the discontinuities between elements (*dis*), and at the boundary (*bc*). The vectors $\hat{\mathbf{q}}_{\sigma}$, $\hat{\mathbf{q}}_t^{dis}$, and $\hat{\mathbf{q}}_t^{bc}$ collect all nodal degrees of freedom related to stress-like quantities and surface tractions. Note that, for an arbitrary vector \mathbf{x} , the symbol $\hat{\mathbf{x}} = \int_{\Omega_e} \mathbf{x} dV$ refers to the volume-integrated quantity over each element. The remaining constraints represent a second-order cone formulation of a general quadratic yield function for both the solid material (*mat*) and the discontinuities (*dis*), with i and j ranging from 1 to the number of stress and traction evaluation nodes, respectively. Thereby, the matrices $\hat{\mathbf{a}}$ and \mathbf{B} contain strength parameters and the matrices \mathbf{R} represent transformation operators, rotating the stress tensors into the principal material direction and the surface traction vector into the direction of the corresponding discontinuity. The external work rate in discretised form can be written as

$$W_{ext} = \sum_{bc=1}^{UBC} \sum_{i=1}^6 \beta \mathbf{q}_{\dot{u},loc}^{bc,i} \text{T} \hat{\mathbf{q}}_{t,loc}^{bc,i} \tag{2.7}$$

where UBC denotes the number of 6-noded boundary surface triangular elements with a prescribed local traction field $\hat{\mathbf{q}}_{t,loc}^{bc}$ and $\mathbf{q}_{\dot{u},loc}^{bc}$ represents the related velocity degrees of freedom.

In previous upper bound formulations (Sloan and Kleeman, 1995; Krabbenhoft *et al.*, 2005; Makrodimopoulos and Martin, 2008) only isotropic yield functions based on shear failure mechanisms, e.g. the von Mises or the Mohr-Coulomb yield function, were considered, leading to a straightforward definition of failure at the discontinuities between elements. On the contrary, in the upper bound formulation Eq. (2.6), the quite general orthotropic yield function according to Tsai-Wu can be implemented, reading

$$\mathbf{q}^i \text{T} \mathbf{P} \mathbf{q}^i + \left(\frac{1}{2} \mathbf{F}^{+\text{T}} \mathbf{q}^i \right)^2 - \left(1 - \frac{1}{2} \mathbf{F}^{-\text{T}} \mathbf{q}^i \right)^2 \leq 0 \tag{2.8}$$

with i as the evaluation point of \mathbf{q} either for the stress field (with subscript σ) in the element or for the traction field (with subscript t) at a discontinuity. The vectors \mathbf{F}^+ , \mathbf{F}^- and matrix \mathbf{P} are related to the terms in Eq. (2.6) as follows

$$\mathbf{a} = \begin{bmatrix} 1 \\ \mathbf{0} \end{bmatrix} \quad \mathbf{B} = \begin{bmatrix} -\frac{1}{2} \mathbf{F}^{-\text{T}} \\ \mathbf{D} \\ \frac{1}{2} \mathbf{F}^{+\text{T}} \end{bmatrix} \tag{2.9}$$

where \mathbf{D} is the decomposed product of $\mathbf{P} = \mathbf{D}^T \mathbf{D}$. Note that the matrix dimensions are $\mathbf{F}_\sigma^+ \in \mathfrak{R}^6$, $\mathbf{F}_\sigma^- \in \mathfrak{R}^6$, $\mathbf{P}_\sigma \in \mathfrak{R}^{6 \times 6}$, $\mathbf{D}_\sigma \in \mathfrak{R}^{6 \times 6}$ for the stress-based yield function and $\mathbf{F}_t^+ \in \mathfrak{R}^3$, $\mathbf{F}_t^- \in \mathfrak{R}^3$, $\mathbf{P}_t \in \mathfrak{R}^{3 \times 3}$, $\mathbf{D}_t \in \mathfrak{R}^{3 \times 3}$ for the traction-based yield function.

In the above, it is assumed that there exists a traction-based yield function for the discontinuities which can also be formulated as a second-order cone. Additionally, it needs to be consistent with the stress-based Tsai-Wu criterion to allow for the description of a homogeneous strength distribution within a body. Since a surface traction state within a discontinuity cannot directly be related to a unique 3D stress state at a material point, the derivation of such a traction-based yield function is not straightforward. However, according to Wu and Cervera (2014), we can assume a 3D plastic strain-rate state to be localised with respect to a certain discontinuity if the following constraints are satisfied, for orthotropic yield functions which are differentiable everywhere (e.g. Tsai-Wu yield function):

$$\begin{aligned} \Lambda_{mm}^{dis}(\boldsymbol{\sigma}_{loc}^{dis}) &= \frac{\dot{\varepsilon}_{mm}}{\dot{\lambda}_\sigma} = \frac{\partial f(\boldsymbol{\sigma}_{loc}^{dis}, \text{strength par.})}{\partial \sigma_{mm}^{dis}} = 0 \\ \Lambda_{pp}^{dis}(\boldsymbol{\sigma}_{loc}^{dis}) &= \frac{\dot{\varepsilon}_{pp}}{\dot{\lambda}_\sigma} = \frac{\partial f(\boldsymbol{\sigma}_{loc}^{dis}, \text{strength par.})}{\partial \sigma_{pp}^{dis}} = 0 \\ \Lambda_{mp}^{dis}(\boldsymbol{\sigma}_{loc}^{dis}) &= \frac{\dot{\varepsilon}_{mp}}{\dot{\lambda}_\sigma} = \frac{\partial f(\boldsymbol{\sigma}_{loc}^{dis}, \text{strength par.})}{\partial \tau_{mp}^{dis}} = 0 \end{aligned} \quad (2.10)$$

where $\boldsymbol{\sigma}_{loc}^{dis}$ denotes a 3D stress state at a discontinuity with the local coordinate basis (n - m - p) with the normal vector of the discontinuity pointing in the n -direction. Note that each of the constraints in Eq. (2.10) can be formulated as a function of the local stress field $\boldsymbol{\sigma}_{loc}^{dis}$. By reformulating Eq. (2.10) using the definition of the Cauchy stress tensor, giving $t_n^{dis} = \sigma_{nn}^{dis}$, $t_m^{dis} = \tau_{nm}^{dis}$, $t_p^{dis} = \tau_{np}^{dis}$, the three remaining stress tensor components σ_{mm}^{dis} , σ_{pp}^{dis} , and τ_{mp}^{dis} can be expressed as functions, hereafter referred to as L^{dis} , of t_n^{dis} , t_m^{dis} , t_p^{dis} , and certain strength parameters, reading

$$\begin{aligned} \sigma_{mm}^{dis} &= L_{mm}^{dis}(\mathbf{t}_{loc}^{dis}, \text{strength par.}) & \sigma_{pp}^{dis} &= L_{pp}^{dis}(\mathbf{t}_{loc}^{dis}, \text{strength par.}) \\ \sigma_{mp}^{dis} &= L_{mp}^{dis}(\mathbf{t}_{loc}^{dis}, \text{strength par.}) \end{aligned} \quad (2.11)$$

Therefrom, a relationship between the local stress field and the local traction field on Γ_{dis} , $\boldsymbol{\sigma}_{loc}^{dis} = \mathbf{L}_t^{dis} \mathbf{t}_{loc}^{dis}$, under the condition of plastic strain localisation, can be derived. Finally, by making use of this relationship, it is possible to “project” the stress-based formulation of the Tsai-Wu yield function $f(\boldsymbol{\sigma}_{loc}^{dis}) \leq 0$ onto a discontinuity, delivering a consistent traction-based yield function $f(\mathbf{t}_{loc}^{dis}) \leq 0$.

The main focus of this work is the performance assessment of this approach and to point out how such an approach could be utilised for future concepts of numerical limit analysis. For this reason, in the next Section, several numerical examples are presented and discussed in detail.

3. Numerical results

In this Section, numerical results obtained using the proposed upper bound formulation with selectively activated velocity discontinuities are discussed. Two benchmark problems with isotropic yield functions are used for basic verification of the presented approaches. By means of further examples, it is demonstrated that orthotropic plastic failure can also be handled appropriately. Moreover, it will be shown that through the introduction of velocity discontinuities across properly-arranged prescribed interfaces, high-quality upper bound results can be obtained with relatively coarse meshes and, thus, very efficiently. Note that, for convenience, the upper bound

results obtained using formulations, with and without velocity discontinuities, are referred to as continuous and discontinuous upper bound results, respectively.

All computations presented in the following have been performed on a Linux desktop machine with an AMD Phenom(tm) II X6 1090T CPU (6 cores) and 8GB of RAM. The commercial software package Abaqus was used for mesh generation, but all other pre- and post-processing tasks as well as the assembly of the SOCP optimisation problems were carried out by self-written codes in Fortran. The SOCP optimisation problems themselves were solved using the commercial software MOSEK (2014), which is based on the conic interior-point algorithm described in Andersen *et al.* (2003).

3.1. Rigid strip footing

The rigid strip footing problem, as illustrated in Fig. 1a, with a weightless purely cohesive material is a common benchmark for limit analysis approaches. Upon the assumption of material failure according to Tresca, $\tau \leq c$, the ultimate load can be obtained by the classical Prandtl solution $N_c^{ref} = P_{lim}/c = 2 + \pi$ (Prandtl, 1920), where N_c is the bearing capacity factor, P_{lim} the collapse load limit, τ the principal shear stress, and c the coefficient of cohesion. Under plane strain conditions, the Tresca yield function is identical to the von Mises yield function $\sqrt{J_2} \leq c$, with J_2 as the second deviatoric stress invariant.

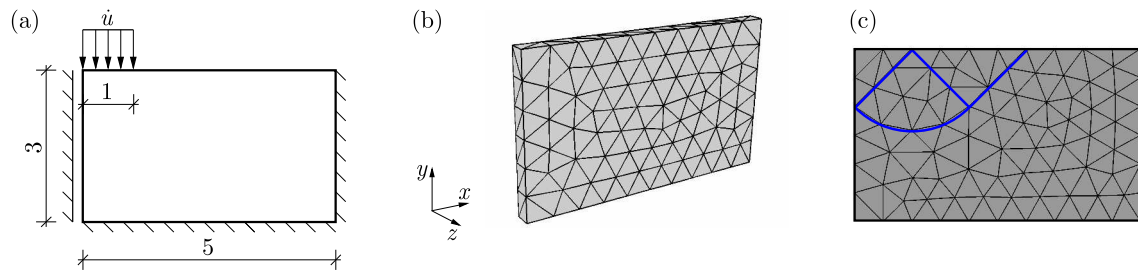


Fig. 1. Rigid strip footing benchmark example: (a) geometry and boundary conditions; (b) example 3D model and illustrative discretisation with 419 elements; (c) the prescribed interfaces for velocity jumps according to Prandtl's failure mechanism (445 elements)

Using the yield function formulation according to Eq. (2.8), the von Mises criterion is defined through

$$\mathbf{P}_\sigma^{mat} = \frac{1}{3c^2} \begin{bmatrix} 1 & -0.5 & -0.5 & 0 & 0 & 0 \\ -0.5 & 1 & -0.5 & 0 & 0 & 0 \\ -0.5 & -0.5 & 1 & 0 & 0 & 0 \\ 0 & 0 & 0 & 3 & 0 & 0 \\ 0 & 0 & 0 & 0 & 3 & 0 \\ 0 & 0 & 0 & 0 & 0 & 3 \end{bmatrix} \quad \mathbf{F}_\sigma^{mat,+} = \mathbf{F}_\sigma^{mat,-} = \mathbf{0} \quad (3.1)$$

A consistent traction-based yield function is easily obtained (Makrodimopoulos and Martin, 2008) by applying the shear strength as the tangential strength at discontinuities, giving

$$\mathbf{P}_t^{dis} = \frac{1}{c^2} \begin{bmatrix} 0 & 0 & 0 \\ 0 & 1 & 0 \\ 0 & 0 & 1 \end{bmatrix} \quad \mathbf{F}_t^{dis,+} = \mathbf{F}_t^{dis,-} = \mathbf{0} \quad (3.2)$$

The geometric boundary conditions and loading are given in Fig. 1a, and an example 3D representation of the model is plotted in Fig. 1b with respect to the global coordinate basis (xyz) and an illustrative discretisation using 419 tetrahedron elements. By applying symmetric boundary conditions at the z^- and z^+ boundary surfaces, plane strain conditions are enforced.

Thus, in the following, all results will be plotted in the xy -plane only. The rough footing interface condition is applied by setting the velocities in the x -direction to zero for all nodes in the footing region.

The obtained numerical upper bound results for different fineness of discretisation or degrees of freedom (DOF) are plotted in Fig. 2a. The black curve represents the results for continuous velocity fields, and shows clear convergence behaviour. Measuring the difference between the upper bound results and the analytical reference N_c^{ref} , as $diff(\%) = (N_c^{ub} - N_c^{ref}) \cdot 100 / (N_c^{ub} + N_c^{ref})$, a $diff$ of 12.92% (2790 DOF) for point a and 0.95% for point c with 188685 DOF are obtained. The corresponding CPU times are 2.09 min versus 41.85 min.

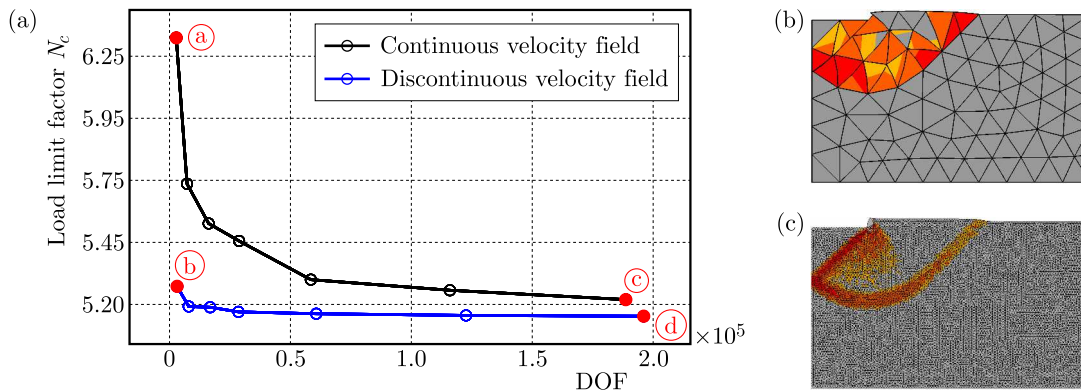


Fig. 2. Numerical upper bound results for the rigid strip footing problem: (a) load limit factor N_c obtained using continuous and discontinuous velocity fields as a function of DOF; (b) upper bound failure mode using discontinuities and 445 elements (range of plotted yield function values (robjv) $[-3 \cdot 10^{-8} : 0]$); (c) upper bound failure mode using continuous velocity field with 31081 elements (robjv $[-5 \cdot 10^{-9} : 0]$)

In the next step, partitions are introduced into the model according to Prandtl's failure mechanism (Prandtl, 1920), see Fig. 1c, to allow velocity jumps across prescribed discontinuities. Since velocity jumps are only allowed through these prescribed interfaces, the number of DOF is not increased significantly. The blue curve in Fig. 2a shows the related results, again for different numbers of DOF. A $diff$ of 1.60% is obtained for point b (3147 DOF) and 0.13% for point d (196077 DOF), with corresponding CPU times of 0.56 min and 41.62 min.

With a minimum difference of below 1% for the obtained best upper bounds compared to the analytical solution, the proposed formulations withstand this basic verification and can be assessed as performing well. Especially when velocity discontinuities are introduced, very good upper bounds can be obtained even with coarse meshes (see point b and the related failure mechanism in Fig. 2b). Of course, this is only possible if the failure mechanism is known in advance and, thus, does not yet represent an added value for general calculations. However, the potential of velocity discontinuities to capture very localised failure is evidently huge and, sensibly used, can greatly increase computational efficiency.

3.2. Block with asymmetric holes

The block with asymmetric holes under tensile loading is a commonly-used benchmark for so-called direct methods (e.g. limit analysis and shakedown analysis) firstly studied by Zouain *et al.* (2002), as illustrated in Fig. 3a. Later on, this problem was studied by Makrodimopoulos and Martin (2007) using an upper bound formulation with a continuous quadratic velocity field, and the plane strain Mohr-Coulomb yield function was applied to the material. Their results are used for verification and as the reference solution in the following. Moreover, the benefit

of using sensibly-arranged velocity discontinuities is further discussed, and a simple strategy to find such arrangements based on preliminary upper bound results is proposed. Geometry, material properties, and boundary conditions (see Fig. 3a) are assigned as in the reference (Makrodimopoulos and Martin, 2007). The model is built by 3D finite elements with the global coordinate basis (xyz) , similarly to Fig. 1b, and again symmetric boundary conditions at the $z-$ and $z+$ boundary surfaces are applied.

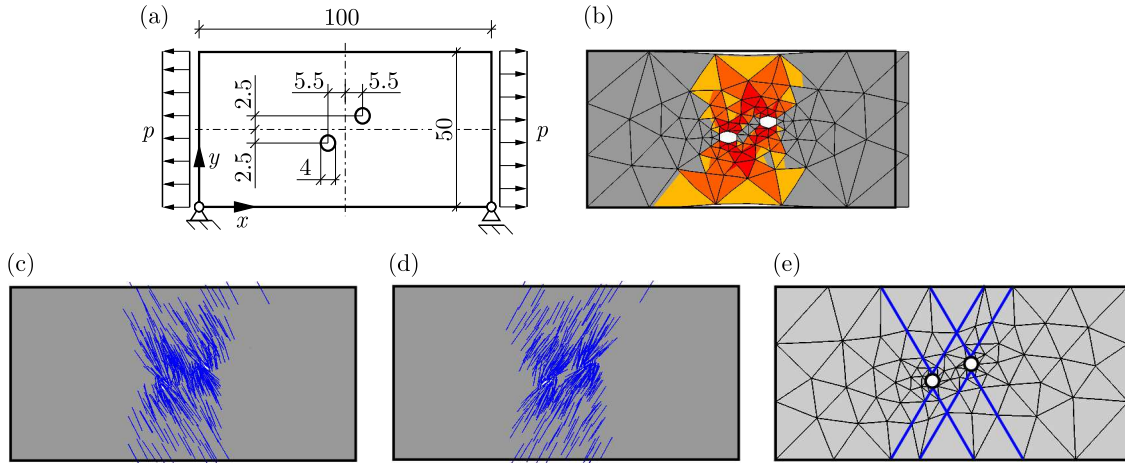


Fig. 3. Block with asymmetric holes using the Drucker-Prager failure criterion: (a) geometry and boundary conditions; (b) upper bound failure mode (519 elements, $\text{robjv} [-5 \cdot 10^{-6} : 0]$); (c) and (d) potential orientations of plastic strain localisation; (e) prescribed discontinuities based on (c) and (d)

3.2.1. Mohr-Coulomb failure criterion

In Makrodimopoulos and Martin (2007), the Mohr-Coulomb yield function was used with a friction angle $\phi = 30^\circ$. In our example, the equivalent Drucker-Prager yield function, $\sqrt{J_2} \leq A - BI_1$, is assigned to the material, defined by inserting

$$\mathbf{F}_\sigma^{mat} = \frac{1}{3A^2} \begin{bmatrix} 1 & -0.5 & -0.5 & 0 & 0 & 0 \\ -0.5 & 1 & -0.5 & 0 & 0 & 0 \\ -0.5 & -0.5 & 1 & 0 & 0 & 0 \\ 0 & 0 & 0 & 3 & 0 & 0 \\ 0 & 0 & 0 & 0 & 3 & 0 \\ 0 & 0 & 0 & 0 & 0 & 3 \end{bmatrix} \quad \mathbf{F}_\sigma^{mat,-} = \frac{1}{A^2} \begin{bmatrix} 2AB \\ 2AB \\ 2AB \\ 0 \\ 0 \\ 0 \end{bmatrix} \quad (3.3)$$

$$\mathbf{F}_\sigma^{mat,+} = \mathbf{0}$$

into Eq. (2.8), with the strength parameters $A = 0.8321c$ and $B = 0.1601$. For the consistent traction-based yield function these terms read

$$\mathbf{F}_t^{dis} = \frac{1}{c^2} \begin{bmatrix} -\tan^2 \phi & 0 & 0 \\ 0 & 1 & 0 \\ 0 & 0 & 1 \end{bmatrix} \quad \mathbf{F}_t^{dis,+} = \mathbf{0} \quad \mathbf{F}_t^{dis,-} = \frac{1}{c^2} \begin{bmatrix} 2c \tan \phi \\ 0 \\ 0 \end{bmatrix} \quad (3.4)$$

In the previous example, it has been shown that velocity discontinuities can improve the upper bound significantly if they are appropriately arranged with respect to potential failure surfaces. For this reason, subsequently, the following strategy is pursued. Based on an upper bound calculation with a continuous velocity field and a relatively coarse mesh, as shown in

Fig. 3b, potential discontinuity directions, where plastic failure could localise, are computed at each integration point where plastic flow takes place according to Eq. (2.10). The resulting orientations are plotted in Fig. 3c and Fig. 3d. With respect to the x axis, the mean orientations obtained by taking the volume average over all orientations are approximately $\bar{\theta}_1 = -60^\circ$ and $\bar{\theta}_2 = 60^\circ$, as would be expected from the underlying failure criterion. Next, according to these average directions of possible localised plastic failure, and by referring to the points with maximum plastic strain-rates, the partitions (blue lines) shown in Fig. 3e are implemented into the model. Finally, the model is re-meshed and velocity discontinuities are introduced along the partitions.

This procedure has been applied to several models with different level of mesh refinement (DOF) and compared to calculations performed without such discontinuities. The obtained upper bounds for the limit load factor N_c are plotted in Fig. 4a. Based on the upper bound result with only 3327 DOF (point a), velocity discontinuities were introduced into the model, leading to a strong improvement of the upper bound (point b) by adding only 585 DOF. The failure mechanism associated with point b is shown in Fig. 4b. To achieve a similarly good upper bound result and the related localised failure mechanism without the introduction of discontinuities, the mesh needed to be refined significantly, as shown in Fig. 4c as the associated failure mechanism to point c . The CPU time required to obtain point c and the mechanism in Fig. 4c was 37.87 min, whereas point b with the mechanism shown in Fig. 4b only took 0.38 min. Although an adaptive mesh refinement would probably be more efficient than the uniform mesh refinement performed, the performance of sensibly-arranged discontinuities, even in a coarsely discretised model, is excellent. Comparing the upper bound result of point b ($N_c = 1.062$) to the best result in the reference (Makrodimopoulos and Martin, 2007) ($N_c = 1.063$) there is almost no difference. However, the upper bound indicated by point b was obtained with 3912 DOF compared to 79955 DOF in the reference.

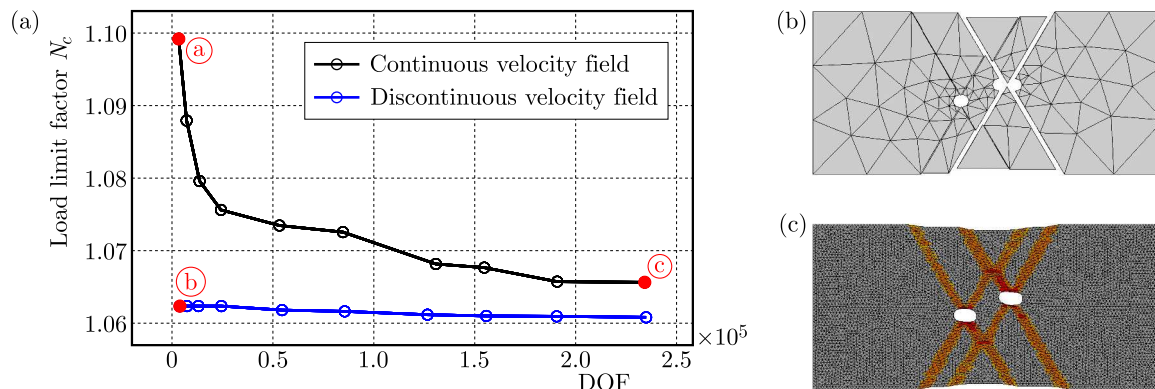


Fig. 4. Numerical upper bound results for the block with asymmetric holes example using the Drucker-Prager yield function: (a) load limit factor N_c obtained using continuous and discontinuous velocity fields as a function of DOF; upper bound results (robjv $[-1 \cdot 10^{-4} : 0]$) (b) with discontinuities using 504 elements and (c) with continuous velocity field using 34875 elements

In the following, this approach is extended to orthotropic material behaviour, using the Tsai-Wu criterion as the indicator for plastic failure.

3.2.2. Tsai-Wu failure criterion

The strength parameters used for the example correspond to the typical orthotropic material spruce wood and are taken from (Dorn, 2012), leading to

$$\mathbf{P}_\sigma^{mat} = \begin{bmatrix} 2.434E-4 & 0 & 0 & 0 & 0 & 0 \\ 0 & 6.588E-2 & 0 & 0 & 0 & 0 \\ 0 & 0 & 6.588E-2 & 0 & 0 & 0 \\ 0 & 0 & 0 & 1.181E-2 & 0 & 0 \\ 0 & 0 & 0 & 0 & 2.973E-2 & 0 \\ 0 & 0 & 0 & 0 & 0 & 1.181E-2 \end{bmatrix} \text{MPa}^{-2} \quad (3.5)$$

$$\mathbf{F}_\sigma^{mat,+} = \mathbf{F}_\sigma^{mat,-} = [-6.573E-3 \quad 8.564E-2 \quad 8.564E-2 \quad 0 \quad 0 \quad 0]^T \text{MPa}^{-1}$$

inserted into the general yield function in Eq. (2.8), defined with respect to the local coordinate basis (*LTR*). Due to the orthotropic characteristics, the consistent traction-based yield function is highly dependent on the orientation of the discontinuity at which it describes plastic failure. Thus, for each introduced discontinuity, a different set of strength parameters had to be computed, determined by the “projection” procedure introduced at the end of Section 2. Then, the equivalence between the material strength within elements and the strength behaviour at discontinuities is guaranteed.

In the following, this orthotropic strength behaviour is assigned to the block with asymmetric holes, for two different material orientations, to assess the capability of the presented approach in handling anisotropic strength behaviour.

Material orientation 1

In the first case, the longitudinal orientation *L* of the material is identical to the *y*-direction, as indicated in Fig. 5a. Moreover, the local material coordinate basis (*LTR*) is defined with *L* and *T* as the in-plane axes and *R* as the out-of-plane axis.

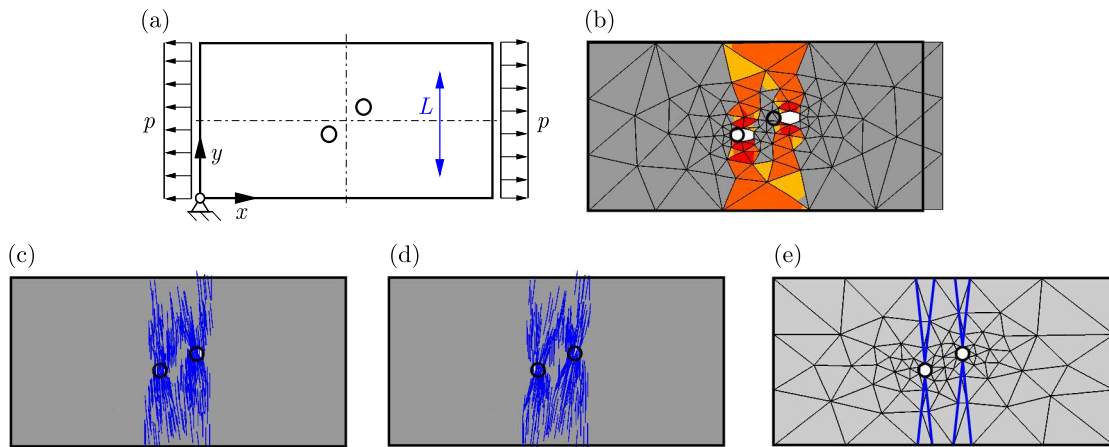


Fig. 5. Block with asymmetric holes using the Tsai-Wu orthotropic failure criterion: (a) geometry, boundary conditions, and the principal material orientation indicated by the blue arrow; (b) upper bound result using 519 elements (robjv $[-1.5 \cdot 10^{-6} : 0]$); (c) and (d) potential orientations of plastic strain localisation; (e) prescribed discontinuities based on (c) and (d)

The preliminary upper bound calculation, based on which the arrangement of discontinuities will be defined, is carried out using a coarse mesh with 519 elements. The corresponding failure mechanism is displayed in Fig. 5b, and the computed orientations of potential discontinuities are shown in Figs. 5c and 5d. Averaging over these orientations results in two mean angle values of $\bar{\theta}_1 = -84^\circ$ and $\bar{\theta}_2 = 84^\circ$ with respect to the *x*-axis. According to these mean angles and starting from the points of highest plastic strain-rates (present at the boundaries of the holes), the velocity discontinuities shown in Fig. 5e are implemented into the model. Subsequently, the model is re-meshed and a further upper bound calculation is performed.

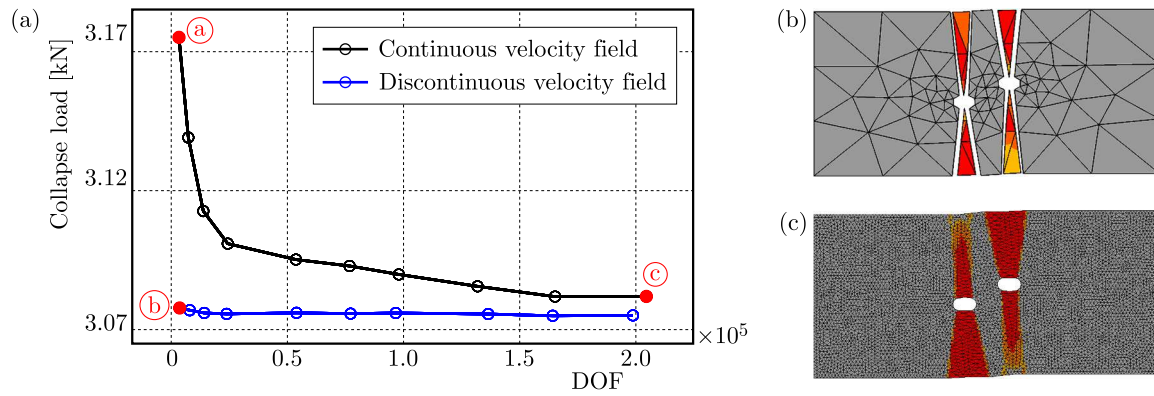


Fig. 6. Numerical upper bound results for the block with asymmetric holes with the principal material direction as defined in Fig. 5a: (a) collapse load using continuous and discontinuous velocity fields as a function of DOF; upper bound failure mode ($\text{robjv} [-9 \cdot 10^{-6} : 0]$) using (b) discontinuities within a coarse mesh (486 elements) and (c) a continuous velocity field with a fine mesh (38 537 elements)

The numerical upper bounds on the collapse load for different levels of mesh refinement (DOF) with and without discontinuities are plotted in Fig. 6. Again, the introduction of velocity discontinuities improves the upper bound significantly, while hardly increasing the DOF. In contrast to the isotropic case before, plastic failure also occurs in the solid finite elements between discontinuities (see Fig. 6b), indicating that the orientation or arrangement of discontinuities could be improved. This can also be seen by looking at the plastic regions in Fig. 6c, which do not exactly match the definition of discontinuities above. It seems that the arrangement of discontinuities does not necessarily have to be ideal in order to achieve considerable improvement in the numerical upper bound results.

Material orientation 2

In the second case, the local material orientation basis (LTR) is rotated by 30° in the xy -plane, as indicated in Fig. 7a. Again, based on an efficient preliminary upper bound calculation (see Fig. 7b), possible orientations of discontinuities are computed, resulting in mean angles of $\bar{\theta}_1 = \pm 80^\circ$ and $\bar{\theta}_2 = -58^\circ$. The introduced velocity discontinuities are shown in Fig. 7e.

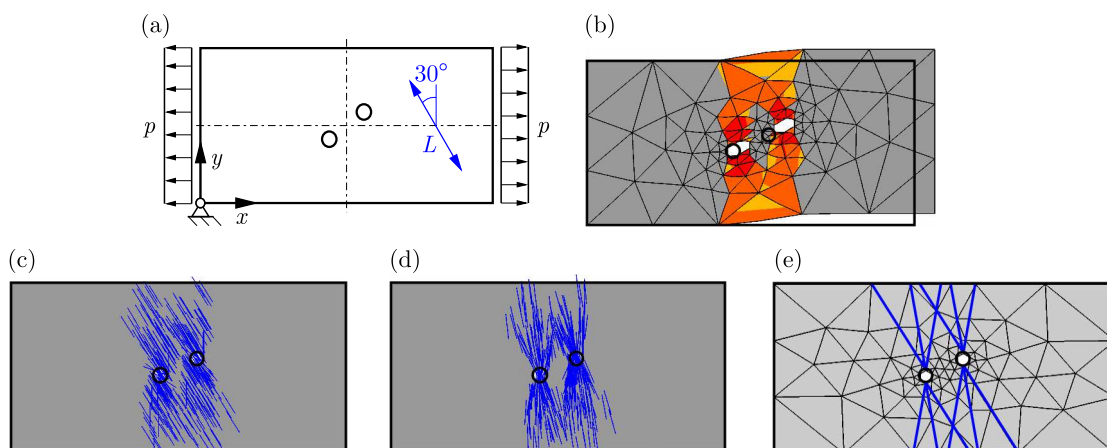


Fig. 7. Block with asymmetric holes using the Tsai-Wu orthotropic failure criterion: (a) geometry, boundary conditions, and the principal material orientation indicated by the blue arrow; (b) upper bound result using 519 elements ($\text{robjv} [-3 \cdot 10^{-6} : 0]$); (c) and (d) potential orientations of plastic strain localisation; (e) prescribed discontinuities based on (c) and (d)

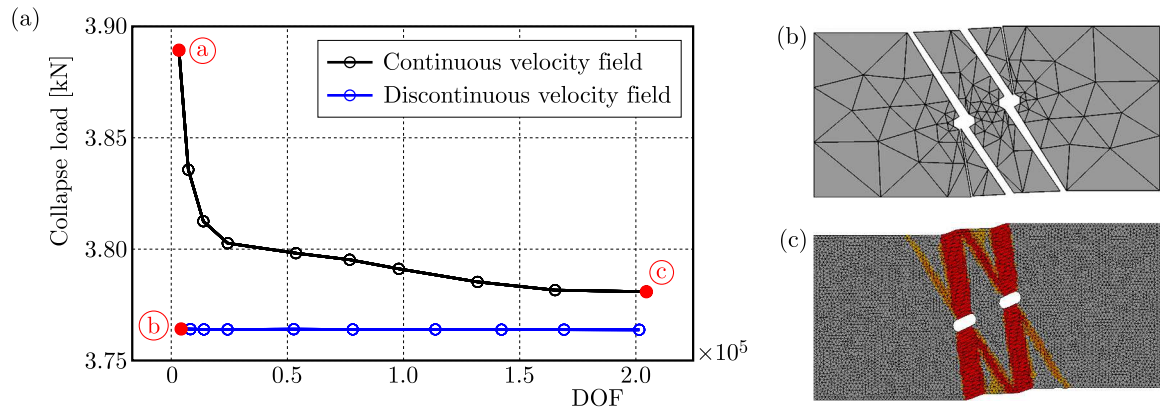


Fig. 8. Numerical upper bound results for the block with asymmetric holes with the principal material direction as defined in Fig. 7a: (a) collapse load using continuous and discontinuous velocity fields as a function of DOF; upper bound failure mode (robjv $[-2 \cdot 10^{-5} : 0]$) using (b) discontinuities within a coarse mesh (524 elements) and (c) a continuous velocity field with a fine mesh (34875 elements)

As before, all numerical upper bounds are plotted in Fig. 8, showing the strong performance increase achieved by the selectively introduced discontinuities. Interestingly, the intensity of localisation of plastic failure is slightly different comparing the approaches with (Fig. 8b) and without (Fig. 8c) discontinuities. It seems that with discontinuities the real failure mechanism can be better represented, since the main plastic failure direction is well aligned with the principal material direction (wood fibre direction) as expected.

3.3. Shear test on block

The last example is used to assess the capability of this upper bound formulation regarding localised shear failure in orthotropic materials. The setup of the model is shown in Fig. 9a and is designed to represent a characteristic as well as often critical loading states in wood-based products, like glued-laminated timber and cross-laminated timber. As in the previous examples, the boundary conditions are chosen so as to represent plane strain conditions, and the Tsai-Wu failure criterion with strength parameters representing spruce wood is assigned to the material.

Again, based on a preliminary upper bound calculation using a very coarse mesh (Fig. 9c1), the orientations of possible discontinuities are determined (Fig. 9c2) and, based on that information, velocity discontinuities are implemented into the model (Fig. 9c3). The result obtained with this discontinuity arrangement is shown in Fig. 9d1, where the dominant plastic failure appears within the solid elements between the introduced discontinuities but not at the discontinuities themselves, and, thus, the potential of the velocity discontinuities has not been activated sufficiently. For this reason, a second iteration was carried out, again computing the orientations of possible discontinuities in all plastic regions (Fig. 9d2). Based on that information, a revised discontinuity pattern was implemented as shown in Fig. 9d3. The corresponding failure mechanism is displayed in Fig. 10b and it can be seen that, now, localised failure occurs exclusively at the last-introduced discontinuity. The related upper bound (point *b* in Fig. 10a) is very good in comparison to the preliminary model without discontinuities (point *a*) but uses a similar number of DOF. Moreover, the failure mechanism agrees well with that obtained using a very fine mesh and no discontinuities (Fig. 10c).

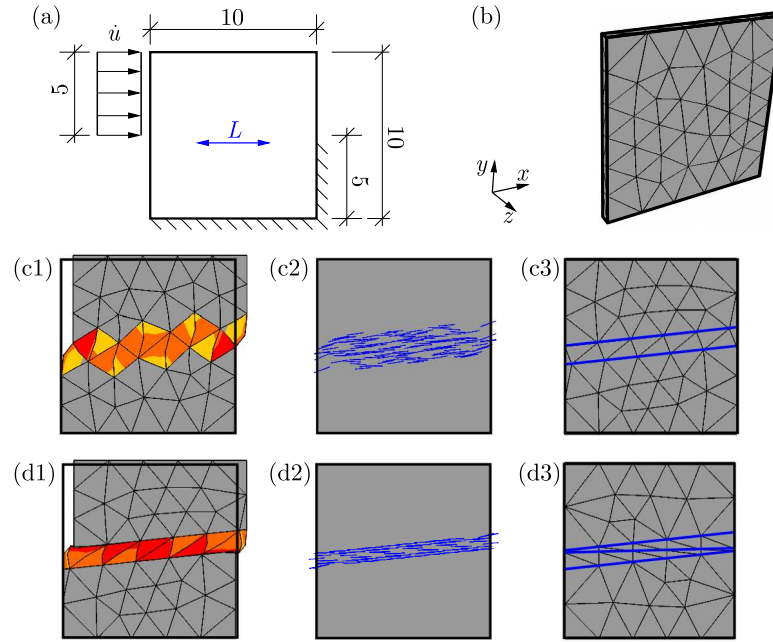


Fig. 9. Block under shear loading: (a) geometry, boundary conditions and the principal material orientation indicated by the blue arrow; (b) illustrative 3D model with 222 finite elements; (c) and (d) two iteration steps for the definition of the discontinuities, with (c1) and (d1) as the upper bound result (robjv $[-2 \cdot 10^{-9} : 0]$), (c2) and (d2) as the potential orientations of plastic strain localisation, and (c3) and (d3) as the prescribed discontinuities based on (c2) and (d2)

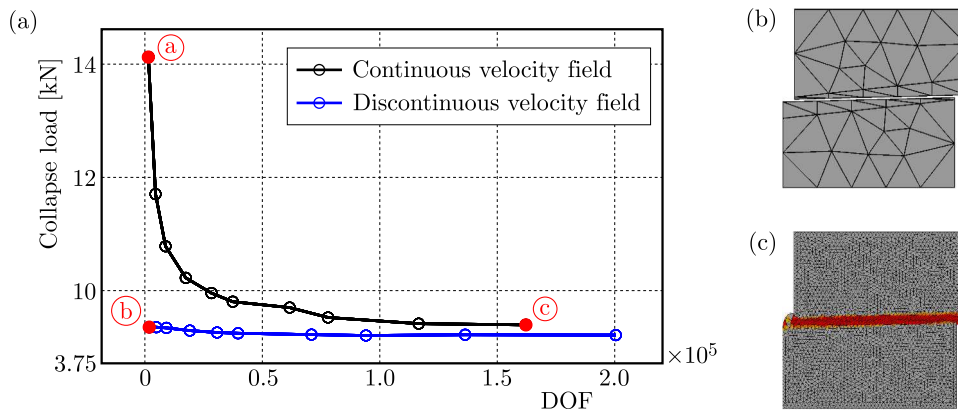


Fig. 10. Numerical upper bound results for the block under shear loading: (a) collapse load using continuous and discontinuous velocity fields as a function of DOF; the upper bound failure mode (robjv $[-4 \cdot 10^{-9} : 0]$) using (b) discontinuities within a coarse mesh (242 elements) and (c) a continuous velocity field with a fine mesh (32 062 elements)

4. Summary and conclusions

In this work, a 3D numerical upper bound formulation using a quadratic approximation of the velocity field and allowing for the implementation of orthotropic yield functions has been briefly proposed. Furthermore, the implementation of velocity discontinuities into this formulation has been presented, along with the concept of how to derive the necessary traction-based yield function which guarantees a consistent description of the material strength behaviour across discontinuities. Based on that formulation, compatibility as well as the associated plastic flow rule are fulfilled throughout the whole body and, thus, rigorous upper bounds are obtained.

The formulation has been verified by means of two classical examples, the rigid strip footing and the block with asymmetric holes. Subsequently, based on preliminary upper bound calculations with very coarse meshes, the orientation of potential slip lines where very localised plastic flow may occur could be determined. Based on that information, sensibly-arranged velocity discontinuities were incorporated into the finite element models. In that way, upper bounds could be improved significantly with essentially no increase of degrees of freedom.

It has also been shown that this concept works very well when assigning orthotropic failure behaviour to the material. If the first introduction of discontinuities does not improve the upper bound significantly, which means that most of the plastic dissipation still takes place in solid elements, a second iteration step can improve the situation, as shown by means of the shear test on a block. This may represent an important finding for future developments, which could lead to a general algorithm for an adaptive introduction and re-arrangement of velocity discontinuities, as an efficient alternative to existing adaptive mesh refinement strategies. Especially for laminated structures and orthotropic materials, where plastic failure often occurs in a very localised mechanism, as shown for wood at the microscale in (Lukacevic *et al.*, 2014; Lukacevic and Füssl, 2016) and at the product scale in (Hochreiner *et al.*, 2013, 2014), such an approach could have great value. Moreover, the efficiency of numerical limit analysis in combination with the accuracy of the extended finite element formulations presented in (Lukacevic *et al.*, 2014; Lukacevic and Füssl, 2016) could lead to more flexible engineering design tools, in which the focus can be switched between accuracy and efficiency as needed.

Acknowledgments

Financial support for this work in the framework of the PhD School DokIn' Holz funded by the Austrian Federal Ministry of Science, Research and Economy and the Austrian Association of Wood Industries is gratefully acknowledged. We also gratefully acknowledge the financial support of this work by the Austrian Science Fund (FWF) through the Erwin Schrödinger Fellowship J3748-N30.

References

1. ANDERHEGGEN E., KNÖPFEL H., 1972, Finite element limit analysis using linear programming, *International Journal of Solids and Structures*, **8**, 12, 1413-1431
2. ANDERSEN E.D., ROOS C., TERLAKY T., 2003, On implementing a primal-dual interior-point method for conic quadratic optimization, *Mathematical Programming*, **95**, 2, 249-277
3. BELYTSCHKO T., HODGE P.G., 1970, Plane stress limit analysis by finite elements, *Journal of the Engineering Mechanics Division*, **96**, 6, 931-944
4. BOTTERO A., NEGRE R., PASTOR J., TURGEMAN S., 1980, Finite element method and limit analysis theory for soil mechanics problems, *Computer Methods in Applied Mechanics and Engineering*, **22**, 1, 131-149
5. CHEN J., YIN J.-H., LEE C.F., 2003, Upper bound limit analysis of slope stability using rigid finite elements and nonlinear programming, *Canadian Geotechnical Journal*, **40**, 742-752
6. CIRIA H., PERAIRE J., 2004, Computation of upper and lower bounds in limit analysis using second-order cone programming and mesh adaptivity, *9th ASCE Specialty Conference on Probabilistic Mechanics and Structural Reliability*
7. CIRIA H., PERAIRE J., BONET J., 2008, Mesh adaptive computation of upper and lower bounds in limit analysis, *International Journal for Numerical Methods in Engineering*, **75**, 8, 899-944
8. DORN M., 2012, *Investigations on the Serviceability Limit State of Dowel-Type Timber Connections*, PhD Thesis, Vienna University of Technology
9. DRUCKER D.C., GREENBERG H.J., PRAGER W., 1951, The safety factor of an elastic-plastic body in plane strain, *Journal of Applied Mechanics*, **18**, 371-378

10. DRUCKER D.C., PRAGER W., GREENBERG H.J., 1952, Extended limit design theorems for continuous media, *Quarterly of Applied Mathematics*, **9**, 381-389
11. FÜSSL J., LACKNER R., EBERHARDSTEINER J., MANG H.A., 2008, Failure modes and effective strength of two-phase materials determined by means of numerical limit analysis, *Acta Mechanica*, **1-4**, 195, 185-202
12. FÜSSL J., LI M., LUKACEVIC M., EBERHARDSTEINER J., MARTIN C.M., 2017, Comparison of unit cell-based computational methods for predicting the strength of wood, *Engineering Structures*, **141**, 427-443
13. HAWKS BEE S., SMITH C., GILBERT M., 2013, Application of discontinuity layout optimization to three-dimensional plasticity problems, *Proceedings of the Royal Society of London A: Mathematical, Physical and Engineering Sciences*, **469**, 2155
14. HOCHREINER G., FÜSSL J., EBERHARDSTEINER J., 2013, Cross-laminated timber plates subjected to concentrated loading – experimental identification of failure mechanisms, *Strain*, **50**, 1, 68-81
15. HOCHREINER G., FÜSSL J., SERRANO E., EBERHARDSTEINER J., 2014, Influence of wooden board strength class on the performance of cross-laminated timber plates investigated by means of full-field deformation measurements, *Strain*, **50**, 2, 161-173
16. KRABBENHØFT K., LYAMIN A.V., HJIAJ M., SLOAN S.W., 2005, A new discontinuous upper bound limit analysis formulation, *International Journal for Numerical Methods in Engineering*, **63**, 7, 1069-1088
17. LE C.V., ASKES H., GILBERT M., 2019, Adaptive element-free Galerkin method applied to the limit analysis of plates, *Computer Methods in Applied Mechanics and Engineering*, **199**, 37, 2487-2496
18. LI M., FÜSSL J., LUKACEVIC M., EBERHARDSTEINER J., MARTIN C.M., 2018, Strength predictions of clear wood at multiple scales using numerical limit analysis approaches, *Computers and Structures*, **196**, 200-216
19. LIU F., ZHAO J., 2013, Upper bound limit analysis using radial point interpolation meshless method and nonlinear programming, *International Journal of Mechanical Sciences*, **70**, 26-38
20. LUKACEVIC M., FÜSSL J., 2016, Application of a multisurface discrete crack model for clear wood taking into account the inherent microstructural characteristics of wood cells, *Holzforschung*, **70**, 9, 845-853
21. LUKACEVIC M., FÜSSL J., LAMPERT R., 2014, Failure mechanisms of clear wood identified at wood cell level by an approach based on the extended finite element method, *Engineering Fracture Mechanics*, **144**, 158-175
22. LYAMIN A.V., SLOAN S.W., 2002a, Lower bound limit analysis using non-linear programming, *International Journal for Numerical Methods in Engineering*, **55**, 5, 573-611
23. LYAMIN A.V., SLOAN S.W., 2002b, Upper bound limit analysis using linear finite elements and non-linear programming, *International Journal for Numerical and Analytical Methods in Geomechanics*, **26**, 2, 181-216
24. LYSMER J., 1970, Limit analysis of plane problems in soil mechanics, *Journal of the Soil Mechanics and Foundations Division*, **96**, 4, 1311-1334
25. MAIER G., ZAVELANI-ROSSI A., BENEDETTI D., 1972, A finite element approach to optimal design of plastic structures in plane stress, *International Journal for Numerical Methods in Engineering*, **4**, 4, 455-473
26. MAKRODIMOPOULOS A., MARTIN C.M., 2006, Lower bound limit analysis of cohesive-frictional materials using second-order cone programming, *International Journal for Numerical Methods in Engineering*, **66**, 4, 604-634
27. MAKRODIMOPOULOS A., MARTIN C.M., 2007, Upper bound limit analysis using simplex strain elements and second-order cone programming, *International Journal for Numerical and Analytical Methods in Geomechanics*, **31**, 6, 835-865

28. MAKRODIMOPOULOS A., MARTIN C.M., 2008, Upper bound limit analysis using discontinuous quadratic displacement fields, *Communications in Numerical Methods in Engineering*, **24**, 11, 911-927
29. MARTIN C., MAKRODIMOPOULOS A., 2008, Finite-element limit analysis of Mohr-Coulomb materials in 3D using semidefinite programming, *Journal of Engineering Mechanics*, **134**, 4, 339-347
30. MILANI G., LOURENÇO P.B., 2009, A discontinuous quasi-upper bound limit analysis approach with sequential linear programming mesh adaptation, *International Journal of Mechanical Sciences*, **51**, 89-104
31. MOSEK ApS, 2014, *The MOSEK optimization tools version 7.0*, User's Manual and Reference, <http://www.mosek.com>
32. PRANDTL L., 1920, Über die Härte plastischer Körper, *Nachrichten von der Gesellschaft der Wissenschaften zu Göttingen, Mathematisch-Physikalische Klasse*, **12**, 74-85
33. SLOAN S.W., KLEEMAN P.W., 1995, Upper bound limit analysis using discontinuous velocity fields, *Computer Methods in Applied Mechanics and Engineering*, **127**, 14, 293-314
34. SMITH C., GILBERT M., 2007, Application of discontinuity layout optimization to plane plasticity problems, *Proceedings of the Royal Society A*, **463**, 2461-2484
35. WU J.-Y., CERVERA M., 2014, On the equivalence between traction- and stress-based approaches for the modeling of localized failure in solids, *Journal of the Mechanics and Physics of Solids*, **82**, 137-163
36. YU S., ZHANG X., SLOAN S.W., 2016, A 3D upper bound limit analysis using radial point interpolation meshless method and second-order cone programming, *International Journal for Numerical Methods in Engineering*, **108**, 13, 1686-1704
37. ZOUAIN N., BORGES L., SILVEIRA J.L., 2002, An algorithm for shakedown analysis with nonlinear yield functions, *Computer Methods in Applied Mechanics and Engineering*, **191**, 23, 2463-2481

Manuscript received January 11, 2017; accepted for print February 5, 2018

ON PROBLEMS WITH SOLUTION-DEPENDENT LOAD

ROMAN BOGACZ

*Warsaw University of Technology, Faculty of Automotive and Construction Machinery Engineering, Warsaw, Poland
e-mail: rbogacz@ippt.pan.pl*

KURT FRISCHMUTH

*University of Rostock, Institute of Mathematics, Rostock, Germany
e-mail: kurt.frischmuth@uni-rostock.de*

In Continuum Physics, general balance problems between internal fluxes and external sources are considered, mostly on some domain Ω called a material body. Typically, the fluxes are determined by a wanted field – the solution or configuration of the body, possibly augmented by derivatives or other suitable quantities specifying the state of the system. In order to obtain a closed problem formulation, initial and boundary conditions need to be provided as well. In this paper, we discuss some issues appearing in the case that the sources, e.g. forces in a mechanical problem, are not known in advance, but related to the wanted configuration in terms of values and/or derivatives of the solution. An analogy between thermodynamic and mechanical problems is shown.

Keywords: feedback, dynamics, stability, columns, follower forces

1. Introduction

Let us consider a problem of the general form

$$H_t = -\operatorname{div} F + G \quad (1.1)$$

Here, by F the flux of some balance quantity is denoted, G is a corresponding source term, and H is the storage of the quantity, which may be scalar or vector-valued. All dependent fields are functions of a space variable x and time t .

As an example, consider internal energy $\epsilon = c\vartheta$ with temperature ϑ , heat flux q and heat sources r , cf. (Kosiński and Frischmuth, 2001), which are related to each other by

$$\epsilon_t = -\operatorname{div} q + r \quad (1.2)$$

In order to find a solution, a constitutive relation for the flux q is introduced by Fourier's law

$$q = -\kappa \nabla \vartheta \quad (1.3)$$

This leads to the partial differential equation

$$c\vartheta_t = \operatorname{div}(\kappa \nabla \vartheta) + r \quad (1.4)$$

with the heat capacity $c > 0$ and the heat conductivity $\kappa > 0$.

For this equation, one considers initial-boundary value problems with given sources $r = r(x, t)$, $x \in \Omega$, $t \geq 0$, given boundary values $\vartheta(x, t) = \bar{\vartheta}(x, t)$, $x \in \partial\Omega$, $t \geq 0$, and a given initial temperature field $\vartheta(x, 0) = \vartheta_0(x)$, $x \in \Omega$.

The above problem is well posed, i.e., it has a unique solution, which depends continuously on the data. Instead of prescribed values of the unknown function ϑ at the boundary, the heat flux $q_n = -\kappa \nabla \vartheta \cdot \vec{n} = -\kappa d\vartheta/d\vec{n}$ may be given. The first case is called Dirichlet conditions, in the second one we speak about a Neumann boundary. There may be a part of the boundary, where Dirichlet conditions are prescribed, while on the remaining part Neumann conditions apply.

In this paper, our focus is on a third type of boundary conditions, the Robin condition, which generalizes both previous cases

$$q_n = -\kappa \frac{d}{d\vec{n}} \vartheta = \gamma(\vartheta - \vartheta_{env}) \quad (1.5)$$

Here ϑ_{env} is a given temperature of the environment, and $\gamma \geq 0$ is the conductivity of a (virtual) layer between the considered body, occupying the domain Ω , and the surroundings. This means that the boundary values of ϑ are no longer known in advance but depend on the normal derivative of the solution ϑ .

Notice that also the assumption of known in advance heat sources r may be not adequate. The intensity of local heating may be a function of temperature, for instance as a result of thermo-chemical coupling, if the kinetics of an exothermal reaction depends on temperature, i.e., $r = r(x, t, \vartheta(x, t))$. In lower-dimensional problems, arising from models of a plate, shell or beam, again the exchange with the environment might be the dominant issue. In such cases, a higher value of the solution leads to a lower source, e.g. by a law of the form $r = \delta(\vartheta_{env} - \vartheta)$. In the reaction case, the opposite effect may lead to an unstable situation: the higher the temperature, the faster it grows. It is a challenge not only to solve an initial-boundary value problem for heat transfer problem (1.4) with the given specifications, but also to find stationary solutions and to determine whether they are stable.

When it comes to mechanics of continua, in the general 3D case, the unknown real valued function ϑ is replaced by a vector field $\mathbf{u} = \mathbf{u}(x, t) \in R^3$, the role of the heat flux is taken by the tensor \mathbf{T} , which comprises the stresses, and the balanced quantity is the linear momentum $\rho \mathbf{u}_{tt}$. The constitutive law, in the simplest elastic case, is given by a linear dependence between strain and stress, with the strain calculated from the gradient of \mathbf{u} , cf. (Bogacz and Janiszewski, 1985). Equation (1.1) takes here the form

$$\rho \mathbf{u}_{tt} = -\operatorname{div} \mathbf{T} + \mathbf{b} \quad (1.6)$$

with the body forces \mathbf{b} playing the role of the former r . A typical, linear, homogeneous and isotropic relation for \mathbf{T} is

$$\mathbf{T} = 2\mu \boldsymbol{\varepsilon} + \lambda \operatorname{tr}(\boldsymbol{\varepsilon}) \mathbf{I} \quad (1.7)$$

where \mathbf{I} is the identity (unit tensor), μ and λ are positive constants (Lamé moduli), and $\boldsymbol{\varepsilon}$ is the tensor of (small) deformations

$$\boldsymbol{\varepsilon} = \frac{1}{2} [\nabla \mathbf{u} + (\nabla \mathbf{u})^T] \quad (1.8)$$

More general situations, anisotropy, large deformations, inelastic materials, etc. are important issues, but out of the focus of this article – we restrict ourselves to linear models, valid in the neighborhood of equilibrium states.

There is one feature common for the thermodynamic and the mechanical master model. Again, the body forces as well as the boundary conditions, i.e. the interface between our model and the environment, may depend on the solution, cf. (Beck, 1952; Timoshenko, 1921). Furthermore, the dependence may be stabilizing, destabilizing, or switch from stable to unstable at certain states. And once more, it will be a challenge to find dynamical solutions, distinguish stationary

ones, and resolve the stability issue, cf. (Bogacz and Frischmuth, 2012; Bogacz *et al.*, 1980, 2008; Bogacz and Janiszewski, 1985; Preumont and Seto, 2008; Ringertz, 1994).

On the other hand, the big difference is that now, in mechanics, second derivatives with respect to time enter the evolution equation.

Since we concentrate on solutions close to a natural state of rest, the assumptions of small deformations (geometric linearity) and material linearity are reasonable. Additionally, we also postulate linearity of the feedback relation between body forces and boundary conditions and the wanted vector field $\mathbf{u} = \mathbf{u}(x, t)$. Due to linearity, the setup

$$\mathbf{u}(x, t) = \mathbf{w}(x)e^{i\omega t} \quad (1.9)$$

is known to work in the context of mechanics. The first order derivatives in the evolution equation are just scalar multiples of the unknown function, and the second order derivatives satisfy

$$\mathbf{u}_{tt}(x, t) = -\omega^2 \mathbf{u}(x, t) \quad (1.10)$$

Using this, the task reduces to an operator eigenproblem of the form

$$\mathbf{L}\mathbf{w} = -\omega^2 \rho \mathbf{u}(x, t) \quad (1.11)$$

where the eigenvalue is $-\omega^2$. The linear operator is composed of two contributions, one corresponds to the stiffness of the classical problem, the other one represents the feedback connected with the solution dependence of the loads. This will be discussed in more detail in the next Section.

After a suitable discretization, e.g. by the FEM or by FDM, a matrix eigenvalue problem emerges, modes of oscillation may be found and superposed. This way, initial conditions may be met and hence initial-boundary value problems solved. A discussion of the real and imaginary parts of the spectrum determines stability of the trivial solution $\mathbf{w} = \mathbf{0}$.

It should be mentioned that other setups are successful as well, e.g. $\exp(\omega t)$ or $\sin(\omega t)$ lead to the same results, bearing in mind Euler's formulas. In the thermodynamic case, where there is only a first order time derivative, obviously $\exp(\omega t)$ is more convenient, while in the mechanical case, when it comes to damping, the exponential representations are advantageous.

2. A classic case

A particular example of the considered class of problems is the 1D Bernoulli-Euler beam model with special loading conditions. Due to the low dimensionality of the domain and due to the fact that the complete solution is represented by a single scalar function, i.e. by the displacement of the middle surface of the beam, this problem is well suited for a qualitative study. For a discussion of the assumptions and applicability of the Bernoulli-Euler beam theory we refer to (Timoshenko, 1921; Tomski *et al.*, 1996).

The equation of balance of linear momentum, after substituting the assumed constraints, takes the form

$$(S(x)u_{xx}(x, t) + Pu(x, t))_{xx} + k(x)u(x, t) = -\rho(x)u_{tt}(x, t) \quad (2.1)$$

Here, S is the bending stiffness (related to the elastic moduli and the cross section of the beam, see Bogacz and Janiszewski (1985)), P a constant compressing axial force, $x \in [0, l]$ the scalar space variable (position), ρ the mass density (per unit length, i.e. the 3D material density multiplied by the area of the cross section). The role of k is the solution dependence of the load – it is well-known as the Winkler constant. Similarly, as in the heat source case, we have a lateral force $-k(x)u(x, t)$, which pushes the displaced beam back to its trivial position.

As a generalization of (2.1), an analogous contribution due to viscous damping may be added (Frischmuth *et al.*, 1993), so that the lateral force from the support becomes $-k(x)u(x, t) - v(x)u_t(x, t)$.

Problems of this class have a great practical relevance in several fields of engineering, see e.g. (Kaliski and Solarz, 1962; Kerr, 1988; Przybyłowicz, 2008; Bogacz *et al.*, 2014).

Introducing, as before, a product setup, this way splitting the time and space dependencies in the form of a standing wave, the heart of the matter will be again an eigenproblem of the form

$$\mathbf{L}_1 \mathbf{w} + P \mathbf{L}_2 \mathbf{w} + k \mathbf{w} = \rho \omega^2 \mathbf{w} \quad (2.2)$$

The name of the eigenvalue, i.e. ω^2 , is no obstacle, as long as ω alone does not enter the equation. This happens, however, if damping is introduced, so that (2.2) becomes

$$\mathbf{L}_1 \mathbf{w} + P \mathbf{L}_2 \mathbf{w} + k \mathbf{w} + i \omega \mathbf{v} \mathbf{w} = \rho \omega^2 \mathbf{w} \quad (2.3)$$

This quadratic eigenproblem may be transformed into a common one for the pair (\mathbf{w}, \mathbf{v}) , where \mathbf{v} stands for the velocity, i.e. $\mathbf{v} = i \omega \mathbf{w}$. With this definition, (2.3) becomes

$$\begin{aligned} \mathbf{v} &= i \omega \mathbf{w} \\ -\frac{1}{\rho} (\mathbf{L}_1 \mathbf{w} + P \mathbf{L}_2 \mathbf{w} + k \mathbf{w} + v \mathbf{v}) &= i \omega \mathbf{v} \end{aligned} \quad (2.4)$$

Now, after discretization, \mathbf{L}_1 and \mathbf{L}_2 become matrices, and (\mathbf{w}, \mathbf{v}) will be represented by n nodal values of the displacement and n more scalar values for the lateral velocities.

The solution of the problem depends in a very sensitive way on the boundary values imposed on the displacement. For a fourth order boundary value problem on a finite interval $[0, l]$, the most straightforward choice is to prescribe zero displacements and zero (space-) derivatives at both ends. This describes a clamped-clamped situation. In the spirit of solution dependence, however, other choices are of greater interest. While at $x = 0$ we demand clamped conditions, at the other end, $x = l$, various linear relations between the angle of inclination $u_x(l, t)$, bending moment $S(l)u_{xx}(l, t)$, lateral force $-(S(x)u_{xx}(x, t) + Pu(x, t))_x$ at $x = l$ may be considered.

Two special cases gained in the past a great deal of attention. One of them is based on the assumption that a lateral force proportional to the axial load P and to the angle of inclination $u_x(l, t)$ is applied at $x = l$. Indeed, this fits into the class of problems with a load dependent on the solution (and its derivatives). If the coefficient is negative, the force is, in fact, stabilizing. If chosen equal to -1 , the boundary condition simplifies to $(S(x)u_{xx}(x, t))_x = 0$ at $x = l$. In the case of constant S , just the third order derivative is set equal to zero. This condition is usually combined with that of a vanishing bending moment, which means a zero second order derivative. Together, these boundary conditions and the equations of motion define Beck's model of a compressed column (Beck, 1952). The second of the mentioned special cases is Reut's column, which is characterized by a vanishing lateral force and a solution dependent bending moment at $x = l$ proportional to P and to the displacement of the tip, $S(l)u_{xx}(l, t) = -Pu(l, t)$, cf. (Imielowski and Mahrenholtz, 1997).

3. Mathematical techniques

In order to solve problems of the discussed class, some analytical background is needed (Euler, 1778a,b); however, eventually, only computational methods give quantitative answers, cf. for instance (Bogacz and Frischmuth, 2012; Bogacz *et al.*, 2008). Analytical properties of the involved operators play a role for qualitative studies, e.g. whether they are coercive or self-adjointed. This decides about the localization of the requested spectrum in (2.4).

The two most essential numerical considerations concern the questions:

- Up to which value of the loading parameter, in the case of the compressed column this is the value of the force P , all solutions are bounded, for instance periodic. In fact, we want to establish stability of the undeformed system at rest.
- Furthermore, when a critical state is reached, what is the form of the displacement that grows out of any limited neighborhood of the trivial state, and what is the way it departs from the state of rest. The later question relates to the effect of flutter, respectively divergent loss of stability.

While in the general case of two- or three-dimensional domains Ω , the method of choice is the discretization of the spatial operator, which leads to a high-dimensional sparse matrix eigenproblem (Frischmuth *et al.*, 1993; Hanaoka and Washizu, 1980; Ringertz, 1994; Tada *et al.*, 1985, 1989), in the one-dimensional case shooting methods are a quite attractive alternative (Bogacz and Frischmuth, 2012; Bogacz and Janiszewski, 1985; Kaliski and Solarz, 1962). Indeed, using explicit formulas for the solution of (2.1) with setup (1.11), the analysis can be reduced to a small matrix problem. This allows an effective and precise calculation of the first eigenmodes and hence the answer to the above formulated questions. This method has been successfully applied e.g. in (Bogacz and Janiszewski, 1985; Kaliski and Solarz, 1962). A weak point of the shooting method is that analytical solutions to the ODE resulting from (1.8), (1.11) and (2.1) are available only in the case of constant coefficients, i.e. prismatic homogeneous beams. To overcome this, segmented columns are studied, which are composed of two or more prismatic pieces. A smooth mass and stiffness distribution would require computational methods. This was done e.g. in (Bogacz *et al.*, 2008) – but the cost increased dramatically. Hence, in the case of a continuously varying cross-section, even a conical one, the shooting method ceases to be efficient.

In this paper, we compare the shooting method – where applicable – with the general approach, based on eigenvalue methods for medium size matrices. This technique is accurate also for higher modes, and it is easily adapted to beams and columns with variable cross-sections. Modifications of the model, e.g. the introduction of supports, elastic or viscous, concentrated or distributed, are extremely easy to implement. Further, elements of the implementation may be re-used for the solution of transient and even nonlinear problems.

The idea of the algorithm is straightforward. We introduce n equally spaced grid points x_j along the middle line of the beam/column. Their distance is $h = l/n$. Between the grid points, exactly at $(j - 1/2)h$, $j = 1, 2, \dots, n - 1, n$, we slice the column into cells. To each cell, its mass is assigned on the basis of the given mass density. Further, for given lateral displacements W_j at the grid points, by central differences the curvature, and hence the bending moment at x_j is calculated as

$$M_j = S_j \frac{W_{j-1} - 2W_j + W_{j+1}}{h^2} \quad (3.1)$$

Taking the first order difference of the M_j -values, adding P times the first order difference of the displacements themselves, one obtains minus the lateral force at the cell boundaries. According to (2.1), allowing for additional lateral support forces if such are present, it is possible to calculate the lateral acceleration with second order accuracy with respect to the step size h .

Special attention is to be paid to the first and last nodes. For the first one, $j = 1$, we are missing the values W_0 and W_{-1} , which according to (3.1) are needed to obtain M_0 and M_1 . Here we may use $W_0 = 0$ and $W_{-1} = W_1$, which follow from the clamped boundary conditions.

The derivation of the equations of motion for the last two nodes was discussed in detail in (Bogacz *et al.*, 2008). Again, application of difference operators requires nodal values beyond the last grid value. These have to be substituted in accordance with the prescribed boundary conditions. For instance in the Beck case, the moment M_n is directly given, the same for Euler

and Reut. In the latter, the moment depends on W_n , which still is easy to implement. Conditions involving the lateral force, i.e. the third and the first derivative, cause more trouble. In particular, in the mentioned examples of Beck's and Reut's columns, the matrix representation of the operator $\mathbf{L} = \mathbf{L}_1 + \mathbf{L}_2$ will be nonsymmetric.

In Beck's case, with constant mass density and stiffness, the shooting method leads to the analysis of the root curves of

$$f(\omega, P) = \det \begin{bmatrix} 0 & 0 & 1 & 0 \\ 0 & P & 0 & 1 \end{bmatrix} \exp(l\mathbf{A}(\omega, P)) \begin{bmatrix} 0 & 0 \\ 0 & 0 \\ 1 & 0 \\ 0 & 1 \end{bmatrix} \quad (3.2)$$

with

$$\mathbf{A}(\omega, P) = \begin{bmatrix} 0 & 1 & 0 & 0 \\ 0 & 0 & 1/S & 0 \\ 0 & 0 & -P & -1 \\ -\rho\omega^2 & 0 & 0 & 0 \end{bmatrix}$$

The zeros of f correspond to pairs of the frequency ω and the compressing force P for which there are nontrivial solutions to a homogeneous system of equations in terms of the moment and lateral force at the foot of the column, which are mapped to the moment and force at the top.

The matrix exponential function used in (3.2) abbreviates the solution formulas for the system

$$\mathbf{y}'(x) = \mathbf{A}(\omega, P)\mathbf{y}(x) \quad (3.3)$$

where $\mathbf{y} = [w, \alpha, M, Q]^T$, meaning the lateral displacement, angle of inclination, bending moment and lateral force. For a given rectangle of interest, the solutions to $f(\omega, P) = 0$ with f from (3.2) have the well-known form shown in Fig. 1.

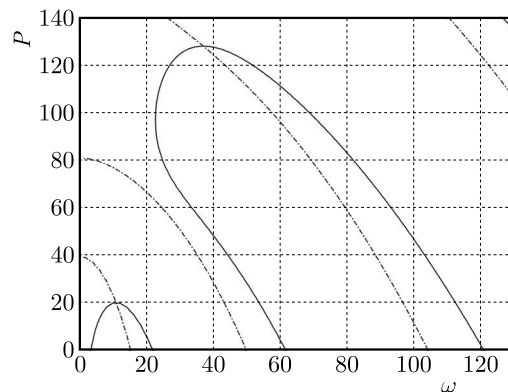


Fig. 1. Root curves in Beck's case, shooting method (density, stiffness and length all equal to 1, dimensionless)

We obtain a critical force of 20.05 together with a critical frequency of 10.87. At this point, the first frequency arc of the first branch of the zero level-set meets with the second one, which we consider the standard topology. Usually, the third meets the fourth and so on. However, in particular for optimized geometries, this alternating sequence of growing and falling arcs becomes disturbed. An example will be shown in Fig. 6, the right part. Moreover, especially in the case of damping, the frequencies are complex-valued from the start on, so that there is no longer a canonical order by their frequencies.

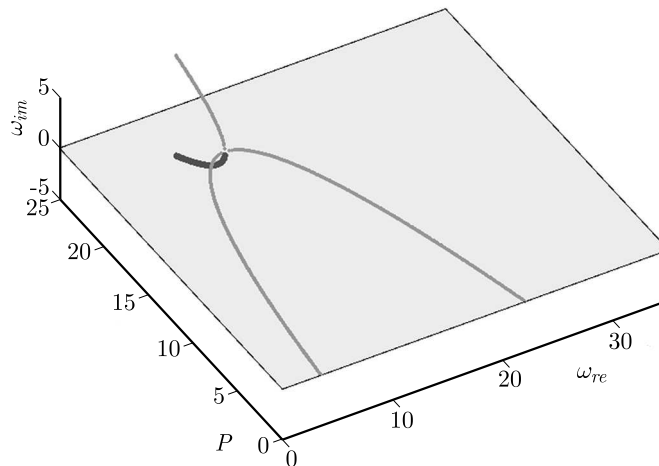


Fig. 2. Eigenfrequencies in dependence on the compressing force. Negative imaginary parts, thick black arc below the 0-plane, indicate instability

The discretization method, followed by an eigenvalue calculation, confirms these values. We used $n = 65$ for Fig. 2.

The minimum of the imaginary parts of the spectrum of the matrix representation of (2.2), here with $k = 0$, is required to be nonnegative. This is true below the critical value of $P_{cr} \approx 20.03$, and it is violated when P exceeds P_{cr} .

4. Improvements

Once we are able to find critical states, an obvious goal is the improvement of the situation in the sense that a higher load can be carried by the structure. There are several options to achieve this. A first way to push the limit of stability higher up is to add supports, i.e. to introduce new loads depending on the values of the displacement, which push or pull the column under consideration back to its original position. Technically, such external forces may be exerted by trusses, which can be modelled as linear springs attached to the column. Further, viscous damping elements may be used to stabilize. Both may be applied alone or together, in series or in parallel, concentrated in a single point, in several points, or continuously distributed. For a detailed analysis, we refer to (Bogacz and Janiszewski, 2008) and our forthcoming book.

An alternative way is to change the considered object – in this case the column – itself. In particular, keeping its length constant, the cross section may be varied, and the material may be changed, so that the mass density and the bending stiffness become design variables. Internal damping may be added, e.g. in the form of a layer of a viscous material, so that a bending moment proportional to the rate of change of the curvature enters the equation of motion. Also graded materials have been studied in the context of damping oscillations in columns (Przybyłowicz, 2008).

Finally, in the age of mechatronics, active control of oscillations of a column may be considered. Assuming that the present deformation of the middle line is known, e.g. measured by optical methods, an optimal position for the application of a lateral force may be determined and applied by an actuator.

In the remaining part of this Section, several versions of modified Beck's columns will be analyzed. Our special interest will be in unexpected effects. Indeed, making a column twice as thick will make it much more stable, which is not a surprise, and which is expensive in terms of material cost, volume and weight. We are looking for intelligent and cost-effective alternatives.

4.1. Mass reduction at the top end

We study the sensitivity of the critical load of Beck's column with respect to changes of its shape. In particular, we will show that it is possible to obtain a higher critical load without using more material. It is enough to reduce the cross section in certain segments, or to redistribute mass, taking material away in some parts, attaching it to others. Here two cases are distinguished: scaled similar profiles and profiles of constant depth. In the first case, stiffness is proportional to the fourth power of the scaling parameter, density changes with its square. In the second case, the exponents are three and one. The effects are analogous, so we pick just one as example.

In Fig. 3, the black curves show the root curves for a segmented column, with the upper part of 15% of the length, reduced in width by 25%. This saves almost 4% of the material, but gives an increase of the critical load from 20.05 to 21.05. Notice the right-shift of the black lines, with reference to the gray ones, corresponding to the column with constant parameters. This means that not only the critical load, but also the critical (resonance) frequency is increased by the modification.

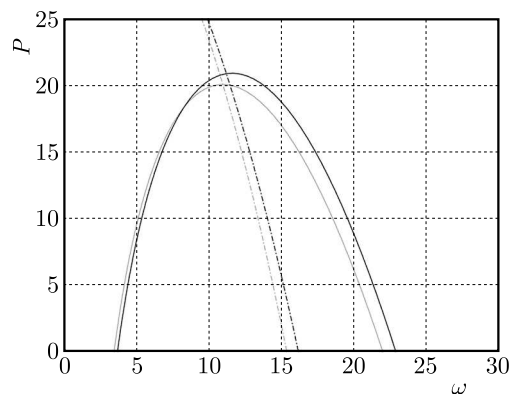


Fig. 3. Improved critical load by reduction of the top segment

It turns out that not much more can be gained by the concept of a two-segment column. A further increase can be obtained, however, by attaching the saved material to the lower segment. Hence, at the same cost of the material, a column with around 8% higher critical load can be found.

The previous case requires just a study of two parameters: fraction of the lower segment and reduction of width of the upper part. This can be done with reasonable accuracy and effort by calculating a full table. Introducing more segments and widths makes a systematic approach too expensive. Further, the results for columns with three or four segments of variable length are not so promising.

Much better results are obtained by a higher number N of segments of equal length, and optimization of the vector of thicknesses of the corresponding cross sections. This fails at $N = 2$, but already at $N = 16$ a considerable improvement of the critical load is possible. This level is kept if the segmented column is replaced by a column with continuous width function, interpolating widths of the segment of the optimally segmented column. A detailed analysis can be found in (Bogacz and Frischmuth, 2012) and the forthcoming book by the authors.

Some remarks on the mechanism of loss of stability may be useful for the understanding of the next Subsections. First, reduction of the cross-section of some segment gives a smaller mass density (per unit of length), and also a smaller stiffness against bending. Looking at the form of oscillations – better even watching an animation – one observes a certain lash-back effect. Both changes, that of mass as well as that of stiffness, contribute positively to the increase of the critical load. In fact, using a lighter material of identical stiffness for the upper segment would yield a small improvement of P_{cr} , same is true for a material (or profile) of the same density

and smaller stiffness. The partial improvements would be around 4% for the change of mass, when keeping the stiffness, and 0.7% for changing the stiffness while keeping the mass in the upper segment. Notice that the combined effect is considerably larger than their sum. Changing simultaneously the mass density with the width, the stiffness with its third power, we gain more than 5%. Hence, there is something like a cross-activity or interaction between both effects.

If we increase the width of the bottom segment by around four per cent, the total mass will be the same as that of the uniform column. Then, instead of 5%, we already obtain a 20% improvement of the critical load.

In the case of the upper segment of a geometrically similar shape as that of the lower segment, e.g. in the case of a circular tower, the improvements are about twice as large. For instance, in the case of the unchanged bottom segment, we can obtain more than 8% saving of the material and more than 9% higher critical load.

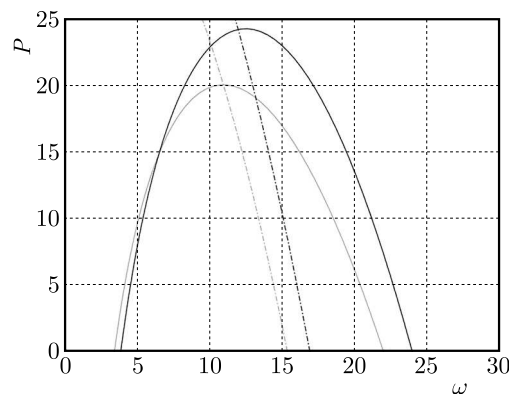


Fig. 4. Increase of the critical load by re-distribution of mass (two segments)

Applying optimization techniques, e.g. an evolution type algorithm, followed by the Nelder-Mead simplex method, columns with 4, 6, 16, ... segments can be tuned to support loads of more than five times higher than those of the uniform width column. For the results, e.g. characteristic curves, shapes and forms of oscillation, we refer to our forthcoming book. However, it should be mentioned that the extremely optimized columns are very sensitive to the slightest changes of their geometry (mass and stiffness distributions), to external forces (e.g. even minimal damping), and boundary conditions, see (Ringertz, 1994).

4.2. Lateral supports

In this Subsection, we consider the influence of lateral supports in the form of elastic and viscous elements. These may act either concentrated at chosen positions or distributed over the length of the column or, finally, combined in the form of a continuous distribution with Dirac-type atoms.

Of particular interest are viscous dampers. Surprisingly, as opposed to elastic ones, their application turns out to be not as promising as might be expected. As previously, effects of cross-influences may be observed. First, we study the influence of forces proportional to the lateral velocity, with a uniform distribution along the length of the column. We found that the influence of such linear viscous damping forces lifts the eigenvalues in Fig. 2 in the direction of the imaginary axis. The effect on the onset of growing modes of oscillation is very small, because the imaginary parts bifurcate out of the horizontal plane containing the lifted characteristic in a parabolic way, so that the increment of P_{cr} is only second order in the damping coefficient ν . Now, if we try a viscous damper giving a concentrated force in a single position, the result is surprisingly bad: depending on the point, where the damper is attached, its effect will be nil or negative. A damper mounted at an inappropriate distance from the fixed end may destabilize

Beck's column. However, if we combine uniform and concentrated damping, a combined advantageous effect can be obtained. So for instance, $\nu = 1$ results in a critical load higher by 0.29% than the undamped column, while $\nu = 10$ already gives 21%. This is more than for the segmented column of the same mass – but quite difficult to implement in practice. A concentrated damper just below the midpoint of the column at $x = 0.48$ gives nothing, but when combined with the small uniform damping $\nu = 1$, an increase of P_{cr} by 50% is possible, see Fig. 5.

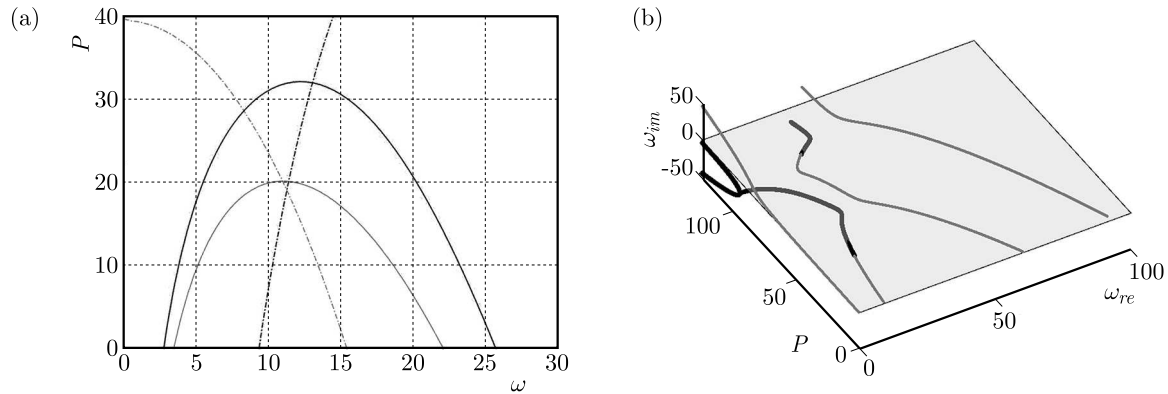


Fig. 5. Combined uniform and concentrated damping

It should be noticed that there is a change in the root curve of the imaginary part of the characteristic determinant on the left part of Fig. 5. On the right part, the complex eigenfrequencies are shown, both real and imaginary parts, for the same parameters of the damping. It is evident that the two arcs of the first branch, the growing and falling one, previously laying in the same plane, do not even touch. The growing part drops below the zero-plane of the imaginary part, $\omega_{im} = \Im(\omega) = 0$, before the maximum is reached. In fact, the maximum of that path does not exist – it appears just in the projection to the real part. Summing up, we can state that the approach using complex eigenvalue problems gives a deeper understanding of the dynamics of the considered construction, while the determinant-based solution gives quicker evaluations of the critical loads, e.g. during optimization.

4.3. Hinged columns

Reshaping the width of a column, using many segments or smooth variation, may be undesirable for several reasons. *Nota bene*, also the applicability of the Bernoulli-Euler theory is limited in the case of jumps in the column diameter. Instead of reducing the diameter, a reduction of the bending stiffness may be obtained as well by connecting two segments by a flexible joint, cf. for example (Bogacz *et al.*, 2008). Using its position and compliance as design parameters, it can be attempted to increase critical loads.

In Fig. 6, the root curves for a column composed of two segments, the lower part of length $0.9l$, the upper of length $0.1l$, is shown. Both segments have identical and uniform mass density and stiffness. They are connected by a hinge with a bending stiffness of 1.0 on the left part of Fig. 6. A 20% increase in the compliance causes considerable changes in the resonance curves, as is shown on the right part. The solution is very sensitive to small changes of the position of the hinge and the stiffness. The obtained increase in P_{cr} of around 20% may be lost if, e.g. due to fatigue, the optimal parameters are not kept with sufficient accuracy. On the right part of Fig. 6, the improvement on P_{cr} is already reduced by 20%, and it quickly drops below the original level of $P_{cr} = 20.05$, if the stiffness of the hinge decreases further.

Thus, hinges should be studied in connection with lateral supports, as discussed in the previous Subsection. Of particular interest are intelligent supports that are neither elastic nor

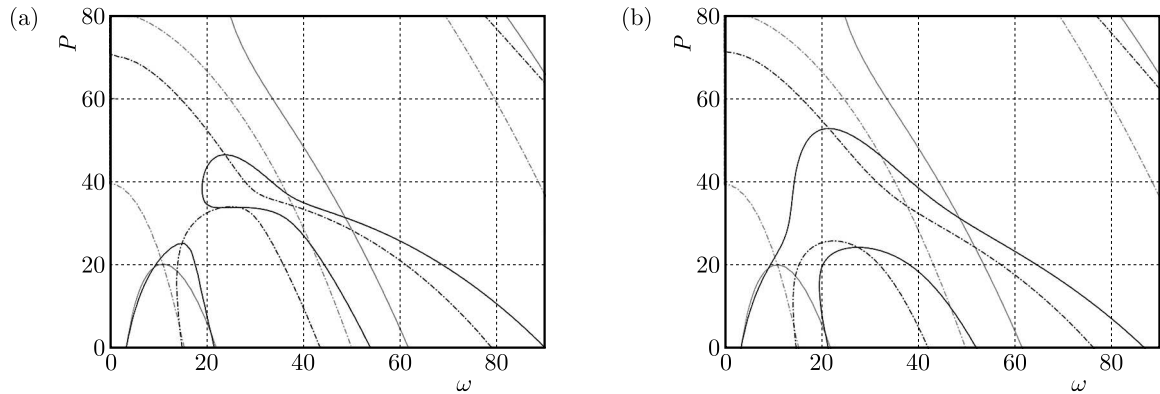


Fig. 6. Characteristics of a hinged column

viscous, but controlled on the basis of observed displacements and speeds. For a detailed analysis, we refer to (Bogacz *et al.*, 2008), in the case of control see also (Preumont and Seto, 2008; Przybyłowicz, 2008).

5. Conclusions

Considerations on the stability of constructions should take into account dynamical effects. Static analysis alone can be very misleading. Secondly, one should be aware that loads may vary if a body gets out of its position of rest; such changes may have a stabilizing or destabilizing effect. Once the limits of stability are calculated, usually efforts will be made to improve the structure. However, effects of changes of the structure or the loading may be very surprising. For instance, weakening by removal of the material and decreasing the bending stiffness may increase the critical load, since it also reduces the inertial forces. Indeed, there may be unexpected cross-effects. If applied in the right region of the body, material may be saved and/or higher critical loads may be achieved. Similarly, adding damping may increase or decrease the critical force, depending on the geometrical details. If combined with mechatronic control, even a hinge may have a positive influence on the stability limit for the compressive load.

Finally, it should be warned that whatever optimized structures are designed and implemented, they should be robust against disturbed parameters and conditions. Such disturbances may be small changes of mass density (e.g. by dirt, corrosion), of stiffness (e.g. by ageing, fatigue, heat) or the loading (e.g. by wind, earthquakes) or a breakdown of the control system (e.g. power outing, shortcut, wear). In a recent paper, the robustness with respect to limited geometrical accuracy was discussed. From the analysis there, it follows that the limit of stability drops by 50% due to the change from the true theoretically optimal shape to a realistic one – that can really be built. Anyway, given the theoretical potential to lift the critical load by a factor of seven, eight or more, there remains quite a good possibility to improve a construction at a low cost and in a save way.

References

1. BECK M., 1952, Die Knicklast des einseitig eingespannten tangential gedrehten Stabes, *ZAMP Zeitschrift für angewandte Mathematik und Physik*, **3**, 3, 225-228
2. BOGACZ R., CZYCZUŁA W., KONOWROCKI R., 2014, Influence of sleepers shape and configuration on track-train dynamics, *Shock and Vibration*, art. ID 393867, 1-7
3. BOGACZ R., FRISCHMUTH K., 2012, On some new aspects of contact dynamics with application in railway engineering, *Journal of Theoretical and Applied Mechanics*, **60**, 1, 119-129

4. BOGACZ R., FRISCHMUTH K., LISOWSKI K., 2008, Interface conditions and loss of stability for stepped columns, *Applied Mechanics and Materials*, **9**, 41-50
5. BOGACZ R., IRRETIER H., MAHREHOLTZ O., 1980, Optimal design of structures subjected to follower forces, *Ingenieur-Archiv*, **49**, 63-71
6. BOGACZ R., JANISZEWSKI R., 1985, Analysis and synthesis of columns, compressed by follower forces, from the stability point of view (in Russian), *Advances in Mechanics*, **8**, 3, 3-52
7. CLAUDON J.L., 1975, Characteristic curves and optimum design of two structures subjected to circulatory loads, *Journal de Mécanique*, **14**, 3, 531-543
8. EULER L., 1778, Determinatio onerum, quae columnae gestare valent, *Acta Academiae Scientiarum Petropolitanae*, **1**, 121-145
9. EULER L., 1778, Examen insignis puradoxi in theoria columnarum occurrentis, *Acta Academiae Scientiarum Petropolitanae*, **1**, 146-162
10. FELDT W.T., NEMAT-NASSER S., PRASAD S.N., HERRMANN G., 1969, Instability of a mechanical system induced by an impinging fluid jet, *Journal of Applied Mechanics*, 693-701
11. FRISCHMUTH K., KOSINSKI W., LEKSZYCKI L., 1993, Free vibrations of finite memory material beams, *International Journal of Engineering Science*, **31**, 3, 385-395
12. HANAOKA M., WASHIZU K., 1980, Optimum design of Beck's column, *Computers and Structures*, **11**, 6, 473-480
13. IMIEŁOWSKI S., MAHREHOLTZ O., 1997, Optimization and sensitivity of stepped columns under circulatory load, *Applied Mathematics and Computer Science*, **7**, 1, 155-170
14. KALISKI S., SOLARZ L., 1962, Aeroelastic vibration and stability of a deformable rotating rocket in a linearized flow, *Proceedings of Vibration Problems*, **3**, 57-68
15. KATSIKADELIS J.T., TSIATAS C.G., 2007, Nonlinear dynamic stability of damped Becks-column with variable cross-section, *International Journal of Nonlinear Mechanics*, **42**, 1, 164-171
16. KERR A.D., 1988, Stability of a water tower, *Ingenieur-Archiv*, **58**, 428-436
17. KOSIŃSKI W., FRISCHMUTH K., 2001, Thermomechanical coupled waves in a nonlinear medium, *Wave Motion*, **34**, 2, 131-141
18. PREUMONT A., SETO K., 2008, *Active Control of Structures*, Wiley
19. PRZYBYŁOWICZ P.M., 2008, Aeroflutter suppression in an FGM panel with active fibers, *Mechanics and Mechanical Engineering*, **12**, 4, 375-387
20. RINGERTZ U. T., 1994, On the design of Beck's column, *Structural Optimization*, **8**, 120-124
21. TADA Y., MATSURNOTO R., OKU A., 1989, Shape determination of nonconservative structural systems, *Proceedings of 1st International Conference of Computer Aided Optimum Design of Structures: Recent Advances*, Springer, Berlin
22. TADA Y., SEGUCHI Y., KEMA K., 1985, Shape determination of nonconservative structural systems by the inverse variational principle, *Memoirs of the Faculty of Engineering, Kobe University*, **32**, 45-61
23. TIMOSHENKO S., 1921, On the correction for shear of the differential equation for transverse vibrations of prismatic bars, *Philosophical Magazine*, **6**, 41, 744-746
24. TOMSKI L., PRZYBYLSKI J., GOŁĘBIEWSKA-ROZANOW M., SZMIDLA J., 1996, Vibration and stability of an elastic column subject to a generalized load, *Archive of Applied Mechanics*, **67**, 105-116

MECHANICAL PROPERTIES AND ADVANCED SUBJECTS IN SHAPE MEMORY ALLOYS AND POLYMERS

RYOSUKE MATSUI, KOHEI TAKEDA, HISAAKI TOBUSHI

Department of Mechanical Engineering, Aichi Institute of Technology, Toyota, Japan

e-mail: r_matsui@aitech.ac.jp; k-takeda@aitech.ac.jp; tobushi@aitech.ac.jp

ELZBIETA A. PIECZYSKA

Institute of Fundamental Technological Research, Polish Academy of Sciences, Warsaw, Poland

e-mail: epiecz@ippt.pan.pl

Advanced subjects in mechanical properties of shape memory alloys and polymers are discussed. In the subloop loading under a stress-controlled condition of the shape memory alloy, the transformation-induced stress relaxation appears due to variation in temperature. The enhancement of corrosion and corrosion fatigue life of the shape memory alloy is discussed. The development of a functionally-graded shape memory alloy and polymer is expected to obtain better performance. Three-way motion appears in the shape memory composite with the shape memory alloy and polymer.

Keywords: shape memory alloy, shape memory polymer, functionally-graded shape memory material, shape memory composite

1. Introduction

The development of shape memory alloys (SMA) has attracted high attention because of the unique properties of the shape memory effect (SME) and superelasticity (SE) appearance (Duerig *et al.*, 1990; Funakubo, 1987; Lagoudas, 2008; LExcellent, 2013; Otsuka and Wayman, 1998; Sun *et al.*, 2017; Tobushi *et al.*, 2013; Ziolkowski, 2015). If we use the SME and SE in practical applications, not only large recovery strain but also high recovery stress, energy storage and energy dissipation can be obtained. The main features of the SME and SE are induced due to martensitic transformation (MT). Since the deformation properties due to the MT depend on temperature, stress and thermomechanical hysteresis, they are, therefore, complex. They also depend on the loading rate. In the case of subloop loading, the deformation behaviors are quite different between strain- and stress-controlled loading conditions. The transformation-induced creep and stress relaxation appear in the subloop loading under the stress-controlled condition. The corrosion and corrosion fatigue properties are important in practical application of SMA elements.

The shape memory polymer (SMP) has also been developed (Hayashi, 1993; Huang *et al.*, 2012; Tandon *et al.*, 2016; Yahia, 2015). The main features of SMP appear due to the glass transition. Elastic modulus differs at temperatures above and below the glass transition temperature, and the rigidity of SMP elements, therefore, varies depending on the temperature change. Based on this property, the shape fixity and shape recovery can be used.

Although elastic modulus and yield stress are high at high temperatures and low at low temperatures in SMAs, they are high at low temperatures and low at high temperatures in SMPs. The dependence of rigidity on temperature is, therefore, quite different between the SMA and SMP. If composite materials with SMA and SMP are developed, new characteristics of the shape memory materials can be obtained.

In order to obtain a better performance, the development of functionally-graded SMAs and SMPs is expected. The 3D-printing of SMPs is requested as a simple method to manufacture complex SMP elements.

In the present paper, advanced subjects in mechanical properties of SMA such as the deformation behavior subjected to the stress-controlled subloop loading and the corrosion fatigue properties of SMA are discussed. Next, the functionally-graded SMA and SMP are discussed. Following these subjects, the mechanical properties of the shape memory composite with SMA and SMP such as the characteristics of the three-way bending properties and the 3D printing of SMP will be discussed.

2. Deformation and fatigue properties of SMAs

2.1. Stress relaxation in subloop loading

SMA elements are subjected to variation in stress, strain and temperature with various ranges accompanying the MT in practical applications. The analysis in the subloop loading is therefore important. Although the return-point memory appears under a low strain rate in the subloop loading, it does not appear under the stress-controlled condition. In the case of the subloop loading under the stress-controlled condition, the transformation-induced creep and creep recovery appear under a constant stress, and the transformation-induced relaxation and stress recovery under a constant strain. It should be noticed that the stress-strain curve depends on the loading rate (Ikeda, 2015; Pieczynska *et al.*, 2006; Yin *et al.*, 2014). The transformation-induced stress relaxation in the subloop loading of the TiNi SMA under various loading conditions will be discussed in this Section.

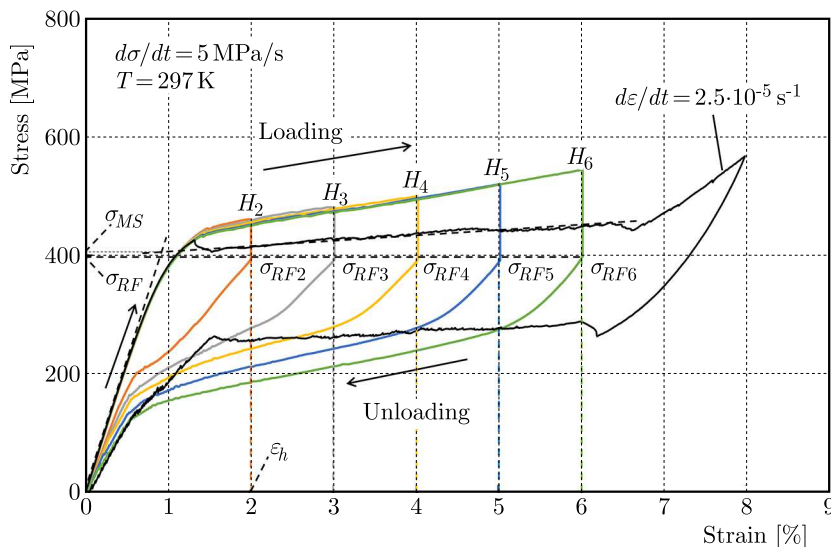


Fig. 1. Stress-strain curves of the TiNi SMA in the stress relaxation test with various holding strains and in the low strain rate $d\varepsilon/dt = 2.5 \cdot 10^{-5} \text{ s}^{-1}$

The stress-strain curves obtained in a stress relaxation test with various holding strains are shown in Fig. 1. The loading conditions of the stress relaxation tests in Fig. 1 were as follows. The load was applied at a stress rate $d\sigma/dt = 5 \text{ MPa/s}$ until a point H_2 (or H_3 , H_4 , H_5 and H_6) at a strain $\varepsilon_h = 2\%$ (or 3% , 4% , 5% and 6%) followed by holding the strain ε_h constant till the decrease in stress finished and thereafter unloaded at a stress rate $d\sigma/dt = -5 \text{ MPa/s}$. The stress-strain curve shown by a black line in Fig. 1 was obtained at a strain rate $d\varepsilon/dt = 2.5 \cdot 10^{-5} \text{ s}^{-1}$ during loading and unloading with the maximum strain 8% . As can be seen in Fig. 1, in the strain

holding process at ε_h following the loading till the strain ε_h at the stress rate $d\sigma/dt = 5 \text{ MPa/s}$, the stress decreases to σ_{RF2} (or σ_{RF3} , σ_{RF4} , σ_{RF5} and σ_{RF6}), resulting in stress relaxation. The stress σ_{RF2} (or σ_{RF3} , σ_{RF4} , σ_{RF5} and σ_{RF6}) at a point ε_h after relaxation is almost the same as the stress of the MT start σ_{MS} in the stress-strain curve at a strain rate $d\varepsilon/dt = 2.5 \cdot 10^{-5} \text{ s}^{-1}$, in which an increase in the stress is smaller than that at a stress rate $d\sigma/dt = -5 \text{ MPa/s}$.

In the loading process at a constant stress rate $d\sigma/dt = 5 \text{ MPa/s}$, strain rate becomes high in the upper stress plateau region, and the heat is generated due to the exothermic MT, resulting in an increase in temperature of the specimen. In the strain holding stage from the point H_2 (or H_3 , H_4 , H_5 and H_6) to σ_{RF2} (or σ_{RF3} , σ_{RF4} , σ_{RF5} and σ_{RF6}), the temperature decreases due to the heat transfer into the ambient air and the condition for the transformation to progress is satisfied, resulting in progress of the MT. As a result, stress relaxation occurs while holding the strain constant.

The relationship between the stress decrease $\Delta\sigma$ and temperature decrease ΔT during holding a constant strain in the stress relaxation tests with various conditions is shown in Fig. 2. Temperature was measured by the infrared thermography. The forced convection was performed by air flow in order to observe the influence of cooling rate on stress relaxation. As can be seen, the stress decrease $\Delta\sigma$ is proportional to the temperature decrease ΔT . The broken line in Fig. 2 is calculated by $\Delta\sigma = a\Delta T$ and shows a good overall match with the experimental results. The value of the coefficient a is 13.2 MPa/K .

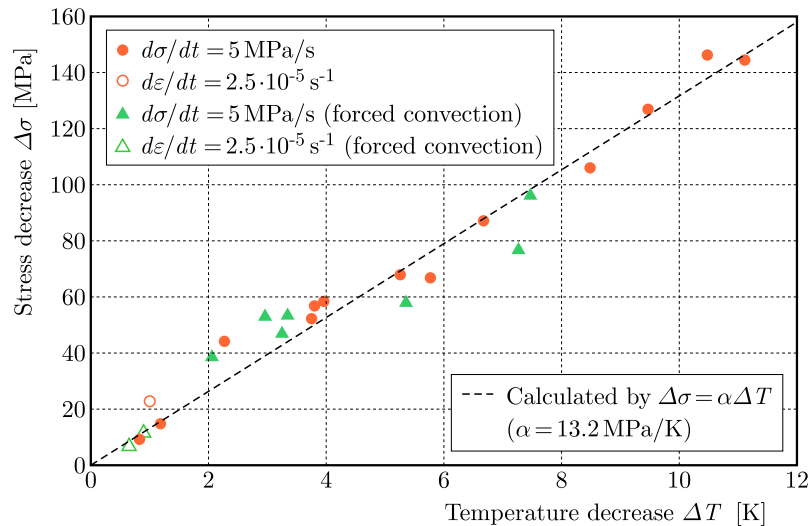


Fig. 2. Relationship between stress decrease and temperature decrease in the stress relaxation test with various conditions

2.2. Corrosion and fatigue properties of SMA

2.2.1. Corrosion fatigue life

The corrosion fatigue life is important in practical applications of SMAs. However, the report on the corrosion fatigue properties is little. The corrosion fatigue life of a TiNi SMA wire was investigated through a bending fatigue test.

The relationships between the strain amplitude ε_a and the number of cycles to failure N_f obtained by the rotating-bending fatigue test in the air and the 10%-NaCl water solution are shown in Fig. 3 (Yamada and Matsui, 2016). The materials used in the experiment were TiNi SMA wires (Ti-49.7 at% Ni) with a diameter of 0.7 mm. The materials were heat-treated in an electrical furnace for 1 h at 673 K. The materials were then allowed to cool inside the furnace. The fatigue life in 10%-NaCl water solution (i.e. the corrosion fatigue life) is shorter than that in the air as shown in Fig. 3. Accordingly, engineers have to be careful with fatigue life of SMA

devices, particularly, when used in corrosive environment (i.e. in human body, seawater, etc.). In order to enhance the corrosion fatigue life, we have developed a thermal treatment to generate a strong and homogeneous passive layer on the surface of TiNi SMAs. This subject will be discussed in the next Section.

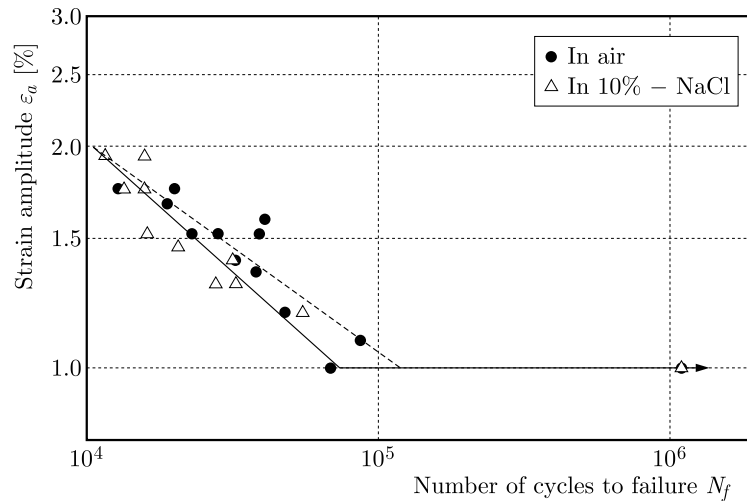


Fig. 3. Fatigue life curves for TiNi shape memory alloys in the air and 10%-NaCl water solution

The enhancement of fatigue life can also be achieved by the surface treatment of materials through the ultrasonic shot peening (USP) and the nitrogen ion implantation (NII). The influence of NII, USP and thermal treatment conditions on the corrosion fatigue life of an SME tape and an SE tape is the future subject.

2.2.2. Corrosion resistance

In order to promote the application of SMAs into devices used in corrosive environment, we have developed a procedure to generate a passive layer on TiNi SMAs. The proposal process called the thermal nitridation (TN) treatment to generate thin and homogeneous passive layers contains heat treatment of a mechanically-polished SMA wire at temperature of 673 K for 3.6 ks in a furnace filled with pure nitrogen gas.

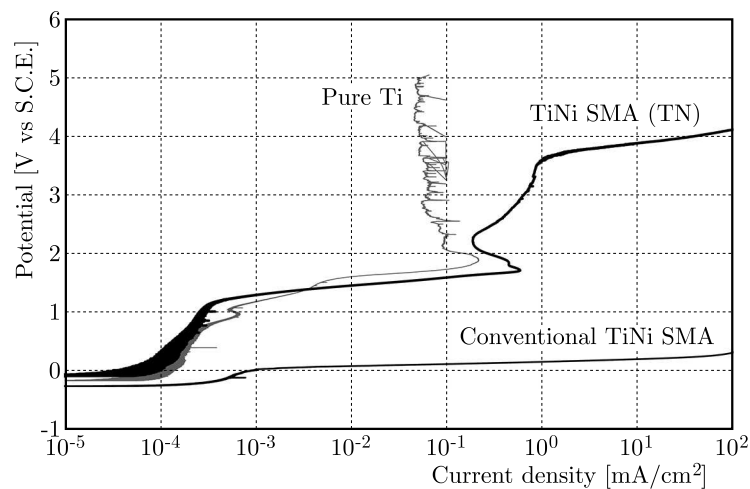


Fig. 4. Anodic polarization curves for TiNi SMA (TN), conventional TiNi SMA and pure Ti

Figure 4 shows anodic polarization curves for TiNi SMA with the passive layer generated by TN process, a conventional TiNi SMA with a thick oxide layer and a pure Ti in a 3%-NaCl water

solution. The results reveal that corrosion resistance of the TN-treated TiNi SMA is much higher than that of the conventional TiNi SMAs and is almost the same as that of pure Ti, which is the most common material as a biomaterial, with current density of up to above $1 \cdot 10^{-2} \text{ mA/cm}^2$. From the energy dispersive X-ray spectrometry analysis and other microscopic investigations, we found that a thin titanium-nitride layer with a thickness of tens of nanometers is generated on the TN-treated TiNi SMA.

Since the corrosion fatigue life for the TN-treated TiNi SMA is one of the important properties to design devices, we are now investing in clarifying the characteristics of corrosion fatigue life from a fatigue test in the 10%-NaCl water solution.

3. Functionally-graded shape memory alloy and shape memory polymer

3.1. Functionally-graded shape memory alloy

In order to develop a more advanced actuator, such as a self-stroke controlling device depending on the ambient temperature, a TiNi SMA having a functionally-graded property of the transformation temperatures will be a major candidate material for the element. If the functionally-graded shape memory alloy (FGSMA) coil is employed to an actuator, the shape-recoverable region exceeding the austenitic transformation finish temperature A_f will change continuously, resulting in length of the coil extending or shortening without a bias element, depending only on its temperature.

Figure 5 shows a demonstration of movement of an FGSMA coil having different transformation temperatures A_f ; $A_{f1} = 293 \text{ K}$, $A_{f2} = 318 \text{ K}$ and $A_{f3} = 338 \text{ K}$. The coil subjected to tensile load along its axial direction and then it was unloaded at temperature $T = 298 \text{ K}$ as shown in Figs. 5b and 5c. In this state, a part of the coil, which had the transformation temperature A_{f1} , recovered its original shape without heating due to superelasticity. The coil was subsequently heated up to $T = 328$ and 348 K , the shape recoverable region extended and length of the coil became shorter as shown in Figs. 5d and 5e.

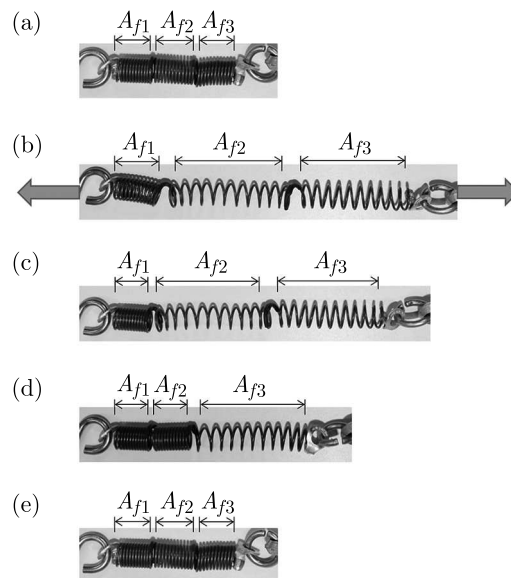


Fig. 5. Movement of the SMA coil having different transformation temperatures; $A_{f1} = 293 \text{ K}$, $A_{f2} = 318 \text{ K}$ and $A_{f3} = 338 \text{ K}$: (a) initial state, (b) loading at $T = 298 \text{ K}$ ($A_{f1} < T < A_{f2} < A_{f3}$), (c) unloading at $T = 298 \text{ K}$ ($A_{f1} < T < A_{f2} < A_{f3}$), (d) heating up to $T = 328 \text{ K}$ ($A_{f1} < A_{f2} < T < A_{f3}$), (e) heating up to $T = 348 \text{ K}$ ($A_{f1} < A_{f2} < A_{f3} < T$)

As an example of manufacturing the functionally-graded shape memory alloy (FGSMA), we have developed a new fabrication process that combines powder metallurgy and hot extrusion to obtain an FGSMA wire in which the transformation temperature varies from high to low along the wire axis depending on gradually changing composition of Ti and Ni. First, a multilayered TiNi green compact in which the Ti-Ni compositions varied layer by layer was sintered using a spark plasma sintering process and then the compact was hot extruded into a wire. We used a characteristic that the phase transformation temperature of TiNi SMA changed depending on the composition of Ti and Ni (Duerig *et al.*, 1990; Funakubo, 1987; Otsuka and Wayman, 1998).

Figure 6 shows the stress-local strain curves at three points of the hot extruded wire with gradually changing composition of Ti and Ni. The wire shows the SE at the position that corresponds to a Ni content of 51.0 at% and the SME at the position of 50.4 at% Ni. These differences appear to be based on the different MT temperatures at each position.

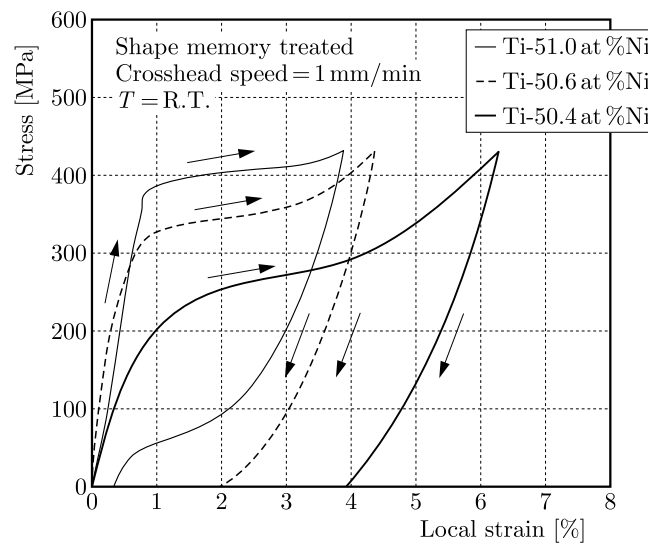


Fig. 6. Stress-local strain curves of FGSMA wire with gradually changing composition

If the FGSMA wire or tape is developed, the temperature-dependent continuous actuation or the multi-way actuation can be obtained by using only one SMA coil or tape, respectively.

3.2. Functionally-graded shape memory polymer

The relationship between force and depth of the functionally-graded shape memory polymer (FGSMP) board in the indentation test is similar to that of the finger (Takeda *et al.*, 2016). The deformation properties of the body differ depending on the region. The FGSMP board corresponding to each region can be developed by a combination of the sheet and foam with appropriate thickness, glass transition temperature and their arrangement. The FGSMP board can therefore be applied to the elements coming into contact with the body as a nursing-care robot in the medical actuators. The basic deformation property of the FGSMP foam will be discussed in this Section.

A polyurethane-SMP foam has been used to fabricate FGSMP foams. The SMP foams having different glass transition temperatures T_g ($T_g = 298$ K and 321 K) and density ρ ($\rho = 43$ kg/m³ and 70 kg/m³) were laminated and the FGSMP was fabricated. Thickness of each SMP foam was 10 mm. The structure of an FGSMP foam is shown in Fig. 7. Two SMP foams with $T_g = 298$ K and $\rho = 43$ kg/m³ were arranged in the upper part, and those with $T_g = 321$ K and $\rho = 70$ kg/m³ in the lower part. The adhesive used to laminate the foam was DW246W produced by SMP Technologies Inc.

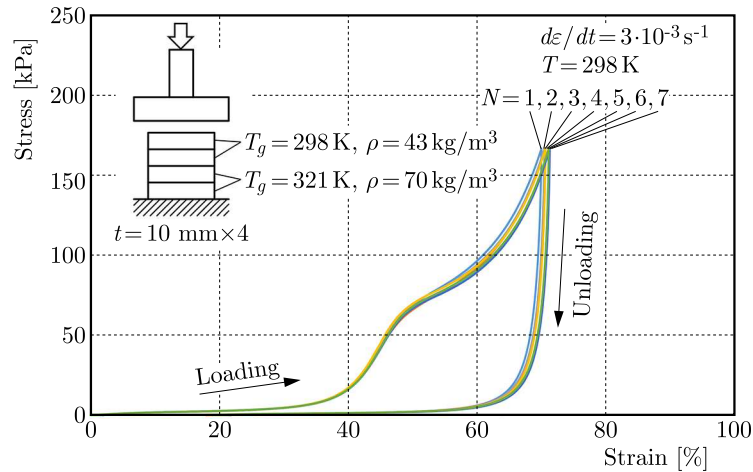


Fig. 7. Stress-strain curves of FGSMF foam in the thermomechanical compression test

The thermomechanical cyclic compression test was performed on the FGSMF foam. At first, it was compressed at a strain rate of $3 \cdot 10^{-3} \text{ s}^{-1}$ in the loading and unloading processes at the room temperature $T = 298 \text{ K}$. Thereafter, the FGSMF foam was heated up to 373 K for 5 minutes in the furnace to recover the residual strain followed by cooling down to the room temperature. These processes were repeated in 7 cycles. The relationship between stress and strain obtained in the cyclic compression test is shown in Fig. 7. As can be seen, the stress increases slightly at the initial stage due to deformation of the SMP foam with $T_g = 298 \text{ K}$ and $\rho = 43 \text{ kg/m}^3$. Then, the stress increases rapidly around a strain of 45% due to completion of local deformation of the upper SMP foam. Thereafter, the SMP foam with $T_g = 321 \text{ K}$ and $\rho = 70 \text{ kg/m}^3$ was deformed accompanying the stress plateau starting from about 70 kPa, resulting in two steps of deformation in the loading process. After unloading, the residual strain of 19% appears under no-load due to the irrecoverable strain of the SMP foam with $T_g = 321 \text{ K}$. This residual strain can be recovered almost to 0% if the FGSMF is heated above $T_g = 321 \text{ K}$ under no-load. The deformation behavior is almost the same in each cycle.

4. Shape memory composite with SMA and SMP

The structure and a photograph of the fabricated shape memory composite (SMC) belt is shown in Fig. 8. As can be seen in Fig. 8a, the 3D-printed SMP sheet, SME wire and SE wire were laminated. Then the laminated material was set in the mold for heat-treating of the SMC belt. The glass transition temperature ($T_g = 328 \text{ K}$) of the SMP sheet was above the both phase transformation temperatures A_f of the SME wire ($A_{f2} = 316 \text{ K}$) and SE wire ($A_{f1} = 306 \text{ K}$) of TiNi alloy. The SME and SE wires were arranged facing in the opposite directions for the memorized U-shape. The SME and SE wires were sandwiched between two 3D-printed SMP sheets from the upper and lower sides. The SMC belt shown in Fig. 8b can be fabricated without bubbles and gaps by using the 3D-printed SMP sheet.

The relationship between the recovery force and temperature of the SMC belt operated by joule heating of both wires is shown in Fig. 9. As can be seen, during heating by joule heat, the recovery force decreases from point (I) to (II) due to the recovery force of SE wire. Then, the recovery force of the SMC belt increases from point (II) to (III) since the recovery force of the SME wire appears. During cooling by the ambient air, the recovery force of the SMC belt decreases from point (III) to (IV) due to decreasing in the recovery force of the SME wire. Then the force of the SMC belt becomes constant since the SMP sheet becomes harder below T_g . The deformation behavior of the SMC belt is almost the same in the cyclic heating and cooling

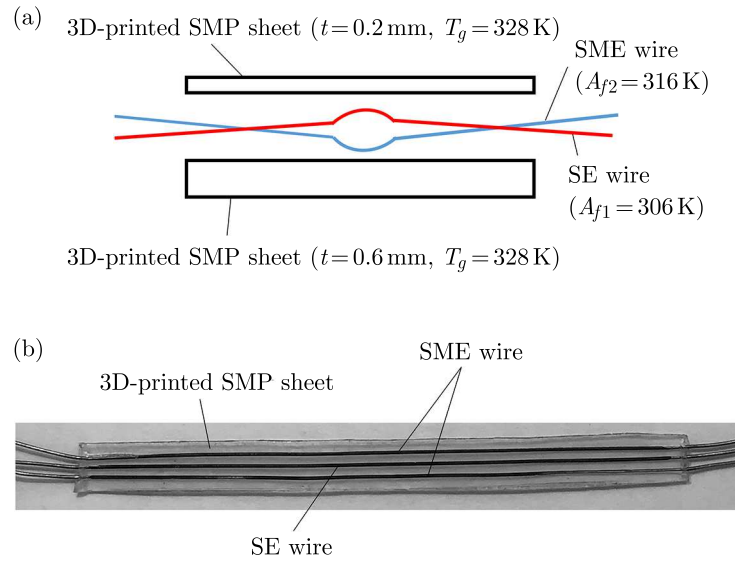


Fig. 8. Structure (a) and photograph (b) of the SMC belt

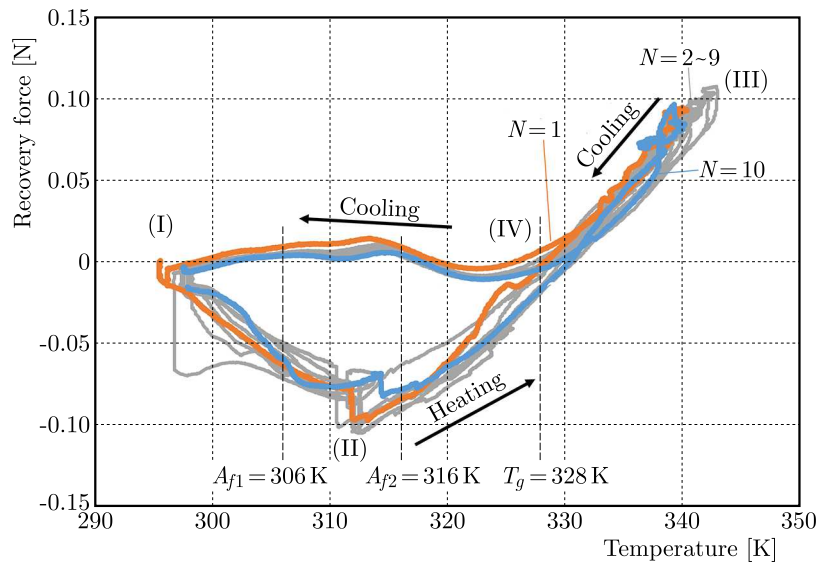


Fig. 9. Variation in the recovery force of the SMC belt during cyclic heating and cooling

processes. The reciprocating three-way behavior of the recovery force can be obtained by a simple SMC structure.

5. 3D-Printed shape memory polymer

Recently, the 3D printer which can make products in a short time without cutting or casting has been attracted worldwide attention. If we use the 3D printer, it is possible that a customized product which is well suited to the individual is fabricated with a low cost and in a short time. If we make a product with SMP using a 3D printer, the new device which is well suited to the individual complex shape can be developed without using expensive metal molds.

The material used to fabricate a 3D-printed SMC belt was a SMP filament which was newly developed by SMP Technologies Inc. and KYORAKU Co., Ltd. The 3D-printed SMP belt was fabricated by a fused deposition modeling (FDM) 3D printer. The nozzle movement during printing the belt is shown in Fig. 10. The pattern of movement of the nozzle during printing was

0° angle with respect to the longitudinal direction of the belt. The thickness of each layer in the printing process was 0.2 mm. The total layers were two and thickness of the belt was 0.4 mm.

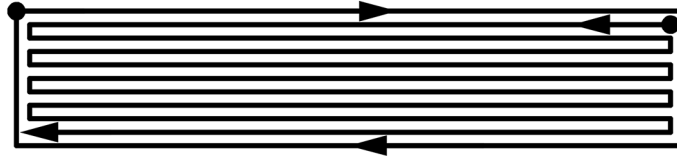


Fig. 10. Nozzle movement during fabricating an SMP belt in 3D-printing

Photographs of motion of the 3D-printed SMP belt for shape fixity and shape recovery are shown in Fig. 11. As can be seen, (1) the 3D-printed SMP belt was deformed at a temperature above T_g . Then, (2) the deformed shape was maintained without a force at temperatures below T_g . Next, (3) the original shape of the belt was recovered by heating above T_g . The shape fixity and shape recovery properties are obtained in the 3D-printed SMP as same as the SMP made by the general method. The thermomechanical properties of the 3D-printed SMP depend on the nozzle temperature, table temperature, printing rate and pattern of each layer (Takeda *et al.*, 2017). These points are the future subjects.

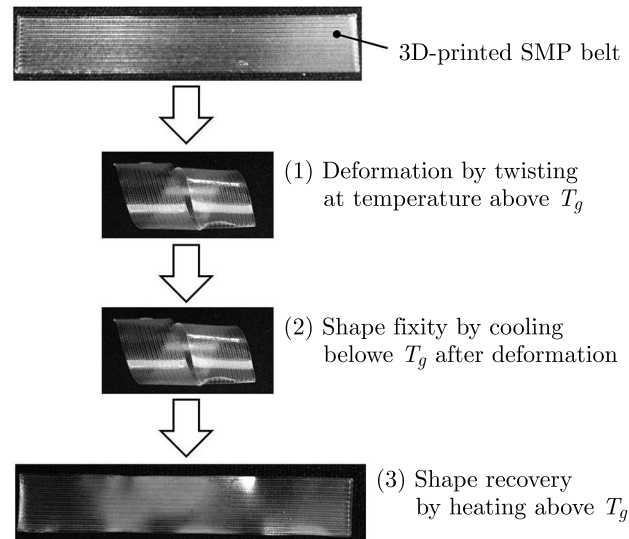


Fig. 11. Photographs of shape fixity and shape recovery of the 3D-printed SMP belt

6. Conclusions

Mechanical properties and advanced subjects in shape memory alloys and polymers have been discussed. The results obtained are summarized as follows.

- The shape memory effect and superelasticity of shape memory alloys depend on thermomechanical loading conditions. The transformation-induced stress relaxation appears in the subloop loading under the stress-controlled condition. The stress decrease is proportional to the temperature decrease during holding the strain constant.
- The thin titanium-nitride layer with thickness of tens of nanometers is generated on TN-treated TiNi SMA. The enhancement of corrosion fatigue life of the shape memory alloy is expected by thermal nitridation treatment.
- The functionally-graded shape memory alloy and polymer with various compositions and phase transformation temperatures are fabricated to obtain better performance of shape memory elements.

- Three-way motion can be obtained by the composite with shape-memory alloys and polymers having various phase transformation temperatures.
- The shape fixity and recovery properties can be obtained by a 3D-printed shape memory polymer element.

Acknowledgement

The authors are grateful for the support of JSPS KAKENHI Grant No. JP15K21477 and the National Science Centre (NCN), Poland, under Grant 2014/13/B/ST8/04280.

References

1. DUERIG T.W., MELTON, K.N., STOKEL D., WAYMAN C.M., EDIT., 1990, *Engineering Aspects of Shape Memory Alloy*, Butterworth-Heinemann, Oxford
2. FUNAKUBO H., EDIT., 1987, *Shape Memory Alloys*, Gordon and Breach Science Pub., New York
3. HAYASHI S., 1993, Properties and applications of polyurethane series shape memory polymer, [In:] *International Progress in Urethanes*, **6**, 90-115
4. HUANG W.M., YANG B., FU Y.Q., 2012, *Polyurethane Shape Memory Polymers*, CRC Press, Boca Raton
5. IKEDA T., 2015, Analytical investigation of strain loading frequency effect on stress-strain-temperature relationship of shape-memory alloy, *Archives of Mechanics*, **67**, 4, 275-291
6. LAGOUDAS D.C., EDIT., 2008, *Shape Memory Alloys*, Springer, New York
7. LEXCELLENT C., 2013, *Shape-Memory Alloys Handbook*, John Wiley & Sons, Hoboken
8. OTSUKA K., WAYMAN C.M., EDIT., 1998, *Shape Memory Materials*, Cambridge University Press, Cambridge
9. PIECZYSKA E.A., TOBUSHI H., GADAJ S.P., NOWACKI W.K., 2006, Superelastic deformation behaviors based on phase transformation bands in TiNi shape memory alloy, *Materials Transactions*, **47**, 3, 670-676
10. SUN Q.P., MATSUI R., TAKEDA K., PIECZYSKA E., EDIT., 2017, *Advances in Shape Memory Materials*, Cham, Springer
11. TAKEDA K., HAYASHI S., UEKI K., 2017, Deformation properties of 3D printed shape memory polymer, *Key Engineering Materials*, **725**, 378-382
12. TAKEDA K., MATSUI R., TOBUSHI H., HAYASHI S., 2016, Functionally-graded shape memory board, *Mechanical Engineering Journal*, **3**, 6, 1-9, DOI: 10.1289/mej.16-00157
13. TANDON G.P., MCCLUNG A.J.W., BAUR J.W., EDIT., 2016, *Shape Memory Polymers for Aerospace Applications*, DEStech Publications, Inc., Lancaster
14. TOBUSHI H., MATSUI R., TAKEDA K., PIECZYSKA E.A., 2013, *Mechanical Properties of Shape Memory Materials*, Nova Science Pub., New York
15. YAHIA L.H., EDIT., 2015, *Shape Memory Polymers for Biomedical Applications*, Elsevier, Amsterdam
16. YAMADA K., MATSUI R., 2016, Improvement of corrosion fatigue strength for TiNi shape memory alloy, *Key Engineering Materials*, **725**, 389-393
17. YIN H., HE Y.J., SUN Q.P., 2014, Effect of deformation frequency on temperature and stress oscillation in cyclic phase transition of NiTi shape memory alloy, *Journal of the Mechanics and Physics of Solids*, **67**, 100-128
18. ZIOLKOWSKI A., 2015, *Pseudoelasticity of Shape Memory Alloys*, Butterworth-Heinemann, Oxford

EXPERIMENTAL INVESTIGATION AND MODELLING OF HOT FORMING B₄C/AA6061 LOW VOLUME FRACTION REINFORCEMENT COMPOSITES

KAILUN ZHENG, JIANGUO LIN

Imperial College London, Department of Mechanical Engineering, United Kingdom
e-mail: k.zheng13@imperial.ac.uk; jianguo.lin@imperial.ac.uk

GAOHUI WU

Harbin Institute of Technology, School of Material Science and Engineering, Harbin, China
e-mail: wugh@hit.edu.cn

ROGER W. HALL

Marbeau Design Consultancy, Paris, France
e-mail: marbeau.dc@sfr.fr

TREVOR A. DEAN

University of Birmingham, Department of Mechanical Engineering, Birmingham, United Kingdom
e-mail: t.a.dean@bham.ac.uk

This paper presents an experimental investigation of the hot deformation behaviour of 15% B₄C particle reinforced AA6061 matrix composites and the establishment of a novel corresponding unified and physically-based visco-plastic material model. The feasibility of hot forming of a metal matrix composite (MMC) with a low volume fraction reinforcement has been assessed by performing hot compression tests at different temperatures and strain rates. Examination of the obtained stress-strain relationships revealed the correlation between temperature and strain hardening extent. Forming at elevated temperatures enables obvious strain rate hardening and reasonably high ductility of the MMC. The developed unified material model includes evolution of dislocations resulting from plastic deformation, recovery and punching effect due to differential thermal expansion between matrix and reinforcement particles during non-steady state heating and plastic straining. Good agreement has been obtained between experimental and computed results. The proposed material model contributes greatly to a more thorough understanding of flow stress behaviour and microstructural evolution during the hot forming of MMCs.

Keywords: Metal Matrix Composite (MMC), hot compression, AA6061, B₄C, dislocation

1. Introduction

Metal matrix composites (MMC) comprise a relatively wide range of materials defined by composition of matrix and of reinforcement together with its geometry (Kaczmar *et al.*, 2000). Particle-reinforced aluminium alloy/B₄C MMC is a popular candidate in automotive, aerospace and nuclear industries, since boron carbide (B₄C) exhibits very high hardness, relatively low density and good thermal and chemical stability (Guo and Zhang, 2017). Raw MMCs are manufactured today using mostly either particle introduction techniques through liquid-stirring or casting, pressure infiltration or powder metallurgy (Ye and Liu, 2004). The final geometry of MMC parts with a high volume fraction reinforcement is usually obtained by machining. Whereas, a low volume fraction MMCs may be processed by extrusion, drawing or rolling in which the plasticity of the matrix material is exploited. The resultant bar or sheet often requires secondary manufacturing operations to produce the final product geometry. It is advisable to perform

such manufacturing processes on MMCs at elevated temperatures where ductility is higher and forming load is lower (Aour and Mitsak, 2016). This combination increases manufacturing capability and results in an increased material yield compared with machining to achieve final part geometry. Therefore, it is important to characterize the deformation behaviour of MMCs with the low volume fraction of reinforcement under hot working conditions, including mechanisms of deformation and corresponding microstructural evolution.

Significant research has been performed on hot forming of MMCs and related deformation mechanisms. The mechanism of matrix strengthening and microstructure evolution during hot deformation becomes more complicated with the addition of reinforcement particles of different materials, shapes and sizes. Wang *et al.* (2017) found that a dynamic recrystallization (DRX) phenomenon, which depends on temperature and strain rate, was the main softening mechanism when hot compressing AA6061/B₄C composite. Ganesan *et al.* (2004) observed dynamic recrystallization and wedge cracking characterising the hot working of AA6061/15% SiC_p. However, although relative microstructural evolutions were identified, steady flow stress was still modelled phenomenologically using the Zener-Hollomon parameter and the Arrhenius constitutive model. The evolution of dislocations associated with hardening was not taken into account. Physically-based models of hot formed MMCs are lacking this phenomenon.

High strength ceramic particles, such as SiC_p, B₄C and ZrB₂, are commonly used to increase MMC strength and thermal stability (Ibrahim *et al.*, 1991). When these MMCs are heated to elevated temperatures, the differential thermal expansion between the particles and matrix alloy can induce dislocation punching (Chawla and Chawla, 2004) during thermal quenching, which is also believed to affect the hardening during deformation. Furthermore, plastic deformation produces temperature increase which can further aggravate dislocation punching. The dominant mechanisms influencing material flow stress behaviour of low volume fraction reinforcement MMCs are punching dislocation and dislocation evolution during deformation of the matrix material, exemplified by plastic strain induced dislocation accumulation and recovery (Lin *et al.*, 2005). Both mechanisms should be included in constitutive models for this type of material.

The objectives of this study are to investigate hot deformation behaviour of MMCs and to further develop a unified physically-based visco-plastic constitutive model for hot forming of discontinuously reinforced MMCs with a low volume fraction of high strength particles. Strengthening mechanisms of discontinuous particle reinforced MMCs are briefly reviewed in this paper, then the development of a visco-plastic material model based on a dislocation evolution mechanism is presented. The feasibility of hot forming of MMCs was proved through hot compression tests. In addition, the constitutive equations of the material model were calibrated using experimentally generated stress-strain relationships. The established model is believed to be the first one ever presented, which is based on the physical mechanisms of particle strengthening and dislocation evolution during hot deformation.

2. Strengthening mechanisms in hot working particle reinforced MMCs

2.1. Modulus

Various methods have been proposed to predict the elastic modulus of composites. Each of the existing models has limits and is unable to cover factors of reinforcement volume fraction, shape, contiguity and distribution. Hashin and Shtrikman (1963) proposed upper and lower bounds for an isotropic aggregate, based on variational principles of linear elasticity. For high volume fraction cases, normally greater than 0.5, Kröner (1958) and Budiansky (1965) proposed a self-consistent methodology to model effective Young's modulus of MMCs with spherical reinforcements. The relationships between Young's modulus E , shear modulus G and bulk modulus K is given in Eq. (2.1)₁. On the assumption of an unchanged Poisson's ratio, Young's

modulus can be obtained from shear and bulk modulus. Mura (1987) provided an estimation of the effective moduli for relatively small volume fractions of reinforcing particles, as shown in Eqs. (2.1)₂ and (2.1)₃. The moduli of a composite are determined by the reinforcement and matrix material for a certain volume percentage of reinforcements. In this theory, the reinforcement geometry is assumed to be spherical. Then, the effective Young's modulus of composite can be obtained from Eq. (2.1)₁. It should be noted that the theory was focused on finite concentrations of reinforcements, and the approach is only valid for a relatively small volume fraction of reinforcements, normally less than 0.25

$$\begin{aligned}
 E &= 2G(1 + \nu) = 3K(1 - 2\nu) \\
 G_c &= G_m \left[1 + V_p(G_m - G_p) / \left\{ G_m + 2(G_p - G_m) \frac{4 - 5\nu_m}{15(1 - \nu_m)} \right\} \right]^{-1} \\
 K_c &= K_m \left[1 + V_p(K_m - K_p) / \left\{ K_m + \frac{1}{3}(K_p - K_m) \frac{1 + \nu_m}{1 - \nu_m} \right\} \right]^{-1}
 \end{aligned} \tag{2.1}$$

where ν is the Poisson's ratio, G is the shear modulus and K is the bulk modulus of the material. G_c , G_m and G_p are the shear modulus of the composite, matrix and reinforcement, respectively. K_c , K_m and K_p are the bulk modulus of the composite, matrix and reinforcement, respectively. ν_c , ν_m and ν_p are the Poisson's ratio of the composite, matrix and reinforcement, respectively. V_p represents the volume fraction of reinforcements.

2.2. Strengthening

2.2.1. Direct strengthening

Direct strengthening is common in continuous fiber-reinforced (Khosoussi *et al.*, 2014) and discontinuously fiber or particle reinforced composites. The main mechanism of direct strengthening is load transfer from the point of application through the low strength matrix to the high strength reinforcement across the matrix/reinforcement interface. Therefore, apparent strengthening results from the additional load carried by the reinforcements. To model such a strengthening phenomenon, Nardone and Prewo (1986) proposed a modified shear-lag model for load transfer in particulate materials. The model incorporates load transfer from the particle ends (which is not applicable to continuous-fiber reinforced composites due to the large aspect ratio). The yield strength of the particulate composite σ_{cy} is increased over the matrix yield strength σ_{my}

$$\sigma_{cy} = \sigma_{my} \left[V_p \left(\frac{S + 4}{4} \right) + V_m \right] \tag{2.2}$$

where S is the aspect ratio of the particle, V_p is the volume fraction of particles, and V_m is the volume fraction of the matrix. The relation shown in Eq. (2.2) does not include effects of particle size and matrix microstructure on the load transfer. Wu *et al.* (2016) investigated the effects of particle size and spatial distribution on the mechanical properties of B₄C reinforced composites. It is demonstrated that for a given volume fraction, reducing the particle size of the B₄C leads to a greater increase in the strength. The contribution of reducing the particle size can be estimated using as

$$\Delta\sigma_d \propto \sqrt{\frac{1}{d}} \tag{2.3}$$

where $\Delta\sigma_d$ represents the increment of the yield strength due to particle size, and d is the average size of particles in the spherical assumption.

2.2.2. Indirect strengthening

Indirect strengthening is believed to be caused by changes of matrix microstructure and properties with the addition of the reinforcement. Thermal expansion mismatch between the reinforcement and matrix alloy can result in a build-up of internal stresses where there is a change in temperature, such as occurs during thermal quenching (Suh *et al.*, 2009). Such a mismatch is a general and important feature of MMCs, especially with the combination of a high coefficient of thermal expansion (CTE) metallic matrix and a low CTE high strength ceramic reinforcement. If the internal stress generated by differential thermal expansion is greater than the yield stress of the matrix, then dislocations form at reinforcement/matrix interfaces and accumulate within a domain surrounding the reinforcement, as shown in Fig. 1. Hence, “thermally induced dislocation

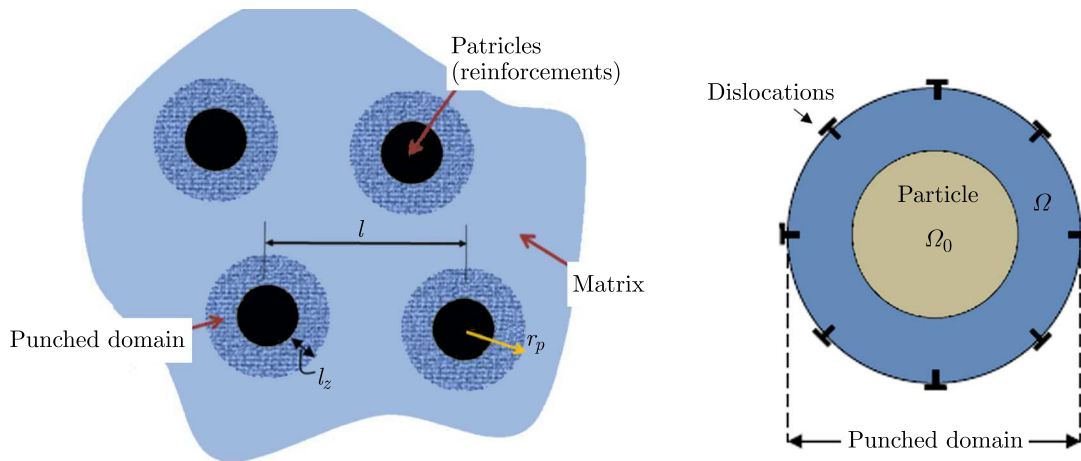


Fig. 1. Schematic of dislocation punching micromechanics (Suh *et al.*, 2009)

punching” results in an indirect strengthening of the matrix. Besides the thermal effects of CTE mismatch during thermal quenching, the internal stress related to differential thermal expansion may also occur if the composite experiences a positive temperature variation under hot forming conditions, such as externally applied heating or temperature rise due to plastic deformation. The matrix domain expands but is constrained by the reinforcements. The matrix material strength is much lower at elevated temperatures, so it is easier for the induced internal stress to exceed the matrix yield strength resulting in dislocations being punched into the matrix. It should be noted that the phenomenon of punched dislocations should be considered only if the heating rate is high and if the soaking time is short. Otherwise, static recovery will eliminate the punched dislocations during the non-steady positive temperature variation. Arsenault and Shi (1986) developed a model to quantify the degree of dislocation punching due to CTE mismatch between a particle and the matrix, schematically shown in Fig. 1. The dislocation density of the punched zone due to differential thermal expansion is given by

$$\rho_{CTE} = \frac{D\varepsilon_{TM}V_p}{b(1-V_p)d} \quad (2.4)$$

where D is a geometric constant, b is the Burgers vector, d is the diameter of the reinforcement particle, and ε_{TM} is the thermal misfit strain, $\varepsilon_{TM} = \Delta\alpha\Delta T$. $\Delta\alpha$ is the difference in the coefficient of thermal expansion between the matrix and reinforcement, and ΔT is the temperature variation. The incremental increase in strength due to dislocation punching can be given as

$$\Delta\sigma_{ind} = \psi G_m b \sqrt{\rho_{CTE}} \quad (2.5)$$

where ψ is a constant. Substituting Eq. (2.4) into Eq. (2.5), the strength increment due to this indirect strengthening mechanism is given by Eq. (2.6) with further consideration of the aspect ratio of the reinforcement particles S

$$\Delta\sigma_{ind} = \psi G_m b \sqrt{\frac{D\varepsilon_{TM} V_p S}{b(1 - V_p)d}} \quad (2.6)$$

3. Development of the visco-plastic constitutive model

3.1. Modelling of modulus

The addition of reinforcement particles significantly increases the stiffness of composites compared with that of the matrix alone. For simplicity, Eq. (2.1)₃ may be used to represent approximately the relationship between Young's modulus and shear modulus by assuming the Poisson's ratio to be constant. Young's modulus of composites can be also approximated by a formulation shown as

$$E_c = E_m \frac{1 + V_p(E_m - E_p)}{E_m + \delta_1(E_p - E_m)\delta_2} \quad (3.1)$$

where δ_1 and δ_2 are constants. E_c , E_m and E_p are Young's moduli of composite, matrix and reinforcement, respectively.

In order to simplify Eq. (3.1), giving $E_1 = \delta_1\delta_2$, substitute E_1 into Eq. (3.1). Equation (3.1) can be rewritten as follows

$$E_c = E_m \left[\frac{(1 - E_1 + V_p)E_m + (E_1 - V_p)E_p}{(1 - E_1)E_m + E_1E_p} \right]^{-1} \quad (3.2)$$

In terms of hot forming low volume fraction composite materials, in this study, Young's modulus of the matrix metal is considered dependent on bulk temperature, while that of reinforcement particles is considered as constant.

3.2. Modelling punched dislocation density

The dislocation punching feature is determined by temperature variation during hot forming, which can be divided into two parts. Contribution of the first part comes from heating the composite from the room temperature to its forming temperature. The initial dislocation density due to differential thermal expansion is considered to be zero. During heating and according to Eq. (2.4), the rate of punched dislocation density can be expressed as a function of temperature history. Considering the instantaneous heating rate, this becomes as defined in

$$\dot{\rho}_{CTE} = \frac{D\Delta\alpha\Delta\dot{T}V_p}{b(1 - V_p)d} \quad (3.3)$$

where $\Delta\dot{T}$ represents the rate of temperature change.

Contribution of the second part results from adiabatic heating during hot working (Bai *et al.* 2013). Adiabatic heating is believed to result from plastic work during hot working (Khan *et al.*, 2004). The temperature increment can be calculated from experimental stress-strain curves using

$$\Delta T = \frac{\eta}{c_m \rho_m} \int_0^{\varepsilon_p} \sigma(\varepsilon_p) d\varepsilon_p \quad (3.4)$$

where η represents the fraction of heat dissipation caused by plastic deformation (Khan *et al.*, 2004), c_m and ρ_m are specific heat and mass density of the matrix material, respectively, σ is the instant flow stress and ε_p is the plastic strain. In this study, the variable related to temperature

increase arising from plastic deformation is expressed in terms of a derivative in order to unify the constitutive equations

$$\dot{T}_\varepsilon = \eta \frac{\sigma}{c_m \rho_m} |\dot{\varepsilon}_p| \quad (3.5)$$

where T_ε is temperature rise due to plastic straining. In ideal isothermal deformation conditions, the instantaneous temperature T is equal to the initial temperature T_0 . However, when heat generated due to large plastic deformation cannot be neglected, the instantaneous temperature T equals $(T_0 + \Delta T)$, where ΔT is the temperature rise regarded as a function of the deformation and deformation rate. According to Eq. (3.5), deformation induced temperature increase can be determined through numerical integration based on the stress-strain relationships for a fixed strain rate and stress state. Therefore, substituting Eq. (3.5) into Eq. (3.3), the rate of accumulated dislocation due to thermal expansion mismatch can be rewritten as

$$\dot{\bar{\rho}}_{CTE} = D \frac{V_p}{1 - V_p} \eta \frac{\sigma}{c_m \rho_m} |\dot{\varepsilon}_p| \quad (3.6)$$

3.3. Formulation of constitutive equations

Physically-based visco-plastic constitutive equations have been proposed for the modelling of plastic deformation of many metals, especially in hot forming conditions. The significant contribution of these models is to enable a variety of phenomena to be modelled, including dislocation accumulation and annealing, dynamic recovery and recrystallization, based on the specific deformation mechanisms. Each aspect of microstructural evolution can be treated as a variable in the constitutive equations. These constitutive equations are also suitable for hot working discontinuous particle reinforced MMCs. However, high strength reinforcement adds new mechanisms and effects on the modulus and microstructural evolutions which also need to be considered and modelled. As interactions between different microstructural phenomena exist, it is impossible to express all the physical phenomena active during hot forming by using a single equation. To thoroughly understand their evolution, this study uses a constitutive model based on an advanced dislocation dominated mechanism (Lin and Dean 2005).

A set of unified visco-plastic constitutive equations is established to model the contribution of particles on the modulus and strength, evolution of dislocation, temperature increase due to adiabatic deformation, and rationalise their effects on the steady plastic flow. This developed material model derives from the dislocation evolution during isothermal hot deformation. The relationships between dislocation density and strain hardening and recovery are characterised in this model. Compared to conventional metals, the dislocation density in this model is divided into plastic deformation induced and thermal expansion induced types. For simplification, several assumptions are used in this model, they are (1) dynamic recrystallization of the material during the initial deformation process is not considered for low-volume fraction reinforcement and relatively high strain rates; (2) thermal strain is not taken into account compared with the great total strain; (3) effects of precipitation on dislocation density are not considered. The set of unified viscoplastic constitutive equations for modelling hot deformation of MMCs with low-volume fraction reinforcements is summarised as follows

$$\dot{\varepsilon}_p = \left(\frac{\sigma - R - k_e}{K} \right)^{n1} \quad \dot{R} = \frac{1}{2} B \frac{\dot{\bar{\rho}}}{\sqrt{\bar{\rho}}} \quad (3.7)$$

and

$$\begin{aligned} \dot{\bar{\rho}}_{str} &= A(1 - \bar{\rho}_{str}) |\dot{\varepsilon}_p| - C \bar{\rho}_{str}^{n2} \\ \dot{\bar{\rho}} &= \dot{\bar{\rho}}_{str} + \dot{\bar{\rho}}_{CTE} \quad \sigma = E_c(\varepsilon - \varepsilon_p) \end{aligned} \quad (3.8)$$

The fundamental equations used are Eq. (3.7)₁ to Eq. (3.8)₃, given above. To make it clear, general description of each equation representing a particular microstructure mechanism is introduced. Details of the form of each equation are given in the literature (Lin and Dean 2005). Equation (3.7)₁ represents the traditional power-law of visco-plastic flow formulation (Mohamed *et al.* 2012), k_e represents the initial yield stress of composites and R represents hardening stress due to dislocation evolution. Equation (3.7)₂ represents the evolution of material hardening, which is a function of the normalised dislocation density $\bar{\rho}$ defined by $\bar{\rho} = (\rho - \rho_i)/\rho_{max}$, where ρ_i is the initial dislocation density and ρ_{max} is the maximum (saturated) dislocation density. Therefore, the range of $\bar{\rho}$ is between 0 and 1 during the whole process. Unlike hot forming of metals, the dislocation density in this study is divided into two parts; dislocation density evolution of hot straining of the matrix material $\bar{\rho}_{str}$ and punched dislocation density evolution due to differential thermal expansion $\bar{\rho}_{CTE}$ as given in Eq. (3.6). Equation (3.8)₁ represents the rate of accumulation of dislocations induced by the plastic deformation, which takes into account deformation and recovery. Equation (3.8)₂ represents the sum of dislocation density arising from plastic deformation and punched dislocations, Eq. (3.6), due to the difference of thermal expansion of the matrix and reinforcement. It should be noted that the difference in thermal expansion arises from the temperature increase resulting from plastic deformation, which is different from the applied heating at the initial stage. Equation (3.8)₃ is Hook's law for a simple uniaxial state. In this equation set, k_e , K , $n1$, B , A , C and E_c are temperature dependent variables defined in Eqs. (3.9) and (3.10), while $n2$ is temperature independent material constant

$$k_e = k_1 \exp\left(\frac{Q_k}{R_g T}\right) (V_p S + V_m) \sqrt{\frac{1}{d}} + k_2 \sqrt{\frac{V_p \Delta T}{(1 - V_p) d}} \quad (3.9)$$

and

$$\begin{aligned} K &= K_0 \exp\left(\frac{-Q_K}{R_g T}\right) & n1 &= \frac{n1_1}{\dot{\epsilon}_p^{n1_2}} \exp\left(\frac{Q_{n1}}{R_g T}\right) \\ B &= B_0 \exp\left(\frac{Q_B}{R_g T}\right) & A &= A_0 \exp\left(\frac{Q_A}{R_g T}\right) \\ C &= C_0 \exp\left(\frac{-Q_C}{R_g T}\right) & E_m &= E_0 \exp\left(\frac{Q_E}{R_g T}\right) \end{aligned} \quad (3.10)$$

Equation (3.9) represents the initial yield strength of the MMC considering direct and indirect strengthening of the reinforcement particles, V_p and V_m represent volume fractions of the reinforcement and matrix respectively. ΔT is the temperature increment during rapid heating. Equations (3.9) to (3.10) represent the Arrhenius equations of temperature dependent variables, where Q describes the activation energy for each variable, and R_g is the universal gas constant. All the material constants in Eqs. (3.9) to (3.10) are temperature independent. It should be noted that Young's modulus of MMC is a function of the matrix modulus and particle modulus, which is modelled in the previous Section. Considering the thermal stability of high strength reinforcements, only Young's modulus of the matrix is temperature dependent, defined in Eq. (3.10), while Young's modulus of reinforcements is considered to be a constant.

4. Hot compression tests

4.1. Materials

Experiments have been undertaken using AA6061/B₄C provided by Harbin Institute of Technology. The composite samples were produced with a 15% volume fraction reinforcement using a pressure infiltration method. Single crystal B₄C particles were used having an average particle

size of $17.5\ \mu\text{m}$ (Zhou *et al.* 2014). The bulk composite material was then extruded into circular bars and then machined into standard cylindrical samples with length of 12 mm and diameter of 8 mm. The selection of sample dimensions was chosen so as to avoid inelastic buckling prior to plastic deformation. The matrix material was AA6061. The main chemical compositions of B_4C and AA6061 are given in Tables 1 and 2, respectively.

Table 1. Main chemical composition of B_4C [%]

Element	B	C	Fe	Si	Ca	F
wt [%]	80.0	18.1	1.0	0.5	0.3	0.025

Table 2. Main chemical composition of AA6061 [%]

Element	Fe	Si	Mn	Cr	Mg	Zn	Al
wt [%]	0.70	0.80	0.15	0.35	1.2	0.25	Remain

4.2. Experimental set-up and test programme

High temperature uniaxial compression tests were performed using the thermo-mechanical simulator Gleeble 3800. Specimens were heated at a pre-determined heating rate by resistance heating, and temperature was precisely controlled by feedback from a thermocouple welded to the middle of the specimen. Graphite foil and high-temperature graphite paste were used at the interfaces between the specimen and Gleeble anvils to reduce interfacial friction and obtain a more uniform deformation. Strain was measured using a C-gauge which detected a change in the specimen diameter. The experimental set-up is shown in Fig. 2.

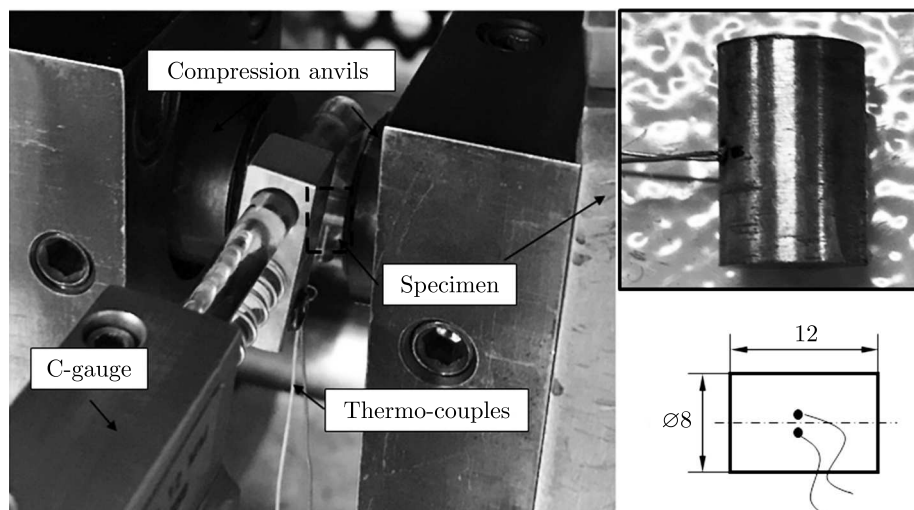


Fig. 2. Experimental set-up for hot compression test (all dimensions are in mm)

Figure 3 shows the temperature profile of a specimen in the hot compression test. A two-stage heating strategy was utilised to obtain a uniform temperature and to avoid overshoot. Initially, the specimen was heated up at a rate of $5^\circ\text{C}/\text{s}$ to 50°C below the specified target deformation temperature. Then, it was further heated to the target temperature at a rate of $2.5^\circ\text{C}/\text{s}$. After soaking for 1 min, the specimen was uniaxially hot compressed at different strain rates. In this study, the temperatures selected were 350°C , 400°C , 450°C . The strain rates used were $0.01\ \text{s}^{-1}$, $0.1\ \text{s}^{-1}$ and $1\ \text{s}^{-1}$.

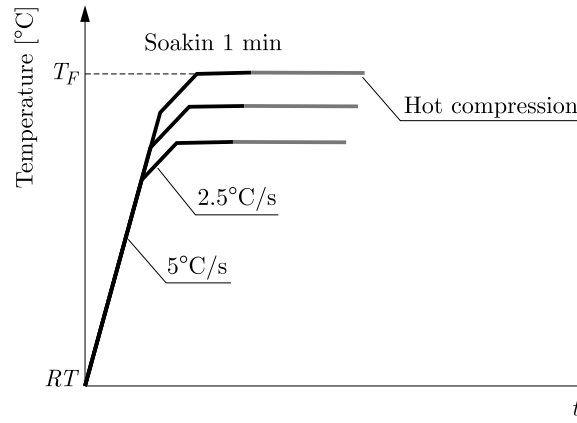


Fig. 3. Temperature profile of the hot compression test

5. Results and discussion

5.1. Determination of constitutive equations

The experimental results from hot compression tests were used to determine material constants in the developed constitutive relationships. Firstly, according to Eqs. (3.2), (3.9) and (3.10), Young’s modulus and the initial yield strength of the composite vary with the temperature from the applied heat, and are also significantly greater than those of the matrix. Figure 4 shows the similarity between the equation fitted and experimentally determined values. Good agreement exists between the fitted curves and experimental results. Differences that exist are believed to be due to the difficulty in determining accurate values from hot compression results, considering the slopes of the modulus are very sharp. Table 3 gives the material properties of the matrix alloy and reinforcement particles at room temperature. Tables 4 lists values of material constants used for calculating the strength variables.

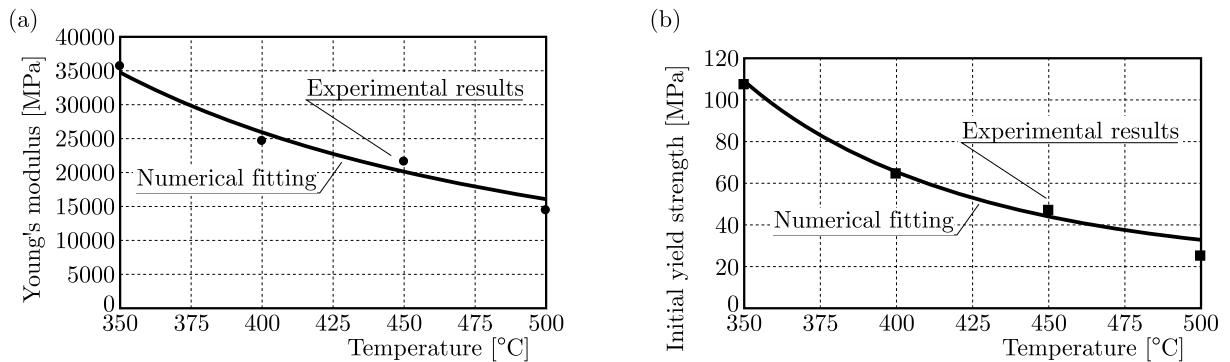


Fig. 4. Comparisons of numerical fitting (solid lines) and experimental results (solid symbols) of strength variables, where (a) Young’s modulus and (b) initial yield strength

Table 3. Material properties of the matrix alloy and reinforcement

V_p	V_m	d [μm]	E_p [MPa]	η	c_m [J/(kg K)]	ρ_m [kg/m ³]
0.15	0.85	17.5	362000	0.9	890	2700

Other material constants in the dominant equation set were determined using a combination of Evolutionary Programming (EP) optimisation techniques (Li *et al.*, 2002) as well as trial and

Table 4. Determined constants for Young's modulus and initial yield strength

E_0	Q_E	E_1	k_1	Q_k	k_2
590	20140	0.67	0.0017	40950	0.075

error methodology. The explanation of the optimisation method and description of numerical procedures for determining the material constants of constitutive equations are described by Cao and Lin (2008). Table 5 shows the determined material constants of Eqs. (3.10)₁₋₅.

Table 5. Determined constants for material constants

K_0	B_0	C_0	A_0	$n1_1$	$n1_2$
326.5	0.2774	114.9	0.144	0.04691	-0.4111
Q_K	Q_B	Q_C	Q_A	Q_{n1}	$n2$
9634	21780	51760	18420	29760	1

5.2. Comparison of experimental results and the constitutive model

Figures 5 and 6 show comparisons between the Gleeble experimental results (symbols) and the modelling results (solid lines). Three typical hot forming temperatures 350°C, 400°C and 450°C and three different strain rates from 0.01 s⁻¹ to 1 s⁻¹ were chosen. As can be seen in both figures, good fitting accuracy was obtained. Dynamic recrystallization at the beginning of deformation which results in the strain softening is neglected in the current model for simplicity of numerical fitting. Figure 5 shows that MMC stress level reduces with the increasing forming temperature, and is lower than that at the room temperature (Chen *et al.*, 2015). When the

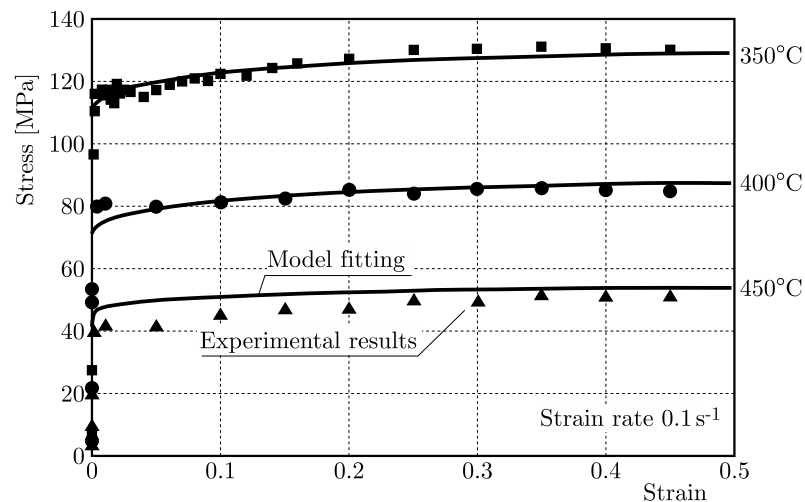


Fig. 5. Comparison of stress-strain relationships from hot compression tests at different temperatures and a strain rate of 0.1 s⁻¹. Symbols represent experimental results and solid lines are computed predictions from the model

composite was compressed at higher temperatures, such as 450°C and lower strain rates, such as 0.01 s⁻¹, the stress level exhibited a plateau. The absence of strain hardening is believed to be beneficial for bulk forming, such as extrusion and forging, as the strain hardening would increase the forming load significantly and may cause cracks of the forming dies. In addition, the extent of strain hardening increased with the decreasing temperature at a fixed strain rate, considering dislocation recovery was not significant and visco-plastic feature was not obvious. The diffusion process was not sufficient at lower temperatures. Moreover, compared with forming at the room

temperature, an increased strain limit without crack was observed representing a reasonable ductility improvement, which enhanced the feasibility of hot forming MMCs. For temperature 400°C , a clear strain rate effect was also observed in the hardening curves. With increasing strain rate, the stress level increased, as shown in Fig. 6. In summary, higher temperatures and lower strain rates are recommended for hot bulk forming the low volume MMC materials.

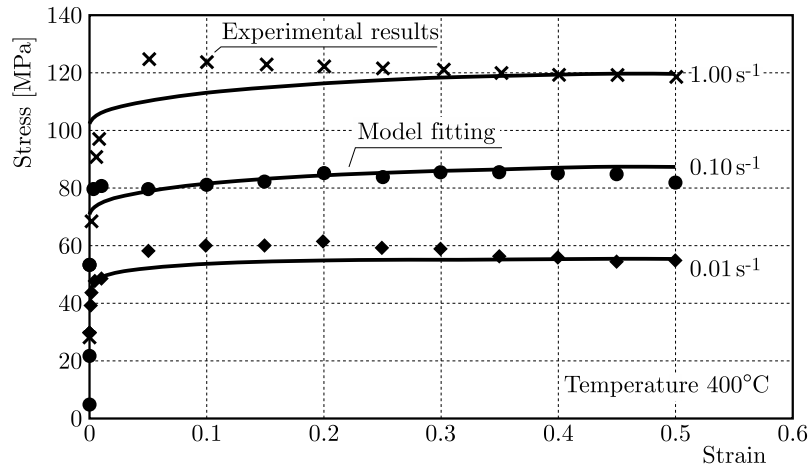


Fig. 6. Comparison of stress-strain relationships from hot compression tests at different strain rates and temperature of 400°C . Symbols represent experimental results and solid lines are computed predictions from the model

6. Conclusions

It is concluded that hot forming processes can be used to shape MMCs with a low volume fraction of reinforcements. Stress-strain relationships obtained from hot compression tests of AA6061/15% B_4C MMC show that strain hardening is only obvious at relatively low temperatures, and the flow stress and the flow stress remains relatively constant at higher temperatures, which is believed to be beneficial for bulk forming. The strain rate hardening is also significant at high temperatures dominated by the visco-plastic mechanism. In addition, the first ever unified physically-based visco-plastic material model has been developed for hot forming of low volume fraction reinforcement MMCs. The evolution of dislocations has been modelled taking into account the effects of temperature history and plastic deformation. This material model, suitable for finite element simulations, can be further extended to predict stress-strain relationships of MMCs under different process conditions.

Acknowledgements

The research in this paper was funded by the European Union's Horizon 2020 research and innovation programme under Grant Agreement No. 723517 as a part of the project "Low Cost Materials Processing Technologies for Mass Production of Lightweight Vehicles (LoCoMaTech)".

References

1. AOUR B., MITSAK A., 2016, Analysis of plastic deformation of semi-crystalline polymers during ECAE process using 135° die, *Journal of Theoretical and Applied Mechanics*, **54**, 1, 263-275, DOI:10.15632/jtam-pl.54.1.263
2. ARSENAULT R.J., SHI N., 1986, Dislocation generation due to differences between the coefficients of thermal expansion, *Materials Science and Engineering*, **81**, 175-187. DOI: 10.1016/0025-5416(86)90261-2

3. BAI Q., LIN J., DEAN T.A., BALINT D.S., GAO T., ZHANG Z., 2013, Modelling of dominant softening mechanisms for Ti-6Al-4V in steady state hot forming conditions, *Materials Science and Engineering A*, **559**, 352-358 DOI: 10.1016/j.msea.2012.08.110
4. BUDIANSKY, B., 1965, On the elastic moduli of some heterogeneous materials, *Journal of the Mechanics and Physics of Solids*, **13**, 4, 223-227, DOI: 10.1016/0022-5096(65)90011-6
5. CAO J., LIN J., 2008, A study on formulation of objective functions for determining material model, *International Journal of Mechanical Sciences*, **50**, 2, 193-204, DOI: 10.1016/j.ijmecsci.2007.07.003
6. CHAWLA K.K., CHAWLA N., 2004, Metal-matrix composites, *Material Science and Technology*, **1**, 1-25, DOI: 10.1016/B978-0-08-050073-7.50011-7
7. CHEN H.S., WANG W.X., LI Y. LI, ZHANG P., NIE H.H., WU Q.C., 2015, The design, microstructure and tensile properties of B₄C particulate reinforced 6061Al neutron absorber composites, *Journal of Alloys and Compounds*, **632**, 23-29, DOI: 10.1016/j.jallcom.2015.01.048
8. GANESAN G., RAGHUKANDAN K., KARTHIKEYAN R., PAI B.C., 2004, Development of processing maps for 6061 Al/15% SiC_p composite material, *Materials Science and Engineering A*, **369**, 1-2, 230-235, DOI: 10.1016/j.msea.2003.11.019
9. GUO H., ZHANG Z., 2017, Processing and strengthening mechanisms of boron-carbide-reinforced aluminum matrix composites, *Metal Powder Report*, DOI: 10.1016/j.mprp.2017.06.072
10. HASHIN Z., SHTRIKMAN S., 1963, A variational approach to the theory of the elastic behaviour of multiphase materials, *Journal of the Mechanics and Physics of Solids*, **11**, 2, 127-140, DOI: 10.1016/0022-5096(63)90060-7
11. IBRAHIM I.A., MOHAMED F.A., LAVERNIA E.J., 1991, Particulate reinforced metal matrix composites – a review, *Journal of Materials Science*, **26**, 5, 1137-1156, DOI: 10.1007/BF00544448
12. KACZMAR J.W., PIETRZAK K., WLOSINSKI W., 2000, The production and application of metal matrix composite materials, *Journal of Materials Processing Technology*, **106**, 1-3, 58-67, DOI: 10.1016/S0924-0136(00)00639-7
13. KHAN A.S., SUH Y.S., KAZMI R., 2004, Quasi-static and dynamic loading responses and constitutive modeling of titanium alloys, *International Journal of Plasticity*, **20**, 12, 2233-2248, DOI: 10.1016/j.ijplas.2003.06.005
14. KHOSOUSI S., MONDALI M., ABEDIAN A., 2014, An analytical study on the elastic-plastic behavior of metal matrix composites under tensile loading, *Journal of Theoretical and Applied Mechanics*, **52**, 2, 323-334
15. KRÖNER E., 1958, Berechnung der elastischen Konstanten des Vielkristalls aus den Konstanten des Einkristalls, *Zeitschrift für Physik*, **151**, 4, 504-518, DOI: 10.1007/BF01337948
16. LI B., LIN J., YAO X., 2002, A novel evolutionary algorithm for determining unified creep damage constitutive equations, *International Journal of Mechanical Sciences*, **44**, 5, 987-1002, DOI: [https://doi.org/10.1016/S0020-7403\(02\)00021-8](https://doi.org/10.1016/S0020-7403(02)00021-8)
17. LIN J., DEAN T.A., 2005, Modelling of microstructure evolution in hot forming using unified constitutive equations, *Journal of Materials Processing Technology*, **167**, 2-3, 354-362, DOI: 10.1016/j.jmatprotec.2005.06.026
18. LIN J., LIU Y., FARRUGIA D.C.J., ZHOU M., 2005, Development of dislocation-based unified material model for simulating microstructure evolution in multipass hot rolling, *Philosophical Magazine*, **85**, 18, 1967-1987, DOI: 10.1080/14786430412331305285
19. MOHAMED M.S., FOSTER A.D., LIN J., BALINT D.S., DEAN T.A., 2012, Investigation of deformation and failure features in hot stamping of AA6082: Experimentation and modelling, *International Journal of Machine Tools and Manufacture*, **53**, 1, 27-38, DOI: 10.1016/j.ijmachtools.2011.07.005
20. MURA T., 1987, *Micromechanics of Defects in Solids*, Springer, ISBN 978-94-009-3489-4

21. NARDONE V.C., PREWO K.M., 1986, On the strength of discontinuous silicon carbide reinforced aluminum composites, *Scripta Metallurgica*, **20**, 1, 43-48, DOI: 10.1016/0036-9748(86)90210-3
22. SUH Y.S., JOSHI S.P., RAMESH K.T., 2009, An enhanced continuum model for size-dependent strengthening and failure of particle-reinforced composites, *Acta Materialia*, **57**, 19, 5848-5861, DOI: 10.1016/j.actamat.2009.08.010
23. WANG K.K., LI X.P., LI Q.L., SHU G.G., TANG G.Y., 2017, Hot deformation behavior and microstructural evolution of particulate-reinforced AA6061/B₄C composite during compression at elevated temperature, *Materials Science and Engineering A*, **696**, 1, 248-256, DOI: 10.1016/j.msea.2017.03.013
24. WU C.D., MA K.K., WU J.L., FANG P., LUO G.Q., CHEN F., SHEN Q., ZHANG L.M., SCHOENUNG J.M., LAVERNA E.J., 2016, Influence of particle size and spatial distribution of B₄C reinforcement on the microstructure and mechanical behavior of precipitation strengthened Al alloy matrix composites, *Materials Science and Engineering A*, **675**, 421-430, DOI: 10.1016/j.msea.2016.08.062
25. YE H.Z., LIU X.Y., 2004, Review of recent studies in magnesium matrix composites, *Journal of Materials Science*, **39**, 20, 6153-6171, DOI: 10.1023/B:JMSC.0000043583.47148.31
26. ZHOU Z.S., WU G.H., JIANG L.T., LI R.F., XU Z.G., 2014, Analysis of morphology and microstructure of B₄C/2024Al composites after 7.62 mm ballistic impact, *Materials and Design*, **63**, 658-663, DOI: 10.1016/j.matdes.2014.06.042

Manuscript received January 5, 2018; accepted for print February 7, 2018

PROTOCOL TO DEFINE MATERIAL BEHAVIOUR AND FAILURE STRAIN LEVEL AT LOW AND HIGH STRAIN RATES BASED ON A COMPRESSION TEST

TOMASZ JANKOWIAK

Poznan University of Technology, Institute of Structural Engineering, Poznań, Poland

e-mail: tomasz.jankowiak@put.poznan.pl

ALEXIS RUSINEK

Laboratory of Microstructure Studies and Mechanics of Materials, UMR-CNRS 7239, Lorraine University,

Metz Cedex, France

AMINE BENDARMA

Poznan University of Technology, Institute of Structural Engineering, Poznań, Poland, and

Universiapolis, Ecole Polytechnique d'Agadir Bab Al Madina, Agadir, Morocco

Compression test is frequently used to define material behaviour. However, this test may be depending on different effects, for example friction, specimen inertia or local stress triaxiality. For this reason, a new design is proposed to analyse the previous effects and to try to minimize it on quantities measured as macroscopic stress and strain. To have a complete understanding, numerical simulations have been performed using finite element method (Abaqus/Standard and Abaqus/Explicit). It allows one to define the macroscopic behaviour and to have an access to the local values not accessible during experiments for a better understanding of the experimental measurements.

Keywords: stress triaxiality, dynamic compression, material behaviour, numerical simulation

1. Introduction

The shape and dimensions of the specimen used during experiments have an important effect on experimental measurements in both static and dynamic loadings. In general, to define the behaviour of a material $\sigma(\varepsilon, \dot{\varepsilon}, T)$, different tests are frequently used: compression, tension, shear, biaxial compression. In this paper, static and dynamic compression tests are considered. This kind of experiments is used to define the behaviour of materials at low and high strain rates and to verify the symmetry of the yield surface comparing to tension, but it induces some problems as it will be discussed in details in this paper. One of the main problems is related to the friction effect between the specimen and the plateau or the split Hopkinson pressure bars (SHPB). This phenomenon is related to the quality of contact and state (lubricated or dry) and it is defined using the friction coefficient value μ . This effect is crucial since it may induce an overstress state as discussed in details in (Jankowiak *et al.*, 2011). Some other quantities are also disturbing the measurements under dynamic loading and using SHPB. These are local inertia of the specimen, puncture of the bars (Safa and Gary, 2010; Małachowski *et al.*, 2014), elastic wave dispersion and shape of the contact zone projectile end – input bar. As observed in (Jankowiak *et al.*, 2011), the stress state is changing when the friction coefficient increases on the contact side. Therefore, an uniaxial compression state cannot be assumed. In the dynamical state, as it was discussed in some papers (Jankowiak *et al.*, 2011; Iwamoto and Yokoyama, 2012; Kii *et al.*, 2014), the ratio length L – diameter D must be in a certain range of values to avoid some problems described

previously. This ratio is defined using the parameter $s = L/D$. In this work, several values of s have been used, see Fig. 1.

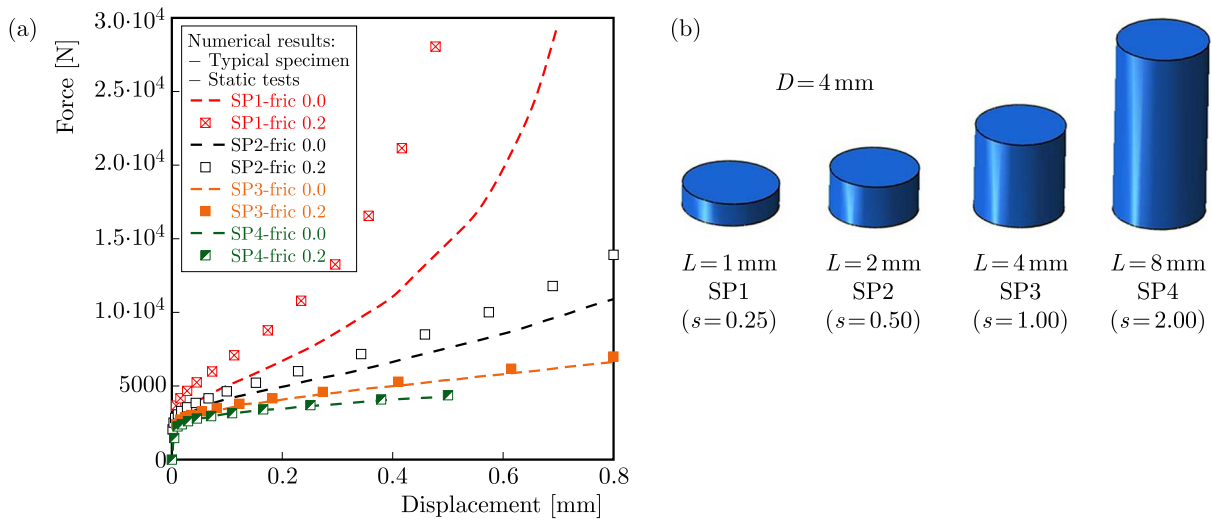


Fig. 1. Force versus displacement for quasi-static compression using standard specimen SP_i

Deformation of the specimen in compression depends on the friction process, Fig. 1. The results reported in this paper are for a constant diameter $D = 4$ mm and different initial length L to vary the ratio s . Therefore, the following configurations have been used: SP1 ($s = 0.25$) with a length of 1 mm and SP4 ($s = 2.0$) with a length of 8 mm. The intermediate specimens SP2 and SP3 have, respectively, a length of 2 mm and 4 mm. It corresponds to a value of s equal to 0.5 and 1.0. The results (force versus displacement curve) for a friction coefficient varying from 0.0 to 0.2 are presented in Fig. 1. In general and following some recommendations, the ratio s equal to 0.5 is frequently used during dynamic tests to avoid some of the problems discussed previously. However, for this ratio, the friction effect is visible (comparing the curves SP2-fric 0.0 and SP2-fric 0.2), see Fig. 1. In the previous picture, Fig. 1, it is observed that the friction coefficient is acting strongly on the specimen having the shortest active length (SP1). In this paper, modified specimens SP_iM , Fig. 2, are used to measure during experiments the intrinsic material behaviour. The SP_iM results will be compared to the original ones to observe if the friction effect may be reduced using a new design. To confirm it, some comparisons will be reported in terms of the force-displacement curve changing the friction coefficient μ . The same ratio s has been considered between SP_i and SP_iM .

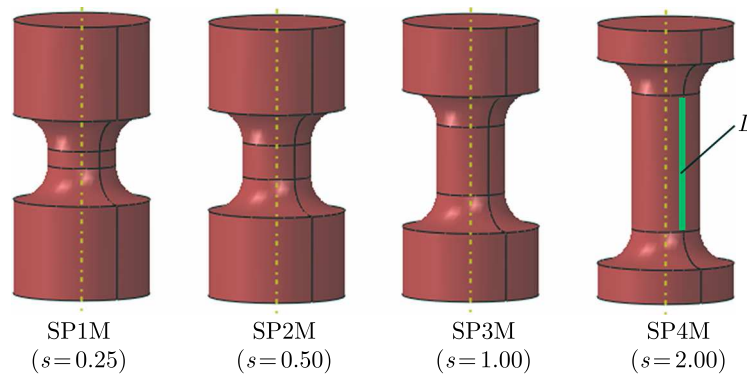


Fig. 2. Modified specimen design SP_iM for the compression test under quasi-static and dynamic compression

2. Geometric effect on the compression force measurement using SP i M specimen

The variation of the stress state defined by η has an effect on the measured force and, in the same way, on the final macroscopic stress level σ estimated during experiments and simulations. Another important parameter is related to the specimen shape ratio s which is inducing a change of the stress triaxiality η , as it will be discussed in this paper. This variable is related to the ratio of the hydrostatic stress p and to the Huber-Mises equivalent stress q . To reduce this phenomenon, a new geometry design is proposed, Fig. 2. The specimens are named SP i M with $i = 1$ to 4 corresponding, respectively, to an active part of 1 mm, 2 mm, 4 mm and 8 mm. Based on it, the shape ratio s is calculated. It corresponds to the ratio of the initial length L divided by the diameter of the active part of the specimen D . For the new geometry, the ratio is respectively equal to 0.25, 0.5, 1.0 and 2.0. To analyze the geometric effect, the following constitutive relation, Eq. (2.1), has been used in FE code. Therefore, just hardening has been considered. The strain rate sensitivity as the temperature sensitivity is not taking into account

$$\sigma = A + B\varepsilon_p^n \quad (2.1)$$

Two material behaviours are assumed, see Table 1, allowing one to demonstrate that the results are just related to geometry and not to material behaviour. Thus, this analysis and geometry can be used with all materials assumed or studied.

Table 1. Constants used to define mild steel ES and aluminum AA6060 assuming Eq. (2.1)

	Mild steel ES (Jankowiak <i>et al.</i> , 2011)	Aluminium AA6060 (Beusink, 2011)
Young modulus E	200 GPa	70 GPa
Yield stress A	154 MPa	70 MPa
Strain hardening B	464 MPa	302 MPa
Strain hardening n	0.37	0.46

The behaviour is depicted in Fig. 3 for a larger yield stress and hardening of mild steel.

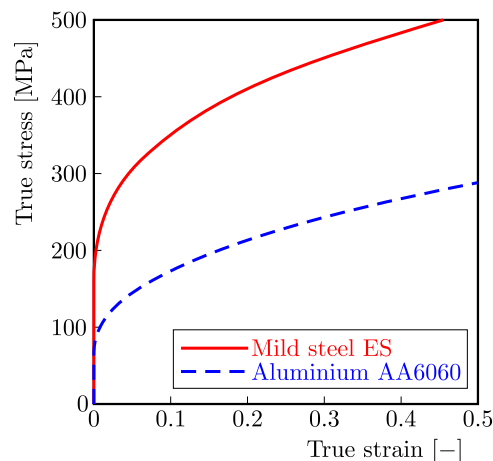


Fig. 3. Comparison of true stress – true strain curve for two different materials

To analyse how the geometry may act on the material behaviour definition using different geometries, mild steel has been considered in the first part of numerical simulations, see Table 1 and Fig. 3. The results for all geometries and two values of the friction coefficient μ are reported in Fig. 4.

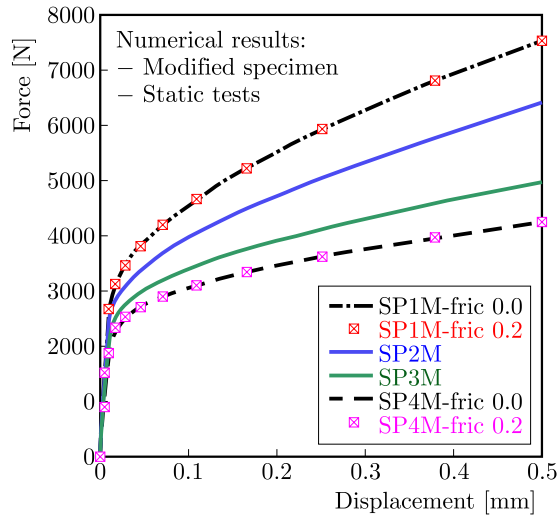


Fig. 4. Force versus displacement for quasi-static compression using the modified specimen SP i M for mild steel

Using the same material behaviour and the same diameter D , it is observed that the material behaviour is depending on the active length of the specimen. On the contrary, the friction coefficient is not acting as it was observed in (Jankowiak *et al.*, 2011). Based on the previous results, it is observed that the ratio s is responsible for different behaviours in terms of force-displacement relationship. To analyse the local distribution of the stress triaxiality with plastic deformation, numerical simulations have been used. Thus, it is observed that the stress triaxiality is equal to -0.34 for $s = 2.0$ (SP4M) which corresponds to the compression value equal to $-1/3$, Fig. 5. The results are reported for each geometry in the following picture, Fig. 5.

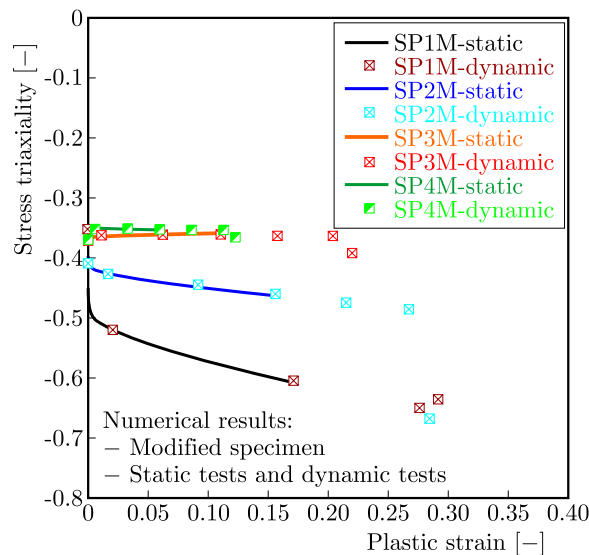


Fig. 5. Average stress triaxiality versus plastic strain for all modified specimens SP i M (static and dynamic loadings using numerical simulations)

It can be seen that η is varying from -0.58 to -0.65 for SP1M and from -0.42 to -0.47 for SP2M. For SP3M, the value is not depending on the plastic strain level and is equal to -0.36 . To estimate the local inertia due to the mass added to both sides of the standard specimen, Fig. 2, numerical simulations have been done at a high velocity $V_0 = 10$ m/s. As the strain rate sensitivity of the material is not considered, Eq. (2.1), the difference in terms of the force

may be due to the mass inertia only. Based on numerical simulations, it is observed that the masses added do not affect the results and, in the same way, do not affect the macroscopic stress (triaxiality) and strain level, Fig. 5. In the following part of the text, the case corresponding to high velocity coupled with the inertial effect is defined as dynamic, and the second case corresponding to low velocity is named static.

In the following curves, Fig. 6, two cases are reported considering the geometry SP1 and SP4 (standard specimens) for different friction coefficients. It is observed for the shortest specimen SP1 that the friction coefficient induces a strong increase of the stress triaxiality η . In the range of plastic deformation considered, the value is varying from 0.6 to 1.5. For SP4, the stress triaxiality is more stable and the value is close to the compression state with $\eta = -1/3$.

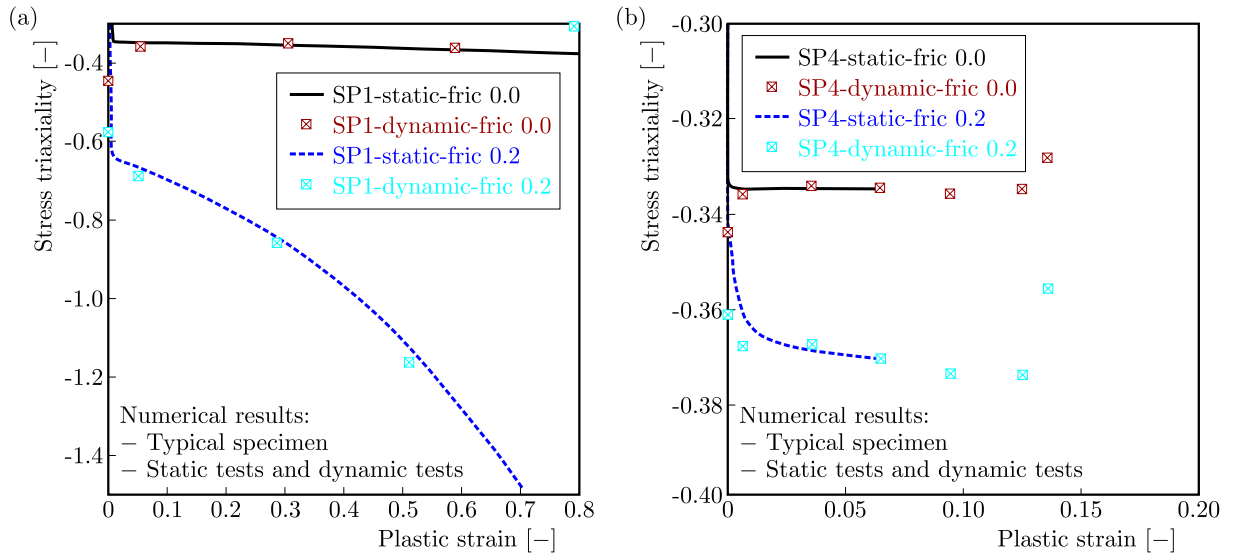


Fig. 6. Average stress triaxiality for standard specimens (SP1 and SP4) for friction coefficients 0.0 and 0.2

3. Material behaviour definition and analysis

For the standard shape specimen SP_i , the behaviour of the material in static and in dynamic conditions can be obtained using the friction correction as discussed in details in (Jankowiak *et al.*, 2011; Zhong *et al.*, 2015). The friction coefficients μ changes the process of plastic deformation and the stress state. Finally, the compressive test with friction coefficient $\mu > 0$ does not predict uniaxial behaviour, and the stress triaxiality η decreases to $-1/3$. Using the modified geometry design SP_iM , friction correction is not required. However, the state of the stress does not correspond to uniaxial compression.

For SP_i geometry and in order to correct the friction coefficient effect, the model proposed by Klepaczko-Malinowski may be used as described in (Jankowiak *et al.*, 2011; Klepaczko and Malinowski, 1977). In a simplified approach and considering that the inertia and the second derivative of the strain rate effect may be neglected, the correction is the following, Eq. (3.1). Therefore, just the geometry effect is taken into account

$$\sigma_{mat} = \sigma_{meas} \left(1 - \frac{\mu}{3s}\right) = \sigma_{meas} C \quad (3.1)$$

where σ_{mat} is the stress in the material and σ_{meas} is the stress measured in the compression test. Using numerical results, the geometrical variable C may be defined for all cases considered SP_i . The value vary from 0.733 to 0.967 considering, respectively, SP1 to SP4, Table 2. In this analysis the friction coefficient is assumed to be equal to 0.2.

Table 2. Definition of the variable C for all cases considered SP_i , Eq. (3.1)

	s	C
SP1	0.25	0.733
SP2	0.5	0.867
SP3	1	0.933
SP4	2	0.967

The method of correction is working correctly for a material without or with reduced plastic strain hardening like pure copper in (Jankowiak *et al.*, 2011). The numerical results (stress-strain curve) are presented for SP4 (the longest) and SP1 (the shortest) in Fig. 7. For a material with strain hardening, the gap between the input model and the method proposed by Klepaczko-Malinowski does not allow one to correctly define the intrinsic behaviour of the material for strain levels $\varepsilon > 15$. For larger plastic deformation levels, the stress state is more complex due to the friction effect and the previous method based on the friction correction is not enough. However, it is observed that the friction effect may be neglected for specimen SP4, see Figs. 7 and 8b.

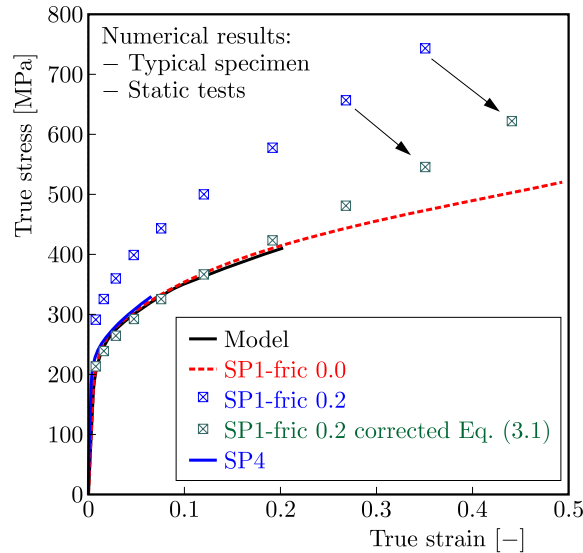


Fig. 7. True stress – true strain curve for the standard specimen

If the specimen length decreases the stress state is changing as reported, Fig. 6. For the specimen SP1, and assuming that the friction coefficient is equal to zero, the numerical results in terms of behaviour are in agreement with the constitutive relation used as an input, Fig. 7. If the friction coefficient increases, $\mu > 0$, a correction is necessary (Jankowiak *et al.*, 2011). Using numerical calculations, two quantities are defined, the Huber-Mises σ_{Mises} equivalent stress and the longitudinal stress σ_{yy} corresponding to the axial loading direction. It has to be noticed that during experiments, the longitudinal stress is the one corresponding to the stress imposed to the specimen. The value of σ_{yy} is obtained dividing the force by the cross section of the specimen. Using these two quantities, the parameter α may be defined. It consists in dividing the longitudinal stress by the equivalent stress as $\alpha = \sigma_{yy}/\sigma_{Mises}$. The value is equal to 1 for uniaxial compression. In other cases, α is varying with the level of plastic deformation as observed for the stress triaxiality, Fig. 8a. To demonstrate this effect, the results for SP4 (the longest) and SP1 (the shortest) are presented in Fig. 8b. If the stress measured during experiments is divided by the α parameter, the material behaviour obtained from numerical simulations is in

agreement with the constitutive relation used. This method is working correctly also for material with plastic strain hardening.

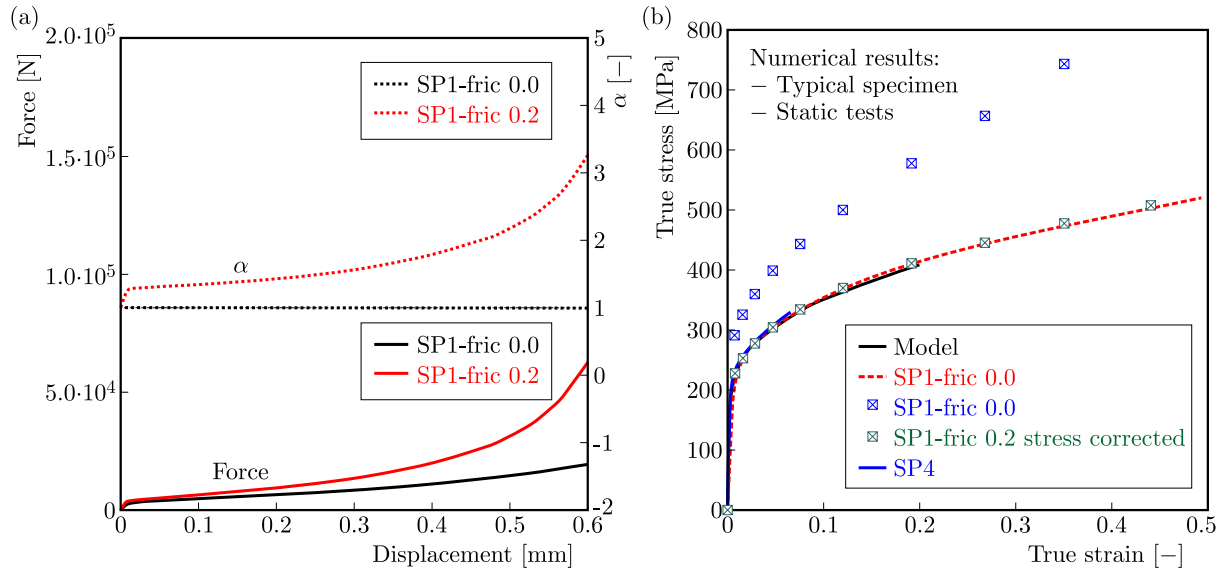


Fig. 8. (a) Influence of the friction coefficient on the measured force and α for model SP1; (b) true stress – true strain curve for the standard specimen SP i with stress correction for mild steel ES

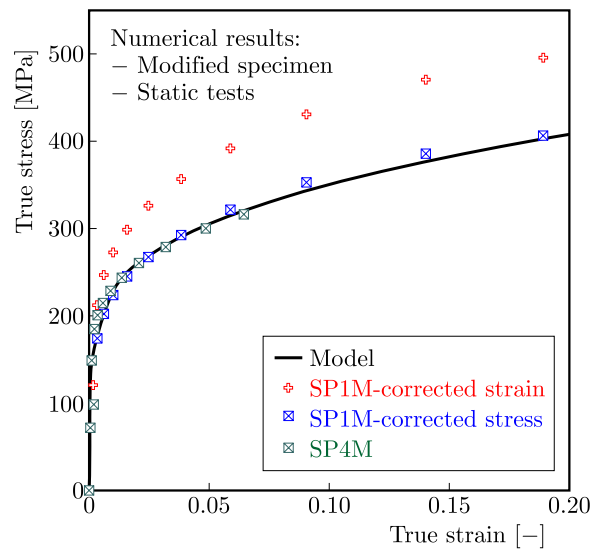


Fig. 9. True stress versus true strain curve for modified specimens under quasi-static loading using mild steel

The specimen modified SP i M has been used to eliminate the friction effect on the stress-strain curve. As demonstrated before, the friction effect was not observed using SP i M, Fig. 4. The true stress-true strain curve for SP4M with and without friction give the same results in agreement with the constitutive relation used, Eq. (2.1), see Fig. 9. However, the triaxiality influence the measured stress as observed for the standard specimen. Analysing the current results, it is visible that these new modified specimens SP i M are much better in describing the failure strain and failure criterion of the materials. However, using these modified short specimens to predict material behaviour, the difficulty is to define the equivalent effective length L_{eff} , different to that reported in Fig. 2 and Fig. 10. To estimate it, numerical simulations have been carried out. The proposed method is presented in this part for the shortest modified specimen SP1M. The

final results are reported in Fig. 9 for specimen SP1M. In this specific case, the final average strain in the active part of the specimen is equal to 0.19. However, if the final strain is calculated from displacements based on the active length of the neck part (1 mm), the final strain level will be equal to 0.551. However, using $L_{eff} = 2.86$ mm, corresponding to the ratio of the strain level described previously, the final strain is equal to 0.19 as the average value in the active part of the specimen. This procedure allows one to correct the strain during the compression test using the modified specimen.

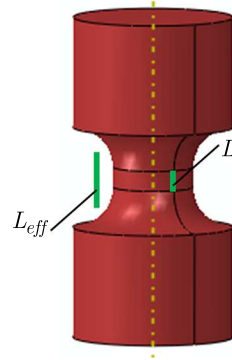


Fig. 10. Definition of the length and effective length used to calculate the strain level

The second step is to correct the stress level using the correction factor $\alpha = \sigma_{yy}/\sigma_{Mises}$. The triaxiality is not strongly changing for this kind of specimen and it is the same for α . In this case, the average value of α during compression is 1.22. To correct the stress measured during experiments or computed by FE code (Małachowski *et al.*, 2014; Dunand and Mohr, 2010), it is necessary to divide the macroscopic stress measured or calculated by 1.22 to estimate the intrinsic material behaviour. The same procedure should be done for other cases. The correction factors for stress should be every time calculated using an inverse method coupling experiments with numerical simulations. To demonstrate that the correction is directly related to the geometry and not to the material tested, numerical simulations have been performed for two materials. It is observed that the correction is related to the applied geometry and not to the material, Fig. 11. The conclusion is the same for SP1M and SP4M. Moreover, it is observed, Fig. 11, that the friction effect does not change the stress triaxiality using SP4M and is not dependent on the

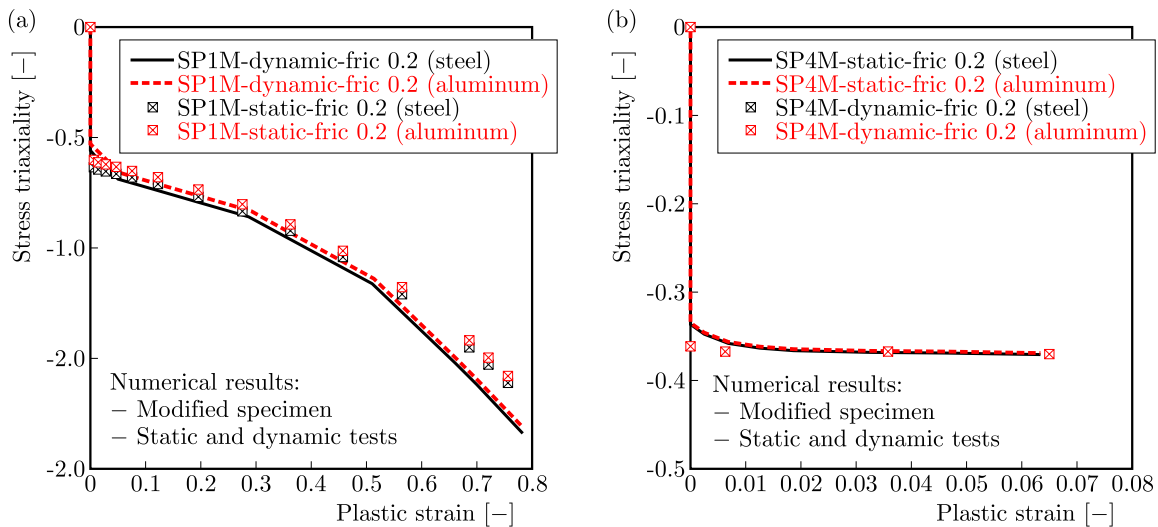


Fig. 11. Comparison of compression results (stress triaxiality versus plastic strain); (a) SP1M and (b) SP4M

material used. Therefore, SP4M may be used to define the material behaviour with the stress triaxiality state corresponding to compression.

Finally, the strain and stress are corrected using Eqs. (3.2)₄ and (3.2)₂, respectively.

$$\varepsilon_{mat} = \kappa_{SPiM} \varepsilon_{meas} \quad \sigma_{mat} = \lambda_{SPiM} \sigma_{meas} \quad (3.2)$$

where λ_{SPiM} and κ_{SPiM} are the geometric coefficients allowing one to define the intrinsic behaviour of the material $\sigma(\varepsilon)$. The first coefficient is related to $1/\alpha$ and the second one to L/L_{eff} . Depending on the geometry SPiM, to obtain the material behaviour, the following corrections are necessary, Table 3.

Table 3. Geometric coefficients for material behaviour definition using SPiM coupled to Eqs. (3.2)

Geometry design, length	λ_{SPiM}	κ_{SPiM}	L_{eff}
SP1M $L = 1$ mm	0.82	0.35	2.86
SP2M $L = 2$ mm	0.92	0.58	3.45
SP3M $L = 4$ mm	0.98	0.78	5.13
SP4M $L = 8$ mm	1	1	8

In addition to material behaviour characterization and for some materials with a reduced ductility, the failure strain ε_f level may be estimated depending on the stress triaxiality, Eq. (3.3). The presented results demonstrate that the use of the specimens with modified shape SPiM in compression tests gives promising results and allows one to eliminate the friction effect, which increases the measured stress as observed during experiments

$$\varepsilon_f = f(\eta) \quad (3.3)$$

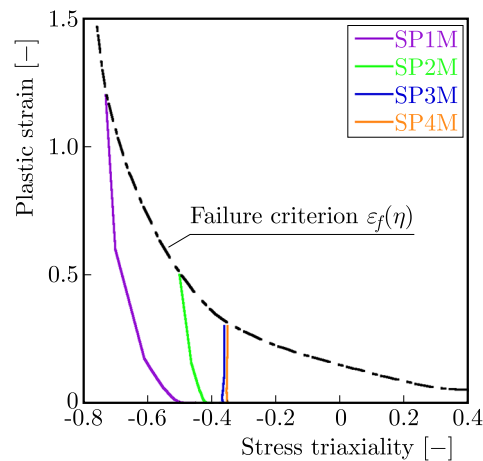


Fig. 12. Failure criterion definition – failure plastic strain as a function of the stress triaxiality η

This kind of approach was previously proposed in shear by Rittel *et al.* (2002). The specimen was used to estimate, after some corrections, the material behaviour and the failure strain level as well. The values of the failure strain level for the new specimens SPiM are reported Fig. 12. The value of triaxiality η is varying from -0.7 to -0.36 . A general example is shown in Fig. 12 and demonstrates how the stress triaxiality changes with plastic deformation mainly for SP1M and SP2M. Using SP3M or SP4M, the value is relatively constant and close to the compression state. An other advantage of having different values of η is the ability precisely define constants of some failure criteria (Bao and Wierzbicki, 2004; Wierzbicki *et al.*, 2005; Rusinek *et al.*, 2007; Dunand and Mohr, 2011), see for example the Johnson-Cook model, Fig. 12.

Now, coupling the new design SPiM with the specimen proposed by Rittel *et al.* (2002), the failure strain level ε_f may be defined for the stress triaxiality η varying between $-0.66 \leq \eta \leq -0.33$ depending on the shear angle inclination. It is also possible to perform, in an easy way, a tensile test to reach a value of $\eta = 0.33$.

4. Conclusions

From the numerical results, it can be seen that using the new design of the compression specimen does not allow one to define the material behaviour without the friction effect only, but also enables estimation of the failure strain level depending on the stress triaxiality. The tests may be complementary to other tests such as tension, shear or biaxial compression (Fraś *et al.*, 2014; Field *et al.*, 2001; Davies and Hunter, 1963; Baranowski *et al.*, 2014).

Thus, comparing all results and basing on the systematic analysis, it is clear that the best solution in terms of the material behaviour is to use the geometry modified SP4M, Fig. 2.

Moreover, it is demonstrated that the parameters calculated to estimate the material behaviour are not dependent on the material used but only on the geometry of SPiM.

References

1. BAO Y., WIERZBICKI T., 2004, On fracture locus in the equivalent strain and stress triaxiality space, *International Journal of Mechanical Sciences*, **46**, 81-98
2. BARANOWSKI P., JANISZEWSKI J., MAŁACHOWSKI J., 2014, Study on computational methods applied to modelling of pulse shaper in split-Hopkinson bar, *Archives of Mechanics*, **66**, 6, 429-452
3. BEUSINK M., 2011, Measurements and simulations on the (dynamic) properties of aluminium alloy AA6060, raport of: Faculty of Mechanical Engineering, Eindhoven University of Technology, SIMLab, Department of Structural Engineering, Norwegian University of Science and Technology, Eindhoven
4. DAVIES E.D.H., HUNTER S.C., 1963, The dynamic compression testing of solids by the method of the split Hopkinson pressure bar, *Journal of the Mechanics and Physics of Solids*, **11**, 155-179
5. DUNAND M., MOHR D., 2010, Hybrid experimental-numerical analysis of basic ductile fracture experiments for sheet metals, *International Journal of Solids and Structures*, **47**, 9, 1130-1143
6. DUNAND M., MOHR D., 2011, On the predictive capabilities of the shear modified Gurson and the modified Mohr-Coulomb fracture models over a wide range of stress triaxialities and Lode angles, *Journal of the Mechanics and Physics of Solids*, **59**, 7, 1374-1394
7. FIELD J.E., PROUD W.G., WALLEY S.M., GOLDREIN H.T., 2001, Review of experimental techniques for high rate deformation and shock studies, [In:] *New Experimental Methods in Material Dynamics and Impact*, W.K. Nowacki, J.R. Klepaczko (Edit.), Vol. 3: *Trends in Mechanics of Materials*, 109-177
8. FRAŚ T., RUSINEK A., PEÇHERSKI R.B., BERNIER R., JANKOWIAK T., 2014, Analysis of friction influence on material deformation under biaxial compression state, *Tribology International*, **80**, 14-24
9. IWAMOTO T., YOKOYAMA T., 2012, Effects of radial inertia and end friction in specimen geometry in split Hopkinson pressure bar tests: A computational study, *Mechanics of Materials*, **51**, 97-109
10. JANKOWIAK T., RUSINEK A., ŁODYGOWSKI T., 2011, Validation of the Klepaczko-Malinowski model for friction correction and recommendations on Split Hopkinson Pressure Bar, *Finite Elements in Analysis and Design*, **47**, 1191-1208

11. KII N., IWAMOTO T., RUSINEK A., JANKOWIAK T., 2014, A study on reduction of friction in impact compressive test based on the Split Hopkinson Pressure Bar method by using a hollow specimen, *Applied Mechanics and Materials*, **566**, 548-553
12. KLEPACZKO J.R., MALINOWSKI J.Z., 1977, Dynamic frictional effects as measured from the Split Hopkinson Pressure Bar, [In:] *High Velocity Deformation of Solids, IUTAM Symposium*, Tokyo, Japan, Springer-Verlag, Berlin, 403-416
13. MAŁACHOWSKI J., BARANOWSKI P., GIELETA R., DAMAZIAK K., 2014, Split Hopkinson Pressure Bar impulse experimental measurement with numerical validation, *Metrology and Measurement Systems*, **21**, 1, 47-58
14. MOĆKO W., KOWALEWSKI Z.L., 2011, Dynamic compression tests – current achievements and future development, *Engineering Transactions*, **59**, 3, 235-248
15. RITTEL D., RAVICHANDRAN G., LEE S., 2002, Large strain constitutive behavior of OFHC copper over a wide range of strain rates using the shear compression specimen, *Mechanics of Materials*, **34**, 627-642
16. RUSINEK A., ZAERA R., KLEPACZKO J.R., 2007, Constitutive relations in 3-D for a wide range of strain rates and temperatures – application to mild steels, *International Journal of Solids and Structures*, **44**, 17, 5611-5634
17. SAFA K., GARY G., 2010, Displacement correction for punching at a dynamically loaded bar end, *International Journal of Impact Engineering*, **37**, 371-384
18. WIERZBICKI T., BAO Y., LEE Y.-W., BAI Y., 2005, Calibration and evaluation of seven fracture models, *International Journal of Mechanical Sciences*, **47**, 4/5, 719-743
19. ZHONG W.Z., RUSINEK A., JANKOWIAK T., ABED F., BERNIER R., SUTTER G., 2015, Influence of interfacial friction and specimen configuration in Split Hopkinson Pressure Bar system, *Tribology International*, **90**, 1-14

Manuscript received December 30, 2017; accepted for print February 8, 2018

NUMERICAL MODELLING OF A DYNAMIC CONTACT PROBLEM WITH NORMAL DAMPED RESPONSE AND UNILATERAL CONSTRAINT

MIKAËL BARBOTEU

Laboratoire de Mathématiques et Physique, University of Perpignan Via Domitia, Perpignan, France
e-mail: barboteu@univ-perp.fr

YOUSSEF OUAFIK

Université Cadi Ayyad, ENSA Safi, Maroc
e-mail: y.ouafik@uca.ma

MIRCEA SOFONEA

Laboratoire de Mathématiques et Physique, University of Perpignan Via Domitia, Perpignan, France
e-mail: sofonea@univ-perp.fr

We consider a mathematical model which describes the dynamic evolution of a viscoelastic body in frictional contact with an obstacle. The contact is modelled with normal damped response and unilateral constraint for the velocity field, associated to a version of Coulomb's law of dry friction. Our aim is to present a detailed description of the numerical modelling of the problem. To this end, we use a penalty method to approximate the constraint. Then, we provide numerical simulations in the study of a two-dimensional example and compare the penalty model with the original one.

Keywords: dynamic contact, viscoelastic material, frictional contact, normal damped response, unilateral constraint, penalty method, numerical simulations

1. Introduction

Contact problems involving deformable bodies arise in many industrial processes as well as in everyday life. For this reason, they have been widely studied in the recent years, with various constitutive laws and boundary conditions, including the normal compliance condition. The studies concern both the mechanical, the mathematical and numerical modelling of the corresponding boundary value problems. References in the field include Oden and Martins (1985), Han *et al.* (2001, 2016), Han and Sofonea (2002), Laursen (2002), Hlaváček *et al.* (1988), Barboteu *et al.* (2015, 2016a,b), Barboteu and Danan (2016), among others. The so-called normal damped response condition represents a version of the normal compliance condition, expressed in terms of velocity. Such a condition seems to be appropriate when contact surfaces are lubricated, as mentioned in (Barboteu and Danan, 2016; Barboteu *et al.*, 2016b; Han *et al.*, 2016; Shillor *et al.*, 2004).

In this current paper, we consider a mathematical model which describes dynamic frictional contact between a body and a deformable foundation. We describe the material behavior with the Kelvin-Voigt viscoelastic constitutive law. The frictional contact is modelled with a normal damped response condition with unilateral constraint for the velocity field associated to a version of Coulomb's law of dry friction. These non standard contact conditions could model the contact with the deformable foundation covered by a lubricant, say oil, as already mentioned.

The current work represents a continuation of (Barboteu *et al.*, 2015, 2016a,b). Its aim is to provide the numerical modelling of the dynamic frictional contact problem supported by numerical simulations. We present a full discretization of the problem and we describe details

of the numerical algorithm we use. The main novelty of our work arises from the fact that we study two problems: an original problem constructed by considering a combination of the normal damped response law with unilateral constraint condition in velocity, and a penalty one constructed with the normal damped response law without a constraint. In this paper, we provide a reliable comparison between numerical solutions of the approximate frictional contact problem and the original one. Finally, we present numerical simulations which validate our approximation method and give information on the mechanical behaviour of the solution.

The paper is organized as follows. In Section 2, we present the original model and provide its variational formulation. Then we introduce the penalty problem and its variational formulation. In Section 3, we introduce a hybrid variational formulation of the two above mentioned problems. A fully discrete scheme is presented in Section 4, based on the finite element method to approximate the spatial variable and the Euler scheme to discretize the time derivatives. Finally, in Section 5, we present numerical simulations in the study of a two-dimensional test problem.

2. The model and its penalty version

We start by presenting the notation and the preliminary material we need in the rest of the paper. Denote by \mathbb{S}^d the space of second order symmetric tensors on \mathbb{R}^d and by “ \cdot ” and $\|\cdot\|$ the inner product and the Euclidean norms on the spaces \mathbb{R}^d and \mathbb{S}^d , respectively. Let $\Omega \subset \mathbb{R}^d$, $d = 1, 2, 3$ be the domain occupied by a viscoelastic body in the reference configuration, with a smooth boundary $\Gamma = \partial\Omega$. We denote by $\boldsymbol{\nu}$ the unit outer normal vector to Γ and assume that Γ is decomposed into three measurable parts $\Gamma_1, \Gamma_2, \Gamma_3$, such that $\text{meas}(\Gamma_1) > 0$. Let $[0, T]$ be the time interval of interest, with $T > 0$. We denote by $\mathbf{x} \in \Omega$ and $t \in [0, T]$ the spatial and the time variable, respectively, and, for simplicity, we do not indicate the dependence of the functions on \mathbf{x} and t . Moreover, a dot above a variable will represent the derivative with respect to time. Finally, we denote by \mathbf{u} the displacement field, by $\boldsymbol{\sigma}$ the stress tensor, and $\boldsymbol{\varepsilon}(\mathbf{u}) = (\varepsilon_{ij}(\mathbf{u}))_{i,j=1}^d$ – the linearized strain field, i.e.

$$\varepsilon_{ij}(\mathbf{u}) = \frac{1}{2} \left(\frac{\partial u_i}{\partial x_j} + \frac{\partial u_j}{\partial x_i} \right)$$

The body is assumed to be viscoelastic and, therefore, we use the constitutive law

$$\boldsymbol{\sigma} = \mathcal{A}\boldsymbol{\varepsilon}(\dot{\mathbf{u}}) + \mathcal{B}\boldsymbol{\varepsilon}(\mathbf{u}) \quad \text{in} \quad \Omega \times (0, T) \quad (2.1)$$

already used in (Duvaut and Lions, 1976), for instance. Here \mathcal{A} and \mathcal{B} are the fourth-order viscosity and elastic tensors, respectively. Since the process is dynamic, the balance equation of the stress field is given by

$$\text{Div} \boldsymbol{\sigma} + \mathbf{f}_0 = \rho \ddot{\mathbf{u}} \quad \text{in} \quad \Omega \times (0, T) \quad (2.2)$$

Here, \mathbf{f}_0 is density of the body forces and ρ stands for density of the material, assumed to be constant for simplicity. Moreover, Div represent the divergence operator, i.e. $\text{Div}(\boldsymbol{\sigma}) = (\sigma_{ij,j})$.

On Γ_1 , the body is clamped and, therefore,

$$\mathbf{u} = \mathbf{0} \quad \text{on} \quad \Gamma_1 \times (0, T) \quad (2.3)$$

Moreover, we assume that a surface force of density \mathbf{f}_2 acts on Γ_2 , i.e.

$$\boldsymbol{\sigma}\boldsymbol{\nu} = \mathbf{f}_2 \quad \text{on} \quad \Gamma_2 \times (0, T) \quad (2.4)$$

The part Γ_3 of the boundary represents the potential contact surface and is assumed to be given. There, the body can arrive in contact with a piston or a device, the so-called foundation. Considering the case of an evolutive (say growing) contact surface leads to various mathematical difficulties and, therefore, is left open. The boundary conditions on Γ_3 are derived from the following assumptions.

— The obstacle prevents motion of the body in such a way that the normal velocity is restricted by an unilateral constraint, i.e.

$$\dot{u}_\nu \leq g \tag{2.5}$$

where $\dot{u}_\nu = \dot{\mathbf{u}} \cdot \boldsymbol{\nu}$ denotes the normal component of $\dot{\mathbf{u}}$ on Γ and $g > 0$ represents a given bound. Here, we assume the non homogeneous case and, therefore, g is a function which could depend on the spatial variable $\mathbf{x} \in \Gamma_3$.

— When the body moves in the opposite direction of the obstacle then the reaction of the obstacle vanishes. Therefore,

$$\dot{u}_\nu < 0 \implies \sigma_\nu = 0 \quad \boldsymbol{\sigma}_\tau = \mathbf{0} \tag{2.6}$$

where σ_ν and $\boldsymbol{\sigma}_\tau$ denote the normal and the tangential components of the stress on Γ , i.e. $\sigma_\nu = (\boldsymbol{\sigma}\boldsymbol{\nu}) \cdot \boldsymbol{\nu}$ and $\boldsymbol{\sigma}_\tau = \boldsymbol{\sigma}\boldsymbol{\nu} - \sigma_\nu\boldsymbol{\nu}$.

— When the body moves towards the obstacle, the contact is described with the normal damped response condition associated to Coulomb’s law of dry friction as far as the normal velocity does not reach the bound g . Therefore,

$$\begin{aligned} 0 \leq \dot{u}_\nu < g \implies & -\sigma_\nu = p(\dot{u}_\nu) & \|\boldsymbol{\sigma}_\tau\| \leq \mu|\sigma_\nu| \\ -\boldsymbol{\sigma}_\tau = \mu|\sigma_\nu| \frac{\dot{\mathbf{u}}_\tau}{\|\dot{\mathbf{u}}_\tau\|} & \text{ if } \dot{\mathbf{u}}_\tau \neq \mathbf{0} \end{aligned} \tag{2.7}$$

Here, p represents a positive function such that $p(r) = 0$ for $r \leq 0$ and μ denotes the coefficient of friction. Details on the normal damped response contact condition associated to Coulomb’s law of dry friction can be found in (Han and Sofonea, 2002; Shillor *et al.*, 2004; Sofonea and Matei, 2012), for instance.

— When the normal velocity reaches the bound g , then the normal stress is larger than $p(g)$ and, moreover, friction follows the Tresca law with the friction bound F_b . Therefore,

$$\begin{aligned} \dot{u}_\nu = g \implies & -\sigma_\nu \geq p(g) & \|\boldsymbol{\sigma}_\tau\| \leq F_b \\ -\boldsymbol{\sigma}_\tau = F_b \frac{\dot{\mathbf{u}}_\tau}{\|\dot{\mathbf{u}}_\tau\|} & \text{ if } \dot{\mathbf{u}}_\tau \neq \mathbf{0} \end{aligned} \tag{2.8}$$

— To accommodate conditions (2.7) and (2.8), we assume the compatibility condition

$$F_b = \mu p(g) \tag{2.9}$$

which guarantees continuity of the friction bound. Note that conditions (2.7) and (2.8) show a natural transition from the Coulomb law (which is valid as far as $0 \leq \dot{u}_\nu < g$) to the Tresca friction law (which is valid when $\dot{u}_\nu = g$).

A careful examination of conditions (2.5)-(2.9) reveals that they can be written, equivalently, as follows

$$\begin{aligned} \dot{u}_\nu \leq g & \quad \sigma_\nu + p(\dot{u}_\nu) \leq 0 & \quad (\dot{u}_\nu - g)(\sigma_\nu + p(\dot{u}_\nu)) = 0 \\ \|\boldsymbol{\sigma}_\tau\| \leq \mu|\sigma_\nu| & \quad -\boldsymbol{\sigma}_\tau = \mu|\sigma_\nu| \frac{\dot{\mathbf{u}}_\tau}{\|\dot{\mathbf{u}}_\tau\|} & \text{ if } \dot{\mathbf{u}}_\tau \neq \mathbf{0} \end{aligned} \tag{2.10}$$

Moreover, conditions (2.10) are equivalent to

$$\begin{aligned} -\sigma_\nu(t) &\in p(\dot{u}_\nu(t)) + \partial I_{(-\infty, g]}(\dot{u}_\nu(t)) && \text{on } \Gamma_3 \times (0, T) \\ -\sigma_\tau(t) &\in \mu p(\dot{u}_\nu(t)) \partial \|\dot{\mathbf{u}}_\tau(t)\| && \text{on } \Gamma_3 \times (0, T) \end{aligned} \tag{2.11}$$

respectively. Here ∂ represents the subdifferential operator in the sense of convex analysis and I_A denotes the indicator function of the set $A \subset \mathbb{R}$. Subdifferential inclusions (2.11) will be considered for the numerical modelling we introduce in Section 3.

Finally, we prescribe the initial displacement and the initial velocity, i.e.

$$\mathbf{u}(0) = \mathbf{u}_0 \quad \dot{\mathbf{u}}(0) = \mathbf{u}_1 \quad \text{in } \Omega \tag{2.12}$$

where \mathbf{u}_0 and \mathbf{u}_1 are given functions defined on Ω .

We now gather relations (2.1)-(2.4), (2.10) and (2.12) to obtain the following formulation of the dynamic frictional contact problem we consider in this paper.

Problem P. Find a displacement field $\mathbf{u} : \Omega \times (0, T) \rightarrow \mathbb{R}^d$ and a stress field $\boldsymbol{\sigma} : \Omega \times (0, T) \rightarrow \mathbb{S}^d$ such that

$$\boldsymbol{\sigma} = \mathcal{A}\boldsymbol{\varepsilon}(\dot{\mathbf{u}}) + \mathcal{B}\boldsymbol{\varepsilon}(\mathbf{u}) \quad \text{in } \Omega \times (0, T) \tag{2.13}$$

$$\text{Div } \boldsymbol{\sigma} + \mathbf{f}_0 = \rho \ddot{\mathbf{u}} \quad \text{in } \Omega \times (0, T) \tag{2.14}$$

$$\mathbf{u} = \mathbf{0} \quad \text{on } \Gamma_1 \times (0, T) \tag{2.15}$$

$$\boldsymbol{\sigma}\boldsymbol{\nu} = \mathbf{f}_2 \quad \text{on } \Gamma_2 \times (0, T) \tag{2.16}$$

$$\dot{u}_\nu \leq g \quad \sigma_\nu + p(\dot{u}_\nu) \leq 0 \quad (\dot{u}_\nu - g)(\sigma_\nu + p(\dot{u}_\nu)) = 0 \quad \text{on } \Gamma_3 \times (0, T) \tag{2.17}$$

$$\|\boldsymbol{\sigma}_\tau\| \leq \mu p(\dot{u}_\nu) \quad -\boldsymbol{\sigma}_\tau = \mu p(\dot{u}_\nu) \frac{\dot{\mathbf{u}}_\tau}{\|\dot{\mathbf{u}}_\tau\|} \quad \text{if } \dot{\mathbf{u}}_\tau \neq \mathbf{0} \quad \text{on } \Gamma_3 \times (0, T) \tag{2.18}$$

$$\mathbf{u}(0) = \mathbf{u}_0 \quad \dot{\mathbf{u}}(0) = \mathbf{u}_1 \quad \text{in } \Omega \tag{2.19}$$

We now turn to the variational formulation of Problem P which is the starting point for the numerical modelling based on the finite element discretization. To this end, we use the notation $H = [L^2(\Omega)]^d$ and we introduce the spaces

$$V = \{\mathbf{v} \in [H^1(\Omega)]^d; \mathbf{v} = \mathbf{0} \quad \text{on } \Gamma_1\}$$

$$Q = \{\boldsymbol{\tau} = (\tau_{ij})_{i,j=1}^d \in [L^2(\Omega)]^{d \times d}; \tau_{ij} = \tau_{ji}, \quad i, j = 1, \dots, d\}$$

The spaces H , V and Q are real Hilbert spaces endowed with the canonical inner products given by

$$(\boldsymbol{\theta}, \boldsymbol{\eta})_H = \int_{\Omega} \boldsymbol{\theta} \cdot \boldsymbol{\eta} \, dx \quad (\mathbf{u}, \mathbf{v})_V = \int_{\Omega} \boldsymbol{\varepsilon}(\mathbf{u}) \cdot \boldsymbol{\varepsilon}(\mathbf{v}) \, dx \quad (\boldsymbol{\sigma}, \boldsymbol{\tau})_Q = \int_{\Omega} \boldsymbol{\sigma} \cdot \boldsymbol{\tau} \, dx$$

On the density of volume forces and surface tractions, we assume that

$$\mathbf{f}_0 \in C([0, T]; H) \quad \mathbf{f}_2 \in C([0, T]; [L^2(\Gamma_2)]^d) \tag{2.20}$$

and, using the Riesz representation theorem, we define the linear function $\mathbf{f} : [0, T] \rightarrow V$ by the equality

$$(\mathbf{f}(t), \mathbf{w})_V = \int_{\Omega} \mathbf{f}_0(t) \cdot \mathbf{w} \, d\mathbf{x} + \int_{\Gamma_2} \mathbf{f}_2(t) \cdot \mathbf{w} \, d\Gamma \quad \forall \mathbf{w} \in V \tag{2.21}$$

Note that assumption (2.20) implies that $\mathbf{f} \in C([0, T]; V)$. Here and below notation $C([0, T]; X)$ represents the space of continuous functions defined on $[0, T]$ with values to X .

Next, we denote by $j : U \times U \rightarrow \mathbb{R}$ the function given by

$$j(\mathbf{u}, \mathbf{w}) = \int_{\Gamma_3} \mu p(u_\nu) \|\mathbf{w}_\tau\| \, d\Gamma \quad \forall \mathbf{u}, \mathbf{w} \in U \tag{2.22}$$

where, $U := \{\mathbf{w} \in V : w_\nu \leq g \text{ a.e. on } \Gamma_3\}$ and $w_\nu = \mathbf{w} \cdot \boldsymbol{\nu}$ and $\mathbf{w}_\tau = \mathbf{w} - w_\nu \boldsymbol{\nu}$, for all $\mathbf{w} \in V$.

Now, using standard arguments based on the Green formula, we obtain the following variational formulation of Problem P .

Problem P_V . Find a displacement field $\mathbf{u} : [0, T] \rightarrow V$ such that $\dot{\mathbf{u}}(t) \in U$ for all $t \in [0, T]$, $\mathbf{u}(0) = \mathbf{u}_0$, $\dot{\mathbf{u}}(0) = \mathbf{u}_1$ and the inequality below holds, for all $t \in (0, T)$:

$$\begin{aligned} & \left(\rho \ddot{\mathbf{u}}(t), \mathbf{w} - \dot{\mathbf{u}}(t) \right)_H + \left(\mathcal{A} \boldsymbol{\varepsilon}(\dot{\mathbf{u}}(t)), \boldsymbol{\varepsilon}(\mathbf{w}) - \boldsymbol{\varepsilon}(\dot{\mathbf{u}}(t)) \right)_Q \\ & + \left(\mathcal{B} \boldsymbol{\varepsilon}(\mathbf{u}(t)), \boldsymbol{\varepsilon}(\mathbf{w}) - \boldsymbol{\varepsilon}(\dot{\mathbf{u}}(t)) \right)_Q + \left(p(\dot{u}_\nu(t)), w_\nu - \dot{u}_\nu(t) \right)_{L^2(\Gamma_3)} + j(\dot{\mathbf{u}}(t), \mathbf{w}) \\ & - j(\dot{\mathbf{u}}(t), \dot{\mathbf{u}}(t)) \geq \left(\mathbf{f}(t), \mathbf{w} - \dot{\mathbf{u}}(t) \right)_V \quad \forall \mathbf{w} \in U \end{aligned} \tag{2.23}$$

Our goal in what follows is to provide a penalty method in order to remove the unilateral constraint $\dot{u}_\nu \leq g$ in (2.17). The penalty form of the Problem P leads to a simpler numerical model which provides a reliable approximation of the solution of the initial problem. Following arguments similar to those in (Chouly and Hid, 2013; Kikuchi and Song, 1981), the penalty contact problem we consider is the following.

Problem P_ε . Find a displacement field $\mathbf{u}_\varepsilon : \Omega \times (0, T) \rightarrow \mathbb{R}^d$ and a stress field $\boldsymbol{\sigma}_\varepsilon : \Omega \times (0, T) \rightarrow \mathbb{S}^d$ such that

$$\boldsymbol{\sigma}_\varepsilon = \mathcal{A} \boldsymbol{\varepsilon}(\dot{\mathbf{u}}_\varepsilon) + \mathcal{B} \boldsymbol{\varepsilon}(\mathbf{u}_\varepsilon) \quad \text{in } \Omega \times (0, T) \tag{2.24}$$

$$\text{Div } \boldsymbol{\sigma}_\varepsilon + \mathbf{f}_0 = \rho \ddot{\mathbf{u}}_\varepsilon \quad \text{in } \Omega \times (0, T) \tag{2.25}$$

$$\mathbf{u}_\varepsilon = \mathbf{0} \quad \text{on } \Gamma_1 \times (0, T) \tag{2.26}$$

$$\boldsymbol{\sigma}_\varepsilon \boldsymbol{\nu} = \mathbf{f}_2 \quad \text{on } \Gamma_2 \times (0, T) \tag{2.27}$$

$$-\sigma_{\varepsilon_\nu} = \frac{1}{\varepsilon} (\dot{u}_{\varepsilon_\nu} - g)_+ + p(\dot{u}_{\varepsilon_\nu}) \quad \text{on } \Gamma_3 \times (0, T) \tag{2.28}$$

$$\|\boldsymbol{\sigma}_{\varepsilon_\tau}\| \leq \mu p(\dot{u}_{\varepsilon_\nu}) \quad - \boldsymbol{\sigma}_{\varepsilon_\tau} = \mu p(\dot{u}_{\varepsilon_\nu}) \frac{\dot{\mathbf{u}}_{\varepsilon_\tau}}{\|\dot{\mathbf{u}}_{\varepsilon_\tau}\|} \text{ if } \dot{\mathbf{u}}_{\varepsilon_\tau} \neq \mathbf{0} \quad \text{on } \Gamma_3 \times (0, T) \tag{2.29}$$

$$\mathbf{u}_\varepsilon(0) = \mathbf{u}_0 \quad \dot{\mathbf{u}}_\varepsilon(0) = \mathbf{u}_1 \quad \text{in } \Omega \tag{2.30}$$

Here and below, ε represents the penalty parameter assumed to be very small, while $\dot{u}_{\varepsilon_\nu}$ and σ_{ε_ν} represent the normal components of the functions $\dot{\mathbf{u}}_\varepsilon$ and $\boldsymbol{\sigma}_\varepsilon$, respectively. Moreover, $\boldsymbol{\sigma}_{\varepsilon_\tau}$ represents the tangential part of the function $\boldsymbol{\sigma}_\varepsilon$. Note that Problem P_ε is constructed by using similar ingredients to those used in Problem P . The differences arise in the fact that here we replace contact condition (2.17) with its penalty version (2.28) and, therefore, Problem P_ε represents a contact problem with the normal damped response, without a unilateral constraint.

Next, using the notation in equations (2.21) and (2.22) and a similar argument to that used in the case of Problem P , we obtain the following variational formulation of Problem P_ε .

Problem P_V^ε . Find a displacement field $\mathbf{u}_\varepsilon : [0, T] \rightarrow V$ such that $\mathbf{u}_\varepsilon(0) = \mathbf{u}_0$, $\dot{\mathbf{u}}_\varepsilon(0) = \mathbf{u}_1$ and the inequality below holds, for all $t \in (0, T)$:

$$\begin{aligned} & \left(\rho \ddot{\mathbf{u}}_\varepsilon(t), \mathbf{w} - \dot{\mathbf{u}}_\varepsilon(t) \right)_H + \left(\mathcal{A} \varepsilon(\dot{\mathbf{u}}_\varepsilon(t)), \varepsilon(\mathbf{w}) - \varepsilon(\dot{\mathbf{u}}_\varepsilon(t)) \right)_Q \\ & + \left(\mathcal{B} \varepsilon(\mathbf{u}_\varepsilon(t)), \varepsilon(\mathbf{w}) - \varepsilon(\dot{\mathbf{u}}_\varepsilon(t)) \right)_Q + \frac{1}{\varepsilon} \left((\dot{u}_{\varepsilon_\nu}(t) - g), w_\nu - \dot{u}_{\varepsilon_\nu}(t) \right)_{L^2(\Gamma_3)} \\ & + \left(p(\dot{u}_{\varepsilon_\nu}(t)), w_\nu - \dot{u}_{\varepsilon_\nu}(t) \right)_{L^2(\Gamma_3)} + j(\dot{\mathbf{u}}_\varepsilon(t), \mathbf{w}) \\ & - j(\dot{\mathbf{u}}_\varepsilon(t), \dot{\mathbf{u}}_\varepsilon(t)) \geq \left(\mathbf{f}(t), \mathbf{w} - \dot{\mathbf{u}}_\varepsilon(t) \right)_V \quad \forall \mathbf{w} \in V \end{aligned} \tag{2.31}$$

Note that Problem P_V represents a second order evolutionary quasivariational inequality with unilateral constraints. In contrast, Problem P_V^ε represents a second order evolutionary quasivariational inequality without unilateral constraints.

3. Hybrid variational formulation

We now turn to a hybrid variational formulation of the model which is more appropriate for the numerical modelling. To this end, consider the trace spaces $X_\nu = \{v_\nu|_{\Gamma_3} : \mathbf{v} \in V\}$ and $X_\tau = \{\mathbf{v}_\tau|_{\Gamma_3} : \mathbf{v} \in V\}$ equipped with their usual norms. Denote by X_ν^* and X_τ^* the duals of the spaces X_ν and X_τ , respectively. Moreover, let $\langle \cdot, \cdot \rangle_{X_\nu^* \times X_\nu}$ and $\langle \cdot, \cdot \rangle_{X_\tau^* \times X_\tau}$ be the corresponding duality pairing mappings.

For the contact conditions, we introduce a function $\varphi_\nu : X_\nu \rightarrow (-\infty, +\infty]$ and an operator $L : X_\nu \rightarrow X_\nu^*$ defined by

$$\begin{aligned} \varphi_\nu(u_\nu) &= \int_{\Gamma_3} I_{\mathbb{R}_-}(u_\nu - g) \, da \quad \forall u_\nu \in X_\nu \\ \langle Lu_\nu, w_\nu \rangle_{X_\nu^* \times X_\nu} &= \int_{\Gamma_3} p(u_\nu) w_\nu \, da \quad \forall u_\nu, w_\nu \in X_\nu \end{aligned}$$

We note that for all $t \in [0, T]$, condition (2.11)₁ leads to the subdifferential inclusion

$$-\sigma_\nu(t) \in \partial\varphi_\nu(\dot{u}_\nu(t)) + L\dot{u}_\nu(t) \quad \text{in } X_\nu^* \tag{3.1}$$

where $\partial\varphi$ denotes the subdifferential of φ .

For the friction law, we introduce a function $\varphi_\tau : X_\tau \rightarrow (-\infty, +\infty]$ defined by

$$\varphi_\tau(\mathbf{u}_\tau) = \int_{\Gamma_3} \|\mathbf{u}_\tau\| \, da \quad \forall \mathbf{u}_\tau \in X_\tau$$

We also note that for all $t \in [0, T]$, condition (2.11)₂ leads to the subdifferential inclusion

$$-\boldsymbol{\sigma}_\tau(t) \in \mu p(\dot{u}_\nu(t)) \partial\varphi_\tau(\dot{\mathbf{u}}_\tau(t)) \quad \text{in } X_\tau^* \tag{3.2}$$

Inclusions (3.1) and (3.2) suggest introduction of the new unknowns λ_ν and $\boldsymbol{\lambda}_\tau$, the so-called Lagrange multipliers, related to the contact and friction stresses on the contact surface, respectively. In our formulation, λ_ν corresponds to $-\sigma_\nu$ and $\boldsymbol{\lambda}_\tau$ corresponds to $-\boldsymbol{\sigma}_\tau$. Thus, proceeding in a standard way and using inclusions (3.1) and (3.2), we obtain the following hybrid variational formulation of Problem P in terms of three unknown fields.

Problem \tilde{P}_V . Find a displacement field $\mathbf{u} : [0, T] \rightarrow V$ with $\mathbf{u}(0) = \mathbf{u}_0$, $\dot{\mathbf{u}}(0) = \mathbf{u}_1$, a normal stress $\lambda_\nu : [0, T] \rightarrow X_\nu^*$ and a tangential stress $\lambda_\tau : [0, T] \rightarrow X_\tau^*$ such that the inequality below holds, for all $t \in (0, T)$:

$$\begin{aligned}
 & (\rho \ddot{\mathbf{u}}(t), \mathbf{w})_H + (\mathcal{A}\varepsilon(\dot{\mathbf{u}}(t)), \varepsilon(\mathbf{w}))_Q + (\mathcal{B}\varepsilon(\mathbf{u}(t)), \varepsilon(\mathbf{w}))_Q \\
 & + \langle \lambda_\nu(t), w_\nu \rangle_{X_\nu^* \times X_\nu} + \langle \lambda_\tau(t), \mathbf{w}_\tau \rangle_{X_\tau^* \times X_\tau} = (\mathbf{f}(t), \mathbf{w})_V \quad \forall \mathbf{w} \in V
 \end{aligned} \tag{3.3}$$

$$-\lambda_\nu(t) \in \partial\varphi_\nu(\dot{u}_\nu(t)) + L\dot{u}_\nu(t) \quad \text{in } X_\nu^* \tag{3.4}$$

$$-\lambda_\tau(t) \in \mu p(\dot{u}_\nu(t))\partial\varphi_\tau(\dot{\mathbf{u}}_\tau(t)) \quad \text{in } X_\tau^* \tag{3.5}$$

The hybrid variational formulation of Problem P_V^ε can be obtained in a similar way and is as follows.

Problem \tilde{P}_V^ε . Find a displacement field $\mathbf{u}_\varepsilon : [0, T] \rightarrow V$ with $\mathbf{u}_\varepsilon(0) = \mathbf{u}_0$, $\dot{\mathbf{u}}_\varepsilon(0) = \mathbf{u}_1$ and a tangential stress field $\lambda_\varepsilon : [0, T] \rightarrow X_\tau^*$ such that the inequality below holds, for all $t \in (0, T)$:

$$\begin{aligned}
 & (\rho \ddot{\mathbf{u}}_\varepsilon(t), \mathbf{w})_H + (\mathcal{A}\varepsilon(\dot{\mathbf{u}}_\varepsilon(t)), \varepsilon(\mathbf{w}))_Q + (\mathcal{B}\varepsilon(\mathbf{u}_\varepsilon(t)), \varepsilon(\mathbf{w}))_Q \\
 & + \left\langle \frac{1}{\varepsilon}(\dot{\mathbf{u}}_{\varepsilon_\nu}(t) - g)_+ + p(\dot{u}_{\varepsilon_\nu}), w_\nu \right\rangle_{X_\nu^* \times X_\nu} + \langle \lambda_\varepsilon(t), \mathbf{w}_\tau \rangle_{X_\tau^* \times X_\tau} = (\mathbf{f}(t), \mathbf{w})_V \quad \forall \mathbf{w} \in V
 \end{aligned} \tag{3.6}$$

$$\lambda_\varepsilon(t) \in \mu p(\dot{u}_{\varepsilon_\nu}(t))\partial\varphi_\tau(\dot{\mathbf{u}}_{\varepsilon_\tau}(t)) \quad \text{in } X_\tau^* \tag{3.7}$$

Note that Problem \tilde{P}_V is formulated in terms of three unknown fields. In contrast, due to the penalty term, Problem \tilde{P}_V^ε is formulated in terms of two unknown fields.

4. Numerical approximation and solution algorithm

4.1. Numerical approximation

We now present a fully discrete approximation of Problems \tilde{P}_V and \tilde{P}_V^ε . First, in order to approximate the spatial variable, we assume that Ω is a polygonal domain and we consider a regular triangulation of Ω , denoted by \mathcal{T}^h , compatible with the boundary decomposition Γ_1 , Γ_2 and Γ_3 . Here and below, $h > 0$ denotes the spatial discretization parameter. Consider the discrete variational space

$$V^h = \left\{ \mathbf{v}^h \in [C(\overline{\Omega})]^d; \mathbf{v}|_{T_{tr}} \in [P_1(T_{tr})]^d \quad \forall T_{tr} \in \mathcal{T}^h, \mathbf{v}^h = \mathbf{0} \text{ at the nodes on } \Gamma_1 \right\}$$

where $P_1(T)$ represents the space of polynomials of the global degree less or equal to one in T_{tr} , and let $U^h = U \cap V^h$. We note that U^h can be obtained as

$$U^h = \{ \mathbf{v}^h \in V^h; v_\nu^h \leq g \text{ a.e. on } \Gamma_3 \}$$

The constraint condition $v_\nu^h \leq g$ on the boundary Γ_3 is satisfied at the nodes, i.e. $v_\nu^h \leq g^I$, where g^I is the linear interpolation of the function g . To discretize the time derivatives, we use a uniform partition of $[0, T]$, denoted by $0 = t_0 < t_1 < \dots < t_N = T$, and let k be the time step size, $k = T/N$. In what follows, we denote $\mathbf{f}_n = \mathbf{f}(t_n)$, $\mathbf{u}_n = \mathbf{u}(t_n)$. For a sequence $\mathbf{u}^{hk} = \{ \mathbf{u}_n^{hk} \}_{n=0}^N$, we use the notation $\delta_n \mathbf{u}_n^{hk} = (\mathbf{u}_n^{hk} - \mathbf{u}_{n-1}^{hk})/k$, $n = 1, \dots, N$, for the backward divided differences, as well as the additional notation $\delta \mathbf{u}^{hk} = \{ \delta_n \mathbf{u}_n^{hk} \}_{n=0}^N$.

We now consider the spaces $X_\nu^h = \{v_\nu^h|_{\Gamma_3} : \mathbf{v}^h \in V^h\}$ and $X_\tau^h = \{\mathbf{v}_\tau^h|_{\Gamma_3} : \mathbf{v}^h \in V^h\}$ equipped with their usual norm. We also consider the discrete space of piecewise constants $Y_\nu^h \subset L^2(\Gamma_3)$ and $Y_\tau^h \subset L^2(\Gamma_3)^d$ related to the discretization of the normal and tangential stress, respectively. Then, conditions (3.1) and (3.2) lead to the following discrete subdifferential inclusions at the time t_n

$$\begin{aligned} \lambda_{\nu_n}^{hk} &\in \partial\varphi_\nu(\delta u_{\nu_n}^{hk}) + L\delta u_{\nu_n}^{hk} & \text{in } & Y_\nu^h \\ \boldsymbol{\lambda}_{\tau_n}^{hk} &\in \mu p(\delta u_{\nu_n}^{hk})\partial\varphi_\tau(\delta \mathbf{u}_{\tau_n}^{hk}) & \text{in } & Y_\tau^h \end{aligned} \quad (4.1)$$

More details about this discretization step can be found in (Khenous *et al.*, 2006).

Let $\mathbf{u}_0^h \in V^h$ and $\mathbf{u}_1^h \in V^h$ be finite element approximations of \mathbf{u}_0 and \mathbf{u}_1 , respectively. Using the previous notation and the backward Euler finite difference $\delta \mathbf{v}_n = (\mathbf{v}_n - \mathbf{v}_{n-1})/k$, the fully discrete approximation of the Problem \tilde{P}_V at the time t_n is the following.

Problem \tilde{P}_V^{hk} . Find a velocity field $\mathbf{v}^{hk} = \{\mathbf{v}_n^{hk}\}_{n=0}^N \subset V^h$, a normal stress $\lambda_{\nu_n}^{hk} = \{\lambda_{\nu_n}^{hk}\}_{n=0}^N \subset Y_\nu^h$ and a tangential stress $\boldsymbol{\lambda}_{\tau_n}^{hk} = \{\boldsymbol{\lambda}_{\tau_n}^{hk}\}_{n=0}^N \subset Y_\tau^h$ such that, for all $n = 1, \dots, N$

$$\begin{aligned} &\left(\frac{\rho}{k}(\mathbf{v}_n^{hk} - \mathbf{v}_{n-1}^{hk}), \mathbf{w}^h\right)_H + \left(\mathcal{A}\boldsymbol{\varepsilon}(\mathbf{v}_n^{hk}), \boldsymbol{\varepsilon}(\mathbf{w}^h)\right)_Q + \left(\mathcal{B}\boldsymbol{\varepsilon}(\mathbf{u}_n^{hk}), \boldsymbol{\varepsilon}(\mathbf{w}^h)\right)_Q \\ &+ \int_{\Gamma_3} \lambda_{\nu_n}^{hk} w_\nu^{hk} da + \int_{\Gamma_3} \boldsymbol{\lambda}_{\tau_n}^{hk} \cdot \mathbf{w}_\tau^{hk} da = \left(\mathbf{f}_n^{hk}, \mathbf{w}^h\right)_V \quad \forall \mathbf{w}^h \in V^h \end{aligned} \quad (4.2)$$

$$\lambda_{\nu_n}^{hk} \in \partial\varphi_\nu(v_{\nu_n}^{hk}) + Lv_{\nu_n}^{hk} \quad \text{in } Y_\nu^h \quad (4.3)$$

$$\boldsymbol{\lambda}_{\tau_n}^{hk} \in \mu p(v_{\nu_n}^{hk})\partial\varphi_\tau(\mathbf{v}_{\tau_n}^{hk}) \quad \text{in } Y_\tau^h \quad (4.4)$$

Here, $\mathbf{u}_0^{hk} = \mathbf{u}_0^h$, $\mathbf{v}_0^{hk} = \mathbf{u}_1^h$ and $\mathbf{u}_n^{hk} = \mathbf{u}_0^{hk} + \sum_{j=1}^n k\mathbf{v}_j^{hk}$.

In a similar way, the discrete version of the penalty Problem \tilde{P}_V^ε can be formulated as follows.

Problem \tilde{P}_V^{hk} . Find a velocity field $\mathbf{v}_\varepsilon^{hk} = \{\mathbf{v}_{\varepsilon_n}^{hk}\}_{n=0}^N \subset V^h$ and a friction stress field $\boldsymbol{\lambda}_\varepsilon^{hk} = \{\boldsymbol{\lambda}_{\varepsilon_n}^{hk}\}_{n=0}^N \subset Y_\tau^h$ such that, for all $n = 1, \dots, N$

$$\begin{aligned} &\left(\frac{\rho}{k}(\mathbf{v}_{\varepsilon_n}^{hk} - \mathbf{v}_{\varepsilon_{n-1}}^{hk}), \mathbf{w}^h\right)_H + \left(\mathcal{A}\boldsymbol{\varepsilon}(\mathbf{v}_{\varepsilon_n}^{hk}), \boldsymbol{\varepsilon}(\mathbf{w}^h)\right)_Q + \left(\mathcal{B}\boldsymbol{\varepsilon}(\mathbf{u}_{\varepsilon_n}^{hk}), \boldsymbol{\varepsilon}(\mathbf{w}^h)\right)_Q \\ &+ \frac{1}{\varepsilon} \int_{\Gamma_3} (v_{\varepsilon_{\nu_n}^{hk}} - g)_+ w_\nu^h da + \int_{\Gamma_3} p(v_{\varepsilon_{\nu_n}^{hk}}) w_\nu^h da \end{aligned} \quad (4.5)$$

$$+ \int_{\Gamma_3} \boldsymbol{\lambda}_{\varepsilon_n}^{hk} \cdot \mathbf{w}_\tau^{hk} da = \left(\mathbf{f}_n^{hk}, \mathbf{w}^h\right)_V \quad \forall \mathbf{w}^h \in V^h$$

$$\boldsymbol{\lambda}_{\varepsilon_n}^{hk} \in \mu p(v_{\varepsilon_{\nu_n}^{hk}})\partial\varphi_\tau(\mathbf{v}_{\varepsilon_{\tau_n}^{hk}}) \quad \text{in } Y_\tau^h \quad (4.6)$$

Here, $\mathbf{u}_{\varepsilon_0}^{hk} = \mathbf{u}_0^h$, $\mathbf{v}_{\varepsilon_0}^{hk} = \mathbf{u}_1^h$ and $\mathbf{u}_{\varepsilon_n}^{hk} = \mathbf{u}_{\varepsilon_0}^{hk} + \sum_{j=1}^n k\mathbf{v}_{\varepsilon_j}^{hk}$.

4.2. The solution algorithm

The algorithm we use to solve the discrete frictional contact Problems \tilde{P}_V^{hk} and \tilde{P}_V^{hk} is based on a combination of the augmented Lagrangian method for the unilateral conditions in velocity and the penalty method for the normal damped response condition. For friction law (4.1)₂, we also use an augmented Lagrangian approach, see (Alart *et al.*, 1991; Khenous *et al.*, 2006; Wriggers, 2002). To this end, we introduce the notation $\boldsymbol{\lambda} = \lambda_\nu \boldsymbol{\nu} + \boldsymbol{\lambda}_\tau$, where $\lambda_\nu = \boldsymbol{\lambda} \cdot \boldsymbol{\nu}$ and $\boldsymbol{\lambda}_\tau = \boldsymbol{\lambda} - \lambda_\nu \boldsymbol{\nu}$. We now introduce the expressions of the functions \mathbf{w}^h , \mathbf{u}^h and $\delta \mathbf{u}^h$ by considering

their values at the i -th node of \mathcal{T}^h and the basis functions α^i of the space V^h for $i = 1, \dots, N_{tot}^h$, i.e.

$$\mathbf{w}^h = \sum_{i=1}^{N_{tot}^h} \mathbf{w}^i \alpha^i \quad \mathbf{u}^h = \sum_{i=1}^{N_{tot}^h} \mathbf{u}^i \alpha^i \quad \delta \mathbf{u}^h = \sum_{i=1}^{N_{tot}^h} \delta \mathbf{u}^i \alpha^i$$

Here and below, N_{tot}^h represents the total number of nodes of \mathcal{T}^h , and $N_{\Gamma_3}^h$ denotes the total number of nodes of \mathcal{T}^h lying on Γ_3 .

The augmented Lagrangian approach shows us that the Problem \tilde{P}_V^{hk} can be governed by the system of nonlinear equations

$$\mathbf{R}(\delta \mathbf{v}_n, \mathbf{v}_n, \mathbf{u}_n, \boldsymbol{\lambda}_n) = \tilde{\mathbf{M}}(\delta \mathbf{v}_n) + \tilde{\mathbf{A}}(\mathbf{v}_n) + \tilde{\mathbf{G}}(\mathbf{u}_n) + \mathcal{F}(\mathbf{v}_n, \boldsymbol{\lambda}_n) = \mathbf{0} \quad (4.7)$$

where the functions $\tilde{\mathbf{M}}$, $\tilde{\mathbf{A}}$, $\tilde{\mathbf{G}}$ and \mathcal{F} are defined below. Here, the vectors $\delta \mathbf{v}_n \in \mathbb{R}^{d \times N_{tot}^h}$, $\mathbf{v}_n \in \mathbb{R}^{d \times N_{tot}^h}$, $\mathbf{u}_n \in \mathbb{R}^{d \times N_{tot}^h}$ and $\boldsymbol{\lambda}_n \in \mathbb{R}^{d \times N_{\Gamma_3}^h}$ represent the generalized velocity, the displacement and the Lagrange multiplier vectors defined by

$$\begin{aligned} \delta \mathbf{v}_n &= \{\delta \mathbf{v}_n^i\}_{i=1}^{N_{tot}^h} & \mathbf{v}_n &= \{\mathbf{v}_n^i\}_{i=1}^{N_{tot}^h} & \mathbf{u}_n &= \{\mathbf{u}_n^i\}_{i=1}^{N_{tot}^h} \\ \boldsymbol{\lambda}_n &= \{\boldsymbol{\lambda}_n^i\}_{i=1}^{N_{\Gamma_3}^h} \quad \text{for all } n = 1, \dots, N \end{aligned}$$

where $\delta \mathbf{v}_n^i$, \mathbf{v}_n^i and \mathbf{u}_n^i denote values of the functions $\delta \mathbf{v}_n^{hk}$, \mathbf{v}_n^{hk} and \mathbf{u}_n^{hk} at the i -th nodes of \mathcal{T}^h . Moreover, $\boldsymbol{\lambda}_n^i$ represents the value of $\boldsymbol{\lambda}_n^{hk}$ at the i -th node of the discretized contact interface. Next, the generalized acceleration term $\tilde{\mathbf{M}}(\mathbf{a}) \in \mathbb{R}^{d \times N_{tot}^h} \times \mathbb{R}^{d \times N_{\Gamma_3}^h}$, the generalized viscous term $\tilde{\mathbf{A}}(\mathbf{v}) \in \mathbb{R}^{d \times N_{tot}^h} \times \mathbb{R}^{d \times N_{\Gamma_3}^h}$ and the generalized elastic term $\tilde{\mathbf{G}}(\mathbf{u}) \in \mathbb{R}^{d \times N_{tot}^h} \times \mathbb{R}^{d \times N_{\Gamma_3}^h}$ are defined by $\tilde{\mathbf{M}}(\mathbf{a}) = (\mathbf{M}(\mathbf{a}), \mathbf{0}_{d \times N_{\Gamma_3}^h})$, $\tilde{\mathbf{A}}(\mathbf{v}) = (\mathbf{A}(\mathbf{v}), \mathbf{0}_{d \times N_{\Gamma_3}^h})$ and $\tilde{\mathbf{G}}(\mathbf{u}) = (\mathbf{G}(\mathbf{u}), \mathbf{0}_{d \times N_{\Gamma_3}^h})$. Here $\mathbf{0}_{d \times N_{\Gamma_3}^h}$ is the zero element of $\mathbb{R}^{d \times N_{\Gamma_3}^h}$; also, $\mathbf{M}(\mathbf{a}) \in \mathbb{R}^{d \times N_{tot}^h}$, $\mathbf{A}(\mathbf{v}) \in \mathbb{R}^{d \times N_{tot}^h}$ and $\mathbf{G}(\mathbf{u}) \in \mathbb{R}^{d \times N_{tot}^h}$ denote the acceleration term, the viscous term and the elastic term, respectively, given by

$$\begin{aligned} (\mathbf{M}(\mathbf{a}) \cdot \mathbf{w})_{\mathbb{R}^{d \times N_{tot}^h}} &= (\rho \mathbf{a}^h, \mathbf{w}^h)_H \quad \forall \mathbf{a}, \mathbf{w} \in \mathbb{R}^{d \times N_{tot}^h}, \quad \forall \mathbf{a}^h, \mathbf{w}^h \in V^h \\ (\mathbf{A}(\mathbf{v}) \cdot \mathbf{w})_{\mathbb{R}^{d \times N_{tot}^h}} &= (\mathcal{A} \boldsymbol{\varepsilon}(\mathbf{v}^h), \boldsymbol{\varepsilon}(\mathbf{w}^h))_Q \quad \forall \mathbf{v}, \mathbf{w} \in \mathbb{R}^{d \times N_{tot}^h}, \quad \forall \mathbf{v}^h, \mathbf{w}^h \in V^h \\ (\mathbf{G}(\mathbf{u}) \cdot \mathbf{w})_{\mathbb{R}^{d \times N_{tot}^h}} &= (\mathcal{B} \boldsymbol{\varepsilon}(\mathbf{u}^h), \boldsymbol{\varepsilon}(\mathbf{w}^h))_Q - (\mathbf{f}_n, \mathbf{w}^h)_V \quad \forall \mathbf{u}, \mathbf{w} \in \mathbb{R}^{d \times N_{tot}^h}, \quad \forall \mathbf{u}^h, \mathbf{w}^h \in V^h \end{aligned}$$

Above, \mathbf{a} , \mathbf{v} , \mathbf{u} and \mathbf{w} represent the generalized vectors of the components \mathbf{a}_i , \mathbf{v}_i , \mathbf{u}_i and \mathbf{w}_i , for $i = 1, \dots, N_{tot}^h$, respectively, and note that the volume and surface efforts are contained in the term $\mathbf{G}(\mathbf{u}_n)$. Finally, the frictional contact operator $\mathcal{F}(\mathbf{v}_n, \boldsymbol{\lambda}_n)$ associated to the boundary condition on the contact surface is given by

$$\begin{aligned} (\mathcal{F}(\mathbf{v}, \boldsymbol{\lambda}), (\mathbf{w}, \boldsymbol{\gamma}))_{\mathbb{R}^{d \times N_{tot}^h} \times \mathbb{R}^{d \times N_{\Gamma_3}^h}} &= \int_{\Gamma_3} \nabla_{\mathbf{v}} \mathcal{P}_c([v_\nu^h]_g) \cdot \mathbf{w}^h \, da \\ &+ \int_{\Gamma_3} \nabla_{\mathbf{v}} (l_\nu^r(\mathbf{v}^h, \boldsymbol{\lambda}^h) + l_\tau^r(\mathbf{v}^h, \boldsymbol{\lambda}^h)) \cdot \mathbf{w}^h \, da + \int_{\Gamma_3} \nabla_{\boldsymbol{\lambda}} (l_\nu^r(\mathbf{v}^h, \boldsymbol{\lambda}^h) + l_\tau^r(\mathbf{v}^h, \boldsymbol{\lambda}^h)) \cdot \boldsymbol{\gamma}^h \, da \\ \forall \mathbf{v}, \mathbf{w} \in \mathbb{R}^{d \times N_{tot}^h}, \quad \forall \boldsymbol{\lambda}, \boldsymbol{\gamma} \in \mathbb{R}^{d \times N_{\Gamma_3}^h}, \quad \forall \mathbf{v}^h, \mathbf{w}^h \in V^h, \quad \forall \boldsymbol{\lambda}^h, \boldsymbol{\gamma}^h \in Y_\nu^h \times Y_\tau^h \end{aligned}$$

Here $\mathcal{P}_c : \mathbb{R} \rightarrow \mathbb{R}$ is a derivable function such that $\nabla_{\mathbf{v}} \mathcal{P}_c = p$ on $(-\infty, g]$, $[\cdot]_g : \mathbb{R} \rightarrow \mathbb{R}$ is the function defined by

$$[s]_g = \begin{cases} s & \text{if } s \leq g \\ g & \text{if } s > g \end{cases}$$

and $\nabla_{\mathbf{x}}$ represents the gradient operator with respect the variable \mathbf{x} . Also l_ν^r and l_τ^r denote the augmented Lagrangian functionals

$$\begin{aligned}
 l_\nu^r(\mathbf{v}^h, \lambda_\nu^h) &= v_\nu^h \lambda_\nu^h + \frac{r_\nu}{2}(v_\nu^h - g)^2 - \frac{1}{2r_\nu} \text{dist}^2\{\lambda_\nu + r_\nu(v_\nu^h - g), \mathbb{R}_-^d\}, \\
 l_\tau^r(\mathbf{v}^h, \boldsymbol{\lambda}_\tau^h) &= \mathbf{v}_\tau^h \cdot \boldsymbol{\lambda}_\tau^h + \frac{r_\tau}{2} |\mathbf{v}_\tau^h|^2 - \frac{1}{2r_\tau} \text{dist}^2\{\boldsymbol{\lambda}_\tau^h + r_\tau \mathbf{v}_\tau^h, C[\mu p(v_\nu^h)]\}
 \end{aligned}
 \tag{4.8}$$

Here, r_ν and r_τ are positive penalty coefficients, $C[\mu p(v_\nu^h)]$ represents the convex disk of constant radius $\mu p(v_\nu^h)$ and $\text{dist}\{x, C\}$ denotes the distance from x to the set C , i.e., $\text{dist}\{x, C\} = \inf_{y \in C} \|x - y\|$.

Note that, in the case of penalty contact condition (2.28), there is no need to use the Lagrange method. Indeed, the penalty method can be used by considering $\lambda_\nu = 0$ in equation (4.8)₁. Then, augmented Lagrangian functional (4.8)₁ takes a simpler expression

$$l_\nu^r(\mathbf{v}^h, 0) = \frac{r_\nu}{2}(v_\nu^h - g)^2 - \frac{1}{2r_\nu} \text{dist}^2\{r_\nu(v_\nu^h - g), \mathbb{R}_-^d\}$$

in which r_ν can be replaced by the penalty parameter ε . Thus, the frictional contact operator $\mathcal{F}(\mathbf{v}, \boldsymbol{\lambda})$ associated with frictional contact conditions (2.28) and (2.29) is given by

$$\begin{aligned}
 (\mathcal{F}(\mathbf{v}, \boldsymbol{\lambda}), (\mathbf{w}, \boldsymbol{\gamma}))_{\mathbb{R}^{d \times N_{tot}^h} \times \mathbb{R}^{d \times N_{\Gamma_3}^h}} &= \int_{\Gamma_3} \nabla_{\mathbf{v}} \mathcal{P}_c([v_\nu^h]_g) \cdot \mathbf{w}^h \, da \\
 &+ \frac{1}{\varepsilon} \int_{\Gamma_3} (v_\nu^h - g)_+ w_\nu^h \, da + \int_{\Gamma_3} \nabla_{\mathbf{v}} l_\tau^r(\mathbf{v}^h, \boldsymbol{\lambda}^h) \cdot \mathbf{w}^h \, da + \int_{\Gamma_3} \nabla_{\boldsymbol{\lambda}} l_\tau^r(\mathbf{v}^h, \boldsymbol{\lambda}^h) \cdot \boldsymbol{\gamma}^h \, da \\
 \forall \mathbf{v}, \mathbf{w} \in \mathbb{R}^{d \times N_{tot}^h}, \quad \forall \boldsymbol{\lambda}, \boldsymbol{\gamma} \in \mathbb{R}^{d \times N_{\Gamma_3}^h}, \quad \forall \mathbf{v}^h, \mathbf{w}^h \in V^h, \quad \forall \boldsymbol{\lambda}^h, \boldsymbol{\gamma}^h \in Y_\nu^h \times Y_\tau^h
 \end{aligned}$$

The solution algorithm consists in a prediction-correction scheme based on a finite differences method (the backward Euler difference method) and a linear iterations method (the Newton method). The finite difference scheme we use is characterized by a first order time integration scheme, both for the acceleration $\delta \mathbf{v}_n$ and the velocity $\mathbf{v}_n = \delta \mathbf{u}_n$. To solve nonlinear system (4.7), at each time increment the variables $(\mathbf{v}_n, \boldsymbol{\lambda}_n)$ are treated simultaneously through the Newton method. For this reason, we use in what follows the notation $\mathbf{x}_n = (\mathbf{v}_n, \boldsymbol{\lambda}_n)$. Inside the loop of the increment of time indexed by n , the algorithm can be developed in three steps which are the following.

For $n = 0$ until N , let $\mathbf{u}_0, \mathbf{v}_0$ and $\boldsymbol{\lambda}_0$ be given.

- **The prediction step:** This step provides the initial values $\mathbf{u}_{n+1}^0, \mathbf{v}_{n+1}^0$ and $\boldsymbol{\lambda}_{n+1}^0$ by the formulas

$$\mathbf{u}_{n+1}^0 = \mathbf{u}_n \quad \boldsymbol{\lambda}_{n+1}^0 = \boldsymbol{\lambda}_n \quad \mathbf{v}_{n+1}^0 = \mathbf{0}
 \tag{4.9}$$

- **The Newton linearization step:** At the iteration i of the Newton method, we have

$$\mathbf{x}_{n+1}^{i+1} = \mathbf{x}_{n+1}^i - \left(\frac{\mathbf{C}_{n+1}^i}{k} + \mathbf{Q}_{n+1}^i + k \mathbf{K}_{n+1}^i + \mathbf{T}_{n+1}^i \right)^{-1} \mathbf{R} \left(\frac{\mathbf{v}_{n+1}^i - \mathbf{v}_n^i}{k}, \mathbf{v}_{n+1}^i, \mathbf{u}_{n+1}^i, \boldsymbol{\lambda}_{n+1}^i \right)$$

where \mathbf{x}_{n+1}^{i+1} denotes the pair $(\mathbf{v}_{n+1}^{i+1}, \boldsymbol{\lambda}_{n+1}^{i+1})$; i and n represent respectively the Newton iteration index and the time index, respectively; $\mathbf{C}_{n+1}^i = D_{\mathbf{v}} \mathbf{M}(\delta \mathbf{v}_{n+1}^i)$ denotes the mass matrix, $\mathbf{Q}_{n+1}^i = D_{\mathbf{v}} \mathbf{A}(\mathbf{v}_{n+1}^i)$ is the damping matrix, $\mathbf{K}_{n+1}^i = D_{\mathbf{v}} \mathbf{G}(\mathbf{u}_{n+1}^i)$ represents the elastic matrix and $\mathbf{T}_{n+1}^i = D_{\mathbf{v}, \boldsymbol{\lambda}} \mathcal{F}(\mathbf{v}_{n+1}^i, \boldsymbol{\lambda}_{n+1}^i)$ is the contact tangent matrix. Also, $D_{\mathbf{v}} \mathbf{M}, D_{\mathbf{v}} \mathbf{A}, D_{\mathbf{v}} \mathbf{G}$ and

$D_{\mathbf{v}, \boldsymbol{\lambda}} \mathcal{F}$ denote the differentials of the functions \mathbf{M} , \mathbf{A} , \mathbf{G} and \mathcal{F} according to the variables \mathbf{v} and $\boldsymbol{\lambda}$. This leads us to solve the resulting linear system

$$\left(\frac{\mathbf{C}_{n+1}^i}{k} + \mathbf{Q}_{n+1}^i + k\mathbf{K}_{n+1}^i + \mathbf{T}_{n+1}^i \right) \Delta \mathbf{x}^i = -\mathbf{R} \left(\frac{\mathbf{v}_{n+1}^i - \mathbf{v}_n^i}{k}, \mathbf{v}_{n+1}^i, \mathbf{u}_{n+1}^i, \boldsymbol{\lambda}_{n+1}^i \right) \quad (4.10)$$

where $\Delta \mathbf{x} = (\Delta \mathbf{v}^i, \Delta \boldsymbol{\lambda}^i)$ with $\Delta \mathbf{v}^i = \mathbf{v}_{n+1}^{i+1} - \mathbf{v}_{n+1}^i$ and $\Delta \boldsymbol{\lambda}^i = \boldsymbol{\lambda}_{n+1}^{i+1} - \boldsymbol{\lambda}_{n+1}^i$.

• **The correction step:** Once system (4.10) is solved, we update \mathbf{x}_{n+1}^{i+1} and \mathbf{u}_{n+1}^{i+1} by

$$\mathbf{x}_{n+1}^{i+1} = \mathbf{x}_{n+1}^i + \Delta \mathbf{x}^i \quad \mathbf{u}_{n+1}^{i+1} = \mathbf{u}_{n+1}^i + k \Delta \mathbf{v}^i$$

Note that formulation (4.7) has been implemented in the open-source finite element library GetFEM++ (see <http://getfem.org/>).

5. Numerical simulations

To verify the performance and the accuracy of the numerical method described in the previous Section, a number of numerical experiments have been performed on a well known test problem. We describe in this Section the numerical results we obtained for Problems P_V and P_{V_ε} in dimension two. The physical setting is depicted in Fig. 1. There, the domain $\Omega = (0, 2) \times (0, 1)$

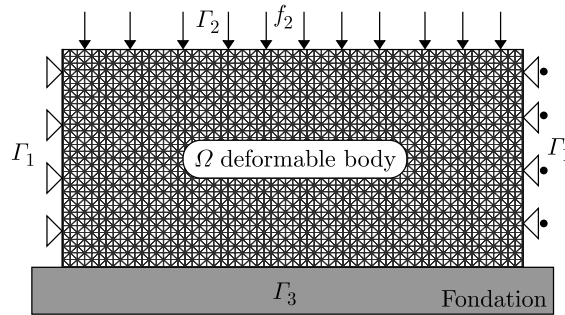


Fig. 1. Physical setting and finite element discretization for $h = 1/33$

is the cross section of a three-dimensional linearly viscoelastic body subjected to the action of tractions in such a way that a plane stress hypothesis is assumed. On the part $\{0\} \times [0, 1]$, the body is clamped and, therefore, the displacement field vanishes there; the horizontal component of the displacement field vanishes on the part $\{2\} \times [0, 1]$. Thus, $\Gamma_1 = (\{0\} \times [0, 1]) \cup (\{2\} \times [0, 1])$. Vertical tractions act on the part Γ_2 of the boundary. No body forces are assumed to act on the viscoelastic body during the dynamic process. The body is in frictional contact with a rigid obstacle on the part $\Gamma_3 = [0, 2] \times \{0\}$ of the boundary. We recall that the contact follows the normal damped response condition associated to Coulomb’s law of dry friction as far as the normal velocity is less than the bound g and, when this bound is reached, it follows a unilateral condition in velocity associated to the Tresca friction law.

The material response is governed by a viscoelastic linear constitutive law defined by the elasticity tensor \mathcal{B} and the viscosity tensor \mathcal{A} given by

$$\begin{aligned} (\mathcal{B}\boldsymbol{\tau})_{\alpha\beta} &= \frac{E\nu}{1-\kappa^2}(\tau_{11} + \tau_{22})\delta_{\alpha\beta} + \frac{E}{1+\kappa}\tau_{\alpha\beta} \\ (\mathcal{A}\boldsymbol{\tau})_{\alpha\beta} &= \mu(\tau_{11} + \tau_{22})\delta_{\alpha\beta} + \eta\tau_{\alpha\beta} \quad 1 \leq \alpha \quad \beta \leq 2 \end{aligned}$$

where E is Young’s modulus, κ is Poisson’s ratio of the material, μ, η are viscosity constants, and $\delta_{\alpha\beta}$ denotes the Kronecker symbol.

In computations, we have used the following data: $T = 1$ s, $\mathbf{u}_0 = \mathbf{0}$ m, $\dot{\mathbf{u}}_0 = \mathbf{0}$ m/s, $\rho = 2000$ Kg/m³, $E = 100$ GPa, $\nu = 0.2$, $\mu_1 = 0.25$ GPa, $\mu_2 = 0.5$ GPa, $\mathbf{f}_0 = (0, 0)$ GPa, $\mathbf{f}_2 = (0, -10t)$ GPam on Γ_2 , $\mu = 0.4$, $g = 0.05$ m/s, $p(r) = c_\nu(r)_+$, $c_\nu = 50$ GPas, $\varepsilon = 1/50000$ GPas.

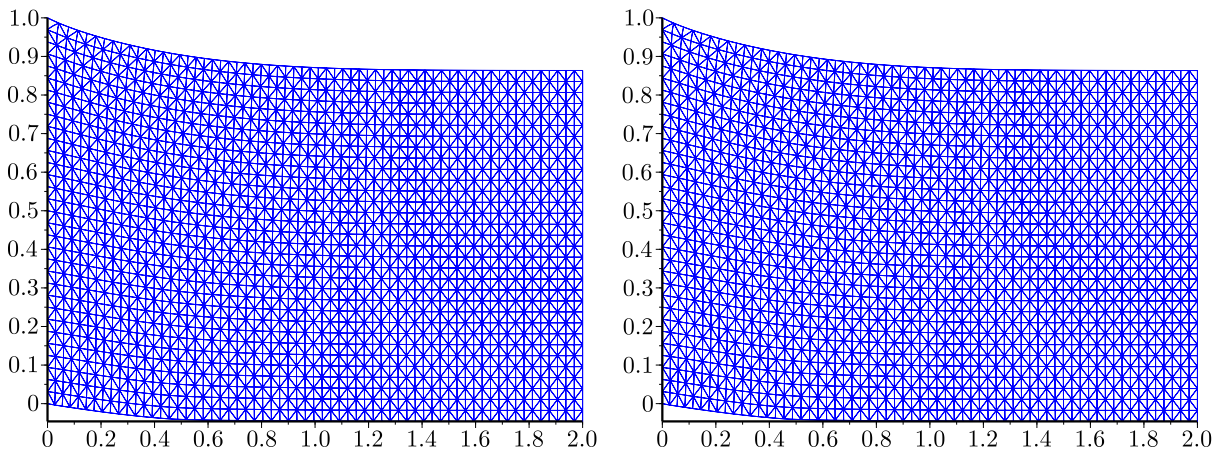


Fig. 2. Deformed configuration at the final time: the original contact problem (left) and the penalty problem (right)

The deformed configuration of the body at the final time $T = 1$ s is represented in Fig. 2 (left), which corresponds to the numerical solution of problem P_V . Note that the vertical displacement of the bottom side is quite large, and this is a consequence of the fact that we model the contact with the normal damped response condition which, in contrast to the unilateral condition in displacement, describes the contact with a deformable foundation and allows penetration. In order to compare the deformed mesh related to Problem P_V with that obtained for the numerical solution of Problem P_V^ε , we plotted in Fig. 2 (right) the deformed configuration for the numerical solution of the penalty problem P_V^ε . Then, in Figs. 3 and 4, we show the reactions and velocities of the nodes of the contact surface for $\mu = 0.4$. The zone AB is a sliding zone formed by 15 nodes which are in a status of the normal damped response; there, the normal velocity is such that $0 < \dot{u}_\nu < g$ and the tangential velocity does not vanishes, i.e., $\dot{\mathbf{u}}_\tau \neq \mathbf{0}$. In this zone, the friction follows the Coulomb law. The zone BC is a sliding zone formed of 29 nodes which are in a status of the unilateral condition in velocity; there, the normal velocity reaches the bound g . In this zone, the friction follows the Tresca law with the friction bound F_b . Next, we have the stick zone CD where the slip vanishes and $\|\sigma_\tau\| < F_b$.

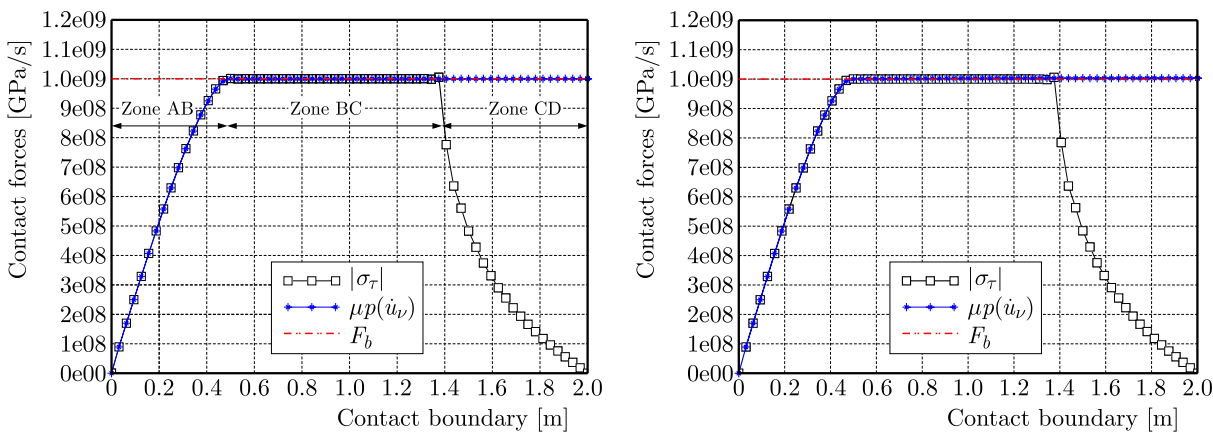


Fig. 3. Frictional contact reactions on Γ_3 at the final time: the original contact problem (left) and the penalty problem (right)

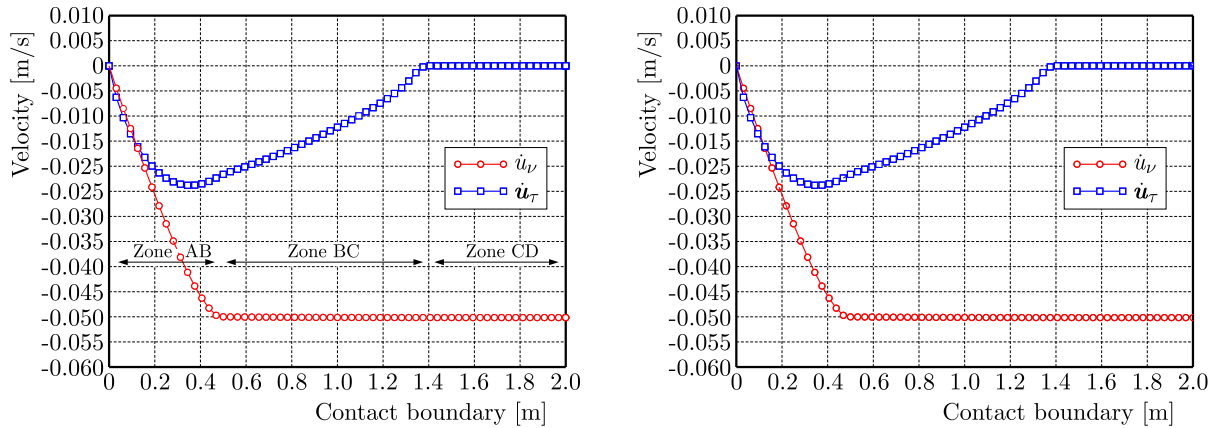


Fig. 4. Velocity on Γ_3 at final time: the original contact problem (left) and the penalty problem (right)

According to the deformed configurations (Figs. 2-4), we observe that the numerical results obtained for the solution of Problem P_V are very well approximated by the solution of Problem P_{V^ϵ} . Next, we lead a parametric study according to the penalty coefficient ϵ . To this end, in Fig. 5 we consider various values of ϵ , and we compare in the left graph the normal velocities profiles on the contact boundary obtained for the solution of the original contact Problem P_V and the penalty Problem P_{V^ϵ} . In the right graph of Fig. 5, we study the convergence on the whole discrete domain Ω^h of the velocity solution obtained for Problem P_{V^ϵ} towards that obtained for Problem P_V . Here, we consider the numerical estimation of the difference $\|\dot{\mathbf{u}}_\epsilon^{hk} - \dot{\mathbf{u}}^{hk}\|$ at the time $T = 1$ s between the numerical solutions obtained for Problems P_V and P_{V^ϵ} . The results depicted in Fig. 5 illustrate that the solution of the penalty problem gives a reliable and accurate approximation of the original problem, provided that the penalty parameter takes very large values.

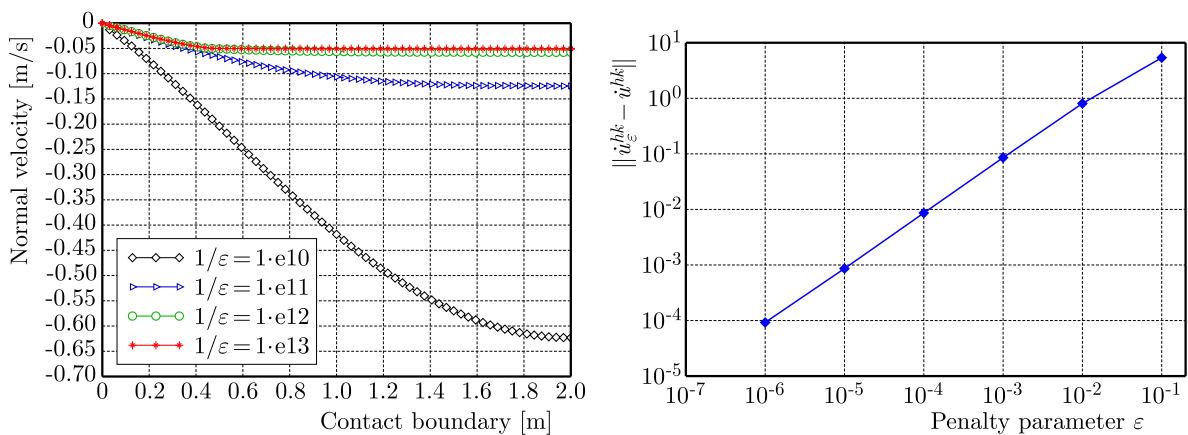


Fig. 5. Normal velocity for different values of the contact penalty parameter (left) and convergence of the penalty method (right)

References

1. ALART P., CURNIER A., 1991, A mixed formulation for frictional contact problems prone to Newton like solution methods, *Computer Methods in Applied Mechanics and Engineering*, **92**, 3, 353-375
2. BARBOTEU M., BARTOSZ K., KALITA P., 2015, A dynamic viscoelastic contact problem with normal compliance, finite penetration and nonmonotone slip rate dependent friction, *Nonlinear Analysis: Real World Applications*, **22**, 452-472

3. BARBOTEU M., CHENG X.L., SOFONEA M., 2016a, Analysis of a contact problem with unilateral constraint and slip-dependent friction, *Mathematics and Mechanics of Solids*, **21**, 791-811
4. BARBOTEU M., DANAN D., 2016, Analysis of a dynamic viscoelastic contact problem with normal compliance, normal damped response, and nonmonotone slip rate dependent friction, *Advances in Mathematical Physics*, **2016**, <http://dx.doi.org/10.1155/2016/1562509>
5. BARBOTEU M., DANAN D., SOFONEA M., 2016b, Analysis of a contact problem with normal damped response and unilateral constraint, *Zeitschrift für Angewandte Mathematik and Mechanik*, **96**, 408-428
6. CHOULY F., HILD P., 2013, On convergence of the penalty method for unilateral contact problems, *Applied Numerical Mathematics*, **65**, 27-40
7. DUVAUT G., LIONS J.L., 1976, *Inequalities in Mechanics and Physics*, Springer Verlag, Berlin
8. HAN J., MIGÓRSKI S., ZENG H., 2016, Analysis of a dynamic viscoelastic unilateral contact problem with normal damped response, *Nonlinear Analysis: Real World Applications*, **28**, 229-250
9. HAN W., SHILLOR M., SOFONEA M., 2001, Variational and numerical analysis of a quasistatic viscoelastic problem with normal compliance, friction and damage, *Journal of Computational and Applied Mathematics*, **137**, 377-398
10. HAN W., SOFONEA M., 2002, *Quasistatic Contact Problems in Viscoelasticity and Viscoplasticity*, American Mathematical Society-International Press
11. HLAVÁČEK I., HASLINGER J., NEČAS J., LOVIŠEK J., 1988, *Solution of Variational Inequalities in Mechanics*, Springer, New York, NY, USA.
12. KHENOUS H.B., LABORDE P., RENARD Y., 2006, On the discretization of contact problems in elastodynamics, [In:] *Analysis and Simulation of Contact Problems*, **27**, 31-38, Lecture Notes in Applied and Computational Mechanics, Springer, Berlin, Germany
13. KIKUCHI N., SONG Y., 1981, Penalty finite element approximations of a class of unilateral problems in linear elasticity, *Quarterly of Applied Mechanics*, **39**, 1-21
14. LAURSEN T.A., 2002, *Computational Contact and Impact Mechanics*, Springer, Berlin, Germany
15. ODEN J.T., MARTINS J.A.C., 1985, Models and computational methods for dynamic friction phenomena, *Computer Methods in Applied Mechanics and Engineering*, **52**, 527-634
16. SHILLOR M., SOFONEA M., TELEGA J., 2004, *Models and Variational Analysis of Quasistatic Contact*, **655**, Lecture Notes in Physics, Springer, Berlin, Germany
17. SOFONEA M., MATEI A., 2012, *Mathematical Models in Contact Mechanics*, **398**, London Mathematical Society Lecture Note Series, Cambridge University Press, Cambridge
18. WRIGGERS P., 2002, *Computational Contact Mechanics*, John Wiley & Sons, Chichester, UK

Manuscript received February 2, 2018; accepted for print February 23, 2018

EFFECT OF CYCLIC HARDENING ON STRESS RELAXATION IN SUS316HTP UNDER CREEP-FATIGUE LOADING AT 700°C: EXPERIMENTS AND SIMULATIONS

NOBUTADA OHNO

Nagoya Industrial Science Research Institute, Nagoya, Japan
e-mail: nobuohno@nagoya-u.jp; nobuohno@nifty.com

TATSUYA SASAKI

Department of Computational Science and Engineering, Nagoya University, Nagoya, Japan
e-mail: t.sasaki@mml.mech.nagoya-u.ac.jp

TAKEHIRO SHIMADA, KENJI TOKUDA, KIMIYAKI YOSHIDA

IHI Corporation, Yokohama, Japan
e-mail: takehiro_shimada@ihi.co.jp; kenji_tokuda@ihi.co.jp; kimiaki_yoshida@ihi.co.jp

DAI OKUMURA

Department of Mechanical Engineering, Osaka University, Osaka, Japan
e-mail: okumura@mech.eng.osaka-u.ac.jp

Cyclic hardening and stress relaxation experiments of SUS316HTP were performed under creep-fatigue loading with tensile strain holding at 700°C. Experiments revealed that under strain holding, the slow stress-relaxation stage satisfying Norton's law with slight cyclic hardening followed a rapid stress-relaxation stage that was noticeably affected by cyclic hardening. This suggests that in the slow stress-relaxation stage, inelastic deformation mechanisms different from that of viscoplasticity occurred. Experiments were simulated using a cyclic viscoplastic-creep model in which the inelastic strain-rate was decomposed into viscoplastic and creep components that were affected differently by cyclic hardening. The simulation accurately reproduced the experiments.

Keywords: creep-fatigue loading, cyclic hardening, stress relaxation, SUS316, constitutive model

1. Introduction

Creep-fatigue tests with tensile and/or compressive strain holding at high temperatures have been performed to investigate the effect of creep damage on the fatigue lives of materials. For polycrystalline metals, creep damage under creep-fatigue loading is caused by grain boundary cavitation that develops with the accumulation of creep strain under strain holding (e.g., Hales, 1980; Priest and Ellison, 1981; Nam, 2002), and has been macroscopically evaluated in terms of the changes in stress and creep strain under strain holding (e.g., Inoue *et al.*, 1989; Takahashi *et al.*, 2008; Yan *et al.*, 2015). To numerically evaluate creep damage in structural components, it is necessary to use a constitutive model that can accurately simulate the stress-strain behavior under cyclic loading with strain holding.

The ductility exhaustion method proposed by Priest and Ellison (1981) and Hales (1983) is a well-known method to evaluate creep damage under creep-fatigue loading (Ainsworth, 2006; Yan *et al.*, 2015). This method assumes that creep damage develops with the accumulation of creep or inelastic strain under strain holding. Priest and Ellison (1981) proposed that creep damage develops when the inelastic strain-rate under strain holding is smaller than the transition rate

below which the diffusion creep and grain boundary sliding become important, whereas Hales (1983) considered that the development of creep damage depends on the variations in inelastic strain in three periods under strain holding. Takahashi (1998) and Takahashi *et al.* (2008) adopted the Priest and Ellison (1981) model and decomposed the inelastic strain-rate under strain holding into viscoplastic and creep components occurring at high and low inelastic-strain rates, respectively, and assumed that only the creep component contributes to the development of creep damage. They thus accurately predicted the creep-fatigue lives of 316 stainless steel at 550°C and 600°C.

The decomposition of inelastic strain-rate is physically valid in the presence of dislocation viscoplasticity at high inelastic strain-rates and diffusion creep at low inelastic strain-rates. In the constitutive modeling of cyclic plasticity, however, the decomposition of inelastic strain into viscoplastic and creep strains has been regarded as a conventional assumption. The work has been focused on the development of unified constitutive models, in which both viscoplasticity and creep are considered to be caused by dislocation movements (Miller, 1976; Krausz and Krausz, 1996; Chaboche, 2008). It is, therefore, worthwhile to investigate the stress relaxation behavior in creep-fatigue tests to examine the appropriateness of the inelastic strain-rate decomposition. This point of view was not taken by Nouailhas (1989) for using a unified model to simulate the creep-fatigue tests of 316 stainless steel at 600°C performed by Goodall *et al.* (1981).

In this study, the stress relaxation behavior under tensile strain holding was measured in creep-fatigue tests of SUS316HTP at 700°C to examine the decomposition of inelastic strain-rate. It was assumed that the increase in dislocation density, which occurs in grains and is observed as cyclic hardening, affected viscoplasticity significantly more than diffusion creep and grain boundary sliding. It was thus suggested that inelastic deformation mechanisms other than viscoplasticity started to operate shortly after the onset of strain holding, and consequently that the inelastic strain-rate consisted of viscoplastic and creep components under strain holding in the creep-fatigue tests. The experiments were then simulated using a cyclic viscoplastic-creep model in which cyclic hardening was assumed to have different effects on the viscoplastic and creep strain-rates.

Throughout this paper, a superposed dot indicates differentiation with respect to time t , a colon represents the inner product between tensors (e.g., $\boldsymbol{\sigma} : \boldsymbol{\varepsilon} = \sigma_{ij}\varepsilon_{ij}$ and $\mathbf{D} : \boldsymbol{\varepsilon} = D_{ijkl}\varepsilon_{kl}$), $\|\cdot\|$ denotes the Euclidean norm of second rank tensors (e.g., $\|\boldsymbol{\sigma}\| = (\boldsymbol{\sigma} : \boldsymbol{\sigma})^{1/2}$), and $\langle \cdot \rangle$ indicates the Macaulay brackets (i.e., $\langle x \rangle = x$ if $x > 0$ and $\langle x \rangle = 0$ if $x \leq 0$).

2. Experiments

2.1. Material tested and cyclic loading conditions

Uniaxial creep-fatigue tests with tensile strain holding were performed at 700°C using an electric-hydraulic servo-type material testing machine MTS810. The material tested was SUS316HTP (a 316 stainless steel), which had the chemical composition and mechanical properties at room temperature given in Tables 1 and 2. Solid bar specimens with the shape illustrated in Fig. 1 were used. The tests performed are listed in Table 3. Hereafter, $\Delta\varepsilon$, $\dot{\varepsilon}$, and t_h indicate the strain range, strain-rate, and strain hold time, respectively, in the creep-fatigue tests.

Table 1. Chemical composition of SUS316HTP by mass percent

C	Si	Mn	P	S	Ni	Cr	Mo
0.07	0.28	1.75	0.27	0.0	11.2	16.6	2.12

Table 2. Mechanical properties at room temperature

0.2% proof stress [MPa]	Tensile strength [MPa]	Tensile rupture strain [%]
267	553	68

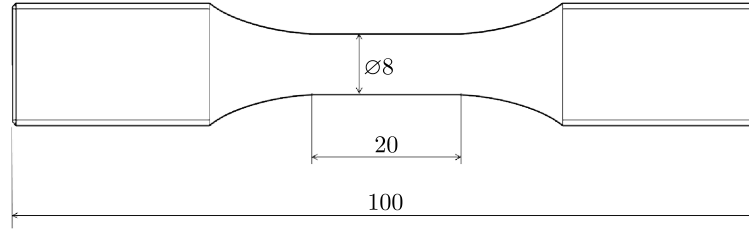


Fig. 1. Shape of the experimental specimens; dimensions in mm

Table 3. Tests performed

Strain rate [1/s]	Strain range [-]	Tensile strain hold time [min]
10^{-3}	0.010	0, 10, 60
10^{-3}	0.007	0, 10, 60
10^{-3}	0.004	0
10^{-4}	0.010	0

2.2. Effect of cyclic hardening on stress relaxation

The effect of cyclic hardening on the stress relaxation behavior under strain holding was investigated using the experimental data obtained in the creep-fatigue tests with $t_h = 60$ min.

Under strain holding, we have

$$\dot{\varepsilon} = \dot{\varepsilon}^e + \dot{\varepsilon}^{in} = 0 \quad (2.1)$$

where $\dot{\varepsilon}^e$ and $\dot{\varepsilon}^{in}$ are the elastic and inelastic parts of $\dot{\varepsilon}$, respectively. Assuming isothermal Hooke's law for $\dot{\varepsilon}^e$ in Eq. (2.1) gives

$$\dot{\varepsilon}^{in} = -\frac{\dot{\sigma}}{E} \quad (2.2)$$

Here, σ and E indicate the uniaxial tensile stress and Young's modulus, respectively. Using a difference approximation for $\dot{\sigma}$ in the above equation, $\dot{\varepsilon}^{in}$ at time t is represented as

$$\dot{\varepsilon}^{in}(t) = -\frac{\sigma(t_{i+1}) - \sigma(t_i)}{(t_{i+1} - t_i)E} \quad (2.3)$$

where t_i and t_{i+1} are times slightly before and after t , respectively.

Applying Eq. (2.3) to the experimental data at $\dot{\varepsilon} = 10^{-3} \text{ s}^{-1}$ with $t_h = 60$ min at $\Delta\varepsilon = 0.007$ and 0.01 provided the relationships between $\log \sigma(t)$ and $\log \dot{\varepsilon}^{in}(t)$ under strain holding (Figs. 2a and 2b). Stress increased with the increasing number of cycles N , especially in the stage just after the onset of strain holding. This is the phenomenon known as cyclic hardening. The relationship became linear to satisfy Norton's law shortly after the onset of tensile strain holding. Hereafter, the stage of stress relaxation satisfying Norton's law is referred to as the Norton stage, and is distinguished from the transient stage in which stress rapidly relaxes just after the onset of strain holding. Figure 2 shows that the Norton stage had much less cyclic hardening than the transient stage.

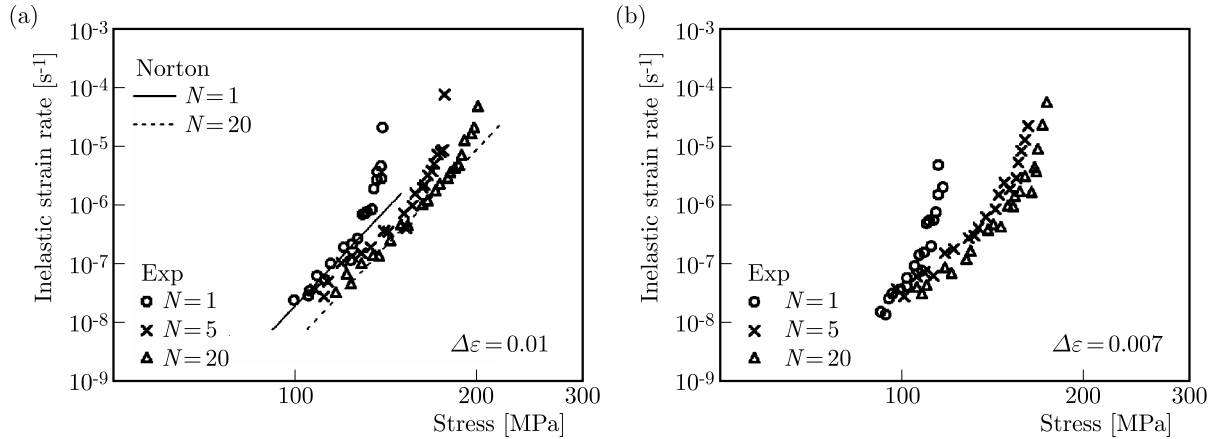


Fig. 2. Relationship between $\dot{\varepsilon}^{in}$ and σ under tensile strain holding in the creep-fatigue tests at $\dot{\varepsilon} = 10^{-3} \text{ s}^{-1}$ with $t_h = 60 \text{ min}$ at: (a) $\Delta\varepsilon = 0.01$ and (b) $\Delta\varepsilon = 0.007$

To discuss the effect of cyclic hardening on the stress relaxation in more detail, the tensile peak stress σ_{+peak} and a representative stress in the Norton stage, σ_{10E-7} , are plotted against N in Fig. 3. Here, σ_{10E-7} denotes the stress at which $\dot{\varepsilon}^{in}$ became equal to 10^{-7} s^{-1} under strain holding. As seen in the figure, σ_{10E-7} increased slightly with N compared to σ_{+peak} , which increased noticeably from $N = 1$ to $N \approx 20$. This confirms that the Norton stage had much less cyclic hardening than the transient stage. It is physically valid to assume that cyclic hardening is primarily caused by an increase in dislocation density, which occurs in grains and is responsible for viscoplasticity. It is thus suggested that the Norton stage is rate-controlled by inelastic deformation mechanisms such as diffusion creep and grain boundary sliding, which are different from viscoplasticity. Therefore, to simulate the creep-fatigue tests performed in this study, the inelastic strain-rate under strain holding should be decomposed into a viscoplastic component responsible for the transient stage and a creep component responsible for the Norton stage.

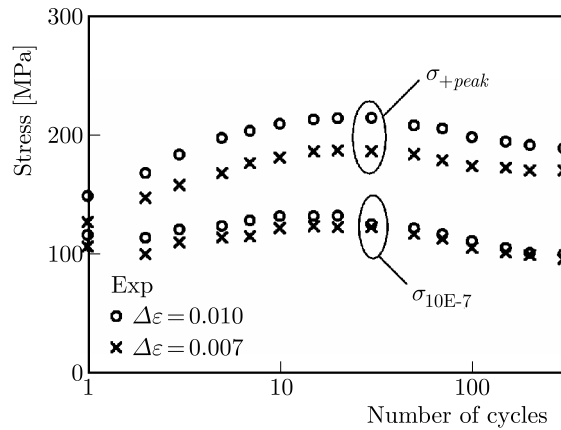


Fig. 3. Variations in σ_{+peak} and σ_{10E-7} with N and $\Delta\varepsilon$ in the creep-fatigue tests at $\dot{\varepsilon} = 10^{-3} \text{ s}^{-1}$ with $t_h = 60 \text{ min}$

3. Constitutive model

Because the inelastic-strain rate under strain holding is decomposed into viscoplastic and creep components (Section 2.2), it is assumed that the strain-rate $\dot{\varepsilon}$ is decomposed into an elastic component $\dot{\varepsilon}^e$ obeying Hooke's law, a viscoplastic component $\dot{\varepsilon}^p$ associated with combined

isotropic-kinematic hardening, and a creep component $\dot{\boldsymbol{\varepsilon}}^c$ satisfying Norton's law¹

$$\dot{\boldsymbol{\varepsilon}} = \dot{\boldsymbol{\varepsilon}}^e + \dot{\boldsymbol{\varepsilon}}^p + \dot{\boldsymbol{\varepsilon}}^c \quad \boldsymbol{\sigma} = \mathbf{D}^e : \boldsymbol{\varepsilon}^e \quad (3.1)$$

and

$$\dot{\boldsymbol{\varepsilon}}^p = \frac{3}{2} \dot{\varepsilon}_0^p \left[\frac{y_{eq}}{(1 + \theta^p) \sigma_0^p} \right]^m \frac{\mathbf{s} - \mathbf{a}}{y_{eq}} \quad \dot{\boldsymbol{\varepsilon}}^c = \frac{3}{2} \dot{\varepsilon}_0^c \left[\frac{\sigma_{eq}}{(1 + \theta^c) \sigma_0^c} \right]^n \frac{\mathbf{s}}{\sigma_{eq}} \quad (3.2)$$

where $\boldsymbol{\sigma}$ is the stress, \mathbf{D}^e is the isotropic elastic stiffness, $\dot{\varepsilon}_0^p$, σ_0^p , and m are viscoplastic parameters, \mathbf{s} is the deviatoric stress, \mathbf{a} is the deviatoric back stress, $\dot{\varepsilon}_0^c$, σ_0^c , and n are creep parameters, θ^p and θ^c are variables representing the effects of cyclic hardening on $\dot{\boldsymbol{\varepsilon}}^p$ and $\dot{\boldsymbol{\varepsilon}}^c$, respectively, and y_{eq} and σ_{eq} are defined as

$$y_{eq} = \sqrt{\frac{3}{2}} \|\mathbf{s} - \mathbf{a}\| \quad \sigma_{eq} = \sqrt{\frac{3}{2}} \|\mathbf{s}\| \quad (3.3)$$

It is further assumed that the back stress can be decomposed into M parts (Chaboche *et al.*, 1979; Chaboche, 2008)², and that cyclic hardening equally affects the drag and back stresses (Ohno *et al.*, 1998, 2017a)³. In addition, it is assumed that the evolution of each part of the back stress is represented by the Ohno-Wang model (Ohno and Wang, 1993). We thus use the following equations for \mathbf{a}

$$\begin{aligned} \mathbf{a} &= (1 + \theta^p) \tilde{\mathbf{a}} \quad \tilde{\mathbf{a}} = \sum_{i=1}^M h^{(i)} \mathbf{b}^{(i)} \\ \dot{\mathbf{b}}^{(i)} &= \frac{2}{3} \dot{\boldsymbol{\varepsilon}}^p - \zeta^{(i)} (\zeta^{(i)} b_{eq}^{(i)})^{k^{(i)}} \left\langle \dot{\boldsymbol{\varepsilon}}^p : \frac{\mathbf{b}^{(i)}}{b_{eq}^{(i)}} \right\rangle \mathbf{b}^{(i)} \end{aligned} \quad (3.4)$$

where $\tilde{\mathbf{a}}$ is the deviatoric back stress free of the effect of cyclic hardening, $\mathbf{b}^{(i)}$ is the i -th non-dimensional back stress related to $\tilde{\mathbf{a}}$, $h^{(i)}$ is the i -th incipient kinematic hardening modulus, $\zeta^{(i)}$ and $k^{(i)}$ are parameters of the back stress evolution, and $b_{eq}^{(i)}$ is defined as

$$b_{eq}^{(i)} = \sqrt{\frac{3}{2}} \|\mathbf{b}^{(i)}\| \quad (3.5)$$

Austenitic stainless steels exhibit a marked dependence of cyclic hardening on the strain range (e.g., Chaboche *et al.*, 1979; Ohno, 1982; Kang *et al.*, 2003). Hence, we assume the following equation for θ^p in Eqs. (3.2)₁ and (3.4)₁

$$\theta^p = \phi(\Delta \varepsilon^p) \kappa \quad (3.6)$$

where $\phi(\Delta \varepsilon^p)$ is the material function representing the dependence of cyclic hardening on the viscoplastic strain range $\Delta \varepsilon^p$, and κ is the cyclic hardening parameter, which evolves as

$$\dot{\kappa} = L(\kappa_0 - \kappa) \dot{p} - R \kappa^\omega \quad (3.7)$$

Here, L and κ_0 are strain hardening parameters, R and ω are thermal recovery parameters, and \dot{p} denotes the accumulating rate of viscoplastic strain

$$\dot{p} = \sqrt{\frac{2}{3}} \|\dot{\boldsymbol{\varepsilon}}^p\| \quad (3.8)$$

¹Eqs. (3.1)-(3.3) based on the decomposition of the inelastic strain-rate into viscoplastic and creep components were assumed for solders in the absence of cyclic hardening (Kobayashi *et al.*, 2003).

²The multiple back stresses can be transformed to the multiple surfaces proposed by Mróz (1967), as shown by Ohno and Wang (1991).

³Trampczynski (1988) experimentally showed the effect of cyclic hardening on the back stress using the technique of successive unloading.

Equation (3.7) does not represent the cyclic softening following cyclic hardening that was observed in the creep-fatigue tests (Fig. 3). However, this limitation is allowed for the purpose of simulating the cyclic hardening and stress relaxation behavior discussed in Section 2.2.

The creep strain-rate $\dot{\epsilon}^c$ may be affected by cyclic hardening because grain boundary sliding can be accommodated with dislocation viscoplasticity as demonstrated by Crossman and Ashby (1975). This effect is represented by θ^c in Eq. (3.2)₂. We assume

$$\theta^c = c\theta^p \quad (3.9)$$

where c is a parameter representing the effect of cyclic hardening on $\dot{\epsilon}^c$.

The constitutive model described in this Section needs $\Delta\epsilon^p$ to be evaluated during computation. We can use the resetting scheme of a viscoplastic strain surface to correctly evaluate $\Delta\epsilon^p$ (Ohno *et al.*, 2017b). This plastic-strain-range (PSR) surface has the same expression as the memory surface of Chaboche *et al.* (1979), and follows the same evolution rule as that of Ohno (1982). In the resetting scheme, however, the PSR surface is reset to a point and re-evolves every cycle under cyclic loading. The resetting thus provides a definite value for the evolution parameter η of the PSR surface irrespective of the amount of cyclic hardening, pre-straining, and ratcheting. In this study, η is set to 0.4, as verified by Ohno *et al.* (2017b).

4. Determination of material parameters

Table 4 gives the material parameters used in this study, which were determined using the following procedure. In the table, E and ν denote Young's modulus and Poisson's ratio, respectively.

Table 4. Material parameters with stress in MPa, strain in mm/mm, and time in s

Elastic	$E = 1.44 \cdot 10^5, \nu = 0.30$
Viscoplastic	$\dot{\epsilon}_0^p = 10^{-3}, \sigma_0^p = 7.53 \cdot 10^1, m = 20.0$
Creep	$\dot{\epsilon}_0^c = 10^{-3}, \sigma_0^c = 2.72 \cdot 10^2, n = 10.9$
Kinematic hardening	$h^{(1)} = 1.63 \cdot 10^5, h^{(2)} = 3.81 \cdot 10^4, h^{(3)} = 9.27 \cdot 10^3,$ $h^{(4)} = 1.59 \cdot 10^3, h^{(5)} = 7.24 \cdot 10^2$
	$\zeta^{(1)} = 6.67 \cdot 10^3, \zeta^{(2)} = 2.00 \cdot 10^3, \zeta^{(3)} = 6.67 \cdot 10^2,$ $\zeta^{(4)} = 2.50 \cdot 10^2, \zeta^{(5)} = 1.25 \cdot 10^2$
	$k^{(i)} = 3.0, (i = 1, 2, \dots, 5)$
Cyclic hardening	$\kappa_0 = 0.726, L = 13.4, R = 0.411, \omega = 13.6, c = 0.32$
	$\lambda = 4.00 \cdot 10^2, \Delta\epsilon_0^p = 6.61 \cdot 10^{-3}$
PSR surface evolution	$\eta = 0.40$

1. The initial tensile curve at $\dot{\epsilon} = 10^{-3} \text{ s}^{-1}$ was fitted, as shown in Fig. 4. This fitting was made using in-house developed Excel software assuming that cyclic hardening and creep strain-rate were negligible under initial tensile loading. The initial tensile curve was on-line fitted by numerically integrating the constitutive equations in the Excel software. Among the parameters, $\dot{\epsilon}_0^p$ was selected to be $\dot{\epsilon}_0^p = 10^{-3} \text{ s}^{-1}$, and $k^{(i)}$, responsible for ratcheting, was set to 3.0 (Ohno *et al.*, 2016a). The viscoplasticity exponent m had almost no influence on $\dot{\epsilon}^p$ at $\dot{\epsilon} = 10^{-3} \text{ s}^{-1}$ because we selected $\dot{\epsilon}_0^p = 10^{-3} \text{ s}^{-1}$ in Eq. (3.2)₁. Thus, $\sigma_0^p, M, h^{(i)}$, and $\zeta^{(i)}$ were determined.
2. Variations in σ_{+peak} with N in the fatigue tests at $\dot{\epsilon} = 10^{-3} \text{ s}^{-1}$ with $\Delta\epsilon = 0.01, 0.007$ and 0.004 were used to determine L, κ_0 , and $\phi(\Delta\epsilon^p)$. It is shown that the constitutive

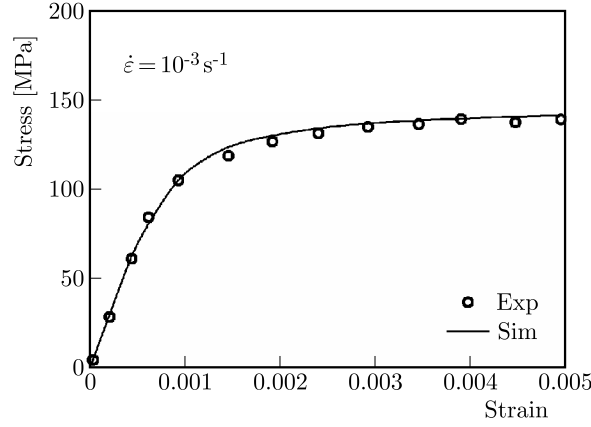


Fig. 4. Tensile stress-strain relationship at $\dot{\varepsilon} = 10^{-3} \text{ s}^{-1}$

model gives the following relationships to σ_{+peak} in the absence of thermal recovery of cyclic hardening (Appendix A)⁴

$$\frac{\sigma_{+peak} - \sigma_{+peak}^{ini}}{\sigma_{+peak}^{sat} - \sigma_{+peak}^{ini}} = 1 - \exp(-Lp) \quad \frac{\sigma_{+peak}^{sat} - \sigma_{+peak}^{ini}}{\sigma_{+peak}^{ini}} = \phi(\Delta\varepsilon^p)\kappa_0 \quad (4.1)$$

where σ_{+peak}^{ini} and σ_{+peak}^{sat} indicate the initial and saturated values of σ_{+peak} . Equations (4.1) were used to determine L , κ_0 , and $\phi(\Delta\varepsilon^p)$ (Figs. 5a and 5b). The following form of $\phi(\Delta\varepsilon^p)$ was found appropriate in the present study

$$\phi(\Delta\varepsilon^p) = \frac{1 - \exp(-\lambda\Delta\varepsilon^p)}{1 - \exp(-\lambda\Delta\varepsilon_0^p)} \quad (4.2)$$

where λ is a fitting parameter, and $\Delta\varepsilon_0^p$ is selected to be equal to the saturated viscoplastic strain range in the fatigue test at $\dot{\varepsilon} = 10^{-3} \text{ s}^{-1}$ and $\Delta\varepsilon = 0.01$.

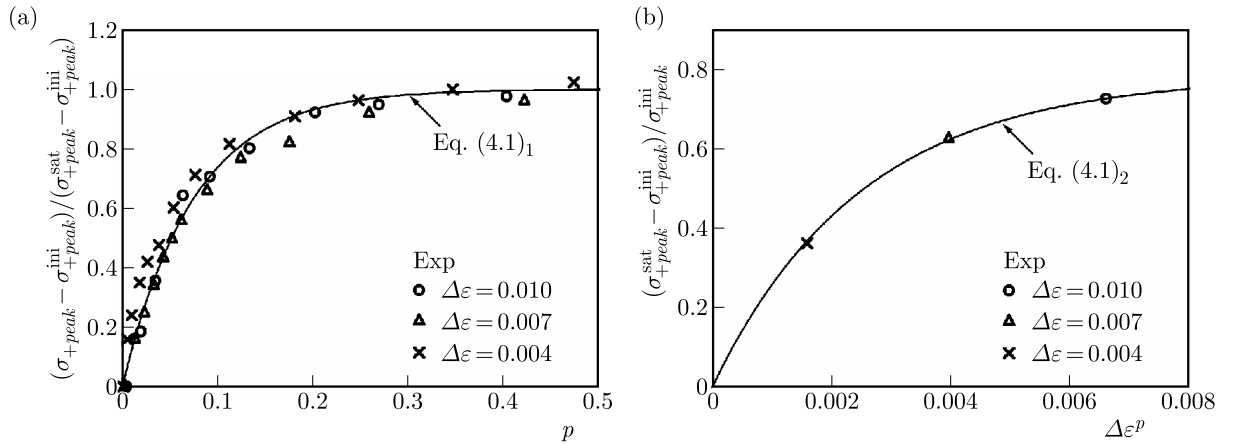


Fig. 5. (a) Change in σ_{+peak} with the accumulated viscoplastic strain p and (b) dependence of saturated σ_{+peak} on the viscoplastic strain range $\Delta\varepsilon^p$ in the fatigue tests at $\dot{\varepsilon} = 10^{-3} \text{ s}^{-1}$

- The thermal recovery parameters R and ω in Eq. (3.7) were determined to represent the effect of strain hold time t_h on σ_{+peak} at $N \approx 20$ in the creep-fatigue tests at $\dot{\varepsilon} = 10^{-3} \text{ s}^{-1}$ with $t_h = 10 \text{ min}$ and 60 min at $\Delta\varepsilon = 0.01$ (Appendix B).

⁴Goodall *et al.* (1981) first showed Eq. (4.1)₁ for fitting the tensile peak stress data of 316 stainless steel at 600°C.

4. The Norton-stage data under strain holding at $N = 1$ and 20 in the creep-fatigue test at $\dot{\epsilon} = 10^{-3} \text{ s}^{-1}$ with $t_h = 60 \text{ min}$ at $\Delta\epsilon = 0.01$ were fitted, as shown by the solid and dashed lines in Fig. 2a. The fitting at $N = 1$ was used to determine σ_0^c and n in Eq. (3.2)₂ by selecting $\dot{\epsilon}_0^c = 10^{-3} \text{ s}^{-1}$ with negligible cyclic hardening, $\theta^c \simeq 0$, at $N = 1$. The fitting at $N = 20$ was then used to estimate c in Eq. (3.9) to reproduce the small increase in σ_{10E-7} depicted in Fig. 3 (Appendix C)

$$c \simeq \frac{\sigma_{10E-7}^{N=20} / \sigma_{10E-7}^{ini} - 1}{\sigma_{+peak}^{N=20} / \sigma_{+peak}^{ini} - 1} \quad (4.3)$$

where $\sigma_{10E-7}^{N=20}$ and $\sigma_{+peak}^{N=20}$ denote the values of σ_{10E-7} and σ_{+peak} at $N = 20$, respectively.

5. The saturated hysteresis loops in the fatigue tests at $\dot{\epsilon} = 10^{-3} \text{ s}^{-1}$ and 10^{-4} s^{-1} at $\Delta\epsilon = 0.01$ were fitted to determine the viscoplasticity exponent m (Fig. 6).

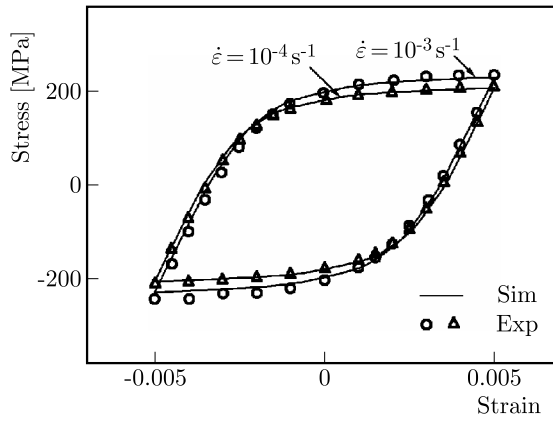


Fig. 6. Saturated stress-strain hysteresis loops in the fatigue tests at $\dot{\epsilon} = 10^{-3} \text{ s}^{-1}$ and 10^{-4} s^{-1} at $\Delta\epsilon = 0.01$

5. Comparison of simulated and experimental results

The creep-fatigue tests were simulated using the constitutive model described in Section 3 with the material parameters given in Table 4. The constitutive model was implemented in Abaqus using a user subroutine UMAT by extending the UMAT program developed by Ohno *et al.* (2016b, 2017b). From here on, t^* denotes the time elapsed after the onset of strain holding, and σ_{relax} indicates the stress attained at the end of stress relaxation under strain holding. It is restated that the cyclic softening following cyclic hardening is disregarded in the constitutive model. This limitation is allowed in simulating the transient and Norton stages affected differently by cyclic hardening. Accordingly, this Section compares the simulated and experimental results with emphasis on the stress relaxation behavior under strain holding at cycles where cyclic softening was not significant.

The tensile peak stress variations and stress relaxation curves observed in the creep-fatigue tests at $\dot{\epsilon} = 10^{-3} \text{ s}^{-1}$ with $t_h = 60 \text{ min}$ at $\Delta\epsilon = 0.007$ and 0.01 were simulated with good accuracy, as shown in Figs. 7 and 8. The variations in σ_{relax} with N in the two tests were also simulated well, though σ_{relax} was slightly inaccurate in the case of $\Delta\epsilon = 0.007$ (Fig. 7). The stress relaxation became more significant as cyclic hardening developed in both the experimental and simulated results. Ignoring $\dot{\epsilon}^c$ in the constitutive model did not affect the transient stage under strain holding, but resulted in considerably under-predicting the stress relaxation, as shown in Figs. 9a and 9b in the case of $\Delta\epsilon = 0.01$ with $t_h = 60 \text{ min}$. Hence, accurate simulation of the

stress relaxation shown in Figs. 7 and 8 was owing to the dominance of $\dot{\epsilon}^p$ and $\dot{\epsilon}^c$ in the transient and Norton stages, respectively. Therefore, the addition of $\dot{\epsilon}^c$ to $\dot{\epsilon}^p$ and the Norton type of creep equation expressed as Eq. (3.2)₂ for $\dot{\epsilon}^c$ enabled accurate simulation of the stress relaxation under strain holding.

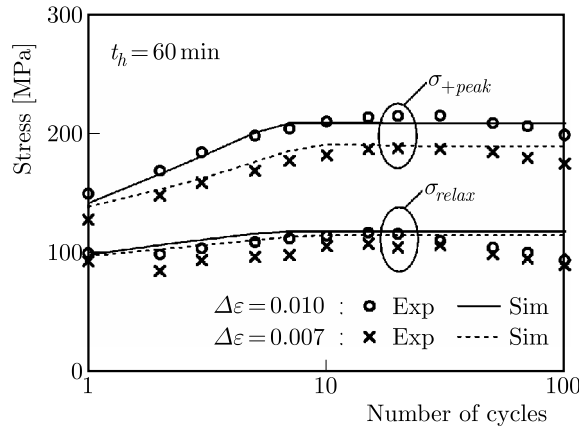


Fig. 7. Variations in σ_{+peak} and σ_{relax} with N and $\Delta\epsilon$ under creep-fatigue loading at $\dot{\epsilon} = 10^{-3} \text{ s}^{-1}$ with $t_h = 60 \text{ min}$

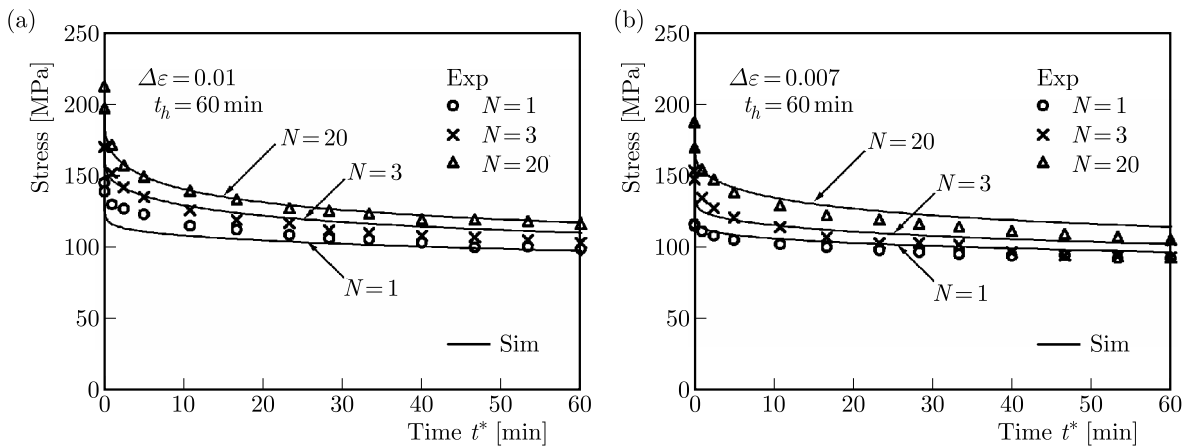


Fig. 8. Stress relaxation under creep-fatigue loading at $\dot{\epsilon} = 10^{-3} \text{ s}^{-1}$ with $t_h = 60 \text{ min}$ at: (a) $\Delta\epsilon = 0.01$ and (b) $\Delta\epsilon = 0.007$

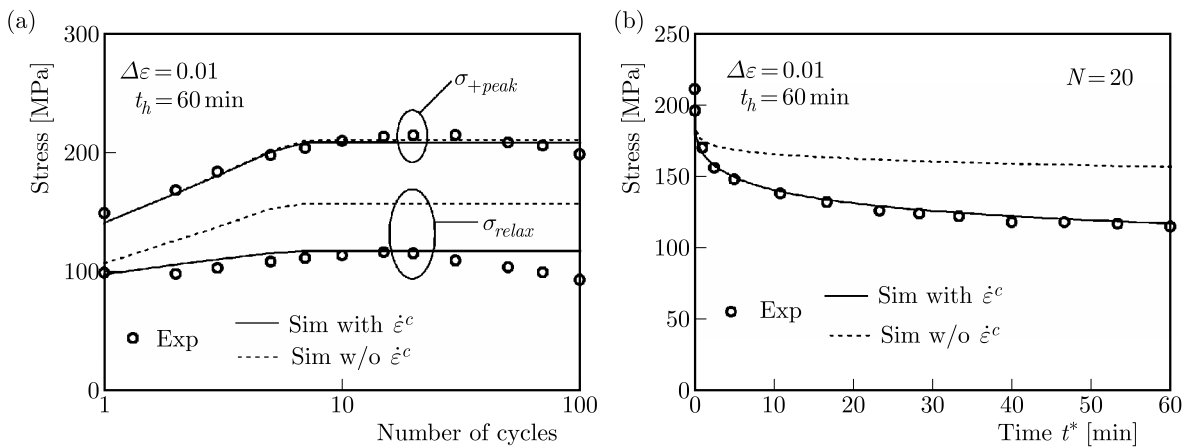


Fig. 9. Effect of the creep strain-rate on (a) variations in σ_{+peak} and σ_{relax} with N and (b) stress relaxation at $N = 20$ under creep-fatigue loading at $\dot{\epsilon} = 10^{-3} \text{ s}^{-1}$ with $t_h = 60 \text{ min}$ at $\Delta\epsilon = 0.01$

The effect of cyclic hardening on $\dot{\epsilon}^c$ was taken into account through θ^c in Eq. (3.2)₂ in the constitutive model, and θ^c was assumed to be proportional to θ^p , $\theta^c = c\theta^p$, in Eq. (3.9). Figure 10 demonstrates the effect of c on the stress relaxation in the simulation of the creep-fatigue test at $\dot{\epsilon} = 10^{-3} \text{ s}^{-1}$ with $t_h = 60 \text{ min}$ at $\Delta\epsilon = 0.01$. As shown in Fig. 10b, the stress relaxation at $N = 20$ was slightly over-predicted if $c = 0$, whereas it was noticeably under-predicted if $c = 1$. If $c = 0$ cyclic hardening had no effect on $\dot{\epsilon}^c$ through θ^c , and if $c = 1$ cyclic hardening had the same effect on $\dot{\epsilon}^c$ and $\dot{\epsilon}^p$. Selecting $c = 0.32$ (i.e., $\theta^c \approx \theta^p/3$) was found to be appropriate for simulating the stress relaxation. It was thus shown that $\dot{\epsilon}^c$ was much less affected by cyclic hardening than $\dot{\epsilon}^p$, leading to suggestion that inelastic deformation mechanisms different from viscoplasticity started to operate shortly after the onset of strain holding, as discussed in Section 2.

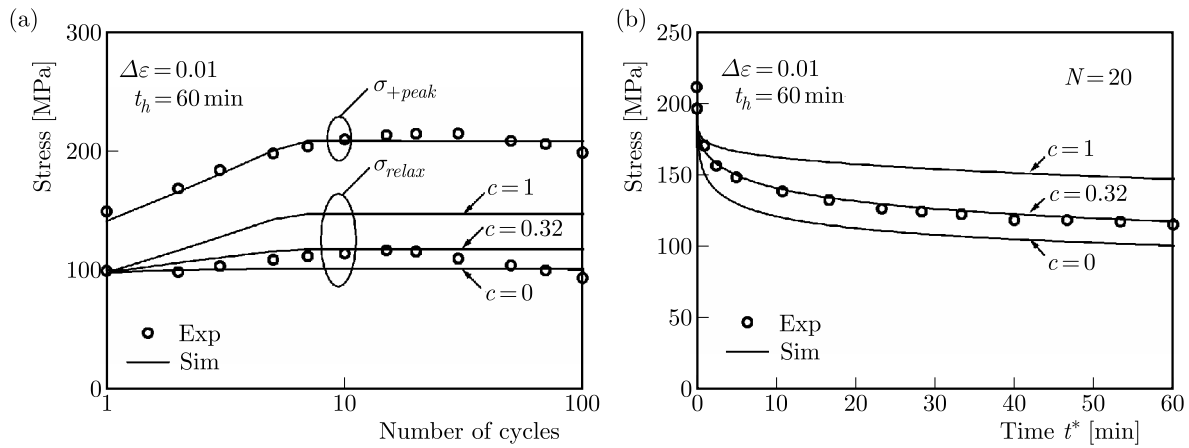


Fig. 10. Effect of the cyclic hardening parameter c on (a) variations in σ_{+peak} and σ_{relax} with N and (b) stress relaxation at $N = 20$ under creep-fatigue loading at $\dot{\epsilon} = 10^{-3} \text{ s}^{-1}$ with $t_h = 60 \text{ min}$ at $\Delta\epsilon = 0.01$

Figure 11 illustrates the effects of t_h on σ_{+peak} and σ_{relax} measured in the creep-fatigue tests at $\dot{\epsilon} = 10^{-3} \text{ s}^{-1}$ with $t_h = 10 \text{ min}$ and 60 min at $\Delta\epsilon = 0.01$. In Fig. 11a, σ_{+peak} for $t_h = 0$ is shown for reference. In the two tests with $t_h = 10$ and 60 min , the effect of t_h on σ_{+peak} appeared slightly after the near-saturation of cyclic hardening, whereas the effect on σ_{relax} became rather large with increasing N before the near-saturation of cyclic hardening. These experimental features were well reproduced by the constitutive model. The creep-fatigue tests at $\Delta\epsilon = 0.007$ with $t_h = 10$ and 60 min were also simulated accurately, though not shown here to save the space.

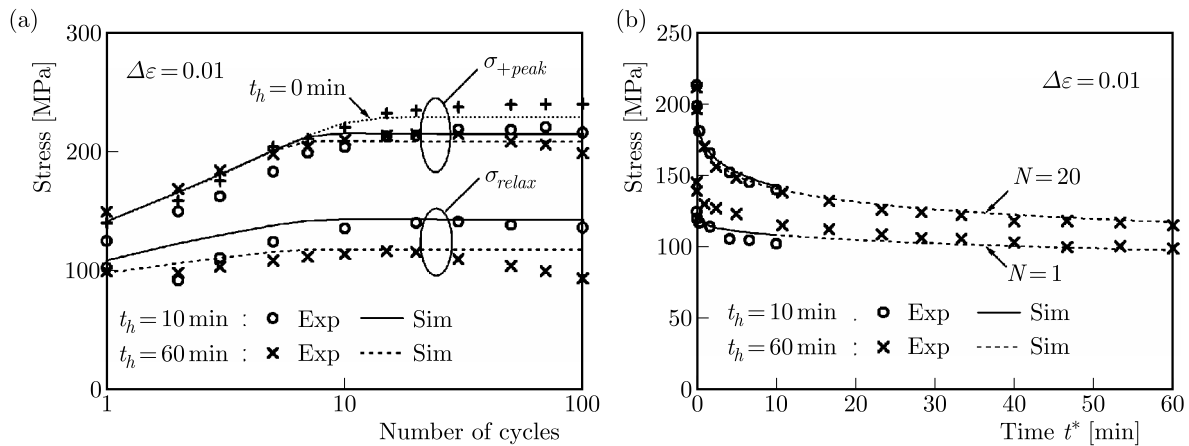


Fig. 11. Effect of the strain hold time t_h on (a) variations in σ_{+peak} and σ_{relax} with N and (b) stress relaxation at $N = 1$ and 20 under creep-fatigue loading at $\dot{\epsilon} = 10^{-3} \text{ s}^{-1}$ at $\Delta\epsilon = 0.01$

The slight effect of t_h on σ_{+peak} described above was successfully simulated because of the thermal recovery of cyclic hardening represented by the second term on the right-hand side of Eq. (3.7). Here, it is noted that the thermal recovery exponent ω in Eq. (3.7) is large (Table 4); as a result, the thermal recovery of cyclic hardening occurred non-linearly to yield the slight effect of t_h on σ_{+peak} despite the factor of six difference in t_h in the two tests with $t_h = 10$ and 60 min. However, the comparatively large effect of t_h on σ_{relax} was well simulated owing to $\dot{\epsilon}^c$ expressed as Eq. (3.2)₂, as depicted in Fig. 11b. Because σ_{relax} denotes the stress attained at the end of stress relaxation, it is seen from Fig. 11b that the difference in σ_{relax} in the two tests was caused by the stress relaxation during $10 \leq t^* \leq 60$ min in the test with $t_h = 60$ min; the stress relaxation from $t^* = 10$ min to $t^* = 60$ min was about 10 MPa and 25 MPa at $N = 1$ and 20, respectively. The stress relaxation during $10 \leq t^* \leq 60$ min was in the Norton stage. Therefore, the difference in σ_{relax} in the two tests was well simulated because of the Norton type of creep equation expressed as Eq. (3.2)₂ for $\dot{\epsilon}^c$.

The stress relaxation under strain holding became larger with the development of cyclic hardening or with the increase in the strain hold time, as shown in this Section. Goodall *et al.* (1981) observed this feature in creep-fatigue tests of 316 stainless steel at 600°C, and Nouailhas (1989) simulated the tests using a unified model of cyclic viscoplasticity. However, Goodall *et al.* (1981) and Nouailhas (1989) did not notice the transient and Norton stages in stress relaxation, which were studied in this work; moreover, Nouailhas (1989) did not show stress relaxation curves under strain holding.

6. Concluding remarks

In this work, the cyclic hardening and stress relaxation behavior of SUS316HTP was experimentally and numerically studied under cyclic loading with tensile strain holding at 700°C. Creep-fatigue tests were performed to show that the slow stress-relaxation stage satisfying Norton's law followed the transient stress-relaxation stage under strain holding. The Norton stage was much less affected by cyclic hardening than the transient stage. Since the transient stage was rate-controlled by viscoplasticity in the presence of the increase in dislocation density in grains to cause cyclic hardening, it was suggested that inelastic deformation mechanisms, such as diffusion creep and grain boundary sliding, operated in the Norton stage.

A cyclic viscoplastic-creep model was developed based on the experimental results described above. In this model, the inelastic strain-rate $\dot{\epsilon}^{in}$ was decomposed into viscoplastic and creep strain-rates, which were dominant in the transient and Norton stages in stress relaxation, respectively. The viscoplastic strain-rate $\dot{\epsilon}^p$ was expressed by incorporating the noticeable effect of cyclic hardening on the drag and back stresses, while the creep strain-rate $\dot{\epsilon}^c$ was ruled by Norton's law and was assumed to be weakly affected by cyclic hardening. The material parameters in the constitutive model were determined to verify the decomposition of $\dot{\epsilon}^{in}$ into $\dot{\epsilon}^p$ and $\dot{\epsilon}^c$, which were affected differently by cyclic hardening.

Finally, the cyclic viscoplastic-creep model was used to simulate the creep-fatigue tests performed in the present study. The constitutive model successfully simulated the stress relaxation behavior in the presence of cyclic hardening, and the stress relaxation in the simulation became more significant as cyclic hardening developed, as observed in the creep-fatigue tests. This was owing to the dominance of $\dot{\epsilon}^p$ and $\dot{\epsilon}^c$ in the transient and Norton stages, respectively, resulting in the transient stage being much more affected by cyclic hardening than the Norton stage. The stress-relaxation curves were also accurately simulated, and the effect of t_h on the stress relaxation was attributed to $\dot{\epsilon}^c$ in the Norton stage.

Appendix A. Change in tensile peak stress

Let us consider rapid, uniaxial cyclic loading with $t_h = 0$ to ignore $\dot{\epsilon}^c$. On the tension side, Eqs. (3.2)₁, (3.4)₁ and (3.6) give the following equation in the viscoplastic region, where $\dot{\epsilon}^p \simeq \dot{\epsilon}$

$$\sigma \simeq (1 + \phi\kappa) \left[\sigma_0^p \left(\frac{\dot{\epsilon}}{\dot{\epsilon}_0^p} \right)^{1/m} + \tilde{\alpha} \right] \quad (\text{A.1})$$

where $\tilde{\alpha}$ indicates the uniaxial component of the cyclic-hardening-free back stress. Because cyclic hardening is negligibly small under the initial loading to the first tensile peak, Eq. (A.1) allows the initial tensile peak stress σ_{+peak}^{ini} to be expressed as

$$\sigma_{+peak}^{ini} \simeq \sigma_0^p \left(\frac{\dot{\epsilon}}{\dot{\epsilon}_0^p} \right)^{1/m} + \tilde{\alpha}_{+peak}^{ini} \quad (\text{A.2})$$

where $\tilde{\alpha}_{+peak}^{ini}$ denotes the initial peak value of $\tilde{\alpha}$. Here, let us assume that the tensile peak value $\tilde{\alpha}_{+peak}$ does not change from $\tilde{\alpha}_{+peak}^{ini}$ with the increasing N because $\tilde{\alpha}$ is regarded as the back stress in the absence of cyclic hardening. Eqs. (A.1) and (A.2) thus provide

$$\sigma_{+peak} \simeq (1 + \phi\kappa) \sigma_{+peak}^{ini} \quad (\text{A.3})$$

When the thermal recovery of cyclic hardening is negligible under rapid cyclic loading, Eq. (3.7) is integrated to give

$$\kappa = \kappa_0 [1 - \exp(-Lp)] \quad (\text{A.4})$$

Hence, Eq. (A.3) leads to Eqs. (4.1).

Appendix B. Determination of thermal recovery parameters

Let us consider rapid, uniaxial cyclic loading with $t_h \neq 0$ to determine the thermal recovery parameters R and ω in Eq. (3.7). Let us suppose that κ decreases from κ_{+peak} to κ_{relax} under tensile strain holding, and that κ increases from κ_{relax} to κ_{+peak} under rapid cyclic loading in one cycle. Here, we assume that the second and first terms on the right-hand side in Eq. (3.7) are active under tensile strain holding and rapid cyclic loading, respectively, to provide

$$\begin{aligned} \kappa_{relax} &= [\kappa_{+peak}^{1-\omega} + R(\omega - 1)t_h]^{1/(1-\omega)} \\ \kappa_{+peak} &= \kappa_{relax} + (\kappa_0 - \kappa_{relax})[1 - \exp(-Lp^*)] \end{aligned} \quad (\text{B.1})$$

where p^* denotes the change in p due to rapid cyclic loading in one cycle

$$p^* = 2 \left(\Delta\epsilon - \frac{\sigma_{relax} + |\sigma_{-peak}|}{E} \right) \quad (\text{B.2})$$

To determine R and ω using Eqs. (B.1), the tensile peak stresses at $N = 30$ in the creep-fatigue tests at $\dot{\epsilon} = 10^{-3} \text{ s}^{-1}$ with $t_h = 10 \text{ min}$ and 60 min at $\Delta\epsilon = 0.01$ are used to evaluate $\kappa_{+peak10}$ and $\kappa_{+peak60}$ using Eq. (A.3) as

$$\kappa_{+peak10} = \frac{1}{\phi} \left(\frac{\sigma_{+peak10}}{\sigma_{+peak}^{ini}} - 1 \right) \quad \kappa_{+peak60} = \frac{1}{\phi} \left(\frac{\sigma_{+peak60}}{\sigma_{+peak}^{ini}} - 1 \right) \quad (\text{B.3})$$

where the subscripts 10 and 60 indicate $t_h = 10 \text{ min}$ and 60 min . Then, $\kappa_{relax10}$ and $\kappa_{relax60}$ are calculated using Eq. (B.1)₂. Here, it is noted that ϕ , κ_0 , and L are determined in Step 2 in Section 4. Finally, R and ω are evaluated by numerically solving the following equations derived from Eq. (B.1)₁

$$\begin{aligned} \kappa_{relax10}^{1-\omega} - \kappa_{+peak10}^{1-\omega} &= R(\omega - 1)t_{h10} & t_{h10} &= 600 \text{ s} \\ \kappa_{relax60}^{1-\omega} - \kappa_{+peak60}^{1-\omega} &= R(\omega - 1)t_{h60} & t_{h60} &= 3600 \text{ s} \end{aligned} \quad (\text{B.4})$$

Appendix C. Cyclic hardening parameter for creep strain-rate

To evaluate c in Eq. (3.9), we consider the changes in σ_{+peak} and σ_{10E-7} with N in the creep-fatigue test at $\dot{\varepsilon} = 10^{-3} \text{ s}^{-1}$ with $t_h = 60 \text{ min}$ at $\Delta\varepsilon = 0.01$. For σ_{+peak} in this creep-fatigue test, Eq. (A.3) is valid, though κ is affected by $t_h \neq 0$. For σ_{10E-7} , Eqs. (3.2)₂, (3.6) and (3.9) provide

$$\sigma_{10E-7} = (1 + c\phi\kappa)\sigma_{10E-7}^{ini} \quad \sigma_{10E-7}^{ini} = \sigma_0^c \left(\frac{\dot{\varepsilon}^c}{\dot{\varepsilon}_0^c} \right)^{1/n} \quad (\text{C.1})$$

where $\dot{\varepsilon}^c = 10^{-7} \text{ s}^{-1}$. The change in κ is considered small under strain holding when ω is large in Eq. (3.7). Thus, using Eqs. (A.3) and (C.1)₁, c is estimated as

$$c \simeq \frac{\sigma_{10E-7}/\sigma_{10E-7}^{ini} - 1}{\sigma_{+peak}/\sigma_{+peak}^{ini} - 1} \quad (\text{C.2})$$

Acknowledgment

We thank Melissa Gibbons, PhD, from Edanz Group (www.edanzediting.com/ac) for editing a draft of this manuscript.

References

1. AINSWORTH R.A., 2006, R5 procedures for assessing structural integrity of components under creep and creep-fatigue conditions, *International Materials Reviews*, **51**, 107-126
2. CHABOCHE J.L., 2008, A review of some plasticity and viscoplasticity constitutive theories, *International Journal of Plasticity*, **24**, 1642-1693
3. CHABOCHE J.L., DANG VAN K., CORDIER G., 1979, Modelization of the strain memory effect on the cyclic hardening of 316 stainless steel, *Proceedings of the 5th International Conference on Structural Mechanics in Reactor Technology*, **L**, L11/3
4. CROSSMAN F.W., ASHBY M.F., 1975, The non-uniform flow of polycrystals by grain-boundary sliding accommodated by power-law creep, *Acta Metallurgica*, **23**, 425-440
5. GOODALL I.W., HALES R., WALTERS D.J., 1981, On constitutive relations and failure criteria of an austenitic steel under cyclic loading at elevated temperature, *Creep in Structures*, Springer-Verlag, 103-127
6. HALES R., 1980, A quantitative metallographic assessment of structural degradation of type 316 stainless steel during creep-fatigue, *Fatigue of Engineering Materials and Structures*, **3**, 339-356
7. HALES R., 1983, A method of creep damage summation based on accumulated strain for the assessment of creep-fatigue endurance, *Fatigue of Engineering Materials and Structures*, **6**, 121-135
8. INOUE T., IGARI T., OKAZAKI M., SAKANE M., TOKIMASA K., 1989, Fatigue-creep life prediction of 2.25Cr-1Mo steel by inelastic analysis, *Nuclear Engineering and Design*, **114**, 311-321
9. KANG G., OHNO N., NEBU A., 2003, Constitutive modeling of strain range dependent cyclic hardening, *International Journal of Plasticity*, **19**, 1801-1819
10. KOBAYASHI M., MUKAI M., TAKAHASHI H., OHNO N., KAWAKAMI T., ISHIKAWA T., 2003, Implicit integration and consistent tangent modulus of a time-dependent non-unified constitutive model, *International Journal for Numerical Methods in Engineering*, **58**, 1523-1543
11. KRAUSZ A.S., KRAUSZ K., 1996, *Unified Constitutive Laws of Plastic Deformation*, Academic Press, San Diego

12. MILLER A., 1976, An inelastic constitutive model for monotonic, cyclic, and creep deformation: Part 1 – equations development and analytical procedures, *Journal of Engineering Materials and Technology*, **98**, 97-105
13. MRÓZ Z., 1967, On the description of anisotropic workhardening, *Journal of the Mechanics and Physics of Solids*, **15**, 163-175
14. NAM S.W., 2002, Assessment of damage and life prediction of austenitic stainless steel under high temperature creep-fatigue interaction condition, *Materials Science and Engineering A*, **322**, 64-72
15. NOUAILHAS D., 1989, Unified modelling of cyclic viscoplasticity: Application to austenitic stainless steels, *International Journal of Plasticity*, **5**, 501-520
16. OHNO N., 1982, A constitutive model of cyclic plasticity with a nonhardening strain region, *Journal of Applied Mechanics*, **49**, 721-727
17. OHNO N., ABDEL-KARIM M., KOBAYASHI M., IGARI T., 1998, Ratchetting characteristics of 316FR steel at high temperature, Part I: strain-controlled ratchetting experiments and simulations, *International Journal of Plasticity*, **14**, 355-372
18. OHNO N., MIZUSHIMA S., OKUMURA D., TANIE H., 2016a, Warpage variation analysis of Si/solder/Cu layered plates subjected to cyclic thermal loading, *Advanced Methods of Continuum Mechanics for Materials and Structures, Advanced Structured Materials*, **60**, 185-204
19. OHNO N., TSUDA M., SUGIYAMA H., OKUMURA D., 2016b, Elastic-viscoplastic implicit integration algorithm applicable to both plane stress and three-dimensional stress states, *Finite Elements in Analysis and Design*, **109**, 54-64
20. OHNO N., WANG J.D., 1991, Transformation of a nonlinear kinematic hardening rule to a multisurface form under isothermal and nonisothermal conditions, *International Journal of Plasticity*, **7**, 879-891
21. OHNO N., WANG J.D., 1993, Kinematic hardening rules with critical state of dynamic recovery, Part I: formulation and basic features for ratchetting behavior, *International Journal of Plasticity*, **9**, 375-390
22. OHNO N., YAMAMOTO R., OKUMURA D., 2017a, Thermo-mechanical cyclic hardening behavior of 304 stainless steel at large temperature ranges: Experiments and simulations, *International Journal of Mechanical Sciences* (article in press)
23. OHNO N., YAMAMOTO R., SASAKI T., OKUMURA D., 2017b, Resetting scheme for plastic strain surface in constitutive modeling of cyclic plasticity, *ZAMM – Zeitschrift für Angewandte Mathematik und Mechanik* (article in press, DOI: 10.1002/zamm.201700298)
24. PRIEST R.H., ELLISON E.G., 1981, A combined deformation map-ductility exhaustion approach to creep-fatigue analysis, *Materials Science and Engineering*, **49**, 7-17
25. TAKAHASHI Y., 1998, Evaluation of creep-fatigue life prediction methods for low-carbon nitrogen-added 316 stainless steel, *Journal of Engineering Materials and Technology*, **120**, 119-125
26. TAKAHASHI Y., SHIBAMOTO H., INOUE K., 2008, Study on creep-fatigue life prediction methods for low-carbon nitrogen-controlled 316 stainless steel (316FR), *Nuclear Engineering and Design*, **238**, 322-335
27. TRAMPCZYNSKI W., 1988, The experimental verification of the evolution of kinematic and isotropic hardening in cyclic plasticity, *Journal of the Mechanics and Physics of Solids*, **36**, 417-441
28. YAN X.L., ZHANG X.C., TU S.T., MANNAN S.L., XUAN F.Z., LIN Y.C., 2015, Review of creep-fatigue endurance and life prediction of 316 stainless steels, *International Journal of Pressure Vessels and Piping*, **126-127**, 17-28

MODEL ORDER REDUCTION OF MIKOTA'S VIBRATION CHAIN INCLUDING DAMPING EFFECTS BY MEANS OF PROPER ORTHOGONAL DECOMPOSITION

WOLFGANG E. WEBER

*Chair of Structural Analysis, Helmut-Schmidt-University/University of the Federal Armed Forces Hamburg,
Hamburg, Germany; e-mail: wolfgang.weber@hsu-hh.de*

BERND W. ZASTRAU

*Institute of Mechanics and Shell Structures, Technische Universität Dresden, Dresden, Germany
e-mail: bernd.zastrau@tu-dresden.de*

In engineering disciplines, both in scientific and practical applications, systems with a tremendous number of degrees of freedom occur. Hence, there is a need for reducing the computational effort in investigating these systems. If the system behaviour has to be calculated for many time instances and/or load scenarios, the need for efficient calculations further increases. Model order reduction is a common procedure in order to cope with such large systems. The aim of model order reduction is to reduce the (computational) effort in solving the given task while still keeping main features of the respective system. One approach of model order reduction uses the proper orthogonal decomposition. This approach is applied to Mikota's vibration chain, a linear vibration chain with remarkable properties, where two cases of an undamped and a damped structure are investigated.

Keywords: Mikota's vibration chain, POD, damping, multibody system, mode shape

1. Introduction

Model order reduction (MOR) is a common method in engineering disciplines allowing for efficient calculations of e.g. dynamic behaviour of structures. The basic concept is to reduce the order of the system, for example by reducing the number of degrees of freedom. However, the resulting loss of information should not exceed a certain level. Several techniques for MOR exist. Some of them are physical subspace methods such as Guyan reduction, modal subspace methods or Krylov subspace method (Freund, 2003; Guyan, 1965). While these methods are physically motivated, there are other approaches which do not take physical meaning into consideration. However, these methods still require extraction of main features of the underlying system. One method for this feature extraction is the proper orthogonal decomposition (POD). Once the arbitrary system has been characterised by POD, it is the task of MOR to only take those characteristics into consideration which are needed to adequately describe the (dynamic) behaviour of the system. In this contribution, the model order reduction is applied to a special vibration chain, namely Mikota's vibration chain. Herein, POD is used. Using Mikota's vibration chain has the advantage that its dynamic characteristics have been investigated quite well, such that there exist analytical solutions which serve as reference solutions for the reduced system. Additionally, damping effects are taken into account as some damage phenomena can be modelled by means of damping.

To cope with these tasks, Mikota's vibration chain is introduced in Section 2. A brief description of the approach of model order reduction involving POD is given in Section 3. In Section 4, POD is applied to Mikota's vibration chain. As a next step, a discrete damping element is added

to Mikota's vibration chain. In doing so, the linearity of the system is kept. POD is then used within MOR to approximate the dynamic behaviour of the damped vibration chain in Section 5. Finally, conclusions and an outlook are given with Section 6.

2. Mikota's vibration chain

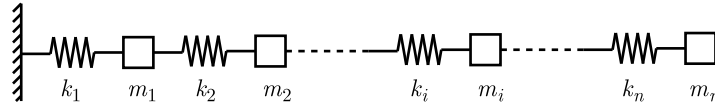


Fig. 1. Undamped vibration chain (Weber *et al.*, 2015)

A linear undamped vibration system with n degrees of freedom (DOF) can be described by

$$\mathbf{M}\ddot{\mathbf{x}}(t) + \mathbf{K}\mathbf{x}(t) = \mathbf{0} \quad (2.1)$$

with $\mathbf{x} = (x_1, \dots, x_i, \dots, x_n)^T$ and $\ddot{\mathbf{x}} = (\ddot{x}_1, \dots, \ddot{x}_i, \dots, \ddot{x}_n)^T$ representing the column matrix of displacements and accelerations, respectively. Herein, \mathbf{M} and \mathbf{K} denote the (diagonal) mass and (tri-diagonal) stiffness matrix, respectively. For a linear vibration chain according to Fig. 1 these matrices are

$$\begin{aligned} \mathbf{M} &= \text{diag}(m_i) \\ \mathbf{K} &= \text{diag}\{(k_1 + k_2, -k_2), \dots, (-k_i, k_i + k_{i+1}, -k_{i+1}), \dots, (-k_n, k_n)\} \end{aligned} \quad (2.2)$$

Mikota set the masses and stiffness coefficients to

$$m_i = \frac{1}{i}m \quad \text{and} \quad k_i = (n - i + 1)k \quad \text{where} \quad i = 1, 2, \dots, n, \quad i \in \mathbb{N} \quad (2.3)$$

cf. (Mikota, 2001). Herein, m is the first mass and k denotes the stiffness of the last spring. Mikota conjectured that this specific vibration chain has eigenfrequencies

$$\Omega_l = l\Omega = l\sqrt{\frac{k}{m}} \quad \text{with again} \quad l = 1, 2, \dots, n, \quad l \in \mathbb{N} \quad (2.4)$$

where $\Omega = \sqrt{k/m}$ is the first eigenfrequency. As can readily be seen, enlarging the system from n DOF to $n + 1$ DOF changes the mass matrix in such a way that the element m_{n+1} is appended at the lower right corner leading to $\mathbf{M}_{n,n} \rightarrow \mathbf{M}_{n+1,n+1}$, while all other entries of the mass matrix remain the same. In contrast, the corresponding matrix $\mathbf{K}_{n+1,n+1}$ is obtained by adding one row and one column at the upper left corner to the former $\mathbf{K}_{n,n}$. For discussion of this opposite behaviour in the set-up of the matrices and the resulting difficulties for proving Mikota's conjecture to be right, one is referred to e.g., (Müller and Hou, 2007; Müller and Gürgöze, 2006). However, two proofs were proposed by Weber *et al.* (2015), Müller and Hou (2007). In order to fully describe Mikota's vibration chain also the mode shapes have to be looked at, which was not the focus of Mikota's work. An approach based on polynomial coefficients is given with (Müller and Hou, 2007), a modification of the well-known Laguerre polynomials allowing for evaluating the mode shapes of Mikota's vibration chain is presented in (Weber *et al.*, 2013). But these approaches are quite laborious and do not reveal a structure in order to obtain general formulae for the mode shapes \mathbf{u}_l . This gap is closed with (Weber *et al.*, 2017), some results of the latter contribution will be used in what follows.

According to Kochendörffer (1963), the coordinates of the eigenvectors of a matrix – and thus the mode shapes dealt with here – can be expressed by polynomials $p_l(i)$ in the coordinate i leading to

$$\mathbf{u}_l = (u_{l,i=1}, u_{l,i=2}, \dots, u_{l,i=n})^T = (p_l(i=1), p_l(i=2), \dots, p_l(i=n))^T \quad (2.5)$$

For an arbitrary n DOF and $l \leq n$, the first three mode shapes of Mikota's vibration chain are represented by the following polynomials

$$\begin{aligned} p_{l=1}(i) &= i \\ p_{l=2}(i) &= i^2 - \frac{2n+1}{3}i \\ p_{l=3}(i) &= i^3 - \frac{3}{5}(2n+1)i^2 + \frac{1}{5}\left[\frac{3}{2}n(n+1) + 1\right]i \end{aligned} \quad (2.6)$$

see (Weber *et al.*, 2017). There, an approach for determining all n polynomials, i.e. all n mode shapes, in a successive manner is suggested, too. For this special vibration chain it could be proved that the polynomial degree of p_l is l . Another neat property of the mode shapes of Mikota's vibration chain is the tri-diagonality of the matrix product $\mathbf{U}^T \mathbf{U}$, where \mathbf{U} denotes the modal matrix. It should be noted that, in general, the mode shapes to different eigenfrequencies are not perpendicular to each other with respect to the (standard) scalar product, as only

$$\mathbf{u}_l \mathbf{M} \mathbf{u}_k^T \begin{cases} = 0 & \text{for } l \neq k \\ \neq 0 & \text{for } l = k \end{cases} \quad \mathbf{u}_l \mathbf{K} \mathbf{u}_k^T \begin{cases} = 0 & \text{for } l \neq k \\ \neq 0 & \text{for } l = k \end{cases} \quad (2.7)$$

holds.

Exemplary, a graphical representation of the eigenvalues $\lambda_l = \Omega_l^2$ and the first five mode shapes of Mikota's vibration chain with $n = 10$ DOF is given in Fig. 2.

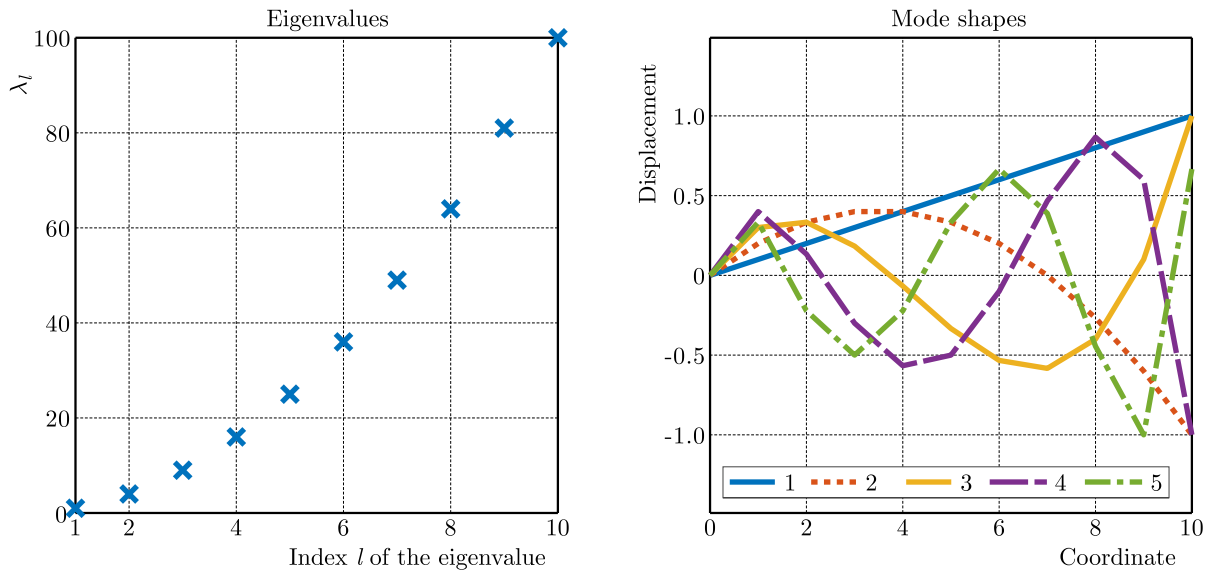


Fig. 2. Eigensolutions of Mikota's vibration chain for $n = 10$ DOF, where only the mode shapes $\mathbf{u}_{l=1}, \dots, \mathbf{u}_{l=5}$ are shown. The displacements between the coordinates i are interpolated linearly, $i = 0$ is at the fixed support according to Fig. 1

3. A brief introduction to MOR by means of POD

The solution of typical large systems of equations, which occur in engineering disciplines, requires a huge computational effort. Thus, strategies are sought which allow for reduction of this

computational cost. One strategy is the model order reduction (MOR). In this strategy, the dimensionality of the underlying mechanical system is reduced while keeping the loss of information within acceptable bounds. For mechanical systems following the system of equations

$$\mathbf{M}\ddot{\mathbf{x}} + \mathbf{D}\dot{\mathbf{x}} + \mathbf{K}\mathbf{x} = \mathbf{f} \quad (3.1)$$

with \mathbf{D} denoting the damping matrix, $\dot{\mathbf{x}}$ the vector of velocities and the vector of applied forces \mathbf{f} , this order reduction can be performed by projecting the involved vectors from the full space \mathbb{R}^n to a lower dimensional space $\mathbb{R}^{n_{red}}$ using a projection matrix Φ of dimension (n, n_{red})

$$\mathbf{x} \approx \Phi \mathbf{x}_{red} \quad \dot{\mathbf{x}} \approx \Phi \dot{\mathbf{x}}_{red} \quad \ddot{\mathbf{x}} \approx \Phi \ddot{\mathbf{x}}_{red} \quad (3.2)$$

Inserting these quantities into Eq. (3.1) leads to

$$\mathbf{M}\Phi\ddot{\mathbf{x}}_{red} + \mathbf{D}\Phi\dot{\mathbf{x}}_{red} + \mathbf{K}\Phi\mathbf{x}_{red} = \mathbf{f} \quad (3.3)$$

Multiplying the transpose of the projection matrix from the left finally yields a reduced problem

$$\begin{aligned} \Phi^T \mathbf{M} \Phi \ddot{\mathbf{x}}_{red} + \Phi^T \mathbf{D} \Phi \dot{\mathbf{x}}_{red} + \Phi^T \mathbf{K} \Phi \mathbf{x}_{red} &= \Phi^T \mathbf{f} \\ \mathbf{M}_{red} \ddot{\mathbf{x}}_{red} + \mathbf{D}_{red} \dot{\mathbf{x}}_{red} + \mathbf{K}_{red} \mathbf{x}_{red} &= \mathbf{f}_{red} \end{aligned} \quad (3.4)$$

The question arises how this projection matrix Φ can be obtained. For reducing the dimensionality, the main features of the system have to be extracted. Within this contribution, the proper orthogonal decomposition (POD) is used to extract the main features and thus shall be introduced in what follows.

In the first step, a suitable amount m of observations is necessary. These observations may result from measurements or from analytical or numerical calculations. In the present case, analytical expressions of the displacements will be evaluated numerically and used as observations. The displacement history obtained by the so-called pre-computations is saved in an observation matrix

$$\mathbf{Q} = [\mathbf{x}_1, \mathbf{x}_2, \dots, \mathbf{x}_m] \quad (3.5)$$

In general, the number m of observations differs from the number n of DOF and, consequently, \mathbf{Q} is a rectangular matrix. This observation matrix is decomposed by means of the singular value decomposition

$$\mathbf{Q} = \mathbf{P}\Sigma\mathbf{V}^T \quad (3.6)$$

according to Golub and Kahan (1965). Herein, \mathbf{P} denotes the matrix of the left-singular vectors ϕ_k , which will be called proper orthogonal modes (POMs) in what follows. For special cases, these POMs are equivalent to the mode shapes of the respective system. This issue will be addressed in Section 4. The matrix Σ is a pseudo-diagonal matrix containing singular values σ_k , with $k \leq \min(n, m)$, in a descending order at its main diagonal, whereas all other entries of the rectangular matrix are zero. The matrix \mathbf{V} of the right-singular vectors will not be used within this contribution.

An energy measure for the matrix \mathbf{Q} consisting of a vector sequence is the Frobenius norm, which itself equals the sum of the squared singular values

$$E_{pseudo}(\mathbf{Q}) = \|\mathbf{Q}\|_F^2 = \frac{1}{m} \sum_{i=1}^n \sum_{j=1}^m Q_{i,j}^2 = \sum_{k=1}^{\min(n,m)} \sigma_k^2 \quad (3.7)$$

see e.g., (Kerschen and Golinval, 2002). Thus, the value of σ_k is related to the so-called pseudo-energy associated to the k -th POM. As a consequence, one may choose the first n_{red} POMs,

with $n_{red} \ll m$, which capture a certain amount of the system total pseudo-energy. From these POMs, the sought projection matrix

$$\Phi = [\phi_1, \phi_2, \dots, \phi_{n_{red}}] \quad n_{red} \ll m \quad (3.8)$$

is constructed.

With this projection matrix, the reduced system according to Eq. (3.4)₂ is solved and the results are transferred back to the full system by using Eqs. (3.2). For a detailed review of the POD and some applications the reader is referred to e.g. (Bamer *et al.*, 2017; Fangye *et al.*, 2016; Radermacher and Reese, 2013; Kerschen *et al.*, 2005; Chatterjee, 2000).

4. Applying POD to Mikota's vibration chain

As the first step, Mikota's vibration chain is exposed to such an initial displacement which only excites its first mode shape. Afterwards, Mikota's vibration chain performs free vibration. By doing so, the POD should identify the first mode shape only. This is due to the fact that the whole (vibrational) energy of the system is kept in this mode shape. Solving the differential equation with the following parameters

$$m = k = 1 \quad \text{and thus} \quad \Omega = \sqrt{\frac{k}{m}} = 1 \quad (4.1)$$

$$n = 10 \quad t_0 = 0 \quad \Delta t = 0.01 \quad t_N = 20 \quad N = 2001 \quad (4.2)$$

where the units have been omitted, yields the displacements x_i for each time step t_j of N . These displacements are written into the observation matrix \mathbf{Q} , which is then analysed by means of the POD according to Section 3. All calculations have been performed with MATLAB®.

As can be seen in Fig. 3, there is indeed only one (dominant) singular value. The remaining singular values are not of practical relevance, as the quotient $\sigma_{k>1}/\sigma_1 < 10^{-15}$ is in the order of numerical accuracy. Consequently, only the first POM is plotted whereas the remaining POMs are not taken into account. As expected, the POM 1 equals the first mode shape as given by Eq. (2.6)₁ and Fig. 2.

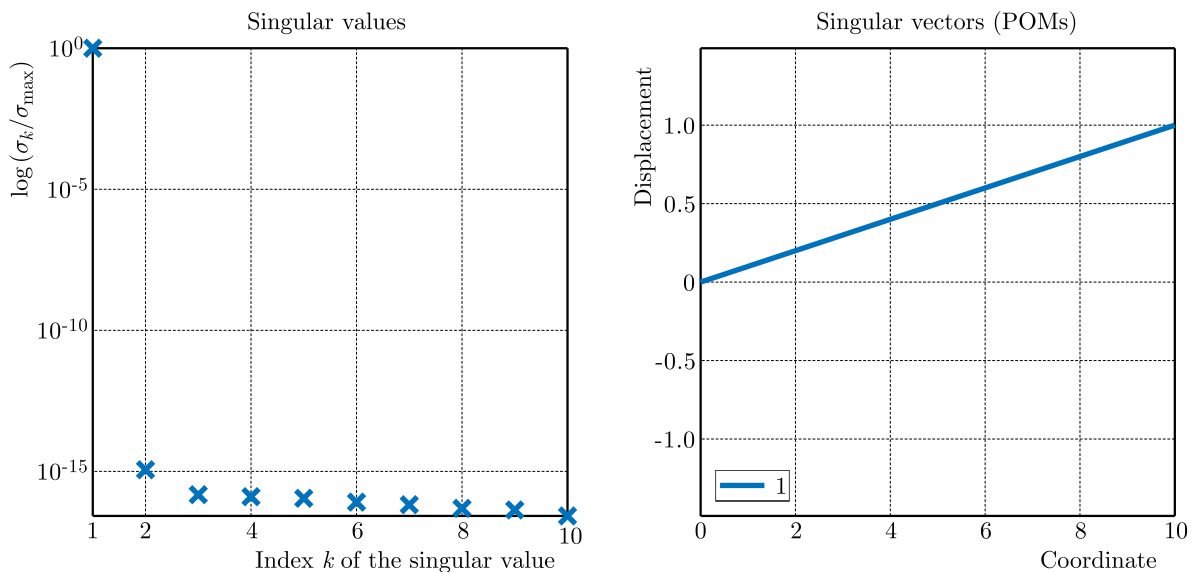


Fig. 3. Singular values and POM of Mikota's vibration chain, $n = 10$ DOF and initial excitation of the 1st mode shape, according to the magnitude of $\sigma_{k>1}/\sigma_1 < 10^{-15}$ only the first POM is plotted

In what follows, Mikota’s vibration chain is exposed to a load with a very short time duration, which simulates an impulse or an impact load. In detail, the force

$$f_1(t) = \begin{cases} 1 & \text{for } 0 \leq t \leq 0.05 = \delta_f \\ 0 & \text{for } \delta_f = 0.05 < t \end{cases} \quad (4.3)$$

is applied to the 1st DOF. Compared to the lowest oscillation period (and thus the highest eigenfrequency), the time duration δ_f of the load is small

$$T_{min} = \frac{2\pi}{\Omega_{10}} \hat{=} \frac{2\pi}{10} \approx 0.628 \gg 0.05 = \delta_f \quad (4.4)$$

with $\Omega_{10} = 10\Omega = 10$ according to Eq. (2.4). The resulting displacements and velocities are given with Figs. 4a and 4b, respectively. Some observations from these figures shall be discussed.

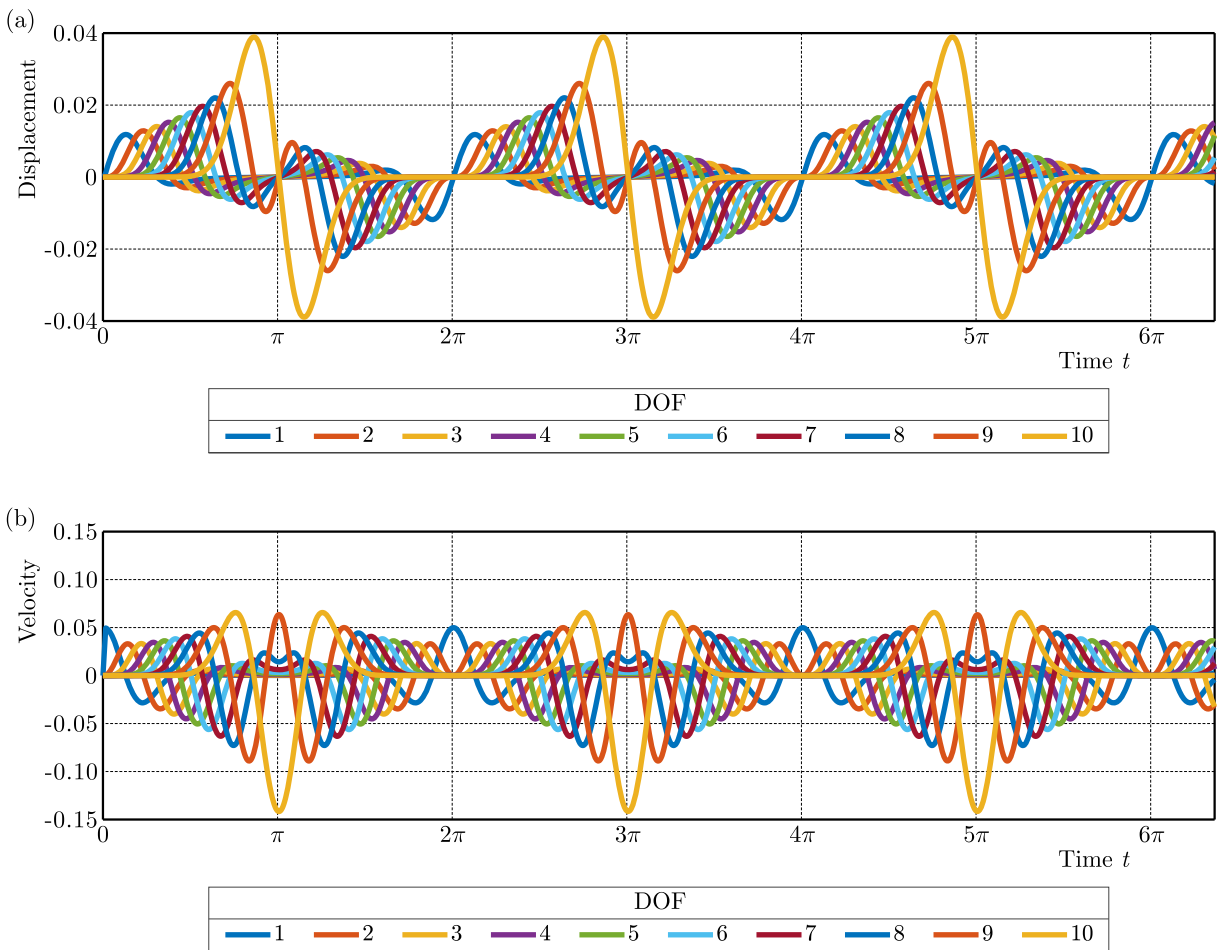


Fig. 4. Displacements and velocities for Mikota’s vibration chain with $n = 10$ DOF and impulse load according to Eq. (4.3) applied to the 1st DOF

From Fig. 4a, it can be seen that beginning from $t > 0$ and starting with the 1st DOF, energy is successively transferred to the remaining DOF. Higher DOFs are characterised by weaker springs and lower masses, see also Eqs. (2.3). The respective displacements increase with the increasing DOF, too. At time instances equal to integer multiples of π , all DOFs have zero displacements. At time instances equal to integer multiples of 2π , all DOFs but the 1st have zero velocities, too. With Eq. (4.4), the impulse load may be regarded as a Dirac-type loading. According to Müller and Schiehlen (1985), such an applied force in fact leads to non-vanishing initial velocities while

maintaining effectively zero initial displacements. In the present case, the 1st DOF gets an initial velocity (more precisely, the initial velocity is at the time instance δ_f). At this time instance, the whole system effectively still is at rest, see Fig. 4a. For this reason, the system starts a free oscillation from a state of zero displacement and, consequently, has to return into this state periodically. This happens at the aforementioned time instances at integer multiples of 2π , where the time duration δ_f has been omitted for clarity. At these time instances, all DOFs but the 1st must have both zero displacements and velocities. The velocity of the 1st DOF equals its initial velocity which is due to the Dirac-type loading, see also Fig. 4b. Due to the special structure of the eigenfrequencies, which is given by Eq. (2.4), the temporal factor at integer multiples of 2π of all n mode shapes is identical and equal to 1. Although Fig. 4a may lead to the assumption that there exist pronounced time intervals within which one or more masses m_i are at rest, it should be emphasised that this is not the case. On the contrary, there are only distinct time instances – at integer multiples of π as discussed above – at which all masses m_j have vanishing displacements. All masses but the first are at rest only at integer multiples of 2π .

The displacements for all time instances according to Eq. (4.2), which are plotted in Fig. 4a, are written in the observation matrix \mathbf{Q} , and the latter is investigated by means of POD according to Section 3. The resulting singular values and some POMs are given in Fig. 5.

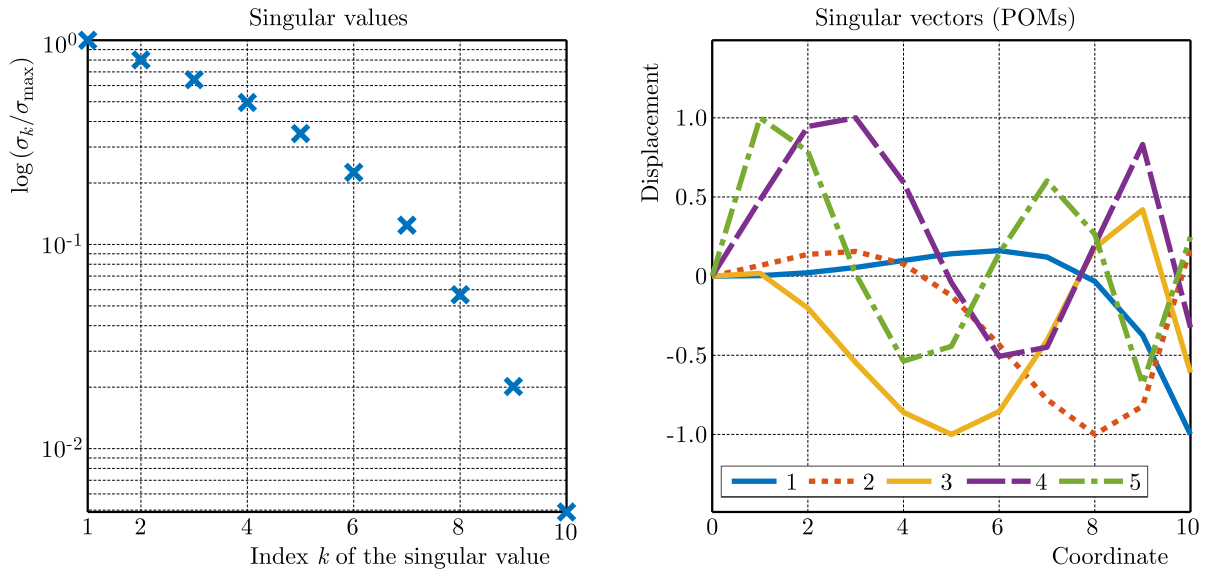


Fig. 5. Singular values and some POMs of Mikota's vibration chain, $n = 10$ DOF and impulse load according to Eq. (4.3) applied to the 1st DOF, only POMs 1, ..., 5 are shown

Compared to Fig. 3, it can readily be seen that in the present load case the so-called pseudo-energy is distributed over all POMs. However, the respective values, i.e. the singular values, are not equal. Hence, the single POMs each have a different contribution to the oscillation pattern of the mechanical system. The descent of the singular values gives an indication of which POMs may be omitted within the model order reduction while not exceeding the given error tolerance. This aspect will be investigated in the next Section, where additionally damping is taken into account.

5. Applying MOR to modified Mikota's vibration chain including damping

In this Section, a single absolute damping element is added to Mikota's vibration chain. By doing so, both the eigenfrequencies and mode shapes of the system are changed. For a general introduction to the topic of (optimal) damping, the reader is referred to e.g. (Gürgöze and

Müller, 1992). For a brief and exemplary discussion concerning the optimal position of absolute and relative damping elements in Mikota’s vibration chain, see Weber *et al.* (2008).

In order to apply a useful model order reduction, the number of DOFs of the system is increased to $n = 300$. The absolute damping element is fixed at the 7th DOF. Only one non-vanishing initial excitation $x_3 = 1$ is prescribed at the 3rd DOF. The other parameters are

$$m = k = d = 1 \quad t_0 = 0 \quad \Delta t = 0.01 \quad t_N = 20 \quad N = 2001 \quad (5.1)$$

where again the units have been omitted. It should be noted that $d = 1$ does not lead to weak damping anymore. However, within this contribution, a parameter study is presented. The resulting displacement history for some DOFs is shown in Fig. 6.

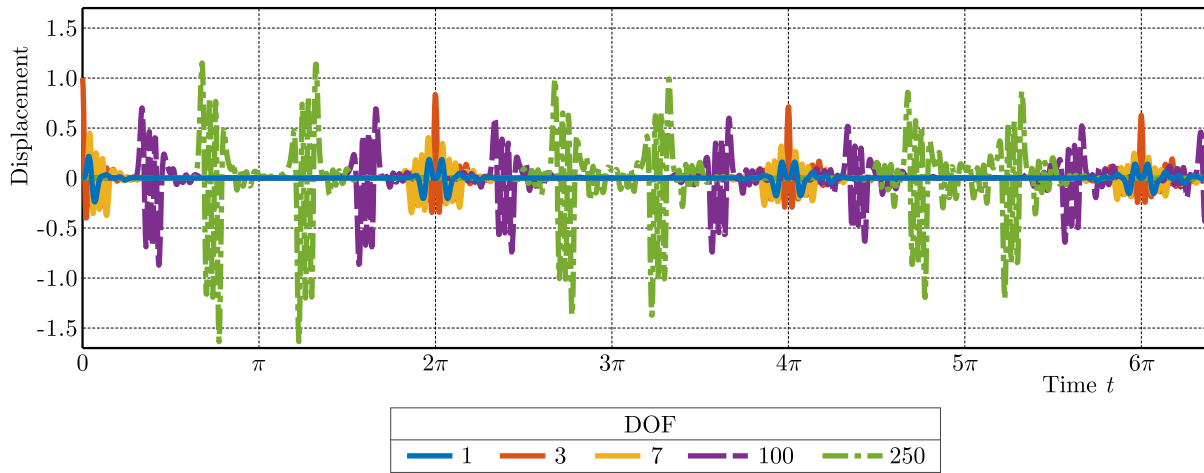


Fig. 6. Displacements for damped Mikota’s vibration chain with $n = 300$ DOF, initial excitation of the 3rd DOF, absolute damping element at the 7th DOF, only DOF 1, 3, 7, 100, 250 are shown

In what follows, the model order reduction using POD is performed. As the initial step, the observation matrix \mathbf{Q} is set by considering the displacements of all $n = 300$ DOFs within the time span $t = 0$ to $t = 10$. The POD is then applied to this observation matrix leading to the singular values and POMs as given in Fig. 7.

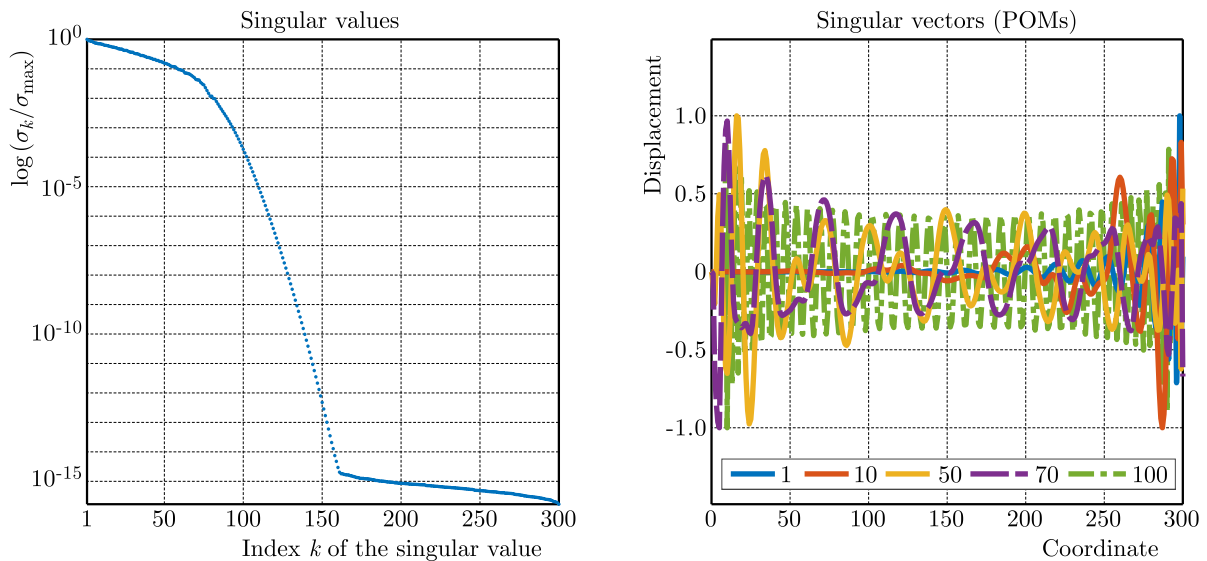


Fig. 7. Singular values and POMs of damped Mikota’s vibration chain, $n = 300$ DOF, initial excitation at the 3rd DOF, absolute damping element at the 7th DOF, only POMs 1, 10, 50, 70, 100 are shown

The so-called pseudo energy E_{pseudo} of the system can be calculated using Eq. (3.7)

$$E_{pseudo} = \sum_{k=1}^{\min(n,m)} \sigma_k^2 = 977.5528^2 \quad (5.2)$$

A common approach to the model order reduction is to consider such an amount n_{red} of POMs that for the corresponding pseudo energy

$$E_{pseudo,red} \approx 0.99E_{pseudo} \quad (5.3)$$

holds (Bamer *et al.*, 2017, Feeny and Kappagantu, 1998). Kerschen *et al.* (2005) even recommend $E_{pseudo,red} \approx 0.9999E_{pseudo}$. For the present case, the former criterion is fulfilled for $n_{red} = 76$ while the latter criterion gives $n_{red} = 98$.

Thus, in the first step, only 76 POMs are considered. As in the present case $\sigma_{77}/\sigma_{max} = 0.0184$, this means that all POMs, for which $\sigma_k \lesssim 0.018\sigma_{max}$ holds, are omitted. Although the observation matrix \mathbf{Q} only contains data up to $t = 10$, the calculations in the reduced system have been performed until $t = 20$. The resulting reduced system is solved and then transferred back to the full system. Both the displacement and velocity history within the time interval $3.25\pi \leq t \leq 3.75\pi$ for the arbitrarily chosen 150th DOF is given in Fig. 8. Additionally, the diagram contains the displacement and velocity history resulting from calculating the full system. As can be seen, there is a good agreement between these two results for both the displacement and velocity history.

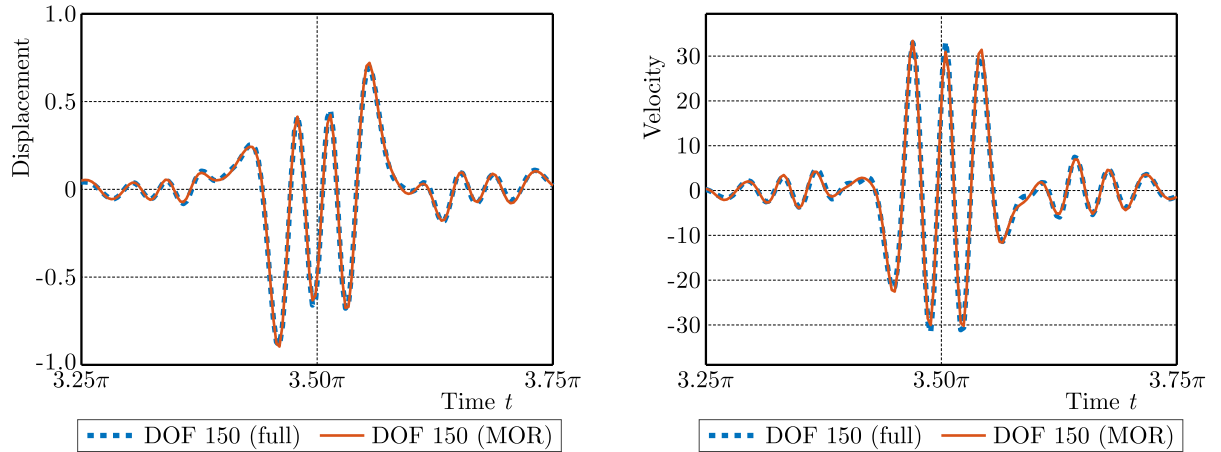


Fig. 8. Displacement and velocity history of the 150th DOF for the full (“full”, $n = 300$) and the reduced (“MOR”, $n_{red} = 76$) system

For comparison, an additional calculation is performed with $n_{red} = 98$, thus neglecting all POMs for which $\sigma_k \lesssim 2.4 \cdot 10^{-4}\sigma_{max}$. The respective results can be taken from Fig. 9 and do not show any (observable) differences between the results obtained with the full and the reduced system. Besides Eq. (5.3), an additional relation is introduced to measure the deviation between the results obtained with the full system and the results obtained with the reduced system

$$\Delta E_{phase} = \sqrt{\frac{\sum_{i=1}^n [(x_i - x_{red,i})^2 + (\dot{x}_i - \dot{x}_{red,i})^2]}{\sum_{i=1}^n (x_i^2 + \dot{x}_i^2)}} \quad (5.4)$$

This relation gives more reliable results as compared to the relation which only takes the pseudo energy into account. This is due to the fact that the latter relation does not reveal pronounced

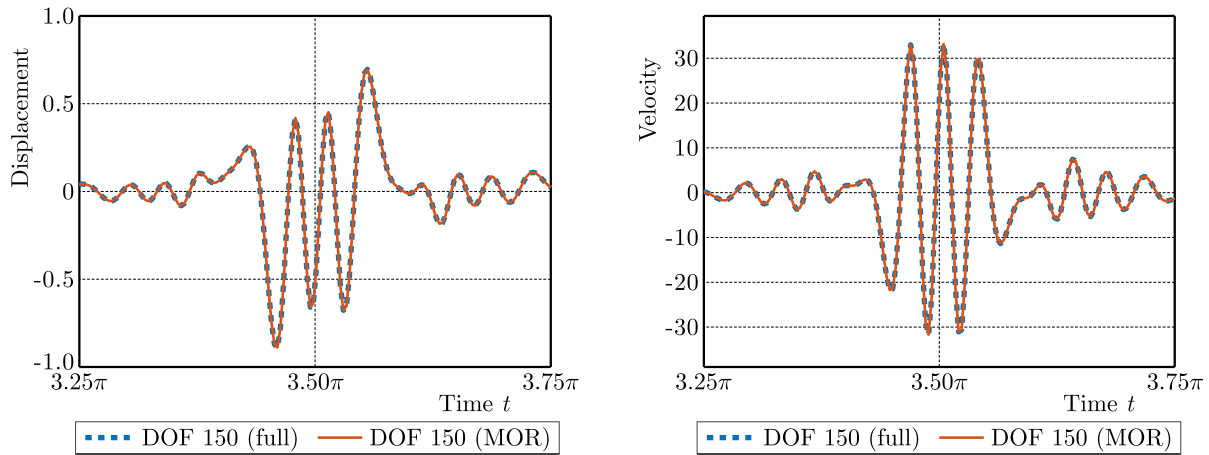


Fig. 9. Displacement and velocity history of the 150th DOF for the full (“full”, $n = 300$) and the reduced (“MOR”, $n_{red} = 98$) system

phase differences within the displacements and velocities, see also (Kappagantu and Feeny, 1999). In the present case, $\Delta E_{phase} = 0.144$ (compared to 0.5149 for $n_{red} = 76$) thus indicating a very good correlation between the results of the full and the reduced ($n_{red} = 98$) system. Hence, the model order reduction has been applied successfully.

6. Conclusions

An approach to the model order reduction has been successively applied to Mikota’s vibration chain, a special vibration chain having remarkable properties. The chosen approach to the model order reduction involves the proper orthogonal decomposition which, therefore, has been shortly introduced. Some basic insights into the proper orthogonal decomposition were given using the standard (that is, undamped) Mikota’s vibration chain with $n = 10$ DOFs. Finally, more advanced calculations including the model order reduction were performed after introducing a single absolute damping element into the vibration chain with $n = 300$ DOFs. It was observed that the dynamic characteristics of Mikota’s vibration chain could be kept if the underlying mechanical system was reduced in such a way, that $> 99\%$ of the so-called pseudo energy was considered. In the present case, an excellent correlation between the results obtained with the full and the reduced system is obtained for $n_{red} = 98$ DOF or – equivalently – for reduction in the dimensionality by $\approx 70\%$.

In this contribution, a linear vibration system has been investigated. However, non-linear systems play an important role in engineering applications, too. Thus, more scientific work has to be done in the field of model order reduction of non-linear systems. This non-linearity may additionally be caused by damage of the respective structure. Such effects must be taken into account if the model order reduction is used in, e.g., structural health monitoring.

References

1. BAMER F., AMIRI A.K., BUCHER C., 2017, A new model order reduction strategy adapted to nonlinear problems in earthquake engineering, *Earthquake Engineering and Structural Dynamics*, **46**, 4, 537-559
2. CHATTERJEE A., 2000, An introduction to the proper orthogonal decomposition, *Current Science*, **78**, 7, 808-818

3. FANGYE Y.F., WEBER W.E., ZASTRAU B.W., BALZANI D., 2016, Some basic ideas for the simulation of wave propagation in microstructures using proper orthogonal decomposition, *Proceedings in Applied Mathematics and Mechanics*, **16**, 1, 333-334
4. FEENY B.F., KAPPAGANTU R., 1998, On the physical interpretation of proper orthogonal modes in vibrations, *Journal of Sound and Vibration*, **211**, 4, 607-616
5. FREUND R.W., 2003, Model reduction methods based on Krylov subspaces, *Acta Numerica*, **12**, 2, 267-319
6. GOLUB G., KAHAN W., 1965, Calculating the singular values and pseudo-inverse of a matrix, *Journal of the Society for Industrial and Applied Mathematics, Series B: Numerical Analysis*, **2**, 2, 205-224
7. GÜRGÖZE M., MÜLLER P.C., 1992, Optimal positioning of dampers in multi-body systems, *Journal of Sound and Vibration*, **158**, 3, 517-530
8. GUYAN R.J., 1965, Reduction of stiffness and mass matrices, *AIAA Journal*, **3**, 2, 380-380
9. KAPPAGANTU R., FEENY B.F., 1999, An "optimal" modal reduction of a system with frictional excitation, *Journal of Sound and Vibration*, **224**, 5, 863-877
10. KERSCHEN G., GOLINVAL J.-C., 2002, Physical interpretation of the proper orthogonal modes using the singular value decomposition, *Journal of Sound and Vibration*, **249**, 5, 849-865
11. KERSCHEN G., GOLINVAL J.-C., VAKAKIS A.F., BERGMAN L.A., 2005, The method of proper orthogonal decomposition for dynamical characterization and order reduction of mechanical systems: an overview, *Nonlinear Dynamics*, **41**, 1-3, 147-169
12. KOCHENDÖRFFER R.K., 1963, *Determinanten und Matrizen*, B.G. Teubner Verlagsgesellschaft, Leipzig
13. MIKOTA J., 2001, Frequency tuning of chain structure multibody oscillators to place the natural frequencies at Ω_1 and $N - 1$ integer multiples $\Omega_2, \dots, \Omega_N$, *Zeitschrift für Angewandte Mathematik und Mechanik*, **81**, S2, 201-202
14. MÜLLER P.C., GÜRGÖZE M., 2006, Natural frequencies of a multi-degree-of-freedom vibration system, *Proceedings in Applied Mathematics and Mechanics*, **6**, 1, 319-320
15. MÜLLER P.C., HOU M., 2007, On natural frequencies and eigenmodes of a linear vibration system, *Zeitschrift für Angewandte Mathematik und Mechanik*, **87**, 5, 348-351
16. MÜLLER P.C., SCHIEHLEN W.O., 1985, *Linear Vibrations*, M. Nijhoff Publishers, Dordrecht
17. RADERMACHER A., REESE S., 2013, A comparison of projection-based model reduction concepts in the context of nonlinear biomechanics, *Archive of Applied Mechanics*, **83**, 8, 1193-1213
18. WEBER W., ANDERS B., MÜLLER P.C., 2015, A proof on eigenfrequencies of a special linear vibration system, *Zeitschrift für Angewandte Mathematik und Mechanik*, **95**, 5, 519-526
19. WEBER W., ANDERS B., ZASTRAU B.W., 2008, Some damping characteristics of a chain structured vibration system, *Proceedings in Applied Mathematics and Mechanics*, **8**, 1, 10391-10392
20. WEBER W., ANDERS B., ZASTRAU B.W., 2013, Calculating the right-eigenvectors of a special vibration chain by means of modified Laguerre polynomials, *Journal of Theoretical and Applied Mechanics, Sofia*, **43**, 4, 17-28
21. WEBER W.E., MÜLLER P.C., ANDERS B., 2017, The remarkable structure of the mode shapes and eigenforces of a special multibody oscillator, *Archive of Applied Mechanics*, to appear, DOI: 10.1007/s00419-017-1327-9

MECHANICAL RESPONSE OF NOTCHED MARBLE BEAMS UNDER BENDING VERSUS ACOUSTIC EMISSIONS AND ELECTRIC ACTIVITY

STAVROS K. KOURKOULIS, ERMIONI D. PASIOU, IOANNA DAKANALI

*National Technical University of Athens, Department of Mechanics, Laboratory for Testing and Materials, Athens, Greece
e-mail: stakkour@central.ntua.gr*

ILIAS STAVRAKAS, DIMOS TRIANTIS

*Technological Educational Institute of Athens, Department of Electronics, Laboratory of Electrical Characterization of
Materials and Electronic Devices, Athens, Greece*

An experimental protocol, including the combined application of both innovative and traditional sensing techniques, is described aiming to explore the mechanical response of marble and also to check the possibilities of detecting precursor phenomena designating upcoming catastrophic fracture. The protocol consisted of three-point bending tests with notched prismatic beams made of Dionysos marble, the material extensively used for restoration of the Acropolis of Athens monuments. The sensing system improvised included techniques relying on completely different physical foundations, which permit simultaneous detection and recording of the Pressure Stimulated Currents, Acoustic Emissions, three dimensional displacement fields and Notch Mouth Opening Displacements. Analysis of the results revealed interesting features of the mechanical response of Dionysos marble and indicated, also, that classical Continuum Fracture Mechanics fails to describe accurately the response of marble, at least in the presence of notches. In addition, strong correlations between the Pressure Stimulated Currents, the rate of acoustic hits and the rate of change of the opening of the pre-existing notch have been enlightened. Moreover, the onset of catastrophic crack propagation appears following distinguishable changes of the Pressure Stimulated Currents recorded. Therefore (and taking into account the very small size of the respective sensors as well as the simple complementary equipment needed), it is concluded that the specific technique could be considered as a simple and reliable tool for an alternative approach to the in-situ Structural Health Monitoring of classical stone monuments.

Keywords: marble, monuments, notch mouth opening displacement, three-point bending, pressure stimulated currents, acoustic emissions, 3D-digital image correlation

1. Introduction

The remaining life and the remaining load-carrying capacity of structural elements seriously concern the engineering community, especially in the case of already damaged or cracked elements. The need for a clear answer to this problem is imperative, among others, for scientists working for conservation projects of ancient stone monuments, given that quite often their structural members are cracked and any extension of pre-existing cracks could be fatal to the structural integrity of the whole monument.

Answering the above question is usually attempted within the frame of Fracture Mechanics by applying various criteria which predict both the load leading a pre-existing crack to initiation and, also, the direction towards which the crack is going to propagate. Such criteria, widely used in engineering praxis, are based on the maximum tangential stress (Yoffe, 1951; Erdogan and Sih, 1963), the strain energy density (Sih, 1973), the maximum energy release rate (Wu, 1978), the maximum dilatational strain energy (Theocaris *et al.*, 1982) etc. In the restoration

praxis of stone monuments, however, the problem is far more complicated due to the anisotropic nature of building materials and the fact that the loading schemes acting on a given element are not easily represented according to standard load-simulation schemes used in the laboratory. Therefore, the classical crack initiation criteria of Fracture Mechanics are not directly applicable, and it is not realistic to expect that closed analytic answers could be obtained. In addition, the direct “transfer” of results from laboratory experimental studies to the structural engineering field is questionable due to the “size effect” (Bažant, 1984; Carpinteri, 1989), i.e., the dependence of material properties on the specimen size. The “size effect” is extremely pronounced in rock and rock-like materials like, for example, those used for the construction of classical monuments of Cultural Heritage in Greece (Sulem and Vardoulakis, 1990; Kourkoulis and Ganniari-Papageorgiou, 2010).

Taking into account the above difficulties, it appears that in-situ continuous Structural Health Monitoring (SHM) of stone monuments is the only preventive tool that could provide on-time warning about upcoming changes, which could be harmful for the structural integrity of such monuments. However, it should be clarified from the very beginning that SHM of monuments of Cultural Heritage is not a trivial task. In order to understand the challenging character of the venture, one could consider the Parthenon Temple in Athens. The structural elements of the most emblematic monument of the “Golden Age of Pericles” (epistyles, column drums, capitals) were made of marble blocks quarried from the Pentelic Mountain. As it can be seen in Fig. 1a, quite a few of these elements are seriously cracked and their load-carrying capacity is questionable (Korres and Bouras, 1983; Zambas, 1994), rendering continuous SHM an imperative demand. The coexistence of authentic and substitute marble (Fig. 1a) together with metallic connectors and cement paste (used to fill the grooves (Fig. 1b) in which the metallic connectors are placed) causes additional difficulties. This coexistence creates internal (hidden) interfaces, along which failure/damage mechanisms are firstly activated, well before any crack extension (or any other damage mode) is observable at the outer surface of the member.

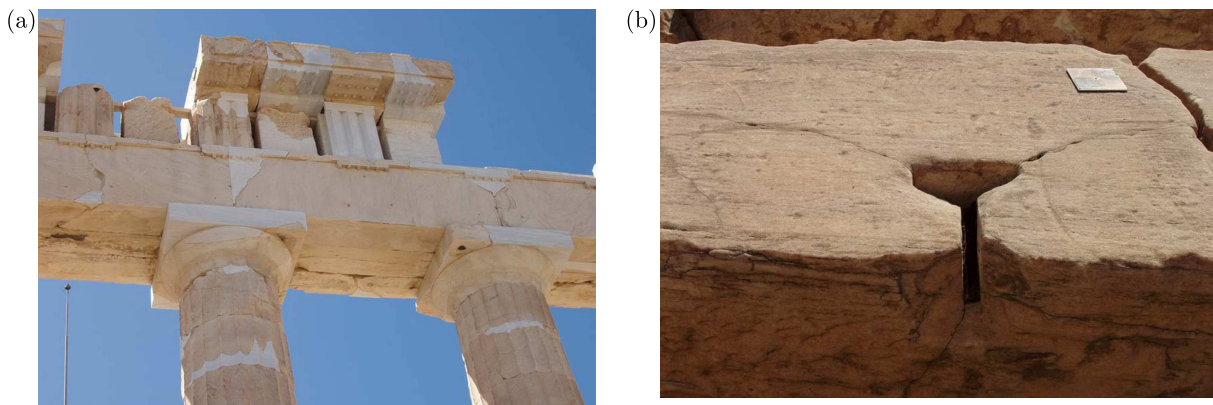


Fig. 1. (a) Typical epistyles of the Parthenon Temple showing the degree of damage and, also, the coexistence of authentic elements (made of Pentelic marble) with patches made of the substitute material (Dionysos marble) joined together by means of invisible metallic elements. (b) The grooves sculptured by ancient Greeks to host the metallic elements used to keep series of epistyles in place

In the frame of the above argumentation, it is easily concluded that questions related to the remaining load-carrying capacity of restored structural members of stone monuments could not be answered unless data from the interior of the element are pumped. Moreover, it is clear that such data can only be pumped using sensors of very small size (to avoid harming the aesthetic harmony of the monument) and also of low cost (considering the number of sensors required to monitor all the cracked structural elements of a given monument, which for the case of the Parthenon Temple are too many). Such sensing systems, widely used today, both in

laboratory and structural scale, include detection of acoustic events, application of optical fibers, quantification of electric resistance changes etc. Their in-situ application is relatively difficult, and for some of them their application necessitates interventions on the monument members, which are usually not permissible.

In this direction, the present study aims to comparatively assess the efficiency of a relatively novel sensing technique, which is based on the detection of extremely weak electric currents, known as the Pressure Stimulated Currents (PSC) (Triantis *et al.*, 2006, 2012). Among the critical advantages of the PSC technique is the very small size of the respective sensors and their low cost as well as the simple complementary equipment of the set-up, rendering the technique quite attractive, especially for long term monitoring of many structural members.

For the study to be accomplished, notched prismatic marble beams are subjected to Three-Point Bending (3PB). The PSC produced is recorded as a function of time, in parallel with the data provided by the Acoustic Emission (AE) technique, which is considered a well-founded and mature sensing technique, widely used worldwide. In addition, the displacement field developed is recorded using the 3D-Digital Image Correlation (3D-DIC) technique while the Notch Mouth Opening Displacement (NMOD) is also recorded using a clip-gauge extensometer.

The data obtained from this combined “attack” (i.e., with both innovative and traditional experimental techniques) are comparatively studied in the direction of correlating critical aspects of their time evolution. Interesting conclusions are drawn about the mechanical behaviour and failure of Dionysos marble, while the possibility of using the critical Notch Opening Displacement (NOD) as a simple easy-to-apply fracture criterion is discussed. Moreover, strong correlations between the PSC, the AE as well as the data obtained using the 3D-DIC technique (properly assessed against the ones of the traditional clip-gauge extensometer) are highlighted. The time evolution of the above quantities was proven to follow internal damage processes in a satisfactory manner. In addition, indications were provided, according to which the time evolution curves of all the quantities mentioned above exhibited changes (either clear or imperceptible) that could be considered as pre-failure indicators well before macroscopic crack initiation.

2. The experimental protocol

2.1. The material and the specimens

The specimens of the experimental protocol were cut out from an almost cubic block of marble quarried from Dionysos Mountain in Attica region. Given that the specific variety of marble is usually considered as a transversely isotropic material, every effort was made for all the specimens to be cut along the strong anisotropy direction and the load to be applied normally to the material layers, in the direction of minimizing the scattering of the results. In general, every effort was made to control (if not to eliminate) the factors responsible for the scattering of the experimental results. All specimens were cut out from the same marble block and they were carefully inspected for visible defects. Moreover, they were cut along the same direction with respect to the material layers, and the notches were machined carefully and by a single technician. After completion of the experimental protocol, Chauvenet’s criterion was used to exclude from the elaboration of the results all tests for which the deviations were unacceptably increased. As a result, the final scattering of the tests included in the analysis was quite affordable (at least for tests with specimens made of a brittle rock-like material).

The specimens were beam-shaped with a rectangular cross section and overall length equal to $L_o = 100$ mm. Two classes of specimens were tested concerning the dimensions of the cross section: a class with width-to-height ratio equal to $b \times h = 20 \times 20$ mm² and the second one with $b \times h = 25 \times 25$ mm². The specimens were mechanically notched at their mid-span with the aid of a cutting disc of thickness $\delta_o = 2.5$ mm and rounded cutting edge. The length of the notch

was constant and equal to $\alpha_o = 4$ mm resulting to two notch length-over-specimen height ratios, i.e., $\alpha_o/h = 0.20$ and $\alpha_o/h = 0.16$, respectively, in an effort to check also the role of the relative notch length. The geometry and dimensions of the specimens are shown in Fig. 2b.

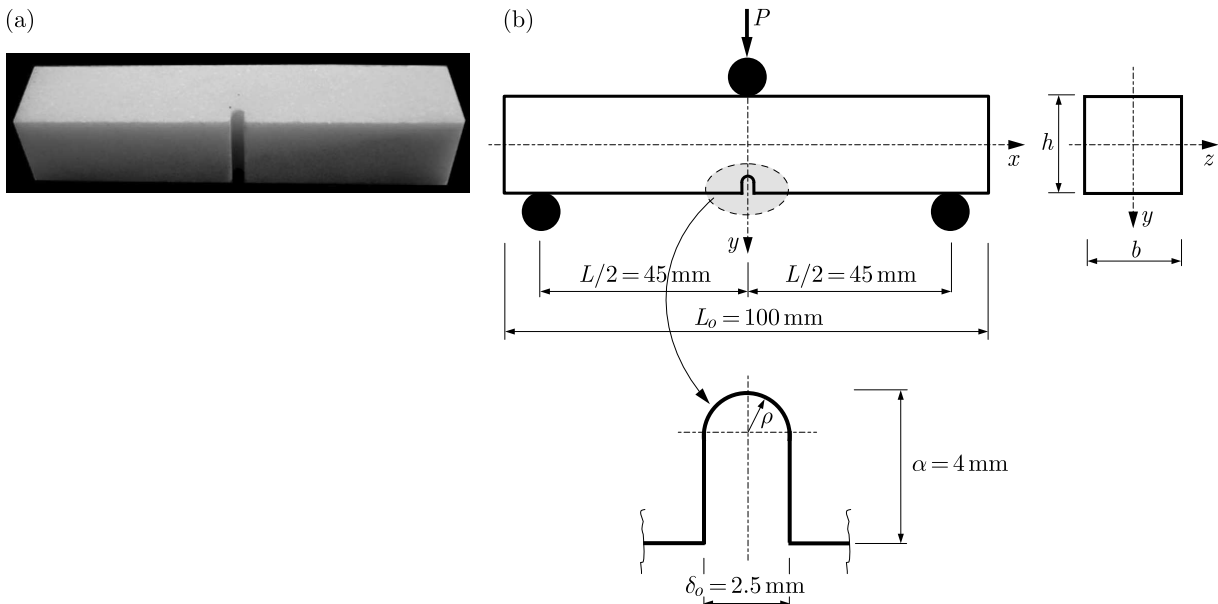


Fig. 2. (a) A typical specimen before testing. (b) The geometry and dimensions of the specimens

Dionysos marble was chosen because it is the material used by the scientific and technical personnel of the restoration project of the Athens Parthenon Temple for constructing copies of missing structural elements and also for preparing patches for partially destroyed members. The project is still in progress and is implemented by the “Acropolis Restoration Service” under the auspices of the “Committee for the Conservation of the Acropolis Monuments”, an interdisciplinary committee of the Greek Ministry of Culture, established in 1975. The methodology adopted and the restoration techniques developed in the frame of the project are worldwide recognized for their pioneering nature and the strict commitment to the restoration principles of “The Venice Charter” (1964).

The properties (mechanical and physicochemical) of Dionysos marble are very similar to those of the authentic building stone of the Parthenon Temple, i.e., Pentelic marble. It is an extremely fine-graded white marble consisting of calcite (about 98%) and very small amounts of muscovite, sericite, quartz and chlorite. It is of almost white colour with a few thin ash-green veins along the marble’s schistosity. Silver areas are detected due to the presence of chlorite and muscovite. Its porosity is very low (varying between 0.3% and 0.7%). Its density is equal to about 2730 kg/m^3 and its absorption coefficient by weight varies around 0.11%. The coefficient of thermal expansion is $9 \cdot 10^{-6}/^\circ\text{C}$ (between 15°C and 100°C). The grain size varies around $0.43 \cdot 10^{-3} \text{ mm}$ and the crystals are polygonic of almost uniform size (between $900 \mu\text{m} \times 650 \mu\text{m}$ and $950 \mu\text{m} \times 874 \mu\text{m}$) (Tassogiannopoulos, 1986).

The mechanical properties of Dionysos marble reported in literature vary within broad limits. This is because they depend, among others, on the exact quarrying point and depth as well as on the orientation of the specimens with respect to the anisotropy directions. The numerical values adopted in this study are based on an exhaustive experimental study by Vardoulakis and Kourkoulis (1997) and are recapitulated in Table 1, for the strong anisotropy direction, which is of importance for the present study.

Table 1. Mechanical properties of Dionysos marble along the strong anisotropy direction (Var-doulakis and Kourkoulis, 1997)

Property	Young's modulus			Tensile strength	Compressive strength	Nominal tensile strength	Poisson's ratio
Test	Tension	Comp-ression	3PB	Tension-Brazilian	Uniaxial compression	3PB	Tension-compression
Unit	GPa	GPa	GPa	MPa	MPa	MPa	–
Value	75	84	109	9.1	78.4	18.4	0.23

2.2. The sensing techniques used

2.2.1. Pressure Stimulated Currents

It has been long ago observed that mechanical stress is responsible for generation of electric signals in brittle materials like rocks. It was Whitworth (1975), in a pioneering work, who demonstrated such an effect in alkali halides. It is worth mentioning, also, that electric signals are generated when brittle non-piezoelectric materials (the porosity of which does not favour electro-kinetic phenomena) are subjected to an abrupt increase of the level of mechanical stress. Nowadays, the most widely accepted model describing qualitatively the generation of these weak electrical signals is the one introduced by Slifkin (1993). The specific model was further developed by Vallianatos and Tzanis (1999) and is commonly designated as the Moving Charged Dislocations (MCD) model.

According to the MCD model, motion of charged dislocations produces a transverse electric polarization P directly related to the electric current density J and, in turn, to the mechanical strain rate, $d\varepsilon/dt$

$$J = \frac{\partial P}{\partial t} \propto \frac{d\varepsilon}{dt} \quad (2.1)$$

The above transient electrical signals are detected in the form of electric currents, known as Pressure Stimulated Currents (PSC), and the respective experimental technique is known as the PSC technique (Triantis *et al.*, 2006). It was used for the first time by Varotsos (2005) in the direction of describing the polarization or depolarization of electric signals, as a result of pressure variations on solids that contain dipoles due to the existence of defects. According to Eq. (2.1), it is expected for the PSC to be related to the accumulation of deformation and more specifically to be proportional to the mechanical strain rate ($d\varepsilon/dt$).

The technique has been applied successfully to rock samples (made either of marble (Stavrakas *et al.*, 2003) or amphibolite (Triantis *et al.*, 2007)), submitted to monotonically increasing compressive load until fracture. Later on, it was applied, also successfully, to cement based specimens under compression (Kyriazopoulos *et al.*, 2011; Triantis *et al.*, 2012).

Experimental studies indicate that the PSC emitted during mechanical loading has a deterministic form and can be used as a tool for detecting the upcoming fracture. Moreover, the form of the PSC can be used to distinguish whether plasticity (non-reversible deformation of the specimen) has appeared or whether fracture is impending (Anastasiadis *et al.*, 2007). It is generally observed that the PSC emissions increase intensively when the applied mechanical stress approaches the strength limit of the tested specimen (Triantis *et al.*, 2012). Experiments with specimens made of cementitious materials indicated that mechanical straining due to axial compression induces electric signals, providing qualitatively similar results with those in rocks and rock-like materials (Kyriazopoulos *et al.*, 2011). However, the PSC recorded is significantly stronger than that in rocks, reaching amplitudes at the nA scale. Moreover, recent experiments with prismatic specimens made either of marble or mortar and subjected to 3PB revealed that

proper evaluation of the electric current emission recordings may provide useful information regarding the proximity of the applied mechanical load to the ultimate stress level of the specimens (Stergiopoulos *et al.*, 2015).

In the laboratory, the PSCs are detected by using extremely sensitive electrometers. The sensors consist of pairs of gold-plated electrodes attached on the specimen's surface by means of a conductive paint. In the present study, the measuring system consisted of an ultra-sensitive programmable electrometer (Keithley, 6517 A) resolving currents from 0.1 fA to 20 mA in 11 ranges. The data of the electrometer were stored in a computer using GPIB interface. The electrodes were installed in the notch and on the upper side of the specimens (Fig. 3a). The overall arrangement of the equipment of the PSC system used is shown in Fig. 4.

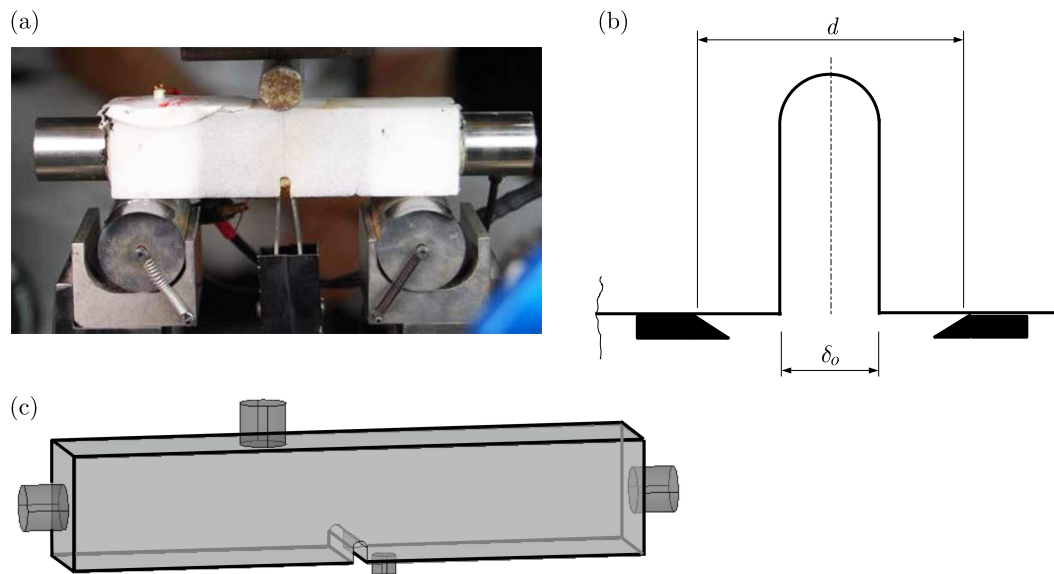


Fig. 3. (a) A specimen placed on the metallic rollers just before testing. (b) A detailed sketch of the knife-edges used to keep the clip-gauge in place. (c) A schematic representation of the position of the Acoustic Emission sensors

2.2.2. Acoustic Emissions

The Acoustic Emission (AE) technique detects acoustic events taking place within a material during mechanical loading, since deformation and failure of materials are accompanied by a sudden release of strain energy. The energy released generates elastic stress waves which travel within the material towards the boundaries of the specimen, where they are detected by proper transducers (usually piezoelectric sensors converting elastic waves to electrical signals). The main advantage of the AE technique is that it can monitor failure processes during the whole loading scheme of either a specimen or a whole structure by just attaching a number of sensors on it. Recalling that acoustic emissions depend mainly on irreversible deformations, it is concluded that this technique is suitable for structural health monitoring. Another advantage of the AE technique is related to its ability to determine the spatial coordinates of the acoustic source employing usually the travel-time-difference method (Sachse *et al.*, 1991).

The underlying principle of the technique is dated back to 1933, when the process of shock occurrence in a wood specimen under flexural loading was studied by Kishinoue with the aid of a phonograph pick-up and a steel needle. His original article (in Japanese) was translated into English by Ono in 1990 (Kishinoue, 1990). The first studies concerning the acoustic emissions in geomaterials were carried out by Obert (1941). Till today, the AE technique has been applied to various materials, i.e., rocks, concrete, mortars, metals etc. under various loading

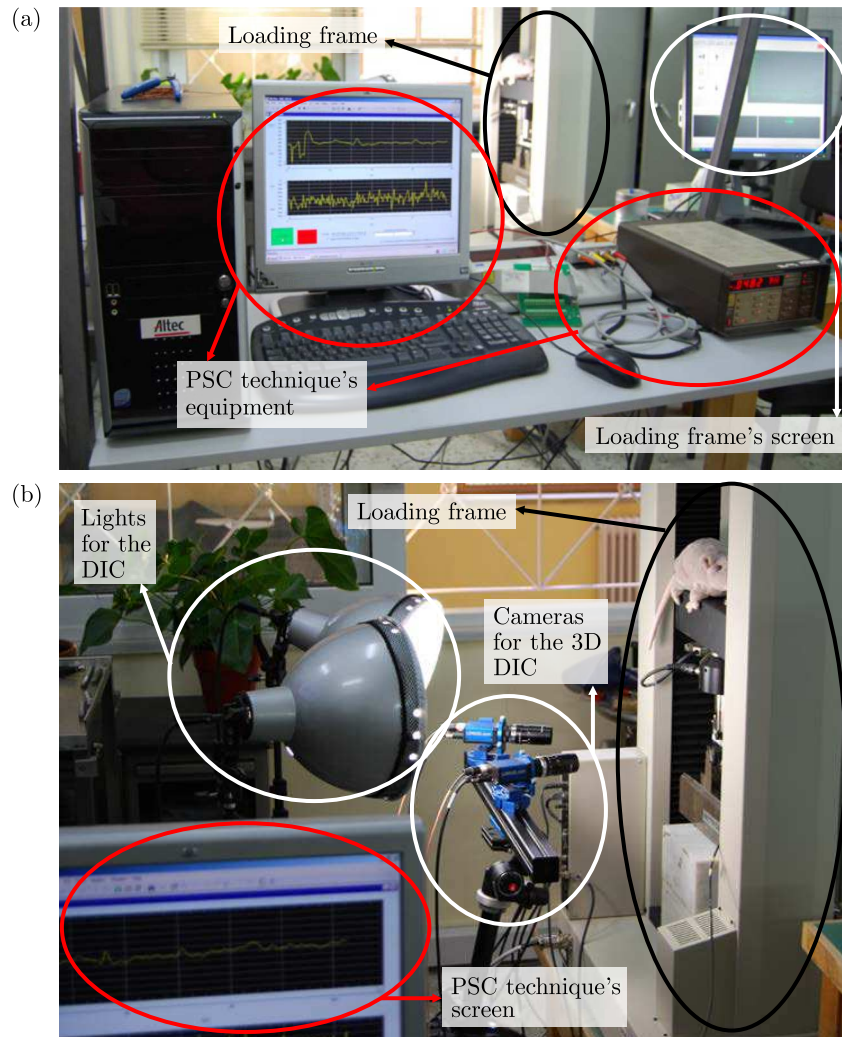


Fig. 4. An overview of the experimental set-up. (a) The equipment for recording the PSC. (b) The arrangement for the application of the DIC technique

modes. Maji and Shah (1988), for example, determined the fracture process zone in pre-cracked concrete specimens under tension by means of the source location of acoustic emissions. Labuz *et al.* (2001) quantified the intrinsic process zone in cementitious specimens of various size subjected to diametral compression (Brazilian-disc test) and 3PB. The dimensions of the fracture process zone based on the location of the acoustic events were determined also for rock specimens (Muralidhara *et al.*, 2010). Another very interesting application of the AE technique is the estimation of the critical values of the SIF and the J-integral, dated back to 1984 (Blanchette *et al.*, 1984). Later on, Hashida (1993) applied the same approach for rock-like materials. Recently, the AE technique has been used for the classification of the failure modes, also, in rock-like materials. For example, bending tests were carried out by Aggelis *et al.* (2013) in marble specimens, in an effort to correlate the frequency and the waveform shape of the AE with the fracture mode.

Quite often the data recorded by the AE sensors are analyzed using the b -value (Rao and Prasanna Lakshmi, 2005), correlating events of high amplitude and lower frequency with events of low amplitude and higher frequency. Nowadays, an “Improved b -value” concept (Ib -value), proposed by Shiotani *et al.* (2001), is employed. It is based on statistical parameters (such as the mean and standard deviation of the AE amplitude), which vary during the test. The

time variation of the Ib -values is considered as providing valuable indications concerning the proximity of the system to its “critical stage” (impending failure). The Ib -value is defined as

$$Ib = \frac{\log_{10} N(\mu - \alpha_1\sigma) - \log_{10} N(\mu + \alpha_2\sigma)}{(\alpha_1 + \alpha_2)\sigma} \quad (2.2)$$

where σ is the standard deviation and μ is the mean value of the AE amplitude distribution. Moreover, α_1 is related to the smaller amplitude while α_2 is related to the fracture level. The numerical values of α_1 , α_2 vary within broad limits ($0.5 < \alpha_1, \alpha_2 < 5.0$). Attributing to them values within this range does not significantly affect the Ib -value (Shiotani *et al.*, 1994). In this context, it is here assumed that $\alpha_1 = \alpha_2 = 1.0$.

Besides providing valuable information concerning the intensity of the internal damage process and its spatiotemporal evolution, it is generally accepted, nowadays, that the data recorded by the AE technique offer interesting information concerning the nature of the source of acoustic signals (Ohno and Ohtsu, 2010; Ohtsu, 2010; Aggelis, 2011; Aggelis *et al.*, 2013). More specifically, the relationship between the RA parameter (Rise Time/Amplitude) and the Average Frequencies (AF) (counts/duration) permits classification of the cracks formed during loading to Mode I and/or Mode II. According to this approach, acoustic emission signals of high AF and low RA values are due to “tensile” (mode I) cracks. On the other hand, acoustic emission signals of low AF and high RA values are due to other crack modes (mode II crack or mixed-mode cracks) or even due to shear phenomena (friction).

In the present study, four acoustic emission sensors were properly attached on the free transverse sections of the specimens with the aid of silicone. Three of the sensors were of the R15 α type while the fourth one was a pico-sensor. The positions of the sensors are shown schematically in the sketch in Fig. 3c.

2.2.3. Digital Image Correlation

The third innovative technique used is the Digital Image Correlation (DIC). It is based on the combined use of two high definition cameras. Its theoretical background is dated 30 years ago (Sutton *et al.*, 1986), and it has been since then continuously developed further (Sutton *et al.*, 2000). For its application, the surfaces monitored are covered by a dense grid of paint dots the displacements of which during loading are used to calculate the full-field 3D displacement-field. DIC has been already used for the determination of Crack Tip Opening Displacement and Stress Intensity Factors (SIFs) of brittle materials (Brynk *et al.*, 2012).

In this study, a novel 3D-DIC system (LIMESS Messtechnik & Software GmbH, Germany) with two cameras (of resolution 1624 \times 1234 pixel) was used. The 3D-DIC active field was a rectangle of dimensions 44 \times 27 mm². The size of the pattern dots was equal to about 0.08 mm. The frequency was set to 1 photo every 3 seconds. The 3D-DIC system used in the present study is shown in Fig. 4.

2.3. The experimental set-up and the experimental protocol

The experiments were implemented using an MTS-INSIGHT loading frame of capacity 10 kN. In parallel to the above mentioned techniques, a traditional clip-gauge extensometer (INSTRON 2670-120) with a 5 mm gauge length and 2 mm range was properly mounted to the notch mouth (Figs. 3a,b) to measure the Notch Mouth Opening Displacement (NMOD). It was calibrated using a micrometer calibrator (High Mag). The TDS-530 data-logger was used for data acquisition and storage. An overview of the whole experimental set-up is shown in Fig. 4.

The specimens were placed on two metallic cylinders of an INSTRON 3PB fixture (Fig. 3a). The diameter of the supporting cylinders was 25 mm and their distance was adjusted (and kept constant for all tests) to $L = 90$ mm, resulting to a span-over-height ratio approaching 4. The

specific value is considered as the lower limit for which the Bernoulli-Euler technical bending theory gives acceptable results, permitting one, in the first approximation, to ignore the influence of shear forces.

The tests were quasi-static realized under displacement-control mode at a rate equal to 0.01 mm/min. The load was applied monotonically until fracture of the specimens. It was linearly distributed along the width of the specimens with the aid of the third steel cylinder of diameter 10 mm (Fig. 3a).

3. Fracture characteristics of Dionysos marble under 3PB

All specimens tested were fractured in the same way: A crack was initiated at the tip of the notch and propagated towards the load application point, almost parallel to the direction of the applied load (Fig. 5a). In some specimens, the crack path deviated slightly (Fig. 5b) indicating some kind of asymmetries of the whole configuration. Considering that every attention was paid to the experimental set-up to be symmetric, it can be concluded that those deviations were due to inevitable local inclinations of the material layers of marble with respect to the specimen's longitudinal axis. The fracture surfaces were almost planar (although slightly wavy) and normal to the longitudinal axis of the specimens, as it can be seen in Figs. 5c and 5d. In general, the fracture plane is very sensitive to local material imperfections (typical for most marble varieties), called “κομμός” at the era of Parthenon builders. These imperfections define locally weak material planes. Obviously, such specimens were not taken into account while elaborating the results of the experiments.

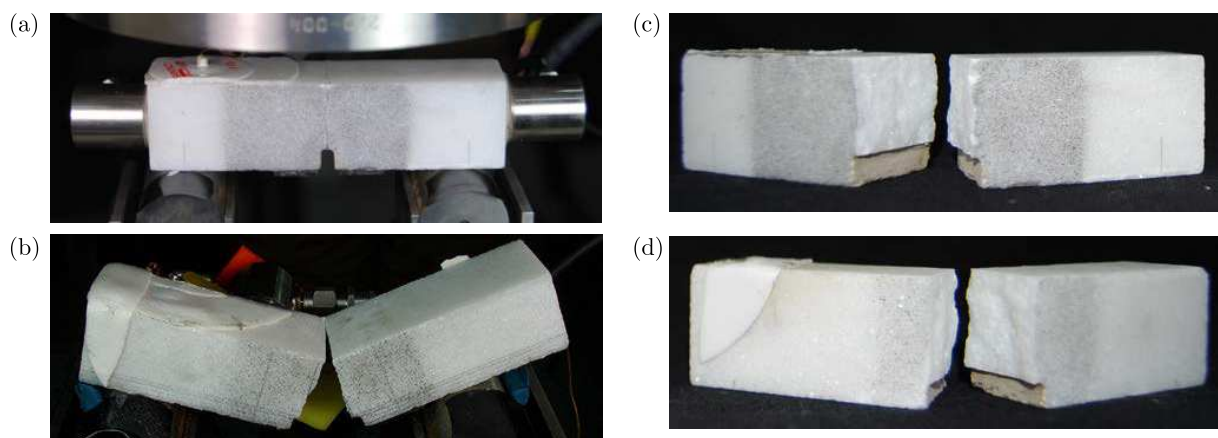


Fig. 5. Typical fractured specimens with fracture planes either parallel to the loading axis (a) or slightly inclined with respect to this axis (b). The wavy shape of typical fracture surfaces (c), (d)

Typical raw data for the variation of the load imposed versus the respective deflection of the central cross section (as provided by the translation of the frame traverse) are plotted in Fig. 6, for some characteristic specimens belonging to both specimen classes. Ignoring inevitable bedding errors, all curves are more or less similar to each other, approaching linearity in a quite satisfactory manner for the whole loading procedure. The fracture load for both specimen classes (around 600 N for the class with $b \times h = 20 \times 20 \text{ mm}^2$ and around 1100 N for the class with $b \times h = 25 \times 25 \text{ mm}^2$) exhibited relatively low scattering in spite of the increased number of unpredictable parameters that could increase scattering for materials like marble (inhomogeneity, anisotropy, internal defects etc.). The maximum deflection of the central cross section was determined equal to about 0.10 mm for the specimens of the first class and equal to about 0.16 mm for those of the second class, again with a relatively low standard deviation.

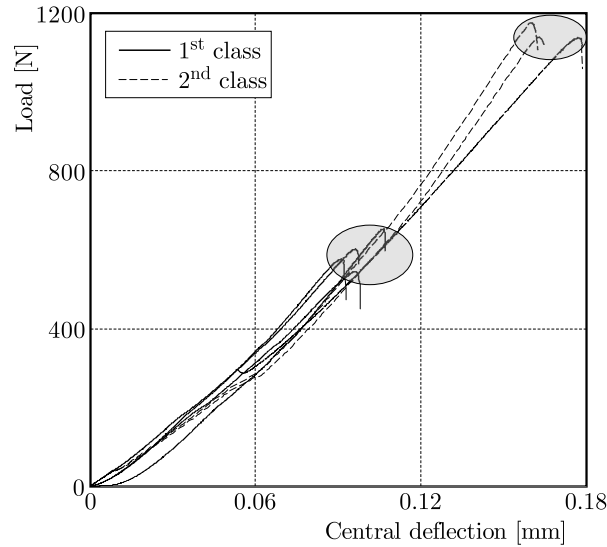


Fig. 6. Raw data of some characteristic experiments of both classes of specimens: variation of the load induced against the displacement of the loading frame traverse

The variation of the Notch Mouth Opening Displacement (NMOD), as it was obtained by the clip-gauge, normalized over the initial distance between the knife edges of the clip-gauge (Fig. 3b), is plotted in Fig. 7 with respect to the maximum “nominal” axial stress developed, also, for some characteristic specimens. The “nominal” stress was calculated by the familiar formula of the classic Bernoulli-Euler technical bending theory (taking into account the effective cross sectional area)

$$\sigma_{nom} = \frac{3PL_o}{2b(h - \alpha_o)^2} \quad (3.1)$$

where P is the force applied. It is seen that after a more or less linear portion these graphs become non-linear, contrary to what is perhaps expected for a material of an increased brittleness like Dionysos marble. It is here clarified that the data of Fig. 7 for the NMOD are plotted up to the maximum stress value. Clearly, the clip-gauge continues recording even after the peak stress is reached, since the fracture of the specimen and its fragmentation into two pieces is macroscopically observed with some delay after the stress attains its maximum level. This phenomenon is the origin of quite a few problems, related to the accurate determination of the critical value of NMOD, in case the latter is considered as a critical quantity (criterion) describing the fracture. Due to its importance, the specific point will be discussed further in Section 5. The average value of the dimensionless critical NMOD for Dionysos marble was found equal to about $7.5 \cdot 10^{-4}$.

The average value of the “nominal” axial fracture stress, in the presence of a notch, was 14.04 MPa with a relatively low (considering the brittleness of the material) standard deviation. The differences between the specimens of the two classes are negligible, indicating that it is the presence of the notch itself rather than its length that dictates the final outcome. The respective value for the “nominal” axial fracture stress of intact Dionysos marble beams under 3PB, as it was determined by Vardoulakis *et al.* (1997), is equal to 18.4 MPa. Both values (i.e., for notched and intact specimens) are considerably higher than the respective one determined from direct tension tests, reported again by Vardoulakis *et al.* (1998), which for the strong anisotropy direction was equal to 9.1 MPa (Table 1). This conclusion supports further the indications concerning the inappropriateness of the 3PB test as a substitute of the direct tension test.

What is to be noted, also, from Fig. 7, is that the stress-NMOD curves deviate from linearity from relatively early load levels, contrary to the respective load-deflection curves. This could

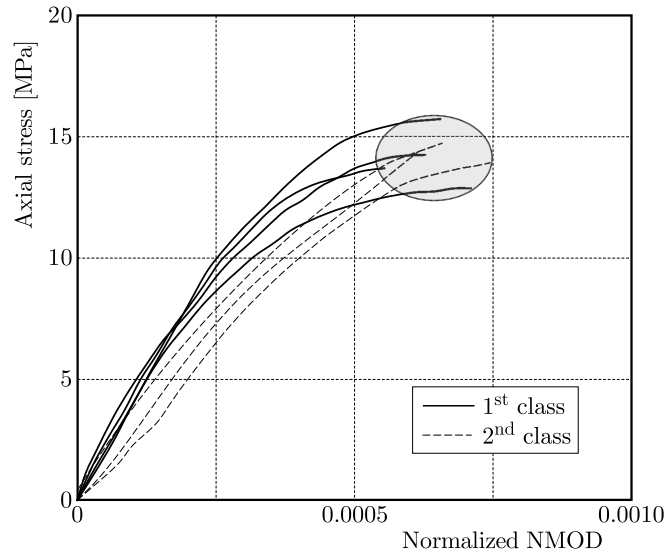


Fig. 7. The variation of the longitudinal “nominal” axial stress against the Notch Mouth Opening Displacement as obtained by the clip-gauge. The values of NMOD are normalized over the initial distance d between the knife edges of the clip-gauge

be explained by the fact that the NMOD strongly depends on the stress field at the immediate vicinity of the notch crown, where the so called “process” zone is formed and the material locally ceases obeying the linearity assumption. On the other hand, the overall deflection depends on the global stress field all over the specimen. Taking into account that the maximum size of the process zone for Dionysos marble is of the order of only a few millimetres (Kourkoulis *et al.*, 1999), it is reasonable to assume that it cannot drastically influence the overall response of the specimen.

In addition, it should be emphasized that the slope of the experimentally obtained stress-NMOD curves is much more abrupt compared to that obtained analytically using the familiar formula for the stress-NMOD relation for a beam with a crack, as it is provided by classical Fracture Mechanics for a beam with length-to-height ratio equal to four (Tada *et al.*, 1973)

$$\delta = \frac{4\sigma_{nom}\alpha}{E'} V_1\left(\frac{\alpha_o}{h}\right)$$

$$V_1\left(\frac{\alpha_o}{h}\right) = 0.76 - 2.28\left(\frac{\alpha_o}{h}\right) + 3.87\left(\frac{\alpha_o}{h}\right)^2 - 2.04\left(\frac{\alpha_o}{h}\right)^3 + \frac{0.66}{\left(1 - \frac{\alpha_o}{h}\right)^2} \quad (3.2)$$

In Eqs. (3.2) E' is the equivalent Young’s modulus of the beam material (depending on whether plane stress or plane strain conditions prevail). The difference exceeds 100%, and it is quite impossible to be addressed to any type of experimental error or to the fact that the length-to-height ratio of the specimens tested was not exactly equal to four for the second class of specimens (it was equal to 3.6). In fact, Eq. (3.2) is only valid for “mathematical” cracks (zero distance between the crack lips) and only approximately describes the stress-NMOD relation in the case of notched specimens. Therefore, it should be used with caution, since it ignores the role of the radius of curvature ρ (see Fig. 2b) of the crown of the notch, which under specific circumstances could be critical (Markides and Kourkoulis, 2016). Moreover, as it was pointed out by Vardoulakis *et al.* (1998) and Kourkoulis *et al.* (1999), 3PB of beams made of Dionysos marble should be described in the frame of gradient elasticity, taking into account the internal microstructure of the specific material. The latter is the only approach permitting description of the size-effect, which is quite pronounced for the specific material.

Before concluding this Section, two additional aspects of the mechanical behaviour of Dionysos marble should be mentioned, which render the theoretical analysis of 3PB in the frame of Linear Elastic Fracture Mechanics even more prone to large discrepancies from experimental reality. The first one is the slight non-linearity characterizing the axial stress-axial strain curve of the specific marble type. The second one is its bimodularity, i.e., the fact that its elastic modulus under tension is not identical to that under compression (Exadaktylos *et al.*, 2001).

Interesting conclusions about the deformed shape of the specimens just before fracture can be drawn from Fig. 8 in which the deflections of both the upper and lower edges of a typical specimen are plotted for its central part from either side of the notch. The deflections are obtained from the data of the DIC system. Any rigid body translation and rotation was removed. It is observed from Fig. 8 that the deformed contours of the upper and lower edges are not self similar. This behaviour could be attributed to:

- (i) The presence of the notch and
- (ii) The decrease of the specimen height due to the relatively short length of the specimen (and the way the load is applied, i.e., to the punch effect).

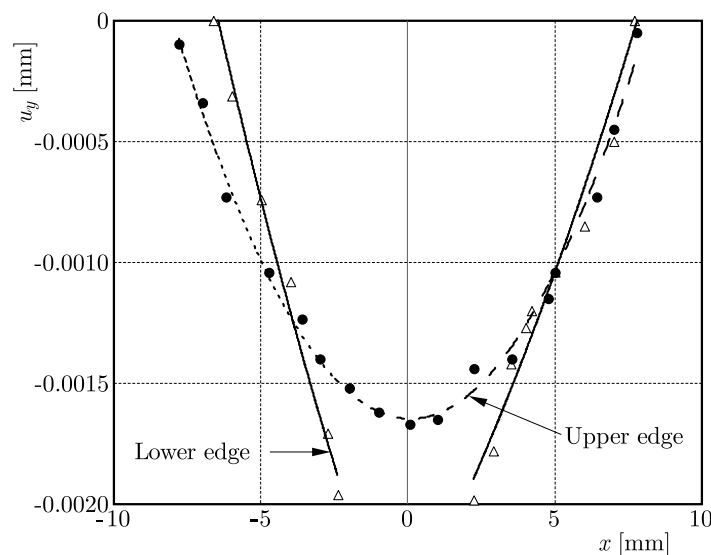


Fig. 8. The vertical (parallel to the load direction) displacement of the upper (filled cycles) and lower (empty triangles) edges of a typical specimen for its central part, as they were obtained with the aid of the 3D-DIC technique (rigid body translations and rotations are removed)

Both these factors are responsible for generation of compressive vertical normal stresses along the height of the central part of the specimens. In Fig. 8, the best fit curves of the experimental data are also shown (continuous lines). For both the upper and lower edges, it is concluded that their deformed shapes are simulated by second order functions of the form

$$y = c_1x^2 + c_2x + c_3 \quad (3.3)$$

with a very satisfactory correlation factor R^2 ranging from 0.97 to 0.99. In Eq. (3.3) c_1 , c_2 and c_3 are constants obtained numerically with the aid of commercial software.

As the next step, the experimental data for the NMOD, as obtained from both the DIC technique and the clip-gauge, are discussed. A typical view of the field of axial displacements u_x (used for the indirect determination of NMOD) is shown in Fig. 9a, as it was captured by the DIC technique just before the final macroscopic fracture of a typical specimen. The impending cracking path is clearly detectable as the locus of zero u_x -values. In order to take advantage of the specific DIC data, two small polygons were isolated on both sides of the notch at its

lowest level and the distance between them was determined as a function of time. Removing the initial distance between the centroids of the two polygons and also removing any rigid body displacements, one obtains the NMOD. The raw data for the time variation of the NMOD as it is obtained from both the DIC technique and the clip-gauge are plotted in Fig. 9b for a typical specimen. Careful inspection of this figure indicates that, although the DIC data are qualitatively similar to the respective ones of the clip-gauge, some quantitative differences exist, mainly for relatively low load levels, where the DIC data appear underestimating the respective NMOD values recorded by the clip-gauge. However, at the ultimate load steps (which are of utmost importance for the determination of the critical NMOD value) the data of the two techniques are very close to each other. In general, according to both techniques, it is only during the very last load steps that the NMOD starts increasing rapidly according to an almost exponential law, and the respective graphs become almost vertical. As a result, the determination of the critical NMOD becomes extremely difficult. Similar conclusions were obtained experimentally by Andrianopoulos *et al.* (1997) for some Metal Matrix Composites under direct tension, although they adopted a completely different recording technique. Saragas *et al.* (1996) published additional data supporting the present conclusions and, moreover, they provided some exponential laws describing accurately enough the dependence of NMOD on the stress level.

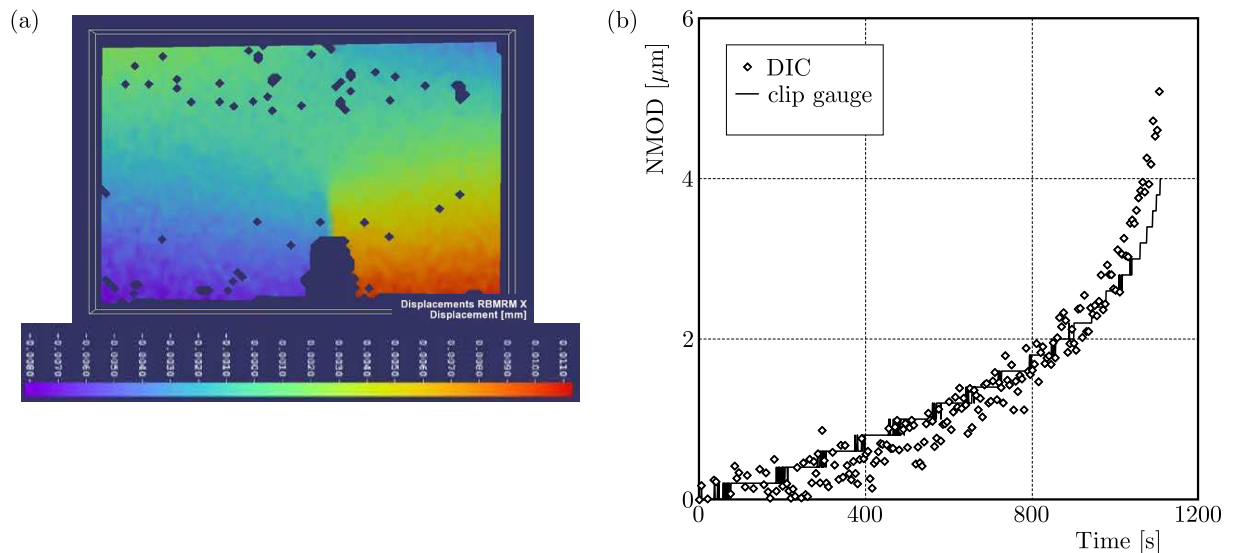


Fig. 9. (a) Axial displacements as recorded by the 3D-DIC technique. The crack path to be followed is visible as the locus with the zero axial displacement. (b) The time variation of the NMOD as it was measured by the clip-gauge (continuous line) versus that recorded by the 3D-DIC system (empty rhomboid symbols)

The deformed notch contour can be deduced from Fig. 10a, in which the horizontal displacements of the points of a locus s , closely surrounding the notch are plotted against the variable s (the contour of the specific locus approaches the actual boundary of the notch as close as it is permitted by the resolution of the DIC system). It is interesting to observe that the flanks of the notch remain linear, thus justifying a geometric extrapolation of the NMOD values in order to obtain the Notch Opening Displacement (NOD). The maximum value of this quantity is in fact the geometry-independent parameter that could be potentially used as fracture criterion. Taking advantage of Fig. 10a, it can be concluded that the critical NMOD for Dionysos marble (at least for the block tested in the present protocol) is equal to about $7.5 \mu\text{m}$ (after removing the initial distance between the knife-edges of the clip-gauge). Then, adopting the procedure shown in Fig. 10b (Knauf and Riedel, 1981) with $\varphi = 60^\circ$, the respective value for the critical NOD (which according to some fracture criteria could be considered as a material constant) is found equal to about $4.4 \mu\text{m}$.

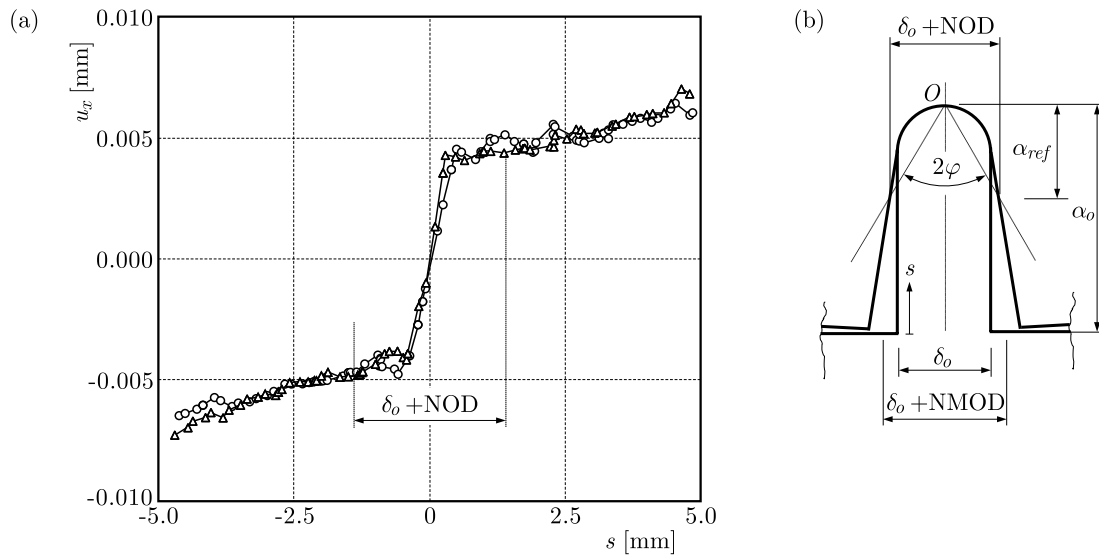


Fig. 10. (a) Axial (horizontal) displacements of a linear locus s closely surrounding the notch (as close as the resolution of the DIC system permits). (b) The procedure adopted to determine the Notch Opening Displacement based on data for the respective NMOD

4. Acoustic and electric activity during three-point bending

4.1. An overview of the whole loading procedure

The time variation of the PSC, recorded during the whole loading process, is plotted in Fig. 11a, in juxtaposition to the respective variation of the load induced, for a representative specimen with a cross section equal to $b \times h = 20 \times 20 \text{ mm}^2$. It is seen that during the initial loading steps (i.e., for load levels lower than 50% of the fracture load) the PSC increases very smoothly, in fact it is almost constant. At a load level equal to about 50% of the fracture load (point A in Fig. 11a), the magnitude of the PSC starts increasing at a different (much higher) rate while the respective load-time plot exhibits an imperceptible slope change (see the shadowed rectangle in Fig. 11a). According to the literature (Triantis *et al.*, 2006, 2007), the onset of an intense PSC increase designates the onset of micro-cracking within the volume of the specimen and, therefore, it can be concluded that point A corresponds to the onset of intense damage processes. Moreover, at a time instant t_1 , a little before the load attains its ultimate value, it is observed that the value of PSC holds back instantaneously (point B in Fig. 11a). The specific point indicates the generation of a local macro-crack which interrupts instantaneously the local electric paths. From this point on, it is considered that the system (specimen) entered its “critical stage”, and final fracture is impending (Stergiopoulos *et al.*, 2015; Triantis *et al.*, 2012).

In Fig. 11b, the aforementioned quantities are plotted for a characteristic experiment of the second class, i.e., with a specimen of the cross section equal to $b \times h = 25 \times 25 \text{ mm}^2$. Although the PSC-time curve exhibits qualitatively similar behaviour to that of Fig. 11a, there are some interesting differences: While at the very early loading levels the PSC-value is again almost constant, it starts increasing relatively earlier (see point A in Fig. 11b), following an “anomaly” of the respective load-time curve. This “anomaly” is characterized by a slight drop of the load-time curve, which then keeps increasing but with a clearly different slope (see the shadowed rectangle in Fig. 11b). Again, at a time instant t_1 , a little before the load attains its ultimate value, the PSC holds back instantaneously (point B in Fig. 11b), indicating again that the system entered its “critical stage” and fracture is impending.

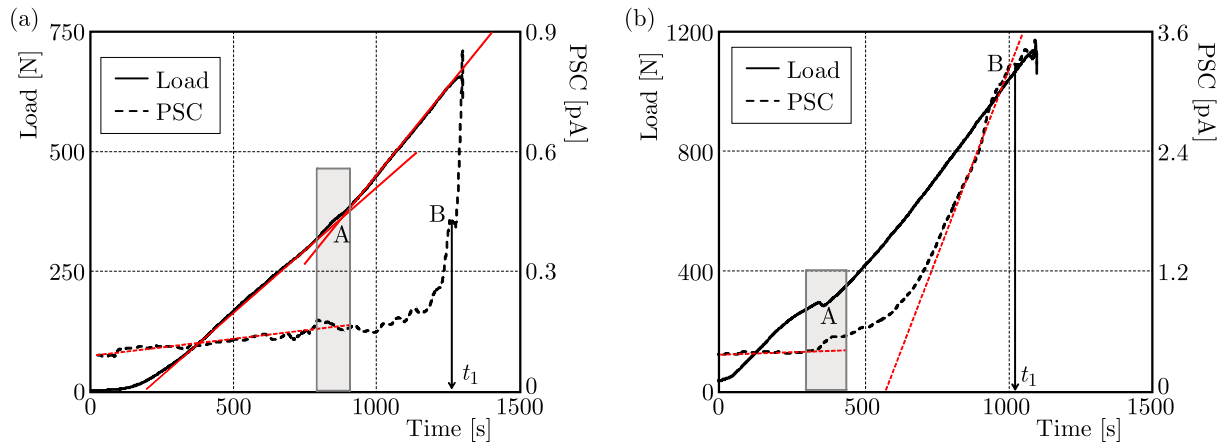


Fig. 11. The time evolution of the load induced in juxtaposition to the respective one of the PSC recorded for a specimen with $b \times h = 20 \times 20 \text{ mm}^2$ (a) and $b \times h = 25 \times 25 \text{ mm}^2$ (b)

Considering the overall behaviour of the two specimens just discussed (and besides any differences which are expected due to the inhomogeneous and anisotropic nature of the material studied), it can be concluded that the time-variation of the PSC offers characteristic indications concerning both the onset of intense micro-cracking within the specimen volume and also the entrance of the system (specimen) to its “critical stage”. Moreover, it is worth noticing that the above indications are not accompanied by similar indications of the load-time curve, which is more or less a continuous and monotonous line (see also Fig. 6) with imperceptible slope changes which do not offer clear hints of the upcoming catastrophic failure.

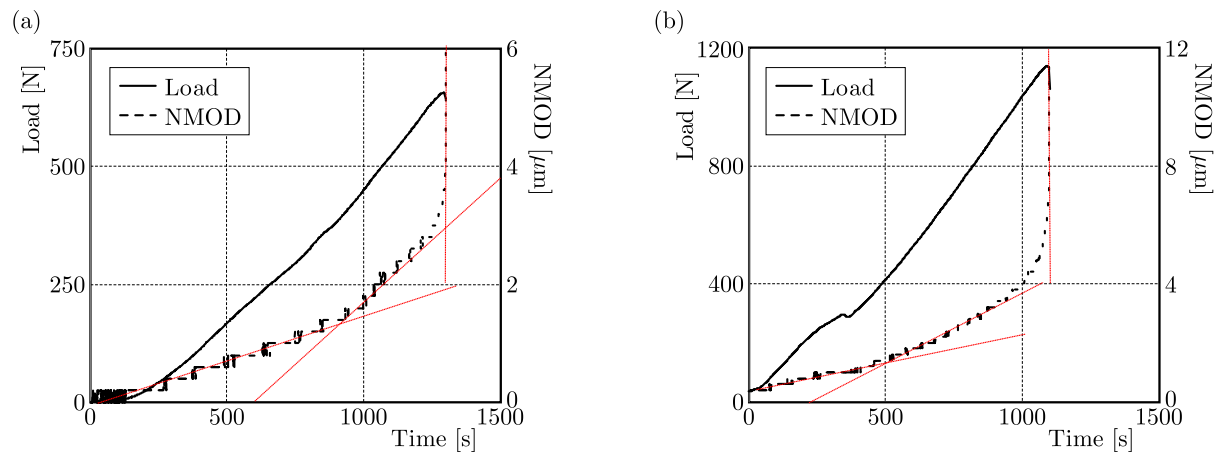


Fig. 12. The time evolution of the load induced in juxtaposition to the respective one of the NMOD, as recorded by the clip-gauge for a specimen with $b \times h = 20 \times 20 \text{ mm}^2$ (a) and $b \times h = 25 \times 25 \text{ mm}^2$ (b)

In an effort to detect a purely mechanical quantity that could, perhaps, offer such hints (i.e., warnings of upcoming catastrophic fracture), the time-variation of the NMOD, as obtained from the clip-gauge, is plotted in Fig. 12 in juxtaposition to the respective load-time variation (for the same as previously two specimens). In good qualitative accordance with the variation of the PSC-values, the NMOD-time curve consists, for both specimens, of three well distinguishable intervals: one of smooth and almost linear increase, a second one, which is again more or less linear but of definitely higher slope and, finally, a third one with very steep slope (as the load induced approaches its ultimate value).

4.2. Focusing attention on the very last loading stages

The analysis of the PSC and NMOD data recorded during all tests of the present experimental protocol indicated clearly that the most dramatic changes of both quantities take place during the very last loading stage (and the same is true for the time variation of the acoustic activity, as it will become evident in next Sections). The duration of this stage does not exceed 10% of the tests duration. Given that the changes within this interval are very abrupt, it is quite possible that critical details of damage evolution could be shadowed by the extremely “condensed” nature of the events. It was thus decided to focus attention on this ultimate time-interval by taking advantage of an alternative mode for representing the respective experimental data. In this direction, the time evolution of PSC, NMOD and also of the acoustic activity are considered versus the $(t_f - t)$ parameter in semi-logarithmic scale, where t_f is the time instant at which the specimen failed by catastrophic crack propagation.

Following the above concept, the time variation of the load and the PSC (both normalized over their respective maximum values) are plotted in Fig. 13 versus the $(t_f - t)$ parameter in juxtaposition to the acoustic activity as it is represented by the time rate of the number of acoustic hits detected by the acoustic sensor located just above the notch. The plots are drawn in a semi-logarithmic scale for the two specimens discussed in the previous Sections.

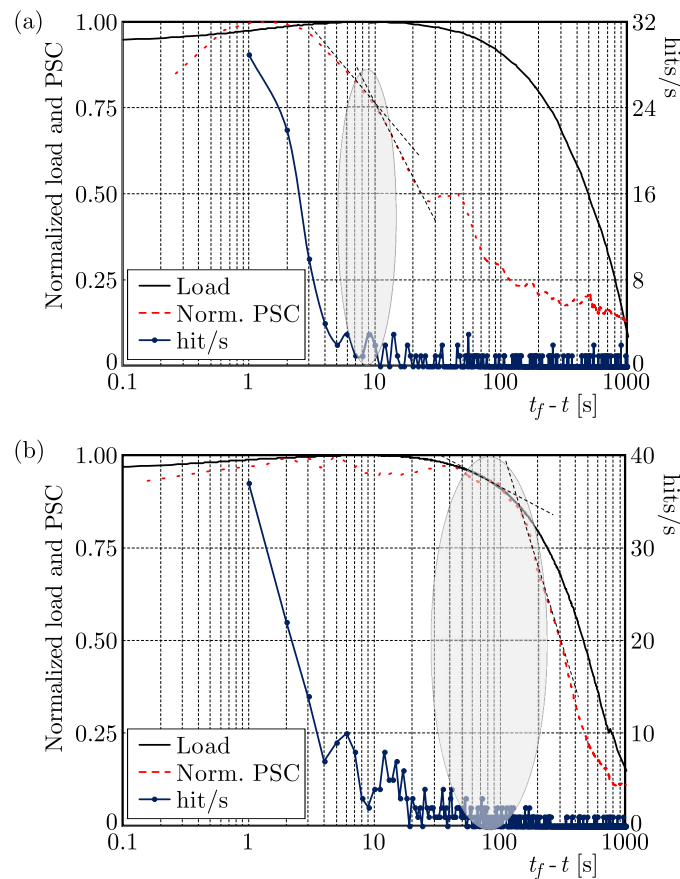


Fig. 13. The time evolution of the load induced (normalized over its maximum value) in juxtaposition to the respective ones of the PSC recorded (also normalized over its maximum value) and of the number of hits recorded per second for a specimen with $b \times h = 20 \times 20 \text{ mm}^2$ (a) and $b \times h = 25 \times 25 \text{ mm}^2$ (b). The quantities are plotted in semi-logarithmic scale against the $(t_f - t)$ parameter to better enlighten the phenomena at the very last loading levels

Figure 13a corresponds to the specimen with $b \times h = 20 \times 20 \text{ mm}^2$. Concerning the acoustic activity, it can be seen that the specimen is almost “silent” for $t_f - t > 10 \text{ s}$. The number of

hits recorded per second is almost equal to zero. Then, at the time instant $t_f - t = 10$ s, the rate of acoustic hits recorded by the acoustic sensor starts increasing dramatically. It is very interesting to observe that the specific time instant corresponds to a clear decrease in the slope of the respective time-PSC curve (see the shadowed ellipse in Fig. 13a).

The overall time evolution of the above quantities (load, PSC and rate of acoustic hits) is qualitatively similar also for the specimens of the second class (i.e., the ones with $b \times h = 25 \times 25$ mm²), as it is shown in Fig. 13b. However, the precursor phenomena designated by the changes of the PSC and the rate of acoustic hits appear now somehow earlier, i.e., at about $t_f - t = 100$ s. Indeed, the specimen is now “silent” for the time interval $t_f - t > 100$ s. Then, the acoustic activity starts increasing relatively smoothly, and only at $t_f - t = 10$ s it starts increasing dramatically. Again, the time instant at which the acoustic activity is amplified for the first time (i.e., the instant $t_f - t = 100$ s) is very close to the time instant at which the respective time-PSC curve changes its slope (see the shadowed ellipse in Fig. 13b). Indeed, while for $t_f - t > 100$ s the PSC increases monotonically (following the respective behaviour of the load), at $t_f - t = 100$ s the rate of the increase of the PSC changes and its value tends to be stabilized. For this specific specimen, at the onset of “explosive” amplification of the acoustic activity (at $t_f - t = 10$ s) the value of the PSC has been already stabilized and it starts decreasing, indicating, obviously, generation of cracks of a higher order (due to the coalescence of already existing cracks of smaller length) which interrupt the electric paths.

Along the same lines, the time variation of the acoustic activity is plotted in Fig. 14 in juxtaposition to the respective variation of the time rate of the NMOD recorded with the aid of clip-gauge. The plots are again considered versus the $(t_f - t)$ parameter in semi-logarithmic scale for the same specimens as previously. The identity of the curves corresponding to the acoustic activity and to the rate of change of the NMOD-values is quite striking.

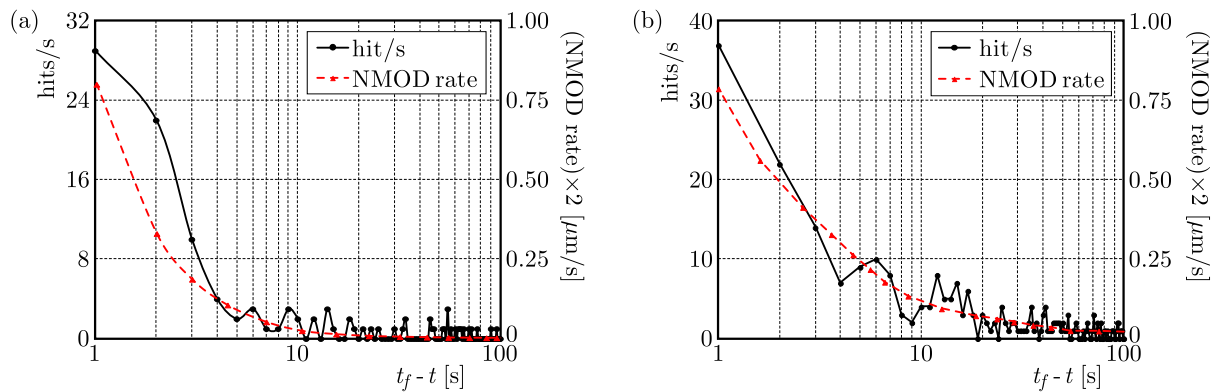


Fig. 14. The time evolution of the NMOD rate in juxtaposition to the respective one of the number of hits recorded per second for a specimen with $b \times h = 20 \times 20$ mm² (a) and $b \times h = 25 \times 25$ mm² (b). The quantities are plotted in semi-logarithmic scale against the $(t_f - t)$ parameter to better enlighten the phenomena at the very last loading levels

Concerning now the Ib -value, its time variation is plotted against the $(t_f - t)$ parameter (again in semi-logarithmic scale), in Fig. 15a, for a characteristic specimen, belonging to the first class. It is seen that the Ib -value starts decreasing towards a level equal to one (considered as an indication that the system enters its “critical stage”) at about the same time instant of the slope change of the respective $(t_f - t)$ -PSC plot. The respective graph for a specimen of the second class, shown in Fig. 15b, is qualitatively similar. The main difference is that now the decrease of the Ib -value towards levels equal to one starts somehow earlier, i.e., at $(t_f - t)$ values around 100 s (again in accordance with the slope change of the respective $(t_f - t)$ -PSC plot).

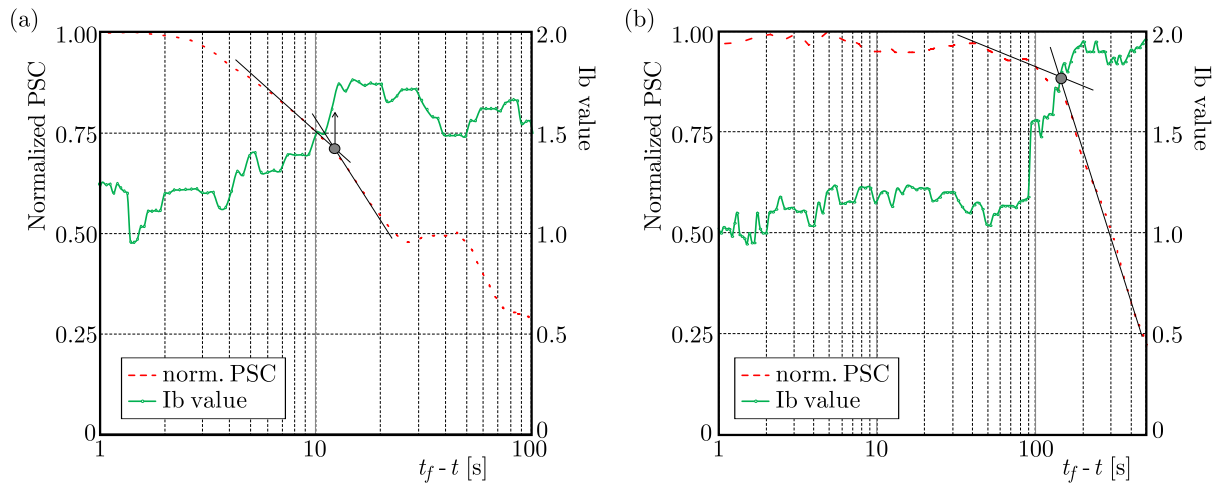


Fig. 15. The time variation of the Ib -value in juxtaposition to the respective one of the PSC for a specimen with $b \times h = 20 \times 20 \text{ mm}^2$ (a) and $b \times h = 25 \times 25 \text{ mm}^2$ (b)

4.3. Classification of the cracking modes

Taking advantage of the characteristics of the acoustic activity, an attempt is now made to classify the cracks generated during the whole loading procedure, focusing again attention on the very last loading stages. Following Ohno and Ohtsu (2010) and Aggelis (2011), the Average Frequency of the acoustic hits is plotted in Fig. 16 either against the RA (Rise Time per Amplitude) parameter (left column of figures) or against the Rise Time (right column of figures) for the above two specimens. It is clear from Fig. 16a (corresponding to the specimen of the first class) that during $t_f - t > 10 \text{ s}$ time interval the acoustic activity is definitely due to exclusively tensile micro-cracking (recall that $t_f - t = 10 \text{ s}$ corresponds to the time instant at which the dramatic changes of the electric and acoustic activity appear for the specific specimen). Indeed, in this time interval the values of both the RA-parameter and the respective Rise Time are very small (tending to zero). It is only during the last ten seconds that events with increasing RA and Rise Time values appear while, at the same time, their average frequency decreases significantly, indicating that Mode II cracking or shear phenomena appear. This phenomenon is even clearer during the very last second of the loading procedure ($t_f - t < 1 \text{ s}$).

The existence of a significant number of non-tensile cracks is, perhaps, somehow astonishing, especially for 3PB tests with pre-notched specimens for which fracture is attributed to tensile stresses around the crown of the notch. A possible explanation could attribute the existence of Mode II and mixed mode cracking (as well as of other type of shear phenomena) to the layered structure of the specific marble type. Indeed, the material layers are somehow wavy and, therefore, they are not uniformly oriented with respect to the loading axis resulting to irregular crack paths (mainly at the microscopic but also at the macroscopic level). These paths, at a given time instant, may be parallel to the material layers (within them), and a few moments later they may become normal to them. As a result, a variety of cracking modes appears (either tensile or shear or mixed mode), in spite of the fact that the macroscopic overall stress field consists of normal stresses (either tensile ones prevailing at the lower portion of the specimens, or compressive ones prevailing at the upper portion). The above described sequence of activation of damage mechanisms is in general agreement with what is widely accepted concerning the fracture of structural materials and the sequence of cracking modes (Aggelis *et al.*, 2013), i.e., that “tensile stresses induce initial micro-cracking and later shear phenomena dominate as damage is being accumulated”.

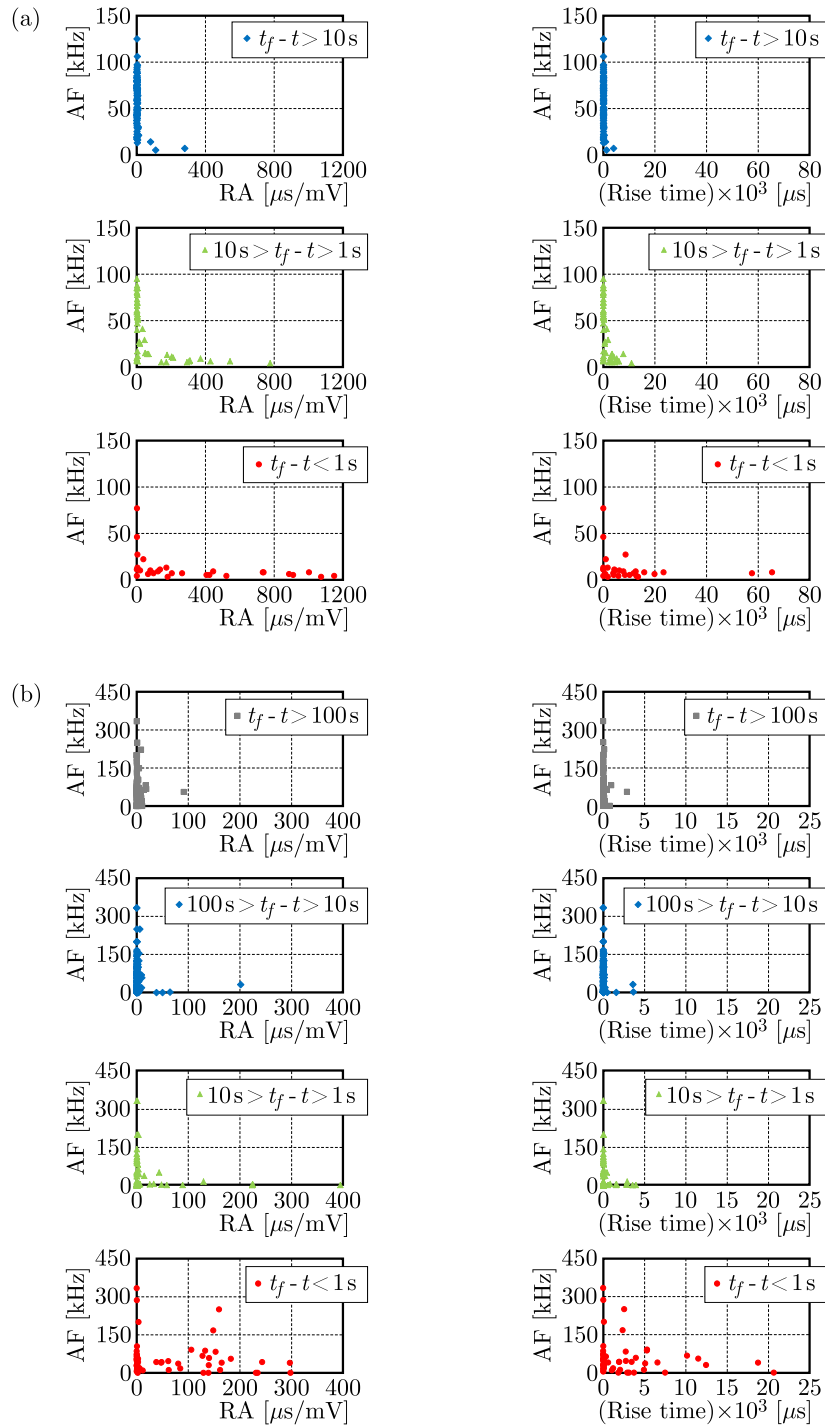


Fig. 16. The Average Frequency of the AE signals recorded versus their RA (Rise Time per Amplitude) parameter (left column) and versus their Rise Time (right column) for a specimen with $b \times h = 20 \times 20 \text{ mm}^2$ (a) and $b \times h = 25 \times 25 \text{ mm}^2$ (b)

The conclusions drawn for the specimen of the second class are almost identical, as it can be seen in Fig. 16b. The only difference is that now the generation of Mode II cracking or shear starts earlier, i.e., at about $t_f - t = 100 \text{ s}$ (again in full accordance with what was observed for the changes of the electric and acoustic activity and the time evolution of the NMOD rate). Exclusively for clarity reasons the duration of the specific test was split into four intervals.

5. Concluding remarks

The response of notched marble beams to mechanical loading under 3PB conditions was studied experimentally, using both traditional and innovative sensing techniques, in an effort to enlighten some critical aspects of their mechanical response and also to check whether it is possible to detect precursor phenomena that could act as signalling effects designating upcoming catastrophic failure.

Concerning the mechanical response, it was concluded that the NMOD-stress relation deviates from linearity from relatively early load levels, contrary to the respective load-deflection relation which is almost linear for the whole loading procedure. The above difference indicates the crucial role of the process zone developed around the crown of the notch. In spite of its very small relative size, this zone affects significantly the evolution of NMOD since the latter depends on the local stress field around the crown of the notch. On the other hand, due to its small size, this zone cannot influence the overall stress field which remains almost linear, explaining the linearity between load and deflection.

Along the same lines, it was pointed out that the slope of the stress-NMOD curve at its linear portion is significantly different from the respective slope predicted using the classical Fracture Mechanics tools. Although some differences were expected due to the fact that in the present protocol notched rather than cracked beams were tested, the magnitude of this difference (exceeding 100%) was astonishing. Following Vardoulakis *et al.* (1998), this huge difference is attributed to the existence of an internal structure, which does not permit characterization of Dionysos marble as an amorphous material. As a result, such materials should be described using tools of gradient elasticity rather than traditional tools of Continuum Mechanics and Fracture Mechanics.

Another interesting finding of the present protocol is that the fracture stress determined by the 3PB tests (with either intact or pre-notched specimens) significantly overestimates the tensile fracture stress obtained by direct tension tests. This observation should be carefully taken into account by engineers since it is a common practice to determine tensile properties of very brittle geomaterials (like rocks and rock-like materials) using bending tests, since their laboratory implementation is quite simple.

Interesting conclusions were also drawn regarding the deformed shape of the specimens just before fracture. Indeed, it was quantitatively pointed out that the deformed shapes of the upper and lower edges of the beams were different. Although such a result should be expected due to the influence of the point load, it was the first time that this difference was experimentally quantified for a material like Dionysos marble, which is extensively used for construction of structural elements subjected to bending schemes.

Regarding the notch itself, it was concluded that its flanks remain linear with excellent accuracy. This observation permits a linear extrapolation of the data recorded at the mouth of the notch (i.e., the NMOD-values recorded by clip-gauges attached at the mouth of the notch) to its tip. As a result, techniques like that proposed by Knauf and Riedel (1981) for the determination of COD and its critical value for completely different materials can be used, also, for the determination of NOD and its critical value for brittle geo-materials like Dionysos marble.

Recapitulating, it became clear that although Dionysos marble is a very brittle material and its overall mechanical response in terms of classical strength of materials is more or less linear, its mechanical behaviour in the presence of notches cannot be adequately described in terms of linear elastic Continuum Fracture Mechanics.

Concerning now the second target of the present experimental protocol, i.e., the detection of precursor phenomena designating impending fracture, interesting conclusions were drawn for all three quantities considered, namely mechanical, electric and acoustic ones. To recapitulate

these conclusions, all three quantities considered, i.e., the PSC, the rate of cumulative acoustic hits per second (dN/dt) and the rate of NMOD, are plotted in Fig. 17 versus the “nominal” stress for a typical specimen of the class with $b \times h = 20 \times 20 \text{ mm}^2$. The similarity of all curves is striking: In spite of their completely different nature (electrical, acoustic and mechanical), all three quantities behave almost according to the same manner with respect to the stress level (or equivalently to the load induced). Initially (i.e., for low stress compared to the fracture one), they are either almost constant (PSC) or they increase very smoothly and, in any case, linearly (dN/dt and NMOD). Then, at a stress level equal to about two thirds of its ultimate value, a dramatic change is observed and the respective curves start increasing according to a completely different slope, tending to become almost vertical.

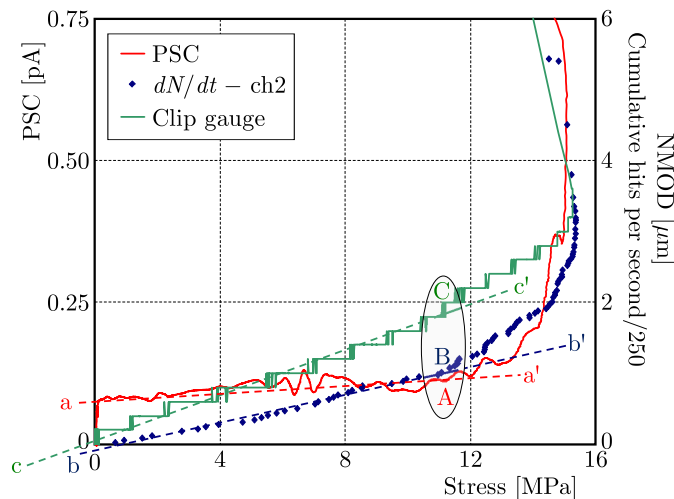


Fig. 17. The evolution of the electric and acoustic activity versus the axial “nominal” stress in juxtaposition to the respective one of the NMOD for a typical specimen with $b \times h = 20 \times 20 \text{ mm}^2$, highlighting the existence of mutually compatible precursor indicators

Considering the above experimental evidence, it is obvious that a relation exists between the mechanical response of Dionysos marble and the respective electric and acoustic processes taking place within the specimen volume. This is schematically shown in Fig. 17 where the narrow shaded elliptic area encompasses all three phenomena:

- (i) Deviation of the stress-PSC plot from its almost constant portion, represented by line aa' (point A).
- (ii) Deviation of the stress- dN/dt plot from its linear portion, represented by line bb' (point B).
- (iii) Deviation of the stress-NMOD rate plot from its linear portion, represented by line cc' (point C).

Taking now into account that the increase of the PSC definitely designates the onset of intense micro-cracking (Triantis *et al.*, 2006; Anastasiadis *et al.*, 2007) and also that the quantity dN/dt is directly related to the number of micro-cracks generated within the specimen’s volume, it can be safely concluded that: At least for the tests of the specific experimental protocol, irreversible processes start taking place at load levels equal to about two thirds of the fracture stress, at rates definitely different from those of the earlier loading stages.

The second very interesting conclusion (which was drawn by considering the very last loading stages through the alternative (inversed) representation of the “time arrow”, see Figs. 13-15) is that a little before the final fracture, the time-PSC plot exhibits well distinguishable changes (in good accordance with the remaining quantities considered), that could be related to the generation of fatal cracks all along the active cross section of the specimen, indicating the exhaust of its load-carrying capacity. From this point on, and in spite of the fact that the load

level will increase slightly (perhaps due to inertia effects), the specimen should be considered fractured. Therefore, these changes of the PSC readings could be used for the determination of the critical NMOD, curing the problems mentioned previously in Section 3, regarding the actual point of the NMOD-stress curve that corresponds to the critical NMOD value.

Along the same lines, it is very interesting to note that the above mentioned changes of the time-PSC plot, designating the exhaust of the specimen's load-carrying capacity, are in good agreement with the respective hints provided by the time evolution of the Ib -value.

Concluding, it can be said that taking advantage of innovative experimental techniques, interesting data can be pumped from the interior of loaded elements, uniquely related to failure mechanisms activated well before any macroscopic fracture is observed.

Research in progress, with double edge notched (DENT) dog-bone marble specimens under direct tension, definitely supports the conclusions of the present study (Kourkoulis *et al.*, 2018). What is more important is that the potentialities of the PSC technique are also supported by a protocol in progress with much more complex structures, as it is for example marble epistyles mutually interconnected with the aid of titanium elements and suitable cementitious materials subjected to pure shear. Although this project is still in progress (given that quite a few difficulties generated by the existence of interfaces are to be overcome), the results are quite encouraging (Pasiou *et al.*, 2018).

Taking into account the conclusions just mentioned, it is indicated that it is worth exploring further the potentialities of the PSC technique to be used as an alternative Structural Health Monitoring tool. This statement is further supported by taking into account the very low cost of the sensors required to record the electric current and also their relatively small size. Especially for restoration projects of ancient monuments, these characteristics of the PSC technique are very attractive because usually there are too many elements restored (thus many sensors are required) and also the aesthetic aspect (and, therefore, the small size of the sensors) is of utmost importance. The excellent agreement of the output of the PSC technique with the respective ones of the AE technique provides a very reliable calibration tool for the PSC technique, considering that nowadays Acoustic Emission is a mature, widely used sensing technique based on well founded natural basis.

Clearly, before definite conclusions are drawn, the qualitative correlations enlightened in the present protocol must be further studied for a much wider class of materials and tests (tension, compression and shear) in the direction of providing quantitative rather than qualitative correlations that could permit calibration of the outcomes of the PSC technique against those of the Acoustic Emissions technique.

Acknowledgements

This research was co-financed by the EU (European Social Fund-ESF) and Greek national funds through the Operational Program "Education and Lifelong Learning" of the National Strategic Reference Framework (NSRF) – Research Funding Program: THALES: Reinforcement of the interdisciplinary and/or inter-institutional research and innovation. The authors gratefully acknowledge the support.

The authors express their sincere thanks to the two anonymous reviewers of the present manuscript. Their comments and suggestions were extremely valuable in the direction of significantly improving the quality and scientific integrity of the present manuscript.

References

1. AGGELIS D.G., 2011, Classification of cracking mode in concrete by acoustic emission parameters, *Mechanics Research Communications*, **38**, 153-157

2. AGGELIS D.G., MPALASKAS A., MATIKAS T.E., 2013, Acoustic signature of different fracture modes in marble and cementitious materials under flexural load, *Mechanics Research Communications*, **47**, 39-43
3. ANASTASIADIS C., STAVRAKAS I., TRIANTIS D., VALLIANATOS F., 2007, Correlation of pressure stimulated currents in rocks with the damage variable, *Annals of Geophysics*, **50**, 1-6
4. ANDRIANOPOULOS N.P., KOURKOULIS S.K., SARAGAS S., 1997, COD measurements and optimum exploitation of metal matrix composites for aerospace applications, *Engineering Fracture Mechanics*, **57**, 565-576
5. BAŽANT Z.P., 1984, Size effect in blunt fracture: concrete, rock, metal, *ASCE Journal of Engineering Mechanics*, **110**, 518-535
6. BLANCHETTE Y., DICKSON J.I., BASSIM M.N., 1984, The use of acoustic emission to evaluate critical values of K and J in 7075-T651 aluminum alloy, *Engineering Fracture Mechanics*, **20**, 359-371
7. BRYNK T., LAPTEV A., TOLOCHYN O., PAKIELA Z., 2012, The method of fracture toughness measurement of brittle materials by means of high speed camera and DIC, *Computational Materials Science*, **64**, 221-224
8. CARPINTERI A., 1989, Decrease of apparent tensile and bending strength with specimen size: Two different explanations based on fracture mechanics, *International Journal of Solids and Structures*, **25**, 407-429
9. ERDOGAN F., SIH G.C., 1963, On the crack extension in plates under plane loading and transverse shear, *ASME Journal of Basic Engineering*, **85D**, 519-527
10. EXADAKTYLOS G.E., VARDOULAKIS I., KOURKOULIS S.K., 2001, Influence of nonlinearity and double elasticity on flexure of rock beams – I. Technical theory, *International Journal of Solids and Structures*, **38**, 4091-4117
11. HASHIDA T., 1993, Fracture toughness testing of core-based specimens by acoustic emission, *International Journal of Rock Mechanics and Mining Sciences and Geomechanics Abstracts*, **30**, 61-69
12. KISHINOUE T., 1990, An experiment on the progression of fracture (preliminary rep.), *Journal of Acoustic Emission*, **9**, 177-180
13. KNAUF C., RIEDEL H., 1981, A comparative study on different methods to measure the crack opening displacement, *Proceedings of the 5th International Conference on Fracture (ICF5)*, Cannes, France, 2547-2553
14. KORRES M., BOURAS H., 1983, *Study for the Restoration of the Parthenon*, Ministry of Culture and Science, Committee for the Preservation of the Acropolis Monuments, Athens, Greece
15. KOURKOULIS S.K., EXADAKTYLOS G. E., VARDOULAKIS I., 1999, U-notched Dionysos-Pentelicon marble beams in three point bending: The effect of nonlinearity, anisotropy and microstructure, *International Journal of Fracture*, **98**, 369-392
16. KOURKOULIS S.K., GANNIARI-PAPAGEORGIOU E., 2010, Experimental study of the size-and shape-effects of natural building stones, *Construction and Building Materials*, **24**, 803-810
17. KOURKOULIS S.K., PASIOU E.D., DAKANALI I., STAVRAKAS I., TRIANTIS D., 2018, Notched marble plates under tension: Detecting pre-failure indicators and predicting entrance to the “critical stage”, *Fatigue and Fracture of Engineering Materials and Structures*, **41**, 776-786
18. KYRIAZOPOULOS A., ANASTASIADIS C., TRIANTIS D., BROWN J.C., 2011, Non-destructive evaluation of cement-based materials from pressure-stimulated electrical emission – Preliminary results, *Construction and Building Materials*, **25**, 1980-1990
19. LABUZ J.F., CATTANEO S., CHEN L.H., 2001, Acoustic emission at failure in quasi-brittle materials, *Construction and Building Materials*, **15**, 225-233
20. MAJI A., SHAH S.P., 1988, Process zone and acoustic-emission measurements in concrete, *Experimental Mechanics*, **28**, 27-33

21. MARKIDES CH.F., KOURKOULIS S.K., 2016, 'Mathematical' cracks versus artificial slits: Implications in the determination of fracture toughness, *Rock Mechanics and Rock Engineering*, **49**, 707-729
22. MURALIDHARA S., PRASAD B.R., ESKANDARI H., KARIHALOO B.L., 2010, Fracture process zone size and true fracture energy of concrete using acoustic emission, *Construction and Building Materials*, **24**, 479-486
23. OBERT L., 1941, Use of subaudible noise for the prediction of rock bursts, Report R13555, U.S. Bureau of Mines, Washington D.C.
24. OHNO K., OHTSU M., 2010, Crack classification in concrete based on acoustic emission, *Construction Building Materials*, **24**, 2339-2346
25. OHTSU M., 2010, RILEM TC 212-ACD: Acoustic emission and related NDE techniques for crack detection and damage evaluation in concrete, *Materials and Structures*, **43**, 1187-1189
26. PASIOU E.D., STAVRAKAS I., TRIANTIS D., KOURKOULIS S.K., 2018, Marble epistyles under shear: An experimental study of the role of "relieving space", submitted to *Frontiers of Structural and Civil Engineering*
27. RAO M.V.M.S., PRASANNA LAKSHMI K.J., 2005, Analysis of b-value and improved b-value of acoustic emissions accompanying rock fracture, *Current Science*, **89**, 1577-1582
28. SACHSE W., YAMAGUCHI K., ROGET J., 1991, *Acoustic Emission: Current Practice and Future Directions*, STP1077, ASTM
29. SARAGAS S., KOURKOULIS S.K., ANDRIANOPOULOS N.P., 1996, A comparative study of COD measurements for novel metal matrix composites and alloys, *International Journal of Fracture*, **79**, 179-187
30. SHIOTANI T., FUJII K., AOKI T., AMOU K., 1994, Evaluation of progressive failure using AE sources and improved b-value on slope model tests, *Progress in Acoustic Emission VII*, **7**, 529-534
31. SHIOTANI T., YUYAMA S., LI Z.W., OHTSU M., 2001, Application of the AE improved b-value to qualitative evaluation of fracture process in concrete-materials, *Journal of Acoustic Emission*, **19**, 118-133
32. SIH G.C., 1973, Some basic problems in Fracture Mechanics and new concepts, *Engineering Fracture Mechanics*, **5**, 365-377
33. SLIFKIN L., 1993, Seismic electric signals from displacement of charged dislocations, *Tectonophysics*, **224**, 149-152
34. STAVRAKAS I., ANASTASIADIS C., TRIANTIS D., VALLIANATOS F., 2003, Piezo stimulated currents in marble samples: Precursory and concurrent-with-failure signals, *Natural Hazards and Earth System Sciences*, **3**, 243-247
35. STERGIPOULOS C., STAVRAKAS I., TRIANTIS D., VALLIANATOS F., STONHAM J., 2015, Predicting fracture of mortar beams under three-point bending using non-extensive statistical modelling of electric emissions, *Physica A*, **419**, 603-611
36. SULEM J., VARDOULAKIS I., 1990, Bifurcation analysis of the triaxial test on rock specimens. A theoretical model for shape and size effect, *Acta Mechanica*, **83**, 195-212
37. SUTTON M.A., CHENG M., PETERS W.H., CHAO Y.J., MCNEILL S.R., 1986, Application of an optimized digital correlation method to planar deformation analysis, *Image and Video Computing*, **4**, 143-150
38. SUTTON M.A., MCNEILL S.R., HELM J.D., CHAO Y.J., 2000, Advances in two-dimensional and three-dimensional computer visio, [In:] *Photomechanics*, Rastogi P.K. (Edit.), Topics in Applied Physics, Springer, Berlin, **77**, 323-372
39. TASSOGIANNPOULOS A.G., 1986, A contribution to the study of the properties of structural natural stones of Greece (in Greek), Ph.D. Dissertation, Supervisor: A. Koroneos, National Technical University of Athens, Greece

40. TADA H., PARIS P.C., IRWIN G.R., 1973, *The Stress Analysis of Cracks Handbook*, Del Research Corporation
41. THEOCARIS P.S., KARDOMATEAS G., ANDRIANOPOULOS N.P., 1982, Experimental study of the T-criterion in ductile fractures, *Engineering Fracture Mechanics*, **17**, 439-445
42. The Venice Charter: International charter for the conservation and restoration of monuments and sites, 1964, *11nd International Congress of Architects and Technicians of Historic Monuments*, ICOMOS, Venice, Italy
43. TRIANTIS D., ANASTASIADIS C., VALLIANATOS F., KYRIAZIS P., NOVER G., 2007, Electric signal emissions during repeated abrupt uniaxial compressional stress steps in amphibolite from KTB drilling, *Natural Hazards and Earth System Science*, **7**, 149-154
44. TRIANTIS D., STAVRAKAS I., ANASTASIADIS C., KYRIAZOPOULOS A., VALLIANATOS F., 2006, An analysis of Pressure Stimulated Currents (PSC) in marble samples under mechanical stress, *Physics and Chemistry of the Earth*, **31**, 234-239
45. TRIANTIS D., STAVRAKAS I., KYRIAZOPOULOS A., HLOUPIS G., AGIOUTANTIS Z., 2012, Pressure stimulated electrical emissions from cement mortar used as failure predictors, *International Journal of Fracture*, **175**, 53-61
46. VALLIANATOS F., TZANIS A., 1999, On possible scaling laws between electric earthquake precursors (EEP) and earthquake magnitude, *Geophysical Research Letters*, **26**, 2013-2016
47. VARDOULAKIS I., EXADAKTYLOS G.E., KOURKOULIS S.K., 1998, Bending of marble with intrinsic length scales: A gradient theory with surface energy and size effects, *Journal de Physique IV*, **8**, 399-406
48. VARDOULAKIS I., KOURKOULIS S.K., 1997, Mechanical properties of Dionysos marble, Final report of the Environment Project EV5V-CT93-0300: Monuments Under Seismic Action, National Technical University of Athens, Athens, Greece
49. VAROTSOS P.A., 2005, *The Physics of Seismic Electric Signals*, TerraPub, Tokyo, Japan
50. WHITWORTH R.W., 1975, Charged dislocations in ionic crystals, *Advances in Physics*, **24**, 203-304
51. WU C.H., 1978, Fracture under combined loads by the maximum-energy release rate criterion, *Journal of Applied Mechanics*, **45**, 553-558
52. YOFFE E. H., 1951, The moving Griffith crack, *Philosophical Magazine*, **42**, 739-750
53. ZAMBAS K., 1994, *Study for the Restoration of the Parthenon*, Vol. 3b, Ministry of Culture, Committee for the Preservation of the Acropolis Monuments, Athens, Greece

VIBRATION OF A MISTUNED THREE-BLADED ROTOR UNDER REGULAR AND CHAOTIC EXCITATIONS

JERZY WARMINSKI, JAROSŁAW LATALSKI, ZOFIA SZMIT

Lublin University of Technology, Department of Applied Mechanics, Lublin, Poland

e-mail: j.warminski@pollub.pl

This study considers forced vibrations of a rotating structure consisting of a rigid hub and three flexible beams. The blades are nominally made of a multilayered laminate with a specific stacking sequence resulting in full isotropic macroscopic material behaviour. However, in the performed analysis it is assumed that the rotor has been mistuned because of manufacturing tolerances of the composite material. These inaccuracies are represented by deviations of reinforcing fibres orientations from their nominal values. The considered tolerances break the intended macroscopic material isotropy and make the laminate to exhibit the fully orthotropic behaviour. Based on previous authors research, the system of four mutually coupled dimensionless ordinary differential governing equations is adopted. Forced responses of the system under regular and chaotic excitations are investigated.

Keywords: rotating beam, multi-bladed rotor, rotor mistuning, chaotic oscillations

1. Introduction

Rotors are important machine components widely used in numerous industrial applications. The most common ones are helicopters, wind power turbines, fans, pumps, airplane propellers etc. Other advanced rotor design examples are rigid disks with a series of beam elements combined in multi-stage assemblies. These are typically found in axial compressors, turbojet aircraft engines, steam and gas turbines etc.

The considered systems are intentionally designed to be perfectly symmetric ones. However, multiple reasons may lead to symmetry break down in actual structures. The most common is rotor unbalance. This happens when mass centerline of the rotor does not coincide with the rotational axis. As a consequence, periodic inertia forces arise and large amplitude lateral vibrations of the structure can occur. The loss of rotor symmetry might happen also due to operating wear of blades airfoil, possible crack development, random variations in material properties and tolerances in manufacturing processes. Any of these factors leads to deviation in mechanical properties of the affected blade. This difference in blade to blade properties is referred to as rotor mistuning.

The impact of system mistuning on the free and forced response of multi-bladed rotors is of great scientific and practical interest. This stems from a few reasons. Primarily, the mistuning phenomenon has a fundamental influence on rotor dynamic characteristics. It turns out that mistuned multiple-bladed rotors can exhibit drastically larger forced response levels than the perfectly tuned designs (Xiao *et al.*, 2004). For example, a 5% variation in the blade cantilever frequencies on a 92-bladed high pressure turbine disk can lead to one blade suffering a response magnitude of over 500% of the one observed on the perfectly tuned equivalent disk (Petrov and Ewins, 2003). This effect leads to large increases in stress and vibration amplitudes resulting in high cyclic fatigue and short lifetime of the rotor. An important observation regarding the increased vibration amplitudes is that they are not evenly distributed around all the rotor

blades. The vibration energy is usually spatially concentrated making the modal motion to be limited to few blades only. This effect is known as mode localisation phenomenon and can be observed in any coupled periodic systems if a group of tuned structure modes forms a complete set along the periodicity direction (Chen and Shen, 2015). The presence of irregularities in such structures restricts propagation of vibrations and confines the energy to a region close to the vibration source. However, as reported by Vakakis *et al.* (1993), the mistuning and the resulting localisation phenomena may originate also from structural nonlinearities and, thus, it may be observed even in perfectly periodic systems.

Several concepts have been developed and discussed in the professional literature to reliably quantify mistuned rotor characteristics. These can be generally divided into either statistical or deterministic approach to the problem.

Studying the dynamics of mistuned rotors within the frame of statistical analysis requires information about forced response probability density functions. These distributions are usually determined within a series of Monte Carlo simulations. To this aim, a random population of test designs has to be given. This can be generated by assuming *a priori* the deviations in system mass and stiffness matrices (Sinha, 1986). More representative designs may be found by Taylor series expansions in terms of variables describing geometric variations of mistuned blades (Bhartiya and Sinha, 2013), from the experimental data tests (Li *et al.*, 2006) or by means of a perturbation technique as proposed by Mignolet and Lin (1993). An alternative approach to approximate the mistuned rotor forced response probability density functions was proposed by Sinha (2006). The author tested the use of polynomial chaos for modal stiffness estimation and to compute the statistics of the forced response of a mistuned bladed disk assembly analytically.

Although the mistuning effect is a stochastic process (due to randomness of geometric and/or material perturbations) several deterministic approaches to the problem have been also developed. The earliest studies considered multi-bladed rotors as a series of springs and lumped masses used to represent the blades and additional springs and dampers to model blade-to-hub and blade-to-blade interactions (Griffin and Hoosac, 1984). Values of these system variables had to be determined through a parameter identification procedure. Despite its simplicity and availability of more advanced models these types of simplified formulations are still in use (Nikolic, 2006).

Around the same time as analytical lumped masses models were being elaborated, the first finite element code software started showing up. This allowed more strict investigation of actual rotor structures, taking into account complicated blades geometry, shrouds, aerodynamics and fluid-structure interactions etc. Over time, a reduced order treatment and sub-structuring techniques were developed to simplify a complete bladed disk finite element model to a smaller and more tractable problem. The most common ones used for mistuned rotors analysis are component mode synthesis (CMS), component mode based (CMB) method, subset of nominal modes (SNM) method and modified modal domain (MMD) analysis (Castanier and Pierre, 2006). For instance, the CMS method proposed by Castanier *et al.* (1997) is capable of reducing the overall number of FE degrees of freedom up to three orders of magnitude if compared to the full structure model. Another deterministic approach to the analysis of mistuned rotors is based on a combination of the perturbation method and sensitivity analysis for natural frequencies and mode shapes (Shapiro, 1999). Alternatively, the analysis of rotors dynamics may be performed in the framework of an exact analytical formulation. The governing equations are usually derived by means of Hamilton's principle. Next, these are solved analytically or numerically to test the system stability, individual blades motion synchronisation etc. (Crespo da Silva, 1998; Chandiramani *et al.*, 2002; Sinha, 2013).

Dynamics of rotating structures was also investigated by the authors of this publication. In particular, in paper (Warminski *et al.*, 2014) a nonlinear system composed of two pendula

attached to a hub and rotating in a horizontal plane was examined. The synchronisation phenomenon and transitions through resonances were analysed considering the influence of the hub inertia and order of nonlinearity in the problem formulation. The existence of chaotic oscillations of the system and paths leading to chaos were demonstrated as well. Next, Latalski *et al.* (2017) studied the dynamics of a hub-composite beam structure. Parametric studies regarding the laminate orientation angle and different regular driving torque scenarios were performed. The possibilities to control this kind of systems by means of the saturation control method were examined in a later research (Warminski and Latalski, 2017).

In the present contribution, the former authors studies are extended to accommodate the three-bladed rotor case. In the performed analysis, it is assumed that the beams are made of a multilayered composite material with manufacturing tolerances of reinforcing fibres orientations. The different magnitude of manufacturing inaccuracies in the individual blades results in their different stiffnesses followed by the rotor mistuning. The forced response of the system under regular and chaotic excitations is investigated as well as synchronisation of individual blades motions.

2. Statement of the problem

Let us consider a rotor consisting of three slender and elastic composite beams clamped at the rigid hub of inertia J_h . The blades are fitted so that their flapwise bending plane coincides with the rotor plane. The system is driven by an external torque T_{ext} inducing rotation about a fixed frame vertical axis CZ_0 . The temporary angular position of the hub is denoted by an angle $\psi(t)$ – see Fig. 1. The beams are made of an eighteen-layered laminate of an unidirectional graphite-epoxy pre-preg material. The adopted specific stacking sequence (0/–60/60/0/–60/60₃/–60₂/0₂/–60/0₂/60₂/–60) results in nominally full isotropic composite material behaviour (Vannucci and Verchery, 2002). However, in the performed analysis it is assumed that the rotor can be mistuned because of manufacturing inaccuracies in the laminate. These are represented by deviations of reinforcing fibres orientations from their nominal values. The discussed misalignments break the intended macroscopic material isotropy and make the laminate exhibit fully orthotropic behaviour. More detailed information regarding the way the rotor is mistuned and the considered mistuning magnitudes is given in the next Section and Table 3.

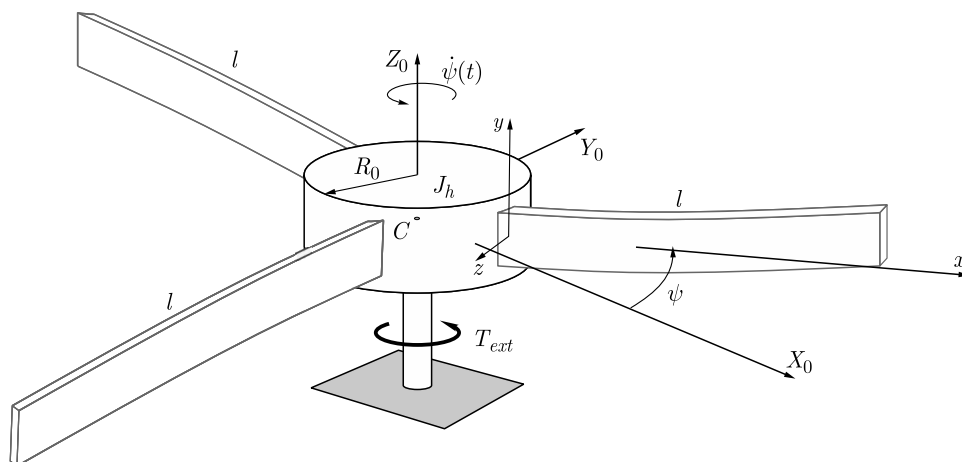


Fig. 1. Model of the rotating hub with three elastic beams

2.1. Equations of motion

The partial differential equations of motion of the considered structure have been derived according to the extended Hamilton's principle

$$\delta J = \int_{t_1}^{t_2} (\delta T - \delta U + \delta W_{ext}) dt = 0 \quad (2.1)$$

where J is the action, T is the kinetic energy, U is the potential energy and the work done by the external forces is given by the W_{ext} term.

The kinetic energy of the structure is defined as

$$T = \frac{1}{2} J_h \dot{\psi}^2(t) + \frac{1}{2} \sum_{i=1}^3 \int_{V_i} \rho \dot{\mathbf{R}}_i^T \dot{\mathbf{R}}_i dV_i \quad (2.2)$$

where the designation ρ refers to the average composite material density, $\dot{\mathbf{R}}_i$ is the velocity vector of an representative infinitesimal element of volume V_i of the beam i . The total potential energy of the system $U = \sum_{i=1}^3 U_i$ comes from elastic deformations of each beam. Posing the assumptions regarding a general shape of an open cross-section and its in-plane non-deformability, the energy U_i for an individual specimen is given by (Latalski *et al.*, 2017)

$$U_i = \frac{1}{2} \int_{V_i} (\sigma_{xx} \varepsilon_{xx} + \sigma_{xz} \gamma_{xz} + \sigma_{xs} \gamma_{xs}) dV_i \quad (2.3)$$

where σ_{xx} , σ_{xn} , σ_{xs} and ε_{xx} , γ_{xz} , γ_{xs} are stresses and strains in the axial direction and transverse and lateral shear planes, respectively (referring to the individual blade). Although the posed mathematical model of the beam is limited to the linear case, the nonlinear axial strain ε_{xx} definition is adopted to represent properly the blade stiffening effect arising from system rotation $\dot{\psi}(t)$ (Latalski *et al.*, 2017; Mayo *et al.*, 2004). Therefore, the appropriate expressions are as follows

$$\begin{aligned} \varepsilon_{xx} &= \frac{\partial D_x}{\partial x} + \frac{1}{2} \left[\left(\frac{\partial D_x}{\partial x} \right)^2 + \left(\frac{\partial D_y}{\partial x} \right)^2 + \left(\frac{\partial D_z}{\partial x} \right)^2 \right] \\ \gamma_{xz} &= \frac{\partial D_x}{\partial z} + \frac{\partial D_z}{\partial x} \\ \gamma_{xs} &= \gamma_{xy} + 2z\varphi' = \frac{\partial D_x}{\partial y} + \frac{\partial D_y}{\partial x} + 2z\varphi' \end{aligned} \quad (2.4)$$

where D_x , D_y and D_z are axial, lateral and transverse displacements of the cross-section representative point written down in the local coordinates frame (x, y, z) . The γ_{xs} strain includes an additional component coming from specimen torsion where φ is the profile twist angle. This is mandatory for the points located out of the beam mid-surface (Librescu and Song, 2006). Moreover, it is worth noting that the first nonlinear term present in ε_{xx} is skipped in further calculations due to the order of magnitude with respect to the other ones (Librescu and Song, 2006).

Bearing in mind least action principle (2.1) and considering energy variations, after integration with respect to time, a set of general partial differential equations of motion of the structure is derived. By neglecting the deformations occurring out of the rotor plane, the problem is simplified. Therefore, in the final formulation, only the lead-lag plane displacement, transverse shear and profile twist for each individual beam are considered. These equations are supplemented by the additional one representing the rigid hub rotation dynamics. For the sake of brevity, the

complex form of the partial differential equations and associated boundary conditions are omitted here. However, their full formulation as well as the detailed step-by-step derivation can be found in the previous authors paper (Latalski *et al.*, 2017).

The derived system of partial differential governing equations is transformed into ordinary differential ones taking into account the normal modes projection and the associated orthogonality condition. To this aim, the Galerkin procedure for the first natural mode is applied. Next, the system is converted into the dimensionless notation. The coupled flexural-torsional mode projection results in the final set of nonlinear ODEs as follows

$$\begin{aligned}
 & \left(J_h + \sum_{i=1}^3 J_{bi} + \sum_{i=1}^3 \alpha_{hi2} q_i^2 \right) \ddot{\psi} + \zeta_h \dot{\psi} + \sum_{i=1}^3 (\alpha_{hi1} \ddot{q}_i + \alpha_{hi3} q_i \dot{q}_i \dot{\psi}) = \mu(\tau) \\
 & \ddot{q}_1 + \zeta_1 \dot{q}_1 + \alpha_{12} \ddot{\psi} + (\alpha_{11} + \alpha_{13} \dot{\psi}^2) q_1 + \alpha_{14} q_1 \dot{q}_1 \dot{\psi} = 0 \\
 & \ddot{q}_2 + \zeta_2 \dot{q}_2 + \alpha_{22} \ddot{\psi} + (\alpha_{21} + \alpha_{23} \dot{\psi}^2) q_2 + \alpha_{24} q_2 \dot{q}_2 \dot{\psi} = 0 \\
 & \ddot{q}_3 + \zeta_3 \dot{q}_3 + \alpha_{32} \ddot{\psi} + (\alpha_{31} + \alpha_{33} \dot{\psi}^2) q_3 + \alpha_{34} q_3 \dot{q}_3 \dot{\psi} = 0
 \end{aligned} \tag{2.5}$$

where J_h , J_{bi} denote the mass moment of inertia of the hub and each subsequent beam, respectively. These are relative values calculated with respect to beam 1. The factors ζ_h and ζ_i are hub and beams viscous damping coefficients. They have been estimated during laboratory experiments. The approximate value for every ζ_i is 0.04 ratio of its corresponding beam natural frequency ω_{0i} , thus $\zeta_i = 0.04\sqrt{a_{i1}}$. The hub damping ζ_h has been set at 0.1. The external dimensionless torque imposed to the hub is denoted by $\mu(\tau)$ where τ is dimensionless time. The parameters α_{hij} ($j = 1, 2, 3$) present in (2.5)₁ and α_{ik} ($k = 1, \dots, 4$) in (2.5)₂₋₄ are coefficients obtained from the modal reduction procedure.

Studying the system of governing equations (2.5) one may observe that the individual beams equations are coupled by inertia terms present in the hub equation. If angular velocity of the structure is constant ($\dot{\psi} = 0$) then all equations become uncoupled. This happens despite the quadratic terms present in the first equation since these terms are of a higher order and can be neglected for a small oscillations case. By contrast, if the angular velocity is not constant ($\dot{\psi} \neq 0$) then all equations are mutually coupled, and the nonlinear quadratic terms as well as Coriolis forces are involved in the full structure dynamics.

2.2. Accounting for reinforcing fibres misalignment

To take into consideration the composite fibres orientation tolerances let us assume that the fiber angle in each k -th ply ($k = 1, \dots, N$) may be deviated from its nominal value α_k by the maximum acceptable tolerance limit $\Delta\alpha_k$. Hence the actual orientation angle stays within a range $\langle \alpha_k - \Delta\alpha_k; \alpha_k + \Delta\alpha_k \rangle$ – see Fig. 2a. Moreover, one assumes that the magnitude of this misalignment is set arbitrary and it does not depend on the nominal fiber orientations α_k . Therefore, the tolerance stays equal for all layers and, thus, $\Delta\alpha_k = \Delta\alpha$.

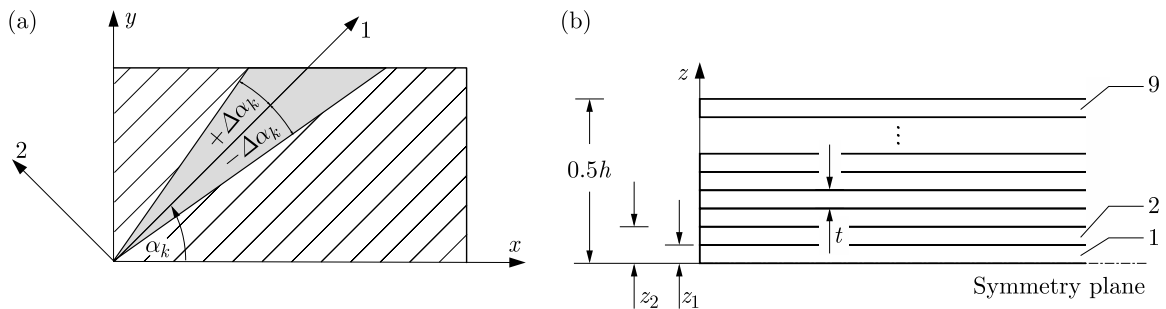


Fig. 2. Modelling the tolerances of laminate reinforcing fibres orientations

This approach to model the imperfect laminate where only the nominal values and peak deviations of fiber orientation angles are given renders their exact values unknown. However, the maximum possible impact of the accepted $\Delta\alpha$ inaccuracies on the mechanical properties of the material may be estimated by means of a sensitivity analysis. To this aim, let us consider the requested beam stiffnesses occurring in the partial differential equations of motion of the hub-composite beam rotor as formulated in (Latalski *et al.*, 2017) Eqs. (24)-(28). These stiffnesses are calculated according to the Librescu composite beam theory (Georgiades *et al.*, 2014; Librescu and Song, 2006) and expressed as

$$\begin{aligned}
a_{33} &= \int_c \left[\left(A_{22} - \frac{A_{12}A_{12}}{A_{11}} \right) z^2 - 2 \left(B_{22} - \frac{A_{12}B_{12}}{A_{11}} \right) \frac{dy}{ds} z + \left(D_{22} - \frac{B_{12}B_{12}}{A_{11}} \right) \left(\frac{dy}{ds} \right)^2 \right] ds \\
a_{37} &= 2 \int_c \left[\left(B_{26} - \frac{A_{12}B_{16}}{A_{11}} \right) z - \left(D_{26} - \frac{B_{12}B_{16}}{A_{11}} \right) \frac{dy}{ds} \right] ds \\
a_{55} &= \int_c \left[\left(A_{66} - \frac{A_{16}A_{16}}{A_{11}} \right) \left(\frac{dz}{ds} \right)^2 + A_{44} \left(\frac{dy}{ds} \right)^2 \right] ds \\
a_{77} &= 2 \int_c \left(D_{66} - \frac{B_{16}B_{16}}{A_{11}} \right) ds
\end{aligned} \tag{2.6}$$

where the dummy variable s represents the beam profile coordinate measured along its width. Terms a_{33} , a_{55} , and a_{77} are flapwise bending, transverse shear and twist stiffnesses, respectively. The parameter a_{37} represents the laminate stiffness in coupled flapwise bending-twist deformation. In the nominal design, this is equal to zero since the considered multilayered laminate is macroscopically isotropic. However, for a material with misaligned layers it is expected to be different from zero. This is confirmed by results given in Table 1.

The above given stiffnesses are expressed in terms of individual elements of \mathbf{A} , \mathbf{D} and \mathbf{B} tensors representing stretching, bending and bending-stretching stiffnesses, respectively. Following the Classical Laminate Theory they are given as

$$\begin{aligned}
A_{ij} &= \sum_{k=1}^{18} \bar{Q}_{ij}^{(k)} (z_k - z_{k-1}) & B_{ij} &= \frac{1}{2} \sum_{k=1}^{18} \bar{Q}_{ij}^{(k)} (z_k^2 - z_{k-1}^2) \\
D_{ij} &= \frac{1}{3} \sum_{k=1}^{18} \bar{Q}_{ij}^{(k)} (z_k^3 - z_{k-1}^3)
\end{aligned} \tag{2.7}$$

where z_k, z_{k-1} are the distances from the reference plane to the two surfaces of the k -th ply (see Fig. 2b) and $\bar{Q}_{ij}^{(k)}$ are the members of the reduced stiffness matrix of this ply. These recent ones depend on the fibres orientation angle α_k

$$\begin{aligned}
\bar{Q}_{11}^{(k)} &= c^4 Q_{11} + s^4 Q_{22} + 2c^2 s^2 (Q_{12} + 2Q_{66}) \\
\bar{Q}_{22}^{(k)} &= s^4 Q_{11} + c^4 Q_{22} + 2c^2 s^2 (Q_{12} + 2Q_{66}) \\
\bar{Q}_{12}^{(k)} &= c^2 s^2 (Q_{11} + Q_{22} - 4Q_{66}) + (c^4 + s^4) Q_{12} \\
\bar{Q}_{66}^{(k)} &= c^2 s^2 (Q_{11} + Q_{22} - 2Q_{12}) + (c^2 - s^2)^2 Q_{66} \\
\bar{Q}_{16}^{(k)} &= cs [c^2 Q_{11} - s^2 Q_{22} - (c^2 - s^2) (Q_{12} + 2Q_{66})] \\
\bar{Q}_{26}^{(k)} &= cs [s^2 Q_{11} - c^2 Q_{22} + (c^2 - s^2) (Q_{12} + 2Q_{66})]
\end{aligned} \tag{2.8}$$

where $c = \cos \alpha_k$ and $s = \sin \alpha_k$.

Bearing the above relations in mind, the impact of the considered reinforcing fibers misalignment $\Delta\alpha_k$ on the beam mechanical properties given by Eqs. (2.6) may be evaluated by performing a sensitivity analysis. The change of any beam stiffness coefficient a_{ij} is

$$\Delta a_{ij} = \sum_{k=1}^{18} \left| \frac{\partial a_{ij}}{\partial \alpha_k} \Delta \alpha_k \right| \tag{2.9}$$

where ij pair is 33, 37, 55 or 77. The term $\partial a_{ij}/\partial \alpha_k$ represents the sensitivity of the specimen stiffness with respect to changes in fibre orientations in the k -th individual laminate layer. Since the signs of the derivative as well as the accepted inaccuracy $\Delta\alpha_k$ are arbitrary, an absolute value operator is used to consider the most unfavourable case. Finally, two limit values for any perturbed stiffness a_{ij} are possible, namely the lower one $a_{ij} - \Delta a_{ij}$ for a decreased stiffness and the upper one $a_{ij} + \Delta a_{ij}$ for an increased value. The presented above treatment based on perturbation calculus is often encountered in reliability based structural design and represents the so called ‘a worst case scenario’ analysis (Gutkowski and Latalski, 2003).

Calculations of $\partial a_{ij}/\partial \alpha_k$ sensitivities involve differentiation of the individual elements of stretching, bending and bending-stretching tensors (2.7) with respect to the fibres angle α . These derivatives are easily found by substituting to Eqs. (2.7) the expressions given by relations (2.8).

The results of stiffnesses (2.6) calculations for the proposed 18 layers stacking sequence laminate beam are collected in Table 1. In the first section, the values for the nominal design are given. Next, the small misalignment $\Delta\alpha = 1^\circ$ is assumed and the perturbed values for increased and decreased stiffnesses are printed. Finally, the $\Delta\alpha = 5^\circ$ case is considered. The graphite-epoxy material data used for these calculations are given in Table 2.

Table 1. Beam stiffnesses for the partial differential equations of motion; nominal design and two perturbed cases by $\Delta\alpha = 1^\circ$ and $\Delta\alpha = 5^\circ$

Nominal design values			
$a_{33} = 0.117568 \text{ Nm}^2$	$a_{37} = 0.0 \text{ Nm}^2$	$a_{55} = 67957.50 \text{ N}$	$a_{77} = 0.081397 \text{ Nm}^2$
Fibres misalignment $\Delta\alpha = 1^\circ$			
perturbed values for increased stiffness			
$a_{33} = 0.121849 \text{ Nm}^2$	$a_{37} = 0.000081 \text{ Nm}^2$	$a_{55} = 68273.55 \text{ N}$	$a_{77} = 0.083996 \text{ Nm}^2$
perturbed values for decreased stiffness			
$a_{33} = 0.113266 \text{ Nm}^2$	$a_{37} = -0.000138 \text{ Nm}^2$	$a_{55} = 67641.44 \text{ N}$	$a_{77} = 0.078523 \text{ Nm}^2$
Fibres misalignment $\Delta\alpha = 5^\circ$			
perturbed values for increased stiffness			
$a_{33} = 0.138754 \text{ Nm}^2$	$a_{37} = -0.000116 \text{ Nm}^2$	$a_{55} = 69537.77 \text{ N}$	$a_{77} = 0.091819 \text{ Nm}^2$
perturbed values for decreased stiffness			
$a_{33} = 0.095806 \text{ Nm}^2$	$a_{37} = -0.001301 \text{ Nm}^2$	$a_{55} = 66377.23 \text{ N}$	$a_{77} = 0.064011 \text{ Nm}^2$

Table 2. Rotor geometric data and material properties used in numerical simulations

Geometric properties			
$l = 0.350 \text{ m}$	$d = 0.034 \text{ m}$	$h = 0.0009 \text{ m}$	$R_0 = 0.1 \times l$
Material properties of the laminate			
$E_1 = 143.2 \text{ GPa}$	$E_2 = E_3 = 3.1 \text{ GPa}$	$G_{23} = 2.05 \text{ GPa}$	$G_{12} = G_{13} = 3.28 \text{ GPa}$
$\nu_{21} = \nu_{31} = 0.00758 [-]$	$\nu_{32} = 0.2439 [-]$	$\rho_c = 1350.0 \text{ kgm}^3$	

The performed numerical calculations confirm the already reported fully isotropic properties of the assumed nominal design stacking sequence laminate ($a_{37} = 0$). However, as can be observed, the discussed stacking sequence configuration is sensitive to possible variations in fibres orientations as confirmed by meaningful changes in the beam stiffnesses. In particular, the possible very small misalignment of the fibres angle leads to anisotropic material behaviour and induces mutual coupling of different components of specimen deformations ($a_{37} \neq 0$). Finally, the values of the coefficients present in the ordinary differential equations of motion (system of Eqs. (2.5)) for the assumed mistuning magnitudes are listed in Table 3. The details regarding the three studied cases of mistuned rotor configurations are also given there.

Table 3. The values of individual coefficients present in the ordinary differential equations of motion; three studied rotor configurations

Case 1. Rotor with nominal design blades				
Beam 1	$\alpha_{11} = 12.364453698$	$\alpha_{12} = 1.779913785$	$\alpha_{13} = 0.350955874$	$\alpha_{14} = -1.551795958$
Beam 2	$\alpha_{21} = 12.364453698$	$\alpha_{22} = 1.779913785$	$\alpha_{23} = 0.350955874$	$\alpha_{24} = -1.551795958$
Beam 3	$\alpha_{31} = 12.364453698$	$\alpha_{32} = 1.779913785$	$\alpha_{33} = 0.350955874$	$\alpha_{34} = -1.551795958$
Hub	$\alpha_{h11} = -0.530660819$	$\alpha_{h12} = -0.402771952$	$\alpha_{h13} = -0.805543905$	
	$\alpha_{h21} = -0.530660819$	$\alpha_{h22} = -0.402771952$	$\alpha_{h23} = -0.805543905$	
	$\alpha_{h31} = -0.530660819$	$\alpha_{h32} = -0.402771952$	$\alpha_{h33} = -0.805543905$	
Case 2. Tolerance $\Delta\alpha = 1^\circ$: beam 1 – nominal, beam 2 – decreased stiffness, beam 3 – increased stiffness				
Beam 1	$\alpha_{11} = 12.364453698$	$\alpha_{12} = -1.779913785$	$\alpha_{13} = 0.350955874$	$\alpha_{14} = 1.551795958$
Beam 2	$\alpha_{21} = 11.911908455$	$\alpha_{22} = -1.779874982$	$\alpha_{23} = 0.350960254$	$\alpha_{24} = 1.551834362$
Beam 3	$\alpha_{31} = 12.814170650$	$\alpha_{32} = -1.779950210$	$\alpha_{33} = 0.350951758$	$\alpha_{34} = 1.551759829$
Hub	$\alpha_{h11} = 0.530660819$	$\alpha_{h12} = -0.402771952$	$\alpha_{h13} = -0.805543905$	
	$\alpha_{h21} = 0.530672090$	$\alpha_{h22} = -0.402790584$	$\alpha_{h23} = -0.805581169$	
	$\alpha_{h31} = 0.530650234$	$\alpha_{h32} = -0.402754446$	$\alpha_{h33} = -0.805508893$	
Case 3. Tolerance $\Delta\alpha = 5^\circ$: beam 1 – nominal, beam 2 – decreased stiffness, beam 3 – increased stiffness				
Beam 1	$\alpha_{11} = 12.364453698$	$\alpha_{12} = -1.779913785$	$\alpha_{13} = 0.350955874$	$\alpha_{14} = 1.551795958$
Beam 2	$\alpha_{21} = 10.072877023$	$\alpha_{22} = -1.779688026$	$\alpha_{23} = 0.350983037$	$\alpha_{24} = 1.552014103$
Beam 3	$\alpha_{31} = 14.591731254$	$\alpha_{32} = -1.780075869$	$\alpha_{33} = 0.350937164$	$\alpha_{34} = 1.551634747$
Hub	$\alpha_{h11} = 0.530660819$	$\alpha_{h12} = -0.402771952$	$\alpha_{h13} = -0.805543905$	
	$\alpha_{h21} = 0.530725703$	$\alpha_{h22} = -0.402879065$	$\alpha_{h23} = -0.805758131$	
	$\alpha_{h31} = 0.530613777$	$\alpha_{h32} = -0.402693994$	$\alpha_{h33} = -0.805387989$	

As the last remark to this Section, it should be noted that density of the material is not affected by the deviations of composite reinforcing fibers from their nominal orientations. Therefore, the inertia coefficients for the nominal and misaligned composite beams are similar.

3. Numerical results

3.1. Forced vibrations – regular oscillations

To get inside into the dynamics of the structure the full nonlinear system of governing equations (2.5) is solved numerically and appropriate diagrams are prepared. To this end, the Auto-07p software (Doedel *et al.*, 1998) adopting the multiparameter continuation method has been used. To start the analysis, let us consider the system response if the structure is excited by an external torque imposed to the hub. In general, we consider the forcing to be composed of two terms, namely the constant and the harmonic one. Thus, the driving torque is defined as

$$\mu(\tau) = \mu_0 + \rho \sin(\omega\tau) \quad (3.1)$$

where μ_0 is a constant component, while ρ and ω correspond to the amplitude and frequency of the periodic term, respectively. For the purpose of an initial analysis, we assume the constant component to be equals to zero, $\mu_0 = 0$. The aim of this analysis is to establish the inherent dynamic properties of the discussed system without the additional stiffening effect resulting from the full rotational motion.

At the first stage, dynamics of the reference structure is examined (nominal design, case 1 in Table 3). In Fig. 3, we present resonance curves for all three beams as well as the angular velocity of the hub (i.e. maximum magnitudes of these four variables) if the constant component of the torque is neglected ($\mu_0 = 0$). One can observe, for the fully symmetric rotor, just a single resonance zone is present with the peak response corresponding to the first natural frequency $\omega_{01} = 3.0217$. In this resonance zone, motions of all the blades are fully synchronised in magnitude and phase and they stay in anti-phase with respect to the hub motion shown in Fig. 3b. It is worth to note that for very small values of excitation frequency ω angular speed of the system gets large values – Fig. 3b. This case corresponds to the zero natural frequency and the excitation of the system with the infinite period. However, this range of excitation is out of our interest in this paper, therefore in next figures we perform analysis around non zero resonance zones only.

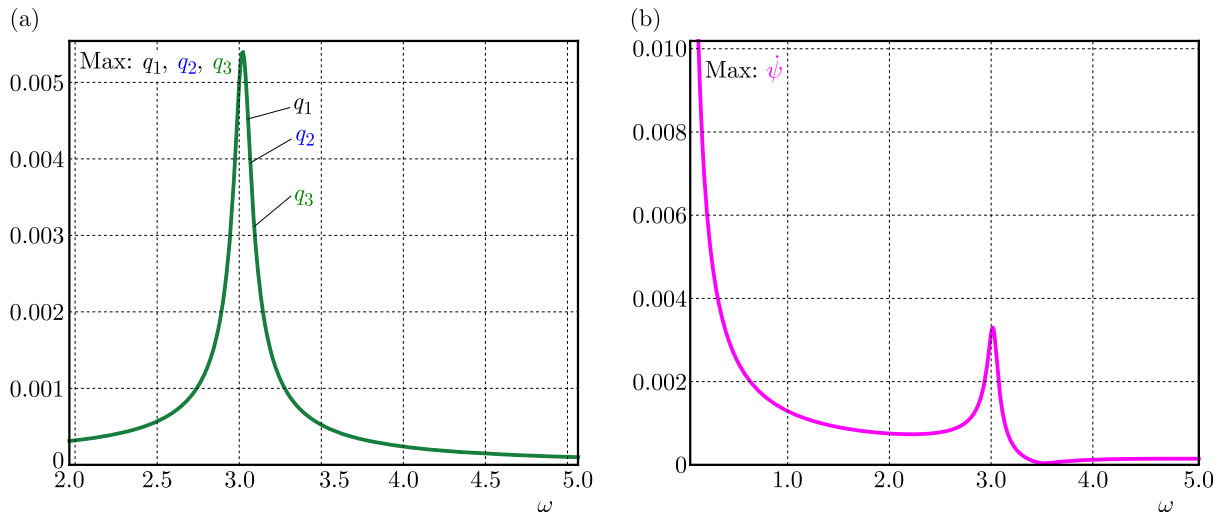


Fig. 3. Resonance curves of beams q_1, q_2, q_3 (a) and angular velocity of the hub $\dot{\psi}$ (b); variant 1 of the three reference (nominal) beams, $\mu_0 = 0, \rho = 0.01, J_h = 5$

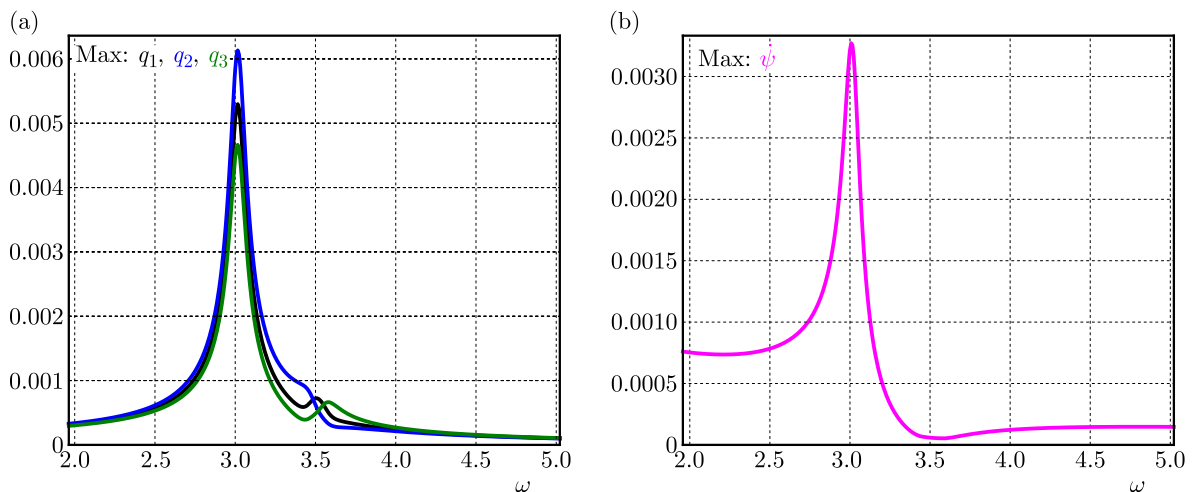


Fig. 4. Resonance curves for individual beams q_1 – black, q_2 – blue, q_3 – green (a) and angular velocity of the hub $\dot{\psi}$ (b). Rotor configuration in variant 2, $\rho = 0.01, J_h = 5$

In the case of marginally mistuned beams ($\Delta\alpha = 1^\circ$) represented by studied variant 2 the response amplitudes of individual blades are slightly different and are dominated by the most flexible beam 2 – presented in Fig. 4a. Similar to the above nominal design case, all the blades are mutually synchronised and oscillate together in anti-phase with respect to the hub – see time histories plots shown in Fig. 5a. Apart from the main resonance, two other minor resonances occur due to the system mistuning. They are shifted to the right with respect to the main resonance peak – Fig. 4a. Time histories for those additional resonances are presented in plots shown in Figs. 5b and 5c. It is to be commented that the phase shift between individual beams and the hub is a constant value. Moreover, note that the response of the hub is not affected in any way by these two minor resonances – Fig. 4b.

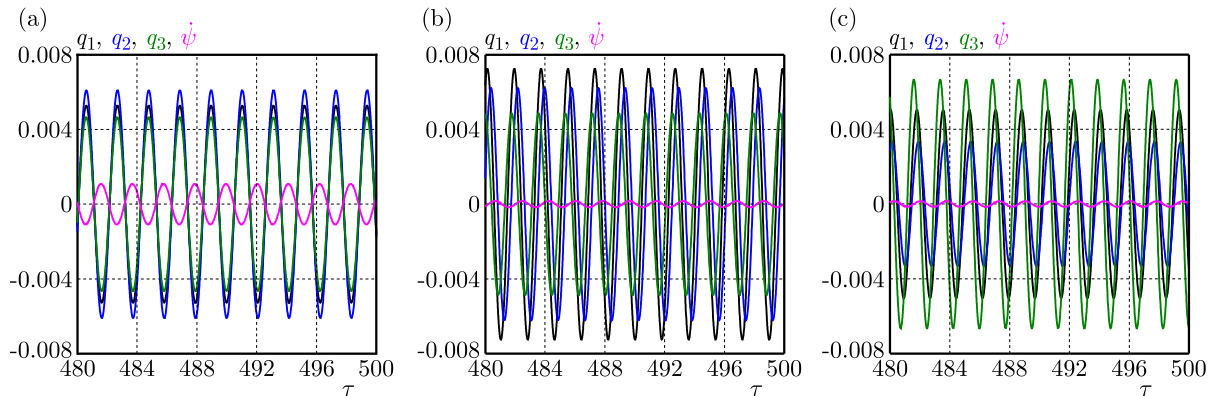


Fig. 5. Time histories of beams q_1 – black, q_2 – blue, q_3 – green and the angle of hub rotation ψ – magenta for variant 2 and $\omega = 3.01$ (a), $\omega = 3.50$ (b), $\omega = 3.58$ (c); $\mu_0 = 0$, $J_h = 5$, $\rho = 0.01$

The effect of blades mistuning is much more evident in variant 3 (see Table 3) corresponding to the fibre orientation tolerance limit $\Delta\alpha = 5^\circ$. The resonance curves and time histories are shown in Fig. 6 and Fig. 7, respectively.

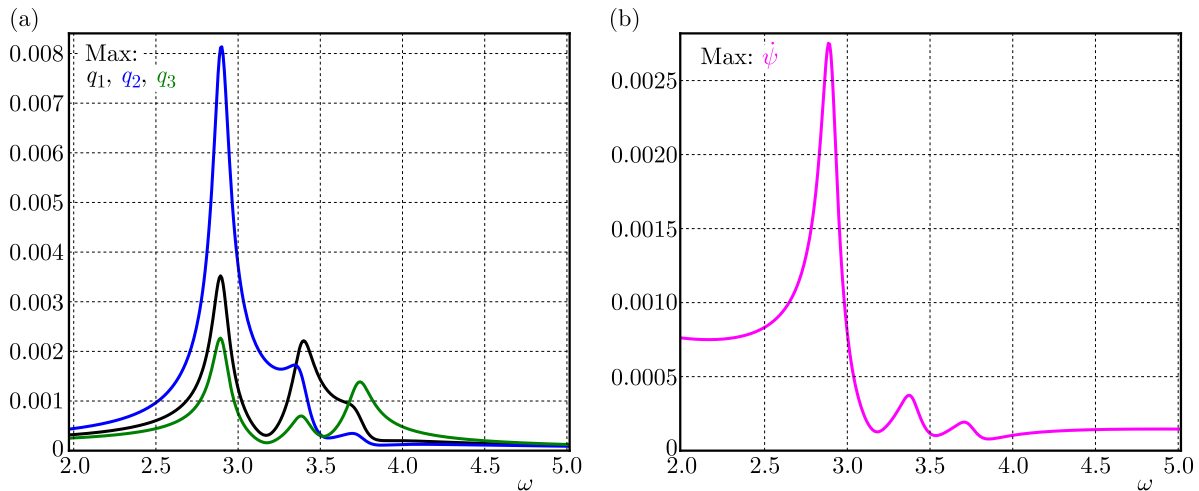


Fig. 6. Resonance curves for individual rotor beams q_1 – black, q_2 – blue, q_3 – green (a) and angular velocity of the hub ψ (b). Rotor configuration in variant 3, $\rho = 0.01$, $J_h = 5$

The direct comparison of system responses for the small and relatively large mistuning – Figs. 4 and 6 – reveals some qualitative differences. Primarily, in the case of a higher structural mistuning (variant 3) all three resonances are distinct and very well observed. This conclusion refers also to the response of the hub which increases in all three resonance zones – Fig. 6b – and is in contrast to the small mistuning case behaviour shown in Fig. 4b. Furthermore, a kind

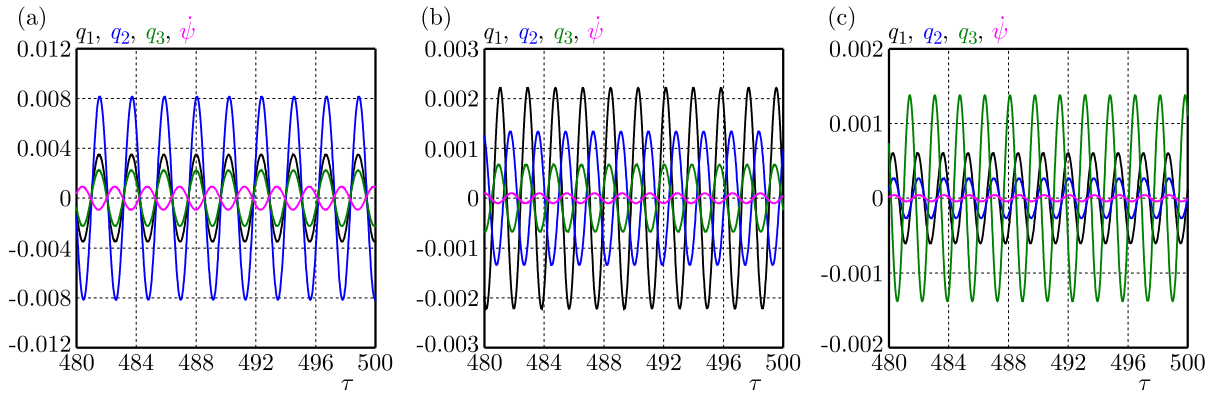


Fig. 7. Time histories of individual beams q_1 – black, q_2 – blue, q_3 – green and the angle of hub rotation ψ – magenta for variant 3 and the frequency of excitation close to the subsequent resonance zones for $\omega = 2.9$ (a), $\omega = 3.4$ (b), $\omega = 3.75$ (c); $J_h = 5$, $\rho = 0.01$

of vibration localisation can be noticed. For the first resonance zone the motion is localised in the second beam (q_2 coordinate in Fig. 6a), for the second resonance the motion is localised in beam number one (q_1 coordinate), and finally for the third resonance the motion is localised in the third beam (q_3 coordinate). This is confirmed by the time history plots and individual blades amplitudes as shown in Figs. 7a-7c.

To examine the influence of rotational motion and anticipated stiffening effects, the relatively large mistuning ($\Delta\alpha = 5^\circ$) variant is studied again and the bifurcation diagram for the μ_0 component of the torque is presented in Fig. 8. It is to be noted here that any non-zero mean value of the driving torque represents the case when the system is accelerating from the zero initial velocity but only up to a certain moment where this torque is balanced by damping on the hub. Finally, the system is performing full rotation with a constant non-zero mean value angular velocity.

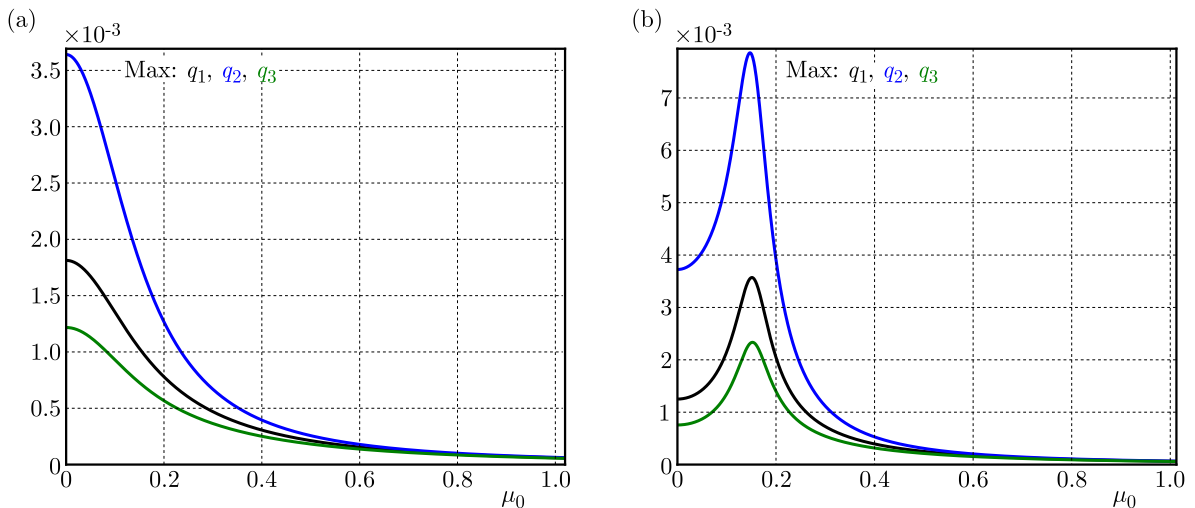


Fig. 8. Bifurcation diagram for the constant torque component μ_0 . Rotor configuration in variant 3, $\omega = 2.8$ (a), $\omega = 3.0$ (b); $\rho = 0.01$, $J_h = 5$

To study the dynamics, we selected two frequencies around the first resonance peak as shown in Fig. 6, namely $\omega = 2.8$ and $\omega = 3.0$. These correspond to the situations before and after the resonance, respectively. As expected, full rotation of the structure changes the amplitudes of blades vibrations due to the centrifugal stiffening effect. However, comparing these two plots, one observes two different possible courses of the beams response while the μ_0 is varied. The first

one (Fig. 8a corresponding to the excitation frequency $\omega = 2.8$) is the monotonic reduction in amplitudes. This occurs particularly up to $\mu_0 \approx 1$ and next becomes much less pronounced. Then the beam vibrations are strongly suppressed, the differences in blades oscillations are negligible and they behave almost like rigid bodies. The different scenario is observed for the case $\omega = 3.0$ (Fig. 8b). While changing the μ_0 component, the amplitudes initially increase and then decrease rapidly to small values. The peak in Fig. 8b is a direct result of the angular speed which shifts to the right the natural frequency of the blades. Therefore, the excitation $\omega = 3.0$ occurs right at the new resonance zone. Nevertheless, the further increase in μ_0 results in a rapid reduction in beam amplitudes, and for $\mu_0 > 1$ they are suppressed similarly to the case presented in Fig. 8a.

To study the influence of the torque amplitude ρ , the last analysis is repeated by setting $\mu_0 = 0.13$ which is similar to the average torque value as assumed in computations for a chaotic signal presented later in Section 3.2. Two torque oscillations amplitudes are analysed, namely $\rho = 0.27$ and $\rho = 1.0$ as shown in Figs. 9 and 10, respectively. Studying these curves, one

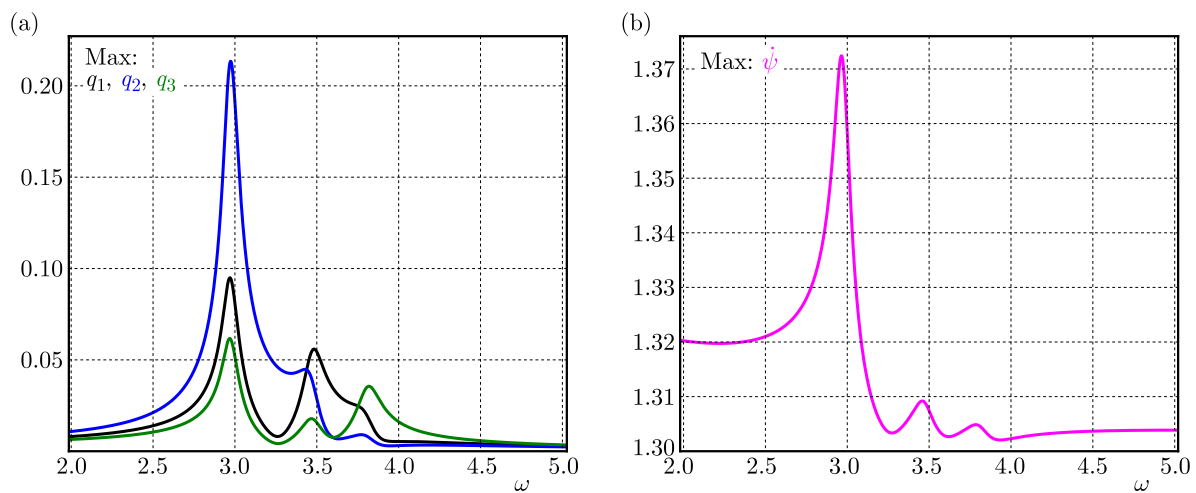


Fig. 9. Resonance curves for individual rotor beams q_1, q_2, q_3 (a) and angular velocity of the hub $\dot{\psi}$ (b). Rotor configuration in variant 3; $\mu_0 = 0.13$, $\rho = 0.27$, $J_h = 5$

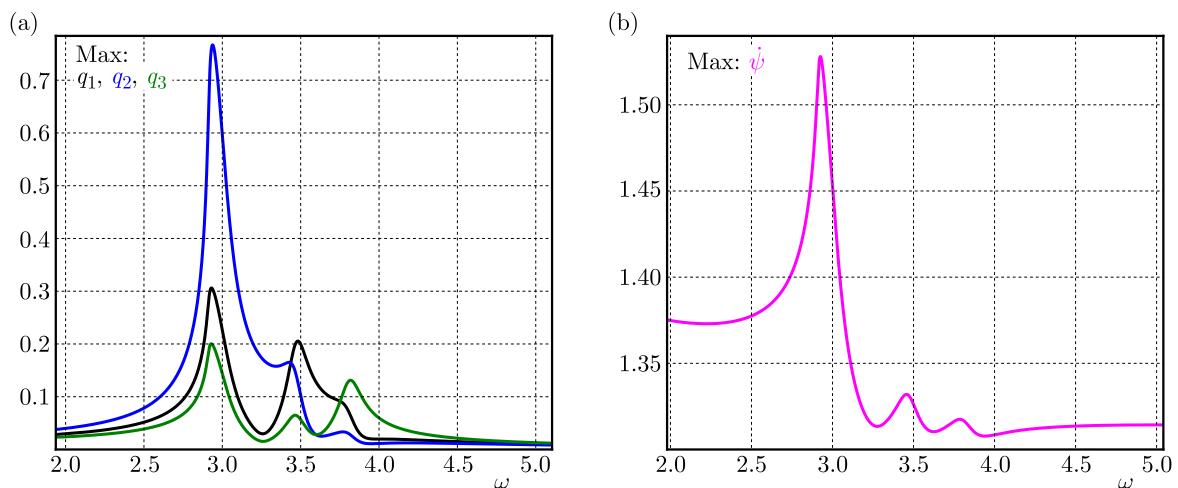


Fig. 10. Resonance curves for individual rotor beams q_1, q_2, q_3 (a) and angular velocity of the hub $\dot{\psi}$ (b). Rotor configuration in variant 3; $\mu_0 = 0.13$, $\rho = 1.0$, $J_h = 5$

observes again the centrifugal stiffening effect that shifts the resonance peaks towards higher frequencies – check Fig. 6 for reference. Furthermore, direct comparison of Figs. 9 and 10 reveals the linear nature of the response curves for relatively small oscillations. By contrast, if the

amplitude of excitation is increased then the resonance curves presented in Fig. 10 demonstrate a minor nonlinear softening phenomenon. However, these results are out of real dynamics of the structure. Therefore, it can be concluded that the higher order terms present in governing equations (2.5) do not have a significant impact on structural dynamic properties.

When studying the system of governing equations (2.5), we may expect that the hub motion plays essential role in the entire rotor dynamics. To get more insight into this relation, let us consider the solution corresponding to the peak in the first resonance zone occurring at $\omega = 2.9$, as shown in Fig. 6, and vary the mass moment of inertia J_h of the hub. The performed simulations show the response peak to be reduced if the mass moment of inertia $J_h = 5$ is changed either towards lower or higher values. The outcomes of these tests are shown in the bifurcation diagram presented in Fig. 11.

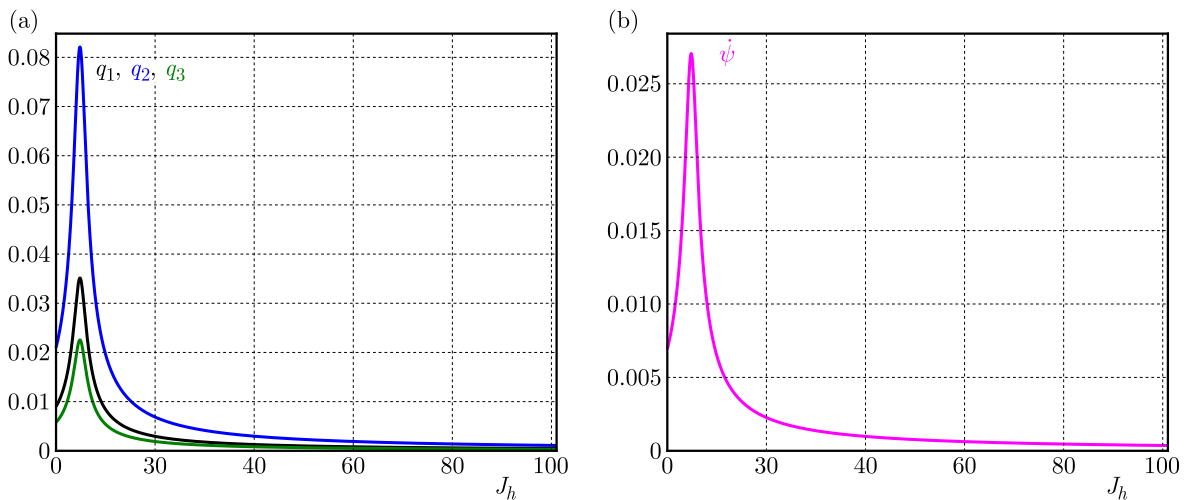


Fig. 11. Influence of hub inertia on the beams responses q_1 – black, q_2 – blue, q_3 – green (a) and angular velocity of the hub ψ (b). Calculations for the data corresponding to variant 3; $\rho = 0.1$, $\omega = 2.9$

The next series of simulations demonstrates the influence of hub inertia if the excitation frequency is varied. The tests are performed for different hubs starting from very light ones with $J_h = 0.1$ up to the heaviest with $J_h = 50$. The corresponding curve plots are shown in Fig. 12. Evidently, larger hub inertias lead to vibration reduction. Moreover, we may also observe an interesting phenomenon of vibrations localisation clearly visible around frequencies $\omega = 3.1$ and $\omega = 3.5$, which is independent of the hub inertia (Fig. 12).

3.2. Chaotic oscillations

Let us consider the case when the discussed three-bladed rotor is excited by a chaotic Duffing type oscillator. The dimensionless driving torque $\mu(\tau)$ in Eq. (2.5)₁ is considered now to be given by the formula $\mu = \alpha_x x$ ($\alpha_x = 1$), where the variable x is calculated from Duffing's equation

$$\ddot{x} + k\dot{x} + x^3 = \beta + \rho \cos(\omega\tau) \quad (3.2)$$

For numerical simulations, the constants $k = 0.05$, $\beta = 0.03$, $\omega = 1$ and $\rho = 0.16$ are adopted as originally used by Ueda (1980). This results in the chaotic torque characteristic with the mean value of about 0.13, which is the one that has been used for harmonic excitation results presented in Figs. 9 and 10. The presented below Poincaré maps have been obtained by means of direct numerical simulations performed in Dynamics software.

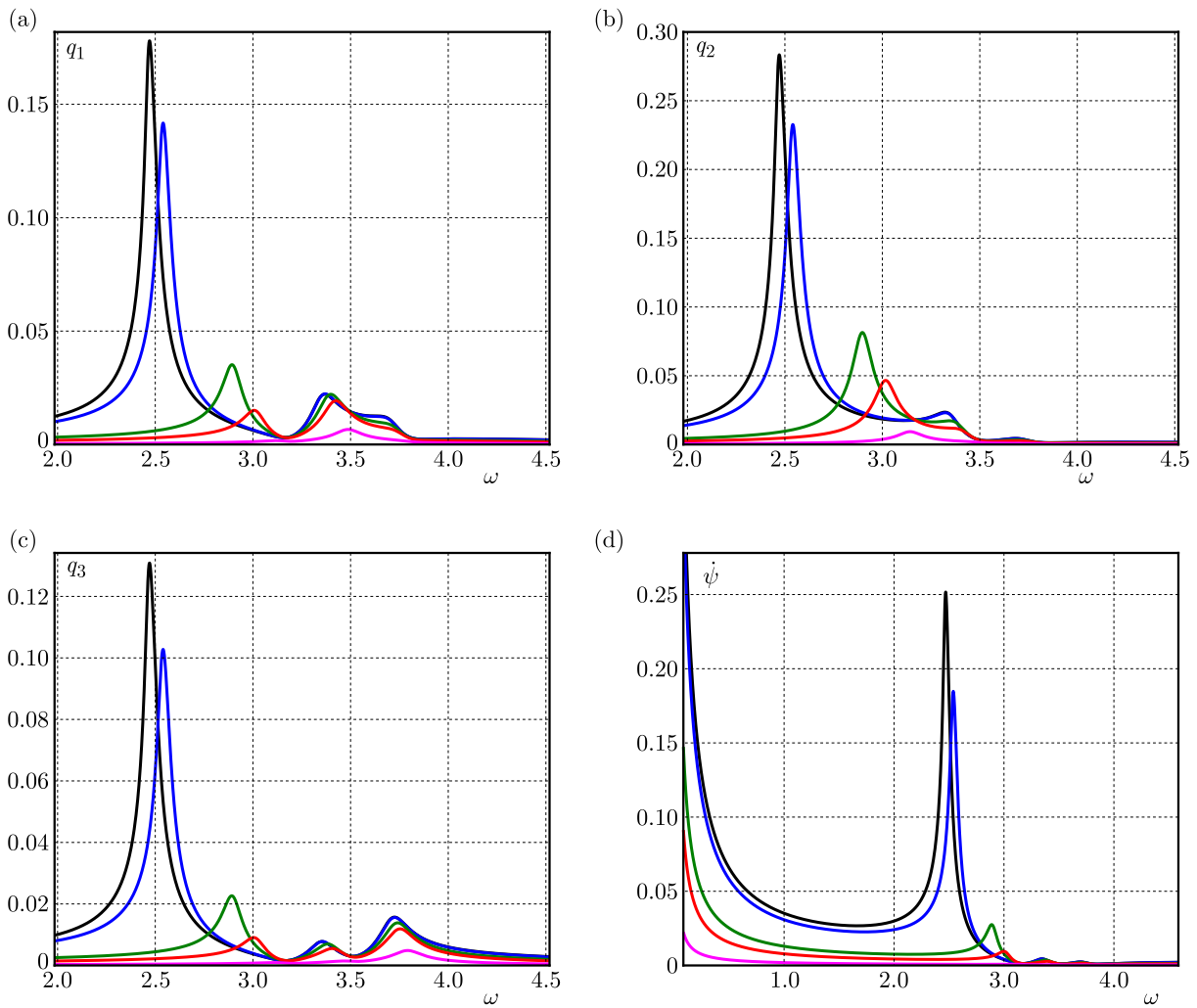


Fig. 12. Resonance curves of beams (a) q_1 , (b) q_2 , (c) q_3 , and (d) angular velocity of the hub $\dot{\psi}$. Calculations for the data corresponding to variant 3 and various hub inertias: $J_h = 0.1$ – black, $J_h = 0.5$ – blue, $J_h = 5$ – green, $J_h = 10$ – red, $J_h = 50$ – magenta; $\rho = 0.1$

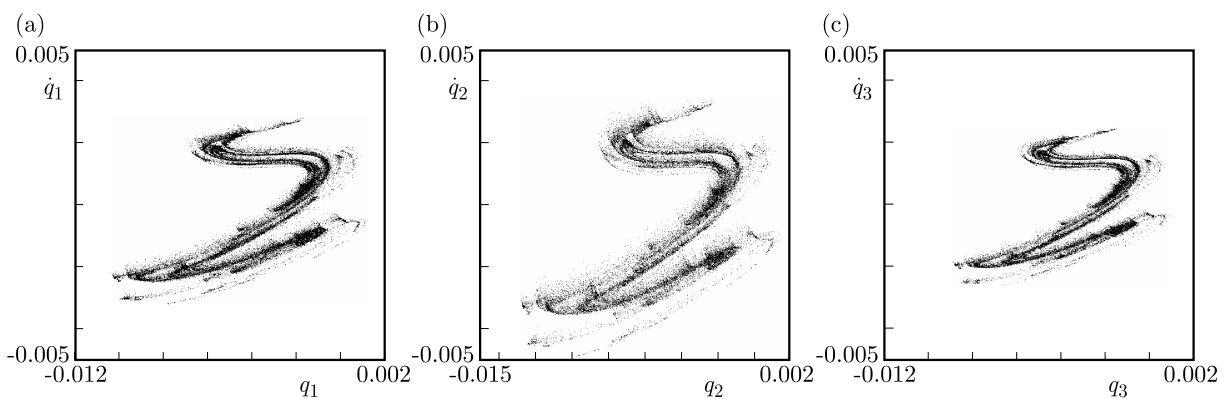


Fig. 13. Poincaré maps of beams responses (a) q_1 , (b) q_2 , (c) q_3 subject to chaotic excitation given by Eq. (3.2). Rotor configuration in variant 3; $J_h = 5$

The strange chaotic attractors are found for all the beams, both for slightly mistuned variant 2 and for highly mistuned configuration given by case 3. The results for this last one are shown in Fig. 13. Since the results for case 2 do not show evident differences between individual blades they are not presented here.

As can be observed in Fig. 13, the strange attractor for the second beam is significantly bigger than the attractor for nominal beam 1 – subplots (a) and (b), respectively. Meanwhile, the strange attractor of beam 3 is smaller – Fig. 13c. This comes from the significant differences in stiffness of individual beams as already reported while discussing the regular excitation case.

To study the possible synchronisation phenomenon, the time series plots are prepared. The time histories for a highly mistuned configuration given by case 3 are shown in Fig. 14. The motions of all the beams are well synchronised, although the amplitudes are slightly different. The amplitude of the second beam is the highest, while the amplitude of the third beam is the smallest one. Again, these disparities can be explained by the differences in specimens stiffnesses.

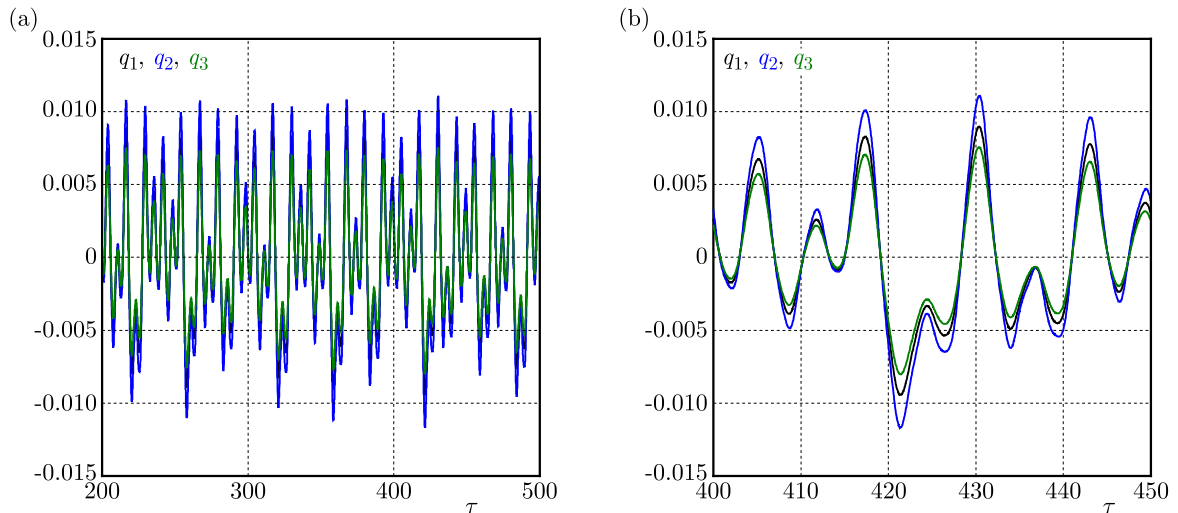


Fig. 14. Time histories of the beams responses, the full time domain (a) and zoom window (b); q_1 – black, q_2 – blue, q_3 – green. Rotor configuration in variant 3, chaotic excitation; $J_h = 5$

The final stage of numerical simulations comprises the studies of system dynamics if both the hub and the first beam are subjected to the same chaotic excitation signal $\mu = \alpha_x x$, as given in the previous example. To this end, the additional forcing term μ is added to the right hand side of the governing equation of beam 1 – Eq. (2.5)₂. The Poincaré maps are plotted for each beam individually as well as for the oscillator itself. Defined variant 3 of high structural mistuning is examined and corresponding plots are gathered in Fig. 15. It can be observed that the strange attractor for the nominal beam is the biggest one. This results from the excitation that has been applied to the hub and directly to this beam as well. Meanwhile, the Poincaré map for the most rigid beam (blade 3) is the smallest – Fig. 15c.

In contrast to the previously studied case of chaotic excitation applied only to the hub now, the synchronisation scenario is different. Beam 1 oscillates in anti-phase with respect to completely synchronised beams 2 and 3.

4. Final remarks and conclusions

The presented paper considers forced vibrations of a rotating structure consisting of a rigid hub and three flexible beams made of a multilayered laminate. In the performed analysis, it is assumed that the rotor has been mistuned due to manufacturing tolerances of reinforcing fibres orientations in the composite material. Based on previous authors research, a system of four mutually coupled dimensionless ordinary differential governing equations has been formulated.

The forced vibrations of the system under a regular excitation supplied to the hub have been investigated. The direct comparison of system responses for small ($\Delta\alpha = 1^\circ$) and relatively large

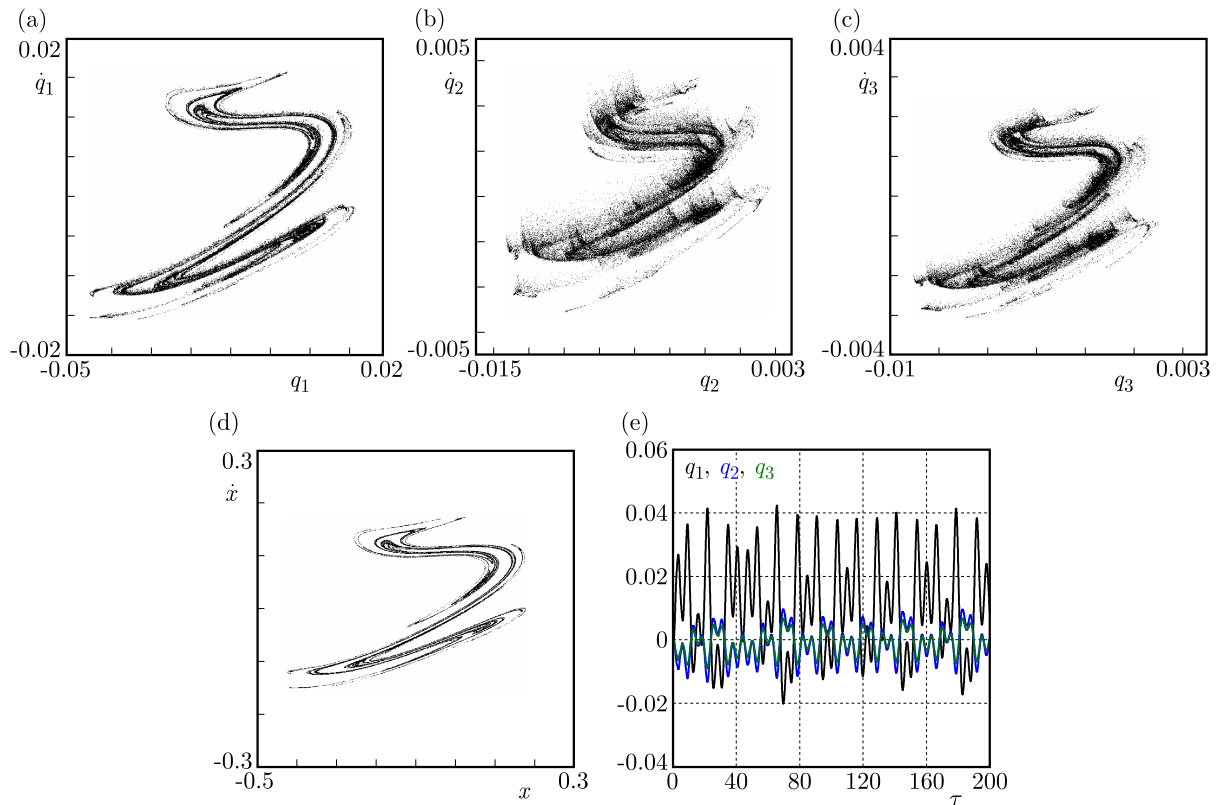


Fig. 15. Poincaré maps of the beams response (a) q_1 , (b) q_2 , (c) q_3 , (d) x chaotic excitation given by Eq. (3.2) and applied to the hub and nominal beam 1. (e) Time histories of individual beams responses q_1 – black, q_2 – blue, q_3 – green. Rotor configuration in variant 3; $J_h = 5$

($\Delta\alpha = 5^\circ$) mistuning cases has revealed some qualitative differences. This has concerned not only oscillation amplitudes but synchronisation of motions as well. Further studies have dealt with the influence of hub inertia on the mistuned system dynamics. An interesting phenomenon of vibrations localisation clearly visible around two distinct frequencies has been observed. This effect has been shown to be independent of the hub inertia magnitude.

Finally, the forced response of the structure under a chaotic excitation has been investigated. Two cases of forcing load have been examined, namely (a) forcing supplied to the hub only and (b) to the hub and to one of the rotor beams. The obtained results for both cases have revealed some disparities in individual beams strange attractors magnitudes due to differences in blades stiffnesses. Analysis of motion of the system with the excitation applied to the hub has showed full synchronisation of the three beams motions despite chaotic motion of the full structure. However, the chaotic excitation applied to the beam and to the hub has resulted in the oscillations of beam 1 in anti-phase with respect to completely synchronised beams 2 and 3.

Acknowledgments

The work is financially supported by the grant DEC-2015/19/N/ST8/03906 from the Polish National Science Centre.

References

1. BHARTIYA Y., SINHA A., 2013, Reduced order modeling of a bladed rotor with geometric mistuning via estimated deviations in mass and stiffness matrices, *Journal of Engineering for Gas Turbines and Power*, **135**, 5, 052501, DOI: 10.1115/1.4007783

2. CASTANIER M.P., ÓTTARSSON G., PIERRE C., 1997, A reduced order modeling technique for mistuned bladed disks, *Journal of Vibration and Acoustics*, **119**, 3, 439, DOI: 10.1115/1.2889743
3. CASTANIER M.P., PIERRE C., 2006, Modeling and analysis of mistuned bladed disk vibration: current status and emerging directions, *Journal of Propulsion and Power*, **22**, 2, 384-396, DOI: 10.2514/1.16345
4. CHANDIRAMANI N.K., LIBRESCU L., SHETE C.D., 2002, On the free-vibration of rotating composite beams using a higher-order shear formulation, *Aerospace Science and Technology*, **6**, 8, 545-561
5. CHEN Y.F., SHEN I.Y., 2015, Mathematical insights into linear mode localization in nearly cyclic symmetric rotors with mistune, *Journal of Vibration and Acoustics*, **137**, 4, 041007, DOI: 10.1115/1.4029945
6. CRESPO DA SILVA M.R.M., 1998, A comprehensive analysis of the dynamics of a helicopter rotor blade, *International Journal of Solids and Structures*, **35**, 7-8, 619-635, DOI: 10.1016/S0020-7683(97)00065-6
7. DOEDEL E., CHAMPNEYS A., FAIRGRIEVE T., KUZNETSOV Y., SANDSTEDE B., WANG X., 1998, *Auto 97: Continuation and Bifurcation Software for Ordinary Differential Equations*, Computational Mathematics and Visualization Laboratory, <http://indy.cs.concordia.ca/aut>
8. GEORGIADES F., LATALSKI J., WARMINSKI J., 2014, Equations of motion of rotating composite beams with a nonconstant rotation speed and an arbitrary preset angle, *Meccanica*, **49**, 8, 1833-1858, DOI: 10.1007/s11012-014-9926-9
9. GRIFFIN J.H., HOOSAC T.M., 1984, Model development and statistical investigation of turbine blade mistuning, *Journal of Vibration Acoustics Stress and Reliability in Design*, **106**, 2, 204, DOI: 10.1115/1.3269170
10. GUTKOWSKI W., LATALSKI J., 2003, Manufacturing tolerances of fiber orientations in optimization of laminated plates, *Engineering Optimization*, **35**, 2, 201-213, DOI: 10.1080/0305215031000091550
11. LATALSKI J., WARMINSKI J., REGA G., 2017, Bending-twisting vibrations of a rotating hub-thin-walled composite beam system, *Mathematics and Mechanics of Solids*, **22**, 6, 1303-1325, DOI: 10.1177/1081286516629768
12. LI J., CASTANIER M.P., PIERRE C., CECCIO S., 2006, Experimental Monte Carlo mistuning assessment of bladed disk vibration using forcing variations, [In:] *47th AIAA/ASME/ASCE/AHS/ASC Structures, Structural Dynamics, and Materials Conference*, pp. AIAA 2006-1964
13. LIBRESCU L., SONG O., 2006, *Thin-Walled Composite Beams: Theory and Application*, Springer, Dordrecht and the Netherlands
14. MAYO J., GARCÍA-VALLEJO D., DOMÍNGUEZ J., 2004, Study of the geometric stiffening effect: comparison of different formulations, *Multibody System Dynamics*, **11**, 4, 321-341, DOI: 10.1023/B:MUBO.0000040799.63053.d9
15. MIGNOLET M.P., LIN C.-C., 1993, The combined closed form-perturbation approach to the analysis of mistuned bladed disks, *Journal of Turbomachinery*, **115**, 4, 771, DOI: 10.1115/1.2929315
16. NIKOLIC M., 2006, *New Insights into the Blade Mistuning Problem*, PhD Thesis, Imperial College London, University of London, London
17. PETROV E.P., EWINS D.J., 2003, Analysis of the worst mistuning patterns in bladed disk assemblies, *Journal of Turbomachinery*, **125**, 4, 623-631, DOI: 10.1115/1.1622710
18. SHAPIRO B., 1999, Solving for mistuned forced response by symmetry, *Journal of Propulsion and Power*, **15**, 2, 310-325, DOI: 10.2514/2.5429
19. SINHA A., 1986, Calculating the statistics of forced response of a mistuned bladed disk assembly, *AIAA Journal*, **24**, 11, 1797-1801, DOI: 10.2514/3.9526
20. SINHA A., 2006, Computation of the statistics of forced response of a mistuned bladed disk assembly via polynomial chaos, *Journal of Vibration and Acoustics*, **128**, 4, 449, DOI: 10.1115/1.2215620

21. SINHA S.K., 2013, Rotordynamic analysis of asymmetric turbofan rotor due to fan blade-loss event with contact-impact rub loads, *Journal of Sound and Vibration*, **332**, 9, 2253-2283, DOI: 10.1016/j.jsv.2012.11.033
22. UEDA Y., 1980, Explosion of strange attractors exhibited by Duffing's equation, *Annals of the New York Academy of Sciences*, **357**, 1, 422-434, DOI: 10.1111/j.1749-6632.1980.tb29708.x
23. VAKAKIS A., NAYFEH T., KING M., 1993, A multiple-scales analysis of nonlinear, localized modes in a cyclic periodic system, *Journal of Applied Mechanics*, **60**, 2, 388, DOI: 10.1115/1.2900806
24. VANNUCCI P., VERCHERY G., 2002, A new method for generating fully isotropic laminates, *Composite Structures*, **58**, 1, 75-82, DOI: 10.1016/S0263-8223(02)00038-7
25. WARMINSKI J., LATALSKI J., 2017, Nonlinear control of flexural-torsional vibrations of a rotating thin-walled composite beam, *International Journal of Structural Stability and Dynamics*, **17**, 5, 1740003-1-1740003-17, DOI: 10.1142/S021945541740003X
26. WARMIŃSKI J., SZMIT Z., LATALSKI J., 2014, Nonlinear dynamics and synchronisation of pendula attached to a rotating hub, *European Physical Journal Special Topics*, **223**, 827847, DOI:10.1140/epjst/e2014-02143-9
27. XIAO B., RIVAS-GUERRA A., MIGNOLET M.P., 2004, Maximum amplification of blade response due to mistuning in multi-degree-of-freedom blade models, *Proceedings of the ASME Turbo Expo: Power for Land, Sea, and Air*, **6**, 427-438

Manuscript received January 24, 2018; accepted for print March 14, 2018

INFORMATION FOR AUTHORS

Journal of Theoretical and Applied Mechanics (JTAM) is devoted to all aspects of solid mechanics, fluid mechanics, thermodynamics and applied problems of structural mechanics, mechatronics, biomechanics and robotics. Both theoretical and experimental papers as well as survey papers can be proposed.

We accept articles in English only. The text of a *JTAM* paper should not exceed **12 pages of standard format A4** (11-point type size, including abstract, figures, tables and references), short communications – **4 pages**.

The material for publication should be sent to the Editorial Office via electronic journal system: <http://www.ptmts.org.pl/jtam/index.php/jtam>

Papers are accepted for publication after the review process. Blind review model is applied, which means that the reviewers' names are kept confidential to the authors. The final decision on paper acceptance belongs to the Editorial Board.

After qualifying your paper for publication we will require L^AT_EX or T_EX or Word document file and figures.

The best preferred form of figures are files obtained by making use of editorial environments employing vector graphics:

- generated in CorelDraw (*.cdr), AutoCad and ArchiCad (*.dwg) and Adobe Illustrator (*.ai). We require original files saved in the standard format of the given program.
- generated by calculation software (e.g. Mathematica) – we need files saved in *.eps or *.pdf formats.
- made in other programs based on vector graphics – we ask for *.eps, *.wmf, *.svg, *.psfiles.

Any figures created without application of vector graphics (scans, photos, bitmaps) are strongly encouraged to be supplied in *.jpg, *.tif, *.png formats with resolution of at least 300 dpi.

Requirements for paper preparation

Contents of the manuscripts should appear in the following order:

- Title of the paper
- Authors' full name, affiliation and e-mail
- Short abstract (**maximum 100 words**) and 3-5 key words (**1 line**)
- Article text (equations should be numbered separately in each section; each reference should be cited in the text by the last name(s) of the author(s) and the publication year)
- References in alphabetical order. See the following:
 1. Achen S.C., 1989, A new boundary integral equation formulation, *Journal of Applied Mechanics*, **56**, 2, 297-303
 2. Boley B.A., Weiner J.H., 1960, *Theory of Thermal Stresses*, Wiley, New York
 3. Canon W., 1955, Vibrations of heated beams, Ph.D. Thesis, Columbia University, New York
 4. Deresiewicz H., 1958, Solution of the equations of thermoelasticity, *Proceedings of Third U.S. National Congress of Applied Mechanics*, 287-305
- Titles of references originally published not in English, should be translated into English and formulated as follows:
 5. Huber M.T., 1904, Specific work of strain as a measure of material effort (in Polish), *Czasopismo Techniczne*, **XXII**, 3, 80-81

All the data should be reported in **SI units**.

Contents

Kurnik W., Kowalewki Z. — From the Editors	337
Kukla S., Siedlecka U. — Fractional heat conduction in a sphere under mathematical and physical Robin conditions	339
Zhao X., Gräbner N., von Wagner U. — Theoretical and experimental investigations of the bifurcation behavior of creep groan of automotive disk brakes	351
Drózdź A., Elsner W., Sikorski D. — Skin friction estimation in a strong decelerating flow	365
Song Y., Voyiadjis G.Z. — A two-dimensional finite element model of the grain boundary based on thermo-mechanical strain gradient plasticity	377
Majchrzak E., Mochnacki B. — Implicit scheme of the finite difference method for the second-order dual phase lag equation	393
Zalewski R., Rutkowski M. — The use of Vacuum Packed Particles with adaptable properties in acoustic applications	403
Li M., Füssl J., Lukacevic M., Eberhardsteiner J., Martin C.M. — A numerical upper bound formulation with sensibly-arranged velocity discontinuities and orthotropic material strength behaviour	417
Bogacz R., Frischmuth K. — On problems with solution-dependent load	435
Matsui R., Takeda K., Tobushi H., Pieczyska E.A. — Mechanical properties and advanced subjects in shape memory alloys and polymers	447
Zheng K., Lin J., Wu G., Hall R.W., Dean T.A. — Experimental investigation and modelling of hot forming B ₄ C/AA6061 low volume fraction reinforcement composites	457
Jankowiak T., Rusinek A., Bendarma A. — Protocol to define material behaviour and failure strain level at low and high strain rates based on a compression test	471
Barboteu M., Ouafik Y., Sofonea M. — Numerical modelling of a dynamic contact problem with normal damped response and unilateral constraint	483
Ohno N., Sasaki T., Shimada T., Tokuda K., Yoshida K., Okumura D. — Effect of cyclic hardening on stress relaxation in SUS316HTP under creep-fatigue loading at 700°C: experiments and simulations	497
Weber W.E., Zastrau B.W. — Model order reduction of Mikota's vibration chain including damping effects by means of proper orthogonal decomposition	511
Kourkoulis S.K., Pasiou E.D., Dakanali I., Stavrakas I., Triantis D. — Mechanical response of notched marble beams under bending versus acoustic emissions and electric activity	523
Warminski J., Latalski J., Szmit Z. — Vibration of a mistuned three-bladed rotor under regular and chaotic excitations	549